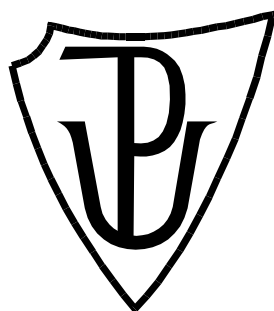# PALACKÝ UNIVERSITY OLOMOUC

Faculty of Science

Department of Biochemistry

Cell division plane regulation in plants by MAPK cascades

PhD Thesis

Author:	**Tereza Vavrdová**
Study program:	P1416 Biochemistry
Study field:	Biochemistry
Form of study:	Full-time study
Supervisor:	doc. George Komis, PhD
Consultant:	Despina Samakovli, PhD
Submitted:	15. June 2020

I hereby declare that this PhD thesis has been written solely by me. All the sources cited in this thesis are listed in the Reference list. All published results included in this work are approved by coauthors.

Olomouc ……………………   …………………………………

Tereza Vavrdová

Acknowledgements

dr. Martijn van Zanten and his PhD student Myrte Praat, but I also benefited greatly from the communication with other lab members, especially dr. Marcel Proveniens and dr. Henriette Schlupmann. Moreover, I would like to thank Jolanda Schuurmans, Evelien Stouten and Sjors van der Horst for their help in my adaptation to both the lab work and life in Utrecht.

Lastly, I would like to acknowledge all the people who never once doubted me and kept on encouraging me during my PhD studies. I would like to especially thank my family and Lukáš Klapka for supporting me by listening to all my troubles and never losing their faith in me.

Bibliografická identifikace

Jméno a příjmení:	Tereza Vavrdová
Název práce:	Role MAPK kaskád ve stanovení roviny buněčného dělení u rostlin
Typ práce:	dizertační
Pracoviště:	Oddělení Buněčné biologie, Centrum Regionu Haná pro biotechnologický a zemědělský výzkum, Přírodovědecká fakulta, Univerzita Palackého v Olomouci
Vedoucí práce:	doc. George Komis, PhD
Konzultant:	Despina Samakovli, PhD
Rok obhajoby:	2020

Abstrakt

Mitogenem aktivované proteinkinázy (MPK) se v rostlinných buňkách zapojují do řady signalizačních drah. Díky tomu propojují reakce na podněty z okolí s mezibuněčnou komunikací. Cílem této práce bylo prozkoumat funkce MPK ve stanovení roviny buněčného dělení. Práce byla zaměřena na signální dráhu skládající se z YODA a MPK3 a MPK6 kináz, pro kterou je známé její zapojení do regulace asymetrických buněčných dělení během ranné embryogeneze a vývoje primárního kořene u modelové rostliny *Arabidopsis thaliana*. Předmětem zájmu bylo zhodnotit, zda je signalizace YODA-MPK3/6 kaskádou ovlivněna proteinovou fosfatázou 2A (PP2A) and proteiny teplotního šoku 90 (HSP90).

Funkce PP2A fosfatázy je spojena s kontrolou stanovení roviny buněčného dělení a předpokládá se, že tuto úlohu plní regulací fosforylace proteinů zapojených do relevantních procesů. Tato práce předkládá hypotézu, podle které PP2A koordinuje funkci YODA-MPK3/6 signální dráhy během stanovení roviny buněčného dělení.

Druhá část této práce je zaměřena na zdokumentování zapojení HSP90 do regulace ranné embryogeneze. I v tomto případě se předpokládá, že HSP90 by embryonální vývoj mohly ovlivňovat skrze interakci s YODA-MPK3/6 signální dráhou.

V této práci jsou též popsány a porovnány pokročilé mikroskopické techniky. Zvláštní důraz je věnován popisu možností jejich praktického využití pro mikroskopické pozorování živých buněk exprimujících chimerické fluorescenční proteiny, nebo fixních preparátů se strukturami značenými pomocí protilátek. Strukturní iluminační mikroskopie a laserová rastrovací konfokální mikroskopie využívající detektor typu Airyscan byly využity pro současné zobrazení mikrotubulů a významných proteinů asociovaných s mikrotubuly, konkrétně protein asociovaný s mikrotubuly 65 2 (MAP65-2) a MAP65-3.

Výsledkem této práce je informování o roli YODA-MPK3/6 signální dráhy při stanovení roviny buněčného dělení a určení buněčného osudu, a dále o interakci této signální kaskády s PP2A and HSP90. Dále je předloženo porovnání pokročilých mikroskopických technik, které mohou být využity v budoucích studiích pro objasnění mechanismů organizace a dynamických změn cytoskeletu v rostlinných buňkách.

Klíčová slova: Mitogenem aktivované proteinkinázy, Proteiny asociované s mikrotubuly, Mikrotubuly, Proteinová fosfatáza 2A, Protein teplotního šoku 90, Stanovení roviny buněčného dělení, Laserová rastrovací konfokální mikroskopie využívající detektor typu Airyscan, Strukturní iluminační mikroskopie, Imunofluorescence

Počet stran: 216

Počet příloh: 9

Jazyk: anglický

Bibliographic identification

Name and surname:	Tereza Vavrdová
Title of thesis:	Cell division plane regulation in plants by MAPK cascades
Type of thesis:	PhD
Department:	Department of Cell Biology, Centre of the Region Haná for Biotechnological and Agricultural Research, Faculty of Science, Palacký University Olomouc
Supervisor:	doc. George Komis, PhD
Consultant:	Despina Samakovli, PhD
Year of defence:	2020

Abstract

Plant mitogen activated protein kinases (MPK) are involved in a plethora of signalling events, integrating extrinsic cues to cellular responses. The focus of this thesis is to examine the role of MPKs in the cell division plane orientation. Specifically, the function of the YODA-MPK3/6 pathway is described in formative cell divisions during early embryonic development and in tissue patterning of the primary root tip of the model plant *Arabidopsis thaliana*. The interaction between the YODA-MPK3/6 pathway and the protein phosphatase 2A (PP2A) and heat shock proteins 90 (HSP90) was assessed.

PP2A phosphatases are known to affect cell division plane orientation and are expected to execute this function by regulating the phosphorylation status of proteins involved in cell division plane positioning. Herein, it is assumed that the PP2A cooperates with the YODA-MPK3/6 in determining the cell division plane orientation.

In the second part of the thesis, the involvement of HSP90s in early embryonic development is investigated in light of their previously described physical partnership with the YODA-MPK3/6 pathway.

Finally, the present thesis also provides a description and comparison of advanced microscopic techniques, with potential applications for imaging live cells expressing appropriate fluorescent protein fusions, or fixed and accordingly immunolabeled samples. Methods such as structured illumination microscopy and Airyscan laser scanning

microscopy are applied to visualize microtubules together with two prominent microtubule associated proteins, microtubule associated protein 65 2 (MAP65-2) and MAP65-3.

Conclusively, this thesis presents information on the role of the YODA-MPK3/6 cascade in the cell division plane orientation and the cell fate determination as well as its interaction with PP2A and HSP90s while executing these functions. Furthermore, it reports on advanced microscopic methods which may be employed in future studies aiming to elucidate mechanisms behind cytoskeleton organization and dynamics in plants.

Keywords: Mitogen Activated Protein Kinase, Microtubule Associated Proteins, Microtubules, Protein Phosphatase 2A, Heat Shock Protein 90, Cell division plane orientation, Airyscan Confocal Laser Scanning Microscopy, Structured Illumination Microscopy, Immunofluorescence

Number of pages: 216

Number of appendixes: 9

Language: English

Content

Objectives

1. Summary of recent knowledge on the role of phosphorylation in cell division plane orientation in both symmetric and asymmetric cell divisions. This part will be focused on describing mitogen-activated protein kinases (MPKs), microtubule associated proteins 65 (MAP65s) and protein phosphatase 2A (PP2A). Additionally, the role of heat shock proteins 90 (HSP90s) in plant development will be reviewed.

2. Documentation of the putative interaction between PP2A and MPK.

3. Phenotypic characterization of mutants defective in genes encoding PP2A subunits regarding the formative cell divisions.

4. Characterization of the role of HSP90s in modulating the function of YODA-MPK pathway in different types of formative cell divisions.

5. Visualization of MAP65s by employing advanced microscopy techniques.

1. Introduction

1.1. Cell division in plants

Plants share two attributes, the sessile life style and rigid cell walls, which compelled them to adapt accordingly the most fundamental processes, among them the cell division. This resulted in a cell division progression exclusive to plants, where microtubules are a driving force of both nuclear and cellular division.

Microtubules are formed through polymerization of tubulins, globular proteins forming a protein superfamily. Among this family, α- and β-tubulin are known to form dimers and then polymerize into microtubules. On the other hand, γ-tubulin is forming the γ-tubulin ring complexes (Fosket and Morejohn 1992). They serve as microtubule nucleation units in plants (Erhardt *et al.* 2002) since plant cells do not have a microtubule organizing centre. The consequence of the absence of microtubule organizing centres is that the formation of plant microtubule arrays depends on an interaction between microtubules and microtubule associated proteins (Bannigan *et al.* 2008; Lee and Liu 2013; Buschmann and Zachgo 2016; Smertenko 2018).

Microtubules form several structures during plant cell mitosis, some of them unique to plants (**Fig. 1**). At the commitment to cell division during interphase, diffusely distributed cortical microtubules coalesce into a progressively narrowing microtubule annulus named the preprophase microtubule band (Dhonukshe and Gadella 2003; Vos *et al.* 2004). Together with actin filaments, organelles, and specific proteins, the preprophase band marks a plasma membrane region denoted as the cortical division zone, which is defining the division site and predicts the cortical sites where the cell plate will fuse with the parent cell walls at the end of the cytokinesis. Apart from marking the cortical division zone, the preprophase band was also shown to affect the spindle morphogenesis and orientation, to serve as a source of microtubules for the assembly of the spindle and to facilitate the anchoring of the nucleus in the central cytoplasm through interactions with perinuclear microtubules (Mineyuki and Furuya 1986; Marcus *et al.* 2005; Ambrose *et al.* 2008; Schaefer *et al.* 2017).
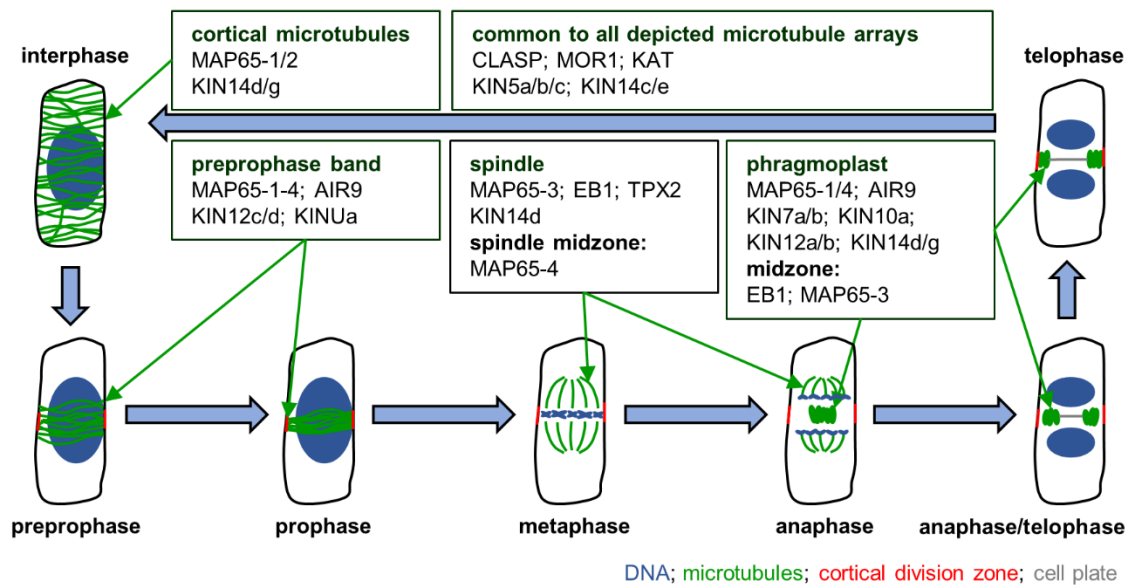
Figure 1. Localization of microtubule associated proteins during mitosis. Adapted from Vavrdová *et al.* (2019). Cortical microtubules reorganize into the preprophase band at the onset of mitosis. The preprophase band starts as a broad ring of microtubules, it narrows during prophase and its site is marked as the cortical division zone, a place of the future cell plate fusion site. The preprophase band is disassembled before the metaphase as the spindle is formed. After the segregation of chromatids, the disc phragmoplast is formed at the center of the cell. The phragmoplast guides the construction of the cell plate. Next, the ring phragmoplast is continuously degraded at its center, where the cell plate is being built, and it expands towards the cell cortex. After the discontinuous phragmoplast reaches the cell plate fusion site, the cell plate is formed and two daughter cells are created, where microtubules again rearrange into cortical microtubules. Abbreviations: AIR9, AUXIN INDUCED IN ROOT CULTURES PROTEIN 9; CLASP, CLIP-ASSOCIATED PROTEIN; EB1, END BINDING 1; KAT, KATANIN; KIN, KINESIN-RELATED PROTEIN; MAP65, MICROTUBULE ASSOCIATED PROTEIN 65; MOR1, MICROTUBULE ORGANIZING 1; TPX2, TARGETING PROTEIN FOR XKLP2.

For a long time, the preprophase band was considered to be crucial for the establishment of the cell division plane orientation in most of the higher plants and a default prerequisite for the plant cell division. Notable exceptions from this rule are cell divisions without the preprophase band in microsporogenesis, pollen grain development, megasporogenesis, embryo sac development, and in the endosperm during syncytial cellularization (Mineyuki 1999; Brown and Lemmon 2001; Otegui and Staehelin 2004). The view of the preprophase band as a default mechanism of the cell division plane orientation was further supported by the observation of the preprophase band-driven mitotic division instead of meiosis I in the maize *ameiotic* mutants (Staiger and Cande 1992). By contrast, the *Arabidopsis thaliana* triple mutant *trm6 trm7 trm8* defective in TON1 RECRUITING MOTIF PROTEINS (TRMs) fails to form the preprophase band, yet its growth and development are mostly unaffected (Schaefer *et al.* 2017). In a revised view, the function of the preprophase band in directing the cell division plane orientation

is less prominent, likely serving as a correction mechanism pivoting the nascent cell plate at the correct plane (Zhang and Dong 2018). It was proposed, that in the absence of the preprophase band, the γ-tubulin and γ-tubulin ring complexes could also control the cell division plane orientation (Kosetsu *et al.* 2017).

In symmetrically dividing cells, the position of the preprophase band is determined by two factors. First, transvascular cytoplasmic strands are under tension during interphase. To minimize the energy of the system, they adopt arrangement with shorter lengths, which pulls the nucleus to the centre. This also affects the position of cortical microtubules and the preprophase band, in accordance to the cell geometry (Flanders *et al.* 1990; Hamant *et al.* 2008; Hamant *et al.* 2019). Second, the position of the nucleus directs the localization of the preprophase band (Murata and Wada 1991), while the nuclear migration itself depends on microtubules (Mineyuki and Furuya 1986; Venverloo and Libbenga 1987; Katsuta *et al.* 1990). This determination of the preprophase band positioning is overridden in asymmetrically dividing cells. The formation of the preprophase band during asymmetric cell division does not correspond to cues from tension or nuclear localization (Marcus *et al.* 2005), but rather it depends on other signals, which will be discussed below.

Initially, the preprophase band is formed as a broad ring structure in the G2 phase, when its major function is marking the cortical division zone. Later on, it narrows during the transition from interphase to mitosis, reaching a maximum of density in prophase at the onset of mitotic spindle formation around the still intact nuclear envelope (Chan *et al.* 2005; Marcus *et al.* 2005). The narrowing of the preprophase band depends on mechanisms underlying the regulation of microtubule organization and dynamics but it is also actin filament-pendant (Mineyuki and Palevitz 1990; Komis *et al.* 2017). At the onset of nuclear envelope breakdown and before prometaphase, the preprophase band is disassembled.

The plant spindle forms in an acentrosomal fashion just before the nuclear envelope breakdown and encompasses the preprophase/prophase nucleus in the form of a bipolar microtubular basket (Buschmann and Zachgo 2016). After the nuclear envelope breakdown, spindle microtubules come in contact with chromosome kinetochores and manage the arrangement of chromosomes at the equatorial plane in metaphase. Then, sister chromatids become separated and mitotic spindle is driving their segregation to two equivalent daughter groups occupying the opposite poles of the spindle in anaphase. Initially, the positioning of the acentriolar spindle depends

on interactions between perinuclear microtubules and the preprophase band. Subsequently, it is robustly regulated by cues originating from the preprophase band, which persistently occupies the cortical division zone (Ambrose and Cyr 2008). Although this does not determine the final division plane, it seems to affect it (Komis *et al.* 2017; Schaefer *et al.* 2017).

Following the spatial separation of the two sister chromatid groups, the process of cytokinesis is marked by two dominant events. The decondensation of chromatin and the progressive reassembly of the nuclear envelope around the sister chromatid groups to reconstitute the daughter nuclei and the formation of the plant-specific cytokinetic apparatus, the phragmoplast. The phragmoplast originates between the sister nuclei in the central part of the cell and it is formed by two antiparallel sets of microtubules, the overlap of which coincides with the equatorial plane and the cell division plane as well. The position and the polarity of the phragmoplast are mirroring the spindle position and polarity. There are two described alterations to its conventional formation: (i) the formation of the phragmoplast outside of the centre of the cell during polarized cytokinesis (Cutler and Ehrhardt 2002; Lucas and Sack 2012); (ii) the formation of phragmoplasts during endosperm cellularization when mitosis is not immediately followed by cytokinesis (Olsen *et al.* 1995; Otegui and Staehelin 2000).

At the beginning of cytokinesis, microtubules occupy the entire surface of the phragmoplast and serve as a frame guiding the movement of Golgi-derived vesicles carrying material for the cell plate assembly. Both the phragmoplast and the nascent cell plate expand centrifugally to meet the parent walls at the cortical division zone and during this process, microtubules are disappearing from the centre of the phragmoplast, being confined at its margins (reviewed in Chen *et al.* 2018; Smertenko 2018). The leading edge of the phragmoplast extends towards the plasma membrane, actively scouting for the cortical division zone (Wu and Bezanilla 2014), thus, fine-tuning the position of the newly built cell wall to the cortical mark. Through the guidance of the phragmoplast, the cell division plane is determined, and the cell plate is assembled, resulting in the completion of the cytokinesis.

Due to the quintessential nature of microtubules for proper cell division, there is a need for strict and exact spatiotemporal regulation of microtubule organization and dynamics during the cell cycle (Dhonukshe and Gadella 2003; Vos *et al.* 2004). This is frequently accomplished through the function of microtubule associated proteins, which

are capable of inducing changes in microtubule nucleation, polymerisation, depolymerisation, stabilization, and destabilization.

1.1.1. Microtubule associated proteins important for cell division

Microtubule associated proteins are interacting with microtubules and regulating them via affecting their nucleation, end-wise dynamics, formation of higher order assemblies, or clearance (**Tables 1, 2**). Unsurprisingly, they are of major importance in precise spatiotemporal control over creation, maintenance, proper function, and disassembly of mitotic microtubule arrays. While some microtubule associated proteins associate with microtubules during every step of the cell cycle, others colocalize only with specific microtubule structures (**Fig. 1**). This situation is mirrored in their *modus operandi*. Microtubule associated proteins persistently colocalizing with microtubules irrespectively of the cell stage include regulators of microtubule organization and dynamics such as MICROTUBULE ORGANIZING 1 (MOR1); CLIP-ASSOCIATED PROTEIN and KATANIN (**Fig. 1**; Kawamura *et al.* 2006; Ambrose *et al.* 2007; Kirik *et al.* 2007; Komis *et al.* 2017) and their proper function is essential for organization and dynamics of any microtubule array (**Table 1**; Kawamura and Wasteneys 2008; Ambrose *et al.* 2013; Pietra *et al.* 2013; Komis *et al.* 2017). Among the microtubule associated proteins with spatial or temporal restrictions of colocalization with microtubules arrays belong AUXIN INDUCED IN ROOT CULTURES PROTEIN 9, END BINDING 1c (EB1c), MICROTUBULE ASSOCIATED PROTEIN 65-3 (MAP65-3) and MAP65-4, all specifically colocalizing only with certain mitotic microtubule arrays (**Fig. 1**; Buschmann *et al.* 2006; Caillaud *et al.* 2008; Fache *et al.* 2010; Komaki *et al.* 2010). Correspondingly, their function is more explicit (**Table 1**; Komaki *et al.* 2010; Ho *et al.* 2012; Buschmann *et al.* 2015; Li *et al.* 2017a).

This clear division is not completely followed by the members of kinesin protein superfamily. This protein superfamily is highly abundant in plants. With 61 predicted kinesins, the Arabidopsis genome exceeds the expected number of kinesins encoded by the human genome (Reddy and Day 2001; Miki *et al.* 2005). Bioinformatic analysis suggested that plant kinesins evolved differently than animal kinesins, assuming distinct functions in plants. While some of the 14 kinesin families are missing in plants, other, specifically kinesin 7 and 14 families, have extensively expanded and diversified (Richardson *et al.* 2006). Out of the 61 known Arabidopsis kinesins, 17 appear to have a role in the cell division (**Table 2**; Zhu and Dixit 2012). Many of these kinesins

colocalize with specific mitotic microtubule arrays and, consequently, their function is limited to these structures, e.g. KINESIN-RELATED PROTEIN 7a (KIN7a) and KIN7b (Nishihama *et al.* 2002; Tanaka *et al.* 2004; Komis *et al.* 2011), KIN12c/d (Walker *et al.* 2007; Xu *et al.* 2008; Lipka *et al.* 2014; Stöckle *et al.* 2016), and KINUa (Malcos and Cyr 2011). Other kinesins are localized to multiple microtubule structures, yet they do not appear to affect the function of all of them, as is the case with KIN5a/b/c (Bannigan *et al.* 2007), KIN14c (Liu *et al.* 1996; Marcus *et al.* 2003), KIN14d (Ambrose *et al.* 2005; Ambrose and Cyr 2007) and KIN14e (Oppenheimer *et al.* 1997; Kao *et al.* 2000; Vos *et al.* 2000). This list is incomplete as many Arabidopsis kinesins remain uncharacterized, yet their homologues in other plants are already known to be involved in the cell division, e.g. members of kinesin 14 family containing calponin homology domains (Frey *et al.* 2010; Klotz and Nick 2012).

Apart from microtubule associated proteins, the microtubule organization and dynamics are modulated by proteins binding to both microtubules and actin filaments (Krtková *et al.* 2016; Takeuchi *et al.* 2017), which are ensuring the collaboration between microtubules and actin filaments, thus, the proper function of plant cytoskeleton (Sampathkumar *et al.* 2011; Wu and Bezanilla 2014; Wu and Bezanilla 2018). Apart from the abovementioned members of the kinesin 14 family (Schneider and Persson 2015; Tian *et al.* 2015), the most notable examples are members of the ACTIN RELATED PROTEIN 2/3 actin nucleation complex (Havelková *et al.* 2015) and formins (Deeks *et al.* 2010; Li *et al.* 2010a; Rosero *et al.* 2013; Wang *et al.* 2013). These proteins affect the assembly of actin filaments, although by employing different mechanisms (Pollard 2007). While its function in plants is not yet properly explored, the ACTIN RELATED PROTEIN 2/3 complex might be involved in cytokinesis similarly to its role in other eukaryotes (Insall *et al.* 2001; Sun *et al.* 2011). On the other hand, plant formins, including those interacting with microtubules, are known to affect the cell division (Li *et al.* 2010a).

Table 1. Overview of plant microtubule associated proteins with a role in cell division

Name	Function	Function in cell division	References
MICROTUBULE ORGANIZING 1 (MOR1)	accelerating of growth/shrinkage of microtubules	proper organization of mitotic arrays	(Kawamura *et al.* 2006; Kawamura and Wasteneys 2008)
AUXIN INDUCED IN ROOT CULTURES PROTEIN 9 (AIR9)	recognition of specific proteins at cell division zone	guidance of phragmoplast to cell plate fusion site	(Buschmann *et al.* 2006; Buschmann *et al.* 2015)
TARGETING PROTEIN FOR XKLP 2 (TPX2)	microtubule polymerization, regulation of Aurora kinases	spindle formation	(Vos *et al.* 2008; Tomaštíková *et al.* 2015)
KATANIN (KAT)	severing microtubules	proper organization of mitotic arrays	(Komis *et al.* 2017)
Plus end interacting proteins			
END BINDING 1c (EB1c)	promoting microtubule polymerization	maintaining spindle bipolarity, chromosomal segregation	(Komaki *et al.* 2010)
CLIP-ASSOCIATED PROTEIN (CLASP)	regulation of microtubule stability, mediating interactions with other proteins	stabilizing mitotic arrays	(Ambrose *et al.* 2007; Kirik *et al.* 2007; Ambrose *et al.* 2013; Pietra *et al.* 2013)
MICROTUBULE ASSOCIATED PROTEIN 65 (MAP65) protein family			
MAP65-1/2	microtubule bundling	non-essential for cell division	(Lucas and Shaw 2012; Boruc *et al.* 2017)
MAP65-3	microtubule bundling	phragmoplast formation	(Caillaud *et al.* 2008; Ho *et al.* 2012)
MAP65-4	microtubule bundling	spindle and phragmoplast formation	(Fache *et al.* 2010; Li *et al.* 2017a)
MAP65-5	microtubule bundling	unknown, possibly non-essential for cell division	(Gaillard *et al.* 2008)

Table 2. Overview of plant KINESIN-RELATED PROTEINS (KIN) with a role in cell division

Name	Alternative name	Function	Function in cell division	References
KIN5a/b/c	KINESIN RELATED PROTEIN 215a/b/c	aligning antiparallel microtubules	spindle and phragmoplast formation	(Bannigan et al. 2007; Walczak and Heald 2008)
KIN7a/b	NPK1-ACTIVATING KINESIN 1/2	activating mitogen-activated protein kinase cascade	phragmoplast expansion	(Nishihama et al. 2002; Tanaka et al. 2004; Komis et al. 2011)
KIN10a	PHRAGMOPLAST ASSOCIATED KINESIN-RELATED PROTEIN 2	possibly transport of vesicles	possibly delivery of Golgi-derived vesicles to phragmoplast midzone	(Lee et al. 2001)
KIN12a/b	PHRAGMOPLAST KINESIN-RELATED PROTEIN 1/ PHRAGMOPLAST KINESIN-RELATED PROTEIN 1-LIKE	possibly microtubule growth inhibition	phragmoplast formation	(Pan et al. 2004; Lee et al. 2007; Zhu and Dixit 2012)
KIN12c/d	PHRAGMOPLAST ORIENTING KINESIN 1/2	transport of other proteins	recruitment of proteins to cell division zone and their retention there	(Müller et al. 2006; Walker et al. 2007; Xu et al. 2008; Lipka et al. 2014; Stöckle et al. 2016)
KIN14a/b	KINESIN CDKA-1-ASSOCIATED PROTEIN 1/2	possibly interaction with actin	negative marking of the cell division zone	(Vanstraelen et al. 2004; Suetsugu et al. 2010)
KIN14c/d	ARABIDOPSIS THALIANA KINESIN 1/5	bundling parallel microtubules, transporting microtubules	spindle formation	(Liu et al. 1996; Marcus et al. 2003; Ambrose et al. 2005; Ambrose and Cyr 2007)
KIN14e	KINESIN-LIKE CALMODULIN BINDING PROTEIN	crosslinking microtubules	possibly role in spindle formation; phragmoplast formation	(Bowser and Reddy 1997; Oppenheimer et al. 1997; Kao et al. 2000; Vos et al. 2000)
KINUa	ARMADILLO-REPEAT KINESIN 3		essential for preprophase band formation	(Malcos and Cyr 2011)

18

1.1.1.1. MAP65 protein family

The MAP65-3 and 4 mentioned above are two out of the nine members of the MAP65 protein family in Arabidopsis (Hussey *et al.* 2002). This protein family is named after the first described member of this protein family, which was discovered in carrot and had a molecular weight of 65 kDa (Chan *et al.* 1999). Plant MAP65 proteins are homologous to fission yeast Anaphase spindle elongation 1 protein (Ase1p) and human PROTEIN REGULATOR OF CYTOKINESIS 1 (PRC1; **Fig. 2**). They bind to microtubule bundles (Chan *et al.* 1999; Smertenko *et al.* 2004) and slow down their depolymerization (Van Damme *et al.* 2004; Fache *et al.* 2010; Lucas *et al.* 2011). Additionally, their function might be to facilitate the recruitment of kinesins (Walczak and Shaw 2010; Lee and Liu 2013). This is supported by reports on changes in subcellular localization of KIN10a, KIN12a/b/d (Ho *et al.* 2011) observed in the *map65-3* mutant (Herrmann *et al.* 2018).
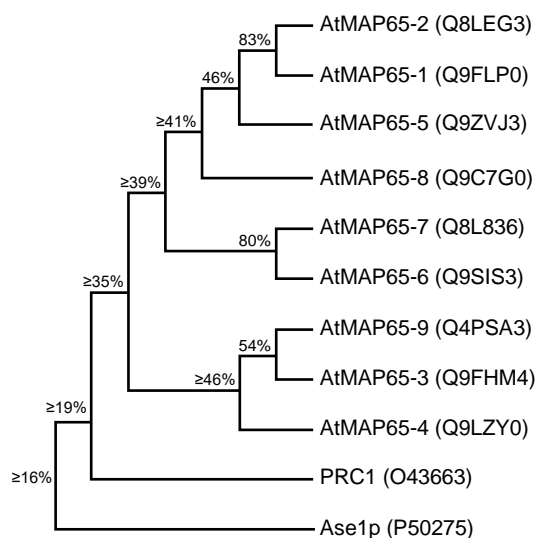
Figure 2. Sequence homology between Arabidopsis MAP65s and their human and yeast homologues. The cladogram illustrates sequence homology between the yeast Anaphase spindle elongation 1 protein (Ase1p), the human PROTEIN REGULATOR OF CYTOKINESIS 1 (PRC1), and Arabidopsis MICROTUBULE ASSOCIATED PROTEINs 65 (AtMAP65s). The cladogram was constructed based on a multiple alignment (Clustal Omega; EMBL-EBI) of sequences (UniProtKB accession numbers are in brackets). Next to each nod, the lowest sequence homology between the respective sequences is stated based on the percent identity matrix.

They differ in their subcellular localization, expression patterns (Van Damme *et al.* 2004), and their regulation throughout the cell cycle (Smertenko *et al.* 2006; Boruc *et al.* 2017). MAP65-1-5 are known to colocalize with mitotic microtubule arrays (**Fig. 1**; Smertenko *et al.* 2004; Caillaud *et al.* 2008; Gaillard *et al.* 2008; Smertenko *et al.* 2008; Fache *et al.* 2010; Lucas and Shaw 2012). MAP65-1 and MAP65-2 share high sequence similarity (**Fig. 2**), they are functionally redundant and more is known about their function during cell growth (**Table 1**; Lucas *et al.* 2011; Lucas and Shaw 2012; Boruc *et al.* 2017) than about their role in the cell division. While MAP65-5 colocalizes to the same microtubule arrays as MAP65-1, their subcellular localization differs (Gaillard *et al.* 2008) and their sequence similarity is

lower than between MAP65-1 and MAP65-2, implying that these MAP65s might have discreet non-redundant functions.

On the other hand, MAP65-3 and MAP65-4 are associated only with mitotic microtubule arrays and their function appears crucial for the cytokinesis (**Table 1**; Müller *et al.* 2004; Ho *et al.* 2012; Li *et al.* 2017a). This is supported by the observation of multinucleated cells with incomplete cell walls in *map65-3* mutants (Müller *et al.* 2004; Caillaud *et al.* 2008), resulting from severe cytokinesis defects. Presumably, these defects originate from abnormal phragmoplast formation, as the phragmoplast in *map65-3* mutants is broader and wider than in wild type plants (Müller *et al.* 2004). While there are conflicting reports on the role of MAP65-3 in karyokinesis through affecting the spindle formation (Müller *et al.* 2004; Caillaud *et al.* 2008), MAP65-3 was also implicated in coordinating the cytokinesis with the karyokinesis together with the TRANSPORT PROTEIN PARTICLE II tethering complex (Steiner *et al.* 2016). Despite the absence of a noticeable phenotype in *map65-4* mutants, *map65-3 map65-4* double mutants were lethal, suggesting partial functional redundancy of these proteins (Li *et al.* 2017a). Interestingly, the multiple alignment analysis of MAP65 protein family revealed that MAP65-3, MAP65-4 and the enigmatic MAP65-9 form a cluster with the lowest sequence homology to the remaining Arabidopsis MAP65 proteins (**Fig. 2**).

The function of MAP65 proteins depends on their ability to bind microtubules and to form dimers, which is facilitated by their domains. They form homodimers through their N-terminal dimerization domains. Their C-terminal domain can be divided into a spectrin-fold domain containing two microtubule-binding sites and a variable domain (**Fig. 3**; Smertenko *et al.* 2004). Interestingly, the C-terminal domain is also involved in the subcellular localization (Smertenko *et al.* 2006; Ho *et al.* 2012). While the Arabidopsis MAP65s share similarities within the N-terminal dimerization domain (**Fig. 4A**), they are most similar to each other in the sequences of the microtubule-binding domain (**Fig. 4B**). On the other hand, the least sequence homology is between their C-terminal variable domains (**Fig. 4C**).

According to one hypothesis, MAP65s form homodimers in solutions, and then they associate with microtubule bundles (Smertenko *et al.* 2004; Smertenko *et al.* 2008). A similar mechanism was described for both Ase1p (Kapitein *et al.* 2008) and PRC1 (Subramanian *et al.* 2010). Supposedly, the homodimer first decodes the microtubule orientation by binding specifically via one of the spectrin domains. Next, the second
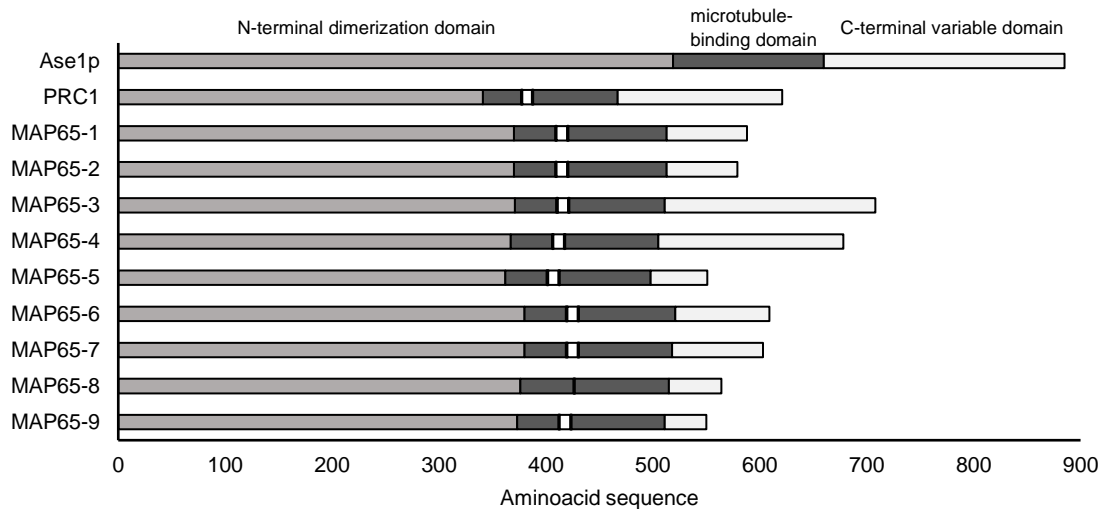
Figure 3. Protein domains of Arabidopsis MAP65s and their homologues. Arabidopsis MICROTUBULE ASSOCIATED PROTEINs 65 (AtMAP65s), the yeast Anaphase spindle elongation 1 protein (Ase1p), and the human PROTEIN REGULATOR OF CYTOKINESIS 1 (PRC1) were compared based on a multiple alignment (COBALT; NCBI) of sequences (UniProtKB accession numbers are in **Fig. 2**). Schema depicts domains and tubulin-binding sites in MAP65s. Localization of tubulin-binding sites was determined based on the information in the UniProtKB database. Generally, there are two tubulin-binding sites within the tubulin-binding domain separated by 10 amino acids, which is symbolized by a white spacer between two black lines marking tubulin-binding sites. For MAP65-8 a single tubulin-binding site was predicted, while no tubulin binding site was predicted for Ase1p so far. The localization of the domains was inferred from the multiple sequence alignment.

microtubule-binding domain might bind to another microtubule, which is affected by the length of the linker between the two spectrin domains and the rigidity of this linker (Subramanian *et al.* 2010). By contrast, alternative hypothesis suggests that MAP65-1 and MAP65-5 are binding microtubules as monomers and stabilize this interaction upon dimerization with adjacent MAP65 molecules in a process called zippering (Gaillard *et al.* 2008; Tulin *et al.* 2012).

Ultimately, the forming of homodimers is essential for the function of MAP65s (Tulin *et al.* 2012). Apart from the length and flexibility of the linker, MAP65s have different association times with the microtubule bundles before their dimerization (Lucas *et al.* 2011). Thus, it is tempting to speculate to which extent is the variability within the plant MAP65 protein family affecting the mechanisms of their functions and how this could affect the biological activity of MAP65s. Taken together, different MAP65 proteins and specific conditions could help the cell to fine-tune its organization of microtubule arrays.
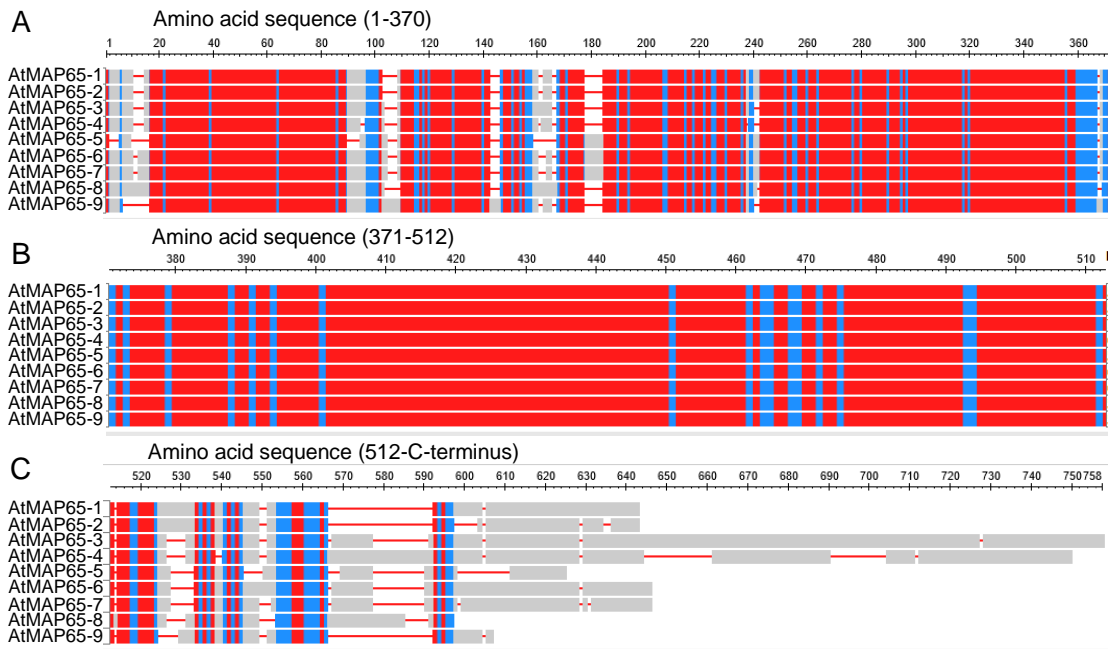
Figure 4. Sequence alignment of Arabidopsis MAP65s. Arabidopsis MICROTUBULE ASSOCIATED PROTEINs 65 (AtMAP65s) were compared based on a multiple alignment (COBALT; NCBI) of sequences (UniProtKB accession numbers are in **Fig. 2**). (A-C) Results of the multiple sequence alignment for N-terminal domain (A), microtubule-binding domain (B) and C-terminal variable domain (C). Colour-coding corresponds to the degree of conservation based on the residue's relative entropy threshold. Alignment columns with gaps are grey, less conserved columns are blue and highly conserved columns are red (Multiple Sequence Alignment Viewer; NCBI).

Within the microtubule bundles, MAP65s form crossbridges 25 nm wide (Chan *et al.* 1999; Smertenko *et al.* 2004) between both parallel and antiparallel microtubules (Van Damme *et al.* 2004; Wicker-Planquart *et al.* 2004; Lucas *et al.* 2011), with a higher preference for antiparallel microtubules (Gaillard *et al.* 2008; Tulin *et al.* 2012). Although most studies reported that MAP65s do not affect polymerization rates (Smertenko *et al.* 2004) nor growth or shortening rates (Lucas *et al.* 2011), it has been suggested that when specific conditions are met, MAP65s increase the number of rescue events leading to the establishment of longer microtubule bundles (Stoppin-Mellet *et al.* 2013). Their canonical function regarding microtubule dynamics remains to be the stabilization of microtubule bundles by slowing down depolymerization rates (Van Damme *et al.* 2004; Gaillard *et al.* 2008; Fache *et al.* 2010). Microtubule bundling promoted by MAP65s also inhibits the severing of microtubules by KATANIN (Burkart and Dixit 2019). Lastly, MAP65s increase the flexibility of microtubules (Portran *et al.* 2013), and they promote bundling of adjacent microtubules meeting each other at shallow angles (Tulin *et al.* 2012).

1.1.2. Phosphorylation of microtubule associated proteins during cell division

The activity of the microtubule associated proteins is in many cases crucial for proper progression of cell division and any aberration may lead to severe defects in cytokinesis. Therefore, there is a need for precise spatiotemporal control of these microtubule associated proteins. Plant cells employ several regulatory mechanisms to achieve this: (i) protein ubiquitination leading to degradation (Malcos and Cyr 2011); (ii) stabilization by other proteins (Stewart and Fang 2005; Pietra *et al.* 2013; Tomaštíková *et al.* 2015); (iii) regulation via the G protein signalling (Gruss *et al.* 2001; Lin *et al.* 2013); (iv) regulation by the Ca^{2+}/calmodulin pathway (Deavours *et al.* 1998); (v) reversible protein de/phosphorylation, which was reported for a number of microtubule associated proteins and other proteins involved in cell cycle progression (**Fig. 5**).

1.1.2.1. Kinases phosphorylating microtubule associated proteins

Several studies pointed out the necessity of the regulation of the phosphorylation status of microtubule associated proteins for proper organization of mitotic microtubule arrays (**Fig. 5**). This is exemplified by CYCLIN DEPENDENT KINASE (CDK) negatively regulating KIN7a/b (Sasabe *et al.* 2011a) and possibly phosphorylating MAP65-1 (Smertenko *et al.* 2006), or AURORA KINASE (AUR) phosphorylating TARGETING PROTEIN FOR XKLP 2 and MPKs (Tomaštíková *et al.* 2015; Boruc *et al.* 2017). Other microtubule associated proteins and markers of cortical division zone, specifically TONNEAU 1 (TON1a), KIN10a and EB1c were predicted to be regulated by either CDK or AUR either based on high-throughput interaction analysis (Leene *et al.* 2007) or *in silico* predictions (STRING 11.0; Szklarczyk *et al.* 2015).

The CDKs and AURs are known regulators of the cell cycle progression, with CDKs being master regulators in controlling mitosis (Costa 2017), while AURs are on a lower hierarchical position (Schecher *et al.* 2017). Both CDK-A and AUR1/2 colocalize with mitotic microtubule structures in Arabidopsis (**Table 3**; Stals *et al.* 1997; Weingartner *et al.* 2001; Demidov *et al.* 2005). There are three members of the AUR protein family in Arabidopsis (Kawabe *et al.* 2005) and AUR1/2 were found to be necessary for formative cell divisions during plant development (Van Damme *et al.* 2011). Based on the information available for animal homologues of plant CDKs, AURs

and microtubule associated proteins (Ookata *et al.* 1997; Vasquez *et al.* 1999; Zhang *et al.* 2008; Ban *et al.* 2009), *in silico* analysis of CDK phosphorylation sites in plant microtubule associated proteins (Hussey *et al.* 2002; Smertenko *et al.* 2006) and results from pharmacological treatment experiments (Weingartner *et al.* 2001), CDKs and AURs are expected to be integrated into the network regulating mitotic microtubule array organization (Weingartner *et al.* 2001). Moreover, CDK-dependent phosphorylation was suggested to promote the disassembly of the preprophase band (Hush *et al.* 1996).
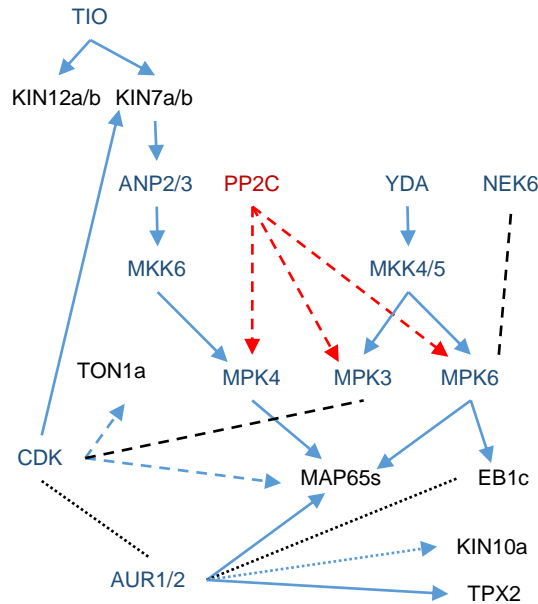
Figure 5. Kinases and phosphatases regulating microtubule associated proteins during cell division. Adapted from Vavrdová *et al.* (2019). A speculative network of protein kinases (dark blue), protein phosphatases (dark red) and targeted microtubule associated proteins or markers of cell division zone (black). Arrows show targets of kinases and/or phosphatases based on published studies (full line), *in vitro* or high-throughput interaction studies (dashed lines; BioGRID), or *in silico* predictions (dotted lines; STRING). Black lines connect putative interaction partners, where the target is unknown. Abbreviations: ANP, ARABIDOPSIS NUCLEUS AND PHRAGMOPLAST-LOCALIZED KINASE, AUR, AURORA KINASE; CDK, CELL DIVISION KINASE; EB1c, END BINDING 1c; KIN, KINESIN-RELATED PROTEIN; MAP65, MICROTUBULE ASSOCIATED PROTEIN 65; MPK, MITOGEN ACTIVATED PROTEIN KINASE; MKK, MITOGEN ACTIVATED PROTEIN KINASE KINASE; NEK6, NIMA-RELATED KINASE 6; PP2C, PROTEIN PHOSPHATASE 2C; TIO, TWO-IN-ONE; TPX2, TARGETING PROTEIN FOR XKLP2; TON1a, TONNEAU 1a; YDA, YODA.

Another family of protein kinases involved in the control over mitosis and mitotic microtubule structures is the NIMA-RELATED KINASE protein family (NEK; Brieño-Enríquez *et al.* 2017). NEKs are highly conserved Ser/Thr protein kinases known to regulate various mitotic events in eukaryotes (O'Connell *et al.* 2003; O'Regan *et al.* 2007). The Arabidopsis genome was described to encode seven members of this protein family (Vigneault *et al.* 2007), but their functions are not well-characterized. So far, they are known to regulate cortical microtubules (Vigneault *et al.* 2007; Takatani *et al.* 2017), thus, to affect the cell expansion and morphogenesis (Motose *et al.* 2008; Sakai *et al.* 2008). Moreover, they are negatively regulated by ARMADILLO-REPEAT KINESIN 1 (Eng *et al.* 2017). The NEK6 was shown to colocalize with the spindle and

the phragmoplast (**Table 3**) and to phosphorylate β-tubulin *in vitro*, however, no phenotypes were noted in single mutants (Motose *et al.* 2011), possibly due to functional redundancy with other NEKs. Therefore, its function in the regulation of cytoskeleton during mitosis remains unknown.

The Ser/Thr protein kinase TWO-IN-ONE (TIO) has been shown to be necessary during cytokinesis in both sporophytes and gametophytes (Oh *et al.* 2005). The orthologue of TIO in animals, the FUSED kinase, phosphorylates a kinesin-like protein (Ruel *et al.* 2007). Similarly, plant TIO interacts with KIN12a/b and KIN7b (**Fig. 5**; Oh *et al.* 2012; Oh *et al.* 2014). These three kinesins are involved in the phragmoplast organization (Tanaka *et al.* 2004; Lee *et al.* 2007). Furthermore, TIO colocalizes with the phragmoplast (Oh *et al.* 2012) highlighting the importance of TIO for correct function of the phragmoplast.

The last protein family implicated in the regulation of mitotic microtubule structures in plants is the MITOGEN ACTIVATED PROTEIN KINASE family (MPKs). MPKs are Ser/Thr kinases well-known to regulate microtubule associated proteins (Hoshi *et al.* 1992). They form signalling cascades, where MPK is activated by MITOGEN ACTIVATED PROTEIN KINASE KINASE (MKK), which is in turn phosphorylated by MITOGEN ACTIVATED PROTEIN KINASE KINASE KINASE (MKKK). The Arabidopsis genome encodes approximately 60 genes for MKKKs, 10 for MKKs, and 20 for MPKs (MAPK Group 2002).

Table 3. Kinases associated with microtubule structures throughout the cell cycle.
Colocalization of kinases with specific microtubule arrays is documented by referring to relevant literature sources.

microtubule array kinases	cortical microtubules	preprophase band	spindle	phragmoplast
AURORA KINASE 1/2 (AUR1/2)			(Demidov *et al.* 2005)	
CYCLIN-DEPENDENT KINASE A (CDK-A)		(Stals *et al.* 1997; Weingartner *et al.* 2001)		
MITOGEN ACTIVATED PROTEIN KINASE 6 (MPK6)		(Müller *et al.* 2010)		(Müller *et al.* 2010)
NIMA-RELATED KINASE 6 (NEK6)	(Motose *et al.* 2011)		(Motose *et al.* 2011)	

All plant MPKs are related to the mammalian family of the EXTRACELLULAR SIGNAL-RELATED KINASEs, which mainly function in mitogenic signal transduction. However, plant MPKs evolved to respond to a broader range of signals (Jonak *et al.* 1999). The activation motif of plant MPKs is usually either Thr-Glu-Tyr or Thr-Asp-Tyr, but unconventional motifs were noted as well (Mohanta *et al.* 2016). As the MPK belong to the same group as CDKs and GLYCOGEN SYNTHASE KINASE 3, they preferentially target Ser-Pro motifs. In plants, two MPK signalling pathways are well-described regarding their activity in the plant cell division.

The MPK pathway, which is essential for proper cell division was initially described in tobacco (Calderini *et al.* 1998; Bögre *et al.* 1999; Calderini *et al.* 2001; Nishihama *et al.* 2001). In Arabidopsis, it is composed of ARABIDOPSIS NUCLEUS AND PHRAGMOPLAST-LOCALIZED KINASE 2 (ANP2) and ANP3 (MKKKs), MKK6, MPK4 and MPK6 (Krysan *et al.* 2002; Strompen *et al.* 2002) and it is activated by KIN7a/b (**Fig. 5**; Tanaka *et al.* 2004; Takahashi *et al.* 2010). This pathway regulates the organization of mitotic structures via the phosphorylation of MAP65s (**Fig. 5**; Smertenko *et al.* 2006; Beck *et al.* 2011; Sasabe *et al.* 2011b; Kohoutová *et al.* 2015; Zhou *et al.* 2017), which directly affects the phragmoplast expansion and cell plate formation (Takahashi *et al.* 2010). Another MAP involved in this pathway is RUNKEL, which is a putative pseudokinase colocalizing with the preprophase band, spindle, and phragmoplast and affecting the cell plate expansion (Krupnova *et al.* 2009; 2013).

Unlike the ANP2/3-MKK6-MPK4/6 pathway, which is fundamental for all types of plant cell divisions, the function of the second MPK pathway is more distinct. It consists of YODA (YDA; MKKK), MKK4 and MKK5, MPK3 and MPK6 (**Fig. 5**; Wang *et al.* 2007; Cristina *et al.* 2010) and its members are involved in stress responses, innate immunity (Colcombet and Hirt 2008) and plant development (reviewed in Komis *et al.* 2018a). Importantly, this pathway has a crucial role in asymmetric cell divisions, specifically in the first division of the zygote (Lukowitz *et al.* 2004) and during stomatal development (Bergmann *et al.* 2004; Wang *et al.* 2007). Moreover, it also affects the cell division plane orientation in regular cell divisions as defects in tissue patterning were observed in *yda, mpk3, mpk6* mutants in roots (Müller *et al.* 2010; Smékalová *et al.* 2014). The role of this pathway in organizing microtubule structures is supported by the observation of MPK6 colocalizing with the preprophase band and the phragmoplast (**Table 3**; Müller *et al.* 2010; Smékalová *et al.* 2014) and by identifying MAP65-1 and

EB1c to be targeted by MPK6 (Smékalová *et al.* 2014; Kohoutová *et al.* 2015). Moreover, the transcript levels of cortical division zone markers, namely TANGLED and KIN12c, were deregulated in *yda* mutants hinting that this pathway is possibly involved at multiple levels in the cell division regulation (Smékalová *et al.* 2014).

1.1.2.2.   Phosphatases dephosphorylating microtubule associated proteins

Protein phosphatases counter the activity of kinases, ensuring the reversibility of protein phosphorylation. Indeed, the interplay of kinases and phosphatases securing correct spatiotemporal regulation of microtubule organization and dynamics seems to be essential for the progression of mitosis (Tournebize *et al.* 1997; Bhaskara *et al.* 2017). Specifically, Ser/Thr specific phosphoprotein phosphatases were pointed out as prominent players in these processes (Samofalova *et al.* 2019).

The involvement of phosphoprotein phosphatases in regulatory mechanisms of microtubule organization and dynamics in plants remains mostly obscure, however, it appears to be complex and encompassing several levels. First, plant PROTEIN PHOSPHATASE 2A (PP2A) and PROTEIN PHOSPHATASE 4 (PP4) interact with α-tubulin and γ-tubulin, respectively (Awotunde *et al.* 2003; Voss *et al.* 2013). Secondly, phosphoprotein phosphatases are known to interact with various microtubule associated proteins as plant PP2A assembles in complexes together with TON1 (Spinner *et al.* 2013). On the other hand, animal homologues of TARGETING PROTEIN FOR XKLP 2 and EB1 were reported to protect AURs from inactivation via PP1 and PP2A-mediated dephosphorylation, respectively (Eyers *et al.* 2003; Sun *et al.* 2008). Thus, microtubule associated proteins can interfere with regulatory function of phosphatases. Finally, plant PP2C negatively regulates CDKs and MPKs (**Fig. 5**; Umbrasaite *et al.* 2010; Kohoutová *et al.* 2015) and other plant phosphoprotein phosphatases are expected to inactivate CDKs, AURs and MPKs similarly to their animal counterparts (Mumby and Walter 1993; Mayer-Jaekel and Hemmings 1994).

The importance of PP2A and PP2C for the function of both interphase and mitotic microtubule arrays is exposed in mutants, as their arrangement of microtubule structures is heavily affected (Traas *et al.* 1995; McClinton and Sung 1997; Song *et al.* 2006; Kirik *et al.* 2012; Kohoutová *et al.* 2015; Bhaskara *et al.* 2017; Qu *et al.* 2018). PP2C affects chromosome segregation, spindle orientation, and alignment of the cell division site (Kohoutová *et al.* 2015). The role of PP2A in the cell division appears to be restricted to

establishing and maintaining the cortical division zone, as spindle and phragmoplast formation are unaffected in mutants, yet guidance of phragmoplast is erroneous (Camilleri *et al.* 2002).

The PP2A functions as a heteromer composed of three subunits – scaffolding (A), regulatory (B) and catalytic (C). The PP2AA scaffolding subunit bridges the regulatory and catalytic domains (Groves *et al.* 1999). There are three isoforms of PP2AA in Arabidopsis, with PP2AA1 (RCN1; ROOTS CURL IN NAPHTYLAMINOACID 1) being fundamental for the activity of PP2A (Zhou *et al.* 2004). The PP2AB regulatory subunit controls subcellular localization and substrate specificity of the PP2A complex. In Arabidopsis, TON2 (alternatively FASS) is a PP2AB" subunit responsible for the regulation of cortical microtubules and the organization of the preprophase band (Traas *et al.* 1995; McClinton and Sung 1997). The PP2A complex containing these two subunits is recruited to the preprophase band by TON1a and TRMs (Drevensek *et al.* 2012; Spinner *et al.* 2013). This complex governs the preprophase band development and, later on, it persists at the cortex, where it maintains the cortical division zone (Wright *et al.* 2009; Spinner *et al.* 2013). MOR1, TON1a, TANGLED and CLIP-ASSOCIATED PROTEIN were proposed to be targeted by PP2A (Twell *et al.* 2002; Kawamura *et al.* 2006; Xu *et al.* 2008; Rasmussen *et al.* 2011). By spatiotemporally restricting activities of microtubule associated proteins, PP2A could enable microtubule stabilization and the formation of the preprophase band (Smertenko *et al.* 2006; Walker *et al.* 2007; Wright and Smith 2007; Wright *et al.* 2009; Lipka *et al.* 2015).

1.1.2.3.   Reversible phosphorylation of MAP65s

The necessity of reversible phosphorylation for the formation of mitotic microtubule arrays has been demonstrated in several studies using either kinase or phosphatase inhibitors (Katsuta and Shibaoka 1992; Ayaydin *et al.* 2000; Smertenko *et al.* 2006). Moreover, the members of the MAP65 family, which are implicated in the formation of the preprophase band and the expansion of the phragmoplast, are known to be regulated by reversible phosphorylation (Smertenko *et al.* 2006; Rasmussen *et al.* 2013; Lipka *et al.* 2015).

The effects of the reversible phosphorylation on the MAP65 activity has been described to be a crucial part of the mechanism behind phragmoplast expansion (Sasabe and Machida 2006, 2012; Smertenko *et al.* 2006). MAP65s are phosphorylated by MPK4

and MPK6 (Smertenko *et al.* 2006; Beck *et al.* 2010; Kosetsu *et al.* 2010; Sasabe *et al.* 2011b), CDKs (Mao *et al.* 2005; Smertenko *et al.* 2006) and AUR (Boruc *et al.* 2017). It has been hypothesized that kinases could contribute to the multisite phosphorylation of MAP65 proteins, which is a type of regulation common for many eukaryotic proteins (Repetto *et al.* 2018). Interestingly, while AUR and MPKs do not interfere with each other in phosphorylating MAP65-1, the targeting motifs for MPK and CDK overlap in this protein (Smertenko *et al.* 2006), thus, they have to compete for them. Moreover, the CDKs impede the MPK4/6 activity via inhibiting the activation of KIN7a/b (Sasabe *et al.* 2011a), with KIN7a/b being the upstream activator of MPK4/6. Since KIN7a/b are kinesins, they probably provide spatial regulation of the MPK4/6 activity, while CDKs ensure proper temporal control of this signalling module. The phosphorylation of MAP65s has two implications: it causes their release from microtubule bundles, which leads to destabilization of microtubules; and it affects their subcellular localization, providing additional spatial regulation. The activity of MAP65 is then re-established via dephosphorylation (Lipka *et al.* 2015), possibly by PP1 or PP2A (Smertenko *et al.* 2006). The putative role of PP2A in dephosphorylating MAP65s was also suggested after observing its function in regulating stabilization and branching of cortical microtubules (Kirik *et al.* 2012).

1.2.   Asymmetric cell divisions in plants

The position of the cell division plane in most symmetrical divisions complies to the geometrical rule, which prefers the shortest distance of the cell division plane, with the additional role of mechanical forces in cells of more complex shapes (Besson and Dumais 2011). These rules are overridden during asymmetric cell divisions, which are indispensable for all multicellular organisms as they generate daughter cells with diverging cell fates (Shao and Dong 2016). There are two major mechanisms behind asymmetric cell division. The intrinsic mechanisms lead to the polarization of the mother cell before the asymmetric cell division. This symmetry breaking is achieved by an uneven distribution of various proteins, signalling pathways, mRNAs, organelles, cytoskeletal components, and other molecules (Freisinger *et al.* 2013), and after the asymmetric cell division, it leads to divergent cell differentiation of daughter cells. On the other hand, there are cases when the division itself does not generate visible physical differences in daughter cells, but the extrinsic mechanisms drive their diversification by placing them in distinct microenvironments (Fuller and Spradling 2007). In plants, intrinsic mechanisms often overlap with extrinsic mechanisms (Shao and Dong 2016).

Generally, the organization of the asymmetric cell division in plants begins with the dedication of cells. Then, the polarity of these cells is established by several factors, among them, by the positioning of the nucleus. This is followed by the cell division with the cell division plane orientation corrected according to the polarization cues. Finally, after the cell division, the asymmetrically distributed and/or expressed cell fate factors determine the cell fate of daughter cells (De Smet and Beeckman 2011; Gaillochet and Lohmann 2015).

Among the mechanisms of polarity establishment described in plants belong: (i) cell-to-cell communication including asymmetries in ligand concentrations (Ito *et al.* 2006; Hara *et al.* 2007; De Smet *et al.* 2009; Hirakawa *et al.* 2010; Jewaria *et al.* 2013; Stahl *et al.* 2013; Costa *et al.* 2014), auxin transport proteins (Geldner *et al.* 2003; Richter *et al.* 2010), and trafficking of mobile transcription factors (Nakajima *et al.* 2001; Schlereth *et al.* 2010); (ii) auxin gradient (Sabatini *et al.* 1999; Robert *et al.* 2013; Le *et al.* 2014); (iii) protein polarity (Cartwright *et al.* 2009; Dong *et al.* 2009; Humphries *et al.* 2011; Pillitteri *et al.* 2011); (iv) nucleus positioning (Park *et al.* 1998; Oh *et al.* 2010a); (v) cell wall modifications (Geshi *et al.* 2013; Sekereš *et al.* 2015; Zhang and

Dong 2018). All these events are interconnected in intricate regulatory networks, which often involve spatially organized cell signalling, feedback loops, and reversible phosphorylation (Zhang *et al.* 2015; 2016a).

There are numerous formative cell divisions during the plant ontogenesis. In two of these asymmetric cell divisions, the YDA-MPK signalling pathway has been described to have a major role, specifically during the first division of the zygote and the stomatal differentiation pathway.

1.2.1.   First division of the zygote

The embryonic development of Arabidopsis is comprised of an extremely ordered sequence of cell divisions (Yoshida *et al.* 2014). This begins with the first asymmetric division of the zygote. The zygote is polarized and after its division, the apical cell and the basal cell emerge. While the apical cell further develops into the embryo proper, the basal cell lineage results in creating a suspensor, which connects the embryo proper to maternal tissues (**Fig. 6A**; ten Hove *et al.* 2015).

The asymmetric cell division is a result of a signalling pathway consisting of multiple components (**Fig. 6B**). After the fertilization, the transcript of the membrane-associated receptor-like pseudokinase SHORT SUSPENSOR (Bayer *et al.* 2009) is transported from the sperm cell to the zygote. Upon its translation and in collaboration with the ZYGOTE ARREST 1, it activates YDA (Yu *et al.* 2016). YDA is also activated by the EMBRYO SURROUNDING FACTOR 1 (Costa *et al.* 2014), however, the activation by SHORT SUSPENSOR is of special importance for it provides temporal cue enabling the synchronization of the fertilization with the activity of YDA (Bayer *et al.* 2009). True to the nature of an MKKK, YDA activates MKK4/5, which, in turn, activate MPK3/6 (Zhang *et al.* 2017a). MPK3/6 phosphorylate the WRKY DNA-BINDING PROTEIN 2 (WRKY2; Ueda *et al.* 2017). Together with the maternally-originated HOMEODOMAIN GLABROUS 11/12, WRKY2 activates transcription of WUCHSEL-RELATED HOMEOBOX PROTEIN 8 (WOX8; Ueda *et al.* 2011; 2017). In this way, both maternal and paternal inputs are integrated into promoting *WOX8* transcription (Bayer *et al.* 2009; Yu *et al.* 2016; Ueda *et al.* 2017). Ultimately, this pathway leads to the polarization of the zygote and this results in the asymmetric cell division. It should be noted that the signalling between the YDA and the WOX8 is not linear (Breuninger *et al.*
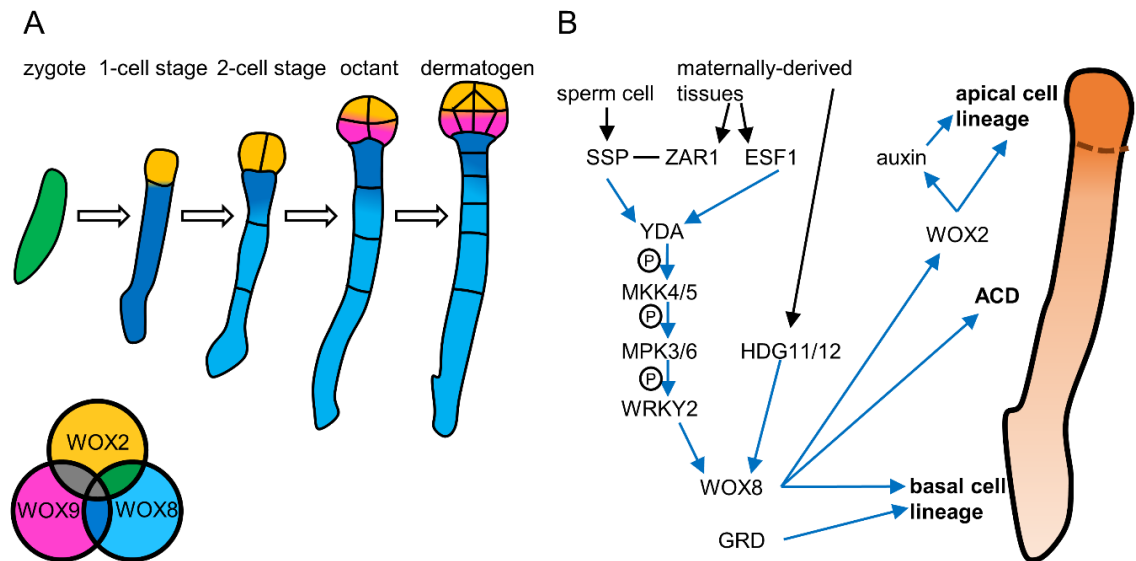
Figure 6. Overview of early embryonic development. (A) The layout of early developmental stages (the 4-cell stage was omitted from the picture). Expression domains of selected WUCHSEL-RELATED HOMEOBOX PROTEINs (WOXs) are colour-coded: yellow for WOX2, azure for WOX8, magenta for WOX9, green for both WOX2 and WOX8, blue for both WOX8 and WOX9. (B) A scheme of signalling events regulating asymmetric cell division (ACD) and the establishment of cell fates in daughter cells. The image on the right depicts auxin gradient in the 1-cell stage embryo, with dark orange showing auxin maxima. Black arrows mark tissue of origin; black line connects proteins interacting with each other; blue arrows show positive regulation; P in a circle marks phosphorylation events. Abbreviations: ESF1, EMBRYO SURROUNDING FACTOR 1; GRD, GROUNDED; HDG11/12, HOMEODOMAIN GLABROUS 11/12; MPK, MITOGEN ACTIVATED PROTEIN KINASE; MKK, MITOGEN ACTIVATED PROTEIN KINASE KINASE; SSP, SHORT SUSPENSOR; WRKY2, WRKY DNA-BINDING PROTEIN 2; YDA, YODA; ZAR1, ZYGOTIC ARREST 1.

2008). After the asymmetric cell division, the WOX8 and the WOX2, despite not being previously polarized (Ueda *et al.* 2011), become restricted to the basal and apical cell, respectively (**Fig. 6A**; Haecker *et al.* 2004).

Apart from the polarization of the zygote and the asymmetric cell division, this signalling pathway also affects the cell fate determination of apical and basal cells. The WOX8, WOX9, and GROUNDED are responsible for proper development of the basal cell (Breuninger *et al.* 2008; Jeong *et al.* 2011). Moreover, through a non-cell autonomous mechanism, WOX8 controls the activity of WOX2 in the apical cell (Breuninger *et al.* 2008), which promotes the development of the embryo proper.

Auxin is indispensable for early embryonic development. It is distributed in a gradient after the first division of the zygote (**Fig. 6B**) owing to the positioning of PIN-FORMED 7 at the apical membrane of the basal cell (Friml *et al.* 2003). The higher amount of auxin in the apical cell leads to the degradation of the BODENLOS, which

releases the MONOPTEROUS (Hamann *et al.* 2002). This signalling ultimately leads to the determination of the apical cell fate (Friml *et al.* 2003). The auxin signalling is regulated by WOX2 (Zhang *et al.* 2017b), RAF-LIKE MAPKKK 22 and 28 (Wang *et al.* 2018), and a putative spliceosome subunit JANUS (Xiong *et al.* 2019).

Proper orientation of the first asymmetric cell division of the zygote is necessary for guiding daughter cells towards their respective cell fates and founding the apical-basal axis, thus, establishing a fundamental framework for the next steps in embryogenesis. During the embryonic development, there are other cases of asymmetric cell divisions, e.g. tangential division in the embryo proper at the dermatogen stage (**Fig. 6A**) or asymmetric division of hypophysis, the uppermost cell of the suspensor (Pillitteri *et al.* 2016). These asymmetric cell divisions are important for differentiation of cell fates and they lead to the initiation of all basic tissues at the globular stage (ten Hove *et al.* 2015).

1.2.2. Stomatal differentiation pathway

Stomata are specialized cells in the epidermis, which facilitate gas exchange and transpiration. Due to their role in the photosynthesis and water use, not only their aperture but also the development of new stomata is regulated by many environmental cues (Endo and Torii 2019). Stomata emerge upon a series of asymmetric and symmetric divisions (**Fig. 7A**), with basic helix-loop-helix transcription factors SPEECHLESS (SPCH), MUTE and FAMA as master regulators (Ohashi-Ito and Bergmann 2006; MacAlister *et al.* 2007; Pillitteri *et al.* 2007). High levels of SPCH in meristemoid mother cell lead to the asymmetric cell division into smaller meristemoid and larger stomatal lineage ground cell. The level of the SPCH remains high in the meristemoid advancing its asymmetric cell division (MacAlister *et al.* 2007). Once SPCH levels decrease, MUTE levels rise and the guard mother cell is formed (Pillitteri *et al.* 2007). Then, the expression pattern changes again with FAMA driving the symmetrical division, from which a pair of guard cells emerge (**Fig. 7A**; Ohashi-Ito and Bergmann 2006).

Out of the three transcription factors, SPCH has a superior role in the stomatal development, as it governs the first asymmetric cell division, thus, the entry into the stomatal lineage (Lau *et al.* 2014). Therefore, the regulation of SPCH incorporates numerous internal and external cues (Lee and Bergmann 2019). The inactivation and downregulation of SPCH are facilitated through the phosphorylation by MPK3/6 and
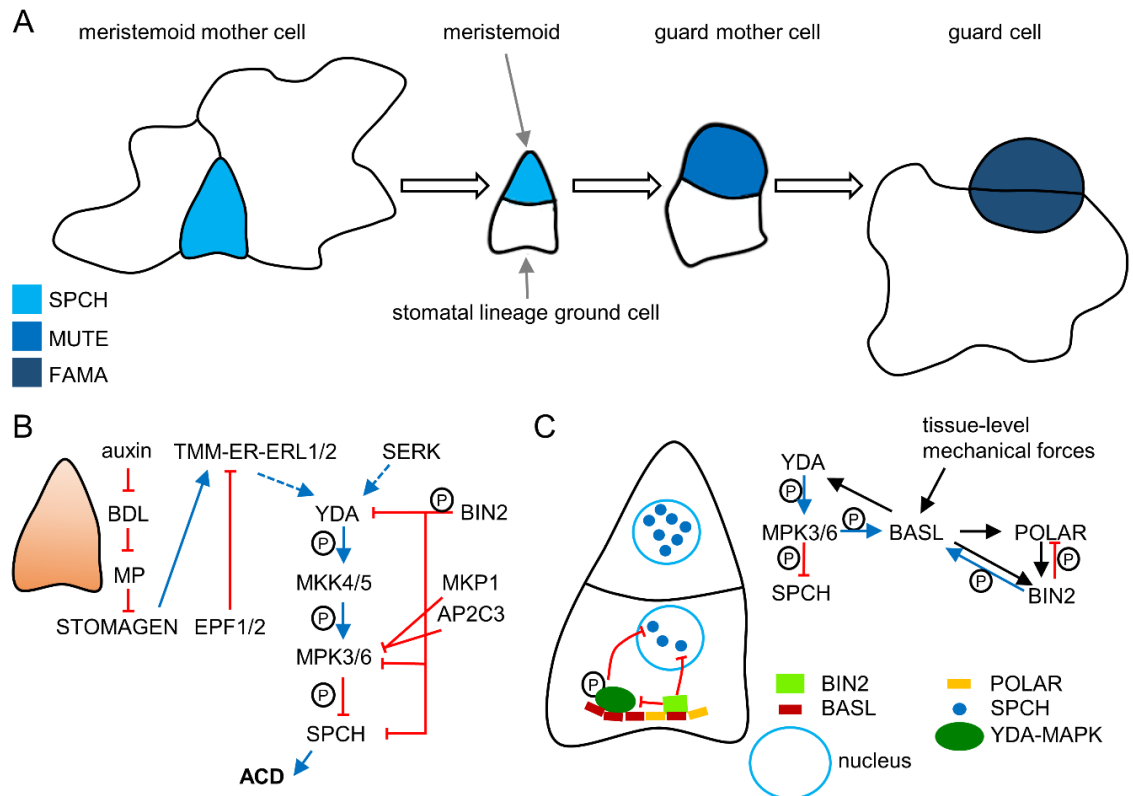
Figure 7. Overview of stomatal development. (A) A depiction of stomata differentiation from precursor cells. Cell-type specific expression of transcription factors regulating stomatal differentiation is colour-coded: azure for SPEECHLESS (SPCH), blue for MUTE and dark blue for FAMA. (B) A scheme of signalling events regulating the asymmetric cell division (ACD). The image on the left depicts auxin gradient in the meristemoid mother cell before the ACD, with dark orange showing the auxin maxima. (C) An overview of polarized proteins after the ACD of the meristemoid mother cell (on the left) and a scheme of interaction between key regulators of the ACD and polarized proteins (on the right). Blue arrows show activation; red lines mark repression, dashed lines symbolize putative links in the signalling pathway; black arrows show modulation of activity; P in a circle marks phosphorylation event. Abbreviations: AP2C3, ARABIDOPSIS PROTEIN PHOSPHATASE 2C 3; BASL, BREAKING OF ASYMMETRY IN THE STOMATAL LINEAGE; BDL, BODENLOS; BIN2, BRASSINOSTEROID INSENSITIVE 2; EPF, EPIDERMAL PATTERNING FACTOR; ER, ERECTA; ERL, ERECTA-LIKE; MP, MONOPTEROUS; MKP1, MAPK PHOSPHATASE 1; MPK, MITOGEN ACTIVATED PROTEIN KINASE; MKK, MITOGEN ACTIVATED PROTEIN KINASE KINASE; POLAR, POLAR LOCALIZATION DURING ASYMMETRIC DIVISION AND REDISTRIBUTION; SERK, SOMATIC EMBRYOGENESIS RECEPTOR-LIKE KINASE; TMM, TOO MANY MOUTH; YDA, YODA.

BRASSINOSTEROID INSENSITIVE 2 (BIN2; **Fig. 7B**; Lampard *et al.* 2008; Gudesblat *et al.* 2012). The BIN2 is a GLYCOGEN SYNTHASE KINASE 3/SHAGGY-LIKE KINASE negatively regulated by brassinosteroid signalling, therefore implementing the brassinosteroid phytohormones into the regulation of stomatal development.

In stomatal development, the MPK signalling module is similar to the one in embryogenesis. It consists of YDA, MKK4/5/7/9 and MPK3/6 (Wang *et al.* 2007;

Lampard *et al.* 2009; Wengier *et al.* 2018). This pathway is probably activated by receptor signalling complex consisting of the ERECTA, ERECTA-LIKE PROTEINS, TOO MANY MOUTH and SOMATIC EMBRYOGENESIS RECEPTOR KINASEs (**Fig. 7B**; Shpak *et al.* 2004; Shpak *et al.* 2005; Meng *et al.* 2015), which receives signalling peptides EPIDERMAL PATTERNING FACTOR 1 and 2, activating the MPK pathway (Gray *et al.* 2008; Hunt and Gray 2009). This can be intercepted through the ligand competition by STOMAGEN (**Fig. 7B**; Hunt *et al.* 2010; Kondo *et al.* 2010; Sugano *et al.* 2010). YDA is negatively regulated by the BIN2, as are MPK3/6 (Kim *et al.* 2012; Khan *et al.* 2013). MPK3/6 are also inactivated by the MAPK PHOSPHATASE 1 (MKP1) or the ARABIDOPSIS PROTEIN PHOSPHATASE 2C 3 (AP2C3; Umbrasaite *et al.* 2010; Tamnanloo *et al.* 2018). Apart from targeting the SPCH and SCREAM, both nuclear transcription factors (Lampard *et al.* 2008; Li *et al.* 2017b), MPK3/6 were recently found to affect stomatal development via phosphorylating MAPK SUBSTRATES IN THE STOMATAL LINEAGE proteins, which are localized in both the nucleus and at the plasma membrane (Xue *et al.* 2020).

The phytohormone auxin takes part in regulating stomatal division as it is locally depleted from meristemoids before their differentiation into guard mother cells (**Fig. 7B;** Le *et al.* 2014). This is in contrast with the increased auxin levels in the apical cell, the smaller cell emerging after the asymmetric cell division of the zygote (Friml *et al.* 2003). On the other hand, the auxin-responsive signalling in the stomatal development employs the same proteins as in the embryogenesis, which means that higher levels of auxin lead to the activation of the MONOPTEROUS and, in turn, to the activation of the STOMAGEN (Zhang *et al.* 2014). Since higher levels of auxin result in the activation of the STOMAGEN, a positive regulator of the asymmetric cell division, the depletion of auxin in the meristemoid might facilitate its cell fate determination through the symmetric cell division (Le *et al.* 2014).

Apart from the cell-to-cell signalling and phytohormones, the initiation of the stomatal development depends on polarity proteins, which coordinate the asymmetric cell divisions. The plant-specific proteins BREAKING OF ASYMMETRY IN STOMATAL LINEAGE (BASL) and POLAR LOCALIZATION DURING ASYMMETRIC DIVISION AND REDISTRIBUTION (POLAR) were found to localize in a polarity crescent at the cell cortex opposite of the future site of the asymmetric cell division and to serve as a scaffold for BIN2 and YDA-MPK cascade (**Fig. 7C**; Dong *et al.*

2009; Pillitteri *et al.* 2011; Houbaert *et al.* 2018). The BASL is phosphorylated by BIN2 and MPK3/6 (Zhang *et al.* 2015; Zhang *et al.* 2016a) and BIN2 also phosphorylates POLAR (Houbaert *et al.* 2018). Additionally, both BASL and POLAR are targets of the SPCH (Dong *et al.* 2009; Pillitteri *et al.* 2011), which makes them a platform integrating multiple regulatory inputs. According to a model suggested by Houbaert *et al.* (2018), BIN2 and MPKs initiate the polarization of BASL and POLAR, which leads to sequestering BIN2 and YDA-MPK cascade at the polarity crescent. This relieves the inhibition of SPCH, allowing the accumulation of SPCH in the nucleus and, ultimately, the asymmetric cell division. After the asymmetric cell division, the complex of kinases and proteins determining their subcellular localization is present only in the stomatal lineage ground cell, which can exit the stomatal lineage pathway and differentiate into the pavement cell. If the levels of BASL and POLAR decrease, it leads to the release of BIN2 and YDA-MPK pathway from the polarity crescent, enabling them to inhibit SPCH and to further repress the asymmetric cell divisions.

1.2.3. Role of kinases and phosphatases in orienting asymmetric cell divisions

The prerequisite for a successful asymmetric cell division is overriding the rules governing the symmetric cell division. Initially, actin was placed as a factor overcoming these rules by altering the positioning of the nucleus during the asymmetric cell division instead of microtubules, which are responsible for this function in symmetrical cell divisions (Mineyuki and Palevitz 1990; Kennard and Cleary 1997). Nevertheless, microtubules and their microtubule associated proteins seem to be essential for the progression of the asymmetric cell division as well. One example is that a mutation in *MOR1* and its tobacco homologue negatively affects the nuclear positioning before the asymmetric cell divisions in the male germline (Park *et al.* 1998; Oh *et al.* 2010b). Similarly, the homologue of TON2 in maize appears to be crucial for the orientation of the preprophase band in asymmetric cell divisions in leaf epidermis (Gallagher and Smith 1999). As described above, MPK6 is polarized in stomatal precursors before the asymmetric cell division and this might affect the formation of mitotic arrays since MPK6 regulates several microtubule associated proteins implicated in the cytokinesis (Zhang and Dong 2018).

Most of the microtubule associated proteins were described regarding their roles in the interphase or during the symmetric cell division. The exception is the plant-specific kinesin KINUa, which colocalizes with the preprophase band before the nuclear breakdown in the asymmetrically dividing stomatal precursors (Sakai *et al.* 2008; Malcos and Cyr 2011). Since the microtubule associated proteins utilized for building mitotic microtubule arrays during the symmetric cell division are also necessary for the asymmetric cell division (Park *et al.* 1998; Caillaud *et al.* 2008), the difference in the cell division plane orientation most likely stems from adjusting their regulation according to the polarization cues.

Indeed, several kinases and phosphatases have been implicated in the asymmetric cell divisions. When these kinases and phosphatases are placed in a bigger picture of the regulatory network behind asymmetric cell divisions, they are frequently associated with the cell fate determination (**Fig. 6B, 7B**). They are expected to also affect mitotic array positioning via their interactions with microtubule associated proteins. This is also supported by the experimental data showing the participation of kinases and phosphatases in formative cell divisions as evidenced by the requirement of AUR kinases for proper orientation of the anticlinal cell division initiating the lateral root development (Van Damme *et al.* 2011). A plethora of other kinases affecting the pattern formation was described (Tanaka *et al.* 2002; Nodine *et al.* 2007), including SOMATIC EMBRYOGENESIS RECEPTOR KINASEs (Meng *et al.* 2015; Zhang *et al.* 2016b; Li *et al.* 2019) and MPKs (Komis, Šamajová, *et al.* 2018; Wang *et al.* 2018).

The function of phosphoprotein phosphatases in asymmetric division has been mostly described as indirect. They are known to target PIN-FORMED proteins changing their subcellular distribution (Michniewicz *et al.* 2007; Dai *et al.* 2012), or to counter the CLAVATA signalling (Stone *et al.* 1994; Song *et al.* 2006). However, judging from their apparent importance for various types of asymmetric cell divisions (Song *et al.* 2008; Spinner *et al.* 2013), it seems that phosphoprotein phosphatases are involved in symmetry breaking more directly. So far, this has been confirmed for PP2C kinases POLTERGEIST and POLTERGEIST-LIKE (Song and Clark 2005; Song *et al.* 2008).

1.2.3.1. YDA-MPK3/6 cascade affects pattern formation

The YDA-MKK4/5-MPK3/6 signalling cascade appears to target both master regulators of the cell fate determination (**Fig. 6B, 7B**; Lampard *et al.* 2009; Ueda *et al.* 2017) and microtubule associated proteins involved in the formation of mitotic microtubule arrays (**Fig. 5**; Smertenko *et al.* 2006; Kohoutová *et al.* 2015). Thus, this pathway affects both cell fate determination and pattern formation, two key mechanisms behind formative cell divisions. Moreover, members of this module affect several pattern formation events throughout the plant ontogenesis (reviewed in Komis *et al.* 2018a). The whole YDA-MKK4/5-MPK3/6 module functions in the embryonic development, stomatal differentiation pathway and the establishment of the inflorescence architecture (Bergmann *et al.* 2004; Lukowitz *et al.* 2004; Wang *et al.* 2007; Meng *et al.* 2012). Both YDA and MPK6 affect the root development (Müller *et al.* 2010; López-Bucio *et al.* 2013; Smékalová *et al.* 2014), even though no root development phenotypes were described in *mpk3* mutants so far. Moreover, MPK3 and MPK6 are involved in the anther, ovule and floral development (Bush and Krysan 2007; Hord *et al.* 2008; Wang *et al.* 2008; López-Bucio *et al.* 2013).

Because of the extensive integration of this MPK pathway in the plant ontogenesis, it is apparent that its signalling specificity must be secured. For ensuring signalling specificity of MPKs, plant cells generally employ several mechanisms: (i) distinct cell types differ in the expression of upstream effectors and/or substrates; (ii) specific combinations of ligand-receptor lead to distinct outcomes (Sugano *et al.* 2010); (iii) involvement of various MKKs in the module, for MKKs are the point of convergence (Lampard *et al.* 2014); (iv) quantitative differences in the signal strength and/or timing (Beck *et al.* 2010); (v) specific subcellular localization arranged by scaffolding, adaptor or anchoring proteins (Kohoutová *et al.* 2015; Zhang *et al.* 2015); (vi) cross-inhibition and feedback control.

Additionally, MPK3 and MPK6 have partially redundant functions with overlapping substrate specificity (Popescu *et al.* 2009; Sörensson *et al.* 2012), yet in some cases, they seem to be noninterchangeable (Bush and Krysan 2007; López-Bucio *et al.* 2013). The negative regulation of MPK3/6 in these developmental events seems to be executed by reversible de/phosphorylation. The only known kinase capable of inactivating MPK3/6 remains BIN2 (Kim *et al.* 2012). On the other hand, the AP2C3 and MKP1 phosphatases were described to inhibit the activity of MPK3/6 (Umbrasaite *et al.*

2010; Tamnanloo *et al.* 2018). By regulating MPK3/6, both AP2C3 and MKP1 markedly affect stomatal differentiation, which is apparent in mutants deficient in these phosphatases (Umbrasaite *et al.* 2010; Tamnanloo *et al.* 2018). Moreover, the loss of MKP1 rescued various growth and developmental defects of *yda* mutants indicating that MKP1 may govern YDA-MPK3/6 in other developmental events as well (Tamnanloo *et al.* 2018). Presumably, other phosphatases are regulating the activity of MPK3/6 as well.

1.3. The role of HSP90s in plant development

The members of the protein family HEAT SHOCK PROTEIN 90 (HSP90s) are present in prokaryotes and eukaryotes, showing the high evolutionary conservation. Primarily, they function as chaperones aiding other proteins to correctly fold or re-fold their tertiary structures. To achieve this, they cooperate with cochaperones to bind their clients and to alter their structure during the chaperone cycle (Taipale *et al.* 2010). HSP90s are constantly expressed and their protein levels rapidly rise in response to stress conditions.

There are seven members of the HSP90 protein family in Arabidopsis. In cytoplasm and nucleus are present HSP90.1-4, while HSP90.5-7 are localized in chloroplasts, mitochondria and the endoplasmic reticulum, respectively (Krishna and Gloor 2001). Three of the cytoplasmic HSP90s, HSP90.2-4, are constitutively expressed. Not only do they share high sequence homology, but their single loss-of-function mutants also show low penetrance phenotypes while double mutants are lethal (Hubert *et al.* 2003). This is related to the fact that their genes originated in a relatively recent gene duplication events and that they are functionally redundant (Krishna and Gloor 2001; Xu *et al.* 2012). On the other hand, the expression of HSP90.1 is low under normal conditions and dramatically increases under stress conditions (Haralampidis *et al.* 2002) making it a profound heat shock protein.

The *hsp90* mutants have pleiotropic phenotypes owing to the fact that HSP90s provide plant cells with genetic buffering (Queitsch *et al.* 2002). The genetic buffering is the ability of HSP90s to correctly fold mutated proteins, thus, to mask mutations or polymorphisms. Once HSP90s are depleted, the mutants exhibit relatively mild defects under normal conditions, but stronger phenotypes under stress conditions that challenge protein homeostasis (Taipale *et al.* 2010). Conclusively, HSP90s provide plants with a buffering system coordinating organismal development with internal inputs and environmental cues.

The expression of plant HSP90s was shown to be developmentally regulated (Prasinos *et al.* 2005). Moreover, the loss-of-function mutants show morphological defects (Xu *et al.* 2012). These observations suggest that HSP90s are important for plant development.

The uncovering of the role of HSP90s in plant development is especially challenging due to their functional redundancy and complex interactions with

cochaperones and a plethora of client proteins. Nevertheless, several studies revealed their integration in developmental signalling networks (reviewed in Tichá *et al.* 2020). The cytoplasmic HSP90s interact with signalling networks, serving as a central hub connecting these pathways with environmental cues. Moreover, they are known to colocalize with cortical microtubules and the phragmoplast (Freudenreich and Nick 1998; Krtková *et al.* 2012) and to affect microtubule remodelling through yet unknown mechanism, which possibly includes other client or interacting proteins (Queitsch *et al.* 2002; Weis *et al.* 2010). Their integration in developmental signalling pathways and their activity in microtubule remodelling nominate them as candidates for modulation the cell division plane orientation during asymmetric cell division.

2. Materials and methods

2.1. Plant material and growth conditions

Arabidopsis thaliana (L.) Heynh. plants of the Columbia (Col-0) ecotype were used as wild type. All mutant lines and marker lines used in this study are listed in **Tables 4, 5**. Arabidopsis seeds were sterilized in 1% (v/v) NaOCl supplemented with 0.02% (v/v) Tween 20. Seeds were planted onto half-strength Murashige Skoog medium supplemented with 1% (w/v) sucrose.

Table 4: **List of lines used in this study.**

Genotype	Description	Reference/source
hsp90.1	T-DNA insertional mutation in *HSP90.1* (At5g52640; SALK_007614)	(Hubert *et al.* 2009)
hsp90.2	T-DNA insertional mutation in *HSP90.2* (At5g56030; SALK_038646)	(Hubert *et al.* 2003)
hsp90^RNAi	RNAi silencing of cytoplasmic HSP90s (*RAC2::HSP90RNAi*)	(Samakovli *et al.* 2020)
mpk3-1	T-DNA insertional mutation in *MPK3* (At3g45640; SALK_151594)	(Alonso *et al.* 2003)
mpk6-2	T-DNA insertional mutation in *MPK6* (At2g43790; SALK_073907)	(Liu and Zhang 2004)
mpk6AEF	TEY activation loop motif changed to AEF in *MPK6*; dominant-negative version of *MPK6* (At2g43790)	(Bush and Krysan 2007)
rcn1-6	T-DNA insertional mutation in *RCN1* (At1g25490; SALK_059903)	(Blakeslee *et al.* 2008)
ton2-5	nonsense mutation in *TON2* (At5g18580)	(Camilleri *et al.* 2002)
yda	insertional mutation in *YDA* (At1g63700)	(Lukowitz *et al.* 2004)
ΔNyda	deletion in N-terminal regulatory domain of *YDA* (At1g63700); gain-of-function	(Bergmann *et al.* 2004)
CaMV35S::TUA6:GFP (TUA6-GFP)	GFP-labelled tubulin driven under constitutively active promoter	(Shaw *et al.* 2003)
DR5::GFP	GFP driven under synthetic auxin responsive promoter	(Friml *et al.* 2003)
MAP65-2::eGFP:MAP65-2 (eGFP-MAP65-2)	eGFP-MAP65-2 fusion protein driven under native promoter	Pavel Křenek
MAP65-2::tagRFP:MAP65-2 (tagRFP-MAP65-2)	tagRFP-MAP65-2 fusion protein driven under native promoter	Pavel Křenek
MAP65-2::eGFP:MAP65-3 (eGFP-MAP65-3)	eGFP-MAP65-3 fusion protein driven under native promoter	Pavel Křenek
WOX8::NLS:YFP	NLS-YFP driven under *WOX8* promoter	(Breuninger *et al.* 2008)

Table 5: **List of crossed lines used in this study.**

First parental line	Second parental line	Authors
mpk6-2	*rcn1-6*	Tereza Vavrdová
yda	*hsp90.1; hsp90.2; hsp90^{RNAi}*	Despina Samakovli
ΔNyda	*hsp90.1; hsp90.2; hsp90^{RNAi}*	Despina Samakovli
DR5::GFP	*yda; ΔNyda; mpk3-1; mpk6-2; mpk6AEF; rcn1-6; ton2-5; hsp90.1; hsp90.2; hsp90^{RNAi}; hsp90.1 yda*	Despina Samakovli, Tereza Vavrdová
WOX8::NLS:YFP	*yda; ΔNyda; mpk3-1; mpk6-2; mpk6AEF; rcn1-6; ton2-5; hsp90.1; hsp90.2; hsp90^{RNAi}*	Despina Samakovli, Tereza Vavrdová
tagRFP-MAP65-2	TUA6-GFP; eGFP-MAP65-3	Tereza Vavrdová

Media were solidified either with Phytoagar (Duchefa Biochemie, Czech Republic) or agarose (catalogue designation A9539; Sigma-Aldrich, USA), in case cantharidin was added. Plants were grown in the long day conditions (16 h light/8 h dark) at 22ºC. For phosphatase inhibitor treatment, 1 mM cantharidin (Sigma-Aldrich, USA) diluted in dimethyl sulfoxide was added to the media to the final concentrations of 1/3/5/10 µM. For the mock treatment, dimethyl sulfoxide was added to the media in the amount corresponding to the amount of dimethyl sulfoxide in 10 µM cantharidin treatments. The experimental setup, specifically the cantharidin concentration and planting seeds directly onto media containing cantharidin, was based on previous studies (Deruere *et al.* 1999; Shin *et al.* 2005).

Generally, for the molecular biology techniques, standard protocols (Green *et al.* 2012) and manufacturer instructions were followed. Mutant lines were genotyped using primers listed in **Table 6**, and the Phire Plant Direct Kit (Thermo Fisher Scientific, USA). Briefly, plant tissue was resuspended in the dilution buffer (Phire Plant Direct Kit) and after incubation for 30 min at -20ºC, this was used as a template in a PCR reaction (1 µl sample, 0.4 µl Phire Hot Start II DNA Polymerase, 1× dedicated buffer, 0.5 µM of each primer; final volume 20 µl). The experimental setup was: initial denaturation at 98ºC for 3 min; 40× cycle of denaturation at 98ºC for 5 s, annealing at the temperature specific for the primer pair for 5 s and extension at 72ºC for 40 s; final extension at 72ºC for 5 min. The annealing temperature for specific primer pairs was set at 68ºC for RP+LP primer pairs, 65ºC for RP+LB primer pairs, and 64ºC for genotyping *ton2-5*; these values were based on the instructions from the manufacturer. In the case of the ethyl methane sulfonate-induced mutant *ton2-5*, PCR genotyping was followed by digestion with *Pst*I, because the point mutation disrupts the restriction site for *Pst*I. The enzymatic digestion

of the PCR product (5 µl sample, 1 U *Pst*I, 1× buffer O (Thermo Fisher Scientific, USA); final volume 20 µl) was performed by incubation at 37ºC for 1 h. Results from the PCR and enzymatic digestion were visualized by 1% agarose electrophoresis in 1× TAE buffer (40 mM Tris-HCl, 20 mM acetic acid, 1 mM EDTA with pH 8) with the equipment and source from the Bio-Rad (USA). The DNA stained with the Midori Green Advance DNA stain (Nippon Genetics, Japan) was visualized by the Gel Doc™ EZ Imager (Bio-Rad, USA) and the software Image Lab (Bio-Rad, USA).

Young seedlings and embryos of sterile mutants, specifically *yda, ΔNyda* and *ton2-5,* were selected based on previously described phenotypes (Camilleri *et al.* 2002; Bergmann *et al.* 2004; Lukowitz *et al.* 2004). Similarly, the dominant negative *mpk6AEF* plants were selected based on their stomatal clustering phenotype (Bush and Krysan 2007). Double mutants and crosses between mutant and marker lines were analyzed as homozygous mutants in the F3 generation.

Table 6: **List of primers used in this study.**

Genotyping primers	
hsp90.1 LP	5'-TCAGACCCAACTTCAACATCC-3'
hsp90.1 RP	5'-TGACCAATGACTGGGAAGATC-3'
hsp90.2 LP	5'-TCCATAGGTTATTGCACTGGC-3'
hsp90.2 RP	5'-CACAAAAAGCTTCGCAACTTC-3'
yda Ler F1	5'-CGACGACGTGATGAGATTGTG-3'
yda Ler R1	5'-GCTGAGTAGCCATATCTCCACC-3'
yda APR Rv2	5'-CCACCGGAGACATACTCCAG-3'
yda APR Fw2	5'-CACGCTGTCAGAGTTTTGCAG-3'
yda APR Rv2	5'-CCACCGGAGACATACTCCAG-3'
yda APR Rv3	5'-TAGAAGCTCGAGGTGCATGC-3'
mpk3-1 LP	5'-ATTTTTGTCAACAATGGCCTG-3'
mpk3-1 RP	5'-TCTGCCTTTTCACGGAATATG-3'
*mpk*6-2 LP	5'- CTCTGGCTCATCGCTTATGTC-3'
*mpk*6-2 RP	5'-ATCTATGTTGGCGTTTGCAAC -3'
rcn1-6 LP	5'-GGCCAGCCAGTTAGGTATAGG-3'
rcn1-6 RP	5'-AAACATAGCCACACGCATTTC-3'
ton2-5 Fw	5'-AGTCGTCCTACCTGCAAATGT-3'
ton2-5 Rv	5'-ACAAAATAGCACACCCACCA-3'
LBb1.3	5'-ATTTTGCCGATTTCGGAAC-3'
Primers for cloning	
RCN1 Fw EcoRI	5'-AAAAgaattcATGGCTATGGTAGATGAACC-3'
RCN1_Rv_BamHI	5'-TTTTggatccTCAGGATTGTGCTGCTGT-3'

2.2. Methods

2.2.1. Yeast two-hybrid assay

For yeast two-hybrid assay, the Matchmaker GAL4 two-hybrid system was used (Clontech, USA). The strategy for cloning was planned either in A plasmid Editor software (M. Wayne Davis; available at jorgensen.biology.utah.edu/wayned/ape/) or the SnapGene® software (from GSL Biotech; available at snapgene.com), which was also used for generating **Fig. 8-10**. The sequence of *RCN1* cDNA was accessed from The Arabidopsis Information Resource (At1g25490; Berardini *et al.* 2015).

The RNA was extracted by phenol-chloroform extraction from the tissue from the wild type plants. Briefly, homogenized plant tissues were mixed with 1:1 RNA-extraction buffer (100 mM Tris-HCl pH 9.5, 0.5% (w/v) SDS):phenol while working in liquid nitrogen. Samples were centrifuged repeatedly ($16000\times$ g; 10 min) and the supernatant was transferred first to 25:24:1 phenol:chloroform:isoamyl alcohol, then to 24:1 chloroform:isoamyl alcohol, and finally to absolute ethanol supplemented with 130 mM CH_3COONa. After overnight incubation at -80ºC, samples were centrifuged ($16000\times$ g; 40 min; 4ºC), and the dried pellet was diluted in RNAse free water. The sample was treated with DNAse I (50 µl sample, 4 U DNAse I (Thermo Fisher Scientific, USA), 1 U rRNasin® (Promega, USA), $1\times$ DNAse I-dedicated buffer; final volume 100 µl) at 37ºC for 1 h. Then, the phenol-chloroform extraction was repeated. The quality of the RNA was assessed by 1% agarose electrophoresis and the quantity was measured by the NanoDrop Lite spectrophotometer (Thermo Fisher Scientific, USA). By reverse transcription (1.5 µg RNA, 160 U M-MLV RT (Promega, USA), 20 U rRNasin®, 5 µM oligo(dT), 0.5 mM dNTPs; final volume 20 µl; incubated 1 h at 42ºC), the cDNA was generated.

Using the primers listed in **Table 6**, the cDNA of RCN1 was first amplified using the iProof™ High-Fidelity DNA Polymerase (Bio-Rad, USA). The template (1 µl) was mixed with other reagents (1 U High-Fidelity DNA Polymerase, 0.5 µM of each primer, 200 µM dNTPs, $1\times$ dedicated buffer; final volume 50 µl) and the reaction was set up as follows: initial denaturation at 98ºC for 30 s; $30\times$ cycle of denaturation at 98ºC for 10 s, 64ºC for 20 s and extension at 72ºC for 60 s; final extension at 72ºC for 10 s. The PCR product was extended by Taq polymerase (2.5 U Taq polymerase (Thermo Fisher Scientific, USA); incubated at 95ºC for 5 min, then 72ºC for 10 min). Following the

agarose electrophoresis, the PCR product was excised and purified using the NucleoSpin® Gel and PCR Clean-up (Macherey-Nagel, Germany).

The purified PCR product was cloned into the pGEM®-T Easy (Promega, USA) by ligation (90 ng PCR product, 50 ng pGEM®-T Easy vector, 3 U T4 DNA ligase, 1× dedicated buffer; final volume 10 μl). The ligation product was used for the transformation of chemocompetent *Escherichia coli* Top10 cells (Green *et al.* 2012). From the selected clones, plasmid DNA was extracted via the QIAprep® Spin Miniprep Kit (Qiagen, Germany). The region of interest was excised using *Eco*RI and *Bam*HI (1 μg plasmid DNA; 1 U *Eco*RI, 2 U *Bam*HI, 2× Tango buffer (Thermo Fisher Scientific, USA); final volume 30 μl); and similar reaction was used to prepare the *pGADT7* vector (**Fig. 8**) for the ligation. The products of restrictions were subjected to agarose electrophoresis, then the regions corresponding to the insert and vector, were excised,
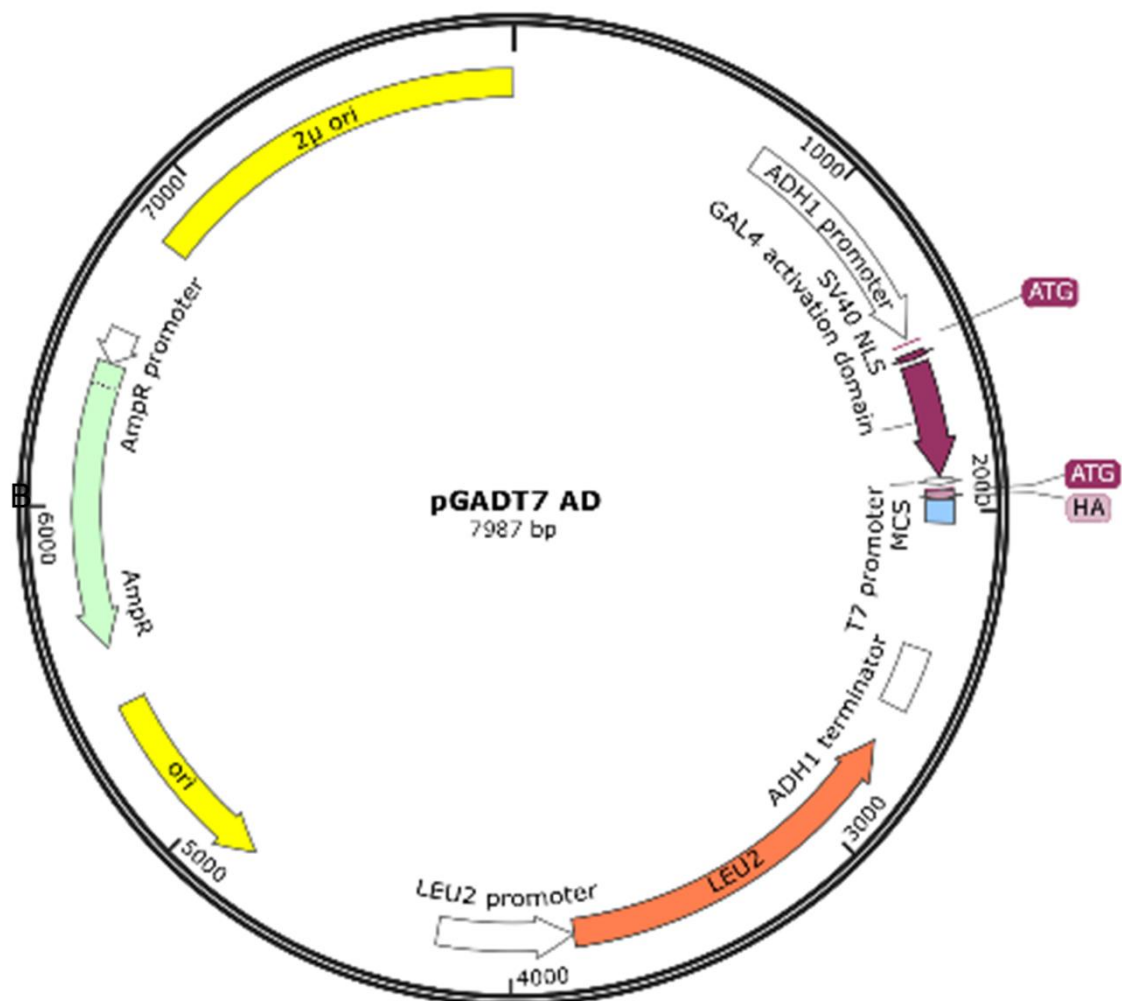
Figure. 8. Plasmid map of pGADT7. The SnapGene software was used for the visualization of a plasmid map provided by Clontech (USA).

purified and used for ligation (60 ng insert, 60 ng pGADT7; 5 U T4 DNA ligase, 1× dedicated buffer (Thermo Fisher Scientific, USA), 5% (v/v) polyethylene glycol). The product of ligation was used for the transformation of chemocompetent cells. Plasmid DNA was isolated from clones growing on selection media and restriction analysis confirmed the successful preparation of pGADT7-RCN1 (**Fig. 9, 10**). The other plasmids used for the yeast two-hybrid assay were prepared similarly by Despina Samakovli, Ivan Luptovčiak and Tereza Tichá.

The yeast strain SG335 was used to prepare yeast cotransformants and they were tested on Syntetic Dropout$^{-Leu,Trp}$ (SD$^{-Leu,Trp}$) medium (Sigma-Aldrich, USA). Interactions were tested on SD$^{-Leu,Trp,His}$; SD$^{-Leu,Trp,His}$ supplemented with 10 mM 3-amino-1,2,4-triazole (Sigma-Aldrich, USA); or SD$^{-Leu,Trp,His,Ade}$.
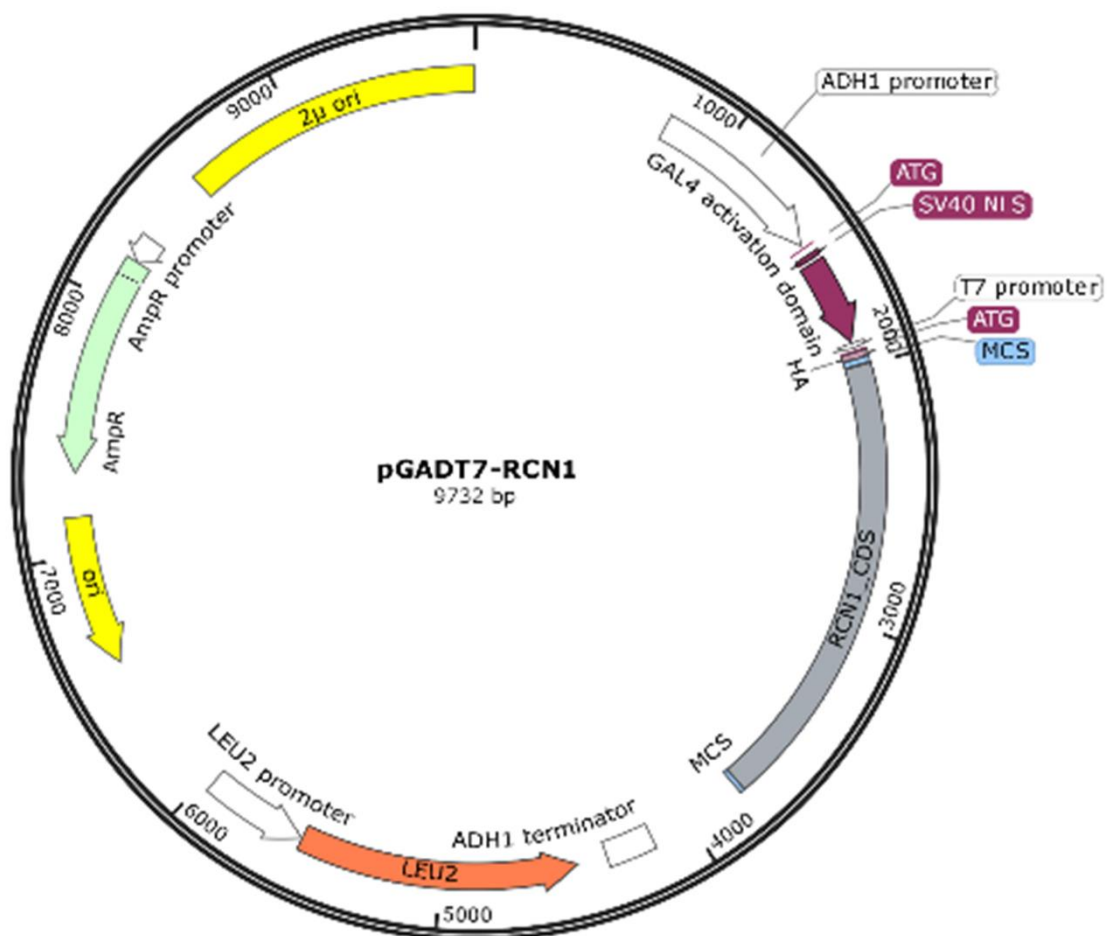
Figure 9. Plasmid map of pGADT7-RCN1. The SnapGene software was used for the construction of a plasmid map.
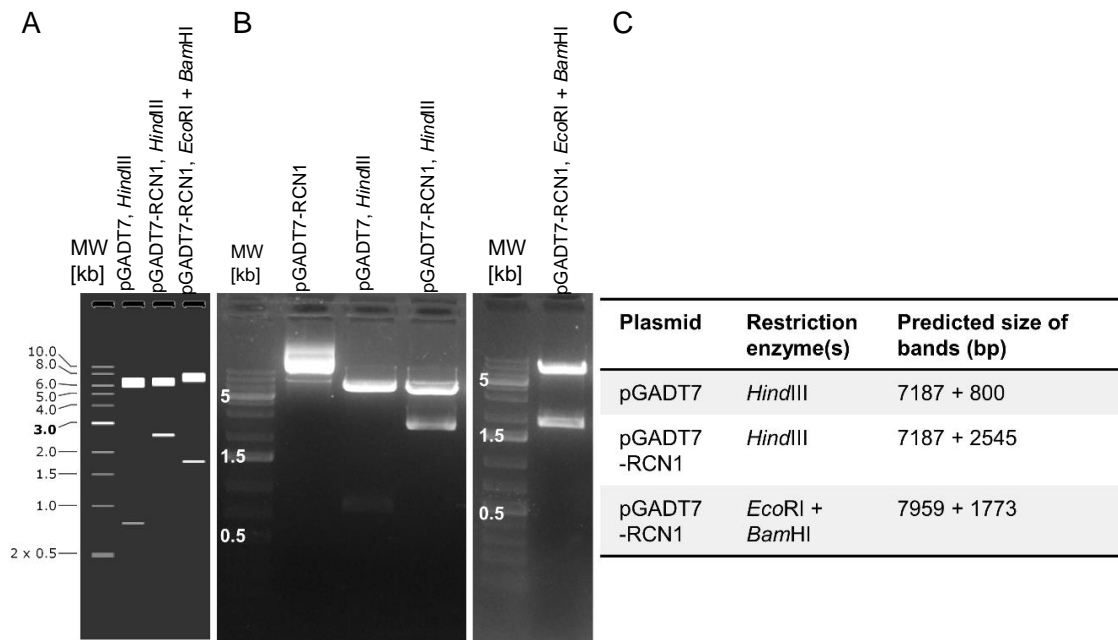
Figure 10. Confirmation of clonning the pGADT7-RCN1. (A) *In silico* prediction of electrophoresis of plasmids digested by restriction enzymes. (B) Results from electrophoresis of plasmids digested by the indicated restriction enzymes. For molecular weight (MW) estimation was used GeneRuler 1 kb Plus DNA Ladder (Thermo Fisher Scientific, USA). (C) Table lists predicted sizes of bands upon digestion of plasmids by restriction enzymes. (A,C) The SnapGene software was used for the *in silico* analysis.

2.2.2. Protein immunodetection

Proteins were extracted using the extraction buffer (50 mM HEPES, pH 7.5, 75 mM NaCl, 1 mM EGTA, 1 mM $MgCl_2$, 1 mM NaF, 10% (v/v) glycerol, 50 mM dithiothreitol) supplemented with cOmplete™ and PhosSTOP™ (Roche, Switzerland) and their concentration was measured via Bradford assay using bovine serum albumin (BSA) as a standard. Denaturated proteins were loaded on the Mini PROTEAN® 10% TGX™ Stain-Free gels (Bio-Rad, USA) containing 0.1% (w/v) sodium dodecyl sulfate. Afterwards, proteins were transferred on polyvinyl difluoride membranes. After blocking with 5% (w/v) BSA in Tween 20-supplemented Tris-buffered saline (TBS-T; 100 mM Tris-HCl, pH 7.4, 1.5 mM NaCl, 0,1% (v/v) Tween 20) overnight, the membranes were incubated with primary antibodies appropriately diluted in TBS-T: polyclonal rabbit pTEpY (anti-phospho-Thr-Glu-phospho-Tyr; Cell Signaling Technology, Czech Republic) diluted 1:1000, monoclonal rabbit anti-MPK3 (Sigma-Aldrich, USA) diluted 1:3000, monoclonal rabbit anti-MPK6 (Sigma-Aldrich, USA) diluted 1:15000, monoclonal mouse anti-β-tubulin (Sigma-Aldrich, USA) diluted 1:1000 in 5% BSA in TBS-T during overnight incubation. The secondary antibodies, horseradish

peroxidase-conjugated goat anti-rabbit or anti-mouse IgG antibody (Santa Cruz Biotechnology, USA), were diluted 1:5000 and incubation was for 2 h. For chemiluminescence detection, Clarity™ Western ECL kit (Bio-Rad, USA) and the ChemiDoc™ MP imaging system (Bio-Rad, USA) were used and the following densitometric analysis was performed in the software Image Lab (Bio-Rad, USA).

The signal intensities measured by the densitometric analysis were used for calculating the relative protein levels:

$$\text{relative level of MPK} = \frac{\text{MPK}_{\text{rcn1-6}}/\text{MPK}_{\text{Col-0}}}{\text{TUB}_{\text{rcn1-6}}/\text{TUB}_{\text{Col-0}}}$$

where "MPK" refers to signal intensity measured for either MPK3 or MPK6 and "TUB" refers to signal intensity measured for the tubulin. The formula for calculating the relative levels of phosphorylated proteins was:

$$\text{relative level of pMPK} = \frac{\text{pMPK}_{\text{rcn1-6}}/\text{pMPK}_{\text{Col-0}}}{\text{TUB}_{\text{rcn1-6}}/\text{TUB}_{\text{Col-0}}} \times \frac{\text{MPK}_{\text{rcn1-6}}/\text{MPK}_{\text{Col-0}}}{\text{TUB}_{\text{rcn1-6}}/\text{TUB}_{\text{Col-0}}}$$

where "pMPK" refers to signal intensity measured for either pMPK3 or pMPK6, "MPK" refers to signal intensity measured for either MPK3 or MPK6 and "TUB" refers to signal intensity measured for the tubulin. Relative protein levels and relative levels of phosphorylated proteins were first calculated separately for each membrane, then the values were averaged.

2.2.3. Microscopic analysis

2.2.3.1. Live cell imaging

The marker lines expressing the respective chimeric fluorescent protein were selected on the stereo microscope M165 FC (Leica, Germany) or, in the case of eGFP-MAP65-3, on the epifluorescent microscope Imager M2 (Carl Zeiss, Germany). Macroscopic images of seedlings were taken on the stereo microscope.

For analyzing *DR5::GFP* (Friml *et al.* 2003) and *WOX8::NLS:YFP* (Breuninger *et al.* 2008) in reproductive tissues, ovules and seeds were extracted into the water onto a slide and observed in the epifluorescent microscope. The *DR5::GFP* marker line was also examined in roots of 5 days after germination (DAG) old seedlings, which were stained with 5 μM FM4-64 staining (Thermo Fisher Scientific, USA) for 10 min, and observed under confocal laser scanning microscope (CLSM) LSM 710 (Carl Zeiss,

Germany). The setup of CLSM was: 10×/0.30 NA Plan-Neofluar or 20×/0.80 NA Plan-Apochromat objectives, 488 nm excitation laser line and pinhole opened at 1 AU; detected wavelengths 493-579 nm and 622-759 nm; photomultiplier tube detector.

The visualization of TUA6-GFP, eGFP-MAP65-2, tagRFP-MAP65-2, and eGFP-MAP65-3 was performed on either the Axio Observer LSM 880 with Airyscan (ACLSM; Carl Zeiss, Germany) or the Axio Observer Z.1 equipped with the Elyra PS.1 superresolution system supporting the structured illumination microscopy (SIM) module (Carl Zeiss, Germany). For these experiments, 3-4 DAG old seedlings were first selected according to the signal expression, then they were transferred onto a slide into liquid half-strength Murashige Skoog medium.

The setup of the ACLSM and SIM platforms was: 40×/1.40 NA, 63×/1.40 NA, 100×/1.46 NA or 100×/1.57 NA, oil-immersion, Plan-Apochromat objectives with appropriate oil (Immersol 518F with the refractive index of 1.518, and Immersol HI with the refractive index of 1.66 for 100×/1.57 NA objective, respectively; Carl Zeiss, Germany). Samples were illuminated with a 488 nm laser line for GFP and a 561 nm laser line for tagRFP. While working with the super-resolution mode of the ACLSM platform, emission was collected via beam splitter and emission filters BP420-480+BP495-550 for GFP detection and BP495-550+LP570 for tagRFP; the signal was detected by a 32 GaAsP (gallium arsenide phosphide) detector with a fully opened pinhole. Splitter beams and emission filters used in the SIM platform were BP495-575+LP750 for GFP and BP570-620+LP750 for tagRFP. The SIM platform was equipped with a PCO.Edge 5.5 scientific complementary metal-oxide-semiconductor camera (PCO AG, Germany). For the setup for SIM, either five rotations and five phase steps or three rotations and five phase steps were used when acquiring time lapsed images (Komis *et al.* 2014).

To prepare samples for the light-sheet Axio Observer SPIM (Carl Zeiss, Germany), 2-3 DAG old plants expressing both GFP and tagRFP were mounted into solidified culture medium within the fluorinated ethylene propylene tubes (Wolf-Technik, Germany) according to the "open system" protocol (Ovečka *et al.* 2015). The sample was inserted into the observation chamber, which was filled with a sterile liquid medium, in a way enabling imaging of the root in the block of the solidified medium outside the tube and during a constant temperature of 22ºC. For image

acquisition the following setup was used: W Plan-Apochromat 40x/1.0 NA objective and two light-sheet fluorescence microscopy (LSFM) 10x/0.2 NA illumination objectives; the excitation laser lines 488 and 561 nm; the detection wavelength 498 and 571 nm; the PCO.Edge 5.5 complementary metal-oxide-semiconductor camera (PCO AG, Germany).

2.2.3.2. Microscopy of fixed samples

For Nomarski microscopy, siliques were fixed in 3:1 (v/v) ethanol:acetic acid solution, then the seeds were mounted in chloral hydrate solution (8 g chloral hydrate, 1 ml glycerol, 3 ml water). Samples were observed in the epifluorescent microscope.

Modified pseudo-Schiff propidium iodide staining was performed as described previously (Truernit *et al.* 2008). Briefly, siliques were slit open at one side and fixed (50% (v/v) methanol, 10% (v/v) acetic acid). After incubation in 1% (w/v) SDS and 0.2 M NaOH, samples were discoloured in 10% (v/v) NaOCl (Sigma-Aldrich, USA). Before the propidium iodide staining, samples were pre-treated with 1% (w/v) periodic acid. Finally, staining was achieved with Schiff reagent solution (100 mM $Na_2S_2O_5$, 0.15 M HCl, 100 µg ml^{-1} propidium iodide). Samples were mounted in chloral hydrate, then observed on CLSM. The setup was similar as described above with the 40x/1.4 NA Plan-Apochromat, oil immersion objective; 514 nm excitation laser line, and detection of the wavelength range 566-719 nm.

The root wholemount immunolocalization was based on previously published protocols (Sauer *et al.* 2006; Šamajová *et al.* 2014) with notable changes. Seedlings were fixed in 4% (v/v) formaldehyde (Polysciences, USA) in microtubule stabilizing buffer (MTSB; 25 mM K-PIPES, pH 6.8; 2.5 mM EGTA; 2.5 mM $MgSO_4 \times 7H_2O$) supplemented with 0.01% (v/v) Triton X-100) and incubated for 1 h at room temperature. Next, cell walls were digested using enzyme solution (2% (w/v) Cellulase Onozuka R10, 0.5% (w/v) Cellulase Onozuka RS, 1% (w/v) Macerozyme R10, 1% (w/v) Meicelase, 0.1% (w/v) Pectolyase Y23; all enzymes were from Desert Biologicals, USA) for 30 min at room temperature. After washing with MTSB and phosphate buffered saline (PBS; pH 7.4), samples were incubated in the permeabilization solution (10% (v/v) dimethyl sulfoxide, 2% (v/v) Nonidet P40, 0.01% (v/v) Triton X-100 in PBS, pH 7.4) for 15 min and washed in PBS afterwards. Blocking was performed overnight in blocking solution (3% (w/v) BSA and 0.5% (w/v) polyacetylated BSA in PBS). Subsequently,

samples were incubated in primary antibody: rat monoclonal anti-α tubulin antibody (Bio-Rad, USA) diluted 1:300, Atto 488-conjugated alpaca anti-GFP nanobody (Chromotek, Germany) diluted 1:100, or rabbit polyclonal anti-RFP antibody (Thermo Fisher Scientific, USA) diluted 1:100; in blocking solution at room temperature overnight. Next day, samples were extensively washed with PBS, then blocked with blocking solution for 1 h and incubated with secondary antibody: Alexa Fluor 647-conjugated goat anti-rat antibody (Thermo Fisher Scienticific, USA), or Alexa Fluor 546-conjugated goat anti-rabbit antibody (Thermo Fisher Scienticific, USA) diluted 1:500; in blocking solution overnight at 37°C (this step was omitted when using the anti-GFP nanobody). After washing in PBS, samples were counterstained with DAPI (4',6-diamidino-2-phenylindole dihydrochloride) and mounted on slides using the mounting media (90% (v/v) glycerol with 100 mM tris(hydroxymethyl)aminomethane-HCl, pH 8.8; supplemented with 0.1% (w/v) paraphenylenediamine). Samples were observed on the SIM platform using settings described above; with laser lines 405 nm for DAPI, 488 nm for Atto 488, 561 nm for Alexa Fluor 546, and 642 nm for Alexa Fluor 647; and emission filters BP420-480+LP750 for DAPI, BP495-550+LP750 for Atto 488, BP570-620+LP750 for Alexa Fluor 546, and LP655 for Alexa Fluor 647.

2.2.4. Image processing and data analysis

All microscopic data were reconstructed and analysed on appropriate Zeiss Zen software (Carl Zeiss, Germany), either Blue or Black version, depending on the microscopic platform. Zen software was also used for suspensor length measurement, fluorescence intensity profiling and for generating kymographs (Komis *et al.* 2014). Root length, the distance between the root tip and first root hair, angles and distances in kymographs were measured in ImageJ (Schneider *et al.* 2012).

For measuring the full-width at half maximum (FWHM), the profile measurements were first normalized based on the minimum-maximum scaling according to the formula:

$$X' = \frac{X - X_{min}}{X_{max} - X_{min}}$$

where X' is the normalized value of the measured value X, X_{min} and X_{max} are the minimum and maximum values within the dataset of the profile intensity measurement. Under the

condition of the Gaussian distribution of the normalized profile intensity measurement, the value of FWHM is equal to 2.3555 SD. However, the ImageJ was used to measure the FWHM in the graphs presenting the normalized signal intensity plotted against the distance.

Images of propidium-iodide stained embryos had their colour inverted in ImageJ.

The parameters describing MAP65-2 dynamics were calculated as described previously (Smal *et al.* 2010); growth and shrinkage rates were established by correcting the tangent of measured angles (corresponding to either growth or shrinkage) with the pixel size and the frame rate specific for each acquisition. Specifically, the formula used for calculating the growth rates was:

$G = \tan_{\theta} \times \text{pixel size} \times \text{fps}$

where $\tan_{\theta}$ is tangential of the growth slope, pixel size is in µm, and fps is the frame rate of the acquisition (frames×sec^{-1}). Similarly, the shrinkage rate was calculated as:

$S = \tan_{\varphi} \times \text{pixel size} \times \text{fps}$

where $\tan_{\varphi}$ is tangential of the shrinkage slope, pixel size is in µm, and fps is the frame rate of the acquisition (frames×sec^{-1}). The rescue and catastrophe rates were calculated by dividing the sum of shrinkage/growth onset events observed by the total amount of time spent in growth or shrinkage phases, respectively (Kapoor *et al.* 2019). The equation for the catastrophe frequency is:

$$f_{cat} = \frac{N_{cat}}{\Sigma t_{growth}}$$

where the N_{cat} is the total number of catastrophe events and Σt_{growth} is the total time spent in growth, regarding all the growth events considered. The rescue frequency was calculated according to the following equation:

$$f_{res} = \frac{N_{res}}{\Sigma t_{shrinkage}}$$

where N_{res} is the total number of rescue events and $\Sigma t_{shrinkage}$ is the total time spent in shrinkage, regarding all the shrinkage events considered.

2.2.5. *In silico* and statistical analysis

In silico analysis were used for several schemes presented in **Fig. 2-4**. The amino acid sequences of Arabidopsis MAP65s and their homologues were obtained from the UniProtKB database (The UniProt Consortium 2019). The multisite alignment was calculated both by the Clustal Omega (Madeira *et al.* 2019) and the COBALT (Papadopoulos and Agarwala 2007) using the default settings. The subsequent analysis was performed in the Jalview (version 2.11; Waterhouse *et al.* 2009) and the Multiple Sequence Alignment Viewer (version 1.13.1.; Madeira *et al.* 2019). The position of domains within Arabidopsis MAP65s and the yeast Ase1p was determined based on the multisite sequence alignment, the information on the localization of domains in the PRC1, and the predicted localization of tubulin-binding sites presented in the UniProtKB.

The speculative network of protein kinases and phosphatases targeting microtubule associated proteins and the cortical division zone markers (**Fig. 5**) is constructed from the information presented in previous studies, which are cited accordingly in the text of Chapter 1, *in vitro* interaction studies recorded in BioGRID (Oughtred *et al.* 2019) or *in silico* predictions listen in STRING (Szklarczyk *et al.* 2015).

For the statistical analysis, the software STATISTICA (version 13.4.0.14; Statsoft, USA) was used. Generally, all datasets were first subjected to Shapiro-Wilk W test and Levene's test to test the normality and homogeneity. Based on their results, appropriate tests were chosen. For pair-wise comparisons was used Mann-Whitney U test. For comparison of three or more categories were employed ANOVA or Welch´s ANOVA followed by Tukey's test of honest significant difference corrected for unequal sample size, or Scheffé's test; or Kruskal-Wallis test. Statistical significance was determined based on the calculated p-values. In the case of datasets with a high number of measurements, p-values were subjected to Holm-Bonferroni correction in the Microsoft Excel Workbook (Gaetano 2013).

3. Results

3.1. PP2A affects the function of MPK3 and MPK6 in plant development

3.1.1. Loss-of-function *mpk3, mpk6* mutants are less sensitive to phosphatase inhibitor treatment

Even though both the YDA-MPK pathway and PP2A are functionally implicated in the cell division plane orientation, it has remained unclear whether these two regulatory elements interact with each other. To investigate the putative connection between them, loss-of-function *mpk3* and *mpk6* mutants were subjected to the phosphatase inhibitor treatment (**Fig. 11**). For the treatment was chosen cantharidin, an inhibitor of both PP1 and PP2A (Honkanen 1993), which is known to bind to PP2A (Li and Casida 1992) and it has higher selectivity towards PP2A (Li *et al.* 2010b) compared to other phosphatase inhibitors. Moreover, it has been previously shown in plants that especially at lower concentrations (in the range from 3 to 10 µM), cantharidin primarily targets the regulatory activity of RCN1 (Deruere *et al.* 1999; Shin *et al.* 2005) and at the concentration of 3 µM, it phenocopies *rcn1* loss-of-function mutant in cell elongation processes leading to shorter hypocotyls and roots (Deruere *et al.* 1999).
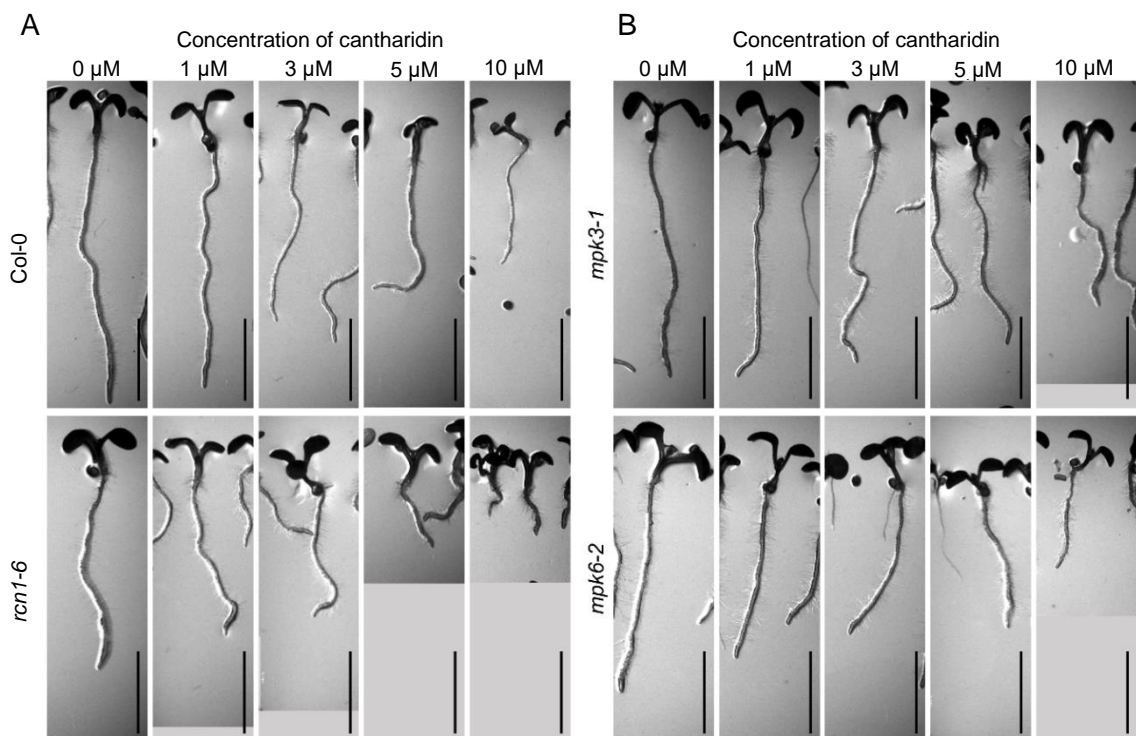
Figure 11. *mpk3, mpk6* mutants are less sensitive to phosphatase inhibitor cantharidin.
Representative pictures of 5 days old seedlings of Col-0, *rcn1-6* (A) and *mpk3-1, mpk6-2* (B) grown on media with the indicated concentration of cantharidin. Scale bars, 5 mm.

In line with previously published results, the cantharidin treatment of wild type plants leads to decreased root length (Deruere *et al.* 1999; **Fig. 11A, 12A**) and a smaller distance between root tip and first root hair (**Fig. 13A**). Moreover, the inhibitory effects of cantharidin on the root length and the distance between root tip and first root hair were more pronounced in the *rcn1-6* mutant (**Fig. 11A**) and with the increasing concentrations of cantharidin, the changes were more progressive (**Fig. 12B, 13B**). This confirms the sensitivity of the *rcn1-6* mutant towards cantharidin.

The distance between the root tip and first root hair in wild type seedlings grown in either 3 or 5 μM cantharidin was comparable to the same parameter in the *rcn1-6* seedlings grown on control medium (in both cases, p=1.0000; **Table S2**), leading to the assumption that this concentration of cantharidin leads to the phenocopy of *rcn1-6.* Moreover, the root length of *rcn1-6* grown on control medium was shorter than that of wild type seedlings grown on 5 μM cantharidin, yet longer than wild type seedlings grown on 10 μM cantharidin, suggesting that concentrations between 5 and 10 μM of cantharidin lead to phenocopy of *rcn1-6* in root length.
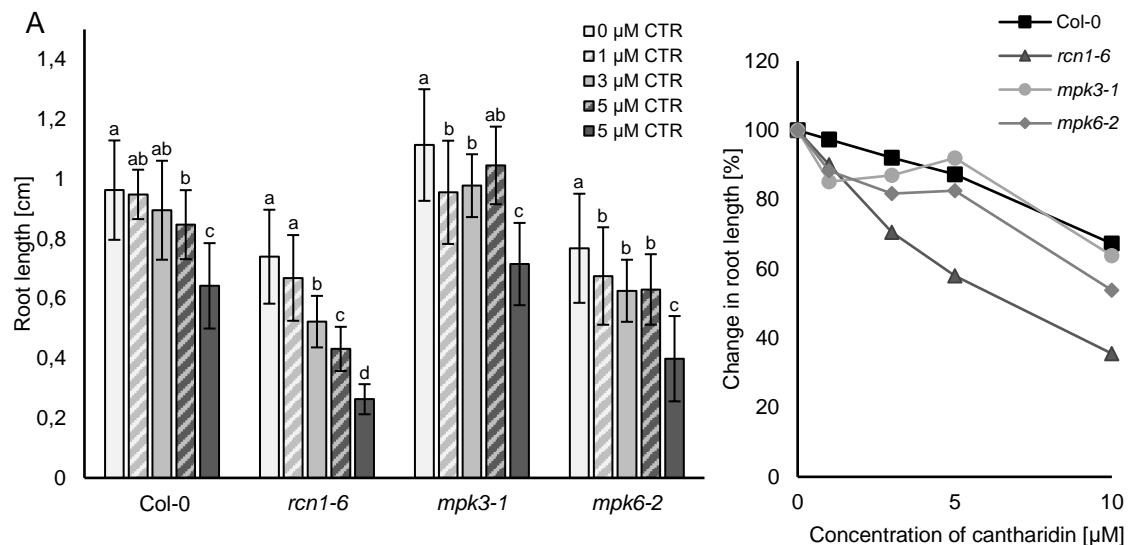
Figure 12. The effects of cantharidin treatment on root length in *rcn1, mpk3, mpk6* mutants. Plants of the indicated genotypes were grown on media with different concentration of catharadin (CTR; 0/1/3/5/10 μM) up to 5 days after germination. (A) Root length measurements presented as mean±SD (N≥120, three technical repetitions; two-way ANOVA followed by Scheffé's test and Holm-Bonferroni correction; statistical comparison is shown within groups sharing the same genotype; letters in the graph are shared by groups without statistically significant differences at the 0.001 probability level; results are in **Table S1**). (B) Change in the root length relative to the root length in media without cantharidin.
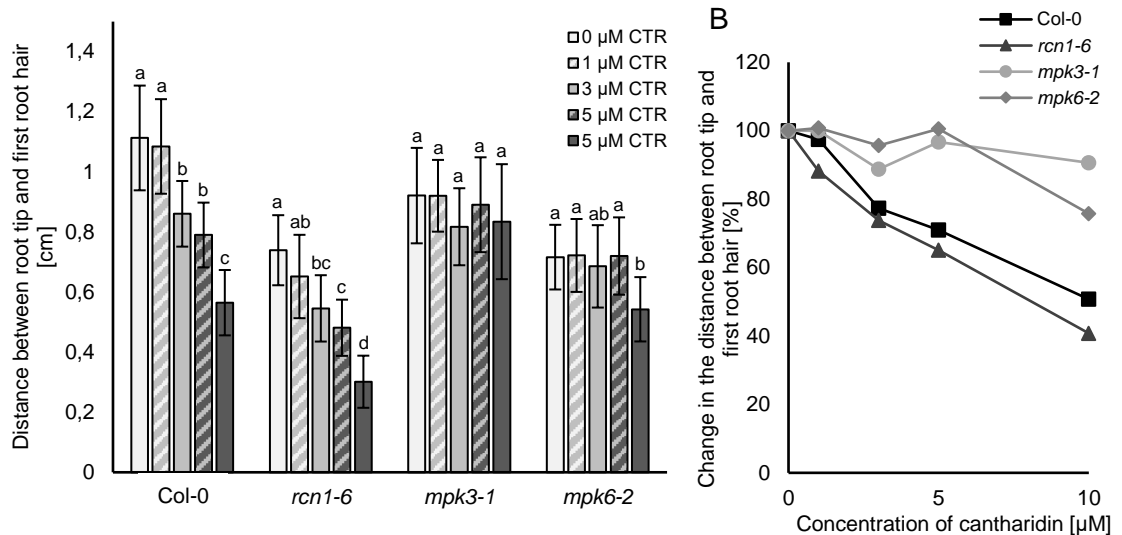
Figure 13. The effects of cantharidin treatment on the distance between the root tip and the first root hair in *rcn1, mpk3, mpk6* mutants. Plants of the indicated genotypes were grown on media with different concentration of cataradin (CTR; 0/1/3/5/10 µM) up to 5 days after germination. (A) Measurements of distances between the root tip and the first root hair presented as mean±SD (N≥50, three technical repetitions; two-way ANOVA followed by Scheffé's test and Holm-Bonferroni correction; statistical comparison is shown within groups sharing the same genotype; letters in the graph are shared by groups without statistically significant differences at the 0.001 probability level; results are in **Table S2**. (B) Change in the distance between the root tip and the first root hair relative to the same parameter in media without cantharidin.

The growth of *mpk3-1* and *mpk6-2* mutants was visibly affected by the presence of cantharidin in media (**Fig. 11B**) with the most pronounced phenotype observed at the concentration of 10 µM. Nevertheless, the *mpk3-1* and *mpk6-2* mutants were less sensitive to cantharidin at lower concentrations. Decreased sensitivity of *mpk3-1* and *mpk6-2* mutants in lower concentrations of cantharidin is supported by the observation of smaller changes in both the root length (**Fig. 12**) and the distances between root tip and first root hair (**Fig. 13**). Although the root length was decreased in *mpk3-1* and *mpk6-2* mutants in concentrations ranging from 1 to 5 µM, partial rescue in this trait was observed for *mpk3-1* at 5 µM concentration of cantharidin (**Fig. 12A**). Regarding the distance between the root tip and first root hair, both *mpk3-1* and *mpk6-2* mutants appeared to be insensitive to the concentrations of cantharidin (ranging from 1 to 5 µM; **Fig. 13A**).

Conclusively, the root growth of *mpk3-1* and *mpk6-2* mutants is less affected by lower doses of cantharidin compared to wild type seedlings. Cantharidin is a phosphatase inhibitor exhibiting higher sensitivity to PP2A than to other phosphatases in low concentrations. Therefore, the observed partial insensitivity of *mpk3-1* and *mpk6-2* mutants to cantharidin suggests that PP2A and MPK3/6 might interact together in regulating cellular processes involved in root growth and development.

3.1.2. Genetic depletion of RCN1 partially rescues root tip phenotype in *mpk6*

To better describe the role of MPK3, MPK6 and RCN1 in the cell division plane orientation and how it affects the root development, *mpk3, mpk6,* and *rcn1-6* mutants were crossed with line stably expressing GFP under a synthetic auxin responsive promoter (*DR5::GFP;* Ulmasov *et al.* 1997; Friml *et al.* 2003), which has been extensively used to mark auxin maxima during Arabidopsis development (Friml *et al.* 2003; Thomann *et al.* 2009; Poulios and Vlachonasios 2018). Through the visualization by the *DR5::GFP* reporter, the auxin maxima can be observed in the primary root tip, specifically in the quiescent centre, columella initials and columella cells (**Fig. 14A**). The expression of *DR5::GFP* can be used to pinpoint the localization of the quiescent centre, which is especially important in mutants with distorted organization of root tips. Additionally, seedlings were stained with FM4-64, a lipophilic dye staining plasma membrane, to assess their root tip anatomy (**Fig. 14B,C**).

In both *mpk3-1* and *mpk6-2,* abnormal organization of root tip anatomy was observed (**Fig. 14D-I**). While the defects were milder in *mpk3-1*, with cell walls being tilted rather than completely shifted, *mpk6-2* had a strong phenotype with severe disorganization of cell

Figure 14. Abnormal development of root tip in *mpk3, mpk6, rcn1* mutants. Adapted from Samakovli *et al.* (unpublished). Primary root architecture and auxin maxima distribution in 5 days old seedlings of the wild type (A-C), *mpk3-1* (D-F), *mpk6-2* (G-I), *mpk6AEF* (J-L), *rcn1-6* (M-O), expressing *DR5::GFP* and stained with FM4-64. Images show either merged pictures from magenta and green channel depicting both *DR5::GFP* expression and FM4-64 staining (A,D,G,J,M) or only FM4-64 staining (B,E,H,K,N). Boxed areas in (B,E,H,K,N) are enlarged in (C,F,I,L,O). White stars mark cells of the quiescent center, white arrowheads point to the abnormally positioned cell walls. Scale bars, 20 μm.

divisions (**Fig. 14I**). The cells in the root tip of the *mpk6AEF* mutant were less organized compared to the wild type, but the root anatomy was affected to a much smaller extent than in either *mpk3-1* or *mpk6-2* (**Fig. 14J-L**). Similarly, the *rcn1-6* mutant was also compromised regarding the cell division plane orientation (**Fig. 14M-O**). These observations are in line with previously published results (Zapletalová and Šamajová, personal communication; Blakeslee *et al.* 2008; Müller *et al.* 2010; Floková 2016).

Since *mpk6-2* mutant had more severe phenotype than *mpk3-1*, and it has been suggested by previous work (Müller *et al.* 2010) that MPK6 is important for proper organization of formative cell divisions in the root, a question arose whether RCN1 and MPK6 are in a common pathway when establishing the cell division plane orientation during primary root development. Therefore, the *mpk6-2 rcn1-6* double mutant was created. Compared to the wild type (**Fig. 15A**) and the parent lines (**Fig. 15B,C**), *mpk6-2 rcn1-6* double mutant exhibited pleiotropic phenotype regarding the root tip anatomy, ranging from mild defects (**Fig. 15D,E**) to phenotype comparable with wild type (**Fig. 15F,G**). When compared with the original single mutants (**Fig. 15B,C**), it is apparent that despite the phenotype not being completely rescued, it is significantly improved. This finding supports the hypothesis that RCN1 and MPK6 belong to the same pathway regulating cell division plane orientation during the primary root development.
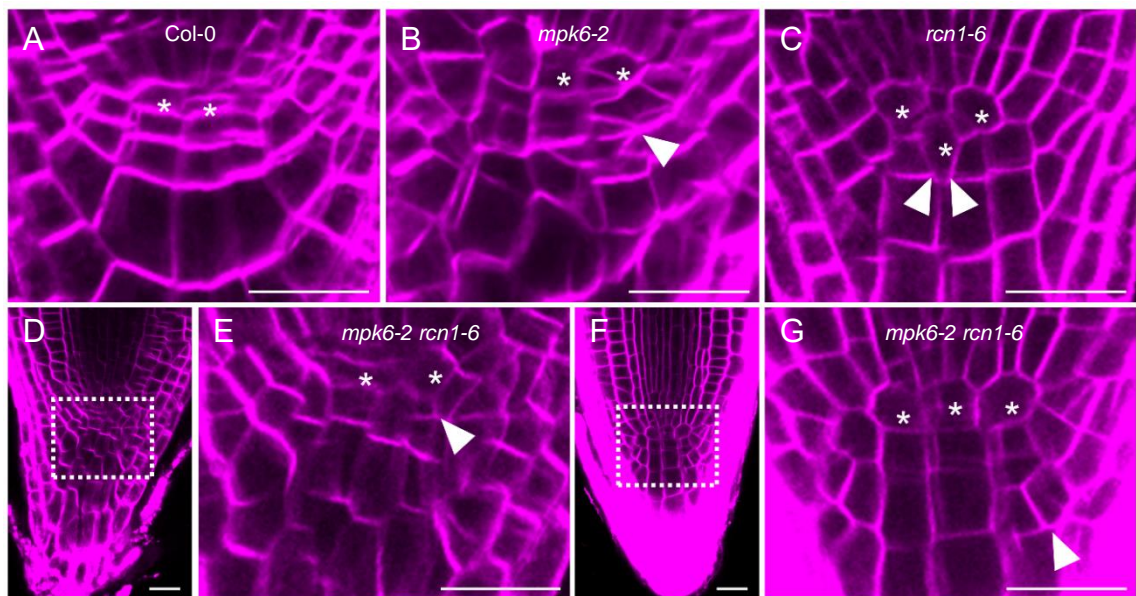
Figure 15. *RCN1* depletion partially rescues morphological defects in root tip of *mpk6* mutant. Primary root architecture in 5 days old seedlings stained with FM4-64. (A-C) Images of the root tip meristem area of the indicated genotypes presented previously in **Fig. 14C,I,O**. (D-G) Pictures show root tips of *mpk6-2 rcn1-6* double mutants with either obvious morphological defects (D,E) or less pronounced phenotype (F,G). Boxed areas in (D) and (F) are enlarged in (E) and (G), respectively. White stars mark cells of the quiescent centre, white arrowheads point to the abnormally positioned cell walls. Scale bars, 20 μm.

3.1.3. RCN1, a scaffolding subunit of PP2A, interacts with MPK3

Next, to investigate the possibility of RCN1 directly interacting with MPK3, MPK6 and YDA, an upstream regulator of both MPK3 and MPK6, yeast two-hybrid assays were performed. The aim was to test protein-protein interactions using RCN1 as a prey and MPK3, MPK6 and N-terminal domain of YDA as a prey (**Fig. 16**). The N-terminal domain of YDA was chosen for the experiments since expressing the entire YDA protein might negatively affect the viability of yeast. Moreover, the N-terminal domain has regulatory function and it contains multiple putative phosphorylation sites making it a target for reversible phosphorylation (Kim *et al.* 2012). The assay confirmed *in vitro* interaction between MPK3 and RCN1 and suggested a weak interaction between RCN1 and N-terminal YDA domain (**Fig. 16**). Unfortunately, the MPK6 fused to the binding domain proved to be autoactivating the binding domain resulting in false positive results for negative controls (**Fig. 16**), thus, the question regarding the *in vitro* interaction between RCN1 and MPK6 remained unaddressed.
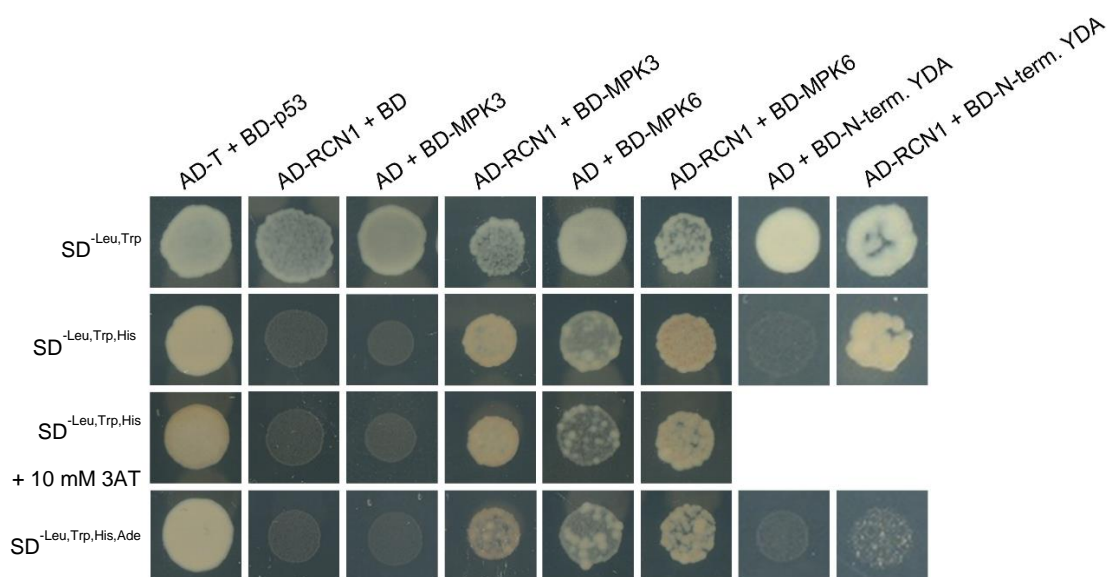
Figure 16. **RCN1 interacts *in vitro* with MPK3 and YDA.** Yeast two-hybrid assays using MPK3, MPK6 and N-terminal domain of YDA (N-term. YDA) as bait (BD, binding domain) and RCN1 as prey (AD, activation domain). The $SD^{-Leu,Trp}$ medium positively selects yeast cotransformants, while the $SD^{-Leu,Trp,\ His}$, $SD^{-Leu,Trp,\ His}$ supplemented with 3-aminotriazole (3AT), and $SD^{-Leu,Trp,\ His,Ade}$ are selective towards interaction between bait and prey with increasing stringency. The AD-T + BD-p53 combination serves as a positive control. Photos were taken 8 days after inoculation.

3.1.4. RCN1 affects phosphorylation levels of MPK3 and MPK6

The partial insensitivity of *mpk3* and *mpk6* to cantharidin treatment and the *in vitro* interaction between MPK3 and RCN1 suggested that RCN1, a scaffolding subunit of PP2A, might direct dephosphorylation of MPK3 and/or MPK6 by the PP2A. To test the effects of genetic depletion of RCN1 on phosphorylation levels of MPK3 and MPK6, protein immunodetection was performed using anti-MPK3 and anti-MPK6 antibodies as well as anti-pTEpY antibody detecting phosphorylated MPK3 (pMPK3) and pMPK6 (**Fig. 17, S1**). Since MPK3, MPK6 and RCN1 are differentially expressed throughout plant ontogenesis (Klepikova *et al.* 2016), proteins were extracted from different tissues, specifically young seedlings (14 DAG), rosettes (21 DAG), flowers and siliques. Proteins extracted from these tissues were used for semiquantitative analysis of relative protein and phosphorylation levels of MPK3 and MPK6 (**Fig. 17**).

The genetic depletion of RCN1 affected protein levels of both MPK3 and MPK6 only in specific tissues. The relative protein levels of MPK3 and MPK6 were increased in siliques of *rcn1-6* mutants (1.8930±0.6499 and 1.9617±0.6278, respectively; **Fig. 18A**). On the other hand, relative protein levels of MPK3 and MPK6 were detected
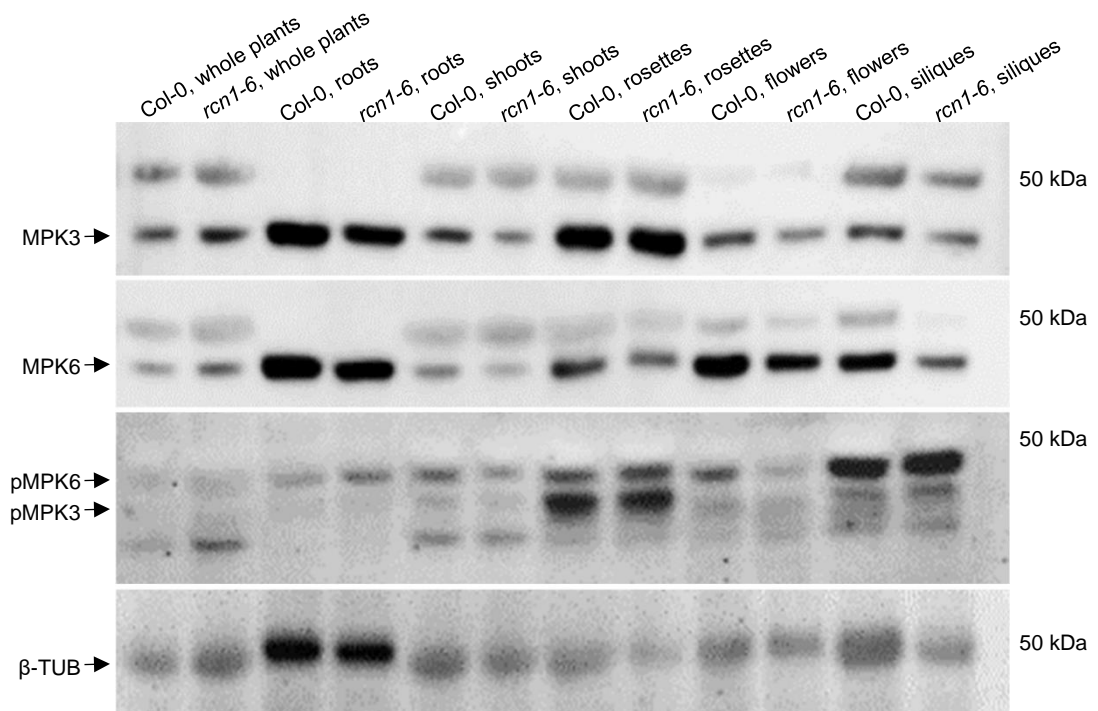
Figure 17. **RCN1 affects levels of phosphorylated MPK3 and MPK6.** Protein and phosphorylated protein levels detected by immunolabelling in tissue extracted from Col-0 or *rcn1-6* whole plants, roots or shoots (14 days after germination), rosettes (21 days after germination), flowers and siliques (6 days after pollination). On the right side of the images is shown the approximate position where proteins with the size of 50 kDa should be localized according to the protein standard. Original images of membranes are in **Fig. S1**.
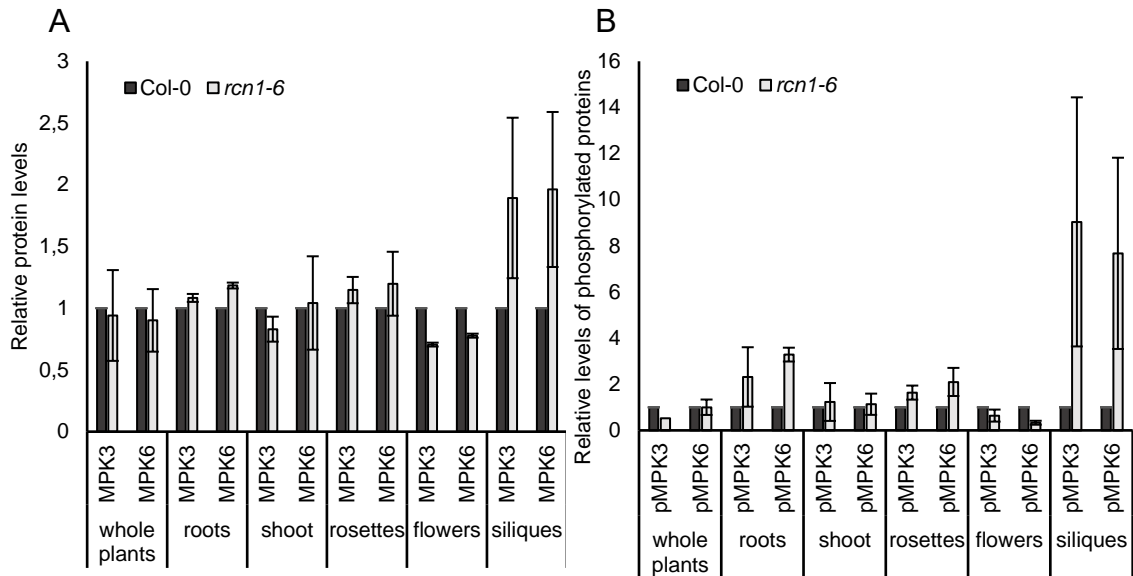
Figure 18. Quantification of the effects of RCN1 genetic depletion on the levels of MPK3/6 and phosphorylated MPK3/6. Graphs presents protein levels of MPK3/6 relative to tubulin protein levels (A) and relative phosphorylated protein levels of pMPK3/6, which were calculated in relation to total protein levels of MPK3/6 (B). Protein levels were detected by immunolabelling in tissue extracted from Col-0 or *rcn1-6* whole plants, roots or shoots (14 day after germination), rosettes (21 day after germination), flowers and siliques (6 days after pollination). Data are presented as mean±SD (N≥three biological and technical replicates).

in flowers of *rcn1-6* mutants (0.7052±0.0157 and 0.7776±0.0162, respectively; **Fig. 18A**). These changes in protein abundance also affected the relative phosphorylated protein levels of MPK3/6 in these tissues. Specifically, the amount of pMPK3/6 was decreased in flowers of *rcn1-6* mutants (0.6418±0.2609 and 0.3323±0.0856, respectively; **Fig. 18B**). The levels of pMPK3/6 in siliques of *rcn1-6* mutants were markedly increased (9.0379±7.6748 and 5.3985±4.1451, respectively; **Fig. 18B**). Moreover, a higher abundance of pMPK3/6 was also noted in roots of *rcn1-6* mutants (2.3164±1.2890 and 3.2858±0.2992, respectively; **Fig. 18B**). Despite the semiquantitative nature of the protein immunolabelling, the significant increase in both pMPK3 and pMPK6 in siliques of *rcn1-6* points towards putative interaction of the YDA-MPK pathway and PP2A in the regulation of the development of generative tissues.

3.1.5. PP2A and MPK3/6 modulate cell division plane orientation during embryogenesis

The early embryogenic development in Arabidopsis follows a simple and highly regular pattern (Mansfield *et al.* 1991) making it an excellent model for describing defects in the cell division plane orientation. Moreover, the involvement of both PP2A and YDA-

MKK4/5-MPK3/6 cascade during embryonic development has been previously described (Torres-Ruiz and Jurgens 1994; Lukowitz *et al.* 2004; Spinner *et al.* 2013; Zhang *et al.* 2017a). However, the defects in the cell division plane orientation have been extensively discussed only for *rcn1* and *ton2* mutants, but not for *mpk3*, *mpk6* mutants. Therefore, the first aim was to compare the *rcn1-6, ton2-5* and *mpk3-1, mpk6-2* mutants regarding their phenotypes in the early embryogenesis. For this purpose, two sets of experiments were conducted; modified pseudo-Schiff propidium iodide staining (Truernit *et al.* 2008) for qualitative description (**Fig. 19, 20**) and Nomarski microscopy of cleared seeds for quantitative analysis of defects in the cell division plane orientation (**Fig. 21, 22**).

Compared to the highly regular positioning of cell walls in the wild type (**Fig. 19A,B, 21A**), the embryos of both *rcn1-6* and *ton2-5* exhibited either tilted (**Fig.19D,E, 21B**) or wrongly oriented cell walls (**Fig. 19C,F, 21C,D**). As expected, the *ton2-5* mutant had the most prominent phenotype with 92% of observed embryos (N=13; **Fig. 22A**) and 62% of suspensors (N=13; **Fig. 22B**) exhibiting wrongly oriented cell walls. Although these defects were less prominent in *rcn1-6,* nearly half of the observed embryos were noted to have either tilted or wrongly positioned cell walls. Again, this was observed in both embryo proper (46%, N=57; **Fig. 22A**) and suspensor (43%, N=56; **Fig. 22B**). Since the defects were in both mutants noted in embryo proper
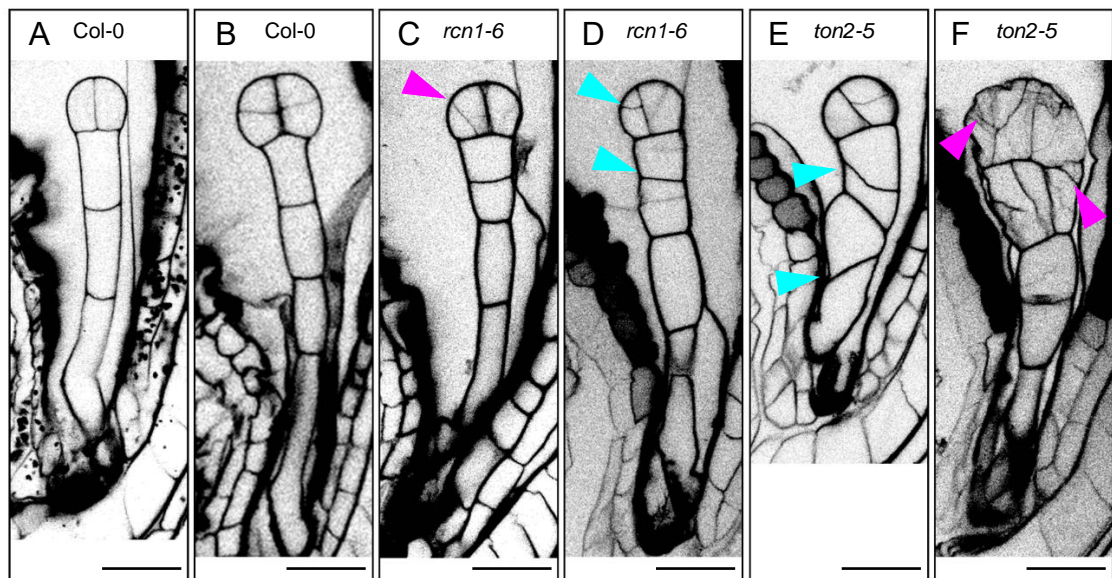
Figure 19. Cell division plane orientation defects in *rcn1, ton2* in early embryogenesis. Embryos of the wild type (A,B), *rcn1-6* (C,D), and *ton2-5* (E,F) were stained with propidium iodide. Magenta arrowheads point to wrongly oriented cell walls, blue arrowheads mark tilted positions of cell walls indicating less severe problems with the cell division plane orientation. Scale bars, 20 μm.
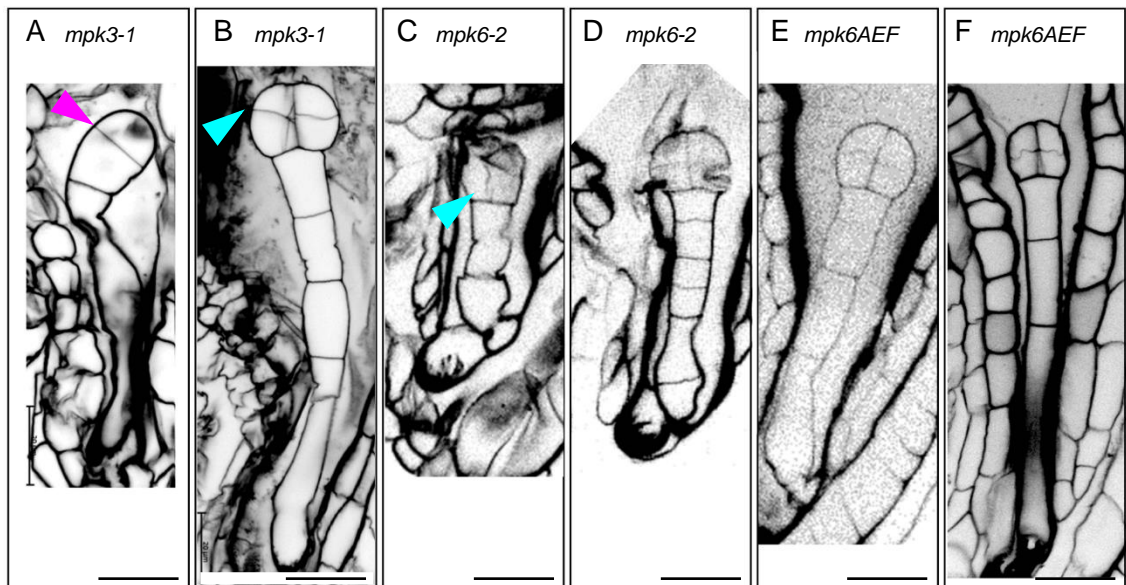
Figure 20. Cell division plane orientation defects in *mpk3, mpk6* mutants in early embryogenesis. Adapted from Samakovli *et al.* (unpublished). Embryos of *mpk3-1* (A,B), *mpk6-2* (C,D), and *mpk6AEF* (E,F) were stained with propidium iodide. Magenta arrowheads point to wrongly oriented cell walls, blue arrowheads mark tilted positions of cell walls indicating less severe problems with the cell division plane orientation. Scale bars, 20 μm.

and suspensor with similar occurrence, PP2A appears to be equally important for the cell division plane orientation in both suspensor and embryo proper.

Similarly, the cell division plane orientation was distorted in both embryos and suspensors of *mpk* mutants (**Fig. 20A-F**). In both *mpk3-1* and *mpk6-2* mutants were observed tilted cell walls (**Fig. 20B,C, 21E,F**) and occasionally, wrongly oriented cell walls were noted (**Fig. 20A, 21G**). The *mpk6AEF* mutant appeared to be the least affected (**Fig. 20E,F, 21H**). This was also supported by the quantitative analysis of the observed defects in the cell division plane orientation. In more than 20% of the examined *mpk6-2* mutant embryos, the tilted or wrongly oriented cell walls were observed (N=83; **Fig. 22A,B**), while there were fewer cases noted in the *mpk3-1* (≥11%, N=38; **Fig. 22A,B**) and *mpk6AEF* mutant embryos (≥17%, N=56; **Fig. 22A,B**).

Apart from the abnormal cell division plane orientation, alterations in the suspensor length were noted in the mutants. The observed changes in suspensor length were quantified (**Fig. 22C**). Only *mpk3-1* had suspensor length comparable to wild type.
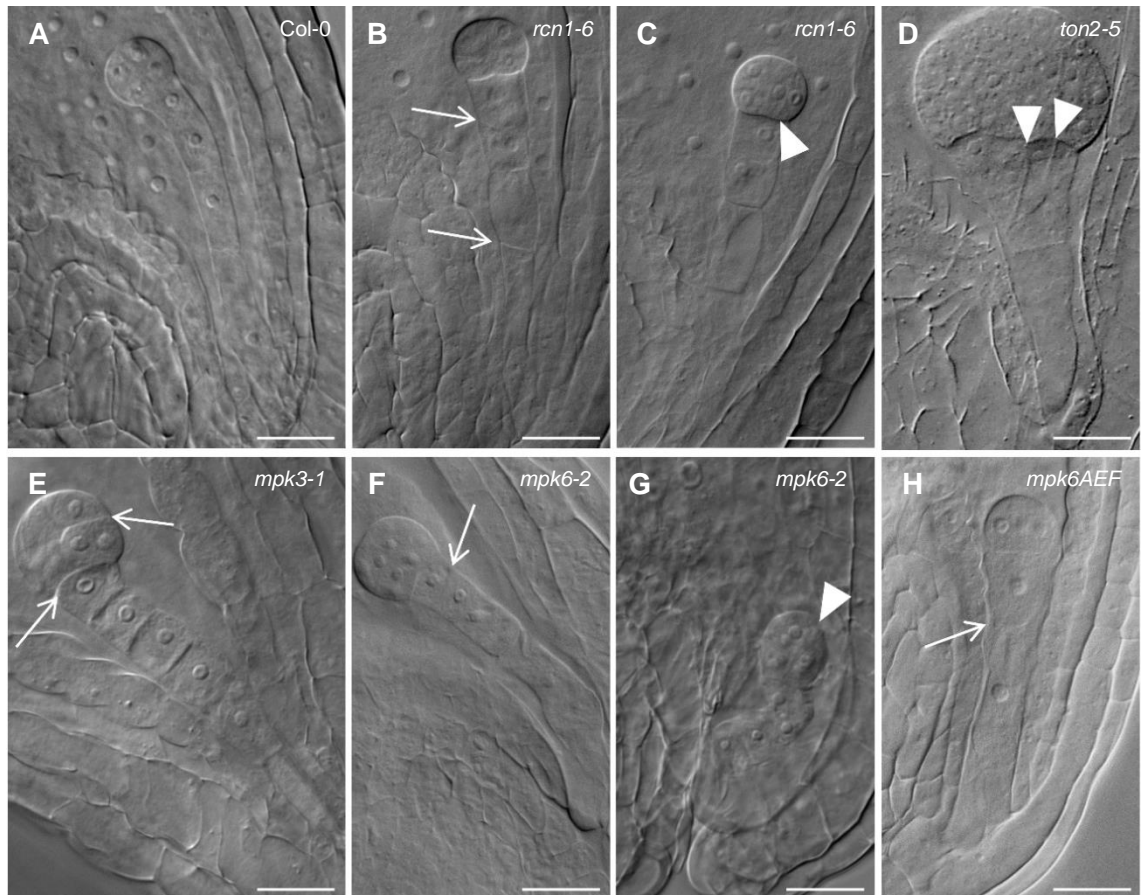
Figure 21. Cell division plane orientation defects in *rcn1, ton2, mpk3, mpk6* in embryogenesis. Nomarski microscopy was used for imaging embryos of the wild type (A), *rcn1-6* (B,C), *ton2-5* (D), *mpk3-1* (E), *mpk6-2* (F,G), and *mpk6AEF* (H) at the octant or dermatogen stage. White arrowheads point to wrongly oriented cell walls, white arrows mark less severe defects in cell wall positioning. Scale bars, 20 μm.

The *rcn1-6, mpk6-2* and *mpk6AEF* mutants had significantly shorter suspensor compared to wild type, with *mpk6-2* having the most prominent phenotype.

In summary, all the examined mutants, namely *rcn1, ton2, mpk3, mpk6*, exhibited aberrations in the cell division plane orientation during early embryogenesis in both the embryo proper and the suspensor. The proper orientation of the cell plane is quintessential for proper progression of the formative cell divisions, which are responsible for the diversification of the cell fates of daughter cells. On the other hand, the cell fate specification during early embryogenesis depends on cell fate determining factors, such as auxin distribution and differential expression of members of the WOX protein family. It is yet unclear, to which extent can incorrect cell division plane orientation impede the cell fate specification established by other factors or *vice versa*.
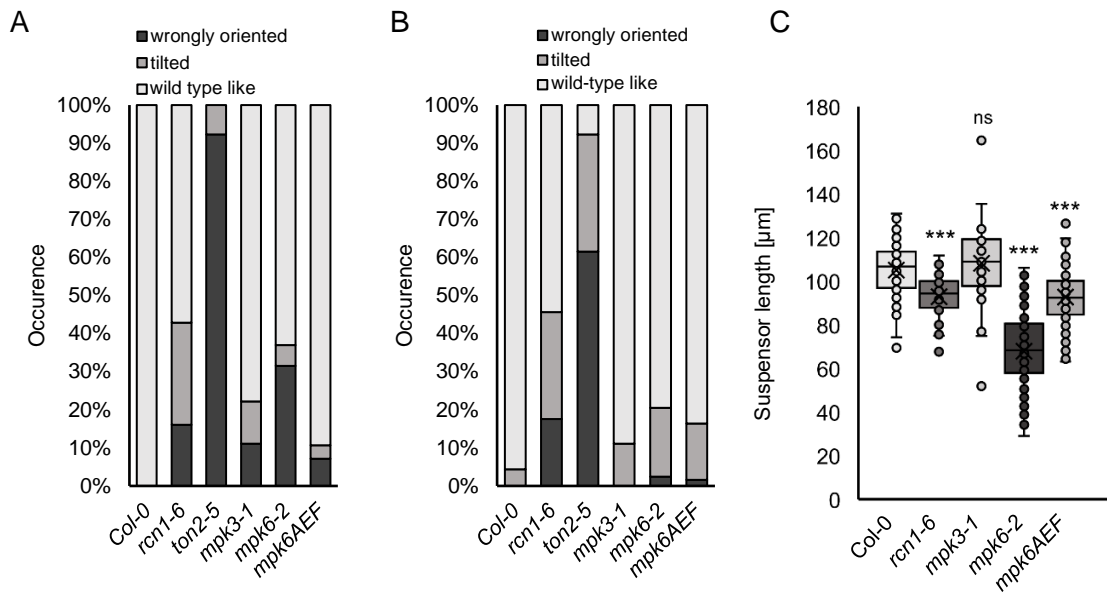
Figure 22. Quantification of cell division plane orientation defects in *rcn1, ton2, mpk3, mpk6* embryos. Adapted from Samakovli *et al.* (unpublished). Quantification of observed phenotypes in images of embryos visualized by either propidium staining or Nomarski microscopy. (A, B) Quantification of abnormal cell division plane orientation in either embryo proper (A; N≥45 except for *ton2-5,* N=13) or suspensor (B; N≥38 except for *ton2-5,* N=13). (C) Quantification of the suspensor length measured at octant or dermatogen stages. (N≥50; Welch's ANOVA was followed with Tukey's test corrected for unequal N, statistically significant differences to Col-0 are shown, *** significant at p<0.001, ns not statistically significant). Results from the statistical analysis are in **Table S3**. Description of box plot: the middle line in the box represents median, the x shows mean, the bottom line depicts the first quartile, while the top line describes the third quartile; the vertical lines (whiskers) extend to minimum and maximum value within the 1.5× interquartile range (distance between the first and the third quartile); points outside of the whiskers mark outliers (values outside of the 1.5× interquartile range).

3.1.6. Abnormal expression pattern of *WOX8* in *rcn1, mpk3, mpk6* mutants

The transcriptional factor WOX8 serves as a major determinant of the cell fate during early embryogenesis (Haecker *et al.* 2004). The WOX8 promotes development of the basal cell into the suspensor and regulates the expression of other members of the WOX protein family (Breuninger *et al.* 2008). After the first division of the zygote, WOX8 is exclusively expressed in the basal cell and later on in the suspensor (Haecker *et al.* 2004). Therefore, if the expression domain of *WOX8* is irregular, it informs on problems with the cell fate determination. Moreover, since transcription of *WOX8* is known to depend on WRKY2, which requires phosphorylation by YDA-MPK3/6 pathway for its activity (Ueda *et al.* 2011), it is expected that the regulation of *WOX8* expression is compromised in case of *yda* or *mpk* mutants.

To examine whether the expression domain of *WOX8* is affected in the genotypes of interest, crosses were generated between mutants and a line expressing the *WOX8::NLS:YFP* reporter. The expression of *WOX8::NLS:YFP* was restricted to the suspensor in the wild type (**Fig. 23A,B, 24A**), but this expression pattern was disrupted in mutants (**Fig. 23C-L**). In the *rcn1-6* and *ton2-5* mutants, the *WOX8::NLS:YFP* was ectopically expressed in the apical cell lineage (**Fig. 23E, 24B**), while the signal was not detected in some of the suspensor cells (**Fig. 23D,F, 24B,C**). Similarly, in the *mpk* mutants, the ectopic signal in the embryo proper was observed (**Fig. 23G,K**), while the signal was missing in the basal cell lineage (**Fig. 23J,L**). The observations of the ectopic signal in the embryo proper were most frequently noted in *ton2-5* (5 out of 15 cases) and *mpk3-1* (16%, N=64), while no such case was noted in the *mpk6-2* mutant embryos (**Fig. 23M**). On the other hand, the missing signal in the suspensor was regularly observed in *mpk6-2* (55%, N=29; **Fig. 23M**).
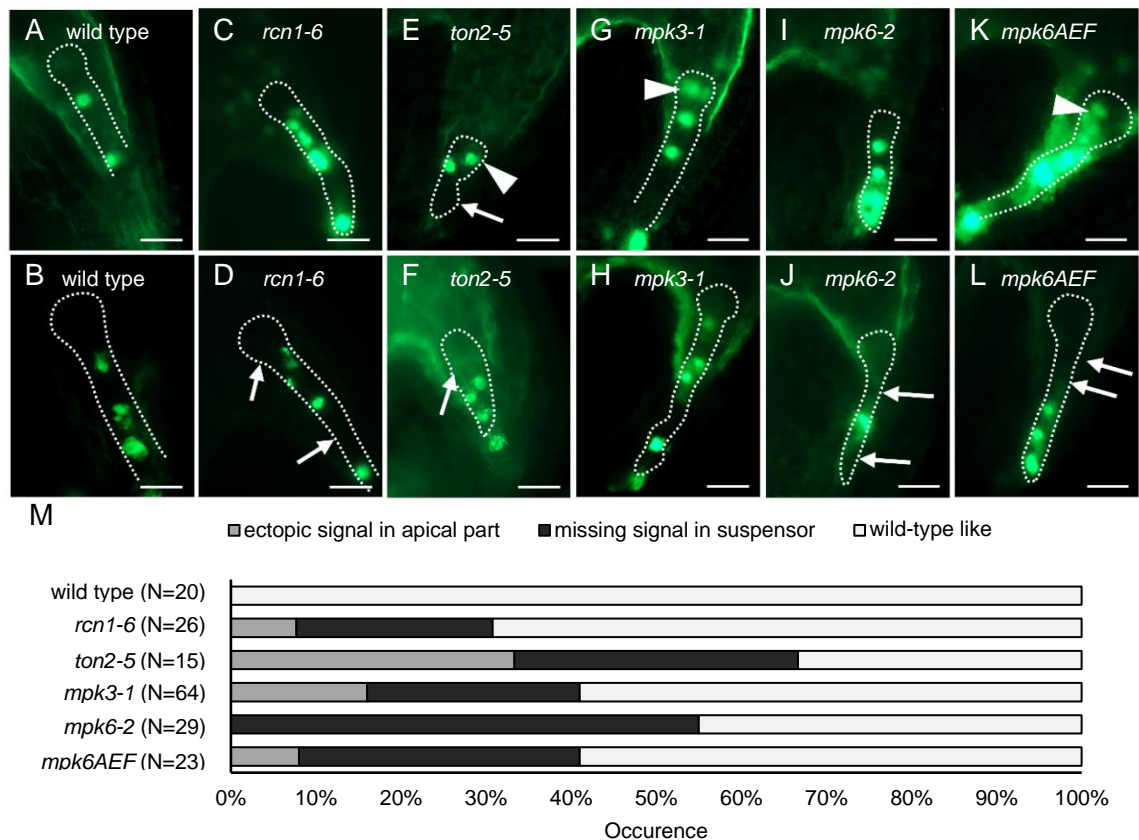
Figure 23. Aberrant *WOX8* expression in *rcn1, ton2, mpk3, mpk6* mutants. Adapted from Samakovli *et al.* (unpublished). (A-L) Distribution of *WOX8::NLS:YFP* signal was examined during early embryogenesis in wild type (A,B), *rcn1-6* (C,D), *ton2-5* (E,F), *mpk3-1* (G,H), *mpk6-2* (I,J), and *mpk6AEF* (K,L). White arrowheads point to ectopic signal in the embryo proper, white arrows mark the nuclei of suspensor cells without signal. Scale bars, 20 μm. (M) Quantitative analysis of observed defects in *WOX8::NLS:YFP* signal localization (N=number of observed embryos).
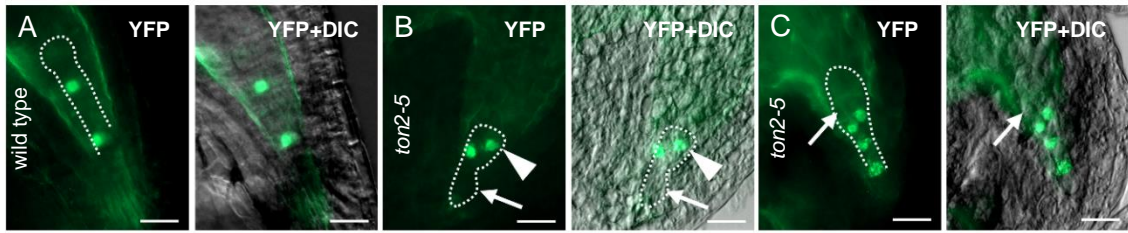
Figure 24. TON2 affects *WOX8* expression pattern in developing embryos. Localization of *WOX8::NLS:YFP* signal during early embryogenesis in wild-type (A; **Fig. 23A**) and *ton2-5* (B-C; **Fig. 23E,F**). Images show *WOX8::NLS:YFP* (YFP) and merged picture of *WOX8::NLS:YFP* and DIC image (YFP+DIC; differential interference contrast microscopy). White arrowheads point to ectopic signal in embryo proper, white arrows mark nuclei of suspensor cells without signal. Scale bars, 20 μm.

The *mpk6-2* mutant appeared to be affected more prominently than the other two mutants, corroborating the findings of the cell division plane orientation defects and suspensor length phenotypes (**Fig. 20-22**). Since similar defects were also found in *rcn1-6* and *ton2-5* mutants, it appears that genetic depletion in PP2A subunits leads to alteration of the expression pattern of *WOX8*.

3.1.7. Auxin distribution is compromised in *rcn1, mpk3, mpk6* mutants

Together with the YDA-MPK cascade and the members of the WOX protein family, auxin belongs to three major factors in establishing apical-basal polarity in early embryogenesis (Friml *et al.* 2003). Moreover, auxin signalling is coordinated by the YDA-MPK-WOX8 regulatory module (Zhang *et al.* 2017b). For this reason, the distribution of auxin maxima during embryonic development was surveyed by documenting the expression of GFP, driven by the synthetic auxin-responsive promoter *DR5* (Ulmasov *et al.* 1997; Friml *et al.* 2003) and by deciphering how such expression patterns are modulated in *rcn1, ton2, mpk3, mpk6* mutants expressing *DR5::GFP*.

At the earliest stages of the embryonic development, auxin is imported to the embryo proper from maternal tissues via the suspensor. However, this changes at the globular stage, when the apical-basal auxin transport is established in the embryo proper. Consequently, auxin maxima are observed at the basal pole of the embryo proper and at the uppermost cell of the suspensor, the hypophysis, which can be observed in embryos of the *DR5::GFP* line (**Fig. 25A,B**; Friml *et al.* 2003). Furthermore, with the continuous auxin synthesis in the apical poles of the embryo proper, auxin maxima can be observed in the apical poles from late heart stages (**Fig. 25B**).

The distribution of auxin maxima was first documented in *mpk3, mpk6* mutants (**Fig. 25C-H**). In the *mpk3-1* mutant, the basal auxin maximum seems to be unaffected compared to the wild type (**Fig. 25C,D, Fig. 26A**), but in the apical pole the signal appears earlier (**Fig. 25C, 26B**). In *mpk6-2* embryos, the basal auxin maxima were at large comparable to those of the wild type, but a significant number of *mpk6-2* embryos exhibited lower signal intensity (14%, N=57; **Fig. 25F, 26A**). The early occurrence of auxin maxima at the apical pole reported for *mpk3-1* was also observed in *mpk6-2* mutant (52%, N=29; **Fig. 25E, 26B**). Lastly, the *mpk6AEF* embryos had their auxin maxima distribution resembling that of wild type (**Fig. 25G,H, 26A,B**).

Subsequently, the expression of the *DR5::GFP* reporter was observed in the *rcn1-6* mutant background. In this case, both phenotypes described for *mpk3, mpk6* mutants were noted (**Fig. 27A,B**). Interestingly, both *mpk-2* and *rcn1-6* mutants had a similar frequency of occurrence for the early signal in apical pole (53%, N=40; **Fig. 26B**), however, *rcn1-6* mutants were more frequently exhibiting weaker signal in the basal pole of the embryo proper as opposed to *mpk6-2* mutants (38%, N=66; **Fig. 26A**). In *ton2-5*
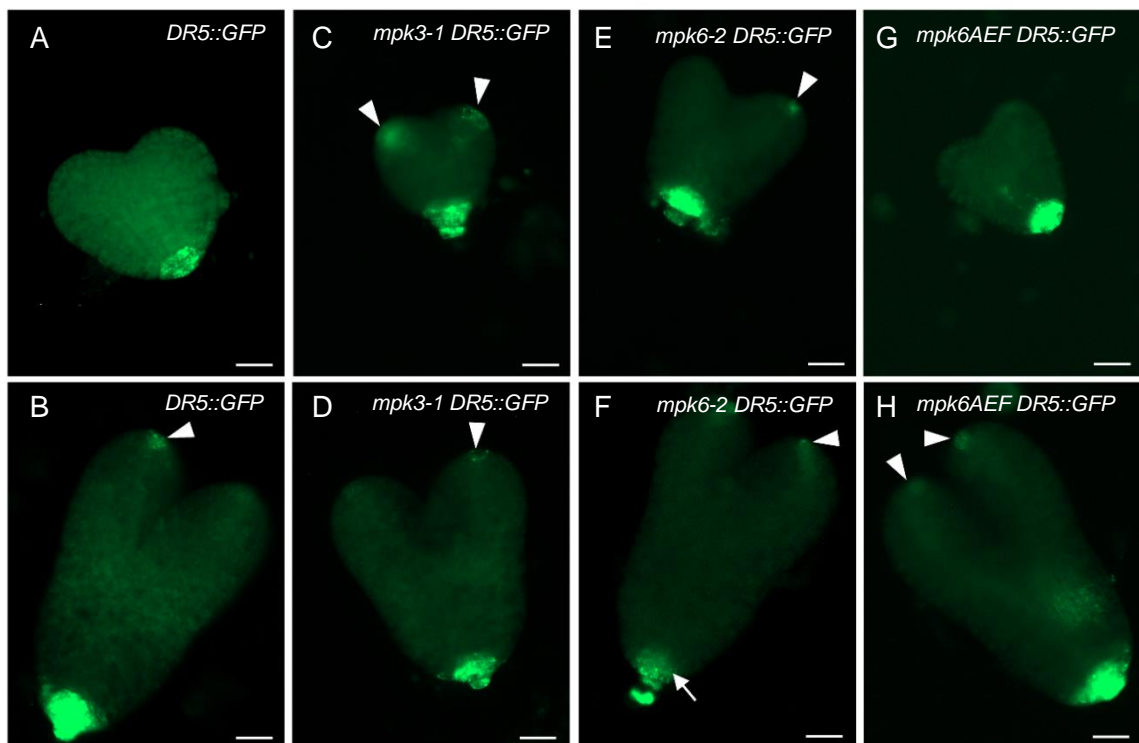
Figure 25. Abnormal auxin maxima distribution during embryonic development in *mpk3, mpk6* mutants. Adapted from Samakovli *et al.* (unpublished). Auxin maxima were visualized during embryonic development in the line stably expressing *DR5::GFP* (A, B) or mutants crossed with this line, specifically *mpk3-1* (C, D), *mpk6-2* (E, F), and *mpk6AEF* (G, H). Embryonic stages early heart and late heart are shown in the pictures. White arrowheads mark GFP signal in the apical part of the embryo; white arrow points to weak signal in the basal pole. Scale bars, 20 μm.
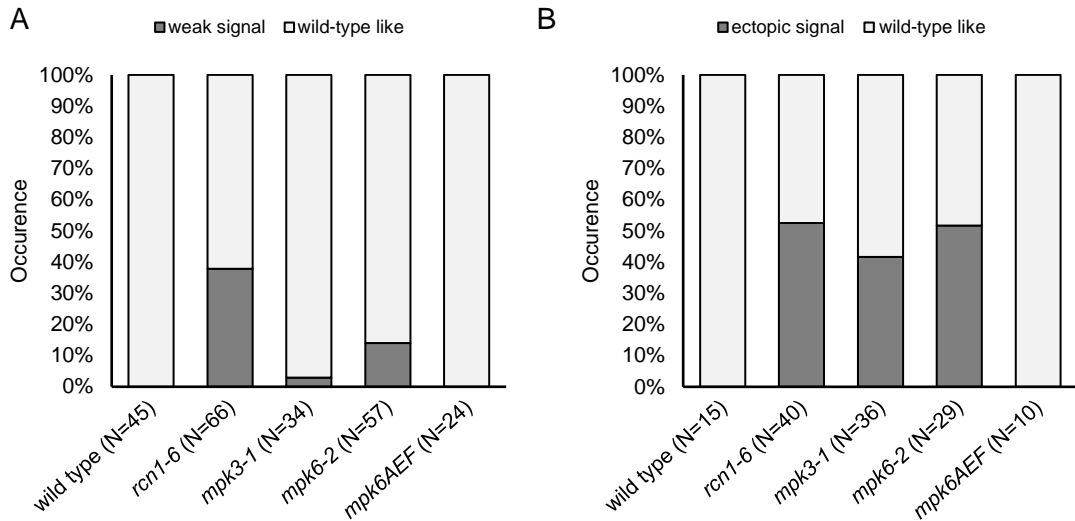
Figure 26. Quantification of abnormal auxin maxima distribution during embryonic development in *rcn1, ton2, mpk3* and *mpk6* mutants. Adapted from Samakovli *et al.* (unpublished). Auxin maxima were visualized in embryos of the indicated genotypes, which were expressing *DR5::GFP*. (A, B) Quantification of observed abnormalities in auxin maxima localization and/or distribution: (A) weak signal in the basal part of embryos in heart stages; (B) ectopic signal in the apical part of embryos in early heart stages (N=number of observations).

embryos, the signal in the apical pole was frequently observed in the early heart stages (7 out of 7 cases; **Fig. 27C**). Moreover, the dwarfed later stages often had more than two proto cotyledons (10 out of 13 cases; **Fig. 27D**). Surprisingly, no alterations of *DR5::GFP* expressions were noted in the basal pole of *ton2-5* embryos. This is in contrast with the high occurrence of abnormal *WOX8::NLS:YFP* expression in *ton2-5* embryos. Conclusively, in *rcn1, mpk3* and *mpk6* mutants, abnormalities of the cell division plane orientation occurred concurrently to the misexpression of *WOX8* and spatiotemporal alterations of the auxin maxima distribution.
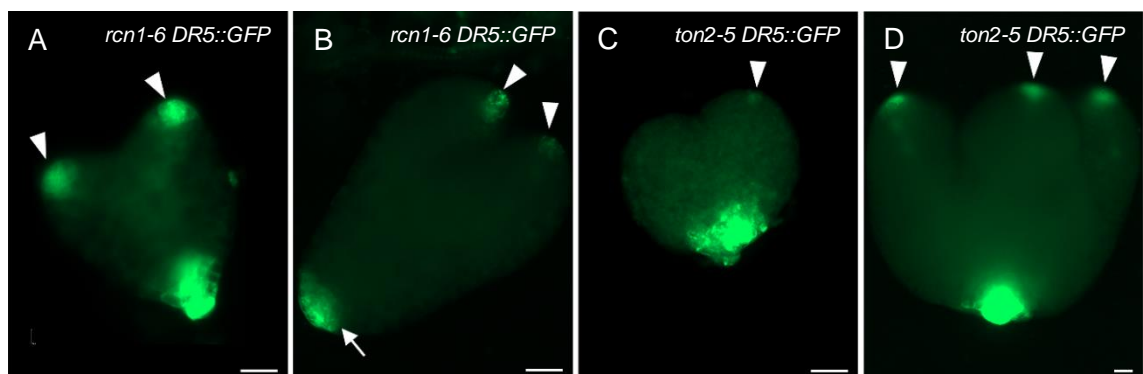
Figure 27. Abnormal auxin maxima distribution during embryonic development in *rcn1, ton2* mutants. Auxin maxima were visualized during embryonic development in *rcn1-6* (A, B), and *ton2-5* (C, D) mutants stably expressing *DR5::GFP*. Embryonic stages early heart and late heart are shown in the pictures. White arrowheads mark GFP signal in the apical part of the embryo; white arrow points to weak signal in the basal pole. Scale bars, 20 μm.

3.2. HSP90s are affecting asymmetric cell divisions via modulating YDA-MPK pathway

3.2.1. Genetic depletion of HSP90s rescues cell division plane orientation defects in *yda* mutants during embryogenesis

Previous experiments have shown that cytoplasmic HSP90.1 and HSP90.2 isoforms modulate stomatal differentiation pathway via their direct interaction with YDA (Samakovli *et al.* 2020). Since YDA is a regulator of the cell division plane orientation in other developmental processes and specifically in early embryogenesis (Lukowitz *et al.* 2004) and in primary root tissue patterning (Smékalová *et al.* 2014), it is likely that its function in these processes might be also affected by interactions with HSP90s. To explore this possibility, the embryonic development in *hsp90, yda* single mutants and *hsp90 yda* double mutant was assessed by employing modified pseudo-Schiff propidium iodide staining and Nomarski microscopy.

For the experiments, three *hsp90* mutants were chosen. Two of them are loss-of-function mutants, while the third is an RNA interference (RNAi) line (*hsp90^{RNAi}*) where expression of cytoplasmic HSP90 isoforms is decreased (Samakovli *et al.* 2020).

The highly ordered cell division plane orientation, which is characteristic for early embryonic development in Arabidopsis (**Fig. 28A,B**), was compromised in the examined *hsp90* mutants (**Fig. 28C-H**), especially in *hsp90.1* (**Fig. 28C**) and *hsp90^{RNAi}* (**Fig. 28H**).
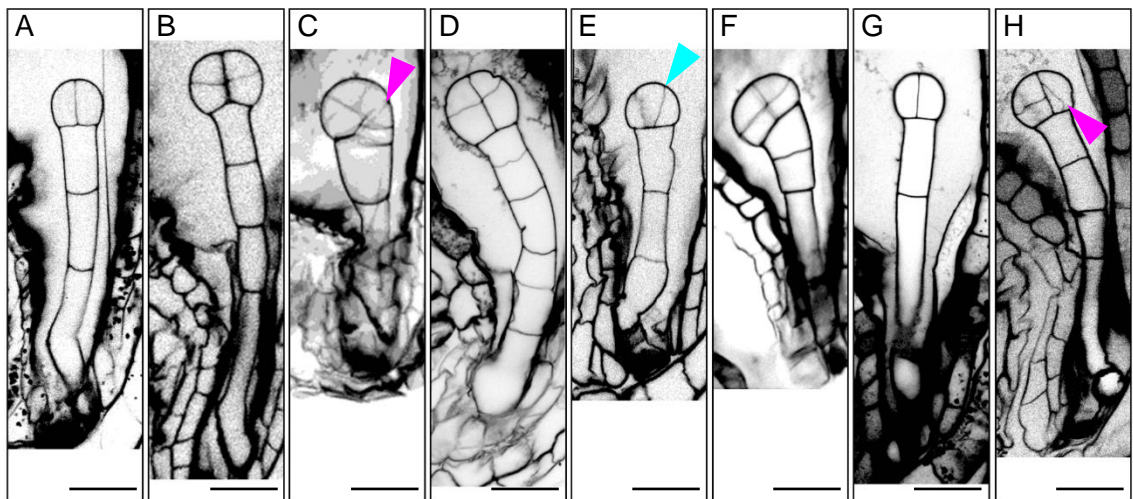
Figure 28. Genetic depletion of HSP90s leads to minor defects in the cell division plane orientation during early embryogenesis. Adapted from Samakovli *et al.* (unpublished). Early embryonic development of the wild type (A,B; **Fig. 19A,B**), *hsp90.1* (C,D), *hsp90.2* (E,F), *hsp90^{RNAi}* (G,H) was visualized by propidium iodide staining. Magenta arrowheads point to wrongly oriented cell walls, blue arrowheads mark tilted positions of cell walls indicating less severe problems with the cell division plane orientation. Scale bars, 20 μm.

On the other hand, the cell division plane orientation was relatively well-ordered in *hsp90.2* mutant (**Fig. 28E,F**) suggesting a differential role of HSP90 isoforms in plant development.

For both loss-of-function *yda* and gain-of-function *ΔNyda* mutants, severe embryonic phenotypes were described, among them altered cell division plane orientation and dramatic changes in the length of the suspensor (Lukowitz *et al.* 2004). As expected, both mutants exhibited disturbed cell division patterning originating from wrongly positioned cell walls, frequently shifted 90° against the typical cell division plane orientation at that stage (**Fig. 29A,B, 30A,B**).

In *hsp90 yda* double mutants, the genetic depletion of HSP90 resulted in partial rescue of the severe *yda* phenotype (**Fig. 29**). While the overall phenotype of double mutants was abnormal (**Fig. 29C-H**), fewer defects in the cell division patterning were noted. Similarly, the *hsp90 ΔNyda* double mutants were less affected in this phenotypic trait (**Fig. 30**) with their overall phenotype being closer to the wild type than to the *ΔNyda* phenotype (**Fig. 30C-H**).

Despite the absence of severe deviations in the cell division plane orientation patterning in *hsp90* mutants, milder defects were still observed in double mutants. To quantify these defects in both the embryo proper (**Fig. 31A**) and the suspensor (**Fig. 31B**), Nomarski microscopy was used. As expected, the cell division plane orientation was strongly affected in both *yda* and *ΔNyda*. While in *yda*, both suspensor and embryo proper
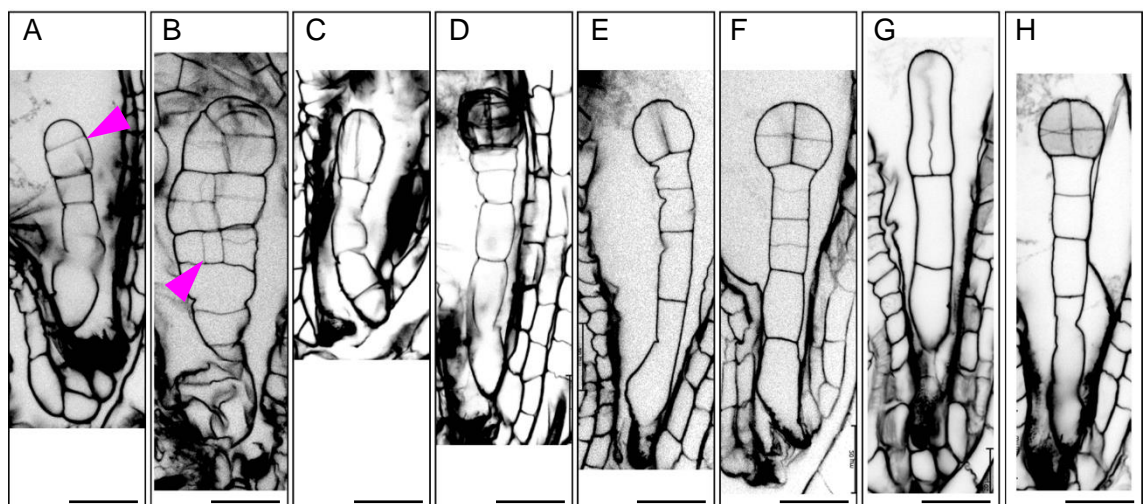
Figure 29. Genetic depletion of HSP90s restores defects in the cell division plane orientation in early embryogenesis of *yda* loss-of-function mutant. Adapted from Samakovli *et al.* (unpublished). Early embryonic development of yda (A,B), *hsp90.1 yda* (C,D), *hsp90.2 yda* (E,F), *hsp90^RNAi yda* (G,H) was visualized by propidium iodide staining. Magenta arrowheads point to wrongly oriented cell walls. Scale bars, 20 μm**.**
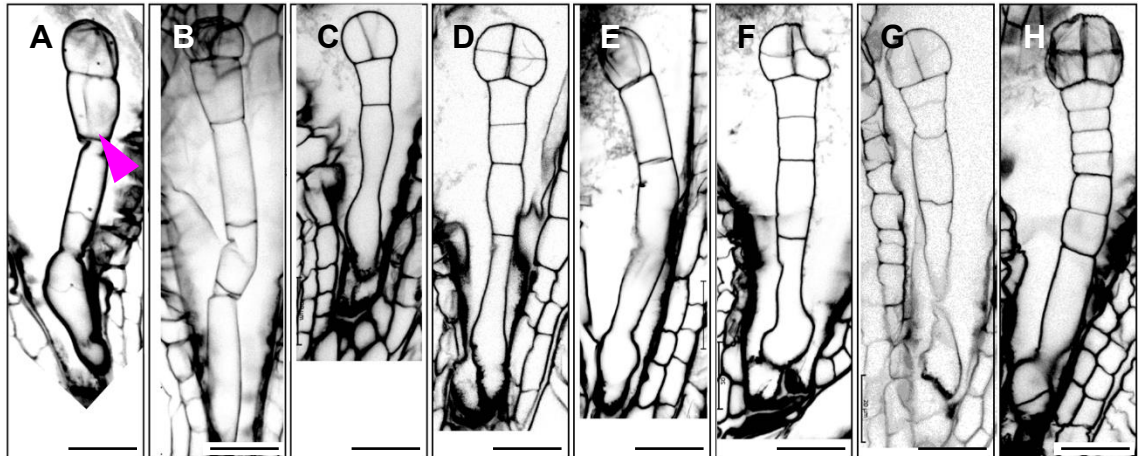
Figure 30. Genetic depletion of HSP90s restores defects in the cell division plane orientation in early embryogenesis of *yda* gain-of-function mutant. Adapted from Samakovli *et al.* (unpublished). Early embryonic development of *ΔNyda* (A,B), *hsp90.1 ΔNyda* (C,D), *hsp90.2 ΔNyda* (E,F), *hsp90^RNAi ΔNyda* (G,H) was visualized by propidium iodide staining. Magenta arrowheads point to wrongly oriented cell walls. Scale bars, 20 μm.

were similarly affected (≥80%, N=20; **Fig. 31**), the cell division plane orientation in suspensor of *ΔNyda* was more frequently altered that in embryo proper (64% compared to 33%, N=45; **Fig. 31**). In *hsp90* mutants, both the embryo proper and the suspensor appeared to be affected with similar frequencies. Out of the three examined *hsp90* mutants, *hsp90.1* had the highest number of cases with abnormal cell division plane orientation (≥38%, N=70; **Fig. 31**). The *yda* and *ΔNyda* phenotypes were alleviated in *hsp90.1 yda, hsp90.1 ΔNyda, hsp90.2 yda, hsp90^RNAi yda* and partially in *hsp90.2 ΔNyda* double mutants (**Fig. 31**). Moreover, the *hsp90.1 yda, hsp90.1 ΔNyda* had also improved phenotype compared to *hsp90.1*. Conversely, the *hsp90^RNAi ΔNyda* double mutant exhibited stronger phenotype than its parent lines.

In summary, *hsp90* mutants have milder embryonic phenotype compared to *yda* mutants. Nevertheless, the cell division patterning is altered in *hsp90* mutants, most notably in *hsp90.1* and *hsp90^RNAi*. The irregular cell division plane orientation phenotype is rescued in *hsp90.1 yda, hsp90.1 ΔNyda* double mutants and alleviated in *hsp90.2 yda, hsp90^RNAi yda,* and *hsp90.2 ΔNyda*. Conclusively, HSP90s affect early embryogenesis with different involvement of the HSP90.1 and HSP90.2 isoforms. The genetic depletion of HSP90.1 alleviates *yda, ΔNyda* embryonic phenotype suggesting that HSP90.1 modulates embryonic development downstream of YDA.
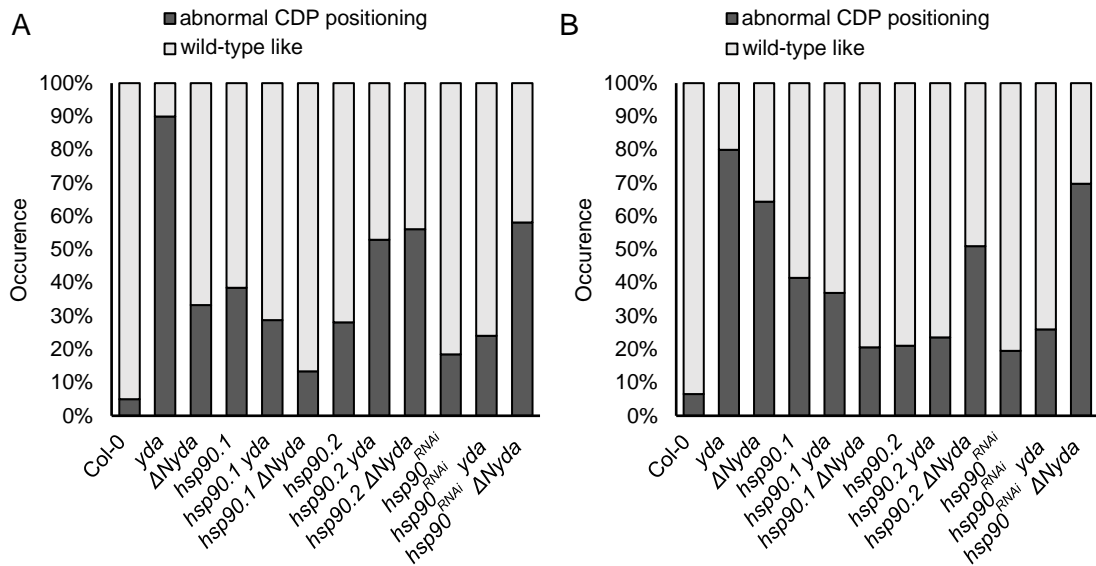
Figure 31. Quantification of observed defects in the cell plane orientation in *hsp90, yda* single and double mutants. Adapted from Samakovli *et al.* (unpublished). (A, B) Abnormal cell division plane orientation was examined in embryos of the indicated genotypes. For the analysis, images from Nomarski microscopy and propidium iodide staining were used. Abnormal cell division plane (CDP) orientation in the embryo proper was analysed separately for the embryo proper (A) and the suspensor (B). In both cases, the N≥34, with the exception of *yda* (N=20).

3.2.2. HSP90s affect the expression of *WOX8*

YDA-MPK pathway is known to regulate the transcription of *WOX8* (Ueda *et al.* 2011), a gene encoding a transcription factor specifying the cell fate of the basal cell (Breuninger *et al.* 2008) with its expression being restricted to the basal cell lineage (Haecker *et al.* 2004; **Fig. 23A,B, 32A**). As shown above, the expression of *WOX8::NLS:YFP* is compromised in *mpk3, mpk6* mutants as documented by either ectopic expression of the *WOX8::NLS:YFP* reporter in the embryo proper, or missing signal in some of the suspensor cells (**Fig. 23**). To investigate whether HSP90s affect *WOX8* expression pattern, the expression of *WOX8::NLS:YFP* was examined in *hsp90* and *yda* mutant background.

In agreement with previous results (**Fig. 23**), the expression pattern of *WOX8* was distorted in *yda* mutants, and both ectopic signal in embryo proper (**Fig. 32C,D**) and missing signal in suspensor cells were observed (**Fig. 32B,E**). Over 45% of examined embryos of *yda* and *ΔNyda* exhibited one of these phenotypes, with *yda* having a higher frequency of the ectopic signal in the embryo proper (25%, N=24; **Fig. 33**), while *ΔNyda*
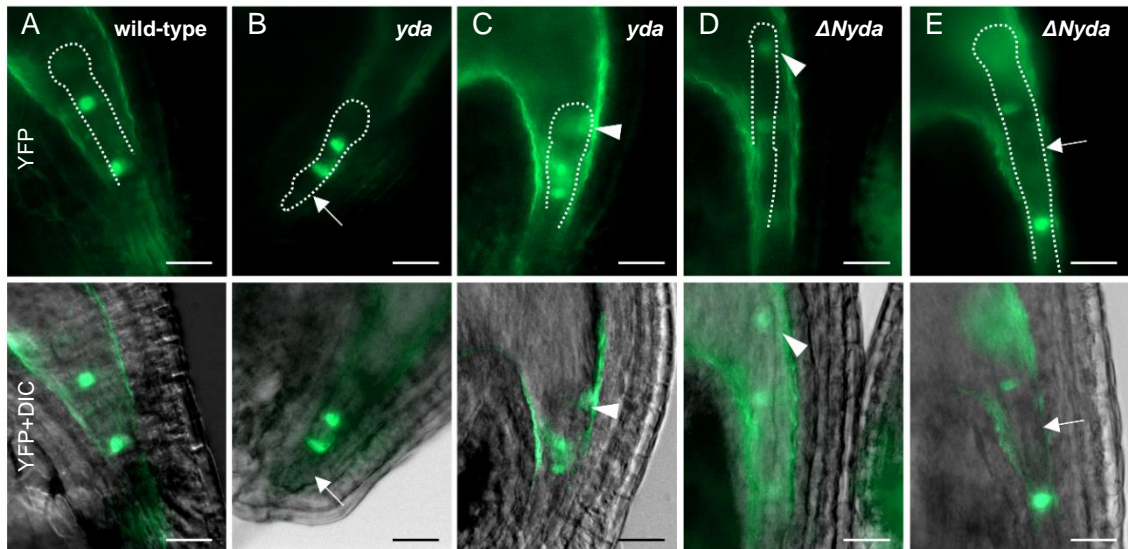
Figure 32. YDA affects the specification of the basal cell fate in developing embryos. Localization of the *WOX8::NLS:YFP* signal during early embryogenesis in wild-type (A; **Fig. 23A**), *yda* (B,C), and *ΔNyda* (D,E). Images show *WOX8::NLS:YFP* (YFP) and merged picture of *WOX8::NLS:YFP* and DIC image (YFP+DIC; differential interference contrast microscopy). White arrowheads point to the ectopic signal in the embryo proper, white arrows mark the nuclei of suspensor cells without signal. Scale bars, 20 μm.

embryos had higher occurrence of the missing signal in the suspensor (36%, N=34; **Fig. 33**). In *hsp90.1, hsp90.2* mutants, both the ectopic expression in the apical cell lineage (**Fig. 34A-C**) and the missing signal in some suspensor cells (**Fig. 34B,D**) were noted. These alterations in the expression of the *WOX8::NLS:YFP* reporter were less frequently observed compared to *yda* mutants. While 45% of *yda* and 50% of *ΔNyda* embryos exhibited one of these traits (**Fig. 33**), the occurrence in *hsp90* mutants was 35% in *hsp90.1* and 30% in *hsp90.2* embryos (N=128 and 75, respectively; **Fig. 33**).
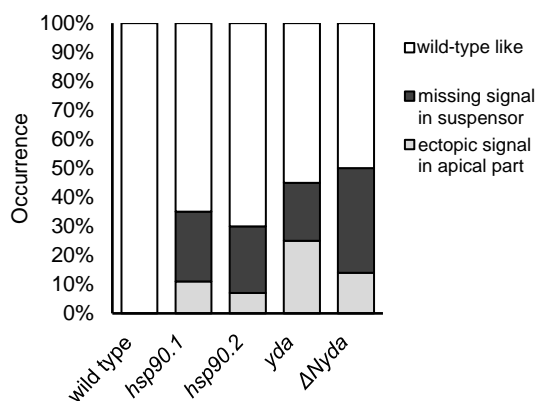
Figure 33. Quantification of the observed defects in *WOX8* expression. Adapted from Samakovli *et al.* (unpublished). Quantification of observed abnormal *WOX8::NLS:YFP* signal localization in the indicated genotypes (N≥34, with the exception of *yda* (N=24)).

In both *hsp90* mutants, the missing signal in suspensor was more prevalent than the observation of the ectopic signal in the apical part of the embryo.

The expression of WOX8 is not only compromised in *yda* mutants, as would be expected based on previous studies but also in *hsp90.1, hsp90.2* mutants. Moreover, the *hsp90.1, hsp90.2* mutant embryos appeared to be similarly affected regarding the expression of the *WOX8::NLS:YFP* reporter.
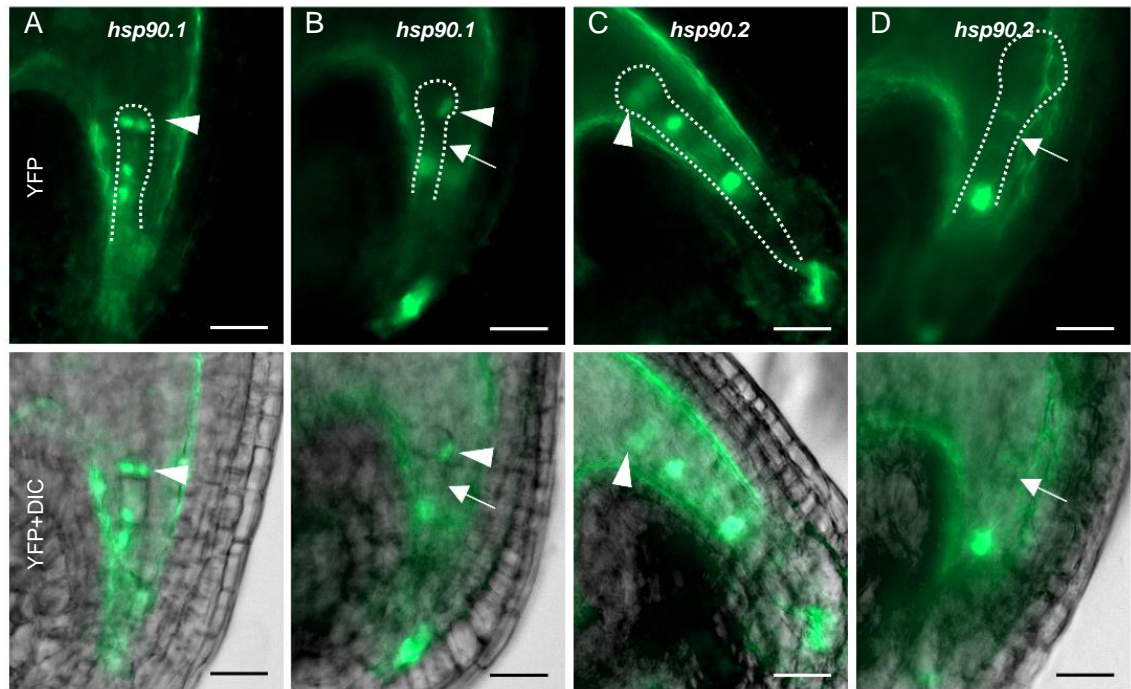
Figure 34. HSP90s affect the specification of the basal cell fate in developing embryos.
Localization of the *WOX8::NLS:YFP* signal during early embryogenesis in *hsp90.1* (A,B), and *hsp90.2* (C,D). Images show *WOX8::NLS:YFP* (YFP) and merged picture of *WOX8::NLS:YFP* and DIC image (YFP+DIC). White arrowheads point to ectopic signal in the embryo proper, white arrows mark the nuclei of suspensor cells without signal. Scale bars, 20 μm.

3.2.3. Auxin distribution is altered in *hsp90, yda* mutants

The uneven distribution of auxin provides cells with positional cue regarding the apical-basal polarity axis during early embryogenesis. Auxin signalling is influenced by WOX8, which expression is, in turn, regulated by the YDA-MPK cascade (Breuninger *et al.* 2008; Ueda *et al.* 2017; Zhang *et al.* 2017b). Moreover, as shown above (**Fig. 25**), auxin distribution is affected in *mpk3, mpk6* mutants during early embryogenesis. Thus, to investigate putative disturbances in auxin distribution, auxin maxima were investigated in *hsp90* and *yda* mutants. For this purpose *hsp90* and *yda* mutants were crossed with the line expressing the *DR5::GFP* reporter (Ulmasov *et al.* 1997; Friml *et al.* 2003).

The analysis of auxin maxima localization in *hsp90* mutants showed that generally, the same pattern of signal localization as in wild type embryos was observed (**Fig. 35A-H**). This means that at the late heart and torpedo stages, the auxin maxima were detected at the apical poles, where auxin biosynthesis takes place, and at the basal pole of the embryo proper and the hypophysis, where auxin accumulates from the globular stage onward due to the polarized localization of auxin transporters (Friml *et al.* 2003).
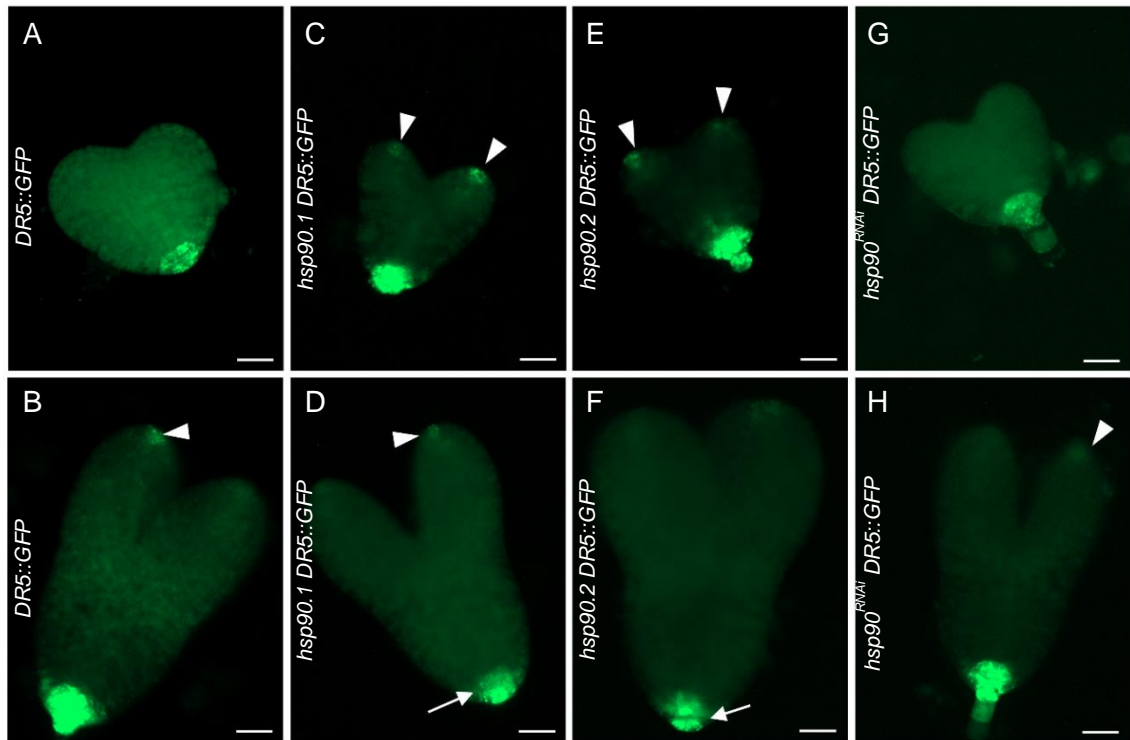
Figure 35. Abnormal distribution of auxin maxima during embryogenesis in *hsp90* mutants. Adapted from Samakovli *et al.* (unpublished). Auxin maxima in embryos were visualized in the line stably expressing *DR5::GFP* (A,B; **Fig. 25A,B**) or mutants crossed with this line, specifically *hsp90.1* (C,D)*, hsp90.2* (E,F)*,* and *hsp90^RNAi^* (G,H). Images show *DR5::GFP* signal distribution in early heart and late heart stages. White arrowheads mark GFP signal in the apical part of the embryo; white arrow points to weak signal in the basal pole. Scale bars, 20 μm.

However, it was noted that in some cases, either the signal in the basal pole of the embryo proper was weaker than in wild type embryos (**Fig. 35D,F**), or the signal was detected in apical poles earlier than in the wild type, specifically in the early heart stages (**Fig. 35C,E**). The early signal in the apical pole and the weak signal in the basal pole were both most frequently observed in *hsp90.1* mutant embryos compared to *hsp90.2* and *hsp90^RNAi^* mutants (**Fig. 36A,B**).

In *yda* mutants, the auxin maxima in the apical poles were mostly showing the same pattern of *DR5::GFP* expression as the wild type (**Fig. 37A-F**). Together with the *hsp90^RNAi^*, the *yda* and *ΔNyda* mutants had the lowest occurrence of the early signal in the apical pole (approximately 1 out of 15 cases; **Fig. 36A**). On the other hand, the *yda* mutants often exhibited peculiar distribution of the auxin maxima in the basal pole (**Fig. 37A,B,E,F**). In *yda* mutants, a specific phenotype was observed, where the signal was less restricted within the basal pole of the embryo proper, and a diffuse signal was

77
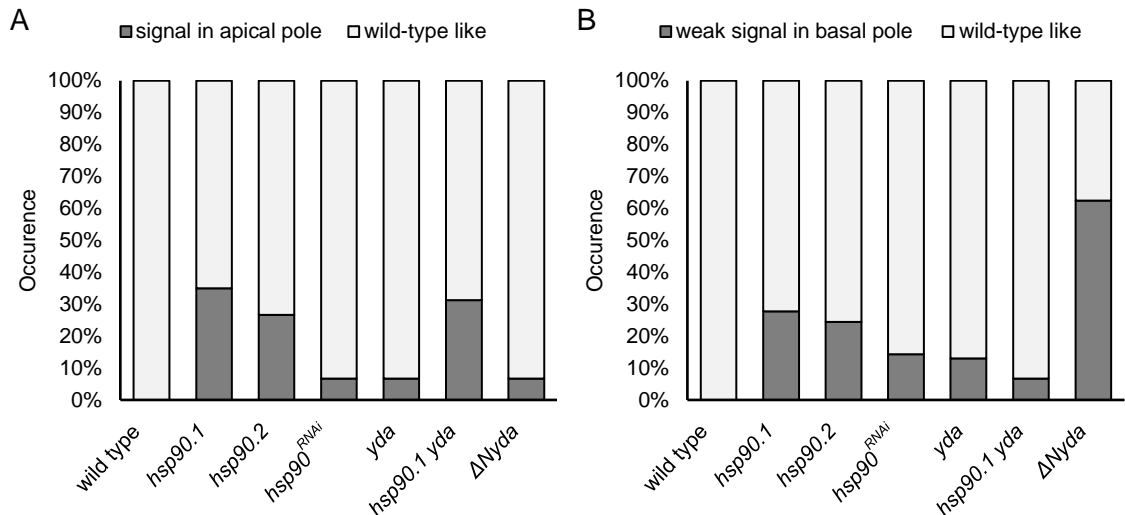
Figure 36. Quantification of the observed defects in auxin maxima localization during embryogenesis in *hsp90* and *yda* mutants. Adapted from Samakovli *et al.* (unpublished). Auxin maxima were visualized in embryos of the indicated genotypes and expressing *DR5::GFP*. (A, B) Quantification of observed abnormalities in auxin maxima localization and/or distribution: (A) ectopic signal in the apical part of embryos in the early heart stages (N≥15); (B) weak signal in the basal part of embryos in the heart stages (N≥32).

observed within the lower tier of the embryo proper (Fig. **37A,B**). Moreover, in some cases the auxin maxima in the basal pole were weaker compared to the wild type, similarly to the weak signal of the *DR5::GFP* reporter observed in *mpk, hsp90* mutants (**Fig. 25, 35**). The *ΔNyda* also exhibited a peculiar phenotype, which was the strongest of all phenotypes observed in the examined mutants. In *ΔNyda*, the signal was frequently weak in the basal pole of the embryo proper (63%, N=32; **Fig. 36B**), while remaining strong in the suspensor. Moreover, the signal was less restricted to the areas where auxin maxima would be expected and it appeared to be diffuse, making it difficult to delineate the areas where it was expressed (**Fig. 37E,F**).

The expression of *DR5::GFP* was examined in *hsp90.1 yda* double mutant (**Fig. 37C,D**). The weaker signal in the basal pole of embryo proper was observed less frequently (7%, N=60; **Fig. 36B**) than in both *hsp90.1* (28%) and *yda* (13%) single mutants suggesting that *hsp90.1 yda* double mutant is partially rescued regarding the auxin distribution in the basal pole. Conversely, the signal in apical poles of early heart stages was observed in more cases in *hsp90.1 yda* double mutant (31%, N=16; **Fig. 36A**) than in *yda* mutants (7%), however, it was less frequent than in *hsp90.1* mutant (35%).

While *hsp90* mutant embryos exhibit defects in auxin maxima localization in both the apical and the basal pole of embryo proper, only the weaker signal in the basal pole
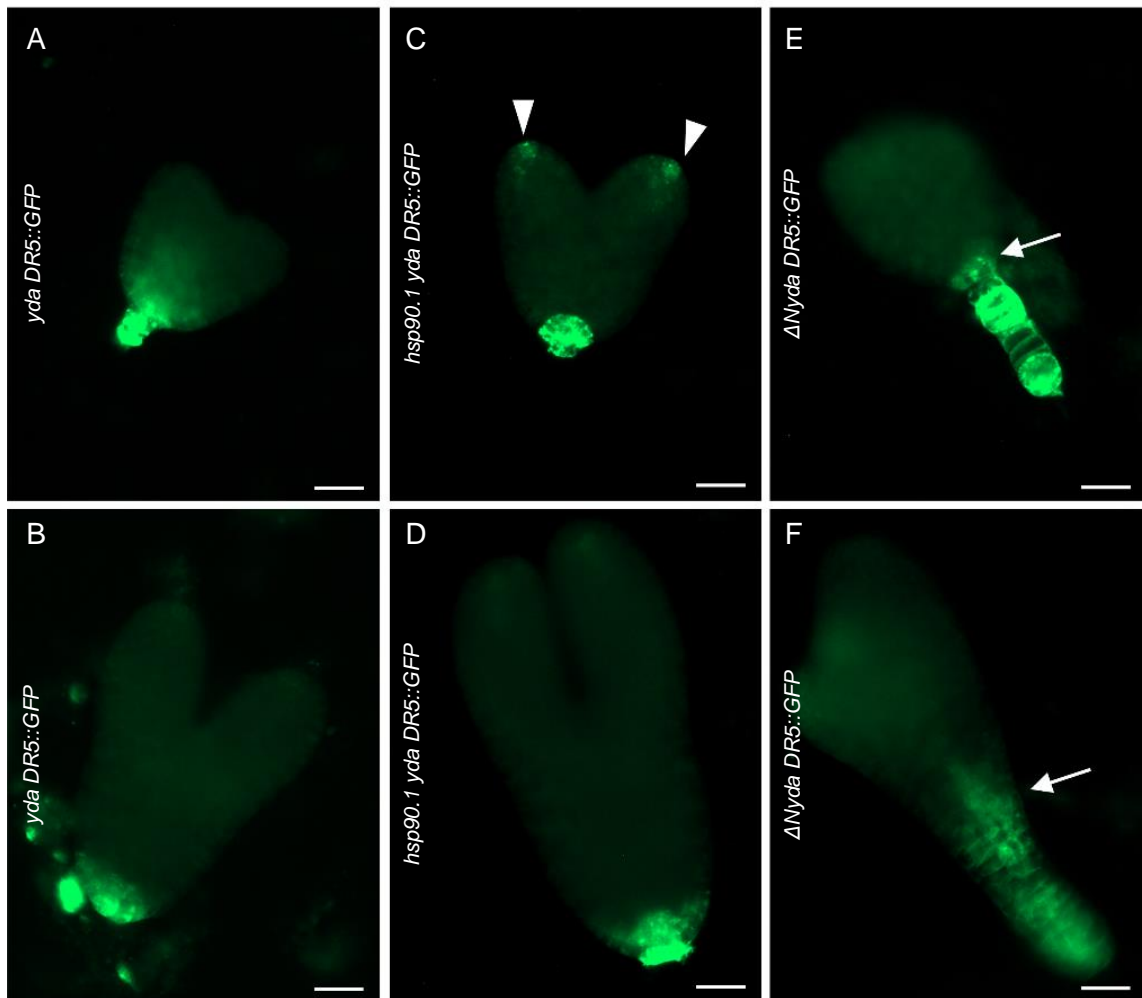
Figure 37. Abnormal distribution of auxin maxima during embryogenesis in *yda* mutants and *hsp90.1 yda* double mutant. Adapted from Samakovli *et al.* (unpublished). Auxin maxima in embryos were visualized in *yda* (A,B)*, hsp90.1 yda* (C,D)*, ΔNyda* (E,F) stably expressing *DR5::GFP*. Images show *DR5::GFP* signal distribution in early heart and late heart or torpedo stages. White arrowheads mark GFP signal in the apical part of the embryo; white arrow points to weak signal in the basal pole. Scale bars, 20 μm.

of the embryo proper is notable in *ΔNyda* mutants. Surprisingly, the yda mutant, with otherwise strong developmental phenotypes, is not markedly affected regarding the auxin maxima localization during early embryogenesis. Moreover, the *hsp90.1 yda* double mutant shows partial rescue in the phenotype of the weaker signal in the basal pole of the embryo proper, but it is similar to *hsp90.1* single mutant in the early detection of auxin maxima in the apical poles of the embryo. Therefore, it appears that the HSP90s affect the auxin maxima both in the apical and the basal pole of the embryo, while the function of YDA regarding the auxin distribution is restricted to the basal pole of the embryo.

3.2.4. Genetic depletion of HSP90.1 alleviates cell division plane orientation defects in primary root tip of *yda* mutants

While the role of HSP90s in plant development is not yet completely elucidated, the YDA-MPK pathway is known to affect both embryonic and postembryonic development (Bergmann *et al.* 2004; Lukowitz *et al.* 2004; Smékalová *et al.* 2014). Among these developmental events belong the establishment of root tip architecture, which begins during the embryogenesis at the globular stage and it is determined by properly oriented cell divisions. To examine whether HSP90s also affect primary root development, the roots of *hsp90* and *yda* seedlings stably expressing *DR5::GFP* (Ulmasov *et al.* 1997; Friml *et al.* 2003) had their plasma membranes stained with FM4-64 and then their root tip architecture was observed (**Fig. 38A-E**). Moreover, the *DR5::GFP* reporter was used to locate the quiescent centre, which was of special importance in mutants with highly distorted root tip anatomy. Moreover, root anatomy was also examined in *hsp90.1 yda, hsp90.1 ΔNyda* double mutants (**Fig. 39**).

In the primary root tip, the auxin maxima are localized in the quiescent centre, columella initials and columella root cap cells, which is a pattern observed in wild type seedlings as well as in *hsp90.1, hsp90.2* mutants (**Fig. 38A-C**). Moreover, their root tip anatomy of *hsp90.1, hsp90.2* mutants appeared normal and without any defects in the cell division plane orientation (**Fig. 39A-D**). Conversely, both root tip anatomy and auxin maxima distribution were altered in *yda* and*, ΔNyda* mutants, with severe defects in cell organization stemming from abnormal cell division plane orientation (**Fig. 39E,F,I,J**). Moreover, ectopic expression of *DR5::GFP* in lateral root cap cells was observed in *yda,*
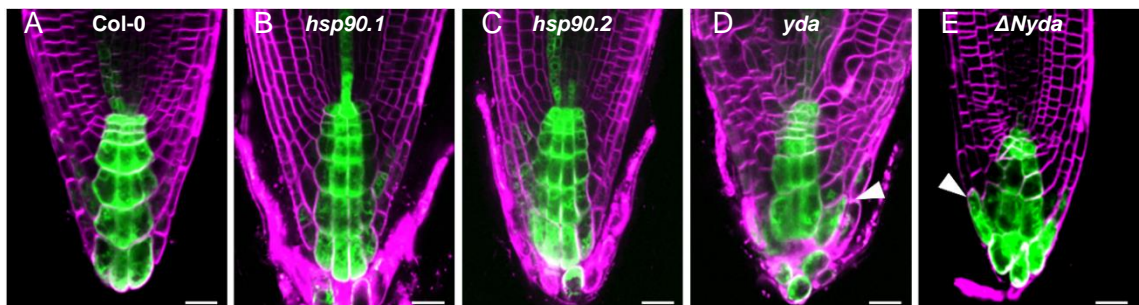
Figure 38. Analysis of *DR5:GFP* expression in the postembryonic development in *hsp90* and *yda* mutants. Adapted from Samakovli *et al.* (unpublished). To observe the auxin maxima distribution in the primary root, FM4-64 staining was performed on seedlings 5 days after germination, which were expressing *DR5::GFP* (A; **Fig. 14A**) and they had the mutant background of *hsp90.1* (B), *hsp90.2* (C), *yda* (D), and *ΔNyda* (E). White arrowheads point to ectopic signal distribution. Scale bars, 20 μm.
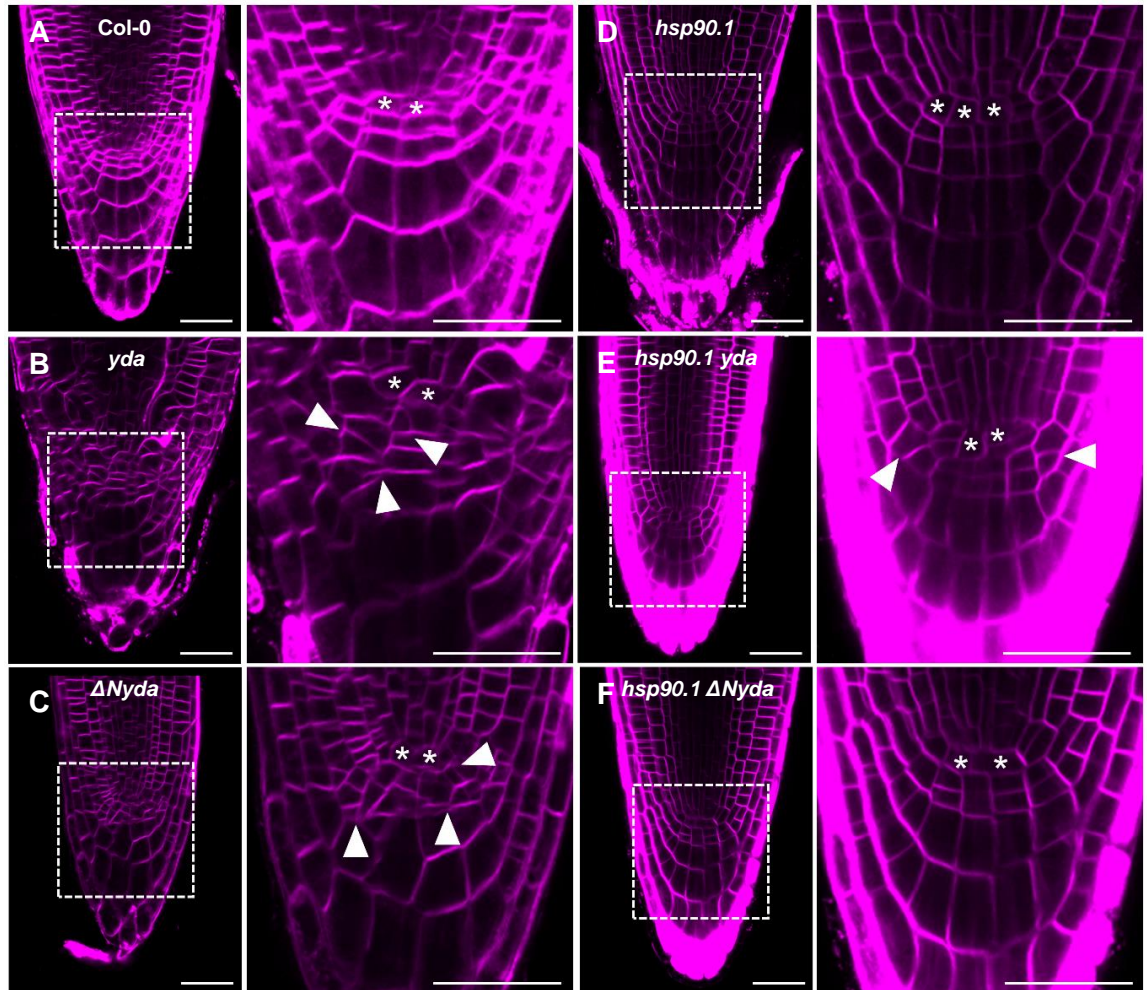
Figure 39. HSP90 depletion rescues morphological defects in root tip of *yda* mutants.
5 days after germination old seedlings were stained with FM4-64 to observe the primary root architecture in Col-0 (A,B; **Fig. 14A**), *hsp90.1* (C,D; **Fig. 38B**), *yda* (E,F; **Fig. 38D**), *hsp90.1 yda* (G,H), *ΔNyda* (I,J; **Fig. 38E**) and *hsp90.1 ΔNyda* (K,L). White stars mark the quiescent centre, white arrowheads point to the abnormally positioned plasma membranes. Scale bars, 20 μm.

ΔNyda mutants (**Fig. 38D,E**). The pattern organization was most heavily distorted in the quiescent centre and columella initials (**Fig. 39F,J**).

The root tip anatomy was also examined in *hsp90.1 yda, hsp90.1 ΔNyda* double mutants (**Fig. 39G,H,K,L**). While some abnormal positioning of the cell division plane was noted, no severe malformations in the root tip anatomy were found (N≥10). Therefore, genetic depletion of HSP90.1 partially rescues *yda, ΔNyda* defects in the cell division plane orientation in postembryonic root development.

3.3. Visualization of MAP65s with advanced microscopy techniques

The MAP65 proteins localize within microtubule arrays, where they promote their bundling (Van Damme *et al.* 2004) and protect them from depolymerization (Burkart and Dixit 2019). Hypothesis on the molecular mechanisms of MAP65 activity are often endorsed by results of *in vitro* experiments, thus, they should be tested *in planta*. To achieve this, microscopy methods ought to be improved and optimized to enable resolving the colocalization of MAP65s with microtubules and tracking their dynamic behaviour. This chapter aims to report on such advancements in microscopy techniques.

3.3.1. Resolution of MAP65-2 decorating cortical microtubules

To describe the organization and dynamics of MAP65 decorating cortical microtubules, two super-resolution approaches were chosen, specifically ACLSM and SIM. To compare these two platforms in terms of their resolution potential, the FWHM was used as a quantitative measure (**Fig. 40-42**). The imaging was performed on hypocotyl epidermal
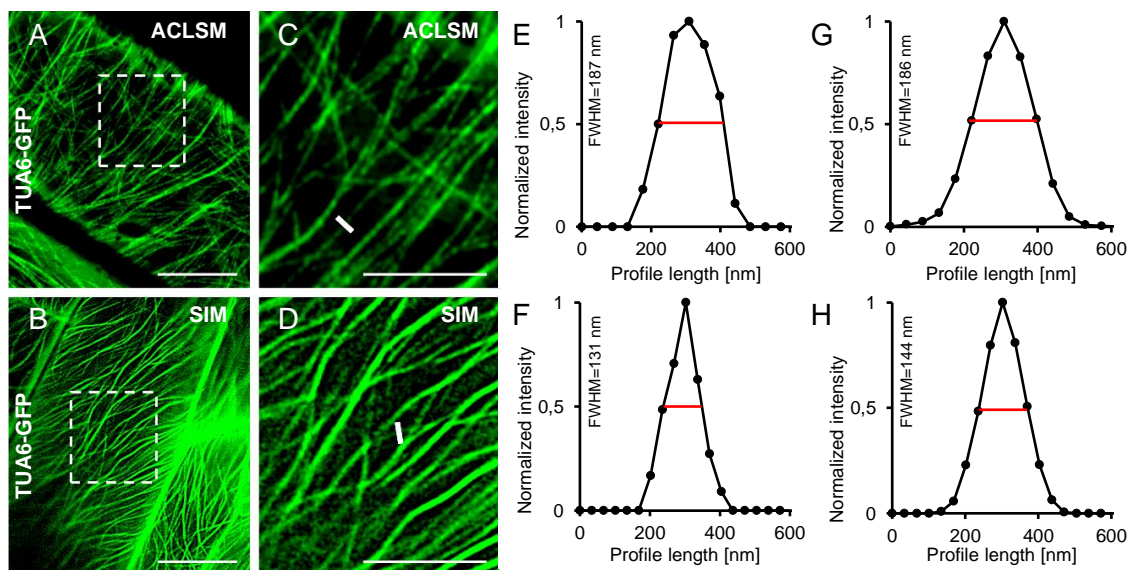
Figure 40. Resolution reached by either ACLSM or SIM in depicting cortical microtubules. Adapted from Vavrdová *et al.* (2020). Cortical microtubules in hypocotyl epidermal cells were visualized with TUA6-GFP marker. (A) Image from the ACLSM (objective 63×/1.40 NA); (B) image from the SIM (objective 63×/1.40 NA); (C, D) show area boxed in (A) and (B), respectively; (E, F) present normalized intensity measurement for the profile measurements marked by white line in (C) and (D), respectively; (G, H) provide a quantitative analysis showing averaged, coaligned, and normalized intensity profiles of TUA6-GFP-labeled microtubules from the ACLSM (G; N=43) and the SIM (H; N=44). Scale bars, 10 μm (A, B), or 5 μm (C, D), respectively. Abbreviations: ACLSM, Airyscan confocal laser scanning microscopy; FWHM, full-width at half maximum; SIM, structured illumination microscopy.

cells, which are generally the tissue of interest when examining interphase microtubule array (Kawamura *et al.* 2006; Pastuglia *et al.* 2006). For measuring the FWHM were used images of cortical microtubules in hypocotyl epidermal cells expressing TUA6-GFP (*CaMV35S::GFP:TUA6;* **Fig. 40A,B**) and pictures of MAP65-2 decorating cortical microtubules in the same type of cells expressing either eGFP-MAP65-2 (*MAP65-2::eGFP:MAP65-2*; **Fig. 41A,B**) or tagRFP-MAP65-2 (*MAP65-2::tagRFP:MAP65-2*; **Fig. 42A,B**). Within these images, fluorescence intensity profiles were drawn perpendicular to the thinnest observed microtubules and MAP65-2 decorating microtubules (**Fig. 40C,D, 41C,D, 42C,D**). The intensity profiles were normalized and used for generating graphs, where the normalized signal intensity was plotted against distance (**Fig. 40E,F, 41E,F, 42E,F**). These graphs were used for measuring the FWHM. With this approach, the resolution was determined for the abovementioned chimeric fluorescent proteins visualized by either ACLSM or SIM. In both platforms, the 63×/1.40 NA oil immersion objective was used.

GFP-TUA6-labeled microtubules were resolved at 186±27 nm (mean±SD; N=43, **Fig. 40G**) by the ACLSM, while with the SIM, the resolution of
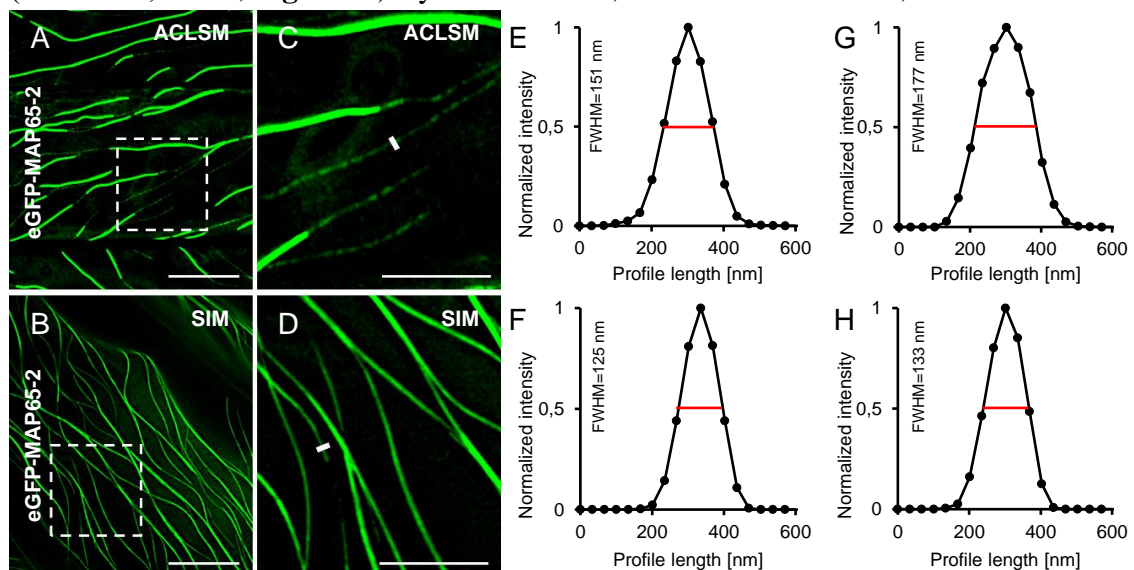
Figure 41. Resolving details of eGFP-MAP65-2 decoration of cortical microtubules by either ACLSM or SIM. Adapted from Vavrdová *et al.* (2020). MAP65-2 decoration of cortical microtubules in hypocotyl epidermal cells was visualized with eGFP-MAP65-2. (A) Image from the ACLSM (objective 63×/1.40 NA); (B) Image from the SIM (objective 63×/1.40 NA); (C-D) show area boxed in (A) and (B), respectively; (E-F) present normalized intensity measurements for the profile measurements marked by white line in (C) and (D), respectively; (G-H) provide a quantitative analysis showing averaged, coaligned, and normalized intensity profiles of individual eGFP-MAP65-2-labeled microtubule bundles from the ACLSM (G; N=36) and the SIM (H; N=36). Scale bars, 10 μm (A, B), or 5 μm (C, D), respectively. Abbreviations: ACLSM, Airyscan confocal laser scanning microscopy; FWHM, full-width at half maximum; SIM, structured illumination microscopy,

Figure 42. Resolving details of tagRFP-MAP65-2 decoration of cortical microtubules by either ACLSM or SIM. Adapted from Vavrdová *et al.* (2020). MAP65-2 decoration of cortical microtubules in hypocotyl epidermal cells was visualized with tagRFP-MAP65-2. (A) Image from the ACLSM (objective 63×/1.40 NA); (B) Image from the SIM (objective 63×/1.40 NA); (C-D) show area boxed in (A) and (B), respectively; (E-F) present normalized intensity measurements for the profile measurements marked by white line in (C) and (D), respectively; (G-H) provide a quantitative analysis showing averaged, coaligned, and normalized intensity profiles of individual tagRFP-MAP65-2-labeled microtubule bundles from the ACLSM (G; N=36) and the SIM (H; N=36). Scale bars, 10 μm (A, B), or 5 μm (C, D), respectively. Abbreviations: ACLSM, Airyscan confocal laser scanning microscopy; FWHM, full-width at half maximum; SIM, structured illumination microscopy.

labelled microtubules was measured at 144±25 nm (mean±SD; N=44, **Fig. 40H**), which is a statistically significant improvement (**Fig. 43A**). Regarding the MAP65-2 tagged with fluorescent proteins, the ACLSM resolved the eGFP-MAP65-2 at 177±19 nm (mean±SD; N=36, **Fig. 41G**) and tagRFP-MAP65-2 at 176±18 nm (mean±SD; N=47, **Fig. 42G**), thus, reaching similar resolution details for both fluorescent proteins. This was also the case for measurements from the SIM platform, specifically 133±20 nm (mean±SD; N=39, **Fig. 41H**) for eGFP-MAP65-2 and 129±14 nm (mean±SD; N=43, **Fig. 42H**) for tagRFP-MAP65-2. In summary, when comparing red and green labelled MAP65-2, no difference was found regardless of the used platform (**Fig. 43A**).

Taken together, the SIM platform was found out to provide significantly better resolution than ACLSM while visualizing TUA6-GFP, eGFP-MAP65-2 (**Fig. 43A**) or tagRFP-MAP65-2 (**Fig. 43B**).
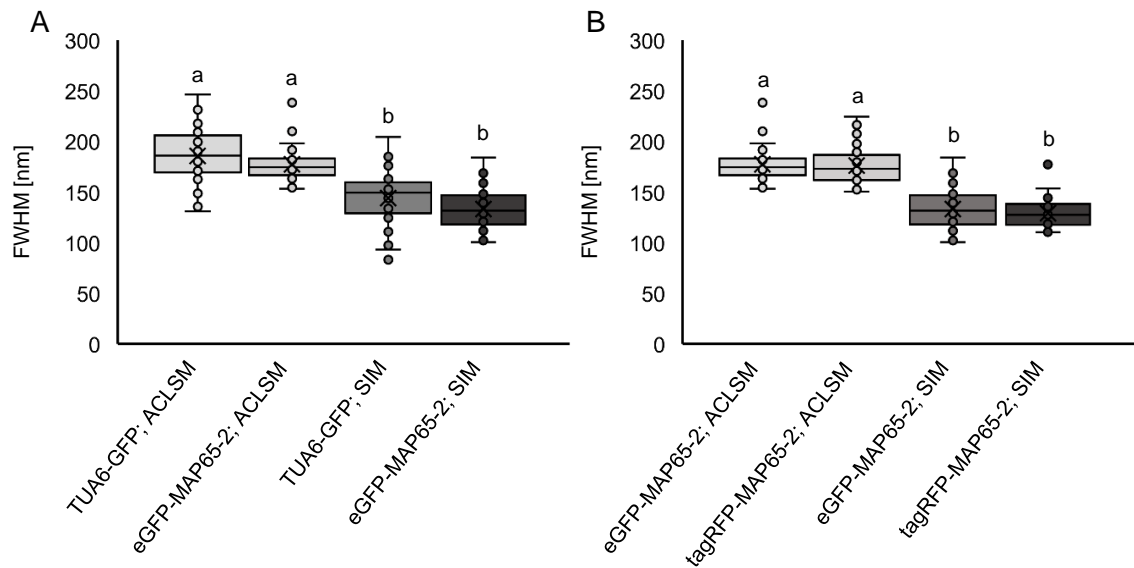
Figure 43. Comparison of ACLSM and SIM in resolving details of cortical microtubules or MAP65-2 decoration of cortical microtubules. Adapted from Vavrdová *et al.* (2020). (A,B) Boxplots show full-width at half maximum (FWHM) values measured on data obtained from either Airyscan confocal laser scanning microscopy (ACLSM) or structured illumination microscopy (SIM) platform. They present comparison of resolution reached for TUA6-GFP and eGFP-MAP65-2 (A) or eGFP-MAP65-2 and tagRFP-MAP65-2 (B). For statistical analysis, Kruskal-Wallis test was used (letters in the graph are shared by groups without statistically significant differences at the 0.001 probability level) and results are in **Table S4**. Description of box plot: average is represented by ×, median by the middle line, first quartile by the bottom line, third quartile by the top line; the whiskers lie within the 1.5× interquartile range (defined from the first to the third quartile), outliers are marked by points.

3.3.2. MAP65-2 decorates cortical microtubules

The next objective was to covisualize MAP65-2 and cortical microtubules to characterize their relations, especially in composite cortical microtubule bundles. Despite the SIM platform outperforming ACLSM regarding the resolution capacity, the ACLSM is advantageous for sequential imaging of two different fluorophores. Firstly, the sequential imaging was considerably faster on the ACLSM platform compared with the SIM platform (regarding the configuration which was at disposal). Secondly, the photon collection is better in the ACLSM even at sub-optimal levels of signal-to-noise ratios (Huff 2016). Moreover, in the pilot experiments, bleaching was particularly affecting the imaging of tagRFP-MAP65-2 by the SIM. Therefore, by choosing the ACLSM over the SIM, the bleaching issues linked with the application of the SIM were avoided.

Since the aim was to describe the MAP65-2 decoration of cortical microtubules, the MAP65-2 localization was examined by using two approaches described previously for characterizing cortical microtubules (Komis *et al.* 2014), for it was of interest to

examine whether MAP65-2 colocalizing with microtubules follow the same trends. Namely, the cortical microtubules are known to create bundles consisting of various numbers of individual filaments. The composite nature of cortical microtubules can be discriminated as the fluorescence intensity maximum of a bundle is increased compared to the fluorescence intensity maximum of its respective branches and this increase is linear (Komis *et al.* 2014).

To determine whether there is a linear increase in maximum fluorescence intensity of fluorescently labelled MAP65-2 upon the joining of two microtubule bundles into one, images of line expressing both tagRFP-MAP65-2 and TUA6-GFP were searched to find such events. Specifically, in places where microtubule bundles were branching into two smaller bundles (**Fig. 44A-C**), the fluorescence intensity profiles were drawn perpendicularly to the two smaller bundles and the larger bundle. Since both tagRFP-MAP65-2 and TUA6-GFP exhibit local deviations in fluorescence intensity maxima, the intensity profiles were independently drawn five times and measurements from these repetitions were averaged. Then, measurements from eight branching events were averaged and plotted against distance (**Fig. 44D-E**). The fluorescence intensity maxima of both TUA6-GFP (**Fig. 44D,F**) and tagRFP-MAP65-2 (**Fig. 44E,G**) are distinctly different for the composite bundle and its smaller and larger branch. The linear correlation coefficient calculated for the absolute fluorescence intensity maxima of these three types of microtubule bundles reached high values for TUA6-GFP (R^2=0.9966; **Fig. 44F**) corroborating the previous observation of a linear increase in maximum fluorescence intensity upon the inclusion of microtubules within a bundle (Komis *et al.* 2014). The MAP65-2 appears to follow this trend as the linear correlation coefficient was also high for tagRFP-MAP65-2 (R^2=0.9786; **Fig. 44G**). This means that the maximum signal intensity of tagRFP-MAP65-2 corresponds to the amount of individual microtubules constituting the bundle.

The images of the line coexpressing tagRFP-MAP65-2 and TUA6-GFP, we also used to examine the signal intensity fluctuation alongside the cortical microtubules labelled with TUA6-GFP. For this purpose, longitudinal profiles were drawn along cortical microtubules (**Fig. 45A-C**). Because the absolute signal intensity values differ greatly between tagRFP-MAP65-2 and TUA6-GFP, the measurements from longitudinal profiles were normalized and then they were plotted against distance (**Fig. 45D**). The signal intensity fluctuation of TUA6-GFP reported previously was also observed
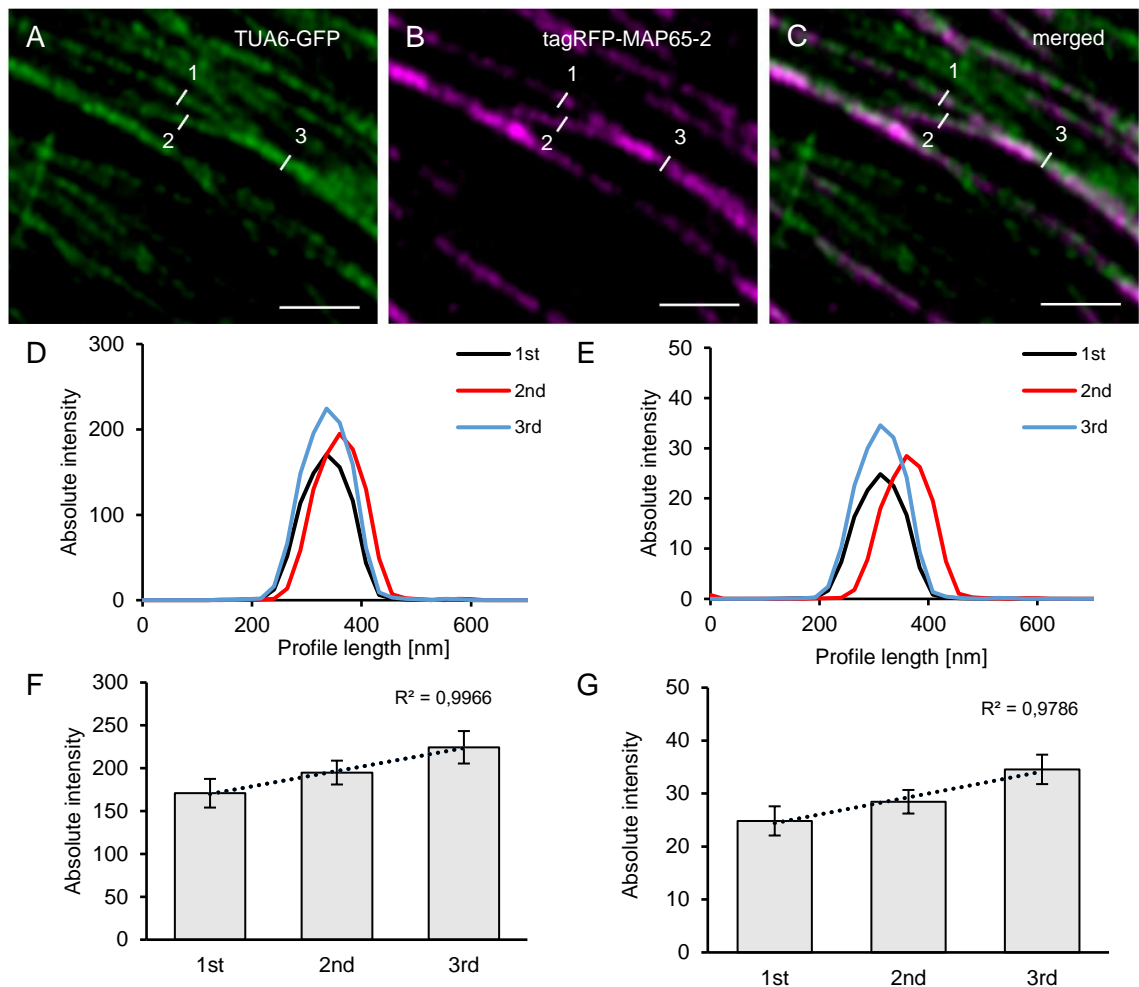
Figure 44. Signal intensity of tagRFP-MAP65-2 reflects the microtubule bundle composition. Adapted from Vavrdová *et al.* (2020). Hypocotyl epidermal cells of stably transformed lines expressing both tagRFP-MAP65-2 and TUA6-GFP were observed in the Airyscan confocal laser scanning microscope (objective 63×/1.40 NA). (A-C) overview of an area with microtubule branching with TUA6-GFP shown in the green channel (A), tagRFP-MAP65-2 in the magenta channel (B) and (C) is a merged picture; measured microtubule bundles are visualized with white lines and labeled with numbers according to their strength (1 being the weakest and 3 the strongest bundle). Microtubule bundles were quantified by fluorescence intensity profiling and averaged values are shown in (D) for TUA6-GFP and (E) for tagRFP-MAP65-2. Quantitative evaluation is given in (F) for TUA6-GFP and in (G) for tagRFP-MAP65-2 (mean±SD; R^2, linear correlation coefficient; N=8, 5 technical repetitions). Scale bars, 2 μm.

here, reflecting the uneven binding of TUA6-GFP into microtubules (Komis *et al.* 2014). Similarly, the signal intensity fluctuation of tagRFP-MAP65-2 signifies the uneven incorporation of tagRFP-MAP65-2 alongside microtubule bundles (**Fig. 45D**). The signal intensity changes in tagRFP-MAP65-2 were not completely following the signal intensity fluctuation of TUA6-GFP. Nevertheless, the overall changes in signal intensity were similar for both tagRFP-MAP65-2 and TUA6-GFP. This leads to a conclusion, that signal intensity of tagRFP-MAP65-2 reflects the microtubule bundle composition.
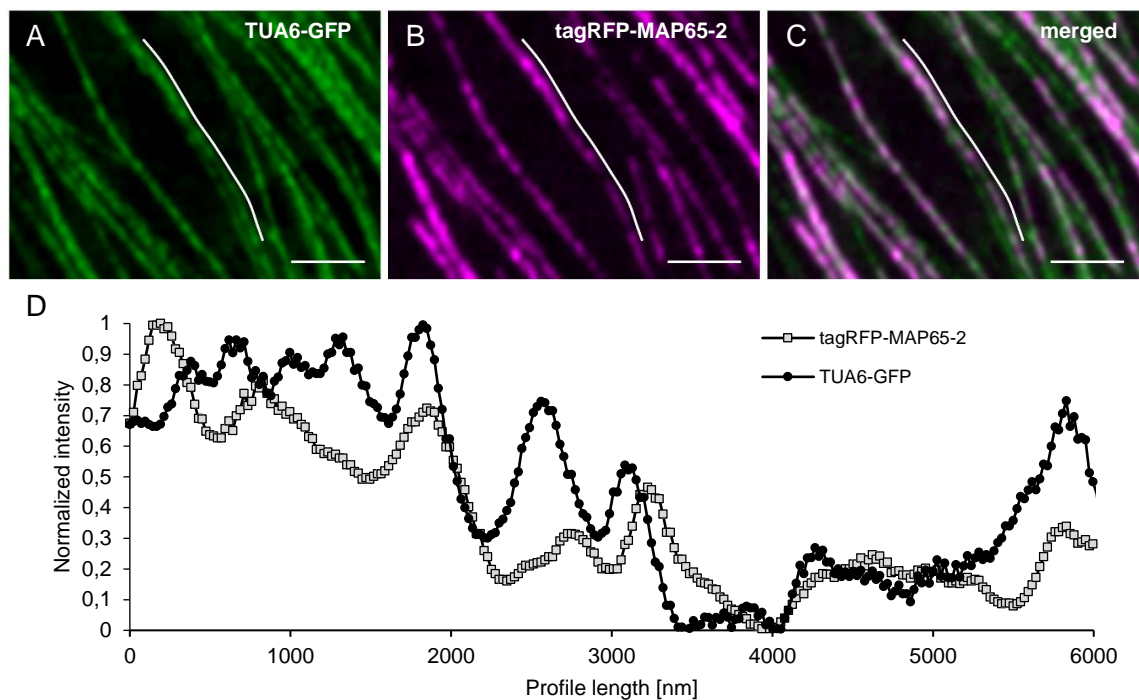
Figure 45. Oscillation of tagRFP-MAP65 signal along cortical microtubules. Adapted from Vavrdová *et al.* (2020). Hypocotyl epidermal cells of stably transformed lines expressing both tagRFP-MAP65-2 and TUA6-GFP were observed in the Airyscan confocal laser scanning microscope (objective 63×/1.40 NA). (A-C) overview of a microtubule bundle, TUA6-GFP shown in the green channel (A), tagRFP-MAP65-2 in the magenta channel (B) and (C) is a merged picture; white line visualizes longitudinal profile, which is shown in (D), where normalized fluorescence intensities are plotted against distance. Scale bars, 2 μm.

While analysing the images of the line coexpressing tagRFP-MAP65-2 and TUA6-GFP, it was observed that in certain places, tagRFP-MAP65-2 localized not only within the microtubule bundles but also in between two close parallel microtubule bundles (**Fig. 46A-C**). This phenomenon was also documented on fluorescence intensity profiles drawn perpendicularly to such events (**Fig. 46D-F**). Graph showing the normalized measurements plotted against distance (**Fig. 46G**) further validate these observations.

As mentioned above, the SIM platform outperforms the ACLSM regarding resolution, thus, this line was observed also on this platform to verify these findings. The images from this line taken on the SIM platform (100x/1.57 NA objective) also displayed this peculiarity, where within the bundles of cortical microtubules (**Fig. 46H-J**), the signal specific for tagRFP-MAP65-2 was observed in between two microtubule bundles (**Fig. 46K-N**).
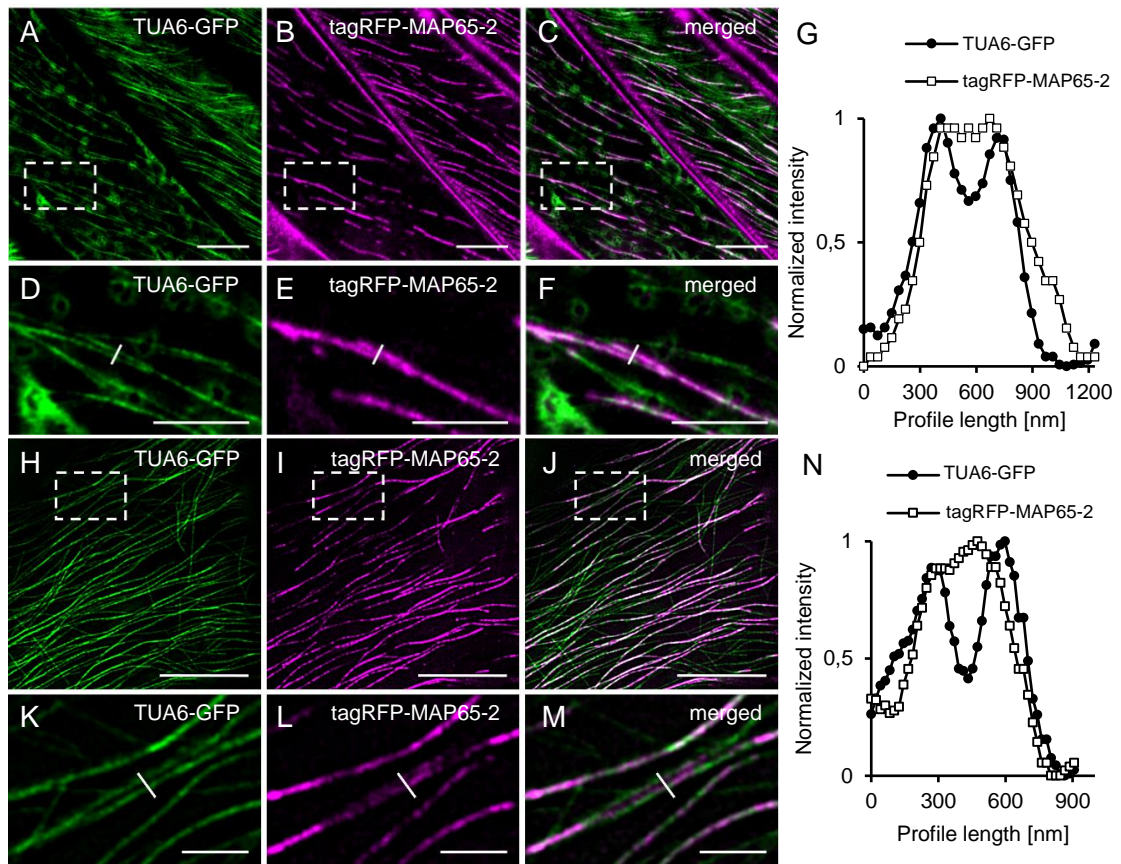
Figure 46. Colocalization of MAP65-2 with microtubules. Adapted from Vavrdová *et al.* (2020). The colocalization of MAP65-2 with microtubules was visualized with either the Airyscan laser scanning microscopy (A-G) or the structured illumination microscopy (H-N). (A-C) images of the line stably coexpressing TUA6-GFP (A) and tagRFP-MAP65-2 (B), an overlay is in (C). Boxed area in (A-C) is shown in (D-F); (D) TUA6-GFP, (E) tagRFP-MAP65-2 and in (F) is an overlay; white line in (E-F) represents a perpendicularly drawn fluorescence intensity profile. After normalization, the profile intensity measurement was plotted against distance and the graph is in (G). (H-J) images of the line stably coexpressing TUA6-GFP (H) and tagRFP-MAP65-2 (I), an overlay is in (J). Boxed area in (H-J) is shown in (K-M); (K) TUA6-GFP, (L) tagRFP-MAP65-2 and in (M) is an overlay; white line in (K-M) represents a perpendicularly drawn fluorescence intensity profile. After normalization, the profile intensity measurement was plotted against distance and the graph is in (N). Scale bars, 10 μm (A-C,H-J), 5 μm (D-F), 2 μm (K-M).

3.3.3. Dynamics of MAP65-2

For cortical microtubules is typical their dynamic behaviour as they constantly switch between the phases of growth and shrinkage (Shaw *et al.* 2003; Komis *et al.* 2014). The MAP65s crosslink predominantly antiparallel microtubules and it is decorating plus ends of antiparallel microtubules as long as the microtubules are bundled together, leading to changes in the length of MAP65-2 mirroring the end-wise microtubule dynamics (Lucas *et al.* 2011).

To describe the dynamic behaviour or MAP65-2, time-lapsed images of the line expressing eGFP-MAP65-2 were taken on the SIM platform, which enables fast scanning at high resolution. The effective time interval was 4.231 s and the time-lapsed images have usually been taken for 10 min (**Fig. 47**). This setting should provide data collection faithfully reporting on the MAP65-2 dynamics (Shaw *et al.* 2003; Komis *et al.* 2014).

The time-lapsed imaging showed that eGFP-MAP65-2 signal exhibits dynamic behaviour (**Fig. 47A-C**), where the growth in length is followed by rapid shrinkage. This behaviour resembles the threadmilling of the plus end of cortical microtubules, which is
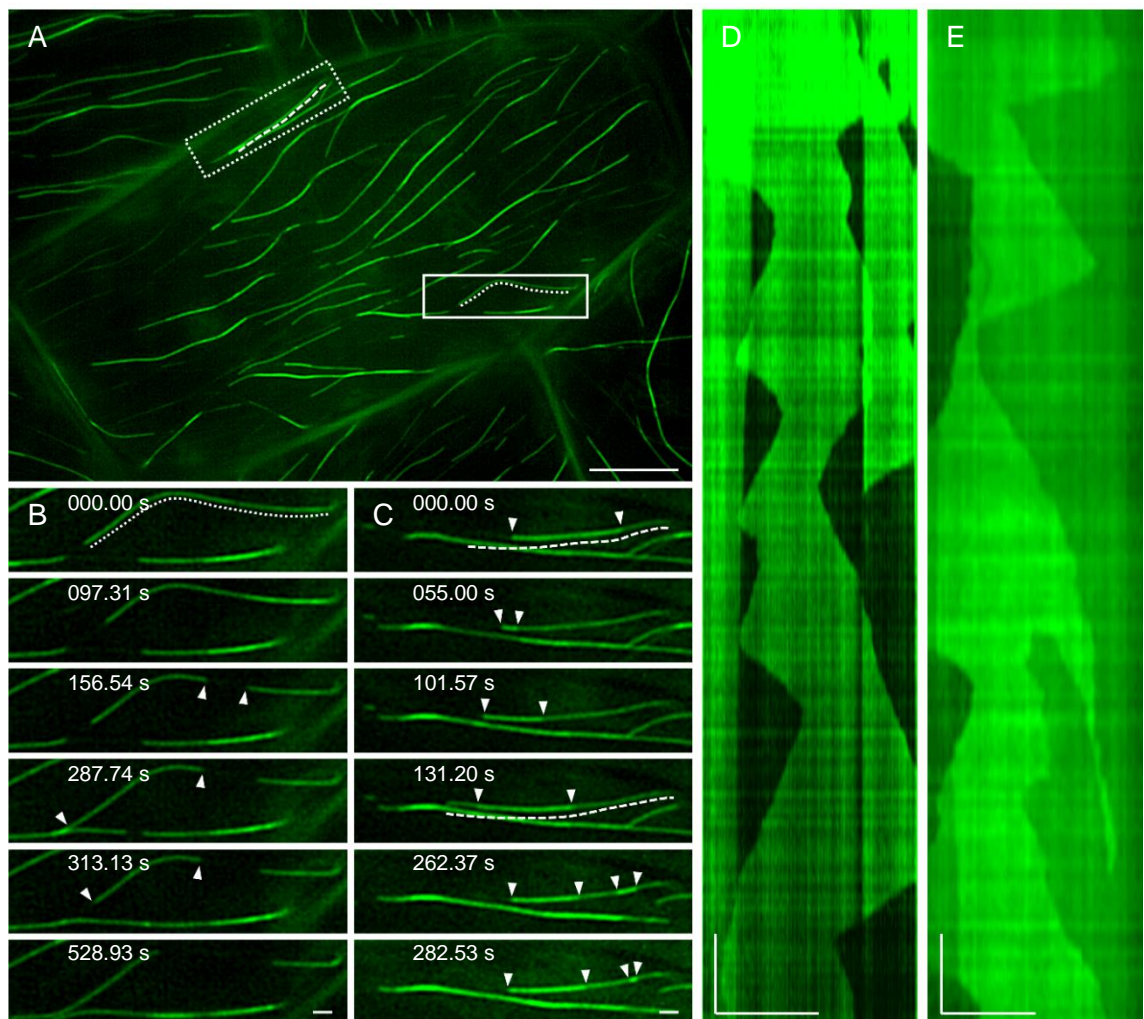
Figure 47. MAP65-2 dynamics. Adapted from Vavrdová *et al.* (2020). (A) an overview of a hypocotyl epidermal cell of stably transformed line expressing eGFP-MAP65-2 observed by structured illumination microscopy (objective 63×/1.40 NA). In full-line box is area, which is magnified in stills in (B); while in dotted-line box is area depicted in stills in (C). Stills in (B) show growth of an individual microtubule bundle as is demonstrated on a kymograph (D), which was generated based on region of interest marked by the dotted line in (A). Complex dynamics within composite microtubule bundle is demonstrated in stills in (C) and in a corresponding kymograph in (E), which was generated based on region of interest marked by the dashed line in (A); white arrowheads point to microtubule ends. Scale bars, 10 µm (A), or 1 µm (B-E); time bars, 1 min (D,E).
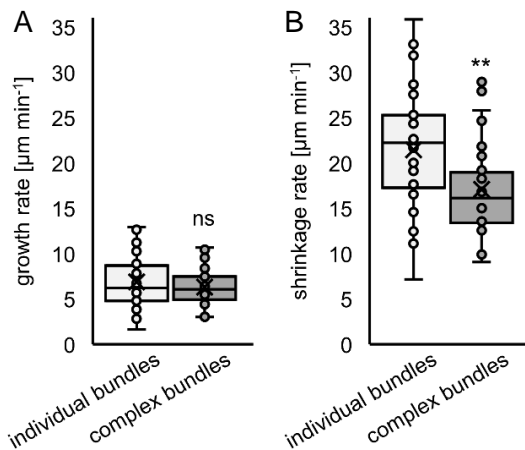
Figure 48. Quantification of MAP65-2 dynamics. Adapted from Vavrdová *et al.* (2020). Time-lapsed imaging of line expressing eGFP-MAP65-2 made on the structured illumination microscopy platform (objective 63×/1.40 NA) was used for generating kymographs. From the measurements made on the kymographs, the growth and shrinkage rates were calculated. (A, B) Boxplots present comparison of the growth (A) and shrinkage (B) rates for individual and complex bundles. Statistical analysis: Mann-Whitney U test; (A) U (N=99)=1081, p=0.4115 (ns - not statistically significant); (B) U (N=73)=382, p=0.0032 (** significant at p<0.01). Description of the box plot: average is presented by ×, median by the middle line, first quartile by the bottom line, third quartile by the top line; the whiskers lie within the 1.5× interquartile range (defined from the first to the third quartile), outliers are presented by points.

in line with previous studies (Van Damme *et al.* 2004; Lucas *et al.* 2011). Time-lapsed images were used for generating kymographs (**Fig. 47D**), which were then used for determining parameters describing dynamics (**Fig. 48**). The MAP65-2 end dynamic, which supposedly corresponds to the plus ends of antiparallel microtubule pairs, was characterized with growth and shrinkage rates of 6.87±2.72 µm min^{-1} (N=57; **Fig. 48A**) and 21.35±6.38 µm min^{-1} (N=43; **Fig. 48B**), respectively, and with the frequencies of rescue and catastrophe reaching 0.0107 and 0.0446, respectively.

Similarly, this dynamic behaviour was also examined in more complex bundles (**Fig. 47A,C**). Dynamic parameters were again extrapolated from data measured within kymographs (**Fig. 47E**). Within these complex bundles, the growth and shrinkage rates were 6.32±2.00 µm min^{-1} (N=42; **Fig. 48A**) and 17.08±4.84 µm min^{-1} (N=30; **Fig. 48B**), respectively. The frequencies of rescue and catastrophe were 0.0114 and 0.0404, respectively. While the growth rates within individual bundles were comparable to those within complex bundles (**Fig. 48A**), the shrinkage rate within complex bundles were significantly smaller compared to the rate within individual bundles (**Fig. 48B**). Despite the MAP65-2 dynamic behaviour mimicking that of plus end cortical microtubules, the difference in shrinkage rate within individual and complex bundles suggests that apart from following cortical microtubule dynamics, it has its own methods of operation.

3.3.4. MAP65-2 and MAP65-3 colocalize with mitotic microtubular structures

Apart from cortical microtubules, MAP65-2 is known to colocalize with specific mitotic microtubule arrays, namely the preprophase band and phragmoplast (Lucas and Shaw 2012). Conversely, MAP65-3 is known to associate only with mitotic microtubule arrays, specifically the preprophase band and phragmoplast (Müller *et al.* 2004; Caillaud *et al.* 2008). Inferring from the reports on differential subcellular localization of individual members of the MAP65 protein family (Gaillard *et al.* 2008), in order to properly understand the possible differences in functions of individual MAP65s, it is necessary to first characterize the subtle nuances in their subcellular localization throughout the cell cycle.

To confirm the colocalization of MAP65-2 and MAP65-3 with specific mitotic microtubule arrays, the lines coexpressing tagRFP-MAP65-2 and TUA6-GFP, or tagRFP-MAP65-2 and eGFP-MAP65-3, were first observed using LSFM (**Fig. 49-51**). At the cost of lower resolution, the LSFM is capable of time-lapsed imaging of whole
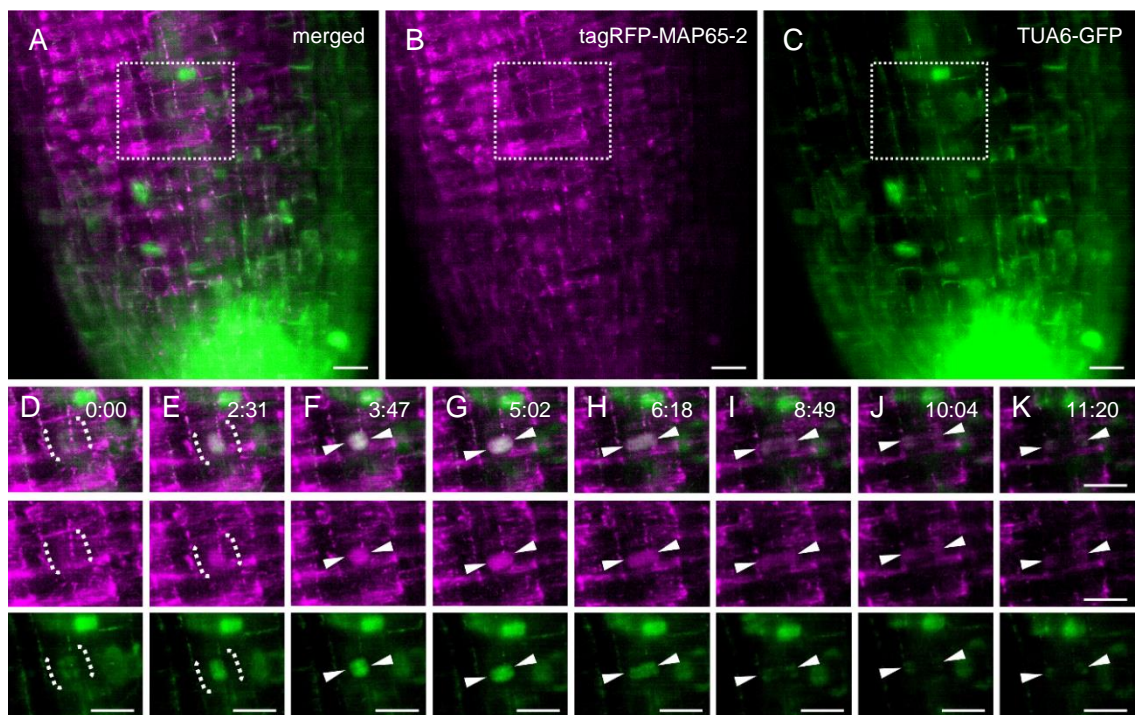
Figure 49. MAP65-2 decorates mitotic microtubular structures. Light sheet microscopy was used to capture growing root of the line expressing both tagRFP-MAP65-2 and TUA6-GFP. (A-C) an overview showing merged picture (A), the magenta channel reporting on tagRFP-MAP65-2 signal (B) and the green channel depicting TUA6-GFP signal (C). The boxed areas in (A-C) are shown in stills in (D-K). (D-K) presents selected stills, where bellow the merged picture are corresponding images from the magenta and green channels. White dotted brackets mark the spindle (D, E), white arrowheads point to the phragmoplast, specifically the disc (F, G), ring (H, I) and discontinuous phragmoplast (J, K). Scale bars, 10 μm; time format, min:s. Image acquisition by Miroslav Ovečka.

roots spanning days (Ovečka *et al.* 2015). In this way, imaging the roots of these lines as they were growing in the media was possible. In the resulting videos, the colocalization of MAP65-2 and MAP65-3 with different mitotic microtubule arrays could be observed. As the whole root tips with multiple cell divisions were visualized, repeated examination of MAP65-2, MAP65-3 localization throughout cell division was possible, resulting in verifying the observations.

Firstly, tagRFP-MAP65-2 subcellular localization was compared to GFP-labelled microtubules (**Fig. 49A-C**). As expected, the tagRFP-MAP65-2 signal is not present in metaphase spindle (**Fig. 49D**), but a weak specific signal is detected in the anaphase spindle when microtubules start to assemble into the disc phragmoplast (**Fig. 49E**). The MAP65-2 is present at the emergence of the disc phragmoplast (**Fig. 49F**) and it colocalizes with microtubules throughout the phragmoplast expansion (**Fig. 49G-K**).
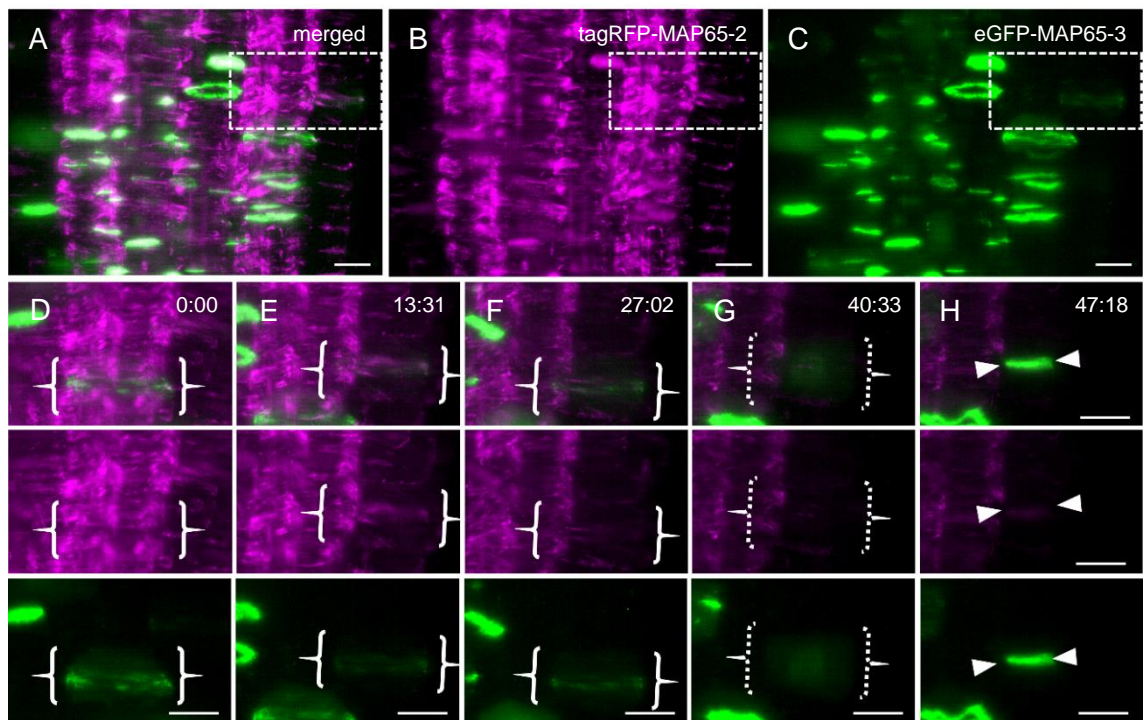
Figure 50. Colocalization of MAP65-2 and MAP65-3 with mitotic structures. Light sheet microscopy was used to capture growing root of the line expressing both tagRFP-MAP65-2 and eGFP-MAP65-3. (A-C) an overview showing merged picture (A), the magenta channel reporting on tagRFP-MAP65-2 signal (B) and the green channel depicting eGFP-MAP65-3 signal (C). The boxed area marked by dashed line in (A-C) is shown stills in (D-H). In (D-H), the stills are presented as merged pictures, with corresponding images from the magenta and green channels bellow them. White full-line brackets mark the preprophase band (D-F), dotted brackets surround the spindle (G), white arrowheads point to the disc phragmoplast (H). Scale bars, 10 μm; time format, min:s. Image acquisition by Miroslav Ovečka.

Next, the colocalization of tagRFP-MAP65-2 and eGFP-MAP65-3 during cell division was compared (**Fig. 50A-C, 51A-C**). Both tagRFP-MAP65-2 and eGFP-MAP65-3 decorate the preprophase band (**Fig. 50D-F**), while they are absent from the metaphase spindle (**Fig. 50G, 51D**; the position of the spindle was determined based on time progression of the time-lapsed imaging and the position of tagRFP-MAP65-2 and eGFP-MAP65-3 signal marking the preprophase band before the spindle assembly, and the phragmoplast after the spindle disassembly). The signal of tagRFP-MAP65-2 and eGFP-MAP65-3, respectively, reappears as the disc phragmoplast is formed (**Fig. 50H, 51E**) and both proteins relocalize from the centre of the cell to the cell division site as the phragmoplast expands (**Fig. 51F-I**).

Although the LSFM provided information on the general localization of MAP65-2 and MAP65-3 during the cell cycle, precise analysis of the subcellular localization of these proteins is needed. Therefore, the SIM platform was employed as it enables
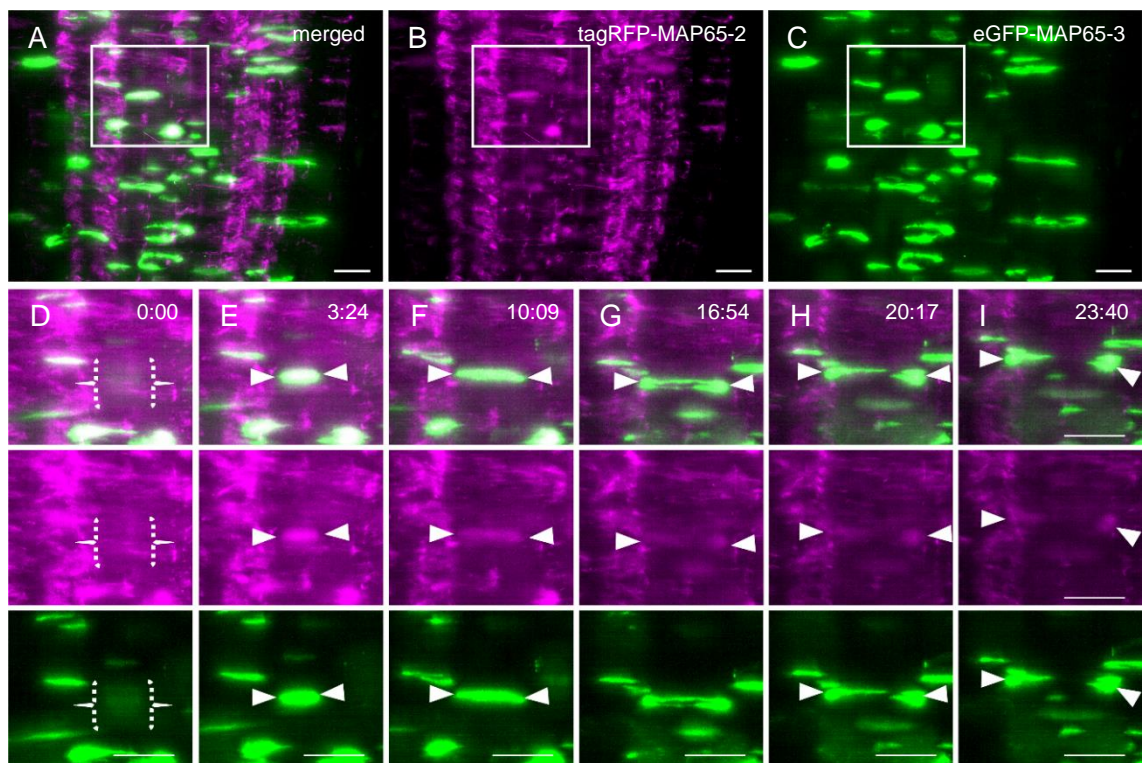
Figure 51. Colocalization of MAP65-2 and MAP65-3 with mitotic microtubular structures. Light sheet microscopy was used to capture growing root of the line expressing both tagRFP-MAP65-2 and eGFP-MAP65-3. (A-C) an overview showing merged picture (A), the magenta channel reporting on tagRFP-MAP65-2 signal (B) and the green channel depicting eGFP-MAP65-3 signal (C). The boxed area marked by full line in (A-C) is shown stills in (D-H). In (D-H), the stills are presented as merged pictures, with corresponding images from the magenta and green channels bellow them. White dotted brackets surround the spindle (D), white arrowheads point to the phragmoplast, specifically disc (E), ring (F, G) and discontinuous phragmoplast (H, I). Scale bars, 10 μm; time format, min:s. Image acquisition by Miroslav Ovečka.

the acquisition of images with high resolution. Live cell time-lapsed imaging of eGFP-MAP65-2 (**Fig. 52**) confirmed the observations from the LSFM on the absence of e-GFP-MAP65-2 at the spindle (**Fig. 52A,B**). It also enabled better description of the transition between spindle and phragmoplast (**Fig. 52C,D**) and its presence at the phragmoplast (**Fig. 52D-F**). From the stills of the time-lapsed imaging is apparent, that during the anaphase, the previously absent specific signal for e-GFP-MAP65-2 appears again to decorate microtubule bundles. Moreover, this happens during the assembly of the disc phragmoplast (**Fig. 52D**), suggesting that MAP65-2 stabilizes microtubule bundles which form into phragmoplast. At the time the disc phragmoplast is formed it is strongly marked by e-GFP-MAP65-2 (**Fig. 52E**). As the disc phragmoplast develops first into ring phragmoplast, and then in discontinuous phragmoplast, the MAP65-2 signal is following the presumed localization of microtubules. At the early stages of the phragmoplast, MAP65-2 decorates the entire phragmoplast. As the phragmoplast expansion progresses, the MAP65-2-decoration of microtubules begins to narrow towards the phragmoplast midzone.

The SIM platform was used for providing high-resolution images of mitotic structures labelled by eGFP-MAP65-3 (**Fig. 53**). Corroborating the observations from LSFM, eGFP-MAP65-3 localizes at the preprophase band and phragmoplast (**Fig. 53A**). While the arrangement of MAP65-3 closely mimics the organization of microtubules in the preprophase band (**Fig. 53B**), the organization of MAP65-3 in the phragmoplast differs from the pattern of MAP65-2 (**Fig. 52E, 53C**). Rather than broadly decorating
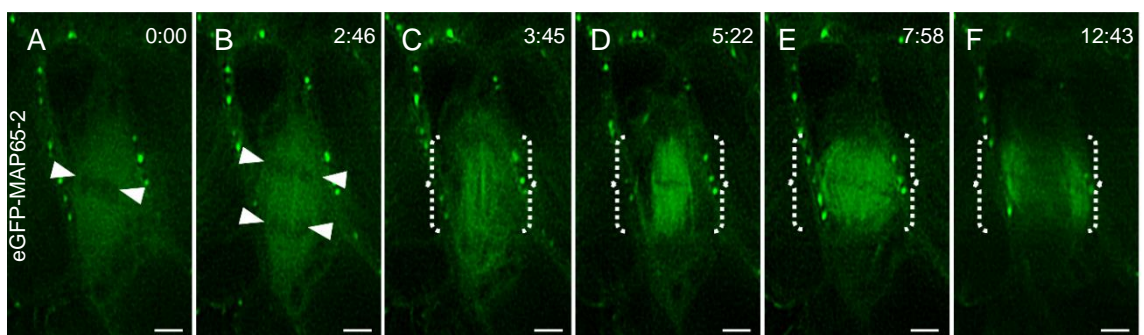
Figure 52. Details of MAP65-2 localization during the cell division. Visualization of eGFP-MAP65-2 by the structured illumination microscopy. (A-F) present stills from time-lapsed imaging. White arrowheads point to places without strong background signal, where chromosomes are supposed to be during metaphase before their segregation (A) and in early anaphase after their segregation (B). White dotted brackets surround area where eGFP-MAP65-2 signal was detected, specifically at the beginning of the phragmoplast formation during the anaphase (C), in the disc phragmoplast (D), in the ring phragmoplast (E) and in the discontinuous phragmoplast (F). Scale bars, 2 µm (A-F); time format, min:s. Image acquisition by Pavlína Floková.
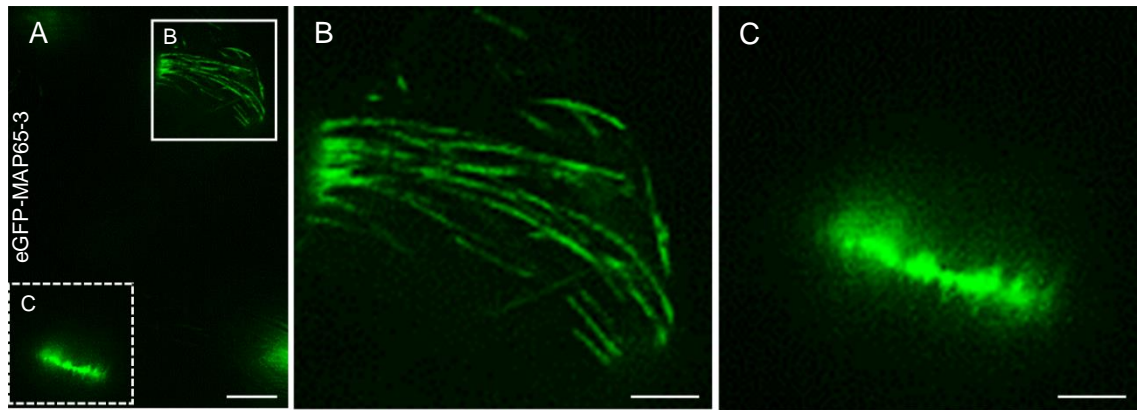
Figure 53. Details of MAP65-3 localization. Visualization of eGFP-MAP65-3 by the structured illumination microscopy. In (A) is presented an overview; in (B) and (C) are shown details from the boxed areas in (A) bordered by full-line and dotted-line, respectively. Scale bars, 5 μm (A), 2 μm (B, C). Image acquisition by Pavlína Floková.

the entire microtubules of the phragmoplast, MAP65-3 appears to localize more discretely at the phragmoplast midzone.

The colocalization of MAP65-2 and MAP65-3 at the preprophase band was confirmed by live cell imaging employing the SIM platform (**Fig. 54A,B**). Interestingly, the signal specific for MAP65-3 was detected on microtubule bundles outside of the preprophase band (**Fig. 54B**). The MAP65-2 and MAP65-3 appear to have similar signal patterns while decorating the preprophase band (**Fig. 54C**).

Taken together, the SIM platform enabled detailed depiction of MAP65-2 and MAP65-3 localization at specific cell cycle stages, improving the comprehension of subcellular localization of MAP65-2 and MAP65-3. Indeed, the live cell imaging enables observation of dynamic changes within the plant cell. Therefore, it provides profound
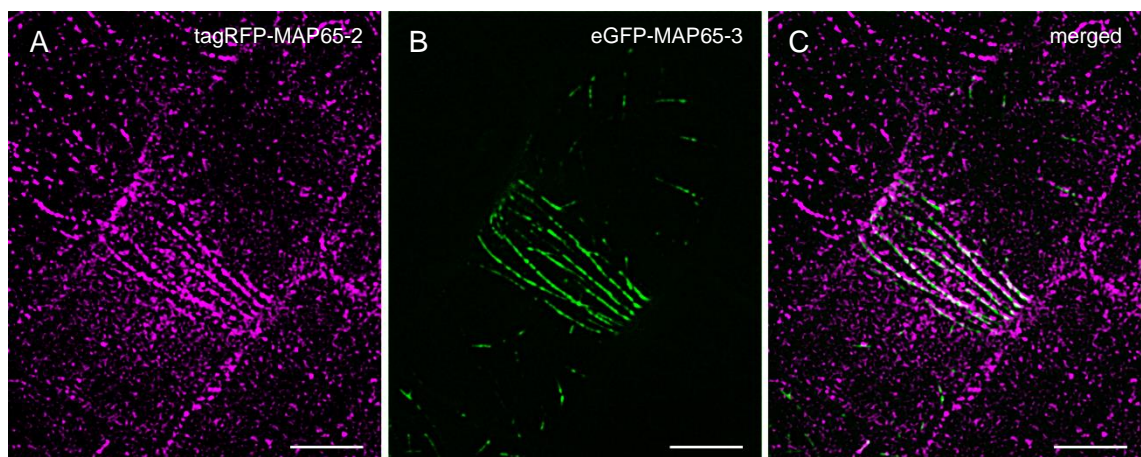
Figure 54. Details of MAP65-2 MAP65-3 colocalization in the preprophase band. Visualization of the preprophase band in a line coexpressing tagRFP-MAP65-2 (A) and eGFP-MAP65-3 (B) by the structured illumination microscopy. In (C) is presented a merged image. Scale bars, 5 μm.

insight into cellular processes compared to other approaches. The live cell imaging employing the SIM, ACLSM and LSFM platforms proved to produce valuable information on MAP65-2 and MAP65-3 organization, dynamics and colocalization with microtubules.

However, the strength of each platform regarding colocalization studies is limited. The SIM platform, which outperforms the others in terms of resolution, proved to be excessively phototoxic for the tagRFP fluorescent protein and the used microscope setup did not enable sequential imaging. On the other hand, LSFM provided possibilities for long term imaging of two different fluorophores, but at the cost of lower resolution. Additionally, the live cell imaging was limited to the visualization of two different fluorophores, narrowing the colocalization studies to the simultaneous observation of two out of three proteins of interest.

To colocalize all three proteins of interest, specifically MAP65-2, MAP65-3, and tubulin, it was decided to visualize these proteins through the immunolabelling in fixed samples. In spite of the benefits of live cell imaging, there are some advantages of the immunolabelling, notably: (i) the fluorescent labels are less prone to photobleaching as they are mounted in appropriate protective media; (ii) the fixation conserves native protein structures, which then enables imaging with higher laser power; (iii) the static nature of the structures alleviates the requirement of high acquisition speed characteristic for live cell imaging. These specifics provide the possibility for detailed visualization of cytoskeletal structures by the SIM.

The immunolabelling of Arabidopsis roots has been described previously (Sauer *et al.* 2006; Šamajová *et al.* 2014) and by optimizing the protocol, concurrent immunolabelling of three proteins was possible. Since there were no available specific antibodies against MAP65-2 and MAP65-3, these proteins were localized by immunolabelling fluorescent proteins in lines stably coexpressing tagRFP-MAP65-2 and eGFP-MAP65-3. Specifically, the Atto 488-conjugated anti-GFP nanobodies were used for detecting the eGFP-MAP65-3. Tubulin was localized by labelling with a rat anti-tubulin antibody and Alexa Fluor 647-conjugated anti-rat antibody. Finally, the tag-RFP-MAP65-2 was labelled with rabbit anti-RFP antibody and Alexa Fluor 546-conjugated anti-rabbit antibody. To visualize the DNA, the DAPI staining was used. The imaging or these samples was performed on the SIM platform.

By covisualizing MAP65-2, MAP65-3, tubulin and DNA in fixed samples, the colocalization of the proteins during the mitotic progression of the cell cycle was possible (**Fig. 55, 56**). The microtubules forming the metaphase spindle and the ring phragmoplast (**Fig. 55A**) and the localization of both MAP65-2 and MAP65-3 (**Fig. 55B,C**) at these stages was documented. The cell cycle stages were determined based on the position of DAPI-stained DNA (**Fig. 55D,E**). The metaphase spindle was devoid of both MAP65-2 and MAP65-3 (**Fig. 55F-H**). This is in line with the observations from live cell imaging (**Fig. 49-52**).

The microtubules constituting the disc and ring phragmoplasts (**Fig. 56A**) and the localization of both MAP65-2 (**Fig. 56B**) and MAP65-3 (**Fig. 56C**) at these stages was documented. Again, the stage of the cell division was confirmed by localizing DAPI-stained DNA (**Fig. 56D,E**). The MAP65-2 appeared to colocalize along the whole phragmoplast microtubule bundles (**Fig. 55F, 56F**) validating the observation from live
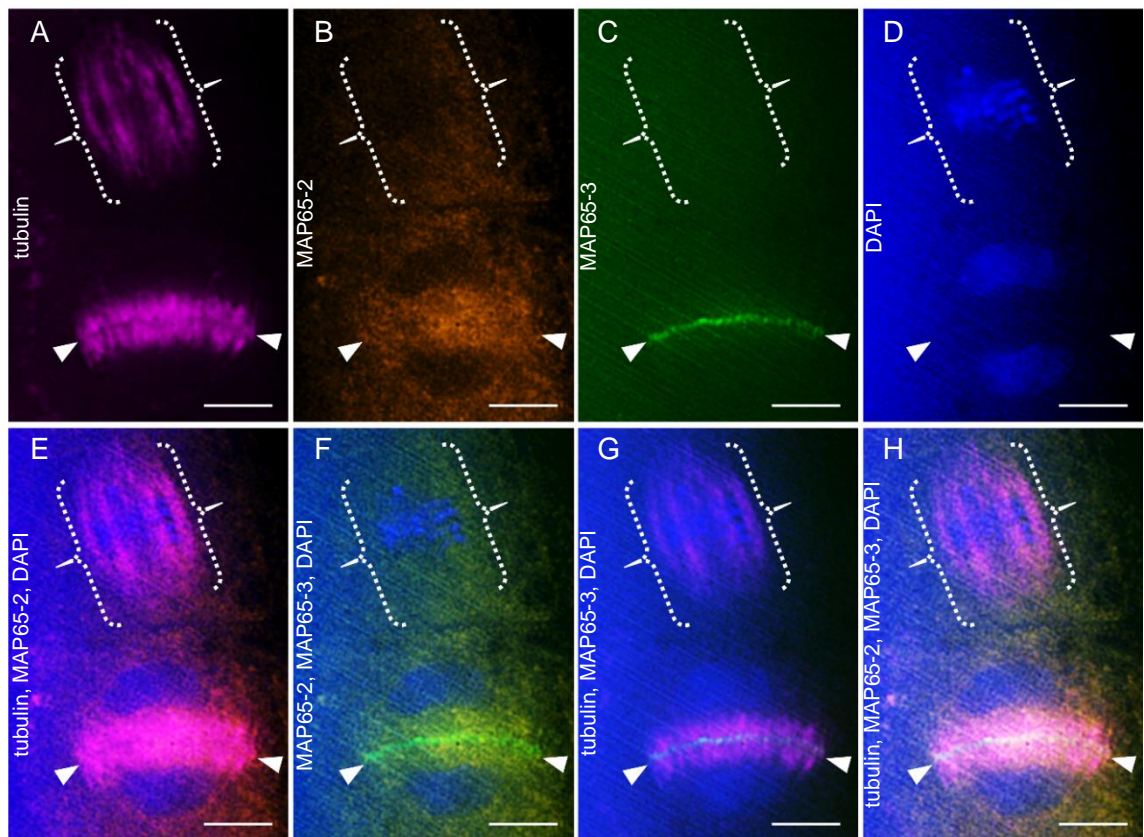
Figure 55. Colocalization of MAP65-2 and MAP65-3 with mitotic microtubular arrays. Immunolocalization of tubulin (A), tagRFP-MAP65-2 (B) and eGFP-MAP65-3 (C) combined with DAPI staining (D) in roots of line coexpressing tagRFP-MAP65-2 and eGFP-MAP65-3. (E-H) present merged images showing combinations of: tubulin, MAP65-2, DAPI (E); MAP65-2, MAP65-3, DAPI (F); tubulin, MAP65-3, DAPI (G); tubulin, MAP65-2, MAP65-3, DAPI (H). White dotted brackets mark the metaphase spindle, white full arrowheads point to the ring phragmoplast. Arrowheads and brackets are positioned at the same places in all images. Scale bars, 2 μm. Image acquisition by Renata Šnaurová.
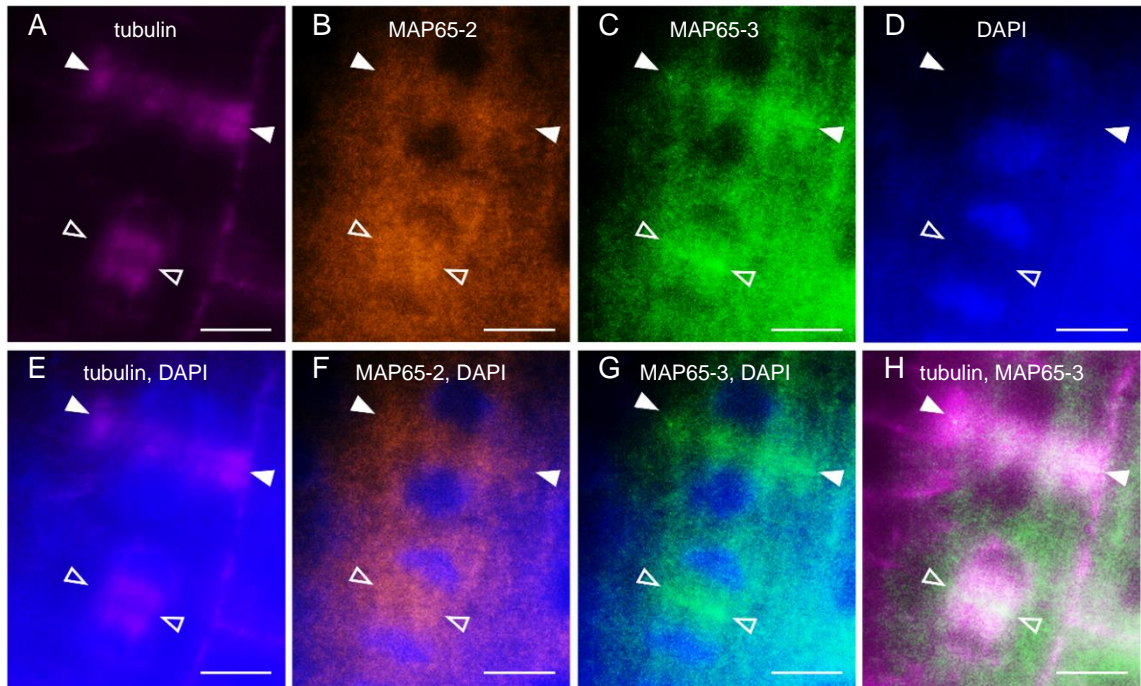
Figure 56. Colocalization of MAP65-2 and MAP65-3 with phragmoplasts. Immunolocalization of tubulin (A), tagRFP-MAP65-2 (B) and eGFP-MAP65-3 (C) combined with DAPI staining (D) in roots of the line coexpressing tagRFP-MAP65-2 and eGFP-MAP65-3. (E-H) present merged images showing combinations of: tubulin, DAPI (E); MAP65-2, DAPI (F); MAP65-3, DAPI (G); tubulin, MAP65-3 (H). White empty arrowheads point to the disc phragmoplast, white full arrowheads point to the ring phragmoplast. Arrowheads are positioned at the same places in all images. Scale bars, 5 μm. Image acquisition by Renata Šnaurová.

cell imaging (**Fig. 49**). On the other hand, MAP65-3 was detected only in the phragmoplast midzone showing different localization pattern to both MAP65-2 and microtubules (**Fig. 55F-H, 56G,H**). This is again in line with the results from live cell imaging (**Fig. 53**).

Distinct localization pattern of MAP65-3 was further depicted by comparing the localization of mitotic microtubule arrays (**Fig. 57A**), MAP65-3 (**Fig. 57B**) and DNA (**Fig. 57C**). Different cell cycle stages were determined by comparing microtubule and DNA organization (**Fig. 57D**). The MAP65-3 signal was not detected at the metaphase spindle (**Fig. 57E-F**), but it was present at the midzone of the disc, ring and discontinuous phragmoplasts (**Fig. 57E-F**), further strengthening the perception of differential localization of MAP65-2 and MAP65-3 at the phragmoplast.

In spite of the inferiority of the fixed-sample microscopy to the live cell imaging regarding the information value on cellular processes, this approach proved to be useful in validating the observations from live cell imaging and providing additional information on localization of proteins and DNA. By covisualizing microtubules, MAP65-2, MAP65-

3 and DNA, it was possible to specify the localization of MAP65-2 and MAP65-3 in relation to each other and to microtubules at different stages of the cell cycle.
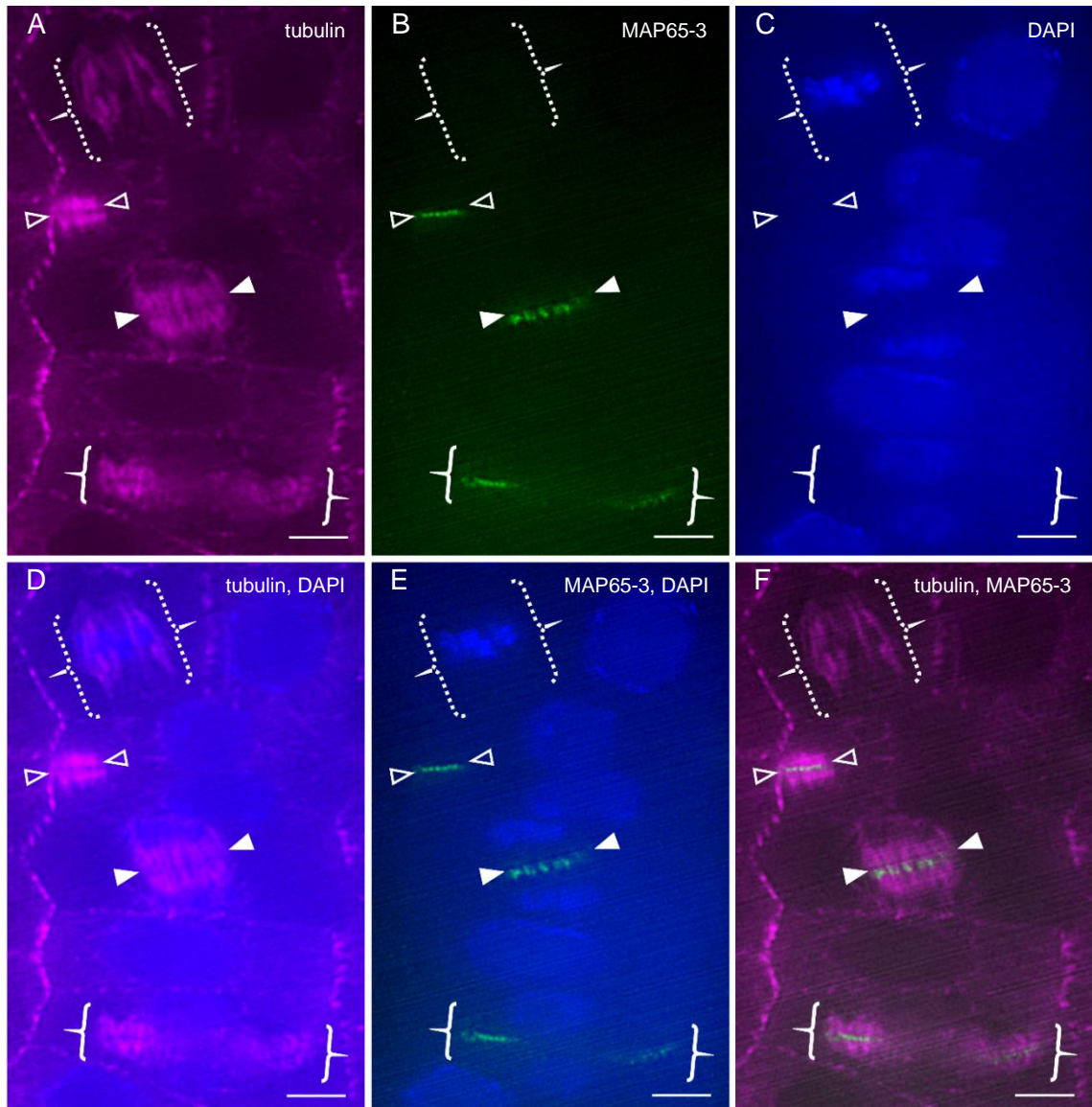
Figure 57. Colocalization of MAP65-3 with mitotic microtubular arrays. Immunolocalization of tubulin (A), eGFP-MAP65-3 (B) combined with DAPI staining (C) in roots of the line expressing eGFP-MAP65-3. (D-F) present merged images showing combinations of: tubulin, DAPI (D); MAP65-3, DAPI (E); tubulin, MAP65-3 (F). White dotted brackets mark the metaphase spindle, white empty arrowheads point to the disc phragmoplast, white full arrowheads point to the ring phragmoplast, white full-line brackets mark the discontinuous phragmoplast. Arrowheads and brackets are positioned at the same places in all images. Scale bars, 2 μm. Image acquisition by Renata Šnaurová.

4. Discussion

4.1. The interplay of PP2A and MPK3, MPK6 in cell division plane orientation

Plant phosphoprotein phosphatases dephosphorylate a plethora of substrates, which leads to their involvement with numerous plant processes. Consequently, many phosphoprotein phosphatases are known to affect plant development, either through exerting control over hormonal signalling, responses to environmental cues, cell proliferation or cell division plane orientation (reviewed in Boyer and Simon, 2015). The impact of phosphoprotein phosphatases on formative cell divisions is in most cases indirect as exemplified by PP2A and PP6 in the regulation polar localization of PIN-FORMED transporters (Michniewicz *et al.* 2007; Dai *et al.* 2012; Ballesteros *et al.* 2013). However, PP2C kinases POLTERGEIST and POLTERGEIST-LIKE are known to be more directly involved in the control over the asymmetric cell division (Song and Clark 2005; Song *et al.* 2008). Thus, it is reasonable to speculate that other phosphatases might directly regulate the cell division plane orientation.

Phosphoprotein phosphatases were shown to be essential for cell division and assembly and disassembly of mitotic microtubule arrays (Bhaskara *et al.* 2017; Samofalova *et al.* 2019). Similarly to their animal counterparts, which are well-known to regulate important players of cell division, namely CDKs, AURs, and MPKs (Mumby and Walter 1993; Mayer-Jaekel and Hemmings 1994), plant phosphoprotein phosphatases were either proved or predicted to interact with tubulin (Awotunde *et al.* 2003; Kirik *et al.* 2012; Voss *et al.* 2013), microtubule associated proteins and markers of the cortical division zone (Twell *et al.* 2002; Kawamura *et al.* 2006; Xu *et al.* 2008; Rasmussen *et al.* 2011; Spinner *et al.* 2013), CDKs and MPKs (Umbrasaite *et al.* 2010; Kohoutová *et al.* 2015). Importantly, two plant phosphoprotein phosphatases were found to inactivate MPKs during specific developmental stages with profound effects on formative cell divisions. The AP2C3 (from the PP2C family) and MKP1 inactivate MPK3/6 in stomatal precursors acting as positive regulators of stomatal differentiation program (Umbrasaite *et al.* 2010; Tamnanloo *et al.* 2018), effectively controlling the commitment to cell fate by integrating MPK signalling and cell cycle regulation (Umbrasaite *et al.* 2010). The regulatory activity of AP2C3 on MPK3/4/6 was also shown in roots, where AP2C3 affects cell division including the spindle and the cell division plane orientation (Kohoutová *et al.* 2015). MKP1 is expected to also regulate MPK3/6

in other developmental events, as the overall phenotype of *mkp1 yda* double mutant was improved compared to *yda* single mutant (Tamnanloo *et al.* 2018).

Concerning plant phosphoprotein phosphatases involved in cell division, PP2A holds a special position as its regulatory subunit TON2 has been associated with the cell division plane orientation for a long time (Traas *et al.* 1995; McClinton and Sung 1997). The mutants in *TON2* exhibit defects in establishing and maintaining the cortical division zone and, consequently, in the phragmoplast guidance (Camilleri *et al.* 2002). The altered cell division patterning results in strong morphological defects, however, the tissue pattern formation remains unaffected (Torres-Ruiz and Jurgens 1994; Scheres *et al.* 1995). Other subunits of PP2A show either significantly weaker phenotype or they are functionally redundant exhibiting these defects only when two subunits are missing (Zhou *et al.* 2004; Blakeslee *et al.* 2008; Spinner *et al.* 2013).

Although PP2A is known to indirectly affect cell divisions through polar localization of PINs (Michniewicz *et al.* 2007), its direct involvement with the cortical division zone maintenance suggests that PP2A profoundly affects the cell division plane orientation. Several studies suggested that the PP2A affects the cell division plane orientation through dephosphorylation of microtubule associated proteins, specifically MOR1, TON1 and MAP65s (Smertenko *et al.* 2006; Kirik *et al.* 2007; Kirik *et al.* 2012).

Another possibility might be that PP2A targets MPKs involved in cell division. Animal PP2A is known to regulate various MPK cascades, among them EXTRACELLULAR SIGNAL-RELATED KINASEs, which are related to plant MPKs (Grethe and Pörn-Ares 2006; Letourneux *et al.* 2006). The candidate MPKs, which could be regulated by PP2A in the context of the cell division plane orientation would be MPK3/4/6. While MPK4 is generally involved in cell division (Beck *et al.* 2010), MPK3 and MPK6 are known to have partially redundant roles in formative cell divisions during several developmental events (Bush and Krysan 2007; Wang *et al.* 2007; Müller *et al.* 2010). Even though they were shown to be regulated by PP2C and MKP1 (Umbrasaite *et al.* 2010; Kohoutová *et al.* 2015; Tamnanloo *et al.* 2018), they are presumed to be regulated by other phosphoprotein phosphatases as well.

To investigate the possibility of MPK3, MPK6 being regulated by PP2A, *mpk3* and *mpk6* loss-of-function mutants were grown in the presence of a phosphatase inhibitor. Even though the chosen phosphatase inhibitor, cantharidin, is not specific only for PP2A,

it has higher selectivity towards PP2A than to PP1 (Li *et al.* 2010b) and it does not interfere with PP2B or PP2C (Li *et al.* 1993) unless it is used in very high concentrations (Bajsa *et al.* 2011). Therefore, the cantharidin treatment should not affect the regulation of MPK3/6 by PP2C (Kohoutová *et al.* 2015). Both *mpk3* and *mpk6* mutants proved to be partially insensitive to cantharidin treatment, especially in low concentrations, in which cantharidin was previously shown to preferentially target the activity of RCN1, a scaffolding subunit of PP2A (Deruere *et al.* 1999; Shin *et al.* 2005).

Since both the root length and the distance between the root tip and first root hair were less affected in mutants compared to wild type, it appears that PP2A and MPK3/6 work synergistically in modulating root growth. Interestingly, *mpk3, mpk6* mutants showed partial insensitivity regarding the overall phenotype and root length, but the distance between root tip and first root hair was completely unaffected by lower concentrations of cantharidin, suggesting that the cooperation between PP2A and MPK3/6 might predominantly affect the root tip. Indeed, *mpk3, mpk6,* and *rcn1* mutants were previously described to have wrongly positioned cell walls within the root tip (Zapletalová and Šamajová, personal communication; Blakeslee *et al.* 2008; Müller *et al.* 2010; Floková 2016), which was confirmed in this study. The *rcn1* mutant exhibits relatively mild defects in the cell wall orientation within the root tip, which is possibly caused by partial functional redundancy with other PP2AA subunits, PP2AA2 and PP2AA3 (Zhou *et al.* 2004; Spinner *et al.* 2013). On the other hand, the severe phenotype of the *ton2-5* mutant prevented imaging of the root tip anatomy by employing the same strategy as in other mutants.

Although the involvement of RCN1 in auxin transport was documented (Garbers *et al.* 1996; Deruere *et al.* 1999; Rashotte *et al.* 2001; Shin *et al.* 2005; Michniewicz *et al.* 2007), and there is a previous report on decreased expression of *DR5::GUS* reporter in *rcn1* mutant (Blakeslee *et al.* 2008), no detectable changes in *DR5* expression were noted in the *rcn1-6* mutant in this study. Herein, a *DR5::GFP* reporter instead of *DR5::GUS* was used, making the assessment of expression levels more straightforward than depending on the histochemical protocol for detection. Additionally, defects in auxin transport in the *rcn1-6* mutant are possibly masked by the other two PP2AA subunits (Michniewicz *et al.* 2007). The *DR5* expression in the root of *mpk3, mpk6* mutants appeared generally unaffected. This justifies the hypothesis that the root tip anatomy defects stemming from the improper orientation of the cell division plane in *mpk3, mpk6*

mutants do not emerge upon the disturbances in auxin transport, but rather after the impairment of the spatiotemporal control of mitotic changes in microtubule arrays (Beck *et al.* 2010).

The pharmacological study was followed up with a genetic study. Since MPK6 is better described regarding its role in root development than MPK3, the *mpk6* mutant was crossed with *rcn1* mutant. The cell wall orientation defects in *mpk6 rcn1* double mutants were alleviated compared to *mpk6* single mutants and in some cases, complete rescue in this trait was observed. This supports the hypothesis that RCN1 and MPK6 are involved in the same pathway controlling the cell division plane orientation in the primary root tip. To which level both proteins counteract during the regulation of the cell division plane orientation remains to be elucidated.

The direct interaction between MPK3 and RCN1 was previously reported in a high-throughput experiment (Interactome 2011). To confirm this, the interaction between MPK3 and RCN1 was assessed by yeast-two hybrid. This *in vitro* assay was also used to test putative interactions between RCN1 and MPK6, and N-terminal regulatory domain of YDA, respectively. While the interaction between MPK3 and RCN1 was confirmed *in vitro*, it could not be assessed for MPK6. Moreover, weak interaction between RCN1 and the N-terminal regulatory domain was detected. In future, the results from *in vitro* assays must be verified by other protein-protein interaction assays.

To elucidate whether MPK3/6 are upstream of RCN1, thus, their phosphorylation is unaffected by its genetic depletion, commercially available antibodies against MPK3/6 and pMPK3/6 were used to detect protein levels in *rcn1* mutants. Since both RCN1 and MPK3/6 have different abundance in various Arabidopsis organs (Klepikova *et al.* 2016), this experiment was performed on several types of tissues. The genetic depletion of RCN1 affected MPK3/6 abundance in flowers and siliques and, more importantly, the phosphorylation levels of MPK3/6 were altered in roots, flowers and siliques.

Although there is a report on the degradation of MKK upon its dephosphorylation (Liu *et al.* 2014), MPKs are generally regarded to be regulated by mechanisms other than protein degradation (Tena *et al.* 2001; Cristina *et al.* 2010). The changes in MPK3/6 protein abundance are therefore more likely resulting from indirect effects of RCN1 genetic depletion, rather than emerging from PP2A-mediated degradation of MPK3/6. On the other hand, the changes in levels of pMPK3/6 might be linked to direct activity of

PP2A on MPK3/6. The increased levels of pMPK3/6 in roots and siliques of *rcn1-6* could be explained by reduced activity of PP2A. This is in line with previous observations of partial insensitivity of *mpk3, mpk6* mutants to cantharidin treatment and the rescue in the root tip anatomy in *mpk6 rcn1* double mutant.

Both protein abundance and phosphorylation levels of MPK3/6 are decreased in flowers of *rcn1-6*, which is in contrast with the observations in other types of tissue signifying that not only the functional interaction between RCN1 and MPK3/6 affects only certain tissues, but it might have different roles in various developmental contexts.

PP2A is known to affect flower development (Zhou *et al.* 2004), embryogenesis (Torres-Ruiz and Jurgens 1994; Spinner *et al.* 2013) and endosperm cellularization (Sorensen 2002). Similarly, MPK3/6 are involved in flower development (Bush and Krysan 2007; Wang *et al.* 2008; Meng *et al.* 2012) and embryogenesis (Wang *et al.* 2007). Thus, both PP2A and MPK3/6 are involved at several events during the development of generative tissues. Nevertheless, both PP2A and YDA-MAPK modules are involved in the cell division plane orientation during early embryogenesis. Cell divisions in early embryogenesis are highly ordered, simplifying the detection of defects in the cell division plane orientation. Therefore, the early embryonic development was examined in *rcn1, ton2, mpk3* and *mpk6* mutants.

The observed cell division plane orientation defects in *rcn1* and *ton2* mutants were in line with previous reports (Camilleri *et al.* 2002; Spinner *et al.* 2013). This type of defects was also noted in *mpk3* and *mpk6* mutants confirming the claim that both PP2A and MPK3/6 are involved in the cell division plane orientation not only in roots but also in embryos. The cell division plane orientation was affected in both embryo proper and suspensor of *rcn1, mpk6* mutants, corroborating previous reports (López-Bucio *et al.* 2013; Spinner *et al.* 2013). Contrary to the previous study, *mpk3* mutant was found to have similar embryonic defects as *mpk6* mutant, albeit with lower occurrence (López-Bucio *et al.* 2013).

During the first asymmetric division of the zygote, the YDA-MPK pathway affects cell polarity through activating WRKY2, which then initiates the activation of *WOX8, WOX9* expression (Ueda *et al.* 2017). Accordingly, the cell division plane orientation defects were described in mutants impaired in *WRKY2, WOX2, WOX8* and *WOX9* (Breuninger *et al.* 2008; Ueda *et al.* 2011), and in *YDA, MPK3, MPK6* (Lukowitz

et al. 2004; this study). Moreover, the expression pattern of *WOX8* is disrupted in *mpk3* and *mpk6* mutants, which could reflect the unequal distribution of cell polarity factors.

TON2 was previously described to affect the cell division plane orientation without affecting pattern formation (Torres-Ruiz and Jurgens 1994). Contrary to the assumption that *WOX8* expression should be unaffected in *ton2* mutants because the pattern formation is unaltered, abnormal expression patterns of the *WOX8* were observed in the *ton2* mutant. The cell division plane orientation defects in *ton2* mutants are assigned to the erroneous regulation of mitotic arrays. Since microtubules are known to affect the asymmetric division of the zygote (Kimata *et al.* 2016), and the asymmetric division during pollen development can be overturned in favour of symmetric divisions after treatment with microtubule inhibitors (Tanaka and Ito 1981), it is possible that by affecting the positioning of the mitotic microtubule arrays, the TON2 is responsible for correct separation of the polarity factors into the daughter cells. The misplaced positioning of the cell division plane in the highly polarized zygote (Zhang and Laux 2011; Kimata *et al.* 2019) might lead to incorrect segregation of the polarity factors into the apical and basal cell, which would explain the incorrect expression pattern of *WOX8* in *ton2* mutants. This problem with the cell fate specification would be only transient, as it would be corrected by other factors involved in the robust mechanism of the cell fate determination. This would be in line with the observation of normal auxin distribution in *ton2* mutants.

Apart from the YDA-MPK cascade and the WOX protein family, auxin contributes to the establishment and maintenance of apical-basal polarity in embryos (Friml *et al.* 2003). The spatiotemporal regulation of auxin maxima distribution were affected in *mpk3, mpk6* mutants, though less significantly than in other mutants, e.g. *wox8 wox9* double mutants (Breuninger *et al.* 2008) and mutants in which auxin transport is altered (Izhaki and Bowman 2007; Mravec *et al.* 2008; Luo *et al.* 2011). Nevertheless, the observation of weaker and less well-defined *DR5* signal is in line with previous observations of similar phenotypes in mutants affecting auxin transport systems (Mravec *et al.* 2008) or the auxin-gibberellic acid crosstalk (Baba *et al.* 2019), whereas the opposite, meaning the overexpression of *DR5*, was observed in *zwille* mutants (Roodbarkelari *et al.* 2015). These reports support the notion that the observed changes in *DR5* expression in *mpk3, mpk6* mutants report on altered auxin signalling in these mutants. Similar defects, though with higher frequency, were also observed in *rcn1*

mutant, corroborating the previous report on decreased signal intensity of *DR5* expression in *rcn1 pp2aa3* double mutants (Michniewicz *et al.* 2007). In contrast, auxin maxima appeared unaffected in *ton2* mutant embryos, suggesting that rather than the whole complex of PP2A, only certain subunits, notably PP2A, affect auxin signalling. This would mean that despite similar defects in *DR5* expression in *mpk3, mpk6,* and *rcn1* mutants, they are probably caused by different mechanisms indirectly affecting auxin signalling.

Properly coordinated auxin synthesis and transport are essential for correctly established division patterns in the embryo (Yoshida *et al.* 2014) and an increase in auxin maxima was linked to earlier onset of organ differentiation leading to morphological defects (Zhang *et al.* 2017b). No defects were noted in postembryonic shoot development of *mpk3, mpk6, rcn1* mutants despite the abnormal expression of *DR5* during embryonic development. This could be explained by other factors affecting auxin signalling and alleviating the predicaments caused by impaired function of these genes.

In conclusion, the MPK3, MPK6 and PP2A seem to be a part of a common signalling pathway in the cell division plane orientation in roots, while the situation in embryos is more ambiguous. The PP2A, together with other kinases and phosphatases, could participate on modulating the phosphorylation status of MPK3 and MPK6, which affects the function, subcellular localization (Zhang *et al.* 2016a) and participation of these kinases in multiprotein complexes (Bequette *et al.* 2018).

4.2. HSP90s affect asymmetric cell divisions through modulating YDA-MPK cascade

The YDA-MPK pathway was described to be involved in several developmental processes (Wang *et al.* 2007; Meng *et al.* 2012; Smékalová *et al.* 2014; Ueda *et al.* 2017). Recently, cytoplasmic HSP90s were shown to directly interact with YDA, and this interaction affected the stomatal differentiation pathway (Samakovli *et al.* 2020). In this way, environmental cues are integrated into developmental pathways.

Another developmental event where YDA plays a major role is embryogenesis (Lukowitz *et al.* 2004), where the role of the YDA-MPK cascade is to establish the first asymmetric cell divisions and to secure spatiotemporal regulation of gene expression of cell fate determination factors (Ueda *et al.* 2017). Previously, *yda* loss-of-function and *ΔNyda* gain-of-function mutants were reported to exhibit defects in the cell division plane orientation only in the suspensor (Lukowitz *et al.* 2004) of the very early stages of embryos, overviewing the possibility that such defects may appear in the embryo proper later. In the present study, this type of defects is indeed shown to occur in the embryo proper, which is in line with phenotypes observed in *mpk3* and *mpk6* mutants (López-Bucio *et al.* 2013; this study). Interestingly, genetic depletion of cytoplasmic HSP90.1 and HSP90.2 rescued the cell division plane orientation defects of *yda* and *ΔNyda* mutants. This suggests that HSP90s play a role in the embryogenesis downstream of YDA similarly to the recently published role of HSP90s in YDA-driven regulation of stomatal differentiation (Samakovli *et al.* 2020).

During embryogenesis, the YDA-MPK pathway targets WRKY2, which activates the expression of *WOX8* (Ueda *et al.* 2017). The expression of *WOX8* needs to be tightly spatiotemporally regulated as it determines the cell fate of the basal cell lineage and it is involved in establishing the apical-basal axis (Breuninger *et al.* 2008; Ueda *et al.* 2011). As a master regulator, it has control over other members of WOX protein family involved in embryogenesis, and it also affects auxin distribution (Breuninger *et al.* 2008; Ueda *et al.* 2011). As expected, the *WOX8* expression pattern was compromised in *yda* and *ΔNyda* mutants. The assumption would be that with the genetic depletion of YDA, a positive regulator of *WOX8* and the basal cell lineage (Ueda *et al.* 2017), the expression of *WOX8* would be decreased and its localization pattern might be compromised. Indeed, the *WOX8::NLS:YFP* signal was missing in some suspensor cells in *yda*, but also in *ΔNyda* mutants. Conversely, with the constitutively active YDA, the ectopic expression

in the apical cell lineage would be expected, which was noted, yet again for both *yda* mutants. As these observations cannot be explained by the model suggested in previous work (Ueda *et al.* 2017), alternative explanations should be discussed.

Generally, the asymmetric cell divisions are controlled by intrinsic and extrinsic factors. The major extrinsic factor in the embryonic development is auxin, however, its role in the very early development is limited as it is supplemented from maternal tissues (Friml *et al.* 2003) and the role of auxin expands once the apical-basal axis is established (Zhang *et al.* 2017b). Thus, the very early development is dependent on intrinsic factors, which is in line with the observed asymmetric distribution of organelles (Kimata *et al.* 2019) and cytoskeleton components (Kimata *et al.* 2016) in the zygote. The adoption of correct cell fate following the asymmetric division depends on the inheritance of proper cell fate determination factors. At the same time, the asymmetric cell division depends on the unequal distribution of the polarity factors (e.g. Terasaka and Niitsu 1987; Houbaert *et al.* 2018; Xue *et al.* 2020). Thus, the impaired positioning of the cell division plane in *yda* mutants could lead to uneven distribution of otherwise well-organized intrinsic factors, which would result in problems with the cell fate determination. As the interaction network establishing the cell fate is rather robust, it is reasonable to speculate that such irregularities would be alleviated later on. This would mirror the polar axis establishment in the zygote of fucal algae, where the polar axis is fixed only after a certain amount of time following its formation (Fowler and Quatrano 1995). In this model, abnormal expression pattern of *WOX8* observed in *yda* mutants would result from the improper spatial distribution of cell fate determinants following the incorrectly oriented cell divisions.

Alternatively, the YDA-MPK pathway might control cell fate determinants through another mechanism which would exist in parallel to the previously described role of the YDA-MPK pathway in the transcriptional activation of *WOX8* (Ueda *et al.* 2017). YDA might alter the expression of *WOX*s by adjusting histone modifications, as WOXs were identified as targets of the POLYCOMB REPRESSIVE COMPLEX 2 (Bouyer *et al.* 2011). This complex is known to modulate transcription of genes involved in the embryonic development (Mozgova *et al.* 2015; Xiao and Wagner 2015) through histone modifications (Köhler *et al.* 2012). HSP90s are known to affect the morphology via epigenetic modulation (Sollars *et al.* 2003; Sangster *et al.* 2007) and the abnormal expression pattern of *WOX8* was also noted for *hsp90.1* and *hsp90.2* mutants. This

supports the hypothesis of the involvement of HSP90s in embryonic developmental processes and it proposes a model in which HSP90s modulate the activity of YDA-MAPK pathway in the context of epigenetic regulation of embryonic development.

Apart from supporting the determination of the basal cell lineage, the YDA-MPK cascade and WOX8 regulate WOX2 and auxin (Breuninger *et al.* 2008; Zhang *et al.* 2017b), two major factors in the embryo proper development. The auxin maxima distribution was affected in both *yda* and *ΔNyda* mutants. The less well-defined auxin maxima in basal pole in *yda* were similar to phenotypes in mutants affecting auxin transport systems (Mravec *et al.* 2008); whereas the severe phenotype of *ΔNyda* is strongly reminiscent of *methyltransferase 1* mutant (Xiao *et al.* 2006). Moreover, the auxin maxima were distorted in the postembryonic root development, corroborating the previous report on the upregulation of auxin biosynthetic enzymes in the roots of these mutants (Smékalová *et al.* 2014).

Defects in the spatiotemporal distribution of auxin maxima were observed in *hsp90* mutant embryos. HSP90s assumably affect the auxin signalling in several ways, as cytoplasmic HSP90s are known to regulate auxin transport (Wang *et al.* 2016; Watanabe *et al.* 2016; Watanabe *et al.* 2017). However, the irregular auxin signalling caused by their genetic depletion appears to be restored by other mechanisms as the auxin maxima distribution appears unaffected in the root of *hsp90* mutants.

The cell division plane orientation defects in the postembryonic root development of both *yda* and *ΔNyda* mutants were rescued by genetic depletion of HSP90.1, which signifies that HSP90s affect the cell division plane orientation downstream of YDA not only during embryogenesis but also in postembryonic development. This is also supported by the observation of the overall improved phenotype of *hsp90 yda* double mutants (Závorková 2019).

The HSP90s fold and stabilize a wide range of proteins, which means that they are securing proper function of various signalling pathways (Li *et al.* 2012; Taipale *et al.* 2012). Recently, YDA has been described to interact with HSP90s (Samakovli *et al.* 2020), adding MPKs into the network surrounding HSP90s, which was suggested to be essential in maintaining order throughout ontogenesis (Samakovli *et al.* 2014; Shigeta *et al.* 2015; Margaritopoulou *et al.* 2016; Wang *et al.* 2016). The role of HSP90s in embryogenesis is supported by embryo abortion phenotypes (Samakovli *et al.* 2007) and differential expression of cytosolic *HSP90s* (Prasinos *et al.* 2005). In this study, the role of cytoplasmic HSP90s in the cell division plane orientation and cell fate

determination during early embryogenesis is documented as well as its cooperation with the YDA-MPK pathway in the proper positioning of cell walls. Moreover, this property was also noted in the postembryonic root development.

The exact mechanism of how HSP90s affect the cell division plane orientation through the YDA-MPK pathway is currently unknown. Generally, the formative cell divisions and cell fate determination are either shaped by spatiotemporally regulated factors or by polarized proteins (Zhang *et al.* 2015). The first group is exemplified by auxin maxima conferring identity of the quiescent center in the primary root (Sabatini *et al.* 1999), and distribution of transcription factors deciding the cell fates during the formative division of hypophysis (Jenik *et al.* 2005). Both HSP90s and YDA were shown to affect WOX8 and auxin, two factors determining cell fates during embryogenesis. However, without additional experiments, it cannot be ruled out that HSP90s and YDA modulate the auxin distribution via different pathways.

The MPK signalling pathways integrate various signals and they frequently share signalling components (reviewed in Komis *et al.* 2018a). There are several mechanisms securing their signalling specificity, among them the spatial restraints executed by scaffold, adaptor or anchoring proteins (Bardwell 2008). The scaffolding enables differential utilization of MAPK modules (Dhanasekaran *et al.* 2007), compartmentization (Müller *et al.* 2001), and it prevents errorneous crosstalk (Nishimura *et al.* 2016). In plants, the only described true scaffold protein is RECEPTOR OF ACTIVATED C KINASE 1 (Guo and Chen 2008). However, other proteins were found to affect the subcellular localization of plant MPKs. Notably, KIN7a/b (Takahashi *et al.* 2010), 14-3-3ω (Kohoutová *et al.* 2015), BASL (Zhang *et al.* 2015), and POLAR (Houbaert *et al.* 2018).

Recently, HSP90.1 was found to affect the polarization of YDA in stomatal precursors (Samakovli *et al.* 2020), which is crucial for asymmetric cell division during the stomatal differentiation pathway (Zhang *et al.* 2015; Houbaert *et al.* 2018; Xue *et al.* 2020). The RHO GTPASE OF PLANTS 3 has been suggested to sequester the subcellular localization of YDA in the zygote to its basal part (Jeong *et al.* 2016). If the subcellular localization of YDA is polarized during early embryogenesis, HSP90s might be involved in the sequestering of YDA localization, similarly to their function in the stomatal differentiation pathway. Lastly, HSP90s could be involved in the cell division plane orientation more directly, because they are known to colocalize with phragmoplast (Krtková *et al.* 2012) and to affect microtubule remodelling (Queitsch *et al.* 2002).

4.3. Visualizing organization and dynamics of MAP65s

Similarly to other eukaryotic cells, the very survival of plant cells depends on plant cytoskeleton as it is at the core of many quintessential processes including cell growth and division. The *in vitro* experiments or studies in heterologous systems do not always accurately report on the events in living cells, therefore they need to be supplemented with *in vivo* visualization of these cellular events (Stoppin-Mellet *et al.* 2013). As the plant cytoskeleton consists of fine structures, the structure of microtubules and the organization of the microtubule associated proteins binding them have been assessed by transmission electron microscopy (Ledbetter and Porter 1963; Chan *et al.* 1999). The transmission electron microscopy possesses an unparalleled resolution capacity, which makes it an indispensable tool for examining protein colocalization and interaction (Kremer *et al.* 2015; Celler *et al.* 2016). Alas, its use is limited to fixed and artificially contrasted samples, which restrains its applicability for observation of dynamic processes. This is of great disadvantage especially in the case of microtubules, as they continuously exhibit dynamic behaviour (Shaw *et al.* 2003; Komis *et al.* 2014).

On the other hand, the resolution obtained by means of light microscopy is bound by the Abbe´s limitation of 200 nm, which is considerably below the resolution capacity needed for precise visualization of microtubule organization. Numerous super-resolution techniques were developed to avoid the Abbe´s limit and they can be generally divided into two groups – the SIM and nanoscopy (reviewed in Komis *et al.* 2018b; Schermelleh *et al.* 2019).

Within the group of light microscopy techniques referred to as nanoscopy belong deterministic approaches limiting emission to subdiffraction size (notably stimulated emission depletion microscopy) and stochastic approaches precisely detecting single fluorophores, also referred to as single molecule localization microscopy methods (e.g. stochastic optical reconstruction microscopy, photoactivation localization microscopy). While the nanoscopy techniques offer possibilities for a substantial decrease in the resolution levels down to 20 nm (Schermelleh *et al.* 2019), they do so at the cost of high irradiation intensity, specific requirements regarding the sample preparation, and, in the case of stochastic approaches, lengthy acquisition time. This tradeoff is acceptable for fixed samples, but it is disadvantageous for live cell imaging. Therefore, the use of nanoscopy in live cells remains limited (Sauer and Heilemann 2017; Takakura *et al.* 2017), especially in plant biology (reviewed in Komis *et al.* 2015; Schubert 2017).

As the classical nanoscopy techniques were deemed inconvenient for live cell imaging, the SIM was more frequently employed (Schubert 2017). Even though its spatial resolution is significantly worse compared to nanoscopy approaches, it is still capable of exceeding the Abbe´s limit, theoretically reaching 100 nm resolution (Komis *et al.* 2015). Furthermore, it provides better conditions for live cell imaging, most importantly the relatively high speed of image acquisition. The SIM scanning extends over a larger field of view compared to other super-resolution methods. Apart from lower resolution, the biggest disadvantage of the SIM is its reliance upon mathematical post-processing, which may lead to reconstruction artifacts (Komis *et al.* 2015; Demmerle *et al.* 2017).

The SIM has lower phototoxicity compared to other super-resolution techniques, but even these levels are burdensome for certain types of fluorescent labels. Lower phototoxicity is the main feature of the CLSM. However, the CLSM used to be rejected for live cell imaging of cytoskeleton, due to the length of acquisition time. This has been changed with the development of both scanning principles and robust deconvolution strategies, resulting in improving the resolution capacity of confocal systems (Müller and Enderlein 2010; Luca *et al.* 2013; York *et al.* 2013). One of the commercially available improved confocal system is the ACLSM using the Airyscan detector (Huff 2016).

Both SIM and ACLSM platforms have been shown to faithfully visualize organization and dynamics or microtubules (Komis *et al.* 2014) or microtubule associated proteins (Herrmann *et al.* 2018), respectively. The SIM should provide better resolution and higher signal-to-noise ratio, however, the SIM and the ACLSM have not been directly compared. In this study, the resolution capacity of the SIM and the ACLSM was evaluated by visualizing cortical microtubules in Arabidopsis lines stably expressing fluorescently labeled tubulin. From the acquired images, the FWHM was calculated as a parameter describing the resolution capacity of the respective platform. In both the SIM and the ACSLM, the objectives used for this experiment had the same magnification and numerical aperture, yet the resolution reached by the SIM platform exceeded that of the ACLSM. The resolution capacity of the SIM measured in these experiments corresponds to previously published data (Komis *et al.* 2014).

This study reports on the visualization of fluorescently labeled MAP65-2 which is expressed under native promoter and the fluorescent protein is fused with the N-terminal sequence of MAP65-2. Therefore, the binding to microtubules is not affected and the proper function and localization of the resulting chimeric protein is secured. This is supported by the lack of differences in the organization and dynamics of MAP65-2

compared to previously published studies (Lucas *et al.* 2011). Even though the constructs carrying genes encoding the fluorescently-labelled MAP65-2 were used for transformation of wild type plants, no growth or morphological defects were noted, especially the traits previously described for *map65-1 map65-2* double mutants (Lucas *et al.* 2011; Lucas and Shaw 2012).

Despite the SIM platform outperforming the ACLSM in resolving microtubules and MAP65s, a major disadvantage of this platform is high phototoxicity, which leads to progressive photobleaching and cell damage especially during long-term acquisition. Although the GFP-labelled proteins were not particularly affected by photobleaching, the phototoxicity of the SIM proved to be exceedingly intense for tagRFP-labelled proteins. Thus, the colocalization of GFP- and tagRFP-labelled proteins was severely impaired. Conversely, the ACLSM subjects samples to lower phototoxicity, which was reflected in the fact that during the simultaneous imaging of GFP- and tagRFP-labelled proteins were noted fewer issues concerning photobleaching. For this reason, the ACSLM proved to be a better choice for parallel imaging of two different fluorescent labels in living cells.

For the colocalization studies, a superresolution fast mode of ACLSM was used allowing to simultaneously track the two channels at high acquisition speed (Huff 2016; Korobchevskaya *et al.* 2017). By parallel imaging of GFP-labelled microtubules and tagRFP-labelled MAP65-2, the relationship between MAP65-2 and cortical microtubules was assessed. The MAP65-2 was found to closely follow trends in the organization, which were previously described for cortical microtubules (Komis *et al.* 2014).

The study of transverse profiles within areas where MAP65-2 and tubulin colocalize show that it is not possible to resolve the MAP65-2 crossbridge at the diffractions limits of SIM and ACLSM.

The dynamic changes in MAP65-2 localization tracked by the SIM were comparable to the end-wise dynamics of microtubules (Komis *et al.* 2014). Specifically, MAP65-2 exhibits periods of growth superseded by rapid retractions, which is mimicking the dynamic behaviour of the plus ends of cortical microtubules as was described previously (Lucas *et al.* 2011). Moreover, the dynamic changes in MAP65-2 localization were observed only at the ends of bundles, with no alterations within them. This supports the hypothesis of stable intrabundle crosslinking and the exclusively end-wise MAP65-2 dynamics.

When tracking the dynamics of MAP65-2, the SIM platform proved to be capable of discriminating dynamics between individual components of a complex bundle, as has been previously shown for GFP-labeled microtubules (Komis *et al.* 2014). By comparing the dynamic parameters measured for individual bundles and within complex bundles, no significant difference was found between the respective growth rates, however, the shrinkage rates in complex bundles were significantly smaller than shrinkage rates in individual bundles. Previously, MAP65-1 was found to have a more profound effect on stabilizing microtubules in larger bundles compared to the smaller ones (Stoppin-Mellet *et al.* 2013). These two observations support the hypothesis that the complexity of microtubule bundles affects the efficiency of MAP65-1/2 executing their functions.

In conclusion, both the SIM and the ACLSM proved to be capable of fast imaging of fluorescently labelled cortical microtubules and MAP65-2 with better resolution compared to classical light microscopy. The SIM surpassed Airyscan in resolution capacity and provided the possibilities of fast tracking of dynamic changes in MAP65-2 localization. The performance of SIM may be further improved in either increasing resolution or decreasing phototoxicity by adding other microscopy techniques into the platform, e.g. total internal reflection fluorescence (Vizcay-Barrena *et al.* 2011), LSFM (Chen *et al.* 2014), or spinning disc (Hayashi and Okada 2015). However, the setup of the SIM microscope used here did not enable simultaneous tracking of two different channels and its use lead to problems with phototoxicity affecting especially tagRFP-labelled proteins.

Although the resolution reached by ACLSM is worse compared to the SIM, the setup used herein enabled fast simultaneous tracking of two channels and the issues with phototoxicity were less noticeable. Thus, the ACLSM has better potential for colocalization studies.

Nevertheless, both ACLSM and SIM do not reach the resolution levels needed for visualizing the mechanisms of the MAP65 functions. For this purpose, the methods of the single molecule localization microscopy might be used, as they provide higher resolution. Despite the technical specifications of these methods favouring fixed samples over living cells (e.g. Hosy *et al.* 2015), photoactivation localization microscopy and stochastic optical reconstruction microscopy have been applied to live cell imaging in plants (Durst *et al.* 2014; Schubert and Weisshart 2015). The recent development of software-based superresolution methods (Dertinger *et al.* 2009; Cox *et al.* 2012; Gustafsson *et al.* 2016) offers employing the fluorophores conventionally used in live cell

imaging in single molecule localization microscopy techniques, thus, increasing the potential of these methods for live cell imaging in plants.

Previously, the localization of MAP65-2 and MAP65-3 at mitotic microtubule arrays was shown (Müller *et al.* 2004; Caillaud *et al.* 2008; Lucas *et al.* 2011). To confirm this observation, LSFM was used for mesoscopic observation of growing roots of Arabidopsis lines expressing either fluorescently labeled microtubules and MAP65-2, or fluorescently labeled MAP65-2 and MAP65-3. The LSFM was chosen as even though its resolution is not remarkable, it provides superior conditions for long-term developmental live cell imaging (Ovečka *et al.* 2015; von Wangenheim *et al.* 2017a). By observing the growing roots of these lines, many cell divisions were observed and the fluorescently labelled MAP65-2 and MAP65-3 were proven to colocalize with mitotic structures. The localization pattern of MAP65-2/3 was then confirmed by high-resolution observations on the SIM platform.

Herein is presented the localization of MAP65-2 at the preprophase band, which is also true for MAP65-1 (Smertenko *et al.* 2004). The presence of MAP65-2 was also documented in the phragmoplast, which is in line with previous observations (Lucas and Shaw 2012). While the immunolabelling displayed MAP65-1 signal more restricted to the phragmoplast midzone compared to the live cell imaging studies (Smertenko *et al.* 2006; Ho *et al.* 2012), the results presented here support the previous observations that MAP65-2 colocalize with microtubules in the entire phragmoplast (Lucas and Shaw 2012).

The localization pattern of MAP65-3 was previously explored by immunolabeling, according to which this protein colocalizes only with the preprophase band and phragmoplast and there is no specific signal detected in the interphase and metaphase (Müller *et al.* 2004; Ho *et al.* 2012). Conversely, a live cell imaging study reported observation of the MAP65-3-GFP signal throughout the entire cell cycle (Caillaud *et al.* 2008). In this study, the eGFP-MAP65-3 signal was detected in the preprophase band and phragmoplast only, corroborating the results of previous immunolabelling studies (Müller *et al.* 2004). The different outcome of the two live cell imaging experiments (Caillaud *et al.* 2008; this study) is most probably caused by the used of different protein fusions. While the protein fusions do not differ significantly in the fluorescent protein nor the length of the promoter region integrated into the final construct, the major difference is that the previous study used C-terminal GFP fusion of MAP65-3 (MAP65-3-GFP; Caillaud *et al.* 2008), while in this study was

used an N-terminal eGFP fusion of MAP65-3 (eGFP-MAP65-3). The N-terminal domain of MAP65-3 is a place of dimerization between MAP65-3 molecules, therefore, the fusion of GFP at the N-terminus should not affect the microtubule-binding activity of MAP65-3. Moreover, this domain has a relatively high sequence homology to the N-terminal domains of other Arabidopsis MAP65s (**Fig. 4A**). The other part of the MAP65-3 closer to the C-terminus consists of the spectrin-fold domain containing tubulin binding sites and the C-terminal variable domain (Smertenko *et al.* 2004). True to its name, the C-terminal variable domain is the place of the least sequence homology within the Arabidopsis MAP65 proteins (**Fig. 4C**). As it has high variability within the MAP65 proteins, it is reasonable to argue that its function is related to the differential subcellular localization of MAP65s, which was indeed proved for both MAP65-1 (Smertenko *et al.* 2006) and MAP65-3 (Ho *et al.* 2012). Thus, the C-terminal GFP fusion of MAP65-3 does not reliably report on the subcellular localization of MAP65-3 protein, and this reasoning also supports the results of immunolabelling of MAP65-3 (Müller *et al.* 2004; Ho *et al.* 2012) and live cell imaging of N-terminal GFP fusion of MAP65-3 presented here.

Herein, the MAP65-3 was found to colocalize with MAP65-2 at the preprophase band. MAP65-3 appeared to have different localization patterns in the phragmoplast, as it was detected in the phragmoplast midzone, whereas MAP65-2 was observed within the whole phragmoplast with a weaker signal in phragmoplast midzone. This is in contrast with previously published study (Ho *et al.* 2012), where MAP65-1 and MAP65-3 were described to be both localized within the phragmoplast midzone. This is probably a result of immunolabelling rather than a true reflection of MAP65s localization pattern in the phragmoplast because this pattern was always observed only in immunolabelled samples of MAP65-1 (Smertenko *et al.* 2006; Ho *et al.* 2012), but pattern similar to that presented here was previously presented for both MAP65-1 and MAP65-2 in live cell imaging experiment (Lucas and Shaw 2012).

Since it was not possible to colocalize MAP65-2, MAP65-3, and microtubules together by means of live cell imaging, immunolabelling was used instead. This approach confirmed the assumptions from live cell imaging and verified the similar but non-overlapping subcellular localization of MAP65-2 and MAP65-3 at the preprophase band, as well as their absence from metaphase spindle. It also proved their differential subcellular localization at the phragmoplast.

In conclusion, the success of live cell imaging stems from the careful design of fusion proteins and the choice of the microscopic platforms, where there is always

a tradeoff between resolution capacity and phototoxicity. Currently, this limits the possibilities of detailed long-term colocalization studies, which may be alleviated with improving microscopic techniques (von Wangenheim *et al.* 2017b). In this study, the immunolabelling proved to be a valuable tool for confirming the observations from live cell imaging.

The high sequence similarity of MAP65-1 and MAP65-2 and their practically identical localization patterns signify their functional redundancy. Both of these proteins stabilize microtubule bundles during interphase and in mitotic microtubule arrays and their binding to microtubules is dictated by their phosphorylation status (Smertenko *et al.* 2006). In this way, the regulators upstream of MAP65s, e.g. MPKs (Smékalová *et al.* 2014), are truly controlling microtubule stabilization by MAP65s, and the role of MAP65s in the cell division plane orientation would be integrating different signalling events by being phosphorylated or dephosphorylated at multiple phosphorylation sites which are present in their sequences (Smertenko *et al.* 2006; Kirik *et al.* 2012).

On the other hand, MAP65-3 colocalizes only with the preprophase band and phragmoplast, granting it more exclusive roles during the cell division. This is supported by findings of MAP65-3 associating with kinesins involved in the recruitment of proteins to the cortical division zone (KIN12d; Herrmann *et al.* 2018), and in the phragmoplast formation (KIN10a, KIN12a; Ho *et al.* 2011). This suggests that MAP65s are not only passively executing regulation of microtubule organization and dynamics, but they might influence these processes more actively. It is an intriguing question, especially because individual members of the MAP65 protein family possibly have different competence in regulating the assembly, maintenance, and disassembly of microtubule arrays. Another challenge for future studies will be finding out whether the functions of MAP65s are universal for all types of tissues and developmental stages, or whether certain members of MAP65 protein family have distinct roles during specific developmental events.

5. Conclusions

This thesis was focused on the role of mitogen activated protein kinases (MPK) in the cell division plane orientation in the context of plant development. Apart from characterizing the involvement of YODA-MPK3/6 pathway in formative cell divisions, potential interaction between this cascade and protein phosphatase 2A (PP2A) and heat shock proteins 90 (HSP90s) was assessed in the model plant *Arabidopsis thaliana*.

The putative interaction between PP2A and members of the YODA-MPK3/6 cascade is presented in the first part of this thesis. Since PP2A is a multiprotein complex, two subunits were chosen for the experiments, regulatory subunit TONNEAU 2 (TON2 and a scaffolding subunit ROOTS CURL IN NAPHTYLAMINOACID 1 (RCN1). Both pharmacological and genetic depletion of PP2A in *mpk3, mpk6* loss-of-function mutants proved that PP2A and YODA-MPK3/6 work together in a common pathway, which affects the cell division plane orientation in the primary root tip. The direct interaction between PP2A and YDA, MPK3 was confirmed by *in vitro* protein-protein interaction assays. Next, the phosphorylated protein levels of MPK3, MPK6 were found to be altered in *rcn1* loss-of-function mutant, supporting the hypothesis of PP2A regulating MPK3/6. The embryonic development in *mpk3, mpk6, rcn1* and *ton2* mutants was examined and all these mutants were found to have defects in the cell division plane orientation in early embryogenesis. During early embryogenesis, the members of the WUCHSEL-RELATED HOMEOBOX PROTEIN (WOX) family and auxin are necessary for proper specification of the apical-basal axis and for the cell fate determination. The expression of *WOX8* and the distribution of auxin maxima was found to be affected in *mpk3, mpk6, rcn1* and *ton2* mutants.

In the second part of this thesis was investigated, whether HSP90s modulate the YODA-MPK3/6 signalling pathway during embryogenesis. This hypothesis is supported by the observation that genetic depletion of HSP90s rescues the cell division plane orientation defects present in embryos of *yda* loss-of-function and gain-of-function mutants. Furthermore, the *WOX8* expression and auxin maxima distribution are altered in *yda* and *hsp90* mutants suggesting that HSP90s fine-tune the signalling in early embryonic development.

The third part of this thesis was dedicated to advanced microscopy techniques used for describing the organization and dynamics of MICROTUBULE ASSOCIATED PROTEINs 65 (MAP65s) and their colocalization with microtubules. For the live cell

imaging, the light sheet microscopy, Airyscan laser scanning microscopy and structured illumination microscopy were used. These platforms were compared regarding their resolution capacity and phototoxicity, and their applicability for specific tasks in live cell imaging was discussed. Lastly, for colocalization studies of three proteins, MAP65-2, MAP65-3 and tubulin, the immunolocalization was used.

These results enhance the understanding of the role of MPKs in formative cell divisions. Moreover, two factors were shown to affect the signalling of the YODA-MPK3/6 pathway during plant development, namely PP2A and HSP90s. Currently, the exact role of HSP90s in plant embryonic development is undisclosed, yet the results presented here suggest that it modulates embryogenesis through the YODA-MPK3/6 pathway. On the other hand, PP2A is expected to regulate the phosphorylation status of MPK3/6, which would explain the observations presented here. This should be verified in future studies. For answering these questions, together with other issues related to the cell division plane orientation, *in planta* experiments will be necessary. For these studies, the advanced microscopy techniques, which are discussed in this thesis, might be employed.

6. References

Alonso, J.M., Stepanova, A.N., Leisse, T.J., Kim, C.J., Chen, H., Shinn, P., … Ecker, J.R. (2003). Genome-Wide Insertional Mutagenesis of Arabidopsis thaliana. *Science* **301**(5633):653–657. doi: https://doi.org/10.1126/science.1086391.

Ambrose, C., Ruan, Y., Gardiner, J., Tamblyn, L.M., Catching, A., Kirik, V., … Wasteneys, G.O. (2013). CLASP Interacts with Sorting Nexin 1 to Link Microtubules and Auxin Transport via PIN2 Recycling in Arabidopsis thaliana. *Developmental Cell* **24**(6):649–659. doi: https://doi.org/10.1016/j.devcel.2013.02.007.

Ambrose, J.C. and Cyr, R. (2007). The Kinesin ATK5 Functions in Early Spindle Assembly in Arabidopsis. *The Plant Cell* **19**(1):226–236. doi: https://doi.org/10.1105/tpc.106.047613.

Ambrose, J.C. and Cyr, R. (2008). Mitotic Spindle Organization by the Preprophase Band. *Molecular Plant* **1**(6):950–960. doi: https://doi.org/10.1093/mp/ssn054.

Ambrose, J.C., Li, W., Marcus, A., Ma, H. and Cyr, R. (2005). A Minus-End–directed Kinesin with Plus-End Tracking Protein Activity Is Involved in Spindle Morphogenesis. *Molecular Biology of the Cell* **16**(4):1584–1592. doi: https://doi.org/10.1091/mbc.e04-10-0935.

Ambrose, J.C., Shoji, T., Kotzer, A.M., Pighin, J.A. and Wasteneys, G.O. (2007). The Arabidopsis CLASP Gene Encodes a Microtubule-Associated Protein Involved in Cell Expansion and Division. *The Plant Cell* **19**(9):2763–2775. doi: https://doi.org/10.1105/tpc.107.053777.

Ambrose, J.C., Wasteneys, G.O. and Drubin, D.G. (2008). CLASP Modulates Microtubule-Cortex Interaction during Self-Organization of Acentrosomal Microtubules. *Molecular Biology of the Cell* **19**(11):4730–4737. doi: https://doi.org/10.1091/mbc.e08-06-0665.

Awotunde, O.S., Lechward, K., Krajewska, K., Zołnierowicz, S. and Muszyńska, G. (2003). Interaction of maize (Zea mays) protein phosphatase 2A with tubulin. *Acta Biochimica Polonica* **50**(1):131–138. doi: https://doi.org/10.18388/abp.2003_3720.

Ayaydin, F., Vissi, E., Mészáros, T., Miskolczi, P., Kovács, I., Fehér, A., … Dudits, D. (2000). Inhibition of serine/threonine-specific protein phosphatases causes premature activation of cdc2MsF kinase at G2/M transition and early mitotic microtubule organisation in alfalfa. *The Plant Journal* **23**(1):85–96. doi: https://doi.org/10.1046/j.1365-313x.2000.00798.x.

Baba, A.I., Valkai, I., Labhane, N.M., Koczka, L., Andrási, N., Klement, É., … Cséplő, Á. (2019). CRK5 Protein Kinase Contributes to the Progression of Embryogenesis of Arabidopsis thaliana. *International Journal of Molecular Sciences* **20**(24):6120. doi: https://doi.org/10.3390/ijms20246120.

Bajsa, J., Pan, Z. and Duke, S.O. (2011). Transcriptional responses to cantharidin, a protein phosphatase inhibitor, in Arabidopsis thaliana reveal the involvement of multiple signal transduction pathways. *Physiologia Plantarum* **143**(2):188–205. doi: https://doi.org/10.1111/j.1399-3054.2011.01494.x.

Ballesteros, I., Domínguez, T., Sauer, M., Paredes, P., Duprat, A., Rojo, E., … Sánchez-Serrano, J.J. (2013). Specialized functions of the PP2A subfamily II catalytic subunits PP2A-C3 and PP2A-C4 in the distribution of auxin fluxes and development in Arabidopsis. *The Plant Journal* **73**(5):862–872. doi: https://doi.org/10.1111/tpj.12078.

Ban, R., Matsuzaki, H., Akashi, T., Sakashita, G., Taniguchi, H., Park, S.-Y., … Urano, T. (2009). Mitotic regulation of the stability of microtubule plus-end tracking protein EB3 by ubiquitin ligase SIAH-1 and Aurora mitotic kinases. *The Journal of Biological Chemistry* **284**(41):28367–28381. doi: https://doi.org/10.1074/jbc.M109.000273.

Bannigan, A., Lizotte-Waniewski, M., Riley, M. and Baskin, T.I. (2008). Emerging molecular mechanisms that power and regulate the anastral mitotic spindle of flowering plants. *Cell Motility* **65**(1):1–11. doi: https://doi.org/10.1002/cm.20247.

Bannigan, A., Scheible, W.-R., Lukowitz, W., Fagerstrom, C., Wadsworth, P., Somerville, C. and Baskin, T.I. (2007). A conserved role for kinesin-5 in plant mitosis. *Journal of Cell Science* **120**(16):2819–2827. doi: https://doi.org/10.1242/jcs.009506.

Bardwell, L. (2008). Signal Transduction: Turning a Switch into a Rheostat. *Current Biology* **18**(19):R910–R912. doi: https://doi.org/10.1016/j.cub.2008.07.082.

Bayer, M., Nawy, T., Giglione, C., Galli, M., Meinnel, T. and Lukowitz, W. (2009). Paternal Control of Embryonic Patterning in Arabidopsis thaliana. *Science* **323**(5920):1485–1488. doi: https://doi.org/10.1126/science.1167784.

Beck, M., Komis, G., Müller, J., Menzel, D. and Šamaj, J. (2010). Arabidopsis Homologs of Nucleus- and Phragmoplast-Localized Kinase 2 and 3 and Mitogen-Activated Protein Kinase 4 Are Essential for Microtubule Organization. *The Plant Cell* **22**(3):755–771. doi: https://doi.org/10.1105/tpc.109.071746.

Beck, M., Komis, G., Ziemann, A., Menzel, D. and Šamaj, J. (2011). Mitogen-activated protein kinase 4 is involved in the regulation of mitotic and cytokinetic microtubule transitions in Arabidopsis thaliana. *New Phytologist* **189**(4):1069–1083. doi: https://doi.org/10.1111/j.1469-8137.2010.03565.x.

Bequette, C.J., Hind, S.R., Pulliam, S., Higgins, R. and Stratmann, J.W. (2018). MAP kinases associate with high molecular weight multiprotein complexes. *Journal of Experimental Botany* **69**(3):643–654. doi: https://doi.org/10.1093/jxb/erx424.

Berardini, T.Z., Reiser, L., Li, D., Mezheritsky, Y., Muller, R., Strait, E. and Huala, E. (2015). The arabidopsis information resource: Making and mining the "gold standard" annotated reference plant genome: Tair: Making and Mining the "Gold Standard" Plant Genome. *Genesis* **53**(8):474–485. doi: https://doi.org/10.1002/dvg.22877.

Bergmann, D.C., Lukowitz, W. and Somerville, C.R. (2004). Stomatal Development and Pattern Controlled by a MAPKK Kinase. *Science* **304**(5676):1494–1497. doi: https://doi.org/10.1126/science.1096014.

Besson, S. and Dumais, J. (2011). Universal rule for the symmetric division of plant cells. *Proceedings of the National Academy of Sciences* **108**(15):6294–6299. doi: https://doi.org/10.1073/pnas.1011866108.

Bhaskara, G.B., Wen, T.-N., Nguyen, T.T. and Verslues, P.E. (2017). Protein Phosphatase 2Cs and *Microtubule-Associated Stress Protein 1* Control Microtubule Stability, Plant Growth, and Drought Response. *The Plant Cell* **29**(1):169–191. doi: https://doi.org/10.1105/tpc.16.00847.

Blakeslee, J.J., Zhou, H.-W., Heath, J.T., Skottke, K.R., Barrios, J.A.R., Liu, S.-Y. and DeLong, A. (2008). Specificity of RCN1-Mediated Protein Phosphatase 2A Regulation in Meristem Organization and Stress Response in Roots. *Plant Physiology* **146**(2):539–553. doi: https://doi.org/10.1104/pp.107.112995.

Bögre, L., Calderini, O., Binarova, P., Mattauch, M., Till, S., Kiegerl, S., … Heberle-Bors, E. (1999). A MAP Kinase Is Activated Late in Plant Mitosis and Becomes Localized to the Plane of Cell Division. *The Plant Cell* **11**(1):101–113. doi: https://doi.org/10.1105/tpc.11.1.101.

Boruc, J., Weimer, A.K., Stoppin-Mellet, V., Mylle, E., Kosetsu, K., Cedeño, C., … Van Damme, D. (2017). Phosphorylation of MAP65-1 by Arabidopsis Aurora Kinases Is Required for Efficient Cell Cycle Progression. *Plant Physiology* **173**(1):582–599. doi: https://doi.org/10.1104/pp.16.01602.

Bouyer, D., Roudier, F., Heese, M., Andersen, E.D., Gey, D., Nowack, M.K., … Schnittger, A. (2011). Polycomb Repressive Complex 2 Controls the Embryo-to-Seedling Phase Transition. *PLoS Genetics* **7**(3):e1002014. doi: https://doi.org/10.1371/journal.pgen.1002014.

Bowser, J. and Reddy, A.S.N. (1997). Localization of a kinesin-like calmodulin-binding protein in dividing cells of Arabidopsis and tobacco. *The Plant Journal* **12**(6):1429–1437. doi: https://doi.org/10.1046/j.1365-313x.1997.12061429.x.

Boyer, F. and Simon, R. (2015). Asymmetric cell divisions constructing *Arabidopsis* stem cell niches: the emerging role of protein phosphatases. *Plant Biology* **17**(5):935–945. doi: https://doi.org/10.1111/plb.12352.

Breuninger, H., Rikirsch, E., Hermann, M., Ueda, M. and Laux, T. (2008). Differential Expression of WOX Genes Mediates Apical-Basal Axis Formation in the Arabidopsis Embryo. *Developmental Cell* **14**(6):867–876. doi: https://doi.org/10.1016/j.devcel.2008.03.008.

Brieño-Enríquez, M.A., Moak, S.L., Holloway, J.K. and Cohen, P.E. (2017). NIMA-related kinase 1 (NEK1) regulates meiosis I spindle assembly by altering the balance between α-Adducin and Myosin X. *PLoS ONE* **12**(10):e0185780. doi: https://doi.org/10.1371/journal.pone.0185780.

Brown, R.C. and Lemmon, B.E. (2001). The cytoskeleton and spatial control of cytokinesis in the plant life cycle. *Protoplasma* **215**(1):35–49. doi: https://doi.org/10.1007/BF01280302.

Burkart, G.M. and Dixit, R. (2019). Microtubule bundling by MAP65-1 protects against severing by inhibiting the binding of katanin. *Molecular Biology of the Cell* **30**(13):1587–1597. doi: https://doi.org/10.1091/mbc.E18-12-0776.

Buschmann, H., Chan, J., Sanchez-Pulido, L., Andrade-Navarro, M.A., Doonan, J.H. and Lloyd, C.W. (2006). Microtubule-Associated AIR9 Recognizes the Cortical Division Site at Preprophase and Cell-Plate Insertion. *Current Biology* **16**(19):1938–1943. doi: https://doi.org/10.1016/j.cub.2006.08.028.

Buschmann, H., Dols, J., Kopischke, S., Pena, E.J., Andrade-Navarro, M.A., Heinlein, M., … Lloyd, C.W. (2015). Arabidopsis KCBP interacts with AIR9 but stays in the cortical division zone throughout mitosis via its MyTH4-FERM domain. *Journal of Cell Science* **128**(11):2033–2046. doi: https://doi.org/10.1242/jcs.156570.

Buschmann, H. and Zachgo, S. (2016). The Evolution of Cell Division: From Streptophyte Algae to Land Plants. *Trends in Plant Science* **21**(10):872–883. doi: https://doi.org/10.1016/j.tplants.2016.07.004.

Bush, S.M. and Krysan, P.J. (2007). Mutational evidence that the Arabidopsis MAP kinase MPK6 is involved in anther, inflorescence, and embryo development. *Journal of Experimental Botany* **58**(8):2181–2191. doi: https://doi.org/10.1093/jxb/erm092.

Caillaud, M.-C., Lecomte, P., Jammes, F., Quentin, M., Pagnotta, S., Andrio, E., … Favery, B. (2008). MAP65-3 Microtubule-Associated Protein Is Essential for Nematode-Induced Giant Cell

Ontogenesis in Arabidopsis. *The Plant Cell* **20**(2):423–437. doi: https://doi.org/10.1105/tpc.107.057422.

Calderini, O., Bogre, L., Vicente, O., Binarova, P., Heberle-Bors, E. and Wilson, C. (1998). A cell cycle regulated MAP kinase with a possible role in cytokinesis in tobacco cells. *Journal of Cell Science* **111**(20):3091–3100.

Calderini, O., Glab, N., Bergounioux, C., Heberle-Bors, E. and Wilson, C. (2001). A Novel Tobacco Mitogen-activated Protein (MAP) Kinase Kinase, NtMEK1, Activates the Cell Cycle-regulated p43Ntf6 MAP Kinase. *Journal of Biological Chemistry* **276**(21):18139–18145. doi: https://doi.org/10.1074/jbc.M010621200.

Camilleri, C., Azimzadeh, J., Pastuglia, M., Bellili, Catherine, Grandjean, O. and Bouchez, D. (2002). The Arabidopsis TONNEAU2 Gene Encodes a Putative Novel Protein Phosphatase 2A Regulatory Subunit Essential for the Control of the Cortical Cytoskeleton. *The Plant Cell* **14**(4):833–845. doi: https://doi.org/10.1105/tpc.010402.

Cartwright, H.N., Humphries, J.A. and Smith, L.G. (2009). A Receptor-Like Protein That Promotes Polarization of an Asymmetric Cell Division in Maize. *Science* **323**(5914):649–651. doi: https://doi.org/10.1126/science.1161686.

Celler, K., Fujita, M., Kawamura, E., Ambrose, C., Herburger, K., Holzinger, A. and Wasteneys, G.O. (2016). Microtubules in Plant Cells: Strategies and Methods for Immunofluorescence, Transmission Electron Microscopy, and Live Cell Imaging. In: Gavin, R. H. (ed.). *Cytoskeleton Methods and Protocols*. New York, NY: Springer New York, pp. 155–184.

Chan, J., Calder, G., Fox, S. and Lloyd, C. (2005). Localization of the Microtubule End Binding Protein EB1 Reveals Alternative Pathways of Spindle Development in Arabidopsis Suspension Cells. *The Plant Cell* **17**(6):1737–1748. doi: https://doi.org/10.1105/tpc.105.032615.

Chan, J., Jensen, C.G., Jensen, L.C.W., Bush, M. and Lloyd, C.W. (1999). The 65-kDa carrot microtubule-associated protein forms regularly arranged filamentous cross-bridges between microtubules. *Proceedings of the National Academy of Sciences* **96**(26):14931–14936. doi: https://doi.org/10.1073/pnas.96.26.14931.

Chen, B.-C., Legant, W.R., Wang, K., Shao, L., Milkie, D.E., Davidson, M.W., … Betzig, E. (2014). Lattice light-sheet microscopy: Imaging molecules to embryos at high spatiotemporal resolution. *Science* **346**(6208). doi: https://doi.org/10.1126/science.1257998.

Chen, H.-W., Persson, S., Grebe, M. and McFarlane, H.E. (2018). Cellulose synthesis during cell plate assembly. *Physiologia Plantarum* **164**(1):17–26. doi: https://doi.org/10.1111/ppl.12703.

Colcombet, J. and Hirt, H. (2008). Arabidopsis MAPKs: a complex signalling network involved in multiple biological processes. *Biochemical Journal* **413**(2):217–226. doi: https://doi.org/10.1042/BJ20080625.

Costa, L.M., Marshall, E., Tesfaye, M., Silverstein, K.A.T., Mori, M., Umetsu, Y., … Gutierrez-Marcos, J.F. (2014). Central Cell–Derived Peptides Regulate Early Embryo Patterning in Flowering Plants. *Science* **344**(6180):168–172. doi: https://doi.org/10.1126/science.1243005.

Costa, S. (2017). Are division plane determination and cell-cycle progression coordinated? *New Phytologist* **213**(1):16–21. doi: https://doi.org/10.1111/nph.14261.

Cox, S., Rosten, E., Monypenny, J., Jovanovic-Talisman, T., Burnette, D.T., Lippincott-Schwartz, J., … Heintzmann, R. (2012). Bayesian localization microscopy reveals nanoscale podosome dynamics. *Nature Methods* **9**(2):195–200. doi: https://doi.org/10.1038/nmeth.1812.

Cristina, M., Petersen, M. and Mundy, J. (2010). Mitogen-Activated Protein Kinase Signaling in Plants. *Annual Review of Plant Biology* **61**(1):621–649. doi: https://doi.org/10.1146/annurev-arplant-042809-112252.

Cutler, S.R. and Ehrhardt, D.W. (2002). Polarized cytokinesis in vacuolate cells of Arabidopsis. *Proceedings of the National Academy of Sciences* **99**(5):2812–2817. doi: https://doi.org/10.1073/pnas.052712299.

Dai, M., Zhang, C., Kania, U., Chen, F., Xue, Q., Mccray, T., … Wang, H. (2012). A PP6-Type Phosphatase Holoenzyme Directly Regulates PIN Phosphorylation and Auxin Efflux in Arabidopsis. *The Plant Cell* **24**(6):2497–2514. doi: https://doi.org/10.1105/tpc.112.098905.

De Smet, I. and Beeckman, T. (2011). Asymmetric cell division in land plants and algae: the driving force for differentiation. *Nature Reviews Molecular Cell Biology* **12**(3):177–188. doi: https://doi.org/10.1038/nrm3064.

De Smet, I., Voß, U., Jürgens, G. and Beeckman, T. (2009). Receptor-like kinases shape the plant. *Nature Cell Biology* **11**(10):1166–1173. doi: https://doi.org/10.1038/ncb1009-1166.

Deavours, B.E., Reddy, A.S.N. and Walker, R.A. (1998). Ca2+/calmodulin regulation of the Arabidopsis kinesin-like calmodulin-binding protein. *Cell Motility* **40**(4):408–416. doi: https://doi.org/10.1002/(SICI)1097-0169(1998)40:4<408::AID-CM8>3.0.CO;2-6.

Deeks, M.J., Fendrych, M., Smertenko, A., Bell, K.S., Oparka, K., Cvrčková, F., … Hussey, P.J. (2010). The plant formin AtFH4 interacts with both actin and microtubules, and contains a newly identified microtubule-binding domain. *Journal of Cell Science* **123**(8):1209–1215. doi: https://doi.org/10.1242/jcs.065557.

Demidov, D., Van Damme, D., Geelen, D., Blattner, F.R. and Houben, A. (2005). Identification and Dynamics of Two Classes of Aurora-Like Kinases in Arabidopsis and Other Plants. *The Plant Cell* **17**(3):836–848. doi: https://doi.org/10.1105/tpc.104.029710.

Demmerle, J., Innocent, C., North, A.J., Ball, G., Müller, M., Miron, E., … Schermelleh, L. (2017). Strategic and practical guidelines for successful structured illumination microscopy. *Nature Protocols* **12**(5):988–1010. doi: https://doi.org/10.1038/nprot.2017.019.

Dertinger, T., Colyer, R., Iyer, G., Weiss, S. and Enderlein, J. (2009). Fast, background-free, 3D super-resolution optical fluctuation imaging (SOFI). *Proceedings of the National Academy of Sciences* **106**(52):22287–22292. doi: https://doi.org/10.1073/pnas.0907866106.

Deruere, J., Jackson, K., Garbers, C., Soll, D. and DeLong, A. (1999). The RCN1-encoded A subunit of protein phosphatase 2A increases phosphatase activity in vivo. *The Plant Journal* **20**(4):389–399. doi: https://doi.org/10.1046/j.1365-313x.1999.00607.x.

Dhanasekaran, D.N., Kashef, K., Lee, C.M., Xu, H. and Reddy, E.P. (2007). Scaffold proteins of MAP-kinase modules. *Oncogene* **26**(22):3185–3202. doi: https://doi.org/10.1038/sj.onc.1210411.

Dhonukshe, P. and Gadella, T.W.J. (2003). Alteration of Microtubule Dynamic Instability during Preprophase Band Formation Revealed by Yellow Fluorescent Protein–CLIP170 Microtubule Plus-End Labeling. *The Plant Cell* **15**(3):597–611. doi: https://doi.org/10.1105/tpc.008961.

Dong, J., MacAlister, C.A. and Bergmann, D.C. (2009). BASL Controls Asymmetric Cell Division in Arabidopsis. *Cell* **137**(7):1320–1330. doi: https://doi.org/10.1016/j.cell.2009.04.018.

Drevensek, S., Goussot, M., Duroc, Y., Christodoulidou, A., Steyaert, S., Schaefer, E., … Pastuglia, M. (2012). The Arabidopsis TRM1-TON1 Interaction Reveals a Recruitment Network Common to Plant Cortical Microtubule Arrays and Eukaryotic Centrosomes. *The Plant Cell* **24**(1):178–191. doi: https://doi.org/10.1105/tpc.111.089748.

Durst, S., Hedde, P.N., Brochhausen, L., Nick, P., Nienhaus, G.U. and Maisch, J. (2014). Organization of perinuclear actin in live tobacco cells observed by PALM with optical sectioning. *Journal of Plant Physiology* **171**(2):97–108. doi: https://doi.org/10.1016/j.jplph.2013.10.007.

Endo, H. and Torii, K.U. (2019). Stomatal Development and Perspectives toward Agricultural Improvement. *Cold Spring Harbor Perspectives in Biology* **11**(5):a034660. doi: https://doi.org/10.1101/cshperspect.a034660.

Eng, R.C., Halat, L.S., Livingston, S.J., Sakai, T., Motose, H. and Wasteneys, G.O. (2017). The ARM Domain of ARMADILLO-REPEAT KINESIN 1 is Not Required for Microtubule Catastrophe But Can Negatively Regulate NIMA-RELATED KINASE 6 in Arabidopsis thaliana. *Plant and Cell Physiology* **58**(8):1350–1363. doi: https://doi.org/10.1093/pcp/pcx070.

Erhardt, M., Stoppin-Mellet, V., Campagne, S., Canaday, J., Mutterer, J., Fabian, T., … Schmit, A.-C. (2002). The plant Spc98p homologue colocalizes with γ-tubulin at microtubule nucleation sites and is required for microtubule nucleation. *Journal of Cell Science* **115**(11):2423–2431.

Eyers, P.A., Erikson, E., Chen, L.G. and Maller, J.L. (2003). A Novel Mechanism for Activation of the Protein Kinase Aurora A. *Current Biology* **13**(8):691–697. doi: https://doi.org/10.1016/S0960-9822(03)00166-0.

Fache, V., Gaillard, J., Van Damme, D., Geelen, D., Neumann, E., Stoppin-Mellet, V. and Vantard, M. (2010). Arabidopsis Kinetochore Fiber-Associated MAP65-4 Cross-Links Microtubules and Promotes Microtubule Bundle Elongation. *The Plant Cell* **22**(11):3804–3815. doi: https://doi.org/10.1105/tpc.110.080606.

Flanders, D.J., Rawlins, D.J., Shaw, P.J. and Lloyd, C.W. (1990). Nucleus-associated microtubules help determine the division plane of plant epidermal cells: avoidance of four-way junctions and the role of cell geometry. *Journal of Cell Biology* **110**(4):1111–1122. doi: https://doi.org/10.1083/jcb.110.4.1111.

Floková, P. (2016). *Úloha mitogenem aktivované protein kinázy MPK6 ve vývoji Arabidopsis thaliana*. Diploma Thesis, Palacký University Olomouc.

Fosket, D.E. and Morejohn, L.C. (1992). Structural and Functional Organization of Tubulin. *Annual Review of Plant Physiology and Plant Molecular Biology* **43**(1):201–240. doi: https://doi.org/10.1146/annurev.pp.43.060192.001221.

Fowler, J.E. and Quatrano, R.S. (1995). Cell polarity, asymmetric division, and cell fate determination in brown algal zygotes. *Seminars in Developmental Biology* **6**(5):347–358. doi: https://doi.org/10.1016/S1044-5781(06)80076-9.

Freisinger, T., Klünder, B., Johnson, J., Müller, N., Pichler, G., Beck, G., … Wedlich-Söldner, R. (2013). Establishment of a robust single axis of cell polarity by coupling multiple positive feedback loops. *Nature Communications* **4**(1):1–11. doi: https://doi.org/10.1038/ncomms2795.

Freudenreich, A. and Nick, P. (1998). Microtubular Organization in Tobacco Cells: Heat-Shock Protein 90 can Bind to Tubulin in Vitro. *Botanica Acta* **111**(4):273–279. doi: https://doi.org/10.1111/j.1438-8677.1998.tb00708.x.

Frey, N., Klotz, J. and Nick, P. (2010). A kinesin with calponin-homology domain is involved in premitotic nuclear migration. *Journal of Experimental Botany* **61**(12):3423–3437. doi: https://doi.org/10.1093/jxb/erq164.

Friml, J., Vieten, A., Sauer, M., Weijers, D., Schwarz, H., Hamann, T., … Jürgens, G. (2003). Efflux-dependent auxin gradients establish the apical–basal axis of Arabidopsis. *Nature* **426**(6963):147–153. doi: https://doi.org/10.1038/nature02085.

Fuller, M.T. and Spradling, A.C. (2007). Male and Female Drosophila Germline Stem Cells: Two Versions of Immortality. *Science* **316**(5823):402–404. doi: https://doi.org/10.1126/science.1140861.

Gaetano, J. (2013). Holm-Bonferroni Sequential Correction: An EXCEL Calculator.

Gaillard, J., Neumann, E., Van Damme, D., Stoppin-Mellet, V., Ebel, C., Barbier, E., … Vantard, M. (2008). Two microtubule-associated proteins of Arabidopsis MAP65s promote antiparallel microtubule bundling. *Molecular Biology of the Cell* **19**(10):4534–4544. doi: https://doi.org/10.1091/mbc.e08-04-0341.

Gaillochet, C. and Lohmann, J.U. (2015). The never-ending story: from pluripotency to plant developmental plasticity. *Development* **142**(13):2237–2249. doi: https://doi.org/10.1242/dev.117614.

Gallagher, K. and Smith, L.G. (1999). discordia mutations specifically misorient asymmetric cell divisions during development of the maize leaf epidermis. *Development* **126**(20):4623–4633.

Garbers, C., DeLong, A., Deruére, J., Bernasconi, P. and Söll, D. (1996). A mutation in protein phosphatase 2A regulatory subunit A affects auxin transport in Arabidopsis. *The EMBO Journal* **15**(9):2115–2124. doi: https://doi.org/10.1002/j.1460-2075.1996.tb00565.x.

Geldner, N., Anders, N., Wolters, H., Keicher, J., Kornberger, W., Muller, P., … Jürgens, G. (2003). The Arabidopsis GNOM ARF-GEF Mediates Endosomal Recycling, Auxin Transport, and Auxin-Dependent Plant Growth. *Cell* **112**(2):219–230. doi: https://doi.org/10.1016/S0092-8674(03)00003-5.

Geshi, N., Johansen, J.N., Dilokpimol, A., Rolland, A., Belcram, K., Verger, S., … Mouille, G. (2013). A galactosyltransferase acting on arabinogalactan protein glycans is essential for embryo development in Arabidopsis. *The Plant Journal* **76**(1):128–137. doi: https://doi.org/10.1111/tpj.12281.

Gray, J.E., Casson, S. and Hunt, L. (2008). Intercellular Peptide Signals Regulate Plant Meristematic Cell Fate Decisions. *Science Signaling* **1**(49):pe53–pe53. doi: https://doi.org/10.1126/scisignal.149pe53.

Green, M.R., Sambrook, J. and Sambrook, J. (2012). *Molecular Cloning: A Laboratory Manual*. 4th ed. Cold Spring Harbor, N.Y: Cold Spring Harbor Laboratory Press.

Grethe, S. and Pörn-Ares, M.I. (2006). p38 MAPK regulates phosphorylation of Bad via PP2A-dependent suppression of the MEK1/2-ERK1/2 survival pathway in TNF-α induced endothelial apoptosis. *Cellular Signalling* **18**(4):531–540. doi: https://doi.org/10.1016/j.cellsig.2005.05.023.

Groves, M.R., Hanlon, N., Turowski, P., Hemmings, B.A. and Barford, D. (1999). The Structure of the Protein Phosphatase 2A PR65/A Subunit Reveals the Conformation of Its 15 Tandemly Repeated HEAT Motifs. *Cell* **96**(1):99–110. doi: https://doi.org/10.1016/S0092-8674(00)80963-0.

Gruss, O.J., Carazo-Salas, R.E., Schatz, C.A., Guarguaglini, G., Kast, J., Wilm, M., … Mattaj, I.W. (2001). Ran Induces Spindle Assembly by Reversing the Inhibitory Effect of Importin α on TPX2 Activity. *Cell* **104**(1):83–93. doi: https://doi.org/10.1016/S0092-8674(01)00193-3.

Gudesblat, G.E., Schneider-Pizoń, J., Betti, C., Mayerhofer, J., Vanhoutte, I., van Dongen, W., … Russinova, E. (2012). SPEECHLESS integrates brassinosteroid and stomata signalling pathways. *Nature Cell Biology* **14**(5):548–554. doi: https://doi.org/10.1038/ncb2471.

Guo, J. and Chen, J.-G. (2008). RACK1 genes regulate plant development with unequal genetic redundancy in Arabidopsis. *BMC Plant Biology* **8**(1):1–11. doi: https://doi.org/10.1186/1471-2229-8-108.

Gustafsson, N., Culley, S., Ashdown, G., Owen, D.M., Pereira, P.M. and Henriques, R. (2016). Fast live-cell conventional fluorophore nanoscopy with ImageJ through super-resolution radial fluctuations. *Nature Communications* **7**(1):1–9. doi: https://doi.org/10.1038/ncomms12471.

Haecker, A., Groß-Hardt, R., Geiges, B., Sarkar, A., Breuninger, H., Herrmann, M. and Laux, T. (2004). Expression dynamics of WOX genes mark cell fate decisions during early embryonic patterning in Arabidopsis thaliana. *Development* **131**(3):657–668. doi: https://doi.org/10.1242/dev.00963.

Hamann, T., Benkova, E., Bäurle, I., Kientz, M. and Jürgens, G. (2002). The Arabidopsis BODENLOS gene encodes an auxin response protein inhibiting MONOPTEROS-mediated embryo patterning. *Genes & Development* **16**(13):1610–1615. doi: https://doi.org/10.1101/gad.229402.

Hamant, O., Heisler, M.G., Jönsson, H., Krupinski, P., Uyttewaal, M., Bokov, P., … Traas, J. (2008). Developmental Patterning by Mechanical Signals in Arabidopsis. *Science* **322**(5908):1650–1655. doi: https://doi.org/10.1126/science.1165594.

Hamant, O., Inoue, D., Bouchez, D., Dumais, J. and Mjolsness, E. (2019). Are microtubules tension sensors? *Nature Communications* **10**(1):2360. doi: https://doi.org/10.1038/s41467-019-10207-y.

Hara, K., Kajita, R., Torii, K.U., Bergmann, D.C. and Kakimoto, T. (2007). The secretory peptide gene EPF1 enforces the stomatal one-cell-spacing rule. *Genes & Development* **21**(14):1720–1725. doi: https://doi.org/10.1101/gad.1550707.

Haralampidis, K., Milioni, D., Rigas, S. and Hatzopoulos, P. (2002). Combinatorial Interaction of Cis Elements Specifies the Expression of the Arabidopsis AtHsp90-1Gene. *Plant Physiology* **129**(3):1138–1149. doi: https://doi.org/10.1104/pp.004044.

Havelková, L., Nanda, G., Martinek, J., Bellinvia, E., Sikorová, L., Šlajcherová, K., … Schwarzerová, K. (2015). Arp2/3 complex subunit ARPC2 binds to microtubules. *Plant Science* **241**:96–108. doi: https://doi.org/10.1016/j.plantsci.2015.10.001.

Hayashi, S. and Okada, Y. (2015). Ultrafast superresolution fluorescence imaging with spinning disk confocal microscope optics. *Molecular Biology of the Cell* **26**(9):1743–1751. doi: https://doi.org/10.1091/mbc.E14-08-1287.

Herrmann, A., Livanos, P., Lipka, E., Gadeyne, A., Hauser, M., Van Damme, D. and Müller, S. (2018). Dual localized kinesin-12 POK2 plays multiple roles during cell division and interacts with MAP65-3. *EMBO reports* **19**(9):e46085. doi: https://doi.org/10.15252/embr.201846085.

Hirakawa, Y., Kondo, Y. and Fukuda, H. (2010). TDIF Peptide Signaling Regulates Vascular Stem Cell Proliferation via the WOX4 Homeobox Gene in Arabidopsis. *The Plant Cell* **22**(8):2618–2629. doi: https://doi.org/10.1105/tpc.110.076083.

Ho, C.-M.K., Hotta, T., Guo, F., Roberson, R.W., Lee, Y.-R.J. and Liu, B. (2011). Interaction of Antiparallel Microtubules in the Phragmoplast Is Mediated by the Microtubule-Associated Protein MAP65-3 in Arabidopsis. *The Plant Cell* **23**(8):2909–2923. doi: https://doi.org/10.1105/tpc.110.078204.

Ho, C.-M.K., Lee, Y.-R.J., Kiyama, L.D., Dinesh-Kumar, S.P. and Liu, B. (2012). Arabidopsis Microtubule-Associated Protein MAP65-3 Cross-Links Antiparallel Microtubules toward Their Plus Ends in the Phragmoplast via Its Distinct C-Terminal Microtubule Binding Domain. *The Plant Cell* **24**(5):2071–2085. doi: https://doi.org/10.1105/tpc.111.092569.

Honkanen, R.E. (1993). Cantharidin, another natural toxin that inhibits the activity of serine/threonine protein phosphatases types 1 and 2A. *FEBS Letters* **330**(3):283–286. doi: https://doi.org/10.1016/0014-5793(93)80889-3.

Hord, C.L.H., Sun, Y.-J., Pillitteri, L.J., Torii, K.U., Wang, H., Zhang, S. and Ma, H. (2008). Regulation of Arabidopsis Early Anther Development by the Mitogen-Activated Protein Kinases, MPK3 and MPK6, and the ERECTA and Related Receptor-Like Kinases. *Molecular Plant* **1**(4):645–658. doi: https://doi.org/10.1093/mp/ssn029.

Hoshi, M., Ohta, K., Gotoh, Y., Mori, A., Murofushi, H., Sakai, H. and Nishida, E. (1992). Mitogen-activated-protein-kinase-catalyzed phosphorylation of microtubule-associated proteins, microtubule-associated protein 2 and microtubule-associated protein 4, induces an alteration in their function. *European Journal of Biochemistry* **203**(1–2):43–52. doi: https://doi.org/10.1111/j.1432-1033.1992.tb19825.x.

Hosy, E., Martinière, A., Choquet, D., Maurel, C. and Luu, D.-T. (2015). Super-Resolved and Dynamic Imaging of Membrane Proteins in Plant Cells Reveal Contrasting Kinetic Profiles and Multiple Confinement Mechanisms. *Molecular Plant* **8**(2):339–342. doi: https://doi.org/10.1016/j.molp.2014.10.006.

Houbaert, A., Zhang, C., Tiwari, M., Wang, K., Serrano, A. de M., Savatin, D.V., … Russinova, E. (2018). POLAR-guided signalling complex assembly and localization drive asymmetric cell division. *Nature* **563**(7732):574–578. doi: https://doi.org/10.1038/s41586-018-0714-x.

Hubert, D.A., He, Y., McNulty, B.C., Tornero, P. and Dangl, J.L. (2009). Specific Arabidopsis HSP90.2 alleles recapitulate RAR1 cochaperone function in plant NB-LRR disease resistance protein regulation. *Proceedings of the National Academy of Sciences* **106**(24):9556–9563. doi: https://doi.org/10.1073/pnas.0904877106.

Hubert, D.A., Tornero, P., Belkhadir, Y., Krishna, P., Takahashi, A., Shirasu, K. and Dangl, J.L. (2003). Cytosolic HSP90 associates with and modulates the Arabidopsis RPM1 disease resistance protein. *The EMBO Journal* **22**(21):5679–5689. doi: https://doi.org/10.1093/emboj/cdg547.

Huff, J. (2016). The Fast mode for ZEISS LSM 880 with Airyscan: high-speed confocal imaging with super-resolution and improved signal-to-noise ratio. *Nature Methods* **13**(11):i–ii. doi: https://doi.org/10.1038/nmeth.f.398.

Humphries, J.A., Vejlupkova, Z., Luo, A., Meeley, R.B., Sylvester, A.W., Fowler, J.E. and Smith, L.G. (2011). ROP GTPases Act with the Receptor-Like Protein PAN1 to Polarize Asymmetric Cell Division in Maize. *The Plant Cell* **23**(6):2273–2284. doi: https://doi.org/10.1105/tpc.111.085597.

Hunt, L., Bailey, K.J. and Gray, J.E. (2010). The signalling peptide EPFL9 is a positive regulator of stomatal development. *New Phytologist* **186**(3):609–614. doi: https://doi.org/10.1111/j.1469-8137.2010.03200.x.

Hunt, L. and Gray, J.E. (2009). The Signaling Peptide EPF2 Controls Asymmetric Cell Divisions during Stomatal Development. *Current Biology* **19**(10):864–869. doi: https://doi.org/10.1016/j.cub.2009.03.069.

Hush, J., Wu, L., John, P.C.L., Hepler, L.H. and Hepler, P.K. (1996). Plant Mitosis Promoting Factor Disassembles the Microtubule Preprophase Band and Accelerates Prophase Progression in Tradescantia. *Cell Biology International* **20**(4):275–287. doi: https://doi.org/10.1006/cbir.1996.0031.

Hussey, P.J., Hawkins, T.J., Igarashi, H., Kaloriti, D. and Smertenko, A. (2002). The plant cytoskeleton: recent advances in the study of the plant microtubule-associated proteins MAP-65, MAP-190 and the Xenopus MAP215-like protein, MOR1. *Plant Molecular Biology* **50**(6):915–924. doi: https://doi.org/10.1023/A:1021236307508.

Insall, R., Müller-Taubenberger, A., Machesky, L., Köhler, J., Simmeth, E., Atkinson, S.J., … Gerisch, G. (2001). Dynamics of the Dictyostelium Arp2/3 complex in endocytosis, cytokinesis, and chemotaxis. *Cell Motility* **50**(3):115–128. doi: https://doi.org/10.1002/cm.10005.

Interactome, A.I.M.C.A. (2011). Mapping Consortium Evidence for network evolution in an Arabidopsis interactome map. *Science* **333**(6042):601–607.

Ito, Y., Nakanomyo, I., Motose, H., Iwamoto, K., Sawa, S., Dohmae, N. and Fukuda, H. (2006). Dodeca-CLE Peptides as Suppressors of Plant Stem Cell Differentiation. *Science* **313**(5788):842–845. doi: https://doi.org/10.1126/science.1128436.

Izhaki, A. and Bowman, J.L. (2007). KANADI and Class III HD-Zip Gene Families Regulate Embryo Patterning and Modulate Auxin Flow during Embryogenesis in Arabidopsis. *The Plant Cell* **19**(2):495–508. doi: https://doi.org/10.1105/tpc.106.047472.

Jenik, P.D., Jurkuta, R.E.J. and Barton, M.K. (2005). Interactions between the Cell Cycle and Embryonic Patterning in Arabidopsis Uncovered by a Mutation in DNA Polymerase ε. *The Plant Cell* **17**(12):3362–3377. doi: https://doi.org/10.1105/tpc.105.036889.

Jeong, S., Bayer, M. and Lukowitz, W. (2011). Taking the very first steps: from polarity to axial domains in the early Arabidopsis embryo. *Journal of Experimental Botany* **62**(5):1687–1697. doi: https://doi.org/10.1093/jxb/erq398.

Jeong, S., Eilbert, E., Bolbol, A. and Lukowitz, W. (2016). Going mainstream: How is the body axis of plants first initiated in the embryo? *Developmental Biology* **419**(1):78–84. doi: https://doi.org/10.1016/j.ydbio.2016.05.002.

Jewaria, P.K., Hara, T., Tanaka, H., Kondo, T., Betsuyaku, S., Sawa, S., … Kakimoto, T. (2013). Differential Effects of the Peptides Stomagen, EPF1 and EPF2 on Activation of MAP Kinase MPK6 and the SPCH Protein Level. *Plant and Cell Physiology* **54**(8):1253–1262. doi: https://doi.org/10.1093/pcp/pct076.

Jonak, C., Ligterink, W. and Hirt, H. (1999). MAP kinases in plant signal transduction. *Cellular and Molecular Life Sciences* **55**(2):204–213. doi: https://doi.org/10.1007/s000180050285.

Kao, Y.-L., Deavours, B.E., Phelps, K.K., Walker, R.A. and Reddy, A.S.N. (2000). Bundling of Microtubules by Motor and Tail Domains of a Kinesin-like Calmodulin-Binding Protein from

Arabidopsis: Regulation by Ca2+/Calmodulin. *Biochemical and Biophysical Research Communications* **267**(1):201–207. doi: https://doi.org/10.1006/bbrc.1999.1896.

Kapitein, L.C., Janson, M.E., van den Wildenberg, S.M.J.L., Hoogenraad, C.C., Schmidt, C.F. and Peterman, E.J.G. (2008). Microtubule-Driven Multimerization Recruits ase1p onto Overlapping Microtubules. *Current Biology* **18**(21):1713–1717. doi: https://doi.org/10.1016/j.cub.2008.09.046.

Kapoor, V., Hirst, W.G., Hentschel, C., Preibisch, S. and Reber, S. (2019). MTrack: Automated Detection, Tracking, and Analysis of Dynamic Microtubules. *Scientific Reports* **9**(1):1–12. doi: https://doi.org/10.1038/s41598-018-37767-1.

Katsuta, J., Hashiguchi, Y. and Shibaoka, H. (1990). The Role of the Cytoskeleton in Positioning of the Nucleus in Premitotic Tobacco BY-2 Cells. *Journal of Cell Science* **95**(3):413–422.

Katsuta, J. and Shibaoka, H. (1992). Inhibition by kinase inhibitors of the development and the disappearance of the preprophase band of microtubules in tobacco BY-2 cells. *Journal of Cell Science* **103**(2):397–405.

Kawabe, A., Matsunaga, S., Nakagawa, K., Kurihara, D., Yoneda, A., Hasezawa, S., … Fukui, K. (2005). Characterization of plant Aurora kinases during mitosis. *Plant Molecular Biology* **58**(1):1–13. doi: https://doi.org/10.1007/s11103-005-3454-x.

Kawamura, E., Himmelspach, R., Rashbrooke, M.C., Whittington, A.T., Gale, K.R., Collings, D.A. and Wasteneys, G.O. (2006). MICROTUBULE ORGANIZATION 1 Regulates Structure and Function of Microtubule Arrays during Mitosis and Cytokinesis in the Arabidopsis Root. *Plant Physiology* **140**(1):102–114. doi: https://doi.org/10.1104/pp.105.069989.

Kawamura, E. and Wasteneys, G.O. (2008). MOR1, the Arabidopsis thaliana homologue of Xenopus MAP215, promotes rapid growth and shrinkage, and suppresses the pausing of microtubules in vivo. *Journal of Cell Science* **121**(24):4114–4123. doi: https://doi.org/10.1242/jcs.039065.

Kennard, J.L. and Cleary, A.L. (1997). Pre-mitotic nuclear migration in subsidiary mother cells of Tradescantia occurs in G1 of the cell cycle and requires F-actin. *Cell Motility* **36**(1):55–67. doi: https://doi.org/10.1002/(SICI)1097-0169(1997)36:1<55::AID-CM5>3.0.CO;2-G.

Khan, M., Rozhon, W., Bigeard, J., Pflieger, D., Husar, S., Pitzschke, A., … Poppenberger, B. (2013). Brassinosteroid-regulated GSK3/Shaggy-like Kinases Phosphorylate Mitogen-activated Protein (MAP) Kinase Kinases, Which Control Stomata Development in Arabidopsis thaliana. *Journal of Biological Chemistry* **288**(11):7519–7527. doi: https://doi.org/10.1074/jbc.M112.384453.

Kim, T.-W., Michniewicz, M., Bergmann, D.C. and Wang, Z.-Y. (2012). Brassinosteroid regulates stomatal development by GSK3-mediated inhibition of a MAPK pathway. *Nature* **482**(7385):419–422. doi: https://doi.org/10.1038/nature10794.

Kimata, Y., Higaki, T., Kawashima, T., Kurihara, D., Sato, Y., Yamada, T., … Ueda, M. (2016). Cytoskeleton dynamics control the first asymmetric cell division in Arabidopsis zygote. *Proceedings of the National Academy of Sciences* **113**(49):14157–14162. doi: https://doi.org/10.1073/pnas.1613979113.

Kimata, Y., Kato, T., Higaki, T., Kurihara, D., Yamada, T., Segami, S., … Ueda, M. (2019). Polar vacuolar distribution is essential for accurate asymmetric division of *Arabidopsis* zygotes.

Proceedings of the National Academy of Sciences:201814160. doi: https://doi.org/10.1073/pnas.1814160116.

Kirik, A., Ehrhardt, D.W. and Kirik, V. (2012). TONNEAU2/FASS Regulates the Geometry of Microtubule Nucleation and Cortical Array Organization in Interphase Arabidopsis Cells. *The Plant Cell* **24**(3):1158–1170. doi: https://doi.org/10.1105/tpc.111.094367.

Kirik, V., Herrmann, U., Parupalli, C., Sedbrook, J.C., Ehrhardt, D.W. and Hülskamp, M. (2007). CLASP localizes in two discrete patterns on cortical microtubules and is required for cell morphogenesis and cell division in Arabidopsis. *Journal of Cell Science* **120**(24):4416–4425. doi: https://doi.org/10.1242/jcs.024950.

Klepikova, A.V., Kasianov, A.S., Gerasimov, E.S., Logacheva, M.D. and Penin, A.A. (2016). A high resolution map of the Arabidopsis thaliana developmental transcriptome based on RNA-seq profiling. *The Plant Journal* **88**(6):1058–1070. doi: https://doi.org/10.1111/tpj.13312.

Klotz, J. and Nick, P. (2012). A novel actin–microtubule cross-linking kinesin, NtKCH, functions in cell expansion and division. *New Phytologist* **193**(3):576–589. doi: https://doi.org/10.1111/j.1469-8137.2011.03944.x.

Köhler, C., Wolff, P. and Spillane, C. (2012). Epigenetic Mechanisms Underlying Genomic Imprinting in Plants. *Annual Review of Plant Biology* **63**(1):331–352. doi: https://doi.org/10.1146/annurev-arplant-042811-105514.

Kohoutová, L., Kourová, H., Nagy, S.K., Volc, J., Halada, P., Mészáros, T., … Binarová, P. (2015). The Arabidopsis mitogen-activated protein kinase 6 is associated with γ-tubulin on microtubules, phosphorylates EB1c and maintains spindle orientation under nitrosative stress. *New Phytologist* **207**(4):1061–1074. doi: https://doi.org/10.1111/nph.13501.

Komaki, S., Abe, T., Coutuer, S., Inze, D., Russinova, E. and Hashimoto, T. (2010). Nuclear-localized subtype of end-binding 1 protein regulates spindle organization in Arabidopsis. *Journal of Cell Science* **123**(3):451–459. doi: https://doi.org/10.1242/jcs.062703.

Komis, G., Illés, P., Beck, M. and Šamaj, J. (2011). Microtubules and mitogen-activated protein kinase signalling. *Current Opinion in Plant Biology* **14**(6):650–657. doi: https://doi.org/10.1016/j.pbi.2011.07.008.

Komis, G., Luptovčiak, I., Ovečka, M., Samakovli, D., Šamajová, O. and Šamaj, J. (2017). Katanin Effects on Dynamics of Cortical Microtubules and Mitotic Arrays in Arabidopsis thaliana Revealed by Advanced Live-Cell Imaging. *Frontiers in Plant Science* **8**. doi: https://doi.org/10.3389/fpls.2017.00866.

Komis, G., Mistrik, M., Šamajová, O., Doskočilová, A., Ovečka, M., Illés, P., … Šamaj, J. (2014). Dynamics and Organization of Cortical Microtubules as Revealed by Superresolution Structured Illumination Microscopy. *Plant Physiology* **165**(1):129–148. doi: https://doi.org/10.1104/pp.114.238477.

Komis, G., Novák, D., Ovečka, M., Šamajová, O. and Šamaj, J. (2018b). Advances in Imaging Plant Cell Dynamics. *Plant Physiology* **176**(1):80–93. doi: https://doi.org/10.1104/pp.17.00962.

Komis, G., Šamajová, O., Ovečka, M. and Šamaj, J. (2015). Super-resolution Microscopy in Plant Cell Imaging. *Trends in Plant Science* **20**(12):834–843. doi: https://doi.org/10.1016/j.tplants.2015.08.013.

Komis, G., Šamajová, O., Ovečka, M. and Šamaj, J. (2018a). Cell and Developmental Biology of Plant Mitogen-Activated Protein Kinases. *Annual Review of Plant Biology* **69**(1):237–265. doi: https://doi.org/10.1146/annurev-arplant-042817-040314.

Kondo, T., Kajita, R., Miyazaki, A., Hokoyama, M., Nakamura-Miura, T., Mizuno, S., … Sakagami, Y. (2010). Stomatal Density is Controlled by a Mesophyll-Derived Signaling Molecule. *Plant and Cell Physiology* **51**(1):1–8. doi: https://doi.org/10.1093/pcp/pcp180.

Korobchevskaya, K., Lagerholm, B.C., Colin-York, H. and Fritzsche, M. (2017). Exploring the Potential of Airyscan Microscopy for Live Cell Imaging. *Photonics* **4**(3):41. doi: https://doi.org/10.3390/photonics4030041.

Kosetsu, K., Matsunaga, S., Nakagami, H., Colcombet, J., Sasabe, M., Soyano, T., … Machida, Y. (2010). The MAP Kinase MPK4 Is Required for Cytokinesis in Arabidopsis thaliana. *The Plant Cell* **22**(11):3778–3790. doi: https://doi.org/10.1105/tpc.110.077164.

Kosetsu, K., Murata, T., Yamada, M., Nishina, M., Boruc, J., Hasebe, M., … Goshima, G. (2017). Cytoplasmic MTOCs control spindle orientation for asymmetric cell division in plants. *Proceedings of the National Academy of Sciences* **114**(42):E8847–E8854. doi: https://doi.org/10.1073/pnas.1713925114.

Kremer, A., Lippens, S., Bartunkova, S., Asselbergh, B., Blanpain, C., Fendrych, M., … Guérin, C.J. (2015). Developing 3D SEM in a broad biological context. *Journal of Microscopy* **259**(2):80–96. doi: https://doi.org/10.1111/jmi.12211.

Krishna, P. and Gloor, G. (2001). The Hsp90 family of proteins in Arabidopsis thaliana. *Cell Stress & Chaperones* **6**(3):238–246.

Krtková, J., Benáková, M. and Schwarzerová, K. (2016). Multifunctional Microtubule-Associated Proteins in Plants. *Frontiers in Plant Science* **7**. doi: https://doi.org/10.3389/fpls.2016.00474.

Krtková, J., Zimmermann, A., Schwarzerová, K. and Nick, P. (2012). Hsp90 binds microtubules and is involved in the reorganization of the microtubular network in angiosperms. *Journal of Plant Physiology* **169**(14):1329–1339. doi: https://doi.org/10.1016/j.jplph.2012.06.010.

Krupnova, T., Sasabe, M., Ghebreghiorghis, L., Gruber, C.W., Hamada, T., Dehmel, V., … Jürgens, G. (2009). Microtubule-Associated Kinase-like Protein RUNKEL Needed for Cell Plate Expansion in Arabidopsis Cytokinesis. *Current Biology* **19**(6):518–523. doi: https://doi.org/10.1016/j.cub.2009.02.021.

Krupnova, T., Stierhof, Y.-D., Hiller, U., Strompen, G. and Müller, S. (2013). The microtubule-associated kinase-like protein RUNKEL functions in somatic and syncytial cytokinesis. *The Plant Journal* **74**(5):781–791. doi: https://doi.org/10.1111/tpj.12160.

Krysan, P.J., Jester, P.J., Gottwald, J.R. and Sussman, M.R. (2002). An Arabidopsis Mitogen-Activated Protein Kinase Kinase Kinase Gene Family Encodes Essential Positive Regulators of Cytokinesis. *The Plant Cell* **14**(5):1109–1120. doi: https://doi.org/10.1105/tpc.001164.

Lampard, G.R., Lukowitz, W., Ellis, B.E. and Bergmann, D.C. (2009). Novel and Expanded Roles for MAPK Signaling in Arabidopsis Stomatal Cell Fate Revealed by Cell Type–Specific Manipulations. *The Plant Cell* **21**(11):3506–3517. doi: https://doi.org/10.1105/tpc.109.070110.

Lampard, G.R., MacAlister, C.A. and Bergmann, D.C. (2008). Arabidopsis Stomatal Initiation Is Controlled by MAPK-Mediated Regulation of the bHLH SPEECHLESS. *Science* **322**(5904):1113–1116. doi: https://doi.org/10.1126/science.1162263.

Lampard, G.R., Wengier, D.L. and Bergmann, D.C. (2014). Manipulation of Mitogen-Activated Protein Kinase Kinase Signaling in the Arabidopsis Stomatal Lineage Reveals Motifs That Contribute to Protein Localization and Signaling Specificity. *The Plant Cell* **26**(8):3358–3371. doi: https://doi.org/10.1105/tpc.114.127415.

Lau, O.S., Davies, K.A., Chang, J., Adrian, J., Rowe, M.H., Ballenger, C.E. and Bergmann, D.C. (2014). Direct roles of SPEECHLESS in the specification of stomatal self-renewing cells. *Science* **345**(6204):1605–1609. doi: https://doi.org/10.1126/science.1256888.

Le, J., Liu, X.-G., Yang, K.-Z., Chen, X.-L., Zou, J.-J., Wang, H.-Z., … Sack, F. (2014). Auxin transport and activity regulate stomatal patterning and development. *Nature Communications* **5**(1):1–8. doi: https://doi.org/10.1038/ncomms4090.

Ledbetter, M.C. and Porter, K.R. (1963). A 'Microtubule' in Plant Cell Fine Structure. *The Journal of Cell Biology* **19**(1):239–250. doi: https://doi.org/10.1083/jcb.19.1.239.

Lee, L.R. and Bergmann, D.C. (2019). The plant stomatal lineage at a glance. *Journal of Cell Science* **132**(8). doi: https://doi.org/10.1242/jcs.228551.

Lee, Y.-R.J., Giang, H.M. and Liu, B. (2001). A Novel Plant Kinesin-Related Protein Specifically Associates with the Phragmoplast Organelles. *The Plant Cell* **13**(11):2427–2439. doi: https://doi.org/10.1105/tpc.010225.

Lee, Y.-R.J., Li, Y. and Liu, B. (2007). Two Arabidopsis Phragmoplast-Associated Kinesins Play a Critical Role in Cytokinesis during Male Gametogenesis. *The Plant Cell* **19**(8):2595–2605. doi: https://doi.org/10.1105/tpc.107.050716.

Lee, Y.-R.J. and Liu, B. (2013). The rise and fall of the phragmoplast microtubule array. *Current Opinion in Plant Biology* **16**(6):757–763. doi: https://doi.org/10.1016/j.pbi.2013.10.008.

Leene, J.V., Stals, H., Eeckhout, D., Persiau, G., Slijke, E.V.D., Isterdael, G.V., … Jaeger, G.D. (2007). A Tandem Affinity Purification-based Technology Platform to Study the Cell Cycle Interactome in Arabidopsis thaliana. *Molecular & Cellular Proteomics* **6**(7):1226–1238. doi: https://doi.org/10.1074/mcp.M700078-MCP200.

Letourneux, C., Rocher, G. and Porteu, F. (2006). B56-containing PP2A dephosphorylate ERK and their activity is controlled by the early gene IEX-1 and ERK. *The EMBO Journal* **25**(4):727–738. doi: https://doi.org/10.1038/sj.emboj.7600980.

Li, H., Cai, Z., Wang, X., Li, M., Cui, Y., Cui, N., … Gou, X. (2019). SERK Receptor-like Kinases Control Division Patterns of Vascular Precursors and Ground Tissue Stem Cells during Embryo Development in Arabidopsis. *Molecular Plant* **12**(7):984–1002. doi: https://doi.org/10.1016/j.molp.2019.04.011.

Li, Hui, Ding, Y., Shi, Y., Zhang, X., Zhang, S., Gong, Z. and Yang, S. (2017b). MPK3- and MPK6-Mediated ICE1 Phosphorylation Negatively Regulates ICE1 Stability and Freezing Tolerance in Arabidopsis. *Developmental Cell* **43**(5):630–642. doi: https://doi.org/10.1016/j.devcel.2017.09.025.

Li, Haoge, Sun, B., Sasabe, M., Deng, X., Machida, Y., Lin, H., … Liu, B. (2017a). Arabidopsis MAP65-4 plays a role in phragmoplast microtubule organization and marks the cortical cell division site. *New Phytologist* **215**(1):187–201. doi: https://doi.org/10.1111/nph.14532.

Li, J., Soroka, J. and Buchner, J. (2012). The Hsp90 chaperone machinery: Conformational dynamics and regulation by co-chaperones. *Biochimica et Biophysica Acta (BBA) - Molecular Cell Research* **1823**(3):624–635. doi: https://doi.org/10.1016/j.bbamcr.2011.09.003.

Li, W., Xie, L., Chen, Z., Zhu, Y., Sun, Y., Miao, Y., … Han, X. (2010b). Cantharidin, a potent and selective PP2A inhibitor, induces an oxidative stress-independent growth inhibition of pancreatic cancer cells through G2/M cell-cycle arrest and apoptosis. *Cancer Science* **101**(5):1226–1233. doi: https://doi.org/10.1111/j.1349-7006.2010.01523.x.

Li, Y., Shen, Y., Cai, C., Zhong, C., Zhu, L., Yuan, M. and Ren, H. (2010a). The Type II Arabidopsis Formin14 Interacts with Microtubules and Microfilaments to Regulate Cell Division. *The Plant Cell* **22**(8):2710–2726. doi: https://doi.org/10.1105/tpc.110.075507.

Li, Y.M. and Casida, J.E. (1992). Cantharidin-binding protein: identification as protein phosphatase 2A. *Proceedings of the National Academy of Sciences* **89**(24):11867–11870. doi: https://doi.org/10.1073/pnas.89.24.11867.

Li, Y.-M., Mackintosh, C. and Casida, J.E. (1993). Protein phosphatase 2A and its [3H]cantharidin/[3H]endothall thioanhydride binding site: Inhibitor specificity of cantharidin and ATP analogues. *Biochemical Pharmacology* **46**(8):1435–1443. doi: https://doi.org/10.1016/0006-2952(93)90109-A.

Lin, D., Cao, L., Zhou, Z., Zhu, L., Ehrhardt, D., Yang, Z. and Fu, Y. (2013). Rho GTPase Signaling Activates Microtubule Severing to Promote Microtubule Ordering in Arabidopsis. *Current Biology* **23**(4):290–297. doi: https://doi.org/10.1016/j.cub.2013.01.022.

Lipka, E., Gadeyne, A., Stöckle, D., Zimmermann, S., Jaeger, G.D., Ehrhardt, D.W., … Müller, S. (2014). The Phragmoplast-Orienting Kinesin-12 Class Proteins Translate the Positional Information of the Preprophase Band to Establish the Cortical Division Zone in Arabidopsis thaliana. *The Plant Cell* **26**(6):2617–2632. doi: https://doi.org/10.1105/tpc.114.124933.

Lipka, E., Herrmann, A. and Mueller, S. (2015). Mechanisms of plant cell division: Mechanisms of plant cell division. *Wiley Interdisciplinary Reviews: Developmental Biology* **4**(4):391–405. doi: https://doi.org/10.1002/wdev.186.

Liu, B., Cyr, R.J. and Palevitz, B.A. (1996). A kinesin-like protein, KatAp, in the cells of Arabidopsis and other plants. *The Plant Cell* **8**(1):119–132. doi: https://doi.org/10.1105/tpc.8.1.119.

Liu, J., Han, L., Li, B., Yang, J., Huen, M.S.Y., Pan, X., … Cheung, A.L.M. (2014). F-Box Only Protein 31 (FBXO31) Negatively Regulates p38 Mitogen-activated Protein Kinase (MAPK) Signaling by Mediating Lysine 48-linked Ubiquitination and Degradation of Mitogen-activated Protein Kinase Kinase 6 (MKK6). *Journal of Biological Chemistry* **289**(31):21508–21518. doi: https://doi.org/10.1074/jbc.M114.560342.

Liu, Y. and Zhang, S. (2004). Phosphorylation of 1-Aminocyclopropane-1-Carboxylic Acid Synthase by MPK6, a Stress-Responsive Mitogen-Activated Protein Kinase, Induces Ethylene Biosynthesis in Arabidopsis. *The Plant Cell* **16**(12):3386–3399. doi: https://doi.org/10.1105/tpc.104.026609.

López-Bucio, José, Dubrovsky, J., Raya Gonzalez, J., Ugartechea-Chirino, Y., López-Bucio, Jesús, De Luna-Valdez, L., … Guevara-Garcia, A. (2013). Arabidopsis thaliana mitogen-activated protein kinase 6 is involved in seed formation and modulation of primary and lateral root development. *Journal of experimental botany* **65**. doi: https://doi.org/10.1093/jxb/ert368.

Luca, G.M.R.D., Breedijk, R.M.P., Brandt, R.A.J., Zeelenberg, C.H.C., de Jong, B.E., Timmermans, W., … Manders, E.M.M. (2013). Re-scan confocal microscopy: scanning twice for better resolution. *Biomedical Optics Express* **4**(11):2644–2656. doi: https://doi.org/10.1364/BOE.4.002644.

Lucas, J.R., Courtney, S., Hassfurder, M., Dhingra, S., Bryant, A. and Shaw, S.L. (2011). Microtubule-Associated Proteins MAP65-1 and MAP65-2 Positively Regulate Axial Cell Growth in Etiolated Arabidopsis Hypocotyls. *The Plant Cell* **23**(5):1889–1903. doi: https://doi.org/10.1105/tpc.111.084970.

Lucas, J.R. and Sack, F.D. (2012). Polar development of preprophase bands and cell plates in the Arabidopsis leaf epidermis. *The Plant Journal* **69**(3):501–509. doi: https://doi.org/10.1111/j.1365-313X.2011.04809.x.

Lucas, J.R. and Shaw, S.L. (2012). MAP65-1 and MAP65-2 promote cell proliferation and axial growth in Arabidopsis roots. *The Plant Journal* **71**(3):454–463. doi: https://doi.org/10.1111/j.1365-313X.2012.05002.x.

Lukowitz, W., Roeder, A., Parmenter, D. and Somerville, C. (2004). A MAPKK Kinase Gene Regulates Extra-Embryonic Cell Fate in Arabidopsis. *Cell* **116**(1):109–119. doi: https://doi.org/10.1016/S0092-8674(03)01067-5.

Luo, Y., Qin, G., Zhang, J., Liang, Y., Song, Y., Zhao, M., … Qu, L.-J. (2011). d-myo-Inositol-3-Phosphate Affects Phosphatidylinositol-Mediated Endomembrane Function in Arabidopsis and Is Essential for Auxin-Regulated Embryogenesis. *The Plant Cell* **23**(4):1352–1372. doi: https://doi.org/10.1105/tpc.111.083337.

MacAlister, C.A., Ohashi-Ito, K. and Bergmann, D.C. (2007). Transcription factor control of asymmetric cell divisions that establish the stomatal lineage. *Nature* **445**(7127):537–540. doi: https://doi.org/10.1038/nature05491.

Madeira, F., Park, Y.M., Lee, J., Buso, N., Gur, T., Madhusoodanan, N., … Lopez, R. (2019). The EMBL-EBI search and sequence analysis tools APIs in 2019. *Nucleic Acids Research* **47**(W1):W636–W641. doi: https://doi.org/10.1093/nar/gkz268.

Malcos, J.L. and Cyr, R.J. (2011). An ungrouped plant kinesin accumulates at the preprophase band in a cell cycle-dependent manner. *Cytoskeleton* **68**(4):247–258. doi: https://doi.org/10.1002/cm.20508.

Mansfield, S.G., Briarty, L.G. and Erni, S. (1991). Early embryogenesis in Arabidopsis thaliana. I. The mature embryo sac. *Canadian Journal of Botany* **69**(3):447–460. doi: https://doi.org/10.1139/b91-062.

Mao, G., Chan, J., Calder, G., Doonan, J.H. and Lloyd, C.W. (2005). Modulated targeting of GFP-AtMAP65-1 to central spindle microtubules during division. *The Plant Journal* **43**(4):469–478. doi: https://doi.org/10.1111/j.1365-313X.2005.02464.x.

MAPK Group (2002). Mitogen-activated protein kinase cascades in plants: a new nomenclature. *Trends in Plant Science* **7**(7):301–308. doi: https://doi.org/10.1016/s1360-1385(02)02302-6.

Marcus, A.I., Dixit, R. and Cyr, R.J. (2005). Narrowing of the preprophase microtubule band is not required for cell division plane determination in cultured plant cells. *Protoplasma* **226**(3–4):169–174. doi: https://doi.org/10.1007/s00709-005-0119-1.

Marcus, A.I., Li, W., Ma, H. and Cyr, R.J. (2003). A Kinesin Mutant with an Atypical Bipolar Spindle Undergoes Normal Mitosis. *Molecular Biology of the Cell* **14**(4):1717–1726. doi: https://doi.org/10.1091/mbc.e02-09-0586.

Margaritopoulou, T., Kryovrysanaki, N., Megkoula, P., Prassinos, C., Samakovli, D., Milioni, D. and Hatzopoulos, P. (2016). HSP90 canonical content organizes a molecular scaffold mechanism to progress flowering. *The Plant Journal* **87**(2):174–187. doi: https://doi.org/10.1111/tpj.13191.

Mayer-Jaekel, R.E. and Hemmings, B.A. (1994). Protein phosphatase 2A — a 'ménage à trois'. *Trends in Cell Biology* **4**(8):287–291. doi: https://doi.org/10.1016/0962-8924(94)90219-4.

McClinton, R.S. and Sung, Z.R. (1997). Organization of cortical microtubules at the plasma membrane in Arabidopsis. *Planta* **201**(3):252–260. doi: https://doi.org/10.1007/s004250050064.

Meng, X., Chen, X., Mang, H., Liu, C., Yu, X., Gao, X., … Shan, L. (2015). Differential Function of Arabidopsis SERK Family Receptor-like Kinases in Stomatal Patterning. *Current Biology* **25**(18):2361–2372. doi: https://doi.org/10.1016/j.cub.2015.07.068.

Meng, X., Wang, H., He, Y., Liu, Y., Walker, J.C., Torii, K.U. and Zhang, S. (2012). A MAPK Cascade Downstream of ERECTA Receptor-Like Protein Kinase Regulates Arabidopsis Inflorescence Architecture by Promoting Localized Cell Proliferation. *The Plant Cell* **24**(12):4948–4960. doi: https://doi.org/10.1105/tpc.112.104695.

Michniewicz, M., Zago, M.K., Abas, L., Weijers, D., Schweighofer, A., Meskiene, I., … Friml, J. (2007). Antagonistic Regulation of PIN Phosphorylation by PP2A and PINOID Directs Auxin Flux. *Cell* **130**(6):1044–1056. doi: https://doi.org/10.1016/j.cell.2007.07.033.

Miki, H., Okada, Y. and Hirokawa, N. (2005). Analysis of the kinesin superfamily: insights into structure and function. *Trends in Cell Biology* **15**(9):467–476. doi: https://doi.org/10.1016/j.tcb.2005.07.006.

Mineyuki, Y. (1999). The Preprophase Band of Microtubules: Its Function as a Cytokinetic Apparatus in Higher Plants. In: Jeon, K. W. (ed.). *International Review of Cytology*. Academic Press, pp. 1–49.

Mineyuki, Y. and Furuya, M. (1986). Involvement of colchicine-sensitive cytoplasmic element in premitotic nuclear positioning of Adiantum protonemata. *Protoplasma* **130**(2):83–90. doi: https://doi.org/10.1007/BF01276589.

Mineyuki, Y. and Palevitz, B.A. (1990). Relationship between preprophase band organization, F-actin and the division site in Allium: Fluorescence and morphometric studies on cytochalasin-treated cells. *Journal of Cell Science* **97**(2):283–295.

Mohanta, T.K., Mohanta, N., Parida, P., Panda, S.K., Ponpandian, L.N. and Bae, H. (2016). Genome-Wide Identification of Mitogen-Activated Protein Kinase Gene Family across Fungal Lineage Shows Presence of Novel and Diverse Activation Loop Motifs. *PLoS ONE* **11**(2). doi: https://doi.org/10.1371/journal.pone.0149861.

Motose, H., Hamada, T., Yoshimoto, K., Murata, T., Hasebe, M., Watanabe, Y., … Takahashi, T. (2011). NIMA-related kinases 6, 4, and 5 interact with each other to regulate microtubule organization during epidermal cell expansion in Arabidopsis thaliana. *The Plant Journal* **67**(6):993–1005. doi: https://doi.org/10.1111/j.1365-313X.2011.04652.x.

Motose, H., Tominaga, R., Wada, T., Sugiyama, M. and Watanabe, Y. (2008). A NIMA-related protein kinase suppresses ectopic outgrowth of epidermal cells through its kinase activity and the association with microtubules. *The Plant Journal* **54**(5):829–844. doi: https://doi.org/10.1111/j.1365-313X.2008.03445.x.

Mozgova, I., Köhler, C. and Hennig, L. (2015). Keeping the gate closed: functions of the polycomb repressive complex PRC2 in development. *The Plant Journal* **83**(1):121–132. doi: https://doi.org/10.1111/tpj.12828.

Mravec, J., Kubeš, M., Bielach, A., Gaykova, V., Petrášek, J., Skůpa, P., … Friml, J. (2008). Interaction of PIN and PGP transport mechanisms in auxin distribution-dependent development. *Development* **135**(20):3345–3354. doi: https://doi.org/10.1242/dev.021071.

Müller, C.B. and Enderlein, J. (2010). Image Scanning Microscopy. *Physical Review Letters* **104**(19):198101. doi: https://doi.org/10.1103/PhysRevLett.104.198101.

Müller, J., Beck, M., Mettbach, U., Komis, G., Hause, G., Menzel, D. and Šamaj, J. (2010). Arabidopsis MPK6 is involved in cell division plane control during early root development, and localizes to the pre-prophase band, phragmoplast, trans-Golgi network and plasma membrane. *The Plant Journal* **61**(2):234–248. doi: https://doi.org/10.1111/j.1365-313X.2009.04046.x.

Müller, J., Ory, S., Copeland, T., Piwnica-Worms, H. and Morrison, D.K. (2001). C-TAK1 Regulates Ras Signaling by Phosphorylating the MAPK Scaffold, KSR1. *Molecular Cell* **8**(5):983–993. doi: https://doi.org/10.1016/S1097-2765(01)00383-5.

Müller, S., Han, S. and Smith, L.G. (2006). Two Kinesins Are Involved in the Spatial Control of Cytokinesis in Arabidopsis thaliana. *Current Biology* **16**(9):888–894. doi: https://doi.org/10.1016/j.cub.2006.03.034.

Müller, S., Smertenko, A., Wagner, V., Heinrich, M., Hussey, P.J. and Hauser, M.-T. (2004). The Plant Microtubule-Associated Protein AtMAP65-3/PLE Is Essential for Cytokinetic Phragmoplast Function. *Current Biology* **14**(5):412–417. doi: https://doi.org/10.1016/j.cub.2004.02.032.

Mumby, M.C. and Walter, G. (1993). Protein serine/threonine phosphatases: structure, regulation, and functions in cell growth. *Physiological Reviews* **73**(4):673–699. doi: https://doi.org/10.1152/physrev.1993.73.4.673.

Murata, T. and Wada, M. (1991). Effects of centrifugation on preprophase-band formation in Adiantum protonemata. *Planta* **183**(3):391–398. doi: https://doi.org/10.1007/BF00197738.

Nakajima, K., Sena, G., Nawy, T. and Benfey, P.N. (2001). Intercellular movement of the putative transcription factor SHR in root patterning. *Nature* **413**(6853):307–311. doi: https://doi.org/10.1038/35095061.

Nishihama, R., Ishikawa, M., Araki, S., Soyano, T., Asada, T. and Machida, Y. (2001). The NPK1 mitogen-activated protein kinase kinase kinase is a regulator of cell-plate formation in plant cytokinesis. *Genes & Development* **15**(3):352–363. doi: https://doi.org/10.1101/gad.863701.

Nishihama, R., Soyano, T., Ishikawa, M., Araki, S., Tanaka, H., Asada, T., … Machida, Y. (2002). Expansion of the Cell Plate in Plant Cytokinesis Requires a Kinesin-like Protein/MAPKKK Complex. *Cell* **109**(1):87–99. doi: https://doi.org/10.1016/S0092-8674(02)00691-8.

Nishimura, A., Yamamoto, K., Oyama, M., Kozuka-Hata, H., Saito, H. and Tatebayashi, K. (2016). Scaffold Protein Ahk1, Which Associates with Hkr1, Sho1, Ste11, and Pbs2, Inhibits Cross Talk Signaling from the Hkr1 Osmosensor to the Kss1 Mitogen-Activated Protein Kinase. *Molecular and Cellular Biology* **36**(7):1109–1123. doi: https://doi.org/10.1128/MCB.01017-15.

Nodine, M.D., Yadegari, R. and Tax, F.E. (2007). RPK1 and TOAD2 Are Two Receptor-like Kinases Redundantly Required for Arabidopsis Embryonic Pattern Formation. *Developmental Cell* **12**(6):943–956. doi: https://doi.org/10.1016/j.devcel.2007.04.003.

O'Connell, M.J., Krien, M.J.E. and Hunter, T. (2003). Never say never. The NIMA-related protein kinases in mitotic control. *Trends in Cell Biology* **13**(5):221–228. doi: https://doi.org/10.1016/S0962-8924(03)00056-4.

Oh, S.A., Allen, T., Kim, G.J., Sidorova, A., Borg, M., Park, S.K. and Twell, D. (2012). Arabidopsis Fused kinase and the Kinesin-12 subfamily constitute a signalling module required for phragmoplast expansion. *The Plant Journal* **72**(2):308–319. doi: https://doi.org/10.1111/j.1365-313X.2012.05077.x.

Oh, S.A., Bourdon, V., Dickinson, H.G., Twell, D. and Park, S.K. (2014). Arabidopsis Fused kinase TWO-IN-ONE dominantly inhibits male meiotic cytokinesis. *Plant Reproduction* **27**(1):7–17. doi: https://doi.org/10.1007/s00497-013-0235-6.

Oh, S.A., Johnson, A., Smertenko, A., Rahman, D., Park, S.K., Hussey, P.J. and Twell, D. (2005). A divergent cellular role for the FUSED kinase family in the plant-specific cytokinetic phragmoplast. *Current Biology* **15**(23):2107–2111. doi: https://doi.org/10.1016/j.cub.2005.10.044.

Oh, S.A., Pal, M.D., Park, S.K., Johnson, J.A. and Twell, D. (2010a). The tobacco MAP215/Dis1-family protein TMBP200 is required for the functional organization of microtubule arrays during male germline establishment. *Journal of Experimental Botany* **61**(4):969–981. doi: https://doi.org/10.1093/jxb/erp367.

Oh, S.A., Park, K.S., Twell, D. and Park, S.K. (2010b). The SIDECAR POLLEN gene encodes a microspore-specific LOB/AS2 domain protein required for the correct timing and orientation of asymmetric cell division. *The Plant Journal* **64**(5):839–850. doi: https://doi.org/10.1111/j.1365-313X.2010.04374.x.

Ohashi-Ito, K. and Bergmann, D.C. (2006). Arabidopsis FAMA Controls the Final Proliferation/Differentiation Switch during Stomatal Development. *The Plant Cell* **18**(10):2493–2505. doi: https://doi.org/10.1105/tpc.106.046136.

Olsen, O.-A., Brown, R.C. and Lemmon, B.E. (1995). Pattern and process of wall formation in developing endosperm. *BioEssays* **17**(9):803–812. doi: https://doi.org/10.1002/bies.950170910.

Ookata, K., Hisanaga, S., Sugita, M., Okuyama, A., Murofushi, H., Kitazawa, H., … Kishimoto, T. (1997). MAP4 Is the in Vivo Substrate for CDC2 Kinase in HeLa Cells: Identification of an M-Phase Specific and a Cell Cycle-Independent Phosphorylation Site in MAP4. *Biochemistry* **36**(50):15873–15883. doi: https://doi.org/10.1021/bi971251w.

Oppenheimer, D.G., Pollock, M.A., Vacik, J., Szymanski, D.B., Ericson, B., Feldmann, K. and Marks, M.D. (1997). Essential role of a kinesin-like protein in Arabidopsis trichome morphogenesis. *Proceedings of the National Academy of Sciences* **94**(12):6261–6266. doi: https://doi.org/10.1073/pnas.94.12.6261.

O'Regan, L., Blot, J. and Fry, A.M. (2007). Mitotic regulation by NIMA-related kinases. *Cell Division* **2**(1):25. doi: https://doi.org/10.1186/1747-1028-2-25.

Otegui, M. and Staehelin, L.A. (2000). Syncytial-Type Cell Plates: A Novel Kind of Cell Plate Involved in Endosperm Cellularization of Arabidopsis. *The Plant Cell* **12**(6):933–947. doi: https://doi.org/10.1105/tpc.12.6.933.

Otegui, M.S. and Staehelin, L.A. (2004). Electron tomographic analysis of post-meiotic cytokinesis during pollen development in Arabidopsis thaliana. *Planta* **218**(4):501–515. doi: https://doi.org/10.1007/s00425-003-1125-1.

Oughtred, R., Stark, C., Breitkreutz, B.-J., Rust, J., Boucher, L., Chang, C., … Tyers, M. (2019). The BioGRID interaction database: 2019 update. *Nucleic Acids Research* **47**(D1):D529–D541. doi: https://doi.org/10.1093/nar/gky1079.

Ovečka, M., Vaškebová, L., Komis, G., Luptovčiak, I., Smertenko, A. and Šamaj, J. (2015). Preparation of plants for developmental and cellular imaging by light-sheet microscopy. *Nature Protocols* **10**(8):1234–1247. doi: https://doi.org/10.1038/nprot.2015.081.

Pan, R., Lee, Y.-R.J. and Liu, B. (2004). Localization of two homologous Arabidopsis kinesin-related proteins in the phragmoplast. *Planta* **220**(1):156–164. doi: https://doi.org/10.1007/s00425-004-1324-4.

Papadopoulos, J.S. and Agarwala, R. (2007). COBALT: constraint-based alignment tool for multiple protein sequences. *Bioinformatics* **23**(9):1073–1079. doi: https://doi.org/10.1093/bioinformatics/btm076.

Park, S.K., Howden, R. and Twell, D. (1998). The Arabidopsis thaliana gametophytic mutation gemini pollen1 disrupts microspore polarity, division asymmetry and pollen cell fate. *Development* **125**(19):3789–3799.

Pastuglia, M., Azimzadeh, J., Goussot, M., Camilleri, C., Belcram, K., Evrard, J.-L., … Bouchez, D. (2006). γ-Tubulin Is Essential for Microtubule Organization and Development in Arabidopsis. *The Plant Cell* **18**(6):1412–1425. doi: https://doi.org/10.1105/tpc.105.039644.

Pietra, S., Gustavsson, A., Kiefer, C., Kalmbach, L., Hörstedt, P., Ikeda, Y., … Grebe, M. (2013). Arabidopsis SABRE and CLASP interact to stabilize cell division plane orientation and planar polarity. *Nature Communications* **4**(1):1–15. doi: https://doi.org/10.1038/ncomms3779.

Pillitteri, L.J., Guo, X. and Dong, J. (2016). Asymmetric cell division in plants: mechanisms of symmetry breaking and cell fate determination. *Cellular and Molecular Life Sciences* **73**(22):4213–4229. doi: https://doi.org/10.1007/s00018-016-2290-2.

Pillitteri, L.J., Peterson, K.M., Horst, R.J. and Torii, K.U. (2011). Molecular Profiling of Stomatal Meristemoids Reveals New Component of Asymmetric Cell Division and Commonalities among Stem Cell Populations in Arabidopsis. *The Plant Cell* **23**(9):3260–3275. doi: https://doi.org/10.1105/tpc.111.088583.

Pillitteri, L.J., Sloan, D.B., Bogenschutz, N.L. and Torii, K.U. (2007). Termination of asymmetric cell division and differentiation of stomata. *Nature* **445**(7127):501–505. doi: https://doi.org/10.1038/nature05467.

Pollard, T.D. (2007). Regulation of Actin Filament Assembly by Arp2/3 Complex and Formins. *Annual Review of Biophysics and Biomolecular Structure* **36**(1):451–477. doi: https://doi.org/10.1146/annurev.biophys.35.040405.101936.

Popescu, S.C., Popescu, G.V., Bachan, S., Zhang, Z., Gerstein, M., Snyder, M. and Dinesh-Kumar, S.P. (2009). MAPK target networks in Arabidopsis thaliana revealed using functional protein microarrays. *Genes & Development* **23**(1):80–92. doi: https://doi.org/10.1101/gad.1740009.

Portran, D., Zoccoler, M., Gaillard, J., Stoppin-Mellet, V., Neumann, E., Arnal, I., … Vantard, M. (2013). MAP65/Ase1 promote microtubule flexibility. *Molecular Biology of the Cell* **24**(12):1964–1973. doi: https://doi.org/10.1091/mbc.e13-03-0141.

Poulios, S. and Vlachonasios, K. (2018). Synergistic action of GCN5 and CLAVATA1 in the regulation of gynoecium development in Arabidopsis thaliana. *New Phytologist* **220**. doi: https://doi.org/10.1111/nph.15303.

Prasinos, C., Krampis, K., Samakovli, D. and Hatzopoulos, P. (2005). Tight regulation of expression of two Arabidopsis cytosolic Hsp90 genes during embryo development. *Journal of Experimental Botany* **56**(412):633–644. doi: https://doi.org/10.1093/jxb/eri035.

Qu, Y., Song, P., Hu, Y., Jin, X., Jia, Q., Zhang, X., … Zhang, Q. (2018). Regulation of stomatal movement by cortical microtubule organization in response to darkness and ABA signaling in Arabidopsis. *Plant Growth Regulation* **84**(3):467–479. doi: https://doi.org/10.1007/s10725-017-0353-5.

Queitsch, C., Sangster, T.A. and Lindquist, S. (2002). Hsp90 as a capacitor of phenotypic variation. *Nature* **417**(6889):618–624. doi: https://doi.org/10.1038/nature749.

Rashotte, A.M., DeLong, A. and Muday, G.K. (2001). Genetic and Chemical Reductions in Protein Phosphatase Activity Alter Auxin Transport, Gravity Response, and Lateral Root Growth. *The Plant Cell* **13**:1683–1697.

Rasmussen, C.G., Sun, B. and Smith, L.G. (2011). Tangled localization at the cortical division site of plant cells occurs by several mechanisms. *Journal of Cell Science* **124**(2):270–279. doi: https://doi.org/10.1242/jcs.073676.

Rasmussen, C.G., Wright, A.J. and Müller, S. (2013). The role of the cytoskeleton and associated proteins in determination of the plant cell division plane. *The Plant Journal* **75**(2):258–269. doi: https://doi.org/10.1111/tpj.12177.

Reddy, A.S. and Day, I.S. (2001). Kinesins in the Arabidopsis genome: A comparative analysis among eukaryotes. *BMC Genomics* **2**(1):2. doi: https://doi.org/10.1186/1471-2164-2-2.

Repetto, M.V., Winters, M.J., Bush, A., Reiter, W., Hollenstein, D.M., Ammerer, G., … Colman-Lerner, A. (2018). CDK and MAPK Synergistically Regulate Signaling Dynamics via a Shared Multi-site Phosphorylation Region on the Scaffold Protein Ste5. *Molecular Cell* **69**(6):938-952.e6. doi: https://doi.org/10.1016/j.molcel.2018.02.018.

Richardson, D.N., Simmons, M.P. and Reddy, A.S. (2006). Comprehensive comparative analysis of kinesins in photosynthetic eukaryotes. *BMC Genomics* **7**(1):18. doi: https://doi.org/10.1186/1471-2164-7-18.

Richter, S., Anders, N., Wolters, H., Beckmann, H., Thomann, A., Heinrich, R., … Jürgens, G. (2010). Role of the GNOM gene in Arabidopsis apical-basal patterning – From mutant phenotype to cellular mechanism of protein action. *European Journal of Cell Biology* **89**(2):138–144. doi: https://doi.org/10.1016/j.ejcb.2009.11.020.

Robert, H.S., Grones, P., Stepanova, A.N., Robles, L.M., Lokerse, A.S., Alonso, J.M., … Friml, J. (2013). Local Auxin Sources Orient the Apical-Basal Axis in Arabidopsis Embryos. *Current Biology* **23**(24):2506–2512. doi: https://doi.org/10.1016/j.cub.2013.09.039.

Roodbarkelari, F., Du, F., Truernit, E. and Laux, T. (2015). ZLL/AGO10 maintains shoot meristem stem cells during Arabidopsis embryogenesis by down-regulating ARF2-mediated auxin response. *BMC Biology* **13**(1):74. doi: https://doi.org/10.1186/s12915-015-0180-y.

Rosero, A., Žárský, V. and Cvrčková, F. (2013). AtFH1 formin mutation affects actin filament and microtubule dynamics in Arabidopsis thaliana. *Journal of Experimental Botany* **64**(2):585–597. doi: https://doi.org/10.1093/jxb/ers351.

Ruel, L., Gallet, A., Raisin, S., Truchi, A., Staccini-Lavenant, L., Cervantes, A. and Thérond, P.P. (2007). Phosphorylation of the atypical kinesin Costal2 by the kinase Fused induces the partial disassembly of the Smoothened-Fused-Costal2-Cubitus interruptus complex in Hedgehog signalling. *Development* **134**(20):3677–3689. doi: https://doi.org/10.1242/dev.011577.

Sabatini, S., Beis, D., Wolkenfelt, H., Murfett, J., Guilfoyle, T., Malamy, J., … Scheres, B. (1999). An Auxin-Dependent Distal Organizer of Pattern and Polarity in the Arabidopsis Root. *Cell* **99**(5):463–472. doi: https://doi.org/10.1016/S0092-8674(00)81535-4.

Sakai, T., van der Honing, H., Nishioka, M., Uehara, Y., Takahashi, M., Fujisawa, N., … Wasteneys, G.O. (2008). Armadillo repeat-containing kinesins and a NIMA-related kinase are required for epidermal-cell morphogenesis in Arabidopsis. *The Plant Journal* **53**(1):157–171. doi: https://doi.org/10.1111/j.1365-313X.2007.03327.x.

Šamajová, O., Komis, G. and Šamaj, J. (2014). Immunofluorescent Localization of MAPKs and Colocalization with Microtubules in Arabidopsis Seedling Whole-Mount Probes. In: Komis, G. and Šamaj, J. (eds.). *Plant MAP Kinases: Methods and Protocols*. New York, NY: Springer, pp. 107–115.

Samakovli, D., Margaritopoulou, T., Prassinos, C., Milioni, D. and Hatzopoulos, P. (2014). Brassinosteroid nuclear signaling recruits HSP90 activity. *New Phytologist* **203**(3):743–757. doi: https://doi.org/10.1111/nph.12843.

Samakovli, D., Thanou, A., Valmas, C. and Hatzopoulos, P. (2007). Hsp90 canalizes developmental perturbation. *Journal of Experimental Botany* **58**(13):3513–3524. doi: https://doi.org/10.1093/jxb/erm191.

Samakovli, D., Tichá, T., Vavrdová, T., Ovečka, M., Luptovčiak, I., Zapletalová, V., … Šamaj, J. (2020). YODA-HSP90 Module Regulates Phosphorylation-Dependent Inactivation of SPEECHLESS to Control Stomatal Development under Acute Heat Stress in Arabidopsis. *Molecular Plant* **13**(4):612–633. doi: https://doi.org/10.1016/j.molp.2020.01.001.

Samofalova, D.O., Karpov, P.A., Raevsky, A.V. and Blume, Y.B. (2019). Protein phosphatases potentially associated with regulation of microtubules, their spatial structure reconstruction and analysis. *Cell Biology International* **43**(9):1081–1090. doi: https://doi.org/10.1002/cbin.10810.

Sampathkumar, A., Lindeboom, J.J., Debolt, S., Gutierrez, R., Ehrhardt, D.W., Ketelaar, T. and Persson, S. (2011). Live Cell Imaging Reveals Structural Associations between the Actin and Microtubule Cytoskeleton in Arabidopsis. *The Plant Cell* **23**(6):2302–2313. doi: https://doi.org/10.1105/tpc.111.087940.

Sangster, T.A., Bahrami, A., Wilczek, A., Watanabe, E., Schellenberg, K., McLellan, C., … Lindquist, S. (2007). Phenotypic Diversity and Altered Environmental Plasticity in Arabidopsis thaliana with Reduced Hsp90 Levels Borevitz, J. (ed.). *PLoS ONE* **2**(7):e648. doi: https://doi.org/10.1371/journal.pone.0000648.

Sasabe, M., Boudolf, V., Veylder, L.D., Inzé, D., Genschik, P. and Machida, Y. (2011a). Phosphorylation of a mitotic kinesin-like protein and a MAPKKK by cyclin-dependent kinases (CDKs) is involved in the transition to cytokinesis in plants. *Proceedings of the National Academy of Sciences* **108**(43):17844–17849. doi: https://doi.org/10.1073/pnas.1110174108.

Sasabe, M., Kosetsu, K., Hidaka, M., Murase, A. and Machida, Y. (2011b). Arabidopsis thaliana MAP65-1 and MAP65-2 function redundantly with MAP65-3/PLEIADE in cytokinesis downstream of MPK4. *Plant Signaling & Behavior* **6**(5):743–747. doi: https://doi.org/10.4161/psb.6.5.15146.

Sasabe, M. and Machida, Y. (2006). MAP65: a bridge linking a MAP kinase to microtubule turnover. *Current Opinion in Plant Biology* **9**(6):563–570. doi: https://doi.org/10.1016/j.pbi.2006.09.010.

Sasabe, M. and Machida, Y. (2012). Regulation of organization and function of microtubules by the mitogen-activated protein kinase cascade during plant cytokinesis. *Cytoskeleton* **69**(11):913–918. doi: https://doi.org/10.1002/cm.21072.

Sauer, M. and Heilemann, M. (2017). Single-Molecule Localization Microscopy in Eukaryotes. *Chemical Reviews* **117**(11):7478–7509. doi: https://doi.org/10.1021/acs.chemrev.6b00667.

Sauer, M., Paciorek, T., Benková, E. and Friml, J. (2006). Immunocytochemical techniques for whole-mount in situ protein localization in plants. *Nature Protocols* **1**(1):98–103. doi: https://doi.org/10.1038/nprot.2006.15.

Schaefer, E., Belcram, K., Uyttewaal, M., Duroc, Y., Goussot, M., Legland, D., … Bouchez, D. (2017). The preprophase band of microtubules controls the robustness of division orientation in plants. *Science* **356**(6334):186–189. doi: https://doi.org/10.1126/science.aal3016.

Schecher, S., Walter, B., Falkenstein, M., Macher-Goeppinger, S., Stenzel, P., Krümpelmann, K., … Tagscherer, K.E. (2017). Cyclin K dependent regulation of Aurora B affects apoptosis and proliferation by induction of mitotic catastrophe in prostate cancer: Cyclin K in prostate cancer. *International Journal of Cancer* **141**(8):1643–1653. doi: https://doi.org/10.1002/ijc.30864.

Scheres, B., Laurenzio, L.D., Willemsen, V., Hauser, M.T., Janmaat, K., Weisbeek, P. and Benfey, P.N. (1995). Mutations affecting the radial organisation of the Arabidopsis root display specific defects throughout the embryonic axis. *Development* **121**(1):53–62.

Schermelleh, L., Ferrand, A., Huser, T., Eggeling, C., Sauer, M., Biehlmaier, O. and Drummen, G.P.C. (2019). Super-resolution microscopy demystified. *Nature Cell Biology* **21**(1):72–84. doi: https://doi.org/10.1038/s41556-018-0251-8.

Schlereth, A., Möller, B., Liu, W., Kientz, M., Flipse, J., Rademacher, E.H., … Weijers, D. (2010). MONOPTEROS controls embryonic root initiation by regulating a mobile transcription factor. *Nature* **464**(7290):913–916. doi: https://doi.org/10.1038/nature08836.

Schneider, C.A., Rasband, W.S. and Eliceiri, K.W. (2012). NIH Image to ImageJ: 25 years of image analysis. *Nature Methods* **9**(7):671–675. doi: https://doi.org/10.1038/nmeth.2089.

Schneider, R. and Persson, S. (2015). Connecting two arrays: the emerging role of actin-microtubule cross-linking motor proteins. *Frontiers in Plant Science* **6**. doi: https://doi.org/10.3389/fpls.2015.00415.

Schubert, V. (2017). Super-resolution Microscopy – Applications in Plant Cell Research. *Frontiers in Plant Science* **8**. doi: https://doi.org/10.3389/fpls.2017.00531.

Schubert, V. and Weisshart, K. (2015). Abundance and distribution of RNA polymerase II in Arabidopsis interphase nuclei. *Journal of Experimental Botany* **66**(6):1687–1698. doi: https://doi.org/10.1093/jxb/erv091.

Sekereš, J., Pleskot, R., Pejchar, P., Žárský, V. and Potocký, M. (2015). The song of lipids and proteins: dynamic lipid–protein interfaces in the regulation of plant cell polarity at different scales. *Journal of Experimental Botany* **66**(6):1587–1598. doi: https://doi.org/10.1093/jxb/erv052.

Shao, W. and Dong, J. (2016). Polarity in plant asymmetric cell division: Division orientation and cell fate differentiation. *Developmental Biology* **419**(1):121–131. doi: https://doi.org/10.1016/j.ydbio.2016.07.020.

Shaw, S.L., Kamyar, R. and Ehrhardt, D.W. (2003). Sustained Microtubule Treadmilling in Arabidopsis Cortical Arrays. *Science* **300**(5626):1715–1718. doi: https://doi.org/10.1126/science.1083529.

Shigeta, T., Zaizen, Y., Sugimoto, Y., Nakamura, Y., Matsuo, T. and Okamoto, S. (2015). Heat shock protein 90 acts in brassinosteroid signaling through interaction with BES1/BZR1 transcription factor. *Journal of Plant Physiology* **178**:69–73. doi: https://doi.org/10.1016/j.jplph.2015.02.003.

Shin, H., Shin, H.-S., Guo, Z., Blancaflor, E.B., Masson, P.H. and Chen, R. (2005). Complex regulation of Arabidopsis AGR1/PIN2-mediated root gravitropic response and basipetal auxin transport by cantharidin-sensitive protein phosphatases: Protein phosphatase regulation of auxin transport and gravitropism. *The Plant Journal* **42**(2):188–200. doi: https://doi.org/10.1111/j.1365-313X.2005.02369.x.

Shpak, E.D., Berthiaume, C.T., Hill, E.J. and Torii, K.U. (2004). Synergistic interaction of three ERECTA-family receptor-like kinases controls Arabidopsis organ growth and flower development by promoting cell proliferation. *Development* **131**(7):1491–1501. doi: https://doi.org/10.1242/dev.01028.

Shpak, E.D., McAbee, J.M., Pillitteri, L.J. and Torii, K.U. (2005). Stomatal Patterning and Differentiation by Synergistic Interactions of Receptor Kinases. *Science* **309**(5732):290–293. doi: https://doi.org/10.1126/science.1109710.

Smal, I., Grigoriev, I., Akhmanova, A., Niessen, W.J. and Meijering, E. (2010). Microtubule Dynamics Analysis Using Kymographs and Variable-Rate Particle Filters. *IEEE Transactions on Image Processing* **19**(7):1861–1876. doi: https://doi.org/10.1109/TIP.2010.2045031.

Smékalová, V., Luptovčiak, I., Komis, G., Šamajová, O., Ovečka, M., Doskočilová, A., … Šamaj, J. (2014). Involvement of YODA and mitogen activated protein kinase 6 in Arabidopsis post-embryogenic root development through auxin up-regulation and cell division plane orientation. *New Phytologist* **203**(4):1175–1193. doi: https://doi.org/10.1111/nph.12880.

Smertenko, A. (2018). Phragmoplast expansion: the four-stroke engine that powers plant cytokinesis. *Current Opinion in Plant Biology*. doi: https://doi.org/10.1016/j.pbi.2018.07.011.

Smertenko, A.P., Chang, H.-Y., Wagner, V., Kaloriti, D., Fenyk, S., Sonobe, S., … Hussey, P.J. (2004). The Arabidopsis Microtubule-Associated Protein AtMAP65-1: Molecular Analysis of Its Microtubule Bundling Activity. *The Plant Cell* **16**(8):2035–2047. doi: https://doi.org/10.1105/tpc.104.023937.

Smertenko, A.P., Cheng, Hsin-Yu, Sosobe, Seiji, Fenyk, Stepan I., Weingartner, M., Bögre, L. and Hussey, P.J. (2006). Control of the AtMAP65-1 interaction with microtubules through the cell cycle. *Journal of Cell Science* **119**(15):3227–3237. doi: https://doi.org/10.1242/jcs.03051.

Smertenko, A.P., Kaloriti, D., Chang, H.-Y., Fiserova, J., Opatrny, Z. and Hussey, P.J. (2008). The C-Terminal Variable Region Specifies the Dynamic Properties of Arabidopsis Microtubule-Associated Protein MAP65 Isotypes. *The Plant Cell* **20**(12):3346–3358. doi: https://doi.org/10.1105/tpc.108.063362.

Sollars, V., Lu, X., Xiao, L., Wang, X., Garfinkel, M.D. and Ruden, D.M. (2003). Evidence for an epigenetic mechanism by which Hsp90 acts as a capacitor for morphological evolution. *Nature Genetics* **33**(1):70–74. doi: https://doi.org/10.1038/ng1067.

Song, S.-K. and Clark, S.E. (2005). POL and related phosphatases are dosage-sensitive regulators of meristem and organ development in Arabidopsis. *Developmental Biology* **285**(1):272–284. doi: https://doi.org/10.1016/j.ydbio.2005.06.020.

Song, S.-K., Hofhuis, H., Lee, M.M. and Clark, S.E. (2008). Key Divisions in the Early Arabidopsis Embryo Require POL and PLL1 Phosphatases to Establish the Root Stem Cell Organizer and Vascular Axis. *Developmental Cell* **15**(1):98–109. doi: https://doi.org/10.1016/j.devcel.2008.05.008.

Song, S.-K., Lee, M.M. and Clark, S.E. (2006). POL and PLL1 phosphatases are CLAVATA1 signaling intermediates required for Arabidopsis shoot and floral stem cells. *Development* **133**(23):4691–4698. doi: https://doi.org/10.1242/dev.02652.

Sorensen, M.B. (2002). Cellularisation in the endosperm of Arabidopsis thaliana is coupled to mitosis and shares multiple components with cytokinesis. *Development* **129**(24):5567–5576. doi: https://doi.org/10.1242/dev.00152.

Sörensson, C., Lenman, M., Veide-Vilg, J., Schopper, S., Ljungdahl, T., Grøtli, M., … Andreasson, E. (2012). Determination of primary sequence specificity of Arabidopsis MAPKs MPK3 and MPK6 leads to identification of new substrates. *Biochemical Journal* **446**(2):271–278. doi: https://doi.org/10.1042/BJ20111809.

Spinner, L., Gadeyne, A., Belcram, K., Goussot, M., Moison, M., Duroc, Y., … Pastuglia, M. (2013). A protein phosphatase 2A complex spatially controls plant cell division. *Nature Communications* **4**(1):1–13. doi: https://doi.org/10.1038/ncomms2831.

Stahl, Y., Grabowski, S., Bleckmann, A., Kühnemuth, R., Weidtkamp-Peters, S., Pinto, K.G., … Simon, R. (2013). Moderation of Arabidopsis Root Stemness by CLAVATA1 and ARABIDOPSIS CRINKLY4 Receptor Kinase Complexes. *Current Biology* **23**(5):362–371. doi: https://doi.org/10.1016/j.cub.2013.01.045.

Staiger, C.J. and Cande, W.Z. (1992). Ameiotic, a gene that controls meiotic chromosome and cytoskeletal behavior in maize. *Developmental Biology* **154**(1):226–230. doi: https://doi.org/10.1016/0012-1606(92)90063-M.

Stals, H., Bauwens, S., Traas, J., Montagu, M.V., Engler, G. and Inzé, D. (1997). Plant CDC2 is not only targeted to the pre-prophase band, but also co-localizes with the spindle, phragmoplast, and chromosomes. *FEBS Letters* **418**(3):229–234. doi: https://doi.org/10.1016/S0014-5793(97)01368-9.

Steiner, A., Rybak, K., Altmann, M., McFarlane, H.E., Klaeger, S., Nguyen, N., … Assaad, F.F. (2016). Cell cycle-regulated PLEIADE/AtMAP65-3 links membrane and microtubule dynamics during plant cytokinesis. *The Plant Journal* **88**(4):531–541. doi: https://doi.org/10.1111/tpj.13275.

Stewart, S. and Fang, G. (2005). Anaphase-promoting complex/cyclosome controls the stability of TPX2 during mitotic exit. *Molecular and Cellular Biology* **25**(23):10516–10527. doi: https://doi.org/10.1128/MCB.25.23.10516-10527.2005.

Stöckle, D., Herrmann, A., Lipka, E., Lauster, T., Gavidia, R., Zimmermann, S. and Müller, S. (2016). Putative RopGAPs impact division plane selection and interact with kinesin-12 POK1. *Nature Plants* **2**(9). doi: https://doi.org/10.1038/nplants.2016.120.

Stone, J.M., Collinge, M.A., Smith, R.D., Horn, M.A. and Walker, J.C. (1994). Interaction of a protein phosphatase with an Arabidopsis serine-threonine receptor kinase. *Science* **266**(5186):793–795. doi: https://doi.org/10.1126/science.7973632.

Stoppin-Mellet, V., Fache, V., Portran, D., Martiel, J.-L. and Vantard, M. (2013). MAP65 Coordinate Microtubule Growth during Bundle Formation. *PLoS ONE* **8**(2). doi: https://doi.org/10.1371/journal.pone.0056808.

Strompen, G., El Kasmi, F., Richter, S., Lukowitz, W., Assaad, F.F., Jürgens, G. and Mayer, U. (2002). The Arabidopsis HINKEL Gene Encodes a Kinesin-Related Protein Involved in Cytokinesis and Is Expressed in a Cell Cycle-Dependent Manner. *Current Biology* **12**(2):153–158. doi: https://doi.org/10.1016/S0960-9822(01)00655-8.

Subramanian, R., Wilson-Kubalek, E.M., Arthur, C.P., Bick, M.J., Campbell, E.A., Darst, S.A., … Kapoor, T.M. (2010). Insights into Antiparallel Microtubule Crosslinking by PRC1, a Conserved Nonmotor Microtubule Binding Protein. *Cell* **142**(3):433–443. doi: https://doi.org/10.1016/j.cell.2010.07.012.

Suetsugu, N., Yamada, N., Kagawa, T., Yonekura, H., Uyeda, T.Q.P., Kadota, A. and Wada, M. (2010). Two kinesin-like proteins mediate actin-based chloroplast movement in Arabidopsis thaliana. *Proceedings of the National Academy of Sciences* **107**(19):8860–8865. doi: https://doi.org/10.1073/pnas.0912773107.

Sugano, S.S., Shimada, T., Imai, Y., Okawa, K., Tamai, A., Mori, M. and Hara-Nishimura, I. (2010). Stomagen positively regulates stomatal density in Arabidopsis. *Nature* **463**(7278):241–244. doi: https://doi.org/10.1038/nature08682.

Sun, L., Gao, J., Dong, X., Liu, M., Li, D., Shi, X., … Zhou, J. (2008). EB1 promotes Aurora-B kinase activity through blocking its inactivation by protein phosphatase 2A. *Proceedings of the National Academy of Sciences* **105**(20):7153–7158. doi: https://doi.org/10.1073/pnas.0710018105.

Sun, S.-C., Wang, Z.-B., Xu, Y.-N., Lee, S.-E., Cui, X.-S. and Kim, N.-H. (2011). Arp2/3 Complex Regulates Asymmetric Division and Cytokinesis in Mouse Oocytes. *PLoS ONE* **6**(4). doi: https://doi.org/10.1371/journal.pone.0018392.

Szklarczyk, D., Franceschini, A., Wyder, S., Forslund, K., Heller, D., Huerta-Cepas, J., … von Mering, C. (2015). STRING v10: protein–protein interaction networks, integrated over the tree of life. *Nucleic Acids Research* **43**(D):D447–D452. doi: https://doi.org/10.1093/nar/gku1003.

Taipale, M., Jarosz, D.F. and Lindquist, S. (2010). HSP90 at the hub of protein homeostasis: emerging mechanistic insights. *Nature Reviews Molecular Cell Biology* **11**(7):515–528. doi: https://doi.org/10.1038/nrm2918.

Taipale, M., Krykbaeva, I., Koeva, M., Kayatekin, C., Westover, K.D., Karras, G.I. and Lindquist, S. (2012). Quantitative Analysis of Hsp90-Client Interactions Reveals Principles of Substrate Recognition. *Cell* **150**(5):987–1001. doi: https://doi.org/10.1016/j.cell.2012.06.047.

Takahashi, Y., Soyano, T., Kosetsu, K., Sasabe, M. and Machida, Y. (2010). HINKEL kinesin, ANP MAPKKKs and MKK6/ANQ MAPKK, which phosphorylates and activates MPK4 MAPK,

constitute a pathway that is required for cytokinesis in Arabidopsis thaliana. *Plant and Cell Physiology* **51**(10):1766–1776. doi: https://doi.org/10.1093/pcp/pcq135.

Takakura, H., Zhang, Y., Erdmann, R.S., Thompson, A.D., Lin, Y., McNellis, B., … Toomre, D. (2017). Long time-lapse nanoscopy with spontaneously blinking membrane probes. *Nature Biotechnology* **35**(8):773–780. doi: https://doi.org/10.1038/nbt.3876.

Takatani, S., Ozawa, S., Yagi, N., Hotta, T., Hashimoto, T., Takahashi, Y., … Motose, H. (2017). Directional cell expansion requires NIMA-related kinase 6 (NEK6)-mediated cortical microtubule destabilization. *Scientific Reports* **7**(1). doi: https://doi.org/10.1038/s41598-017-08453-5.

Takeuchi, M., Staehelin, A. and Mineyuki, Y. (2017). Actin-microtubule interaction in plants. In: Jimenez-Lopez, J. C. (ed.). *Cytoskeleton-Structure, Dynamics, Function and Disease.* IntechOpen, pp. 33–54.

Tamnanloo, F., Damen, H., Jangra, R. and Lee, J.S. (2018). MAP KINASE PHOSPHATASE1 Controls Cell Fate Transition during Stomatal Development. *Plant Physiology* **178**(1):247–257. doi: https://doi.org/10.1104/pp.18.00475.

Tanaka, H., Ishikawa, M., Kitamura, S., Takahashi, Y., Soyano, T., Machida, C. and Machida, Y. (2004). The AtNACK1/HINKEL and STUD/TETRASPORE/AtNACK2 genes, which encode functionally redundant kinesins, are essential for cytokinesis in Arabidopsis. *Genes to Cells* **9**(12):1199–1211. doi: https://doi.org/10.1111/j.1365-2443.2004.00798.x.

Tanaka, H., Watanabe, M., Watanabe, D., Tanaka, T., Machida, C. and Machida, Y. (2002). ACR4, a Putative Receptor Kinase Gene of Arabidopsis thaliana, that is Expressed in the Outer Cell Layers of Embryos and Plants, is Involved in Proper Embryogenesis. *Plant and Cell Physiology* **43**(4):419–428. doi: https://doi.org/10.1093/pcp/pcf052.

Tanaka, I. and Ito, M. (1981). Control of division patterns in explanted microspores of Tulipa gesneriana. *Protoplasma* **108**(3):329–340. doi: https://doi.org/10.1007/BF02224427.

ten Hove, C.A., Lu, K.-J. and Weijers, D. (2015). Building a plant: cell fate specification in the early Arabidopsis embryo. *Development* **142**(3):420–430. doi: https://doi.org/10.1242/dev.111500.

Tena, G., Asai, T., Chiu, W.-L. and Sheen, J. (2001). Plant mitogen-activated protein kinase signaling cascades. *Current Opinion in Plant Biology* **4**(5):392–400. doi: https://doi.org/10.1016/S1369-5266(00)00191-6.

Terasaka, O. and Niitsu, T. (1987). Unequal cell division and chromatin differentiation in pollen grain cells. *The botanical magazine = Shokubutsu-gaku-zasshi* **100**(2):205–216. doi: https://doi.org/10.1007/BF02488324.

The UniProt Consortium (2019). UniProt: a worldwide hub of protein knowledge. *Nucleic Acids Research* **47**(D1):D506–D515. doi: https://doi.org/10.1093/nar/gky1049.

Thomann, A., Lechner, E., Hansen, M., Dumbliauskas, E., Parmentier, Y., Kieber, J., … Genschik, P. (2009). Arabidopsis CULLIN3 Genes Regulate Primary Root Growth and Patterning by Ethylene-Dependent and -Independent Mechanisms. *PLoS Genetics* **5**(1):e1000328. doi: https://doi.org/10.1371/journal.pgen.1000328.

Tian, J., Han, L., Feng, Z., Wang, G., Liu, W., Ma, Y., … Kong, Z. (2015). Orchestration of microtubules and the actin cytoskeleton in trichome cell shape determination by a plant-unique kinesin. *eLife* **4**:e09351. doi: https://doi.org/10.7554/eLife.09351.

Tichá, T., Samakovli, D., Kuchařová, A., Vavrdová, T. and Šamaj, J. (2020). Multifaceted roles of HEAT SHOCK PROTEIN 90 molecular chaperones in plant development. *Journal of Experimental Botany*. doi: https://doi.org/10.1093/jxb/eraa177.

Tomaštíková, E., Demidov, D., Jeřábková, H., Binarová, P., Houben, A., Doležel, J. and Petrovská, B. (2015). TPX2 Protein of Arabidopsis Activates Aurora Kinase 1, But Not Aurora Kinase 3 In Vitro. *Plant Molecular Biology Reporter* **33**(6):1988–1995. doi: https://doi.org/10.1007/s11105-015-0890-x.

Torres-Ruiz, R.A. and Jurgens, G. (1994). Mutations in the FASS gene uncouple pattern formation and morphogenesis in Arabidopsis development. *Development* **120**(10):2967–2978.

Tournebize, R., Andersen, S.S.L., Verde, F., Dorée, M., Karsenti, E. and Hyman, A.A. (1997). Distinct roles of PP1 and PP2A-like phosphatases in control of microtubule dynamics during mitosis. *The EMBO Journal* **16**(18):5537–5549. doi: https://doi.org/10.1093/emboj/16.18.5537.

Traas, J., Bellini, C., Nacry, P., Kronenberger, J., Bouchez, D. and Caboche, M. (1995). Normal differentiation patterns in plants lacking microtubular preprophase bands. *Nature* **375**(6533):676–677. doi: https://doi.org/10.1038/375676a0.

Truernit, E., Bauby, H., Dubreucq, B., Grandjean, O., Runions, J., Barthélémy, J. and Palauqui, J.-C. (2008). High-Resolution Whole-Mount Imaging of Three-Dimensional Tissue Organization and Gene Expression Enables the Study of Phloem Development and Structure in Arabidopsis. *The Plant Cell* **20**(6):1494–1503. doi: https://doi.org/10.1105/tpc.107.056069.

Tulin, A., McClerklin, S., Huang, Y. and Dixit, R. (2012). Single-Molecule Analysis of the Microtubule Cross-Linking Protein MAP65-1 Reveals a Molecular Mechanism for Contact-Angle-Dependent Microtubule Bundling. *Biophysical Journal* **102**(4):802–809. doi: https://doi.org/10.1016/j.bpj.2012.01.008.

Twell, D., Park, S.K., Hawkins, T.J., Schubert, D., Schmidt, R., Smertenko, A. and Hussey, P.J. (2002). MOR1/GEM1 has an essential role in the plant-specific cytokinetic phragmoplast. *Nature Cell Biology* **4**(9):711–714. doi: https://doi.org/10.1038/ncb844.

Ueda, M., Aichinger, E., Gong, W., Groot, E., Verstraeten, I., Vu, L.D., … Laux, T. (2017). Transcriptional integration of paternal and maternal factors in the *Arabidopsis* zygote. *Genes & Development* **31**(6):617–627. doi: https://doi.org/10.1101/gad.292409.116.

Ueda, M., Zhang, Z. and Laux, T. (2011). Transcriptional Activation of Arabidopsis Axis Patterning Genes WOX8/9 Links Zygote Polarity to Embryo Development. *Developmental Cell* **20**(2):264–270. doi: https://doi.org/10.1016/j.devcel.2011.01.009.

Ulmasov, T., Murfett, J., Hagen, G. and Guilfoyle, T.J. (1997). Aux/IAA proteins repress expression of reporter genes containing natural and highly active synthetic auxin response elements. *The Plant Cell* **9**(11):1963–1971. doi: https://doi.org/10.1105/tpc.9.11.1963.

Umbrasaite, J., Schweighofer, A., Kazanaviciute, V., Magyar, Z., Ayatollahi, Z., Unterwurzacher, V., … Meskiene, I. (2010). MAPK Phosphatase AP2C3 Induces Ectopic Proliferation of Epidermal Cells Leading to Stomata Development in Arabidopsis. *PLoS ONE* **5**(12):e15357. doi: https://doi.org/10.1371/journal.pone.0015357.

Van Damme, D., De Rybel, B., Gudesblat, G., Demidov, D., Grunewald, W., De Smet, I., … Russinova, E. (2011). Arabidopsis α Aurora Kinases Function in Formative Cell Division Plane Orientation. *The Plant Cell* **23**(11):4013–4024. doi: https://doi.org/10.1105/tpc.111.089565.

Van Damme, D., van Poucke, K., Boutant, E., Ritzenthaler, C., Inzé, D. and Geelen, D. (2004). In Vivo Dynamics and Differential Microtubule-Binding Activities of MAP65 Proteins. *Plant Physiology* **136**(4):3956–3967. doi: https://doi.org/10.1104/pp.104.051623.

Vanstraelen, M., Acosta, J.A.T., Veylder, L.D., Inzé, D. and Geelen, D. (2004). A Plant-Specific Subclass of C-Terminal Kinesins Contains a Conserved A-Type Cyclin-Dependent Kinase Site Implicated in Folding and Dimerization. *Plant Physiology* **135**(3):1417–1429. doi: https://doi.org/10.1104/pp.104.044818.

Vasquez, R.J., Gard, D.L. and Cassimeris, L. (1999). Phosphorylation by CDK1 regulates XMAP215 function in vitro. *Cell Motility* **43**(4):310–321. doi: https://doi.org/10.1002/(SICI)1097-0169(1999)43:4<310::AID-CM4>3.0.CO;2-J.

Venverloo, C.J. and Libbenga, K.R. (1987). Regulation of the Plane of Cell Division in Vacuolated Cells I. The Function of Nuclear Positioning and Phragmosome Formation. *Journal of Plant Physiology* **131**(3):267–284. doi: https://doi.org/10.1016/S0176-1617(87)80166-9.

Vigneault, F., Lachance, D., Cloutier, M., Pelletier, G., Levasseur, C. and Séguin, A. (2007). Members of the plant NIMA-related kinases are involved in organ development and vascularization in poplar, Arabidopsis and rice. *The Plant Journal* **51**(4):575–588. doi: https://doi.org/10.1111/j.1365-313X.2007.03161.x.

Vizcay-Barrena, G., Webb, S.E.D., Martin-Fernandez, M.L. and Wilson, Z.A. (2011). Subcellular and single-molecule imaging of plant fluorescent proteins using total internal reflection fluorescence microscopy (TIRFM). *Journal of Experimental Botany* **62**(15):5419–5428. doi: https://doi.org/10.1093/jxb/err212.

von Wangenheim, D., Hauschild, R., Fendrych, M., Barone, V., Benková, E. and Friml, J. (2017b). Live tracking of moving samples in confocal microscopy for vertically grown roots. *eLife* **6**:e26792. doi: https://doi.org/10.7554/eLife.26792.

von Wangenheim, D., Hauschild, R. and Friml, J. (2017a). Light Sheet Fluorescence Microscopy of Plant Roots Growing on the Surface of a Gel. *Journal of Visualized Experiments*(119):e55044. doi: https://doi.org/10.3791/55044.

Vos, J.W., Dogterom, M. and Emons, A.M.C. (2004). Microtubules become more dynamic but not shorter during preprophase band formation: A possible "search-and-capture" mechanism for microtubule translocation. *Cell Motility* **57**(4):246–258. doi: https://doi.org/10.1002/cm.10169.

Vos, J.W., Pieuchot, L., Evrard, J.-L., Janski, N., Bergdoll, M., de Ronde, D., … Schmit, A.-C. (2008). The Plant TPX2 Protein Regulates Prospindle Assembly before Nuclear Envelope Breakdown. *The Plant Cell* **20**(10):2783–2797. doi: https://doi.org/10.1105/tpc.107.056796.

Vos, J.W., Safadi, F., Reddy, A.S.N. and Hepler, P.K. (2000). The Kinesin-like Calmodulin Binding Protein Is Differentially Involved in Cell Division. *The Plant Cell* **12**(6):979–990. doi: https://doi.org/10.1105/tpc.12.6.979.

Voss, M., Campbell, K., Saranzewa, N., Campbell, D.G., Hastie, J., Peggie, M., … Cohen, P. (2013). Protein phosphatase 4 is phosphorylated and inactivated by Cdk in response to spindle toxins and interacts with γ-tubulin. *Cell Cycle* **12**(17):2876–2887. doi: https://doi.org/10.4161/cc.25919.

Walczak, C.E. and Heald, R. (2008). Chapter Three - Mechanisms of Mitotic Spindle Assembly and Function. In: Jeon, K. W. (ed.). *International Review of Cytology*. Academic Press, pp. 111–158.

Walczak, C.E. and Shaw, S.L. (2010). A MAP for Bundling Microtubules. *Cell* **142**(3):364–367. doi: https://doi.org/10.1016/j.cell.2010.07.023.

Walker, K.L., Müller, S., Moss, D., Ehrhardt, D.W. and Smith, L.G. (2007). Arabidopsis TANGLED Identifies the Division Plane throughout Mitosis and Cytokinesis. *Current Biology* **17**(21):1827–1836. doi: https://doi.org/10.1016/j.cub.2007.09.063.

Wang, B., Liu, G., Zhang, J., Li, Y., Yang, H. and Ren, D. (2018). The RAF-like mitogen-activated protein kinase kinase kinases RAF22 and RAF28 are required for the regulation of embryogenesis in Arabidopsis. *The Plant Journal* **96**(4):734–747. doi: https://doi.org/10.1111/tpj.14063.

Wang, H., Liu, Y., Bruffett, K., Lee, J., Hause, G., Walker, J.C. and Zhang, S. (2008). Haplo-Insufficiency of MPK3 in MPK6 Mutant Background Uncovers a Novel Function of These Two MAPKs in Arabidopsis Ovule Development. *The Plant Cell* **20**(3):602–613. doi: https://doi.org/10.1105/tpc.108.058032.

Wang, H., Ngwenyama, N., Liu, Y., Walker, J.C. and Zhang, S. (2007). Stomatal Development and Patterning Are Regulated by Environmentally Responsive Mitogen-Activated Protein Kinases in Arabidopsis. *The Plant Cell* **19**(1):63–73. doi: https://doi.org/10.1105/tpc.106.048298.

Wang, J., Zhang, Y., Wu, J., Meng, L. and Ren, H. (2013). AtFH16, an Arabidopsis Type II Formin, Binds and Bundles both Microfilaments and Microtubules, and Preferentially Binds to Microtubules. *Journal of Integrative Plant Biology* **55**(11):1002–1015. doi: https://doi.org/10.1111/jipb.12089.

Wang, R., Zhang, Y., Kieffer, M., Yu, H., Kepinski, S. and Estelle, M. (2016). HSP90 regulates temperature-dependent seedling growth in Arabidopsis by stabilizing the auxin co-receptor F-box protein TIR1. *Nature Communications* **7**(1):1–11. doi: https://doi.org/10.1038/ncomms10269.

Watanabe, E., Mano, S., Hara-Nishimura, I., Nishimura, M. and Yamada, K. (2017). HSP90 stabilizes auxin receptor TIR1 and ensures plasticity of auxin responses. *Plant Signaling & Behavior* **12**(5):e1311439. doi: https://doi.org/10.1080/15592324.2017.1311439.

Watanabe, E., Mano, S., Nomoto, M., Tada, Y., Hara-Nishimura, I., Nishimura, M. and Yamada, K. (2016). HSP90 Stabilizes Auxin-Responsive Phenotypes by Masking a Mutation in the Auxin Receptor TIR1. *Plant and Cell Physiology* **57**(11):2245–2254. doi: https://doi.org/10.1093/pcp/pcw170.

Waterhouse, A.M., Procter, J.B., Martin, D.M.A., Clamp, M. and Barton, G.J. (2009). Jalview Version 2—a multiple sequence alignment editor and analysis workbench. *Bioinformatics* **25**(9):1189–1191. doi: https://doi.org/10.1093/bioinformatics/btp033.

Weingartner, M., Binarova, P., Drykova, D., Schweighofer, A., David, J.-P., Heberle-Bors, E., … Bögre, L. (2001). Dynamic Recruitment of Cdc2 to Specific Microtubule Structures during Mitosis. *The Plant Cell* **13**:1929–1943.

Weis, F., Moullintraffort, L., Heichette, C., Chrétien, D. and Garnier, C. (2010). The 90-kDa Heat Shock Protein Hsp90 Protects Tubulin against Thermal Denaturation. *Journal of Biological Chemistry* **285**(13):9525–9534. doi: https://doi.org/10.1074/jbc.M109.096586.

Wengier, D.L., Lampard, G.R. and Bergmann, D.C. (2018). Dissection of MAPK signaling specificity through protein engineering in a developmental context. *BMC Plant Biology* **18**(1):60. doi: https://doi.org/10.1186/s12870-018-1274-9.

Wicker-Planquart, C., Stoppin-Mellet, V., Blanchoin, L. and Vantard, M. (2004). Interactions of tobacco microtubule-associated protein MAP65-1b with microtubules. *The Plant Journal* **39**(1):126–134. doi: https://doi.org/10.1111/j.1365-313X.2004.02115.x.

Wright, A.J., Gallagher, K. and Smith, L.G. (2009). discordia1 and alternative discordia1 Function Redundantly at the Cortical Division Site to Promote Preprophase Band Formation and Orient Division Planes in Maize. *The Plant Cell* **21**(1):234–247. doi: https://doi.org/10.1105/tpc.108.062810.

Wright, A.J. and Smith, L.G. (2007). Division Plane Orientation in Plant Cells. In: Verma, D. P. S. and Hong, Z. (eds.). *Cell Division Control in Plants*. Berlin, Heidelberg: Springer Berlin Heidelberg, pp. 33–57.

Wu, S.-Z. and Bezanilla, M. (2014). Myosin VIII associates with microtubule ends and together with actin plays a role in guiding plant cell division. *eLife* **3**. doi: https://doi.org/10.7554/eLife.03498.

Wu, S.-Z. and Bezanilla, M. (2018). Actin and microtubule cross talk mediates persistent polarized growth. *Journal of Cell Biology* **217**(10):3531–3544. doi: https://doi.org/10.1083/jcb.201802039.

Xiao, J. and Wagner, D. (2015). Polycomb repression in the regulation of growth and development in Arabidopsis. *Current Opinion in Plant Biology* **23**:15–24. doi: https://doi.org/10.1016/j.pbi.2014.10.003.

Xiao, W., Custard, K.D., Brown, R.C., Lemmon, B.E., Harada, J.J., Goldberg, R.B. and Fischer, R.L. (2006). DNA methylation is critical for Arabidopsis embryogenesis and seed viability. *The Plant Cell* **18**(4):805–814. doi: https://doi.org/10.1105/tpc.105.038836.

Xiong, F., Liu, H.-H., Duan, C.-Y., Zhang, B.-K., Wei, G., Zhang, Y. and Li, S. (2019). Arabidopsis JANUS Regulates Embryonic Pattern Formation through Pol II-Mediated Transcription of WOX2 and PIN7. *iScience* **19**:1179–1188. doi: https://doi.org/10.1016/j.isci.2019.09.004.

Xu, X.M., Zhao, Q., Rodrigo-Peiris, T., Brkljacic, J., He, C.S., Muller, S. and Meier, I. (2008). RanGAP1 is a continuous marker of the Arabidopsis cell division plane. *Proceedings of the National Academy of Sciences* **105**(47):18637–18642. doi: https://doi.org/10.1073/pnas.0806157105.

Xu, Z.-S., Li, Z.-Y., Chen, Y., Chen, M., Li, L.-C. and Ma, Y.-Z. (2012). Heat Shock Protein 90 in Plants: Molecular Mechanisms and Roles in Stress Responses. *International Journal of Molecular Sciences* **13**(12):15706–15723. doi: https://doi.org/10.3390/ijms131215706.

Xue, X., Bian, C., Guo, X., Di, R. and Dong, J. (2020). The MAPK substrate MASS proteins regulate stomatal development in Arabidopsis. *PLOS Genetics* **16**(4):e1008706. doi: https://doi.org/10.1371/journal.pgen.1008706.

York, A.G., Chandris, P., Nogare, D.D., Head, J., Wawrzusin, P., Fischer, R.S., … Shroff, H. (2013). Instant super-resolution imaging in live cells and embryos via analog image processing. *Nature Methods* **10**(11):1122–1126. doi: https://doi.org/10.1038/nmeth.2687.

Yoshida, S., Barbier de Reuille, P., Lane, B., Bassel, G.W., Prusinkiewicz, P., Smith, R.S. and Weijers, D. (2014). Genetic Control of Plant Development by Overriding a Geometric Division Rule. *Developmental Cell* **29**(1):75–87. doi: https://doi.org/10.1016/j.devcel.2014.02.002.

Yu, T.-Y., Shi, D.-Q., Jia, P.-F., Tang, J., Li, H.-J., Liu, J. and Yang, W.-C. (2016). The Arabidopsis Receptor Kinase ZAR1 Is Required for Zygote Asymmetric Division and Its Daughter Cell Fate. *PLoS Genetics* **12**(3). doi: https://doi.org/10.1371/journal.pgen.1005933.

Závorková, N. (2019). *Molekulární a funkční charakterizace embryonálního vývoje u dvojitých mutantů HSP90 a YODA*. Bachelor Thesis, Palacký University Olomouc.

Zhang, H., Lin, X., Han, Z., Wang, J., Qu, L.-J. and Chai, J. (2016b). SERK Family Receptor-like Kinases Function as Co-receptors with PXY for Plant Vascular Development. *Molecular Plant* **9**(10):1406–1414. doi: https://doi.org/10.1016/j.molp.2016.07.004.

Zhang, J.-Y., He, S.-B., Li, L. and Yang, H.-Q. (2014). Auxin inhibits stomatal development through MONOPTEROS repression of a mobile peptide gene STOMAGEN in mesophyll. *Proceedings of the National Academy of Sciences* **111**(29):E3015–E3023. doi: https://doi.org/10.1073/pnas.1400542111.

Zhang, M., Wu, H., Su, J., Wang, H., Zhu, Q., Liu, Y., … Zhang, S. (2017a). Maternal control of embryogenesis by MPK6 and its upstream MKK4/MKK5 in Arabidopsis. *The Plant Journal* **92**(6):1005–1019. doi: https://doi.org/10.1111/tpj.13737.

Zhang, X., Ems-McClung, S.C. and Walczak, C.E. (2008). Aurora A phosphorylates MCAK to control ran-dependent spindle bipolarity. *Molecular Biology of the Cell* **19**(7):2752–2765. doi: https://doi.org/10.1091/mbc.e08-02-0198.

Zhang, Y. and Dong, J. (2018). Cell polarity: compassing cell division and differentiation in plants. *Current Opinion in Plant Biology* **45**:127–135. doi: https://doi.org/10.1016/j.pbi.2018.06.003.

Zhang, Y., Guo, X. and Dong, J. (2016a). Phosphorylation of the Polarity Protein BASL Differentiates Asymmetric Cell Fate through MAPKs and SPCH. *Current Biology* **26**(21):2957–2965. doi: https://doi.org/10.1016/j.cub.2016.08.066.

Zhang, Y., Wang, P., Shao, W., Zhu, J.-K. and Dong, J. (2015). The BASL Polarity Protein Controls a MAPK Signaling Feedback Loop in Asymmetric Cell Division. *Developmental Cell* **33**(2):136–149. doi: https://doi.org/10.1016/j.devcel.2015.02.022.

Zhang, Z. and Laux, T. (2011). The asymmetric division of the Arabidopsis zygote: from cell polarity to an embryo axis. *Sexual Plant Reproduction* **24**(2):161–169. doi: https://doi.org/10.1007/s00497-010-0160-x.

Zhang, Z., Tucker, E., Hermann, M. and Laux, T. (2017b). A Molecular Framework for the Embryonic Initiation of Shoot Meristem Stem Cells. *Developmental Cell* **40**(3):264-277.e4. doi: https://doi.org/10.1016/j.devcel.2017.01.002.

Zhou, H.-W., Nussbaumer, C., Chao, Y. and DeLong, A. (2004). Disparate Roles for the Regulatory A Subunit Isoforms in Arabidopsis Protein Phosphatase 2A. *The Plant Cell* **16**(3):709–722. doi: https://doi.org/10.1105/tpc.018994.

Zhou, S., Chen, Q., Li, X. and Li, Y. (2017). MAP65-1 is required for the depolymerization and reorganization of cortical microtubules in the response to salt stress in Arabidopsis. *Plant Science* **264**:112–121. doi: https://doi.org/10.1016/j.plantsci.2017.09.004.

Zhu, C. and Dixit, R. (2012). Functions of the Arabidopsis kinesin superfamily of microtubule-based motor proteins. *Protoplasma* **249**(4):887–899. doi: https://doi.org/10.1007/s00709-011-0343-9.

7. Abbreviations

3AT	3-amino-1,2,4-triazole
ACD	asymmetric cell division
AIR9	AUXIN INDUCED IN ROOT CULTURES PROTEIN 9
ANP	ARABIDOPSIS NUCLEUS AND PHRAGMOPLAST-LOCALIZED KINASE
AP2C3	ARABIDOPSIS PROTEIN PHOSPHATASE 2C 3
Ase1p	Anaphase spindle elongation 1 protein
AUR	AURORA KINASE
BASL	BREAKING OF ASYMMETRY IN STOMATAL LINEAGE
BDL	BODENLOS
BIN2	BRASSINOSTEROID INSENSITIVE 2
BSA	bovine serum albumin
CDK	CYCLIN DEPENDENT KINASE
CLASP	CLIP-ASSOCIATED PROTEIN
CLSM	confocal laser scanning microscope
• ACLSM	CLSM equipped with Airyscan
CTR	cantharidin
DAG	days after germination
DAPI	4',6-diamidino-2-phenylindole dihydrochloride
DIC	differential interference contrast
EB1	END BINDING 1
EPF	EPIDERMAL PATTERNING FACTOR
ER	ERECTA
ERL	ERECTA-LIKE PROTEIN
ESF1	EMBRYO SURROUNDING FACTOR 1
FWHM	full-width at half maximum
GRD	GROUNDED
HDG	HOMEODOMAIN GLABROUS
HSP90	HEAT SHOCK PROTEIN 90
KAT	KATANIN
KIN	KINESIN-RELATED PROTEIN
LSFM	light-sheet fluorescence microscopy
MAP65	MICROTUBULE ASSOCIATED PROTEIN 65
MKP1	MAPK PHOSPHATASE 1
MOR1	MICROTUBULE ORGANIZING 1
MP	MONOPTEROS
MPK	MITOGEN ACTIVATED PROTEIN KINASE
• pMPK	phosphorylated MPK
• MKK	MITOGEN ACTIVATED PROTEIN KINASE KINASE
• MKKK	MITOGEN ACTIVATED PROTEIN KINASE KINASE KINASE
MTSB	microtubule stabilizing buffer
NEKs	NIMA-RELATED KINASEs
PBS	phosphate buffered saline
POLAR	POLAR LOCALIZATION DURING ASYMMETRIC DIVISION AND REDISTRIBUTION
PP	PROTEIN PHOSPHATASE
PP2A	PROTEIN PHOSPHATASE 2A
PP2C	PROTEIN PHOSPHATASE 2C
PRC1	PROTEIN REGULATOR OF CYTOKINESIS 1
pTEpY	anti-phospho-Thr-Glu-phospho-Tyr
RCN1	ROOTS CURL IN NAPHTYLAMINOACID 1

RNAi	RNA interference
SD	Synthetic Dropout
SERK	SOMATIC EMBRYOGENESIS RECEPTOR KINASE
SIM	structured illumination microscopy
SPCH	SPEECHLESS
SSP	SHORT SUSPENSOR
TBS-T	tris-buffered saline buffer suplemented with Tween 20
TIO	TWO-IN-ONE
TMM	TOO MANY MOUTH
TON	TONNEAU
TPX2	TARGETING PROTEIN FOR XKLP2
TRM	TON1 RECRUITING MOTIF PROTEIN
WOX	WUCHSEL-RELATED HOMEOBOX PROTEIN
WRKY2	WRKY DNA-BINDING PROTEIN 2
YDA	YODA
ZAR1	ZYGOTE ARREST 1

8. Supplementary Data

Supplementary Figures and Supplementary Tables

Figure S1. Uncropped pictures of Western blot analyses illustrated in **Fig. 17**.

Table S1. Statistical tests for **Fig. 12**.

Table S2. Statistical tests for **Fig. 13**.

Table S3. Statistical tests for **Fig. 22C**.

Table S4. Statistical tests for **Fig. 43**.

List of publications

Addendum

Publication 1. <u>Title:</u> Complementary superresolution visualization of composite plant microtubule organization and dynamics.

<u>Authors:</u> Tereza Vavrdová, Pavel Křenek, Miroslav Ovečka, Olga Šamajová, Pavlína Floková, Petra Illešová, Renata Šnaurová, Jozef Šamaj and George Komis

Publication 2. <u>Title:</u> Phosphorylation of plant microtubule-associated proteins during cell division.

<u>Authors:</u> Tereza Vavrdová, Jozef Šamaj and George Komis

Publication 3. <u>Title:</u> Multicolour three dimensional structured illumination microscopy of immunolabeled plant microtubules and associated proteins.

<u>Authors:</u> Tereza Vavrdová, Olga Šamajová, Pavel Křenek, Miroslav Ovečka, Pavlína Floková, Renata Šnaurová, Jozef Šamaj and George Komis

Supplementary Figures and Supplementary Tables
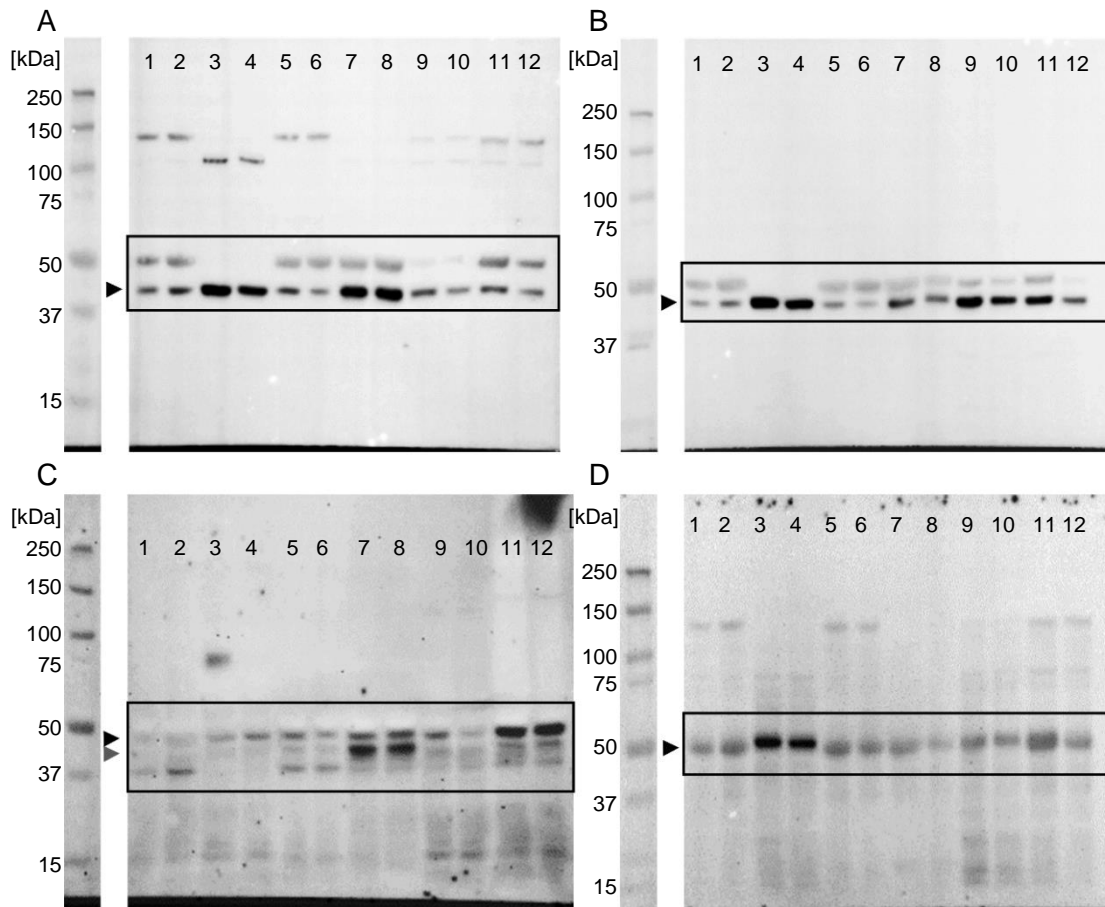
Figure S1. Uncropped pictures of Western blot analyses illustrated in Fig. 17. (A-D) uncropped images showed in **Fig. 17**. Primary antibodies were used against MPK3 (A), MPK6 (B), phosphorylated MPK3 (grey arrowhead) and MPK6 (black arrowhead) (C), and β-tubulin (D). Loaded samples: (1, 3, 5, 7, 9, 11) Col-0, (2, 4, 6, 8, 10, 12) *rcn1-6;* (1, 2) whole plants, 14 days after germination (DAG); (3, 4) roots, 14 DAG; (5, 6) shoots, 14 DAG; (7, 8) rosettes, 21 DAG; (9, 10) flowers; (11, 12) siliques, 6 days after pollination. Protein levels were visualized by Stain-Free™ technology; arrowheads point to detected proteins; black boxes mark areas shown in **Fig. 17**. Next to every image of a membrane is shown corresponding protein standard marking protein sizes.

Table S1. Statistical tests for Fig. 12.

Factorial ANOVA was conducted to compare the main effects of genotype cantharidin treatment and the interaction between cantharidin treatment and genotype on root length (0.05 significance level). Main effect was for genotype $F_{(3, 5623)}=2750$, $p=0.00$; for cantharidin treatment $F_{(4, 5623)}=1474$, $p=0.00$; the interaction effect was significant: $F_{(12, 5623)}=42.5$, $p=0.00$. ANOVA was followed by Scheffé's test and p-values were corrected by Holm-Bonferroni correction.

cat.	g	c_{CTR}	category																			
			1	2	3	4	5	6	7	8	9	10	11	12	13	14	15	16	17	18	19	20
1	Col-0	0 µM		1	0.3	0	0	0	0	0	0	0	0	1	1	1	0	0	0	0	0	0
2		1 µM	1		1	0.003	0	0	0	0	0	0	0	1	1	0.5	0	0	0	0	0	0
3		3 µM	0.3	1		1	0	0	0	0	0	0	0	1	1	0	0	0	0	0	0	0
4		5 µM	0	0.003	1		0	0	0	0	0	0	1	0	0	0	0	0.015	0	0	0	0
5		10 µM	0	0	0	0		0	1	0	0	0	0	0	0	0	1	0	1	1	1	0
6	rcn1-6	0 µM	0	0	0	0	0		0.02	0	0	0	0	0	0	0	1	1	0.3	0	0	0
7		1 µM	0	0	0	0	1	0.02		0	0	0	0	0	0	0	1	0	1	1	1	1
8		3 µM	0	0	0	0	0	0	0		0	0	0	0	0	0	0	0	0	0	0	0
9		5 µM	0	0	0	0	0	0	0	0		0	0	0	0	0	0	0	0	0	0	1
10		10 µM	0	0	0	0	0	0	0	0	0		0	0	0	0	0	0	0	0	0	0
11	mpk3-1	0 µM	0	0	0	1	0	0	0	0	0	0		0	0	1	0	0	0	0	0	0
12		1 µM	1	1	1	0	0	0	0	0	0	0	0		1	0.3	0	0	0	0	0	0
13		3 µM	1	1	1	0	0	0	0	0	0	0	0	1		1	0	0	0	0	0	0
14		5 µM	1	0.5	0	0	0	0	0	0	0	0	1	0.3	1		0	0	0	0	0	0
15		10 µM	0	0	0	0	1	1	1	0	0	0	0	0	0	0		1	1	0.01	0.1	0
16	mpk6-2	0 µM	0	0	0	0.015	0	1	0	0	0	0	0	0	0	0	1		0	0	0	0
17		1 µM	0	0	0	0	1	0.3	1	0	0	0	0	0	0	0	1	0		1	1	0
18		3 µM	0	0	0	0	1	0	1	0	0	0	0	0	0	0	0.01	0	1		1	0
19		5 µM	0	0	0	0	1	0	1	0	0	0	0	0	0	0	0.1	0	1	1		0
20		10 µM	0	0	0	0	0	0	1	0	1	0	0	0	0	0	0	0	0	0	0	

Abbreviations: cat., category; g, genotype; c_{CTR}, concentration of cantharidin.

Table S2. Statistical tests for Fig. 13.

Factorial ANOVA was conducted to compare the main effects of genotype and cantharidin treatment and the interaction between cantharidin treatment and genotype on the distance between root tip and first root hair (0.05 significance level). Main effect was for genotype $F_{(3, 1417)}=527$, $p=0.00$; for cantharidin treatment $F_{(4, 1417)}=295$, $p=0.00$; the interaction effect was significant: $F_{(12, 1417)}=41$, $p=0.00$. ANOVA was followed by Scheffé's test and p-values were corrected by Holm-Bonferroni correction.

cat.	g	c_{CTR}	1	2	3	4	5	6	7	8	9	10	11	12	13	14	15	16	17	18	19	20
1	Col-0	0 µM		1	0	0	0	0	0	0	0	0	0	0	0	0	0	0	0	0	0	0
2		1 µM	1		0	0	0	0	0	0	0	0	0.008	0.006	0	0	0	0	0	0	0	0
3		3 µM	0	0		1	0	1	0	0	0	0	1	1	1	1	1	1	1	0.01	1	0
4		5 µM	0	0	1		0	1	0.8	0	0	0	1	1	1	1	1	1	1	1	1	0
5		10 µM	0	0	0	0		0	1	1	1	0	0	0	0	0	0	0	0	0.6	0	1
6	rcn1-6	0 µM	0	0	1	1	0		1	0	0	0	1	1	1	1	1	1	1	1	1	0
7		1 µM	0	0	0	0.8	1	1		1	1	0	1	1	0.02	1	1	1	1	1	1	0
8		3 µM	0	0	0	0	1	0	1		0	1	0	0	0	0	0	0	0	0.9	0	0
9		5 µM	0	0	0	0	1	0	1	0		0	0	0	0	0	0	0	0	0	0	0
10		10 µM	0	0	0	0	0	0	0	1	0		0	0	0	0	0	0	0	0	0	0
11	mpk3-1	0 µM	0	0.008	1	1	0	1	1	0	0	0		1	1	1	1	1	1	1	1	0
12		1 µM	0	0.006	1	1	0	1	1	0	0	0	1		1	1	1	1	1	1	1	0
13		3 µM	0	0	1	1	0	1	0.02	0	0	0	1	1		1	1	0.01	0.05	1	1	0
14		5 µM	0	0	1	1	0	1	1	0	0	0	1	1	1		1	0.01	0.05	0	1	0
15		10 µM	0	0	1	1	0	1	1	0	0	0	1	1	1	1		1	1	0.02	1	0
16	mpk6-2	0 µM	0	0	1	1	0	1	1	0	0	0	1	1	0.01	0.01	1		1	1	1	0
17		1 µM	0	0	1	1	0	1	1	0	0	0	1	1	0.05	0.05	1	1		1	1	0
18		3 µM	0	0	0.01	1	0.6	1	1	0.9	0	0	1	1	1	0	0.02	1	1		1	0.01
19		5 µM	0	0	1	1	0	1	1	0	0	0	1	1	1	1	1	1	1	1		0
20		10 µM	0	0	0	0	1	0	0	0	0	0	0	0	0	0	0	0	0	0.01	0	

(Columns 1–20 are "category".)

Abbreviations: cat., category; g, genotype; c_{CTR}, concentration of cantharidin.

Table S3. Statistical tests for Fig. 22C.

Welch's ANOVA followed by Tukey's honestly significant difference test corrected for unequal sample size; F (4, N=490)=111.9271, p=0.000

p-values for indicated genotypes	wild type	*rcn1-6*	*mpk3-1*	*mpk6-2*	*mpk6AEF*
wild type		0.0000	0.8006	0.0000	0.0000
rcn1-6	0.0000		0.0000	0.0000	0.9999
mpk3-1	0.8006	0.0000		0.0000	0.0000
mpk6-2	0.0000	0.0000	0.0000		0.0000
mpk6AEF	0.0000	0.9999	0.0000	0.0000	

Table S4: Statistical tests for Fig. 43.

Kruskal-Wallis test for comparing full-width at half maximum (FWHM) reached for different lines by Airyscan confocal laser scanning microscopy (ACLSM) or structured illumination microscopy (SIM); H (3, N=161)=83.6043, p=0.0000

line; platform	TUA6-GFP; ACLSM	eGFP-MAP65-2; ACLSM	TUA6-GFP; SIM	eGFP-MAP65-2; SIM
TUA6-GFP; ACLSM		1.0000	0.0000	0.0000
eGFP-MAP65-2; ACLSM	1.0000		0.0000	0.0000
TUA6-GFP; SIM	0.0000	0.0000		0.4383
eGFP-MAP65-2; SIM	0.0000	0.0000	0.4383	

H (3, N=165)=110.0558 p=0.000

line; platform	eGFP-MAP65-2; ACLSM	tagRFP-MAP65-2; ACLSM	eGFP-MAP65-2; SIM	tagRFP-MAP65-2; SIM
GFP-MAP65-2; ACLSM		1.0000	0.0000	0.0000
tagRFP-MAP65-2; ACLSM	1.0000		0.0000	0.0000
GFP-MAP65-2; SIM	0.0000	0.0000		1.0000
tagRFP-MAP65-2; SIM	0.0000	0.0000	1.0000	

List of publications

Vavrdová, T.[*], Křenek, P.[*], Ovečka, M., Šamajová, O., Floková, P., Illešová, P., Šnaurová, R., Šamaj, J., Komis, G. (2020). Complementary superresolution visualization of composite plant microtubule organization and dynamics. *Frontiers in Plant Sciences* **11**. doi: https://doi.org/10.3389/fpls.2020.00693.

Tichá, T., Samakovli, D., Kuchařová, A., Vavrdová, T., Šamaj, J. (2020). Multifaceted roles of HEAT SHOCK PROTEIN 90 molecular chaperones in plant development. *Journal of Experimental Botany*. doi: https://doi.org/10.1093/jxb/eraa177.

Samakovli, D., Tichá, T., Vavrdová, T., Ovečka, M., Luptovčiak, I., Zapletalová, V., Kuchařová, A., Křenek, P., Krasylenko, Y., Margaritopoulou, T., Roka, L., Milion, D., Komis, G., Hatzopoulos, P., Šamaj, J. (2020). YODA-HSP90 Module regulates phosphorylation-dependent inactivation of SPEECHLESS to control stomatal development under acute heat stress in Arabidopsis. *Molecular Plant* **13**(4):612–633. doi: https://doi.org/10.1016/j.molp.2020.01.001.

Vavrdová, T., Šamaj, J. and Komis, G. (2019). Phosphorylation of plant microtubule-associated proteins during cell division. *Frontiers of Plant Sciences* **10**: 238. https://doi.org/10.3389/fpls.2019.00238.

Vavrdová, T., Šamajová, O., Křenek, P., Ovečka, M., Floková, P., Šnaurová, R., Šamaj, J. and Komis, G. (2019). Multicolour three dimensional structured illumination microscopy of immunolabeled plant microtubules and associated proteins. *Plant Methods* **15**(1): 22. doi: https://doi.org/10.1186/s13007-019-0406-z.

Addendum

Publication 1.

<u>Title:</u> Complementary superresolution visualization of composite plant microtubule organization and dynamics.

<u>Authors:</u> <u>Tereza Vavrdová,</u> Pavel Křenek, Miroslav Ovečka, Olga Šamajová, Pavlína Floková, Petra Illešová, Renata Šnaurová, Jozef Šamaj and George Komis

Frontiers in Plant Sciences 2020; **11**.

My contribution: I was helping with selection of transformed plants and handling plants and I prepared the crossed lines. I was involved in image acquisition on the Axio Observer LSM 880 with the Airyscan and Axio Observer Z.1 with the Elyra PS.1. I made the post-acquisition image processing and quantitative analysis and performed all statistical evaluations. I prepared drafts of the figures and manuscript.

Complementary Superresolution Visualization of Composite Plant Microtubule Organization and Dynamics

Tereza Vavrdová[†], Pavel Křenek[†], Miroslav Ovečka, Olga Šamajová, Pavlína Floková, Petra Illešová, Renáta Šnaurová, Jozef Šamaj and George Komis*

Department of Cell Biology, Centre of the Region Haná for Biotechnological and Agricultural Research, Faculty of Science, Palacký University Olomouc, Olomouc, Czechia

Microtubule bundling is an essential mechanism underlying the biased organization of interphase and mitotic microtubular systems of eukaryotes in ordered arrays. Microtubule bundle formation can be exemplified in plants, where the formation of parallel microtubule systems in the cell cortex or the spindle midzone is largely owing to the microtubule crosslinking activity of a family of microtubule associated proteins, designated as MAP65s. Among the nine members of this family in *Arabidopsis thaliana*, MAP65-1 and MAP65-2 are ubiquitous and functionally redundant. Crosslinked microtubules can form high-order arrays, which are difficult to track using widefield or confocal laser scanning microscopy approaches. Here, we followed spatiotemporal patterns of MAP65-2 localization in hypocotyl cells of Arabidopsis stably expressing fluorescent protein fusions of MAP65-2 and tubulin. To circumvent imaging difficulties arising from the density of cortical microtubule bundles, we use different superresolution approaches including Airyscan confocal laser scanning microscopy (ACLSM), structured illumination microscopy (SIM), total internal reflection SIM (TIRF-SIM), and photoactivation localization microscopy (PALM). We provide insights into spatiotemporal relations between microtubules and MAP65-2 crossbridges by combining SIM and ACLSM. We obtain further details on MAP65-2 distribution by single molecule localization microscopy (SMLM) imaging of either mEos3.2-MAP65-2 stochastic photoconversion, or eGFP-MAP65-2 stochastic emission fluctuations under specific illumination conditions. Time-dependent dynamics of MAP65-2 were tracked at variable time resolution using SIM, TIRF-SIM, and ACLSM and post-acquisition kymograph analysis. ACLSM imaging further allowed to track end-wise dynamics of microtubules labeled with TUA6-GFP and to correlate them with concomitant fluctuations of MAP65-2 tagged with tagRFP. All different microscopy modules examined herein are accompanied by restrictions in either the spatial resolution achieved, or in the frame rates of image acquisition. PALM imaging is compromised by speed of acquisition. This limitation was partially compensated by exploiting emission fluctuations of eGFP which allowed much higher photon counts at substantially smaller time series compared to mEos3.2. SIM, TIRF-SIM, and ACLSM

were the methods of choice to follow the dynamics of MAP65-2 in bundles of different complexity. Conclusively, the combination of different superresolution methods allowed for inferences on the distribution and dynamics of MAP65-2 within microtubule bundles of living *A. thaliana* cells.

INTRODUCTION

Microtubules are essential components of the plant cytoskeleton and are crucial for fundamental cellular functions, including cell division, growth and morphogenesis (reviewed in Panteris and Galatis, 2005; Yamada and Goshima, 2017; Eng and Sampathkumar, 2018; Lazzaro et al., 2018; Sapala et al., 2018). Higher plants are devoid of a structurally discernible microtubule organizing center (MTOC), therefore formation and organization of plant-unique microtubule arrays, such as the interphase cortical system, the premitotic preprophase microtubule band, the acentrosomal mitotic spindle and the cytokinetic phragmoplast, rely on interactions between microtubules and several microtubule associated proteins (MAPs) with diverse functions (Bannigan et al., 2008; Müller et al., 2009; Lee and Liu, 2013; Buschmann and Zachgo, 2016; Smertenko, 2018).

Such proteins are involved in the spatiotemporal control of microtubule nucleation (e.g., Walia et al., 2014; Nakamura, 2015; Tian and Kong, 2019), the regulation of end-wise microtubule dynamics (e.g., Nakamura et al., 2018; Lindeboom et al., 2019), microtubule clearance via severing (e.g., Nakamura et al., 2010; Tulin et al., 2012; Deinum et al., 2017; Wang et al., 2018), the formation of higher order microtubule assemblies via physical microtubule crosslinking (e.g., Ma et al., 2016; Molines et al., 2018; Burkart and Dixit, 2019), or the adjustment of microtubule positioning by different microtubule-dependent motor activities (e.g., Zhu et al., 2015; Oda, 2018). A particular group of proteins associated with microtubules, are those with dual affinity for both the microtubule and the actin filament surface (reviewed in Schneider and Persson, 2015; Krtková et al., 2016). Notable examples include members of the plant FORMIN family (e.g., Sun et al., 2017; Wu and Bezanilla, 2018; Kollárová et al., 2020), members of the ARP2/3 actin nucleation complex (Havelková et al., 2015) and motor proteins of either the kinesin or the myosin superfamilies (e.g., Schneider and Persson, 2015). In this respect kinesins with calponin homology domains such as tobacco KCH1 or cotton KCH2 (e.g., Xu et al., 2009; Buschmann et al., 2010), were found to bind to both cytoskeletal filaments and especially in the case of KCH2, to crosslink actin and microtubules (Xu et al., 2009). Likewise, some plant myosins have been found to colocalize with microtubular structures, such as the mitotic spindle (e.g., Sun et al., 2018 for MYOSIN XI) or to directly interact with microtubules (Wu and Bezanilla, 2014 for MYOSIN VIII).

The plant interphase cortical array is a widespread microtubule system lying at the close vicinity of the plasma membrane, and it is intimately associated with cell growth and differentiation (Elliott and Shaw, 2018b). It can promptly reorganize in response to physical (reviewed in Lindeboom et al., 2013; Nakamura, 2015; Hamant et al., 2019), or hormonal (Vineyard et al., 2013; Elliott and Shaw, 2018a; Adamowski et al., 2019; True and Shaw, 2020) signals, in order to redefine cell growth directionality by blueprinting the orientation of cellulose deposition in the overlying cell wall (Chen et al., 2016).

The directional growth of plant cells requires cortical microtubules of uniform orientation. At large, this is achieved through microtubule interactions mediated by MAPs. Symmetry breaking in the cortical array arises from several different mechanisms, which include the spatial control of microtubule nucleation (Lindeboom et al., 2013), or microtubule severing (reviewed in Luptovčiak et al., 2017), the tight regulation of plus-end (Galva et al., 2014; Lindeboom et al., 2019), or minus-end (Nakamura et al., 2018) stability and dynamics, and the bundling or elimination of microtubules that encounter each other during their end-wise dynamic length fluctuations (Dixit and Cyr, 2004; Wightman and Turner, 2007; Zhang et al., 2013).

Based on the angle of contact, microtubule encounters may have either a constructive, or destructive outcome, leading to sustained microtubule growth at the preferred orientation, or initiating a catastrophe event eliminating microtubules of the unfavorable orientation (Wightman and Turner, 2007; Zhang et al., 2013). The outcome of microtubule convergence depends on the angle of encounter (Chi and Ambrose, 2016). If the angle is greater than 40°, the encounter results in either a catastrophe (a rapid shrinkage initiated at the tip of the microtubule that touches the lattice of another), or a crossover, where katanin-mediated severing may selectively occur and cleave one of the two microtubules (Wightman and Turner, 2007; Zhang et al., 2013). When the angle of encounter is less than 40°, the microtubules tend to co-align and bundle (Dixit and Cyr, 2004) by means of physical crosslinking via MAPs, leading eventually to the formation of a biased array with predominant orientation and parallel microtubule arrangement (van Damme et al., 2004).

From *in vitro* studies based on MAP65-1, it was shown that it can exist in a monomeric state capable of coating individual microtubules, being able to dimerize in a "zippering" process and construct 25 nm cross bridges when two antiparallel microtubules come in close contact (Gaillard et al., 2008; Tulin et al., 2012). In sharp contrast, the human MAP65 homolog PRC1 (Protein Regulator of Cytokinesis 1) and likewise the fission yeast homolog Ase1p (Anaphase spindle

elongation 1), form obligate dimers or homotetramers. In this case, formation of cross bridge depends on the flexibility of the oligomeric molecule, which assumes a rigid structure when confined in the overlap of two antiparallel microtubules (Subramanian et al., 2010).

Regardless of the mechanisms leading to their crosslinking, microtubule bundling is essential for the building of universal microtubule systems, such as the premitotic preprophase microtubule band and the interzonal telophase system. Moreover, the coalescence of adjacent microtubules to tight bundles was shown to be related to the morphogenesis of particular cell types with unique cell wall patterning such as differentiating tracheary (Mao, 2006; Pesquet et al., 2010; Derbyshire et al., 2015) and protoxylem elements (Schneider et al., 2020).

Apart from such developmental processes, environmental factors and hormones also induce symmetry breaking in the cortical array (e.g., Elliott and Shaw, 2018b; True and Shaw, 2020). Although katanin-mediated severing was already shown to have a major contribution in the induction of uniform microtubule orientation (e.g., Chen et al., 2014; Sassi et al., 2014; reviewed in Luptovčiak et al., 2017), the role of bundling by means of physical crosslinking of adjacent microtubules has not been addressed extensively.

From the MAPs related to the formation of microtubule bundles, the MAP65 family is the best characterized. Based on transmission electron micrographs, MAP65 proteins exemplified by MAP65-1 form 25 nm crossbridges between adjacent antiparallel microtubules (Chan et al., 1999; Tulin et al., 2012). Arabidopsis MAP65s bind to microtubules via C-terminal domain-located binding sites, and their function depends on the formation of homodimers via their N-terminal domain (Smertenko et al., 2004). For MAP65-1, MAP65-2, and MAP65-5, it has been shown that they do not promote microtubule polymerization, yet they slow down depolymerization rates (van Damme et al., 2004; Lucas et al., 2011). Moreover, MAP65-1 was recently shown to prohibit katanin from binding to microtubule bundles, thus protecting them from severing (Burkart and Dixit, 2019).

In Arabidopsis, nine genes belonging to this family were identified (Hussey et al., 2002), with different subcellular localizations, expression patterns throughout cell cycle (van Damme et al., 2004) and responses to in/activation during cell cycle (Smertenko et al., 2006; Boruc et al., 2017). Several MAP65s were observed to colocalize with mitotic microtubule arrays, specifically MAP65-1 (Smertenko et al., 2004), MAP65-2 (Lucas and Shaw, 2012), MAP65-3 (Caillaud et al., 2008; Ho et al., 2012; Vavrdová et al., 2019b), MAP65-4 (van Damme et al., 2004), MAP65-5 and MAP65-6 (Smertenko et al., 2008), with some of them being involved in the progression of mitosis (Beck et al., 2010, 2011; Sasabe et al., 2011; Li et al., 2017; Vavrdová et al., 2019a). Particularly in this case, the phosphorylation of MAP65s at their C-terminal domain via MITOGEN ACTIVATED PROTEIN KINASE 4 (MPK4) and MPK6 (Beck et al., 2010; Kosetsu et al., 2010; Sasabe et al., 2011), cyclin dependent kinases (Smertenko et al., 2006) and Aurora kinases, is a universal

negative regulation of their affinity for the microtubule surface (reviewed in Komis et al., 2011; Vavrdová et al., 2019a). More importantly, MAP65-1, MAP65-2 and MAP65-5 colocalize with cortical microtubules (van Damme et al., 2004; Lucas et al., 2011). Owing to their functional redundancy, co-expression and spatiotemporal colocalization (Lucas and Shaw, 2012), single mutants of either *MAP65-1* or *MAP65-2* do not show a discernible phenotype. However, in double *map65-1 map65-2* mutants an overall growth retardation was observed (Lucas et al., 2011).

Microtubule bundles represent a crowded environment hindering the possibilities to track the dynamic behavior of individual components with diffraction limited microscopy approaches. In a previous study, we demonstrated the capacity of structured illumination microscopy (SIM) to delineate the microtubule content of complex bundles in the cell cortex, and within the limitations of the method, to record dynamics of individual microtubules at accepted frame rates (Komis et al., 2014). In the present study, we extend this paradigm to follow the distribution and the dynamics of a universal microtubule crosslinking MAP, either alone or in parallel, to appropriately labeled microtubules.

For this reason, we employ different superresolution microscopy methods to extrapolate information on the organization and the dynamics of MAP65-2 in living *A. thaliana* hypocotyl epidermal cells, expressing appropriate fluorescent protein markers. We use Airyscan confocal laser scanning microscopy (ACLSM) and 2D SIM to obtain high resolution images of fluorescently labeled MAP65-2 and its association with cortical microtubule bundles. Dynamic properties of MAP65-2 are deciphered at different time scales using ACLSM, 2D SIM and total internal reflection (TIRF) SIM. Finally, the specific arrangement of MAP65-2 molecules is approached by single molecule photoactivation localization microscopy (PALM) from either the stochastic photoconversion of a mEos3.2-MAP65-2 molecular marker, or by calculating stochastic optical fluctuations of an eGFP-MAP65-2 fusion protein under specific illumination conditions.

MATERIALS AND METHODS

Plant Material

Arabidopsis thaliana (L.) was used for all experiments presented herein. Stably transformed Arabidopsis lines carrying *proMAP65-2:eGFP:MAP65-2*, *proMAP65-2:tagRFP:MAP65-2*, and *proMAP65-2:mEos3.2:MAP65-2* constructs, were prepared in a wild type ecotype Columbia (Col-0) background. Other Arabidopsis lines were stably transformed with *proCaMV35S:TUA6:GFP* or *proUBQ1:mRFP:TUB6* constructs and for colocalization purposes such lines were crossed with plants expressing appropriate MAP65-2 markers. Plants were grown on Phytagel (Sigma, Czechia) solidified half-strength Murashige–Skoog (1/2 MS) medium supplemented with 1% (w/v)

sucrose and under controlled environmental conditions (Beck et al., 2010).

Transgenic Plant Construction

Constructs for N-terminal fluorescent protein fusions of MAP65-2 were prepared using binary vector pGWB502link (Vavrdová et al., 2019b), a modified version of original destination vector pGWB502 (Nakagawa et al., 2007). All primers used for cloning are listed in **Supplementary Table S1**. PCR product (2616 bp) corresponding to the native promoter region of *MAP65-2* gene was obtained using PCR with primers pMAP65-2-F and pMAP65-2-R, which contain *Pac*I and *Acc*65I restriction site, respectively, and template genomic DNA isolated from *A. thaliana* Col-0. This PCR product was double-digested with *Pac*I and *Acc*65I and ligated into vector pGWB502link, also double-digested with *Pac*I and *Acc*65I, to generate construct pGWB502link-*proMAP65-2*. An open reading frame (ORF) of *MAP65-2* including stop codon was amplified from cDNA (isolated from *A. thaliana* Col-0) using primers MAP65-2cDNA-F and MAP65-2cDNA-R, which contain *Acc*65I and *Bsi*WI restriction site, respectively. PCR product encompassing ORF of *MAP65-2* was double-digested with *Acc*65I and *Bsi*WI and ligated into *Acc*65I digested pGWB502link-*proMAP65-2* to generate construct proGWB502link-*proMAP65-2:MAP65-2*. *Acc*65I and *Bsi*WI are isocaudomers producing the same sticky ends. Therefore, pGWB502link-*pMAP65-2:MAP65-2* contains only a single *Acc*65I restriction site in between *pMAP65-2* region and start codon of *MAP65-2* ORF. Coding region of *EGFP* was amplified with primers eGFP-F and eGFP-R, whereas coding region of *tagRFP* was amplified with primers tagRFP-F and tagRFP-R. All four primers contain a single *Acc*65I restriction site near their 5′-end. In addition, stop codon in the sequence of reverse primers is replaced with in frame stretch of nucleotides coding for a linker (EAAAK)₃ (Werner et al., 2006), which interconnects fluorescent protein tags with MAP65-2. PCR products containing coding regions of *EGFP* and *tagRFP* were digested with *Acc*65I and ligated into *Acc*65I digested pGWB502link-*proMAP65-2:MAP65-2* to generate constructs *proMAP65-2:EGFP:MAP65-2* and *proMAP65-2:tagRFP:MAP65-2*, respectively. To prepare the construct *proMAP65-2:mEos3.2:MAP65-2*, coding sequence of *mEos3.2* (Zhang et al., 2012) was optimized for expression in *A. thaliana* by GeneOptimizer^TM software (Thermo Fisher Scientific, United States) and synthetized by GeneArt^TM (Thermo Fisher Scientific, United States). In the 5′ to 3′ direction synthetic *mEos3.2* DNA fragment contains *Acc*65I restriction site upstream of the start codon, codon optimized ORF of *mEos3.2*, DNA sequence for (EAAAK)₃ linker replacing stop codon and *Acc*65I restriction site immediately following linker encoding sequence. Synthetic *mEos3.2* fragment was digested with *Acc*65I and ligated into *Acc*65I digested construct pGWB502link-*proMAP65-2:MAP65-2*. All prepared constructs were verified by Sanger sequencing and used for the preparation of stably transformed *A. thaliana* Col-0 ecotype transgenic plants as described before (Vavrdová et al., 2019b).

Positive T1 seedlings (i.e., the first generation following transformation) were selected either on the basis of antibiotic resistance, or upon detection of fluorescence. Few positive lines, showing similar fluorescence intensity, were chosen for subsequent propagation for each construct. In the T3 generation of selection, at least one homozygous line showing uniform fluorescence intensity was obtained for each construct. Fluorescence intensity was inspected at the root apex at the seedling stage, because the root apex is devoid of autofluorescence in both channels used for the selection (green channel for eGFP-MAP65-2, TUA6-GFP and unconverted mEos3.2-MAP65-2 and red channel for mRFP-TUB6, tagRFP-MAP65-2 and converted mEos3.2-MAP65-2). All the experiments were performed on T3 generation seedlings of one selected homozygous line for each construct. Functionality of all constructs was deduced by the fact that all transgenic seedlings, had no discernible phenotype and during microscopy exhibited the expected localization patterns of MAP65-2, either when visualized alone, or together with appropriately labeled microtubules.

Sample Preparation

Seedlings grown for 3–4 days after germination were selected according to the expression of constructs under an epifluorescence microscope. Selected seedlings were transferred on a microscopic slide (containing a spacer from double-sided sticky tape) into liquid 1/2 MS medium, and after applying a coverslip, parafilm was used to gently seal the sample at the margins of the coverslip, in order to prevent evaporation of medium and to stabilize samples for microscopic observation. When the 100 × /1.57 NA oil-immersion objective was used, samples were prepared within Attofluor cell chambers (Invitrogen, United States) and sandwiched between a high-precision and low-thickness-tolerance Nexterion round coverslip (facing the objective; coverslip thickness (D) = 0.17 ± 0.003 mm, diameter = 25 mm; Schott, Czech Republic; Komis et al., 2014, 2015), and a common 18 mm OD round coverslip of the same thickness. For TIRF-SIM imaging, 3–4 days old seedlings were secured in Attofluor cell chambers, embedded in 1% (w/v) low gelling temperature agarose dissolved in liquid 1/2 MS medium.

Microscopy Setup and Acquisition

For this study, following microscopes were used: AxioObserver LSM 880 with Airyscan (ACLSM; Carl Zeiss, Germany), AxioImager Z.1 equipped with the Elyra PS.1 superresolution system supporting the SIM and PALM/STORM module (Carl Zeiss, Germany) and a custom built TIRF-SIM microscope maintained in the Advanced Imaging Center of Janelia Research Campus (Kner et al., 2009; Ashburn, United States). With the ACLSM, either 40×/1.40 NA, or 63×/1.40 NA, oil-immersion, Plan Apochromat objectives were used with appropriate oil (Immersol 518F with refractive index of 1.518). Single photon excitation laser lines were used throughout with the 488 nm line for GFP excitation and 561 nm for mRFP and tagRFP excitation. Appropriate beam splitters and emission fluorescence filter blocks (BP420-480+BP495-550 for GFP detection and BP495-550 + LP570 for mRFP and tagRFP detection) were used in ACLSM and signal was detected by a 32 GaAsP detector with fully opened pinhole. Samples were scanned with the super-resolution mode of the ACLSM allowing optimum resolution

for acquired single Z-stacks or time-lapsed 2D acquisitions. Owing to the effective light-collecting capacity of the ACLSM and the sensitivity of the GaAsP detector the laser power at the excitation was set to a level not exceeding 2% of the range available. Acquired data were analyzed with Zen 2014 software (Blue Version; Carl Zeiss, Germany).

For SIM acquisitions with the Zeiss Elyra PS.1 platform, either 63×/1.40 NA or 100×/1.57 NA, oil-immersion, Alpha Plan Apochromat objectives were used with Immersol 518F and Immersol HI (with refractive index of 1.66), respectively. Samples were illuminated with a 488 nm laser line for eGFP excitation and a 561 nm laser line for mRFP or tagRFP excitation. For eGFP a BP495-575/LP750 filter was used while for mRFP or tagRFP a BP570-620/LP750 was used. Recordings were done using a PCO.Edge 5.5 sCMOS camera. For highest resolution possible samples were illuminated with five rotations and five phase steps, while for time lapsed imaging rotations of the patterned light were restricted to three (Komis et al., 2014, 2015). Reconstruction of SIM images and generation of kymographs were done using Zen software with appropriate licenses. The TIRF-SIM recordings were done with a custom built system and house written software as previously published (Kner et al., 2009). Owing to the setup of sample preparation we obtained very stable recordings over periods between 10–30 min, without loss of focus.

PALM localizations were performed on the dedicated Elyra PS.1 microscopy platform. Photoconversion of the green emitter form of mEos3.2 (excited with a 488 nm laser line and visualized through a BP420-480/BP495-560/LP650 dual bandpass/longpass filter) to the red emitter form, was done using a 405 nm laser line and a 561 nm excitation line. For simultaneous activation and excitation of the photoconverting form of mEos3.2 (i.e., molecules converting to the red emitter form), a BP420-480/BP570-640/LP740 dual bandpass/longpass filter was used. Photons were collected by the EM CCD sensor of an Andor iXon 897 Ultra camera without EM gain. Illumination of the sample was done using either the Highly Inclined and Laminated Optical Sheet regime (HILO; Tokunaga et al., 2008), or the ultra-high power TIRF mode of the system. For improving precision of localization, photons of stochastically photoconverting mEos3.2 molecules, were captured in time series experiments of 5,000 – 10,000 time points with exposure times ranging between 40 ms and 80 ms. The readout was processed using the PALM module of Zen software and since localization was done in 2D, overlapping localizations were discarded. In the example given in the appropriate section, results are presented both collectively and for representative examples of individual localizations.

Occasionally, more conventional fluorophores such as GFP and its variants, eGFP and YFP, may exhibit fluorescence intensity fluctuations under special conditions of excitation at or out of their nominal excitation wavelength (reviewed in Bagshaw and Cherny, 2006). For example, eGFP was shown to blink at acidic pH values when illuminated with a 405 nm laser (Haupts et al., 1998) or it may exhibit oxidative photoconversion to a red emitter following excitation with a 532 nm laser line (Sen et al., 2019). The versatility of more conventional fluorophores in SMLM has led to the development of unique methods including Stochastic Optical

Fluctuations Imaging (SOFI; Dertinger et al., 2009) or Bayesian analysis of blinking and bleaching (3B; Cox et al., 2012) with a very big potential to broaden SMLM applications in plants.

Optical fluctuations of eGFP, were recorded in a similar way as described for mEos3.2, by illuminating the sample simultaneously with the 405 nm and the 488 nm laser lines of Elyra PS.1, using the BP420-480/BP495-560/LP650 dual bandpass/longpass filter. The use of 405 nm illumination was previously shown to promote emission fluctuations of eGFP and was used accordingly (Marcus and Raulet, 2013). Better photon counts were achieved under the ultra high power TIRF mode compared to HILO illumination.

Image Processing and Quantitative Analysis

Raw ACLSM and SIM images were acquired with Zen software. Fluorescence intensity profiling was performed as described previously (Komis et al., 2014). Briefly, intensity profiles were measured directly in Zen software. Raw values were exported to Microsoft Excel (Microsoft, United States), normalized to a range between 0 and 1 and plotted against distance. These scatterplots were used to measure full-width at half maximum (FWHM) with Image J (Schneider et al., 2012). TIRF-SIM images were obtained and processed with custom-written software (Kner et al., 2009). In this case, fluorescence intensity profiles were measured in Image J, then previously described workflow was followed (Komis et al., 2014).

Similarly, for analysis of microtubule bundles and differential distribution of MAP65-2 along microtubules, both perpendicular and longitudinal fluorescence intensity profiles were done in Zen software. Due to the fact that MAP65-2 decorates microtubules in a discontinuous manner, for each perpendicular fluorescence intensity measurement five profiles were drawn and their values were averaged. Altogether, eight sets (consisting of measurements of a bundle and two branches stemming from it) of perpendicular profiles were made. After exporting raw values to Microsoft Excel, data were normalized and plotted against distance.

Pearson's (Dunn et al., 2011) and Manders' (Manders et al., 1992) correlation coefficients denoting the extend of colocalization between tagged microtubules and MAP65-2 protein fusions, were automatically extrapolated by means of the colocalization tool of the licensed version of Zen software. Colocalizations were automatically thresholded according to Costes (Costes et al., 2004).

From time-lapsed images taken by ACLSM and SIM, kymographs were generated with the appropriate plugin of Zen software (Blue version). For generating kymographs of TIRF-SIM acquisitions, we instead used the Multi Kymograph plugin of Image J[1]. Angles and distances needed for calculations were measured in ImageJ. Parameters describing MAP65-2 dynamics were calculated as described previously (Smal et al., 2010). Briefly, growth rates were calculated by correcting the tangent values of slopes corresponding to growth or shrinkage phases, with the pixel size and the frame rate of each respective acquisition. Measures deduced from kymographs included plus-end growth

---

[1]https://www.embl.de//eamnet/html/body_kymograph.html

and shrinkage rates and catastrophe/rescue frequencies and time spent in growth and shrinkage. Catastrophe rates were deduced by dividing the sum of shrinkage onset events observed by the total amount of time spent in growth (extension) phases, while rescue frequencies were deduced by dividing the sum of growth onset events observed by the total amount of time spent in shrinkage (retraction) phases (Gardner et al., 2013; Kapoor et al., 2019). Briefly the equations used in this case can be formulated as:

$$f_{cat} = \frac{N_{cat}}{\Sigma t_{growth}}$$

for the calculation of catastrophe frequencies, where f_{cat} is the catastrophe frequency, N_{cat} is the total number of catastrophes measured and Σt_{growth} is the total time spent in growth, while similarly the calculation of rescue frequency is based on the formula:

$$f_{res} = \frac{N_{res}}{\Sigma t_{shrinkage}}$$

where f_{res} is the rescue frequency, N_{res} is the total number of rescues measured and $\Sigma t_{shrinkage}$ is the total time spent in shrinkage.

Statistical Analysis

For statistical analysis, all datasets were first tested for normality of data distribution by means of Shapiro–Wilk test. Based on the results of Shapiro–Wilk test, either unpaired two-sample t-tests or Mann–Whitney U tests were performed. All tests were calculated in STATISTICA (version 13.4.0.14; Statsoft, United States). Statistical significance was inferred according to the calculated p-values.

RESULTS

Superresolution of MAP65-2 Decorating Microtubules

The purpose of our study, was to report the fine structure of microtubule bundles and track the organization and dynamics of fluorescently tagged MAP65-2 within such bundles. We chose for this purpose three methods, namely, ACLSM, widefield 2D SIM and TIRF-SIM, which were initially characterized in terms of spatial resolution at the settings used for time-lapsed imaging. As previously mentioned, the quantitative measure in this case was the FWHM of normalized fluorescence intensity linear profiles encompassing the entire microtubule or MAP65-2 signal width.

When comparing the resolution of TUA6-GFP-labeled individual microtubules visualized by means of ACLSM (**Figures 1A,B**) or 2D SIM (**Figures 1E,F**), we found significant differences especially after defining the FWHM of normalized intensity profiles (**Figures 1C,D** cf. **Figures 1G,H**) using in both cases a 63×/1.40 NA oil immersion objective. Quantitatively the resolution of individual microtubules averaged at 186 ± 27 nm (mean ± SD; N = 43, **Figure 1D**) with ACLSM and at 144 ± 25 nm (mean ± SD; N = 44, **Figure 1H**) with 2D SIM. This difference is statistically significant (t-value = −7.1839; p < 0.001). However the FWHM value reported for 2D SIM

was higher for the 63 × /1.40 NA objective than that reported previously (Komis et al., 2014) owing to the use of lower Wiener filter during image reconstruction to compensate for the lower signal to noise ratio of the hypocotyl cells used herein.

As 2D SIM and TIRF-SIM were used for time lapsed recordings of eGFP-MAP65-2, we compared their resolution potential in cells expressing eGFP-MAP65-2 and referenced them against ACLSM. In this case, eGFP-MAP65-2 decorated microtubules were resolved by ACLSM (**Figures 2A–C**) at 177 ± 19 nm (FWHM of normalized intensity profiles; mean ± SD; N = 36, **Figure 2D**). For 2D SIM (**Figures 2E–G**) and TIRF-SIM (**Figures 2I–K**) the resolution of eGFP-MAP65-2 decorated microtubules was considerably improved (133 ± 20 nm; mean ± SD; N = 39, **Figure 2H** for SIM; 130 ± 28 nm; mean ± SD; N = 55, **Figure 2L** for TIRF-SIM). As denoted, 2D SIM and TIRF-SIM showed significantly better resolution compared to ACLSM with either TUA6-GFP (**Figures 3A,E**) or eGFP-MAP65-2 (**Figures 3B,E**), without showing differences when compared to each other (**Figures 3B,E**). Similarly, when comparing the resolution of the two labeled structures, we did not find considerable difference between them neither by ACLSM (**Figures 3C,E**) or by 2D SIM (**Figures 3D,E**).

For dual channel visualization of both microtubules and MAP65-2, it was necessary to analyze the resolution of red tags for both microtubules (mRFP-TUB6; **Supplementary Figures S1A–C**) and MAP65-2 (tagRFP-MAP65-2) when visualized with both ACLSM and 2D SIM (**Supplementary Figures S1E–G** for ACLSM and **Supplementary Figures S1I–K** for 2D SIM). The mRFP-TUB6-labeled microtubules were only visualized with ACLSM and in this case they were resolved at an average FWHM of 188.044 ± 19.93 nm (mean ± SD; N = 35; **Supplementary Figure S1D**). Likewise, tagRFP-MAP65-2 was resolved by ACLSM at an average FWHM of 176.115 ± 18.08 nm (mean ± SD; N = 47; **Supplementary Figure S1H**) while the respective resolution by 2D SIM was 129.161 ± 14.46 nm (mean ± SD; N = 43; **Supplementary Figure S1L**). Comparison of green with red-labeled structures regardless of the used microscopy platform did not yield any significant differences. The resolution reached for TUA6-GFP and mRFP-TUB6-labeled microtubules was comparable (**Supplementary Figures S2A,E**). Similarly we did not note any significant differences between tagRFP-MAP65-2 and eGFP-MAP65-2 observed on either ACLSM (**Supplementary Figures S2B,E**) or 2D SIM (**Supplementary Figures S2C,E**). By contrast tagRFP-MAP65-2 was considerably better resolved by means of 2D SIM compared to ACLSM (p < 0.001) further corroborating the resolution efficiency differences between the two systems (**Supplementary Figures 2D,E**).

Detailed View on MAP65-2 Colocalizing With Microtubules

One major point in the analysis of microtubule bundles, is the efficiency with which individual microtubules can be deciphered and co-visualized with other molecules inhabiting the bundle, including bundling proteins such as MAP65-2. To co-visualize

FIGURE 1 | Comparison of ACLSM and SIM in resolving details of TUA6-GFP labeled cortical microtubules in hypocotyl epidermal cells of Arabidopsis labeled.
(A) Overview of image from ACLSM (objective 63×/1.40 NA). **(B)** Magnified view of the boxed area in **(A)**. The white line corresponds to a perpendicular profile, for normalized intensity measurement. **(C)** Graph depicting normalized fluorescence intensity corresponding to the profile shown in **(B)**. **(D)** Averaged, coaligned, and normalized intensity profiles of individual TUA6-GFP-labeled microtubules visualized by ACLSM (N = 43; FWHM – full-width at half maximum). **(E)** Overview of image from 2D-SIM (objective 63×/1.40 NA). **(F)** Magnified view of the boxed area in **(E)**. The white line in **(F)** shows a profile, used for normalized intensity measurement. **(G)** Representative plot of a normalized fluorescence intensity corresponding to the profile drawn in **(F)**. **(H)** Averaged, coaligned, and normalized intensity profiles of individual TUA6-GFP-labeled microtubules visualized with 2D-SIM (N = 44). Scale bars = 10 µm **(A,E)**, or 5 µm **(B,F)**, respectively.

microtubules and MAP65-2 and decipher their spatial relations in composite cortical microtubule bundles, we preferentially used ACLSM. 2D SIM was also used, but due to the configuration of the platform, it was possible to acquire images at the two channels sequentially with significant delays compared to ACLSM, where sequential imaging was done considerably faster. Moreover, owing to its detection principle, ACLSM allows the best photon collection even at suboptimal signal-to-noise ratios at approximately the same resolution as 2D SIM (**Figures 1**, **2**; Huff, 2016).

Thus, ACLSM was used for imaging epidermal hypocotyl cells co-expressing eGFP-MAP65-2 with mRFP-TUB6, or tagRFP-MAP65-2 with TUA6-GFP markers. We were able to co-visualize cortical microtubules and MAP65-2, while avoiding bleaching issues that were particularly limiting to tagRFP-MAP65-2 visualization by 2D SIM. To properly address the nature of MAP65-2 colocalization with microtubules, two

approaches based on light intensity profiling were used as described previously (Komis et al., 2014). By employing these approaches, we wanted to verify, whether MAP65-2 follows the same trends that were reported for cortical microtubules (Komis et al., 2014). The first trend specifies the composite nature of cortical microtubules, as microtubule bundles containing different number of microtubules can not only be discriminated from each other, but the fluorescence intensity maximum within a microtubule bundle is linearly depending on the number of microtubules incorporated in it. In composite bundles consisting of many microtubules, intensity fluctuations along linear profiles can reflect the number of individual components (Komis et al., 2014). Apart from this goal, we were also interested whether we could observe cases, where the tagRFP-MAP65-2 signal would be close to the signal corresponding to TUA6-GFP-labeled microtubules, yet the signals would not completely overlap, meaning there is MAP65-2 signal outside of the tightly bound

FIGURE 2 | Comparison of ACLSM, SIM and TIRF-SIM in resolving MAP65-2 decoration of cortical microtubules in hypocotyl epidermal cells of Arabidopsis expressing eGFP-MAP65-2. **(A)** ACLSM overview. **(B)** Close-up image of the boxed area of **(A)** with profile used for normalized intensity measurement (white line). **(C)** Representative quantitative depiction of normalized fluorescence intensity of the individual profile drawn in **(B)**. **(D)** Averaged, coaligned, and normalized intensity profiles of basal MAP65-2 decoration of microtubules (N = 36; FWHM, full-width at half maximum). **(E)** 2D-SIM overview (objective 63×/1.40 NA). **(F)** Magnified view of boxed area in **(E)** with the perpendicular profile, for normalized intensity measurement (white line). **(G)** Graph depiction of the normalized intensity corresponding to the profile drawn in **(F)**. **(H)** Averaged, coaligned, and normalized intensity profiles of basal MAP65-2 decoration of microtubules (N = 39). **(I)** Overview image from TIRF-SIM (objective 100×/1.49 NA). **(J)** Magnification of the boxed area of **(I)**. **(K)** Normalized intensity of the perpendicular profile drawn in **(J)**. **(L)** Averaged, coaligned, and normalized intensity profiles of basal MAP65-2 decoration of microtubules visualized with TIRF-SIM (N = 55). Scale bars = 10 μm **(A,E)**, 5 μm **(B,F,I)**, and 2 μm **(J)** respectively.

FIGURE 3 | Quantitative analysis of resolution achieved by using ACLSM, SIM, and TIRF-SIM in resolving details of cortical microtubules (MTs) with TUA6-GFP marker or eGFP-MAP65-2 decoration of cortical MTs. Boxplots present the full-width at half maximum values (FWHM). **(A)** Comparison of ACLSM and SIM in resolving MTs with TUA6-GFP marker. **(B)** Comparison of ACLSM, SIM, and TIRF-SIM in resolving eGFP-MAP65-2 decoration of MTs. **(C)** Resolution reached by ACLSM for either TUA6-GFP or eGFP-MAP65-2. **(D)** Resolution reached by SIM for either TUA6-GFP or eGFP-MAP65-2. **(A–E)** Unpaired two-sample t-tests were used for statistical analysis (*** significant at p 0.001, * significant at p 0.05, ns, not statistically significant) and the results are in **(E)**. Description of box plot: average is presented by ×, median by the middle line, 1st quartile by the bottom line, 3rd quartile by the top line; the whiskers lie within the 1.5 × interquartile range (defined from the 1st to the 3rd quartile), outliers are marked by points.

microtubules. In quantitative terms, colocalization of tagRFP-MAP65-2 with TUA6-GFP marked microtubules is quite tight as evidenced by colocalization analyses of either the entire cortical microtubule system (**Figures 4A–C,G**) or selected regions of interest that selectively encompass bundled microtubules (**Figures 4D–F,H**). Quantitative assessment of tagRFP-MAP65-2 with TUA6-GFP in the full frame shown in **Figures 4A–C**, showed collinearity of both signals with a Pearson's coefficient value of 0.964 and a Manders coefficient value of 0.891. In the selected rectangular ROI, the respective Pearson's coefficient is 0.604 and the Manders coefficient is 0.92.

To answer the first question regarding the linear increase in signal intensity when microtubule bundles blend together, we searched the images of Arabidopsis line stably expressing both tagRFP-MAP65-2 and TUA6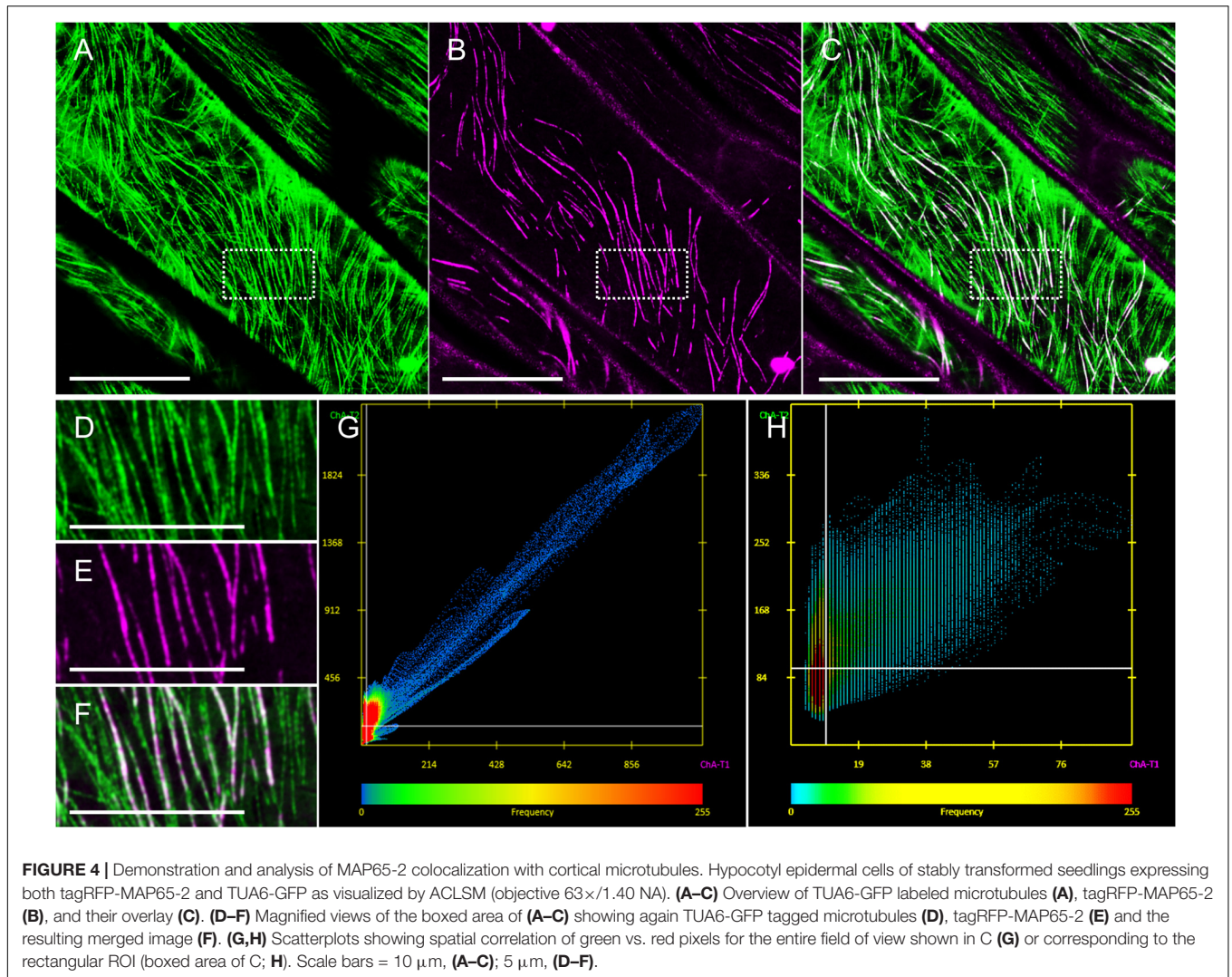-GFP markers for cases showing events of microtubule bundles branching in two smaller branches (**Figures 5A–C**). Then, we measured the fluorescence intensity profiles perpendicularly to the original bundle as well as to its two branches. To prevent errors stemming from local deviations in fluorescence intensity maxima of either fluorescent signal, five independent measurements were performed on each measured branch and these data were averaged. Such averaged measurements ($N = 8$; **Figures 5D,E**), display a clear distinction between the absolute fluorescence intensity maximum of the original bundle, the smaller and the larger branch. Moreover,

the linear correlation coefficient between the two signals was inferred from absolute fluorescence intensity maxima of all three microtubule bundles of different complexity (i.e., differing in the microtubule number they accommodate; **Figures 5F,G**). For both TUA6-GFP-labeled microtubules (**Figure 5F**) and tagRFP-MAP65-2 (**Figure 5G**), the high values of the linear correlation coefficient ($R^2 = 0.9966$, respectively $R^2 = 0.9786$) confirm the observation, that both microtubules and MAP65-2 accumulate equally during the increase of the bundle size.

Next, using the images of the same Arabidopsis line with two markers tagRFP-MAP65-2 and TUA6-GFP, we focused on areas showing signal intensity fluctuation alongside the decorated microtubules. To examine whether these changes in the signal intensity of TUA6-GFP-labeled microtubules would be mirrored in signal intensity changes of tagRFP-MAP65-2, we draw longitudinal profiles along microtubules. A representative measurement is shown in **Figures 5H–K**. Due to considerable differences in absolute intensity values between signals corresponding to tagRFP-MAP65-2 and TUA6-GFP, the values from longitudinal profiles were normalized before they were plotted against distance (**Figure 5K**). Such linear profiles were discontinuous, reflecting the uneven incorporation of TUA6-GFP in the microtubule lattice (Komis et al., 2014) and the similarly uneven binding of MAP65-2 alongside microtubule bundles. Signal intensity fluctuations of tagRFP-MAP65-2 were

FIGURE 4 | Demonstration and analysis of MAP65-2 colocalization with cortical microtubules. Hypocotyl epidermal cells of stably transformed seedlings expressing both tagRFP-MAP65-2 and TUA6-GFP as visualized by ACLSM (objective 63×/1.40 NA). **(A–C)** Overview of TUA6-GFP labeled microtubules **(A)**, tagRFP-MAP65-2 **(B)**, and their overlay **(C)**. **(D–F)** Magnified views of the boxed area of **(A–C)** showing again TUA6-GFP tagged microtubules **(D)**, tagRFP-MAP65-2 **(E)** and the resulting merged image **(F)**. **(G,H)** Scatterplots showing spatial correlation of green vs. red pixels for the entire field of view shown in C **(G)** or corresponding to the rectangular ROI (boxed area of C; **H**). Scale bars = 10 μm, **(A–C)**; 5 μm, **(D–F)**.

not coinciding with those of the TUA6-GFP signal. However, the overall changes along both linear profiles showed the same trend of signal intensity increase pending on the increase in bundle complexity, suggesting that the abundance of MAP65-2 at a specific place depends on the composition of a microtubule bundle at that place.

Last, during a careful analysis of ACLSM images of Arabidopsis lines carrying eGFP-MAP65-2 and mRFP-TUB6, or tagRFP-MAP65-2 and TUA6-GFP marker couples, respectively, we noted that there were cases, where MAP65-2 was observed to localize both within microtubule bundles and in between two parallel microtubule bundles in the near proximity to each other (**Figures 6A–F,H–M**). These observations were addressed by normalized intensity profiles drawn perpendicularly to composite microtubule bundles (**Figures 6G,N**). The graphs confirmed the visual observation and further demonstrated association of MAP65-2 with microtubule bundles and its localization between these bundles by showing that peak intensities of TUA6-GFP and tagRFP-MAP65-2 are offset (**Figures 6G,N**). To strengthen our observation and to dismiss the possibility of noting this

information due to poor resolution, we decided to check whether similar situation can be found in images with higher resolution. For this, we used SIM with a 100×/1.46 NA, oil-immersion objective. Again, the same observation was confirmed (**Figures 6O–T**) and proved in normalized fluorescence intensity profile plotted against distance (**Figure 6U**) showing offset position of peak intensities of TUA6-GFP and tagRFP-MAP65-2.

Dynamics of MAP65-2 Localization

Due to the ever-changing nature of cortical microtubules, MAP65-2, as a protein associated with microtubules, is expected to follow microtubule dynamics (e.g., Lucas et al., 2011). Concomitant recordings tracking the dynamics of both eGFP-MAP65-2 and mRFP-TUB6 were done using the ACLSM at frame rates of ca. 0.67 fps (time interval of 1.5 s). The eGFP-MAP65-2 follows microtubule labeling at areas of potential antiparallel microtubule overlaps (**Figures 7A–F** and **Supplementary Video S1**), whereas the length fluctuations of eGFP-MAP65-2 and mRFP-TUB6 closely follow each other (**Figures 7G–I**).
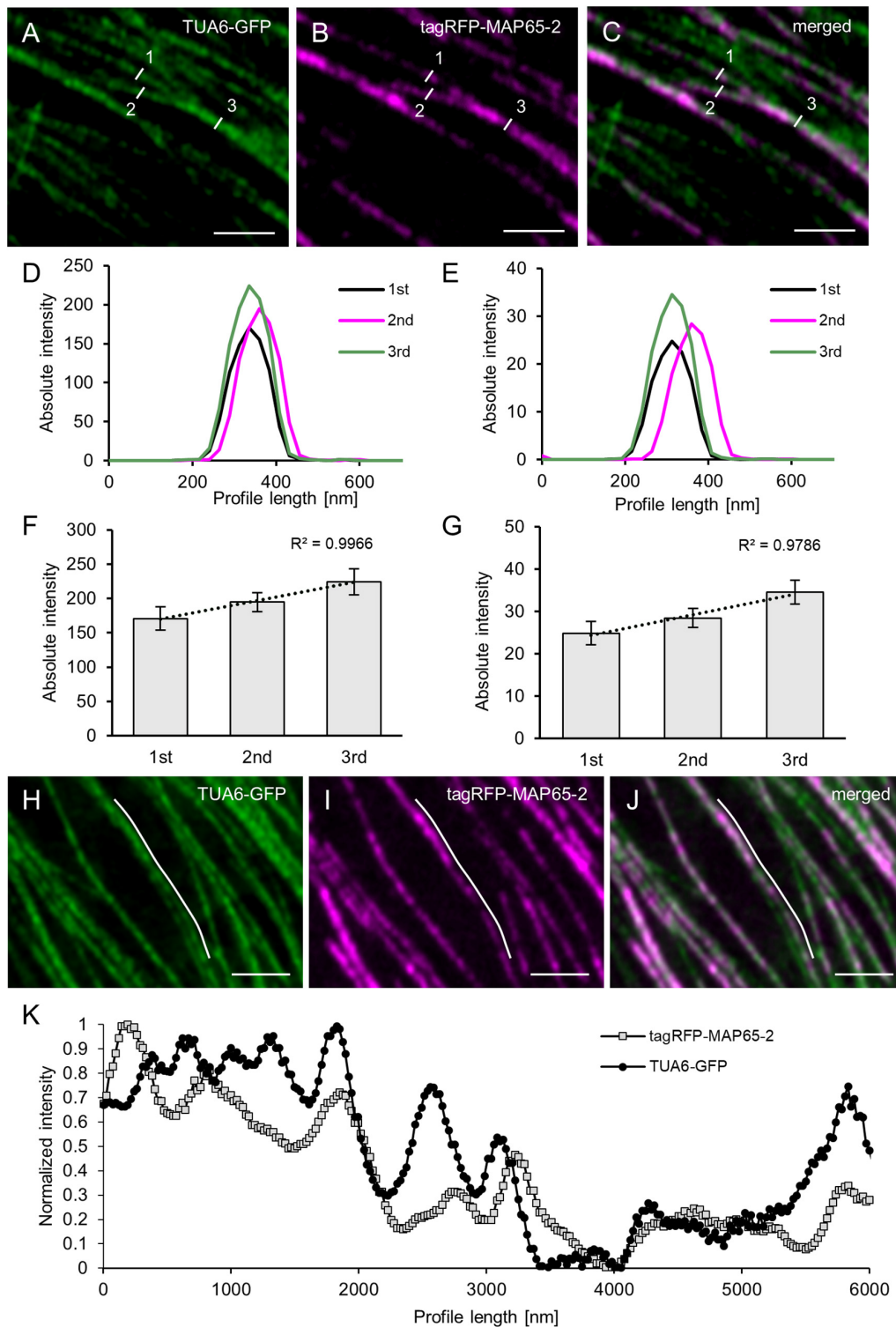
FIGURE 5 | Quantitative analysis of MAP65-2 colocalization with cortical microtubules. Hypocotyl epidermal cells of stably transformed Arabidopsis lines expressing both tagRFP-MAP65-2 and TUA6-GFP were observed in ACLSM (objective 63×/1.40 NA). **(A–C)** Overview of an area with microtubule branching with TUA6-GFP shown in green **(A)**, tagRFP-MAP65-2 in red **(B)** and **(C)** the showing the overlay; measured microtubule bundles are visualized with white lines and labeled with given numbers according to their strength (1 being the weakest and 3 the strongest bundle). Microtubule bundles were quantified by fluorescence intensity profiling and averaged values are shown in **(D)** for TUA6-GFP and **(E)** for tagRFP-MAP65-2. Quantitative evaluation is given in **(F)** for TUA6-GFP and **(G)** for tagRFP-MAP65-2 (mean ± SD; R2, linear correlation coefficient; N = 8, 5 technical repetitions). **(H–J)** Overview of a microtubule bundle, TUA6-GFP shown in green **(H)**, tagRFP-MAP65-2 in red **(I)** and **(J)** is a merged picture; white line visualizes longitudinal profile, which is shown in **(K)**, where is demonstrated fluctuation of fluorescence intensities. Scale bars = 2 μm.

FIGURE 6 | Colocalization of MAP65-2 with microtubules. **(A–C)** ACLSM overview of microtubule bundles in hypocotyl cells coexpressing mRFP-TUB6 **(A)** and eGFP-MAP65-2 **(B)**; merged picture is shown in **(C)**. Boxed area in **(A–C)** is shown in **(D–F)**; **(D)** mRFP-TUB6, **(E)** eGFP-MAP65-2, **(F)** overlay; yellow line in **(D–F)** delineates fluorescence intensity profile, shown in **(G)**. Profile intensity measurement was normalized, plotted against distance and the resulting graph is in **(G)**. **(H–J)** ACLSM co-visualization of microtubule bundles in line coexpressing TUA6-GFP **(H)** and tagRFP-MAP65-2 **(I)**; overlay is displayed in **(J)**. Boxed area in **(H–J)** is shown in **(K–M)**; **(K)** TUA6-GFP, **(L)** tagRFP-MAP65-2 and in **(M)** is overlay; yellow line in **(K–M)** delineates fluorescence intensity profile, shown in **(N)**. After normalization, profile intensity measurement was plotted against distance and the graph is in **(N)**. **(O–Q)** Images of line expressing TUA6-GFP **(O)** and tagRFP-MAP65-2 **(P)** and their colocalization **(Q)**. Boxed area in **(O–Q)** is shown in **(R–T)**; **(R)** TUA6-GFP, **(S)** tagRFP-MAP65-2 and in **(T)** is overlay; yellow line represents a perpendicularly drawn fluorescence intensity profile shown in **(U)**. After normalization, profile intensity measurement was plotted against distance and the graph is in **(U)**. Scale bars = 10 μm **(A–C,H–J,O–Q)**, 5 μm **(D–F,K–M)** or 2 μm **(R–T)**.

For more detailed analysis, we restricted time lapsed imaging to eGFP-MAP65-2. To address this issue, we employed 2D SIM and TIRF-SIM to survey eGFP-MAP65-2 dynamics at different temporal resolutions. In both cases, it was

possible to make recordings of durations ranging between 10 and 30 min, but with markedly different acquisition frame rates. With 2D SIM, images were acquired at frame rates between 0.22 fps to 0.4 fps (time intervals from
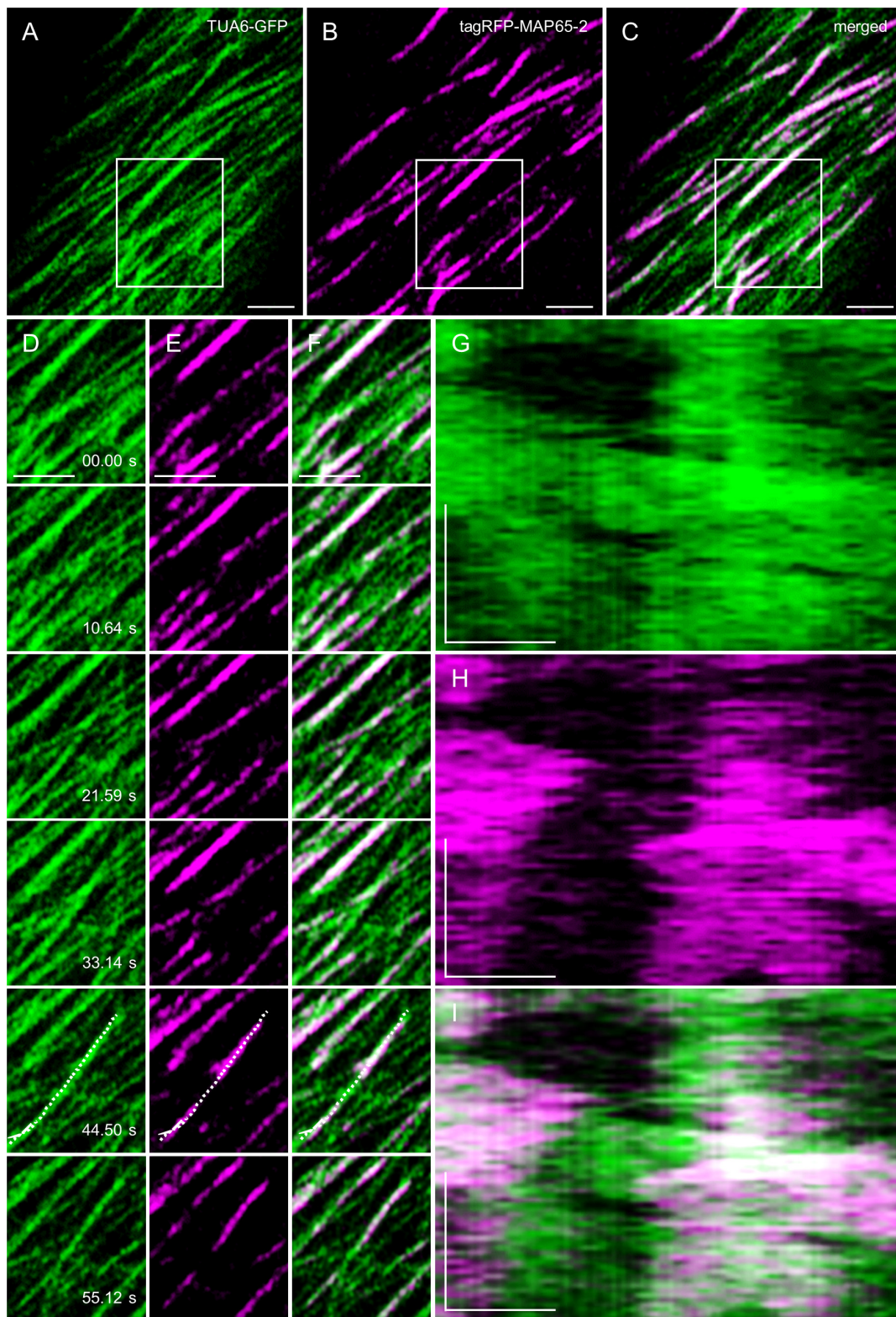
FIGURE 7 | MAP65-2 and microtubule dynamics visualized by ACLSM (see also **Supplementary Video S1**). **(A–C)** Is an overview of a hypocotyl epidermal cell of stably transformed line expressing both TUA6-GFP **(A)** and tagRFP-MAP65-2 **(B)** observed by ACLSM (objective 63×/1.4 NA); in **(C)** is merged picture. Area in boxes is shown in stills **(D–F)**, within which is the region of interest where kymographs were generated **(G–I)**. Stills in **(D)** show TUA6-GFP, in **(E)** show tagRFP-MAP65-2 and in **(F)** are stills from merged picture. In **(G)**, kymograph is shown for TUA6-GFP, in **(H)** for tagRFP-MAP65-2 and in **(I)** for merged picture. Scale bars = 2 μm **(A–F)**, 1 μm **(G–I)**. Time bars = 1 min **(G–I)**.

2.5 s to 4.5 s) while the TIRF-SIM recordings were done at frame rates between 1.33 fps to 10 fps (time intervals from 750 to 100 ms).

Since MAP65-2 is preferentially crosslinking antiparallel microtubules, the end-wise dynamics of eGFP-MAP65-2 do not follow the classical view of microtubule dynamics *per se*. MAP65-2 is closely tracking antiparallel microtubule plus ends and it only persists as long as the overlap between the microtubules does (Lucas et al., 2011). This was previously shown by simultaneous tracking of mCherry-MAP65-2 and GFP-TUA6 (Lucas et al., 2011), proving that end-wise microtubule dynamics are closely followed by approximate changes in the length of the MAP65-2 signal.

In agreement with previous observations (van Damme et al., 2004; Lucas et al., 2011), the dynamic behavior of MAP65-2 is similar to that of cortical microtubules. With 2D SIM, MAP65-2 decorating overlaps of antiparallel cortical microtubules displays periods of growth (extension) followed up with fast shrinkage (retraction; **Figures 8A,B** and **Supplementary Video S2**), mimicking the dynamic instability of plus ends of cortical microtubules. To quantify this behavior, kymographs were generated from the original images and parameters describing MAP65-2 dynamics were extrapolated from these kymographs (**Figure 8D**). In this case, the growth and shrinkage rates were $6.87 \pm 2.72\ \mu m\ min^{-1}$ ($N = 57$) and $21.35 \pm 6.38\ \mu m\ min^{-1}$ ($N = 43$), respectively. Moreover, frequencies of rescue and catastrophe events were 0.0107 and 0.0446, respectively.

2D SIM allowed to pursue dynamics of eGFP-MAP65-2 in more complex bundles, presumably accommodating more than two microtubules (**Figures 8A,C**). This is deemed by the higher fluorescence intensity and it is reflected in the resulting kymographs exhibiting areas of variable intensity above the background fluorescence (**Figure 8E**). Again, inferring from kymographs (**Figure 8E**), the growth and the shrinkage rates were $6.32 \pm 2.00\ \mu m\ min^{-1}$ ($N = 42$) and $17.08 \pm 4.84\ \mu m\ min^{-1}$ ($N = 30$), respectively. The frequencies of rescue and catastrophe events were 0.0114 and 0.0404, respectively.

Similar analysis was done using TIRF-SIM (**Figures 9A–C** and **Supplementary Video S3**), after the subsequent generation of kymographs (**Figures 9D,E**). Growth and shrinkage rates deduced from TIRF-SIM images were calculated as $5.04 \pm 1.30\ \mu m\ min^{-1}$ ($N = 53$) and $18.27 \pm 5.04\ \mu m\ min^{-1}$ ($N = 36$), respectively, which is comparable to the results from SIM. However, the frequencies of rescue and catastrophe events were in both cases higher compared to 2D SIM (0.0381 and 0.0864, respectively), probably due to the higher spatial and temporal resolution, which enabled more detailed measurement of dynamic changes.

Growth rates within individual bundles are similar to those calculated from more complex bundles but shrinkage is slower (**Figures 10A–C,G**). When comparing the two acquisition methods, both growth and shrinkage rates inferred by TIRF-SIM, were significantly slower than those obtained by 2D SIM ($p = 0.0067$ for growth; **Figures 10D,E,G** and $p = 0.0002$ for shrinkage; **Figures 10D,F,G**). This is probably owing to the big difference between the two systems in terms of sampling

frame rates. Since TIRF-SIM has essentially the same resolution potential like 2D SIM, it is probably collecting more frames without detectable length changes compared to 2D SIM.

Single Molecule PALM Localization of mEos3.2-MAP65-2

For visualization of the mEos3.2-MAP65-2 reporter we followed previously published settings to induce photoconversion and collect photons (Hoogendoorn et al., 2014; Hosy et al., 2015). The mEos3.2-based reporter of MAP65-2 reacted reasonably well albeit slowly during photoconversion experiments and image reconstruction after the acquisition of time series consisting of ca. 8,000–12,000 frames. Following the photoconversion of mEos3.2, PALM reconstruction resulted in the localization of well discernible single molecules compared to the respective TIRF image, where the signal was roughly continuous (**Figures 11A,B**). Individual localization events were recorded by variable photon numbers (**Figure 11C**) resulting to a precision ranging between 10 and 80 nm (38 nm $\pm$ 19 nm; mean $\pm$ SD; **Figures 11D,G**). In areas presumably corresponding to microtubule bundles, localization events exhibited an arrayed order by comparison to the continuous localization via TIRF (**Figures 11A,B,E**), which was further proven upon intensity profile quantification (**Figure 11H**). In most cases, localization resulted in the documentation of individual spot-like structures, possibly corresponding to individual mEos3.2-MAP65-2 molecules and not dimers (**Figures 11D,E**). Occasionally we documented spot duplets, i.e., spots that are very closely positioned (**Figure 11F**). Normalized fluorescence intensity profiling and averaging of the Rayleigh distances (at ca. 67% of the peak intensity) proved a resolution of 30.53 $\pm$ 5.28 (mean $\pm$ SD; $N = 17$; **Figure 11I**). Given that the physical length of the closely related MAP65-1 dimer is ca. 25 nm as judged from transmission electron micrographs of *in vitro* reconstituted microtubule bundles after negative staining (Tulin et al., 2012) it is likely that these localization events revealed by optical nanoscopy correspond to true MAP65-2 dimers.

Similar results were obtained when optical fluctuations of eGFP-MAP65-2 were recorded using TIRF illumination, a high laser power input at the sample and simultaneous illumination with the 405 nm laser line of Elyra PS.1 (**Figures 12A–E**). The major difference when comparing with mEos3.2 (**Figures 12F–J**), was that with eGFP-MAP65-2 we achieved much higher photon numbers per position, very rapidly, minimizing the time necessary to yield similar localization precision (**Figures 12E,J**).

DISCUSSION

The plant cytoskeleton consists of fine molecular structures, which cannot be properly characterized by means of light microscopy with the Abbe's limitation of 200 nm due to diffraction. Instead, transmission electron microscopy was used to describe microtubules and their complex nature of interactions with a pleiade of MAPs (e.g., Ledbetter and Porter, 1963; Chan et al., 1999). Despite its superior resolution and its irreplaceable role for examining supramolecular structures,

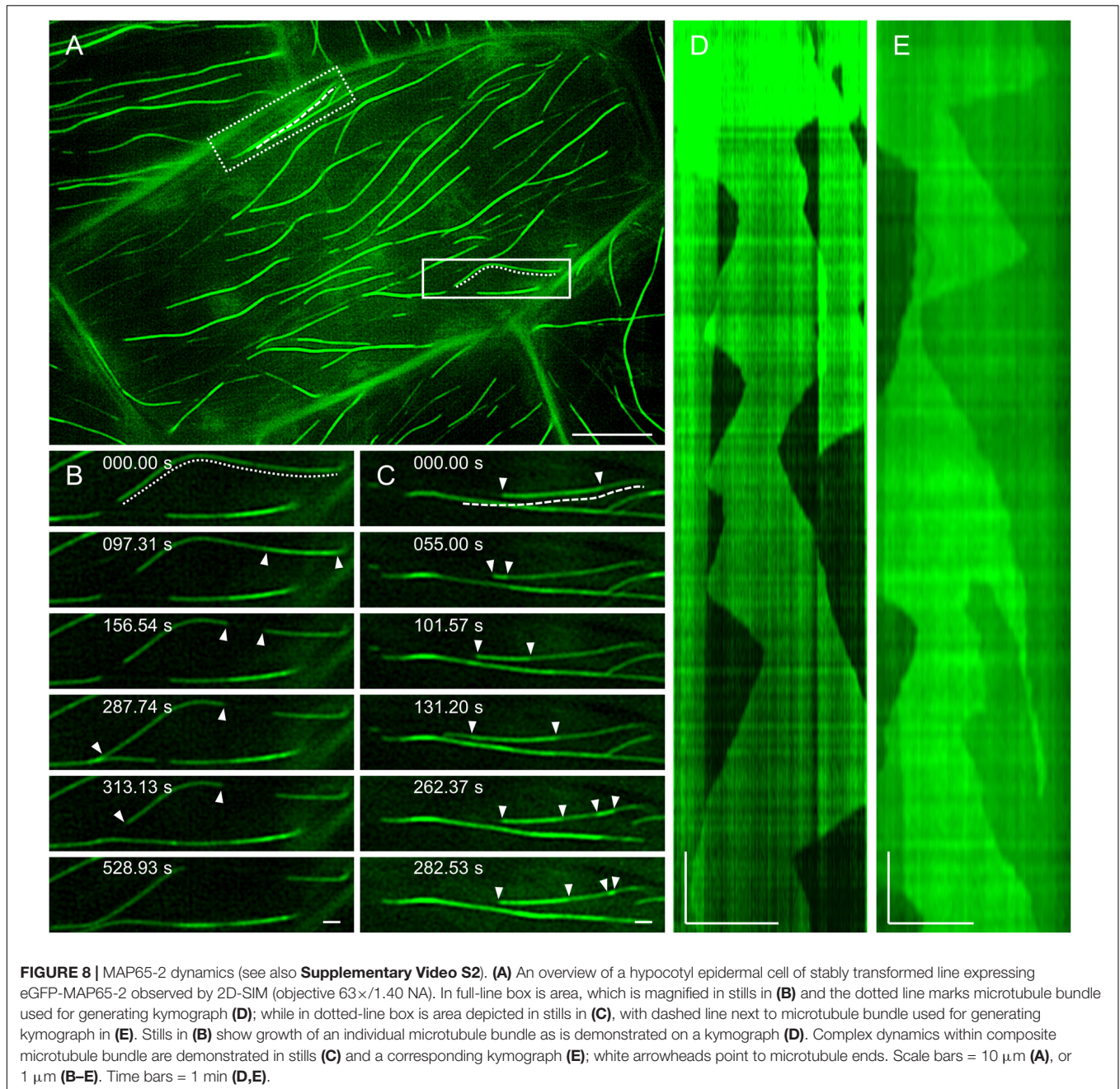**FIGURE 8 |** MAP65-2 dynamics (see also **Supplementary Video S2**). **(A)** An overview of a hypocotyl epidermal cell of stably transformed line expressing eGFP-MAP65-2 observed by 2D-SIM (objective 63×/1.40 NA). In full-line box is area, which is magnified in stills in **(B)** and the dotted line marks microtubule bundle used for generating kymograph **(D)**; while in dotted-line box is area depicted in stills in **(C)**, with dashed line next to microtubule bundle used for generating kymograph in **(E)**. Stills in **(B)** show growth of an individual microtubule bundle as is demonstrated on a kymograph **(D)**. Complex dynamics within composite microtubule bundle are demonstrated in stills **(C)** and a corresponding kymograph **(E)**; white arrowheads point to microtubule ends. Scale bars = 10 μm **(A)**, or 1 μm **(B–E)**. Time bars = 1 min **(D,E)**.

protein colocalization and interaction (Celler et al., 2016), a great disadvantage of electron microscopy is visualization of only fixed and artificially contrasted samples. On the other hand, intracellular structures show inherent dynamic redistribution during the time of observation and cortical microtubules of plant cells represent such an example. Cortical microtubules in *A. thaliana* exhibit rapid length fluctuations preferably at their plus ends, although occasionally they may oscillate via their minus end in a course of hybrid treadmilling (Shaw et al., 2003; Komis et al., 2014). Moreover they tend to accommodate into higher order assemblies incorporating more microtubules which are physically crosslinked by a number

of appropriate microtubule proteins including members of the MAP65 (reviewed in Hamada, 2014) and MAP70 (Korolev et al., 2005, 2007; Pesquet et al., 2010) families. These proteins form subresolution crossbridges that are impossible to discern from microtubules with standard diffraction-limited fluorescence microscopy approaches.

To make ends meet, a plethora of superresolution techniques, which stem from light microscopy and circumvent the Abbe's limit, were developed with the premise to survey and temporally follow intracellular organization at the nanoscale. Among them, several were described as especially suitable for characterizing both organization and dynamics of microtubules
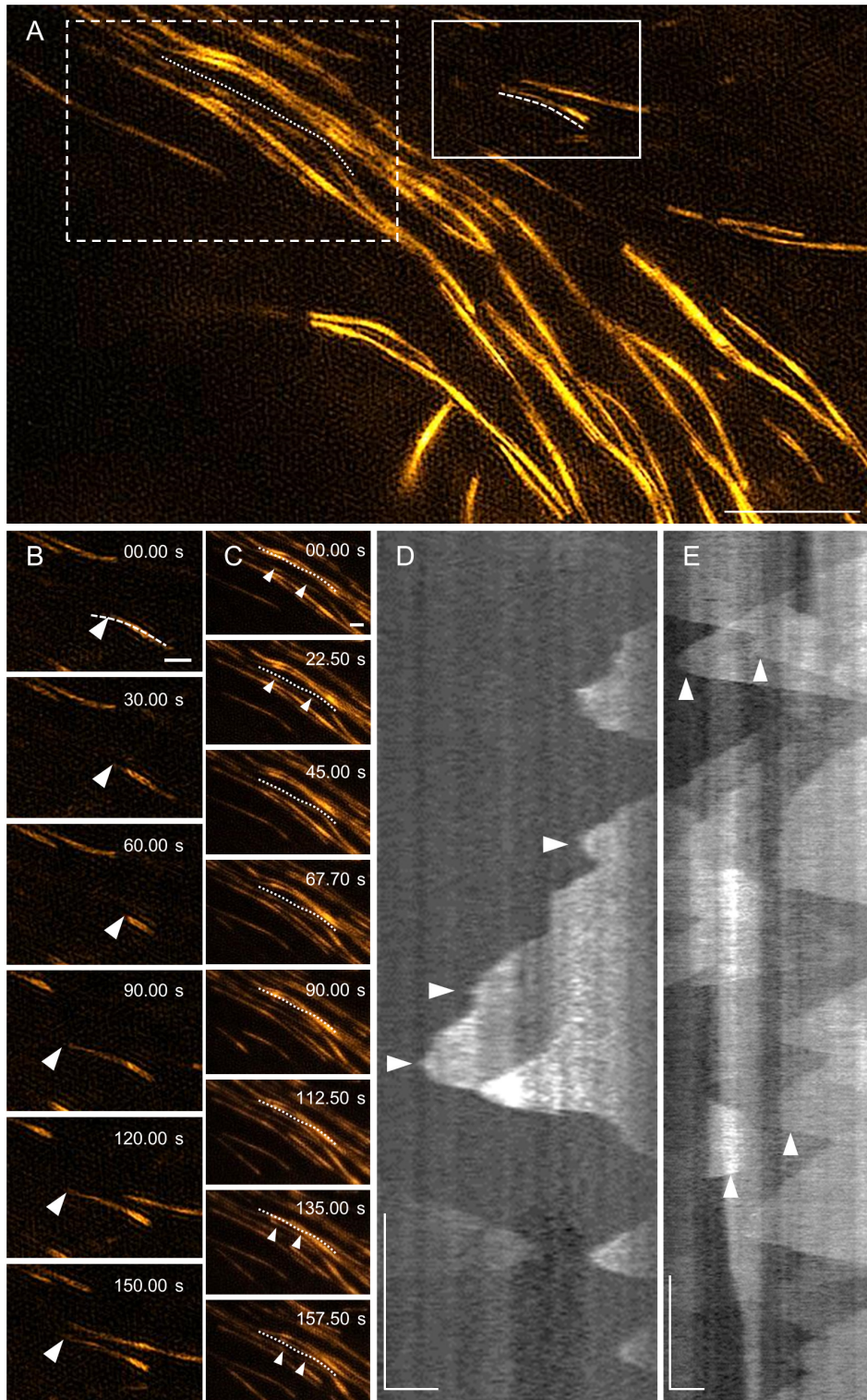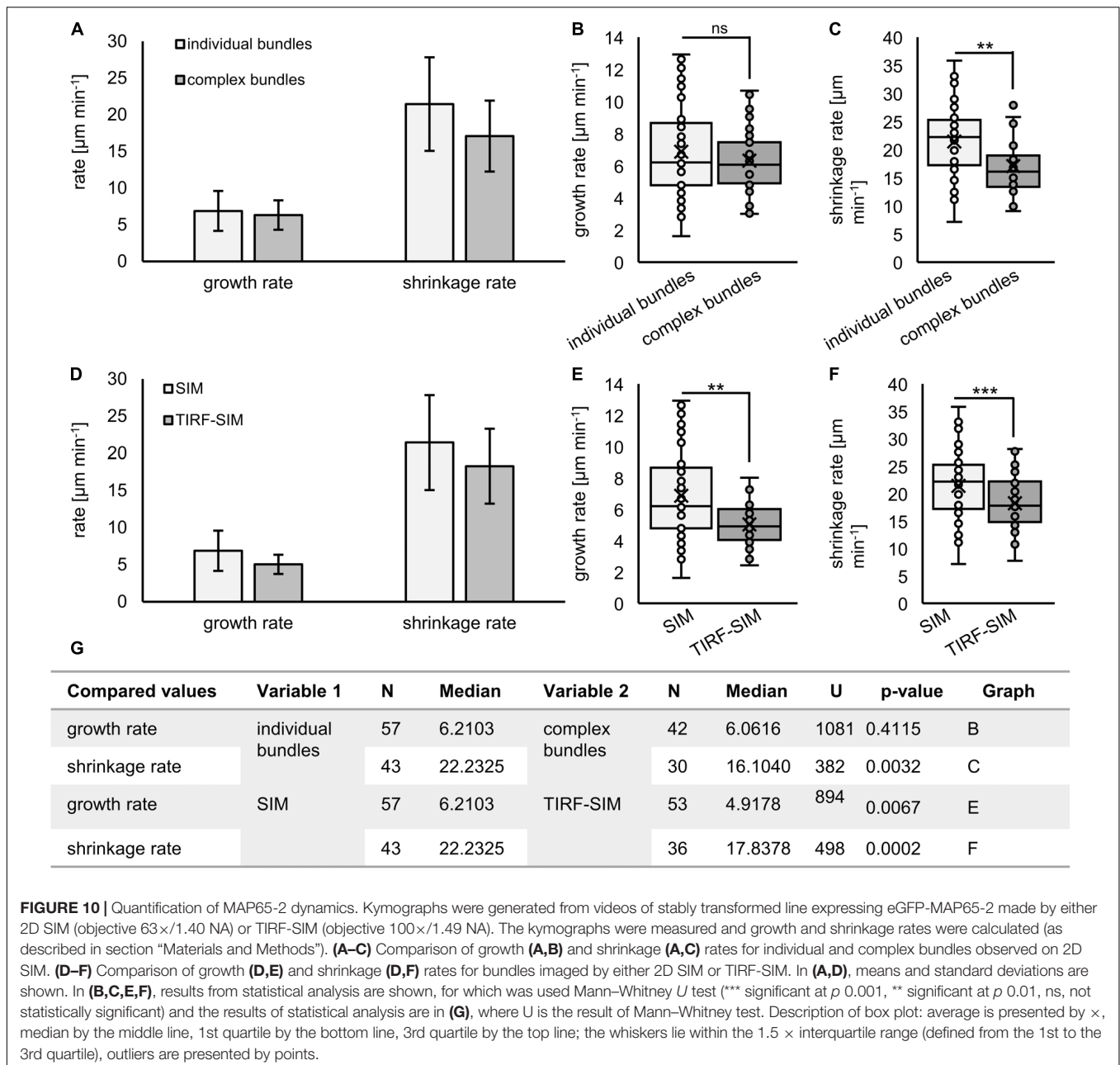
FIGURE 9 | MAP65-2 dynamics visualized by TIRF-SIM (see also **Supplementary Video S3**). **(A)** An overview of a hypocotyl epidermal cell of stably transformed line expressing eGFP-MAP65-2 observed by TIRF-SIM (objective 100×/1.49 NA). In full-line box is area, which is magnified and shown in stills in **(B)**, with dashed line marking microtubule bundle used for generating kymograph in **(D)**, while in dotted-line box is area depicted in stills in **(C)** and the dotted line is next to microtubule bundle, from which kymograph of **(E)** was generated. Stills in **(B)** show growth of a plus end of an individual microtubule bundle as demonstrated on a kymograph **(D)**. A complex dynamics within composite microtubule bundle is demonstrated in stills **(C)** and a corresponding individual kymograph **(E)**; white arrowheads point to microtubule ends. Scale bars = 5 μm **(A)**, or 1 μm **(B–E)**. Time bars = 1 min **(D,E)**.

FIGURE 10 | Quantification of MAP65-2 dynamics. Kymographs were generated from videos of stably transformed line expressing eGFP-MAP65-2 made by either 2D SIM (objective 63×/1.40 NA) or TIRF-SIM (objective 100×/1.49 NA). The kymographs were measured and growth and shrinkage rates were calculated (as described in section "Materials and Methods"). **(A–C)** Comparison of growth **(A,B)** and shrinkage **(A,C)** rates for individual and complex bundles observed on 2D SIM. **(D–F)** Comparison of growth **(D,E)** and shrinkage **(D,F)** rates for bundles imaged by either 2D SIM or TIRF-SIM. In **(A,D)**, means and standard deviations are shown. In **(B,C,E,F)**, results from statistical analysis are shown, for which was used Mann–Whitney U test (*** significant at p 0.001, ** significant at p 0.01, ns, not statistically significant) and the results of statistical analysis are in **(G)**, where U is the result of Mann–Whitney test. Description of box plot: average is presented by ×, median by the middle line, 1st quartile by the bottom line, 3rd quartile by the top line; the whiskers lie within the 1.5 × interquartile range (defined from the 1st to the 3rd quartile), outliers are presented by points.

and MAPs, namely SIM, PALM and STORM (Komis et al., 2015, 2018; Schubert, 2017). The SIM method proved to describe microtubule organization and dynamics with high resolution (Komis et al., 2014), reaching as low as nearly a half of Abbe's diffraction limit. 2D SIM as applied by all existing commercial platforms offers acceptable acquisition frame rates regarding microtubule dynamics (e.g., Shaw et al., 2003; Buschmann et al., 2010; Lucas et al., 2011; Komis et al., 2014, 2015).

With the implementation of TIRF and a unique strategy to generate and move the patterned light, this technique is capable of capturing time-lapsed images with high temporal resolution (Vizcay-Barrena et al., 2011). On the other hand, SIM relies on computer-assisted image reconstruction, which

makes SIM prone to a variety of artifacts (see comments in Komis et al., 2015; Demmerle et al., 2017). Nevertheless, due to the aforementioned advantages and well-established protocols of image acquisition and subsequent reconstruction (Komis et al., 2014, 2015), SIM proved to be a valuable tool for determining cytoskeletal dynamics.

To compare SIM, TIRF-SIM and ACLSM regarding their abilities to resolve microtubular structures, we have used these techniques to visualize cortical microtubules in hypocotyl epidermal cells of *A. thaliana*, an approach generally used when describing interphase microtubular array (Kawamura et al., 2006; Pastuglia et al., 2006). The *A. thaliana* lines carrying fluorescently labeled tubulin (TUA6-GFP or mRFP-TUB6) or
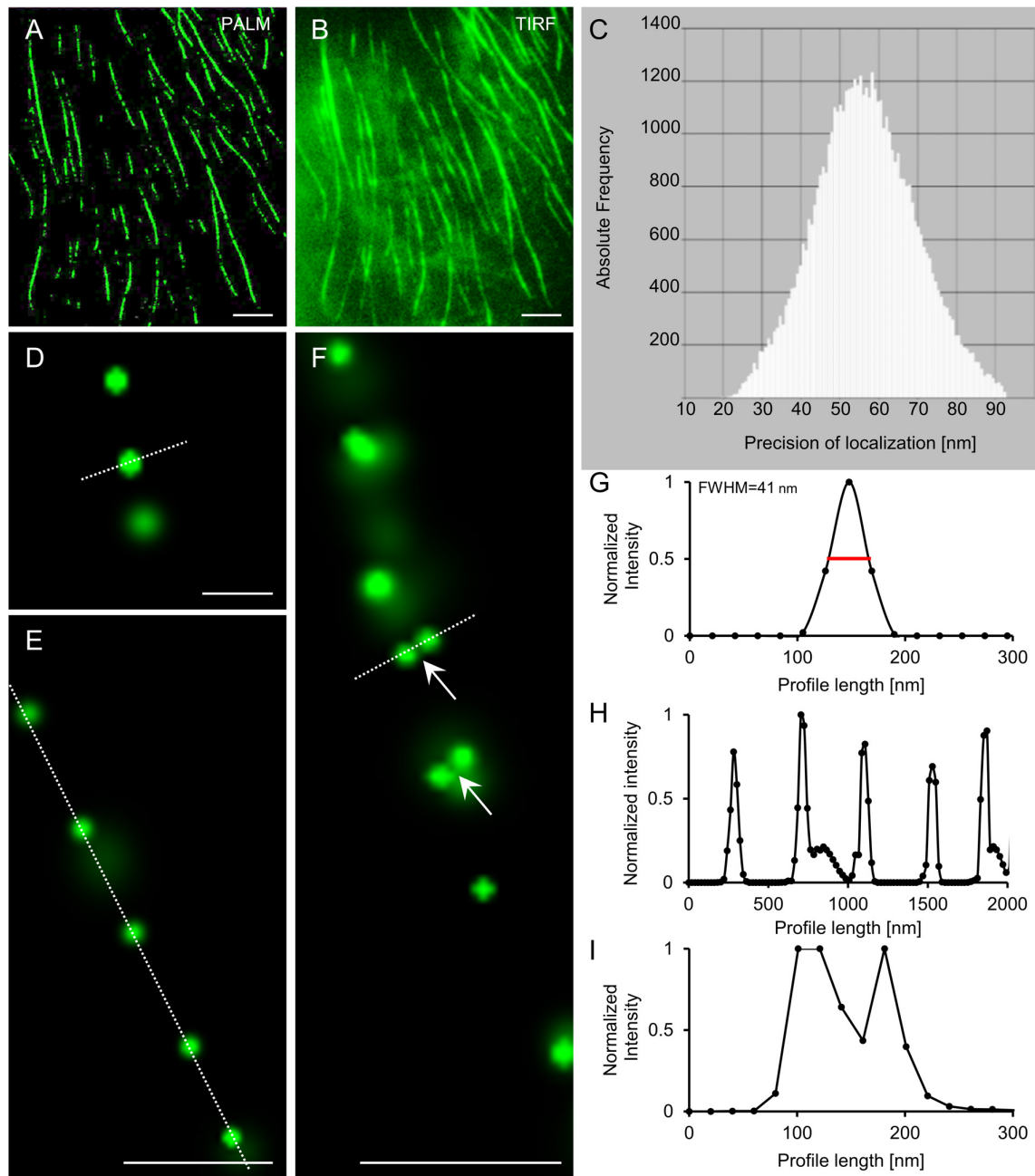
FIGURE 11 | PALM localization of mEos3.2-MAP65-2. **(A,B)** Overview of Arabidopsis hypocotyl epidermal cell expressing mEos3.2-MAP65-2 at the end of an acquisition time series following single molecule localization by PALM **(A)** or TIRF imaging **(B)**. **(C)** Histogram of photon detection frequencies plotted against precision of localization. **(D–F)** Details from PALM imaging in **(D)** are single mEos3.2-MAP65-2 molecule; **(E)** shows a linear array of single mEos3.2-MAP65-2 molecules; and in **(F)** is a linear array of mostly mEos3.2-MAP65-2 molecules with two pairs of spots most likely corresponding to mEos 3.2-MAP65-2 dimers. **(G)** Normalized intensity profiling of the spot delineated with the dotted white line in **(D)**, showing a full-width at half maximum (FWHM) of ca. 41 nm. **(H)** Normalized intensity profiling corresponding to the dotted white line in **(E)**, showing the periodic distribution of mEos3.2-MAP65-2 along a microtubule bundle. **(I)** Normalized intensity profiling along the dotted white line of **(F)**. Scale bars = 5 μm **(A,B)**; 0.2 μm **(D)**; 0.5 μm **(E,F)**.

fluorescent protein fusions with MAP65-2 were used in this study. Previously, the TUA6-GFP marker has been shown not to interfere with microtubule function and dynamics as marked from the lack of phenotypes of the transformants (Shaw et al., 2003).

As for the fluorescently labeled MAP65-2 marker, it was designed in a way to ensure proper function and localization of the resulting chimeric protein. Thus, it is expressed under native promoter while the fluorescent protein is fused with N-terminal sequence of MAP65-2, which is not responsible for binding
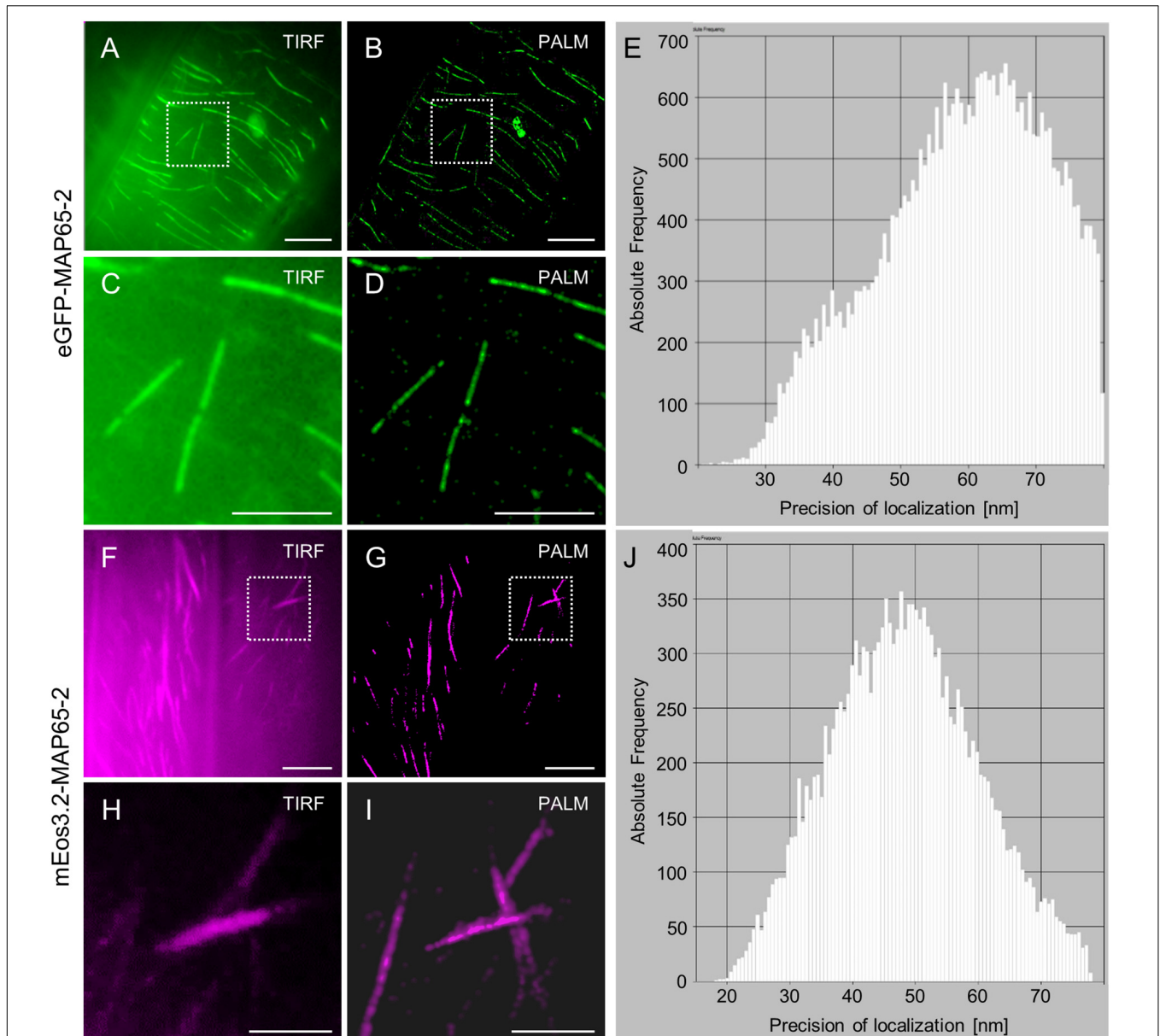
FIGURE 12 | Comparison of single molecule localization microscopy (SMLM) between eGFP-MAP65-2 stochastic optical fluctuations and mEos3.2-MAP65-2 photoconversion. **(A,B)** Comparative overviews of a hypocotyl cell expressing eGFP-MAP65-2 visualized after TIRF illumination **(A)** or following PALM reconstruction **(B)**. **(C,D)** Detailed comparisons of a magnified view of the boxed area in **(A,B)** under TIRF illumination **(C)** or PALM reconstruction **(D)**. **(E)** Histogram of precision of localization plotted against photon frequency. **(F,G)** Comparative overviews of a hypocotyl cell expressing mEos3.2-MAP65-2 by means of TIRF **(F)** or after PALM reconstruction **(G)**. **(H,I)** Detailed view of the boxed areas in **(F,G)** after TIRF acquisition **(H)** or PALM reconstruction **(I)**. **(J)** Histogram of precision of localization plotted against photon frequency. Scale bars = 10 μm **(A,B)**; 5 μm **(C,D,F,G)**; 2 μm **(H,I)**.

to microtubules. All seedlings used herein are T3 generation and were all chosen based on fluorescence intensity uniformity and the absence of phenotype when compared to same age untransformed Col-0 seedlings. Accordingly, we did not observe differences in the dynamics of MAP65-2 nor to its patterns of localization in the cortical array compared to previously published work (Lucas et al., 2011), suggesting the functionality of all MAP65-2 fusion proteins used herein (eGFP-MAP65-2, tagRFP-MAP65-2, and mEos3.2-MAP65-2).

Images acquired from these two lines were quantitatively evaluated, using FWHM as a value of the resolution capacity of each respective microscope. By using the same objective, (63×/1.40 NA), the SIM platform outperformed ACLSM. Accordingly, when using objective with higher magnification and NA (100×/1.49 NA), the resolution reached by TIRF-SIM further increased. Our results are in agreement with previously published data for 2D SIM (Komis et al., 2014). However, both ACLSM and SIM were shown to be capable of nearly

linear titration of bundled microtubule numbers by measuring fluorescence intensity.

Both 2D SIM and TIRF-SIM, allowed us to track end-wise dynamics of MAP65-2 length fluctuations in either microtubule pairs, or more complex microtubule assemblies. Our results show that the dynamics of MAP65-2 length changes are tightly coupled to end-wise length fluctuations of antiparallel microtubules as described before (Lucas et al., 2011). Within bundles, speckles of MAP65-2 remain immobile, further proving the end-wise restriction of MAP65-2 dynamics and the stability of intrabundle crosslinks. Dynamicity values of MAP65-2 excursions of eGFP-MAP65-2 expressors were considerably slower when analyzed with TIRF-SIM compared to 2D SIM. In particular, both extensions and retractions of the MAP65-2 signal as imprinted in the respective kymographs occurred at a slower pace compared to the respective 2D SIM acquisitions. This observation raises the issue of temporal sampling taking into account the resolution of the system used. Tracking of MAP65-2 dynamics is spatially limited by the system. If such changes occur at smaller lengths than what the system is able to resolve, then they will not be recorded as such. Therefore length fluctuations within the 4.5 s interval of the 2D SIM are expected to be bigger than those recorded with the 100–750 ms interval of the TIRF-SIM platform and also account for differences in transition frequencies (designated as catastrophes and rescues to follow the microtubule nomenclature).

The benefit of both systems, however, was the possibility to contrast intensity differences of variable MAP65-2 intensities and discriminate dynamics between individual components as was previously done with uniformly labeled microtubules (Komis et al., 2014). In the future, fast SIM platforms can be used to survey the dynamic nature of microtubule complexity in bundled systems by simultaneously addressing the distribution of more than one component at the time.

In this respect and owing to the default setup of the 2D SIM microscope used herein, it was not possible to acquire simultaneously signals from both tagged MAP65-2 and tagged tubulin. This constitutes a particular problem, since both microtubule length and MAP65-2 dynamics show considerable changes within the time frame of 2D SIM acquisitions followed herein and would not allow the faithful tracking of both components at the sequential mode of acquisition used. For this reason, ACLSM imaging was employed instead, since quantitative analysis of the imaging output showed that it still exhibited a resolution below Abbe's limit although significantly lower than that achieved by 2D SIM. Notwithstanding, with the introduction of Airyscan, an improved detector designed for ACLSM, the scanning time was dramatically shortened, while the main advantage of CLSM for live cell imaging, namely low phototoxicity, remained. So far, a direct comparison between SIM and ACLSM has not been provided.

A clear benefit of 2D-SIM and TIRF-SIM is the highly contrasted discrimination of intrabundle microtubules within the diffraction limitations of both modalities. Quite surprisingly, the recording of intrabundle dynamics consistently yielded statistically significant lower shrinkage rates compared to individual microtubules. This is quite surprising given that

at least *in vitro*, MAP65 proteins did not affect microtubule assembly and disassembly rates (Stoppin-Mellet et al., 2013) but rather the extent and duration of growth and shrinkage. Moreover, they might be also implicated in the decrease of catastrophe frequencies, since they are competing katanin activity (Stoppin-Mellet et al., 2013; Burkart and Dixit, 2019), leading to sustainable intrabundle microtubule elongation. By contrast, *in vivo* observations herein, show striking similarity in both catastrophe and rescue frequencies when comparing intrabundle with individual microtubules. Additionally previous *in vivo* observations, deduced reduced shrinkage rates of intrabundle microtubules as found here (van Damme et al., 2004; Lucas et al., 2011). In contrast to *in vitro* observations, intrabundle microtubule dynamics *in vivo* occur in the context of competitive or synergistic interactions from more protein species than those addressed in *in vitro* assays. Notable interacting partners of bundling proteins such as the fission yeast homolog of MAP65s, Ase1p, are kinesin motors and the plus-end binding protein CLASP (Bratman and Chang, 2007; Janson et al., 2007). This finding will, be further pursued in the near future and it represents a merit of the implementation of live superresolution imaging for *in vivo* observations.

To overcome the dual localization caveat, ACLSM was used in a superresolution fast mode to simultaneously track more than one channel at a time (Huff, 2016; Korobchevskaya et al., 2017). Despite the high resolution capacity of 2D SIM and TIRF-SIM, these platforms exhibit significant phototoxicity resulting in progressive photobleaching of fluorophores and cell damage after the time frames of observation used herein. Although the phototoxicity was not a particular problem for imaging lines expressing GFP-labeled proteins (owing to lower laser inputs and camera exposure times necessary for documentation), it represented a serious predicament for live imaging of mRFP- and tagRFP-labeled proteins. The output of ACLSM is at large comparable in terms of resolution with the output of 2D SIM, excluding the time restrictions of the latter. Taking into account the above advantages and restrictions of the different SIM modules and ACLSM, we used the latter to address aspects of MAP65-2 localization, relationship with microtubules within cortical bundles of variable complexity. Our results show that MAP65-2 either as an eGFP- or as a tagRFP-fusion, partially colocalizes with microtubule overlaps after tracking of microtubules with either TUA6-GFP, or mRFP-TUB6. The labeling of MAP65-2 in all cases was discontinuous without conspicuously following the similar speckled distribution of tagged tubulin. This means that MAP65-2 (as probably happens with other members of the MAP65 family) does not show a binding prevalence to a specific tubulin isoform. Moreover, the uneven distribution of MAP65-2 signifies the fact that microtubule bundles may stochastically recruit different MAP65 proteins during their assembly, including the wild type untagged MAP65-2 protein, which is also expected to be expressed in our transformants. To this extent, it would be of interest in a future study to address the spatial relationships between MAP65-1, MAP65-2, and MAP65-5 which have been shown to coexist in the cortical microtubule array (van Damme et al., 2004; Lucas et al., 2011; Lucas and Shaw, 2012) and to delineate their dynamics.

Diffraction limits of widefield imaging have been surpassed either by physically restricting emission to subdiffraction sizes by means of stimulated emission depletion microscopy (reviewed in Sahl et al., 2017), or by specifying the localization of single fluorophores at nanometer precision. The latter approach encompasses a high number of comparable methods all of which take into account non-linear responses of the fluorophore to excitation conditions. So-called single molecule localization microscopy (SMLM) methods which emerged on this principle rely on either fluorophores switching between on and off states, converting between two different emission peaks, or in intensity fluctuations of single emitters under special excitation conditions.

PALM is based on the first principle and employs photoswitchable, photoactivatable or photoconvertible protein tags (such as PA-GFP, Dronpa, or mEos3.2 as used herein; reviewed in Shcherbakova et al., 2014) which are shifting between two temporally distinct emission states upon appropriate illumination. Stochastic optical reconstruction (STORM) is also based on the on/off transitions of special fluorophores such as AlexaFluor 647 or Atto488 under redox conditions and high irradiance with the excitation wavelength promoting the blinking of individual fluorophores during time-resolved acquisitions only when the sample is embedded in the presence of reducing agents such as β-mercatoethanol or mercaptoethylamine (reviewed in Li and Vaughan, 2018; Jradi and Lavis, 2019).

In plant research, PALM and STORM applications of SMLM are still limited but promising. They have been applied for counting molecules of active and inactive RNA polymerase II in interphase nuclei of Arabidopsis (Schubert and Weisshart, 2015), or to elucidate the organization of perinuclear actin in living tobacco cells (Durst et al., 2014). Together with other studies, which elaborated applications of direct STORM in fixed plant samples interrogating cortical microtubule structure (Dong et al., 2015) or cellulose microfibril arrangement in plant cell walls (Liesche et al., 2013), and PALM combined with single particle tracking of diffusing membrane proteins (Hosy et al., 2015) makes SMLM methods tractable approaches for quantitatively interrogating plant intracellular and extracellular architecture at all spatial dimensions and in time.

Owing to the composite and crowded nature of cortical microtubule bundles and their molecular complement, SMLM methods for visualization of individual components presents ideal means to characterize their molecular composition. To this extend, we followed the PALM principle in order to address the localization of single molecules of mEos3.2-MAP65-2 fusions. The localization process required lengthy time acquisitions, in order to yield photon frequencies necessary for subdiffraction localization precision. Taking into account the dynamic nature of MAP65-2 at the fluctuating ends of overlapping microtubules, the results presented herein are only valid for localizations within the overlap and away from the microtubule tips.

PALM imaging within immotile regions of microtubule bundles showed the definite localization of MAP65-2 crossbridges with outstanding resolution and, most importantly, the discontinuous manner of MAP65-2 decoration as roughly shown by 2D SIM and ACLSM. In our work we could not observe a global periodicity of localized mEos3.2-MAP65-2, compared to TEM observations of reconstituted microtubule bundles. We believe that there might be three reasons for this: (a) not all mEos3.2-MAP65-2 were localized during the acquisition time series, (b) mEos3.2-MAP65-2 is buffered by endogenous MAP65-2 and (c) unlabeled crossbridges may be formed by other members of the MAP65 family such as MAP65-1 (which has overlapping localization with MAP65-2; Lucas et al., 2011) or MAP65-5 (van Damme et al., 2004).

Similar results in terms of precision of localization were obtained when visualizing eGFP-MAP65-2 under conditions of high irradiance with the 488 nm laser and concomitant excitation with the 405 nm line. In terms of efficiency, the photon frequencies necessary for a certain precision of localization were much higher in the case of mEos3.2 photoconverters compared to eGFP molecules with fluctuating intensity. However, in the latter case, precision of localization was roughly similar to that achieved by mEos3.2 photoconversion in much narrower time frames.

Based on our preliminary results, the sparse detection of spot duplets by PALM and the separation distance between individual spot of the duplets, we postulate that these might represent resolved dimers of MAP65-2. The two mEos3.2 moieties of a presumable mEos3.2-MAP65-2 dimer can be separated at a physical distance within the resolution potential of PALM. The robust detection of dimers vs. monomers requires a fluorescent tag with low duty cycle (i.e., the ratio of time spent in the on state vs. the time spent in the off state) and high contrast between the two states in order to avoid overlaps during the detection. Apparently, mEos3.2 fulfils such prerequisites (duty cycle of mEos3.2 is 3×10^{-6} and contrast is 200; Li and Vaughan, 2018) and work is under way to map the oligomerization state of MAP65-2. In this direction, it will be necessary to address the composition of microtubular bundles by multichannel localization of differentially tagged MAP65 isoforms. Further studies awaiting next generation microscopic technologies will help to decipher the topology of MAP65 crossbridging of microtubules in diverse plant microtubule arrays that rely on MAP65-mediated bundling, such as biased parallel cortical microtubule arrays, but especially robust 3-D structures, namely preprophase band, mitotic spindle and phragmoplast. More importantly, the recent release on new SIM platforms allowing faster and more light-efficient imaging at multiple channels (commented in Vavrdová et al., 2019b), will help to dynamically address the process of bundle formation in the cortical cytoplasm in plants co-expressing microtubule and various isoform-specific MAP65 markers.

The possibilities of multichannel PALM will facilitate colocalization studies of either microtubules and single MAP65 isoforms, or the spatial relation between different MAP65 isoforms that may redundantly localize within the same microtubule bundle. TIRF-SIM as well as the recent implementation of lattice SIM in commercially available system (see Komis et al., 2018) allow the high speed tracking of microtubule dynamics and particularly the latter modality is constructed to permit multicolor imaging at very high

frame rates. Unfortunately lattice SIM is limited to the same resolution range as standard SIM used herein, so it will not able to discriminate between microtubules and MAP65 crossbridges. However, the lattice SIM system may be suitable for the volumetric dynamic colocalization of microtubules and different MAP65 isoforms a task currently impossible for most SIM modalities existing today. The intrabundle dynamics of individual MAP65 molecules may be addressed by single particle tracking PALM, which is a goal for the immediate future.

Another limitation of the methods presented herein, is related to the duration of observations. As mentioned before, many events leading to microtubule reordering occur over time and their successful documentation requires excitation light inputs that will not harm the sample. The SIM (and the TIRF-SIM) modalities used herein are likely prone to phototoxicity-related artifacts and cell damage and this is why imaging sequences were time limited. Although this is beyond the scope of the present study, it will be a future goal to investigate the potential of Airyscan CLSM to this respect since by principle of detection, it does not require a high laser input to achieve superresolution output.

DATA AVAILABILITY STATEMENT

All material integral to the present study, will become available upon reasonable request from the corresponding author (GK, georgios.komis@upol.cz).

AUTHOR CONTRIBUTIONS

TV, PK, and PI were involved in generation of all material used herein (cloning, transformations, crosses). TV, PK, PI, PF, and GK were involved in selection of transgenic plants used for propagation and imaging. TV, RŠ, and PF managed plant handling. TV, MO, OŠ, PF, RŠ, and GK were involved in image acquisition and carried out all post-acquisition image processing regarding 2D SIM, ACLSM, TIRF-SIM, and PALM. TV and GK conducted all post-acquisition image analysis. TV and GK drafted the manuscript and figures with input and editing by PK, OŠ, MO, and JŠ. GK and JŠ provided the funding resources. JŠ provided infrastructure.

FUNDING

This work was funded by a grant Nr. 16-24313S from the Czech Science Foundation GAČR and by ERDF project 'Plants as a tool for sustainable global development' (CZ.02.1.01/0.0/0.0/16_019/0000827).

ACKNOWLEDGMENTS

We cordially acknowledge Dr. Teng-Leong Chew, Dr. Jesse Aaron, and Dr. Satya Kuon for organizing all aspects of the research visit of GK and MO, to the Janelia Research Campus

(Howard Hughes Medical Institute, Ashburn, United States) and for guidance and advice during experiments conducted with TIRF-SIM. In this case subsistence and bench expenses were defrayed by funds from the HHMI and the Moore Foundation. We thank Assoc. Prof. Sidney Shaw from the Indiana University for providing *proCaMV35S::TUA6:GFP* line; Prof. Geoffrey Wasteneys from the University of British Columbia for providing the *pUBQ1::mRFP:TUB6* line; Prof. Tsuyoshi Nakagawa from the Shimane University for kindly providing us with vector pGWB502; Dr. David Zalabák from Palacký University Olomouc for his kind gift of Col-0 cDNA and for his suggestions on selection of *A. thaliana* primary transformants. Finally, we thank Dr. Yilmaz Niyaz (Zeiss, Oberkochen, Germany) for helpful advice on SMLM.

SUPPLEMENTARY MATERIAL

The Supplementary Material for this article can be found online at: https://www.frontiersin.org/articles/10.3389/fpls.2020.00693/full#supplementary-material

FIGURE S1 | Resolving details of cortical microtubules with mRFP-TUB6 marker or MAP65-2 decoration of cortical microtubules with tagRFP-MAP65-2. The signal of mRFP-TUB6 and tagRFP-MAP65-2, respectively, was observed in hypocotyl epidermal cells of Arabidopsis by means of ACLSM and/or SIM. **(A)** Overview image from ACLSM (objective 63×/1.40 NA) showing mRFP-TUB6; the boxed area is shown in **(B)**. The white line in **(B)** presents a perpendicular profile, for which normalized intensity measurement is shown in **(C)**. **(D)** Presents quantitative analysis of the resolution of individual TUB6-labeled microtubules by ACLSM. The graph represents averaged, coaligned, and normalized intensity profiles ($N = 35$; FWHM – full-width at half maximum). **(E)** Overview image from ACLSM (objective 63×/1.40 NA) showing tagRFP-MAP65-2; the boxed area is displayed in **(F)**. The white line in **(F)** presents a perpendicular profile, for which normalized intensity measurement is shown in **(G)**. **(H)** Presents quantitative analysis of the resolution of MAP65-2-labeled microtubule bundles by ACLSM. The graph represents averaged, coaligned, and normalized intensity ($N = 47$). **(I)** Overview image from SIM (objective 63×/1.40 NA) showing tagRFP-MAP65-2; the boxed area is displayed in **(J)**. The white line in **(J)** presents a perpendicular profile, for which normalized intensity measurement is shown in **(K)**. **(L)** Presents quantitative analysis of the resolution of MAP65-2-labeled microtubule bundles by SIM. The graph represents averaged, coaligned, and normalized intensity profiles ($N = 43$). Scale bars = 2 μm.

FIGURE S2 | Comparison of resolving details of cortical microtubules or MAP65-2 decoration of cortical microtubules by employing TUA6-GFP, mRFP-TUB6, eGFP-MAP65-2 or tagRFP-MAP65-2 and by the means of ACLSM or SIM platform. **(A–D)** Boxplots present the full-width at half maximum (FWHM) values. **(A)** Comparison of TUA6-GFP and mRFP-TUB6 imaged by ACLSM. **(B,C)** Resolution reached by either ACLSM **(B)** or SIM **(C)** for eGFP-MAP65-2 and tagRFP-MAP65-2. **(D)** Comparison of resolution reached by ACLSM or SIM for tagRFP-MAP65-2. **(A–E)** For statistical analysis, Mann–Whitney U test was used (*** significant at p 0.001, ns, not statistically significant) and the results are in **(E)**, where M is median and U is result of Mann–Whitney test. Description of box plot: average is represented by ×, median by the middle line, 1st quartile by the bottom line, 3rd quartile by the top line; the whiskers lie within the 1.5× interquartile range (defined from the 1st to the 3rd quartile), outliers are marked by points.

TABLE S1 | List of primers used for cloning.

VIDEO S1 | Full frame ACLSM video corresponding to **Figure 7**.

VIDEO S2 | Full frame 2D SIM video corresponding to **Figure 8**.

VIDEO S3 | Full frame TIRF-SIM video corresponding to **Figure 9**.

REFERENCES

Adamowski, M., Li, L., and Friml, J. (2019). Reorientation of cortical microtubule arrays in the hypocotyl of *Arabidopsis thaliana* is induced by the cell growth process and independent of auxin signaling. *Int. J. Mol. Sci.* 20:3337. doi: 10.3390/ijms20133337

Bagshaw, C. R., and Cherny, D. (2006). Blinking fluorophores: what do they tell us about protein dynamics? *Biochem. Soc. Trans.* 34, 979–982. doi: 10.1042/BST0340979

Bannigan, A., Lizotte-Waniewski, M., Riley, M., and Baskin, T. I. (2008). Emerging molecular mechanisms that power and regulate the anastral mitotic spindle of flowering plants. *Cell Motil.* 65, 1–11. doi: 10.1002/cm.20247

Beck, M., Komis, G., Müller, J., Menzel, D., and Šamaj, J. (2010). *Arabidopsis* homologs of nucleus- and phragmoplast-localized kinase 2 and 3 and mitogen-activated protein kinase 4 are essential for microtubule organization. *Plant Cell* 22, 755–771. doi: 10.1105/tpc.109.071746

Beck, M., Komis, G., Ziemann, A., Menzel, D., and Šamaj, J. (2011). Mitogen-activated protein kinase 4 is involved in the regulation of mitotic and cytokinetic microtubule transitions in *Arabidopsis thaliana*. *New Phytol.* 189, 1069–1083. doi: 10.1111/j.1469-8137.2010.03565.x

Boruc, J., Weimer, A. K., Stoppin-Mellet, V., Mylle, E., Kosetsu, K., Cedeño, C., et al. (2017). Phosphorylation of MAP65-1 by Arabidopsis aurora kinases is required for efficient cell cycle progression. *Plant Physiol.* 173, 582–599. doi: 10.1104/pp.16.01602

Bratman, S. V., and Chang, F. (2007). Stabilization of overlapping microtubules by fission yeast CLASP. *Dev. Cell* 13, 812–827. doi: 10.1016/j.devcel.2007.10.015

Burkart, G., and Dixit, R. (2019). Microtubule bundling by MAP65-1 protects against severing by inhibiting the binding of katanin. *bioRxiv [Preprint]* doi: 10.1101/520445

Buschmann, H., Sambade, A., Pesquet, E., Calder, G., and Lloyd, C. W. (2010). "Chapter 20 - microtubule dynamics in plant cells," in *Methods in Cell Biology Microtubules: in vivo*, eds L. Cassimeris and P. Tran (Cambridge, MA: Academic Press), 373–400. doi: 10.1016/S0091-679X(10)97020-9

Buschmann, H., and Zachgo, S. (2016). The evolution of cell division: from streptophyte algae to land plants. *Trends Plant Sci.* 21, 872–883. doi: 10.1016/j.tplants.2016.07.004

Caillaud, M.-C., Lecomte, P., Jammes, F., Quentin, M., Pagnotta, S., Andrio, E., et al. (2008). MAP65-3 microtubule-associated protein is essential for nematode-induced giant cell ontogenesis in *Arabidopsis*. *Plant Cell* 20, 423–437. doi: 10.1105/tpc.107.057422

Celler, K., Fujita, M., Kawamura, E., Ambrose, C., Herburger, K., Holzinger, A., et al. (2016). "Microtubules in plant cells: strategies and methods for immunofluorescence, transmission electron microscopy, and live cell imaging," in *Cytoskeleton Methods and Protocols*, ed. R. H. Gavin (New York, NY: Springer), 155–184. doi: 10.1007/978-1-4939-3124-8_8

Chan, J., Jensen, C. G., Jensen, L. C. W., Bush, M., and Lloyd, C. W. (1999). The 65-kDa carrot microtubule-associated protein forms regularly arranged filamentous cross-bridges between microtubules. *Proc. Natl. Acad. Sci. U.S.A.* 96, 14931–14936. doi: 10.1073/pnas.96.26.14931

Chen, X., Grandont, L., Li, H., Hauschild, R., Paque, S., Abuzeineh, A., et al. (2014). Inhibition of cell expansion by rapid ABP1-mediated auxin effect on microtubules. *Nature* 516, 90–93. doi: 10.1038/nature13889

Chen, X., Wu, S., Liu, Z., and Friml, J. (2016). Environmental and endogenous control of cortical microtubule orientation. *Trends Cell Biol.* 26, 409–419. doi: 10.1016/j.tcb.2016.02.003

Chi, Z., and Ambrose, C. (2016). Microtubule encounter-based catastrophe in Arabidopsis cortical microtubule arrays. *BMC Plant Biol.* 16:18. doi: 10.1186/s12870-016-0703-x

Costes, S. V., Daelemans, D., Cho, E. H., Dobbin, Z., Pavlakis, G., and Lockett, S. (2004). Automatic and quantitative measurement of protein-protein colocalization in live cells. *Biophys. J.* 86, 3993–4003.

Cox, S., Rosten, E., Monypenny, J., Jovanovic-Talisman, T., Burnette, D. T., Lippincott-Schwartz, J., et al. (2012). Bayesian localization microscopy reveals nanoscale podosome dynamics. *Nat. Methods* 9, 195–200. doi: 10.1038/nmeth.1812

Deinum, E. E., Tindemans, S. H., Lindeboom, J. J., and Mulder, B. M. (2017). How selective severing by katanin promotes order in the plant cortical microtubule array. *Proc. Natl. Acad. Sci. U.S.A.* 114, 6942–6947. doi: 10.1073/pnas.1702650114

Demmerle, J., Innocent, C., North, A. J., Ball, G., Müller, M., Miron, E., et al. (2017). Strategic and practical guidelines for successful structured illumination microscopy. *Nat. Protoc.* 12, 988–1010. doi: 10.1038/nprot.2017.019

Derbyshire, P., Ménard, D., Green, P., Saalbach, G., Buschmann, H., Lloyd, C. W., et al. (2015). Proteomic analysis of microtubule interacting proteins over the course of xylem tracheary element formation in Arabidopsis. *Plant Cell* 27, 2709–2726. doi: 10.1105/tpc.15.00314

Dertinger, T., Colyer, R., Iyer, G., Weiss, S., and Enderlein, J. (2009). Fast, background-free, 3D super-resolution optical fluctuation imaging (SOFI). *Proc. Natl. Acad. Sci. U.S.A.* 106, 22287–22292. doi: 10.1073/pnas.0907866106

Dixit, R., and Cyr, R. (2004). Encounters between dynamic cortical microtubules promote ordering of the cortical array through angle-dependent modifications of microtubule behavior. *Plant Cell* 16, 3274–3284. doi: 10.1105/tpc.104.026930

Dong, B., Yang, X., Zhu, S., Bassham, D. C., and Fang, N. (2015). Stochastic optical reconstruction microscopy imaging of microtubule arrays in intact *Arabidopsis thaliana* seedling roots. *Sci. Rep.* 5:15694. doi: 10.1038/srep15694

Dunn, K. W., Kamocka, M. M., and McDonald, J. H. (2011). A practical guide to evaluating colocalization in biological microscopy. *Am. J. Physiol. Cell Physiol.* 300, C723–C742. doi: 10.1152/ajpcell.00462.2010

Durst, S., Hedde, P. N., Brochhausen, L., Nick, P., Nienhaus, G. U., and Maisch, J. (2014). Organization of perinuclear actin in live tobacco cells observed by PALM with optical sectioning. *J. Plant Physiol.* 171, 97–108. doi: 10.1016/j.jplph.2013.10.007

Elliott, A., and Shaw, S. L. (2018a). A cycloheximide-sensitive step in transverse microtubule array patterning. *Plant Physiol.* 178, 684–698. doi: 10.1104/pp.18.00672

Elliott, A., and Shaw, S. L. (2018b). Update: plant cortical microtubule arrays. *Plant Physiol.* 176, 94–105. doi: 10.1104/pp.17.01329

Eng, R. C., and Sampathkumar, A. (2018). Getting into shape: the mechanics behind plant morphogenesis. *Curr. Opin. Plant Biol.* 46, 25–31. doi: 10.1016/j.pbi.2018.07.002

Gaillard, J., Neumann, E., Van Damme, D., Stoppin-Mellet, V., Ebel, C., Barbier, E., et al. (2008). Two microtubule-associated proteins of *Arabidopsis* MAP65s promote antiparallel microtubule bundling. *Mol. Biol. Cell* 19, 4534–4544. doi: 10.1091/mbc.e08-04-0341

Galva, C., Kirik, V., Lindeboom, J. J., Kaloriti, D., Rancour, D. M., Hussey, P. J., et al. (2014). The microtubule plus-end tracking proteins SPR1 and EB1b interact to maintain polar cell elongation and directional organ growth in *Arabidopsis*. *Plant Cell* 26, 4409–4425. doi: 10.1105/tpc.114.131482

Gardner, M. K., Zanic, M., and Howard, J. (2013). Microtubule catastrophe and rescue. *Curr. Opin. Cell Biol.* 25, 14–22. doi: 10.1016/j.ceb.2012.09.006

Hamada, T. (2014). "Chapter one - microtubule organization and microtubule-associated proteins in plant cells," in *International Review of Cell and Molecular Biology*, ed. K. W. Jeon (Cambridge, MA: Academic Press), 1–52. doi: 10.1016/B978-0-12-800178-3.00001-4

Hamant, O., Inoue, D., Bouchez, D., Dumais, J., and Mjolsness, E. (2019). Are microtubules tension sensors? *Nat. Commun.* 10:2360. doi: 10.1038/s41467-019-10207-y

Haupts, U., Maiti, S., Schwille, P., and Webb, W. W. (1998). Dynamics of fluorescence fluctuations in green fluorescent protein observed by fluorescence correlation spectroscopy. *Proc. Natl. Acad. Sci. U.S.A.* 95, 13573–13578.

Havelková, L., Nanda, G., Martinek, J., Bellinvia, E., Sikorová, L., Šlajcherová, K., et al. (2015). Arp2/3 complex subunit ARPC2 binds to microtubules. *Plant Sci.* 241, 96–108. doi: 10.1016/j.plantsci.2015.10.001

Ho, C.-M. K., Lee, Y.-R. J., Kiyama, L. D., Dinesh-Kumar, S. P., and Liu, B. (2012). Arabidopsis microtubule-associated protein MAP65-3 cross-links antiparallel microtubules toward their plus ends in the phragmoplast via its distinct C-terminal microtubule binding domain. *Plant Cell* 24, 2071–2085. doi: 10.1105/tpc.111.092569

Hoogendoorn, E., Crosby, K. C., Leyton-Puig, D., Breedijk, R. M. P., Jalink, K., Gadella, T. W. J., et al. (2014). The fidelity of stochastic single-molecule super-resolution reconstructions critically depends upon robust background estimation. *Sci. Rep.* 4:3854. doi: 10.1038/srep03854

Hosy, E., Martinière, A., Choquet, D., Maurel, C., and Luu, D.-T. (2015). Super-resolved and dynamic imaging of membrane proteins in plant cells reveal

contrasting kinetic profiles and multiple confinement mechanisms. *Mol. Plant* 8, 339–342. doi: 10.1016/j.molp.2014.10.006

Huff, J. (2016). The fast mode for ZEISS LSM 880 with airyscan: high-speed confocal imaging with super-resolution and improved signal-to-noise ratio. *Nat. Methods* 13, i–ii. doi: 10.1038/nmeth.f.398

Hussey, P. J., Hawkins, T. J., Igarashi, H., Kaloriti, D., and Smertenko, A. (2002). The plant cytoskeleton: recent advances in the study of the plant microtubule-associated proteins MAP-65, MAP-190 and the *Xenopus* MAP215-like protein, MOR1. *Plant Mol. Biol.* 50, 915–924. doi: 10.1023/A:1021236307508

Janson, M. E., Loughlin, R., Loïodice, I., Fu, C., Brunner, D., Nédélec, F. J., et al. (2007). Crosslinkers and motors organize dynamic microtubules to form stable bipolar arrays in fission yeast. *Cell* 128, 357–368. doi: 10.1016/j.cell.2006.12.030

Jradi, F. M., and Lavis, L. D. (2019). Chemistry of photosensitive fluorophores for single-molecule localization microscopy. *ACS Chem. Biol.* 14, 1077–1090. doi: 10.1021/acschembio.9b00197

Kapoor, V., Hirst, W. G., Hentschel, C., Preibisch, S., and Reber, S. (2019). MTrack: automated detection, tracking, and analysis of dynamic microtubules. *Sci. Rep.* 9:3794. doi: 10.1038/s41598-018-37767-1

Kawamura, E., Himmelspach, R., Rashbrooke, M. C., Whittington, A. T., Gale, K. R., Collings, D. A., et al. (2006). MICROTUBULE ORGANIZATION 1 regulates structure and function of microtubule arrays during mitosis and cytokinesis in the Arabidopsis root. *Plant Physiol.* 140, 102–114. doi: 10.1104/pp.105.069989

Kner, P., Chhun, B. B., Griffis, E. R., Winoto, L., and Gustafsson, M. G. L. (2009). Super-resolution video microscopy of live cells by structured illumination. *Nat. Methods* 6, 339–342. doi: 10.1038/nmeth.1324

Kollárová, E., Baquero Forero, A., Stillerová, L., Přerostová, S., and Cvrčková, F. (2020). Arabidopsis class II formins AtFH13 and AtFH14 can form heterodimers but exhibit distinct patterns of cellular localization. *Int. J. Mol. Sci.* 21:348. doi: 10.3390/ijms21010348

Komis, G., Illés, P., Beck, M., and Šamaj, J. (2011). Microtubules and mitogen-activated protein kinase signalling. *Curr. Opin. Plant Biol.* 14, 650–657. doi: 10.1016/j.pbi.2011.07.008

Komis, G., Mistrik, M., Šamajová, O., Doskočilová, A., Ovečka, M., Illés, P., et al. (2014). Dynamics and organization of cortical microtubules as revealed by superresolution structured illumination microscopy. *Plant Physiol.* 165, 129–148. doi: 10.1104/pp.114.238477

Komis, G., Mistrik, M., Šamajová, O., Ovečka, M., Bartek, J., and Šamaj, J. (2015). Superresolution live imaging of plant cells using structured illumination microscopy. *Nat. Protoc.* 10, 1248–1263. doi: 10.1038/nprot.2015.083

Komis, G., Novák, D., Ovečka, M., Šamajová, O., and Šamaj, J. (2018). Advances in imaging plant cell dynamics. *Plant Physiol.* 176, 80–93. doi: 10.1104/pp.17.00962

Korobchevskaya, K., Lagerholm, B. C., Colin-York, H., and Fritzsche, M. (2017). Exploring the potential of airyscan microscopy for live cell imaging. *Photonics* 4:41. doi: 10.3390/photonics4030041

Korolev, A. V., Buschmann, H., Doonan, J. H., and Lloyd, C. W. (2007). AtMAP70-5, a divergent member of the MAP70 family of microtubule-associated proteins, is required for anisotropic cell growth in *Arabidopsis*. *J. Cell Sci.* 120, 2241–2247. doi: 10.1242/jcs.007393

Korolev, A. V., Chan, J., Naldrett, M. J., Doonan, J. H., and Lloyd, C. W. (2005). Identification of a novel family of 70 kDa microtubule-associated proteins in Arabidopsis cells. *Plant J.* 42, 547–555. doi: 10.1111/j.1365-313X.2005.02393.x

Kosetsu, K., Matsunaga, S., Nakagami, H., Colcombet, J., Sasabe, M., Soyano, T., et al. (2010). The MAP kinase MPK4 is required for cytokinesis in *Arabidopsis thaliana*. *Plant Cell* 22, 3778–3790. doi: 10.1105/tpc.110.077164

Krtková, J., Benáková, M., and Schwarzerová, K. (2016). Multifunctional microtubule-associated proteins in plants. *Front. Plant Sci.* 7:474. doi: 10.3389/fpls.2016.00474

Lazzaro, M. D., Wu, S., Snouffer, A., Wang, Y., and van der Knaap, E. (2018). Plant organ shapes are regulated by protein interactions and associations with microtubules. *Front. Plant Sci.* 9:1766. doi: 10.3389/fpls.2018.01766

Ledbetter, M. C., and Porter, K. R. (1963). A "microtubule" in plant cell fine structure. *J. Cell Biol.* 19, 239–250. doi: 10.1083/jcb.19.1.239

Lee, Y.-R. J., and Liu, B. (2013). The rise and fall of the phragmoplast microtubule array. *Curr. Opin. Plant Biol.* 16, 757–763. doi: 10.1016/j.pbi.2013.10.008

Li, H., Sun, B., Sasabe, M., Deng, X., Machida, Y., Lin, H., et al. (2017). Arabidopsis MAP65-4 plays a role in phragmoplast microtubule organization and marks the cortical cell division site. *New Phytol.* 215, 187–201. doi: 10.1111/nph.14532

Li, H., and Vaughan, J. C. (2018). Switchable fluorophores for single-molecule localization microscopy. *Chem. Rev.* 118, 9412–9454. doi: 10.1021/acs.chemrev.7b00767

Liesche, J., Ziomkiewicz, I., and Schulz, A. (2013). Super-resolution imaging with pontamine fast scarlet 4BS enables direct visualization of cellulose orientation and cell connection architecture in onion epidermis cells. *BMC Plant Biol.* 13:226. doi: 10.1186/1471-2229-13-226

Lindeboom, J. J., Nakamura, M., Hibbel, A., Shundyak, K., Gutierrez, R., Ketelaar, T., et al. (2013). A mechanism for reorientation of cortical microtubule arrays driven by microtubule severing. *Science* 342:1245533. doi: 10.1126/science.1245533

Lindeboom, J. J., Nakamura, M., Saltini, M., Hibbel, A., Walia, A., Ketelaar, T., et al. (2019). CLASP stabilization of plus ends created by severing promotes microtubule creation and reorientation. *J. Cell Biol.* 218, 190–205. doi: 10.1083/jcb.201805047

Lucas, J. R., Courtney, S., Hassfurder, M., Dhingra, S., Bryant, A., and Shaw, S. L. (2011). Microtubule-associated proteins MAP65-1 and MAP65-2 positively regulate axial cell growth in etiolated *Arabidopsis* hypocotyls. *Plant Cell* 23, 1889–1903. doi: 10.1105/tpc.111.084970

Lucas, J. R., and Shaw, S. L. (2012). MAP65-1 and MAP65-2 promote cell proliferation and axial growth in Arabidopsis roots. *Plant J.* 71, 454–463. doi: 10.1111/j.1365-313X.2012.05002.x

Luptovčiak, I., Komis, G., Takáč, T., Ovečka, M., and Šamaj, J. (2017). Katanin: a sword cutting microtubules for cellular, developmental, and physiological purposes. *Front. Plant Sci.* 8:1982. doi: 10.3389/fpls.2017.01982

Ma, Q., Sun, J., and Mao, T. (2016). Microtubule bundling plays a role in ethylene-mediated cortical microtubule reorientation in etiolated *Arabidopsis* hypocotyls. *J. Cell Sci.* 129, 2043–2051. doi: 10.1242/jcs.184408

Manders, E. M. M., Stap, J., Brakenhoff, G. J., Van Driel, R., and Aten, J. A. (1992). Dynamics of three-dimensional replication patterns during the S-phase, analysed by double labelling of DNA and confocal microscopy. *J. Cell Sci.* 103, 857–862.

Mao, G. (2006). The role of MAP65-1 in microtubule bundling during Zinnia tracheary element formation. *J. Cell Sci.* 119, 753–758. doi: 10.1242/jcs.02813

Marcus, A., and Raulet, D. H. (2013). A simple and effective method for differentiating GFP and YFP by flow cytometry using the violet laser. *Cytometry A* 83, 973–974. doi: 10.1002/cyto.a.22347

Molines, A. T., Marion, J., Chabout, S., Besse, L., Dompierre, J. P., Mouille, G., et al. (2018). EB1 contributes to microtubule bundling and organization, along with root growth, in *Arabidopsis thaliana*. *Biol. Open* 7:bio030510. doi: 10.1242/bio.030510

Müller, S., Wright, A. J., and Smith, L. G. (2009). Division plane control in plants: new players in the band. *Trends Cell Biol.* 19, 180–188. doi: 10.1016/j.tcb.2009.02.002

Nakagawa, T., Suzuki, T., Murata, S., Nakamura, S., Hino, T., Maeo, K., et al. (2007). Improved gateway binary vectors: high-performance vectors for creation of fusion constructs in transgenic analysis of plants. *Biosci. Biotechnol. Biochem.* 71, 2095–2100. doi: 10.1271/bbb.70216

Nakamura, M. (2015). Microtubule nucleating and severing enzymes for modifying microtubule array organization and cell morphogenesis in response to environmental cues. *New Phytol.* 205, 1022–1027. doi: 10.1111/nph.12932

Nakamura, M., Ehrhardt, D. W., and Hashimoto, T. (2010). Microtubule and katanin-dependent dynamics of microtubule nucleation complexes in the acentrosomal *Arabidopsis* cortical array. *Nat. Cell Biol.* 12, 1064–1070. doi: 10.1038/ncb2110

Nakamura, M., Lindeboom, J. J., Saltini, M., Mulder, B. M., and Ehrhardt, D. W. (2018). SPR2 protects minus ends to promote severing and reorientation of plant cortical microtubule arrays. *J. Cell Biol.* 217, 915–927. doi: 10.1083/jcb.201708130

Oda, Y. (2018). Emerging roles of cortical microtubule–membrane interactions. *J. Plant Res.* 131, 5–14. doi: 10.1007/s10265-017-0995-4

Panteris, E., and Galatis, B. (2005). The morphogenesis of lobed plant cells in the mesophyll and epidermis: organization and distinct roles of cortical

microtubules and actin filaments. *New Phytol.* 167, 721–732. doi: 10.1111/j.1469-8137.2005.01464.x

Pastuglia, M., Azimzadeh, J., Goussot, M., Camilleri, C., Belcram, K., Evrard, J.-L., et al. (2006). γ-tubulin is essential for microtubule organization and development in *Arabidopsis. Plant Cell* 18, 1412–1425. doi: 10.1105/tpc.105.039644

Pesquet, E., Korolev, A. V., Calder, G., and Lloyd, C. W. (2010). The microtubule-associated protein AtMAP70-5 regulates secondary wall patterning in *Arabidopsis* wood cells. *Curr. Biol.* 20, 744–749. doi: 10.1016/j.cub.2010.02.057

Sahl, S. J., Hell, S. W., and Jakobs, S. (2017). Fluorescence nanoscopy in cell biology. *Nat. Rev. Mol. Cell Biol.* 18, 685–701. doi: 10.1038/nrm.2017.71

Sapala, A., Runions, A., Routier-Kierzkowska, A.-L., Das Gupta, M., Hong, L., Hofhuis, H., et al. (2018). Why plants make puzzle cells, and how their shape emerges. *eLife* 7:e32794. doi: 10.7554/eLife.32794

Sasabe, M., Kosetsu, K., Hidaka, M., Murase, A., and Machida, Y. (2011). *Arabidopsis thaliana* MAP65-1 and MAP65-2 function redundantly with MAP65-3/PLEIADE in cytokinesis downstream of MPK4. *Plant Signal. Behav.* 6, 743–747. doi: 10.4161/psb.6.5.15146

Sassi, M., Ali, O., Boudon, F., Cloarec, G., Abad, U., Cellier, C., et al. (2014). An auxin-mediated shift toward growth isotropy promotes organ formation at the shoot meristem in Arabidopsis. *Curr. Biol.* 24, 2335–2342. doi: 10.1016/j.cub.2014.08.036

Schneider, C. A., Rasband, W. S., and Eliceiri, K. W. (2012). NIH image to ImageJ: 25 years of image analysis. *Nat. Methods* 9, 671–675. doi: 10.1038/nmeth.2089

Schneider, R., Klooster, K., van't, Picard, K., van der Gucht, J., Demura, T., Janson, M., et al. (2020). Long-term single-cell imaging and simulations of microtubules reveal driving forces for wall pattering during proto-xylem development. *bioRxiv [Preprint]* doi: 10.1101/2020.02.13.938258

Schneider, R., and Persson, S. (2015). Connecting two arrays: the emerging role of actin-microtubule cross-linking motor proteins. *Front. Plant Sci.* 6:415. doi: 10.3389/fpls.2015.00415

Schubert, V. (2017). Super-resolution microscopy – applications in plant cell research. *Front. Plant Sci.* 8:531. doi: 10.3389/fpls.2017.00531

Schubert, V., and Weisshart, K. (2015). Abundance and distribution of RNA polymerase II in *Arabidopsis* interphase nuclei. *J. Exp. Bot.* 66, 1687–1698. doi: 10.1093/jxb/erv091

Sen, T., Mamontova, A. V., Titelmayer, A. V., Shakhov, A. M., Astafiev, A. A., Acharya, A., et al. (2019). Influence of the first chromophore-forming residue on photobleaching and oxidative photoconversion of EGFP and EYFP. *Int. J. Mol. Sci.* 20:5229. doi: 10.3390/ijms20205229

Shaw, S. L., Kamyar, R., and Ehrhardt, D. W. (2003). Sustained microtubule treadmilling in *Arabidopsis* cortical arrays. *Science* 300, 1715–1718. doi: 10.1126/science.1083529

Shcherbakova, D. M., Sengupta, P., Lippincott-Schwartz, J., and Verkhusha, V. V. (2014). Photocontrollable fluorescent proteins for superresolution imaging. *Annu. Rev. Biophys.* 43, 303–329. doi: 10.1146/annurev-biophys-051013-022836

Smal, I., Grigoriev, I., Akhmanova, A., Niessen, W. J., and Meijering, E. (2010). Microtubule dynamics analysis using kymographs and variable-rate particle filters. *IEEE Trans. Image Process.* 19, 1861–1876. doi: 10.1109/TIP.2010.2045031

Smertenko, A. (2018). Phragmoplast expansion: the four-stroke engine that powers plant cytokinesis. *Curr. Opin. Plant Biol.* 46, 130–137. doi: 10.1016/j.pbi.2018.07.011

Smertenko, A. P., Chang, H.-Y., Wagner, V., Kaloriti, D., Fenyk, S., Sonobe, S., et al. (2004). The Arabidopsis microtubule-associated protein AtMAP65-1: molecular analysis of its microtubule bundling activity. *Plant Cell* 16, 2035–2047. doi: 10.1105/tpc.104.023937

Smertenko, A. P., Cheng, H.-Y., Sosobe, S., Fenyk, S. I., Weingartner, M., Bögre, L., et al. (2006). Control of the AtMAP65-1 interaction with microtubules through the cell cycle. *J. Cell Sci.* 119, 3227–3237. doi: 10.1242/jcs.03051

Smertenko, A. P., Kaloriti, D., Chang, H.-Y., Fiserova, J., Opatrny, Z., and Hussey, P. J. (2008). The C-terminal variable region specifies the dynamic properties of *Arabidopsis* microtubule-associated protein MAP65 isotypes. *Plant Cell* 20, 3346–3358. doi: 10.1105/tpc.108.063362

Stoppin-Mellet, V., Fache, V., Portran, D., Martiel, J. L., and Vantard, M. (2013). MAP65 coordinate microtubule growth during bundle formation. *PLoS One* 8:e56808. doi: 10.1371/journal.pone.0056808

Subramanian, R., Wilson-Kubalek, E. M., Arthur, C. P., Bick, M. J., Campbell, E. A., Darst, S. A., et al. (2010). Insights into antiparallel microtubule crosslinking by PRC1, a conserved nonmotor microtubule binding protein. *Cell* 142, 433–443. doi: 10.1016/j.cell.2010.07.012

Sun, H., Furt, F., and Vidali, L. (2018). Myosin XI localizes at the mitotic spindle and along the cell plate during plant cell division in *Physcomitrella patens*. *Biochem. Biophys. Res. Commun.* 506, 409–421. doi: 10.1016/j.bbrc.2018.01.082

Sun, T., Li, S., and Ren, H. (2017). OsFH15, a class I formin, interacts with microfilaments and microtubules to regulate grain size via affecting cell expansion in rice. *Sci. Rep.* 7:6538. doi: 10.1038/s41598-017-06431-5

Tian, J., and Kong, Z. (2019). The role of the augmin complex in establishing microtubule arrays. *J. Exp. Bot.* 70, 3035–3041. doi: 10.1093/jxb/erz123

Tokunaga, M., Imamoto, N., and Sakata-Sogawa, K. (2008). Highly inclined thin illumination enables clear single-molecule imaging in cells. *Nat. Methods* 5, 159–161. doi: 10.1038/nmeth1171

True, J. H., and Shaw, S. L. (2020). Exogenous auxin induces transverse microtubule arrays through TRANSPORT INHIBITOR RESPONSE1/AUXIN SIGNALING F-BOX receptors. *Plant Physiol.* 182, 892–907. doi: 10.1104/pp.19.00928

Tulin, A., McClerklin, S., Huang, Y., and Dixit, R. (2012). Single-molecule analysis of the microtubule cross-linking protein MAP65-1 reveals a molecular mechanism for contact-angle-dependent microtubule bundling. *Biophys. J.* 102, 802–809. doi: 10.1016/j.bpj.2012.01.008

van Damme, D., van Poucke, K., Boutant, E., Ritzenthaler, C., Inzé, D., and Geelen, D. (2004). In vivo dynamics and differential microtubule-binding activities of MAP65 proteins. *Plant Physiol.* 136, 3956–3967. doi: 10.1104/pp.104.051623

Vavrdová, T., Šamaj, J., and Komis, G. (2019a). Phosphorylation of plant microtubule-associated proteins during cell division. *Front. Plant Sci.* 10:238. doi: 10.3389/fpls.2019.00238

Vavrdová, T., Šamajová, O., Křenek, P., Ovečka, M., Floková, P., Šnaurová, R., et al. (2019b). Multicolour three dimensional structured illumination microscopy of immunolabeled plant microtubules and associated proteins. *Plant Methods* 15:22. doi: 10.1186/s13007-019-0406-z

Vineyard, L., Elliott, A., Dhingra, S., Lucas, J. R., and Shaw, S. L. (2013). Progressive transverse microtubule array organization in hormone-induced *Arabidopsis* hypocotyl cells. *Plant Cell* 25, 662–676. doi: 10.1105/tpc.112.107326

Vizcay-Barrena, G., Webb, S. E. D., Martin-Fernandez, M. L., and Wilson, Z. A. (2011). Subcellular and single-molecule imaging of plant fluorescent proteins using total internal reflection fluorescence microscopy (TIRFM). *J. Exp. Bot.* 62, 5419–5428. doi: 10.1093/jxb/err212

Walia, A., Nakamura, M., Moss, D., Kirik, V., Hashimoto, T., and Ehrhardt, D. W. (2014). GCP-WD mediates γ-TuRC recruitment and the geometry of microtubule nucleation in interphase arrays of *Arabidopsis. Curr. Biol.* 24, 2548–2555. doi: 10.1016/j.cub.2014.09.013

Wang, B., Liu, G., Zhang, J., Li, Y., Yang, H., and Ren, D. (2018). The RAF-like mitogen-activated protein kinase kinase kinases RAF22 and RAF28 are required for the regulation of embryogenesis in Arabidopsis. *Plant J.* 96, 734–747. doi: 10.1111/tpj.14063

Werner, S., Marillonnet, S., Hause, G., Klimyuk, V., and Gleba, Y. (2006). Immunoabsorbent nanoparticles based on a tobamovirus displaying protein A. *Proc. Natl. Acad. Sci. U.S.A.* 103, 17678–17683. doi: 10.1073/pnas.0608869103

Wightman, R., and Turner, S. R. (2007). Severing at sites of microtubule crossover contributes to microtubule alignment in cortical arrays. *Plant J.* 52, 742–751. doi: 10.1111/j.1365-313X.2007.03271.x

Wu, S.-Z., and Bezanilla, M. (2014). Myosin VIII associates with microtubule ends and together with actin plays a role in guiding plant cell division. *eLife* 3:e03498. doi: 10.7554/eLife.03498

Wu, S.-Z., and Bezanilla, M. (2018). Actin and microtubule cross talk mediates persistent polarized growth. *J. Cell Biol.* 217, 3531–3544. doi: 10.1083/jcb.201802039

Xu, T., Qu, Z., Yang, X., Qin, X., Xiong, J., Wang, Y., et al. (2009). A cotton kinesin GhKCH2 interacts with both microtubules and microfilaments. *Biochem. J.* 421, 171–180. doi: 10.1042/BJ20082020

Yamada, M., and Goshima, G. (2017). Mitotic spindle assembly in land plants: molecules and mechanisms. *Biology* 6:6. doi: 10.3390/biology6010006

Zhang, M., Chang, H., Zhang, Y., Yu, J., Wu, L., Ji, W., et al. (2012). Rational design of true monomeric and bright photoactivatable fluorescent proteins. *Nat. Methods* 9, 727–729. doi: 10.1038/nmeth.2021

Zhang, Q., Fishel, E., Bertroche, T., and Dixit, R. (2013). Microtubule severing at crossover sites by katanin generates ordered cortical microtubule arrays in *Arabidopsis. Curr. Biol.* 23, 2191–2195. doi: 10.1016/j.cub.2013.09.018

Zhu, C., Ganguly, A., Baskin, T. I., McClosky, D. D., Anderson, C. T., Foster, C., et al. (2015). The fragile Fiber1 kinesin contributes to cortical microtubule-mediated trafficking of cell wall components. *Plant Physiol.* 167, 780–792. doi: 10.1104/pp.114.251462

Publication 2.

My contribution: I wrote the first draft of the manuscript and prepared Figure 1. I contributed to the revision of the manuscript prior to its acceptance.

Phosphorylation of Plant Microtubule-Associated Proteins During Cell Division

Tereza Vavrdová, Jozef Šamaj and George Komis*

Department of Cell Biology, Centre of the Region Haná for Biotechnological and Agricultural Research, Faculty of Science, Palacký University Olomouc, Olomouc, Czechia

Progression of mitosis and cytokinesis depends on the reorganization of cytoskeleton, with microtubules driving the segregation of chromosomes and their partitioning to two daughter cells. In dividing plant cells, microtubules undergo global reorganization throughout mitosis and cytokinesis, and with the aid of various microtubule-associated proteins (MAPs), they form unique systems such as the preprophase band (PPB), the acentrosomal mitotic spindle, and the phragmoplast. Such proteins include nucleators of *de novo* microtubule formation, plus end binding proteins involved in the regulation of microtubule dynamics, crosslinking proteins underlying microtubule bundle formation and members of the kinesin superfamily with microtubule-dependent motor activities. The coordinated function of such proteins not only drives the continuous remodeling of microtubules during mitosis and cytokinesis but also assists the positioning of the PPB, the mitotic spindle, and the phragmoplast, affecting tissue patterning by controlling cell division plane (CDP) orientation. The affinity and the function of such proteins is variably regulated by reversible phosphorylation of serine and threonine residues within the microtubule binding domain through a number of protein kinases and phosphatases which are differentially involved throughout cell division. The purpose of the present review is to provide an overview of the function of protein kinases and protein phosphatases involved in cell division regulation and to identify cytoskeletal substrates relevant to the progression of mitosis and cytokinesis and the regulation of CDP orientation.

Keywords: microtubules, microtubule-associated proteins, mitotic spindle, phragmoplast, protein kinase, protein phosphatase

INTRODUCTION

Owing to their sedentary life style and their encasement within the barriers of rigid cell walls, plant cells adopted unique mechanisms for regulating fundamental eukaryotic processes such as cell division and cell division plane (CDP) orientation establishment (reviewed in Buschmann and Zachgo, 2016). In this respect, plant cells developed unique microtubule-based cytoskeletal structures which underlie the above processes. CDP orientation is marked by a plant-specific cortical microtubule ring, the preprophase band (PPB; Pickett-Heaps and Northcote, 1966) which determines spindle positioning (Schaefer et al., 2017) and coincides with the plane of cell plate deposition during cytokinesis (cell plate fusion site; CPFS; Marcus et al., 2005).
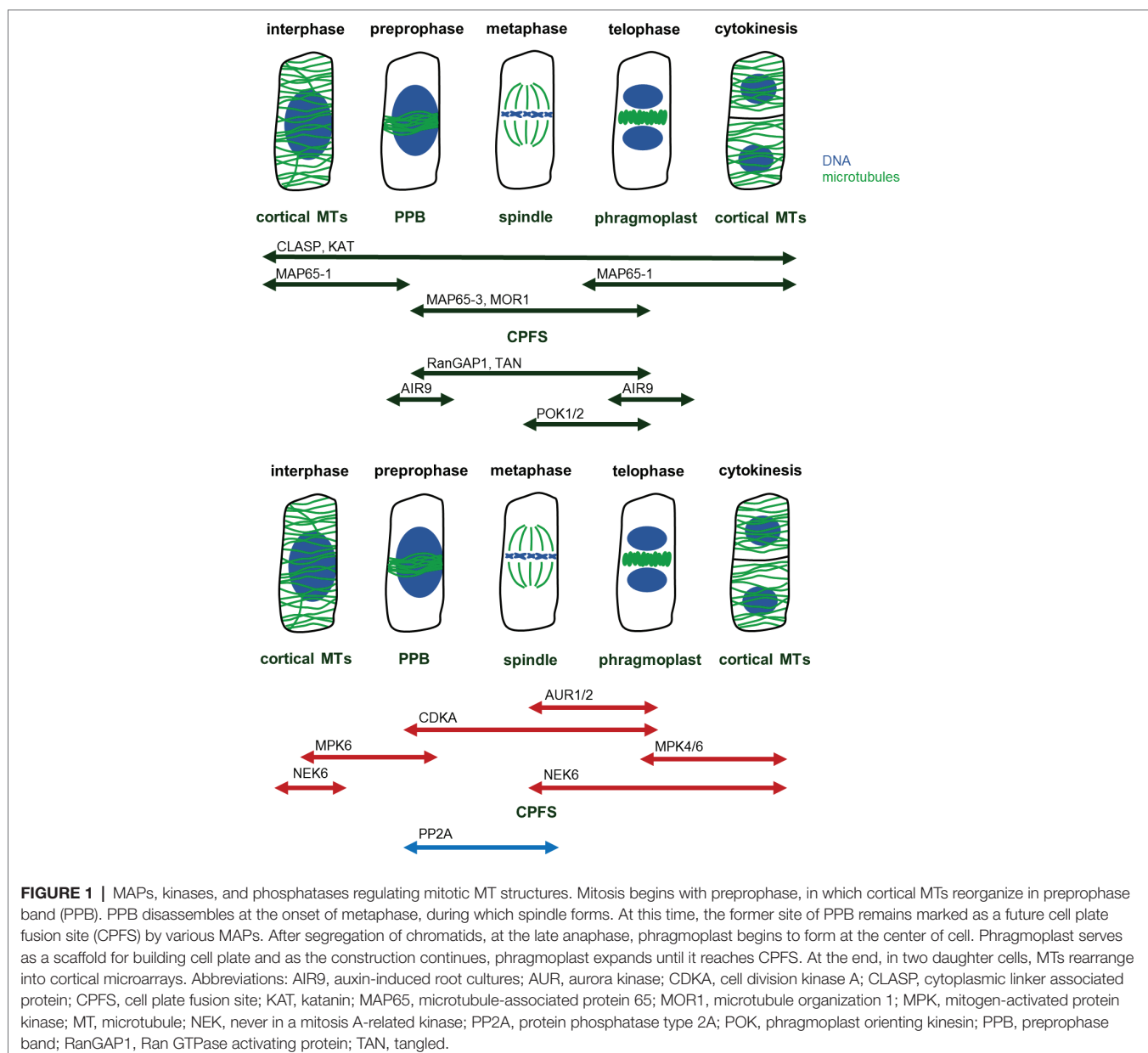
The PPB exhibits a progressive narrowing and finally it disassembles shortly after the mitotic spindle is formed; however, the cortical site which was occupied by the PPB is marked by specific proteins throughout mitosis in a continuous or intermittent manner (e.g., Buschmann et al., 2006; Walker et al., 2007).

The plant mitotic spindle starts to assemble before nuclear envelope breakdown and in contrast to the mammalian or yeast spindle, and it forms in the absence of microtubule organizing center (reviewed in Buschmann and Zachgo, 2016).

Cytokinesis is hallmarked by the formation of another plant specific microtubule machinery, the phragmoplast. It is formed at the end of telophase between the reconstituting daughter nuclei. It comprises two sets of antiparallel microtubules, and it expands centrifugally toward the cell periphery. During its expansion, it guides the deposition of the cell plate until the latter merges with the parent cell wall, after which the phragmoplast disintegrates (Chen et al., 2018).

Throughout the cell cycle, precise temporal and spatial regulation of microtubule organization and dynamics is required for the formation, proper function, and structural transitions of these cytoskeletal structures (Dhonukshe and Gadella, 2003). Such regulation is achieved via microtubule-associated proteins (MAPs) involved in microtubule organization and dynamics. Among these proteins belong motor proteins from the kinesin (Müller et al., 2006; Lipka et al., 2014; Buschmann et al., 2015; de Keijzer et al., 2017) and the myosin superfamilies (Wu and Bezanilla, 2014), plus end-binding proteins and microtubule crosslinkers (Mao et al., 2005; Beck et al., 2010; Kohoutová et al., 2015; Lin et al., 2019). Many of such proteins exhibit a cell cycle dependent localization to mitotic and

FIGURE 1 | MAPs, kinases, and phosphatases regulating mitotic MT structures. Mitosis begins with preprophase, in which cortical MTs reorganize in preprophase band (PPB). PPB disassembles at the onset of metaphase, during which spindle forms. At this time, the former site of PPB remains marked as a future cell plate fusion site (CPFS) by various MAPs. After segregation of chromatids, at the late anaphase, phragmoplast begins to form at the center of cell. Phragmoplast serves as a scaffold for building cell plate and as the construction continues, phragmoplast expands until it reaches CPFS. At the end, in two daughter cells, MTs rearrange into cortical microarrays. Abbreviations: AIR9, auxin-induced root cultures; AUR, aurora kinase; CDKA, cell division kinase A; CLASP, cytoplasmic linker associated protein; CPFS, cell plate fusion site; KAT, katanin; MAP65, microtubule-associated protein 65; MOR1, microtubule organization 1; MPK, mitogen-activated protein kinase; MT, microtubule; NEK, never in a mitosis A-related kinase; PP2A, protein phosphatase type 2A; POK, phragmoplast orienting kinesin; PPB, preprophase band; RanGAP1, Ran GTPase activating protein; TAN, tangled.

cytokinetic microtubule systems (**Figure 1**), and at large this is differentially regulated by protein kinases and phosphatases which become activated/deactivated in a similar cell cycle dependent manner.

Many kinases were directly shown to associate with cytoskeletal systems (Weingartner et al., 2001; Samaj et al., 2002, 2004; Lee et al., 2003; Oh et al., 2005, 2012) and indirect pharmacological (e.g., Binarova et al., 1996; Ayaydin et al., 2000) and subsequently more targeted studies (e.g., Mao et al., 2005; Brumbarova and Ivanov, 2016), establishing the functional reciprocity between protein kinases and cytoskeletal components. Plant microtubule systems can be targeted for phosphorylation-pendant regulation of their components after environmental stimulation (e.g., Ban et al., 2013; Bhaskara et al., 2017), or in a developmental context, which is the aim of this review.

INVOLVEMENT OF MAPS IN THE ORGANIZATION OF MITOTIC STRUCTURES

From numerous plant proteins related to the regulation of microtubule organization and dynamics, some have been inadvertently associated with the progress of mitotic and cytokinetic microtubule arrays and were shown to be regulated by reversible phosphorylation. These proteins are involved in all aspects of microtubule organization and dynamics.

Microtubule nucleation factors such as γ-tubulin and TPX2 (targeting protein for Xklp2) are essential for spindle formation and the establishment of spindle bipolarity (Petrovská et al., 2013), and it was suggested that they are regulated by mitogen-activated protein kinase (MAPK, MPK) and/or Aurora kinase (AUR) phosphorylation (Petrovská et al., 2012; https://string-db.org/cgi/network.pl?taskId=f13kHLYXYV1W). It is likely that γ-tubulin interacts with the FASS B″ subunit of protein phosphatase 2A (https://string-db.org/network/3702.AT5G18580.1; **Figure 2**). Notably, *fass* mutants exhibit altered geometry of microtubule nucleation at least in interphase microtubule arrays (Kirik et al., 2012).

Microtubule dynamics are largely controlled by plus end binding proteins, including end-binding protein 1 isoforms (EB1a, b, and c; Komaki et al., 2010), SPIRAL1 (Sedbrook et al., 2004), CLASP (Ambrose et al., 2007), and GPT1 and 2 (growing plus-end tracking 1 and 2; Wong and Hashimoto, 2017). The plant-specific isoform EB1c was shown to be phosphorylated by MPK6 (**Figure 2**; Kohoutová et al., 2015), however, without apparent functional implications. Similarly, phosphorylation of CLASP was demonstrated only in the context of conditional signaling (Brumbarova and Ivanov, 2016).

Microtubule bundling *via* the MAP65 proteins is essential for the formation of the central spindle, its subsequent reorganization into phragmoplast and for support of its centrifugal expansion (Chang et al., 2005; Smertenko et al., 2008, 2018; Herrmann et al., 2018). From the nine members of the *Arabidopsis* MAP65 family, only MAP65-1, -2, -3, and -4 have been associated with the progression of mitosis and cytokinesis (Chang-Jie and Sonobe, 1993; Chan et al., 1999; Caillaud et al., 2008). MAP65-1

and MAP65-2 are nonessential as proven by the absence of cytokinetic phenotypes of single or double mutants (Lucas and Shaw, 2012). On the other hand, MAP65-3 and MAP65-4 appear to be essential for cytokinesis, in an additive manner (Müller et al., 2004; Li et al., 2017). MAP65-1 and MAP65-2 proteins differentially colocalize with microtubules and mediate their bundling during interphase and preprophase (Murata et al., 2013; Zhou et al., 2017). However, they are excluded from the mitotic spindle until telophase. This suggests that their colocalization with microtubule structures is subjected to temporal control during cell division (Gaillard et al., 2008). One possible mechanism controlling the differential localization of MAP65 proteins with mitotic microtubule systems is proteolytic degradation, since several *map65* genes harbor a "destruction box" motif, which is a target for the ubiquitin degradation pathway. More importantly, at least MAP65-1, -2, and -3 are targeted for phosphorylation in their C-terminal microtubule binding domains by several kinases with cell cycle functions, such as cyclin-dependent kinases [CDKs (Smertenko et al., 2006), MAPKs (Kosetsu et al., 2010; Smékalová et al., 2014), and AURs (Boruc et al., 2017)]. Generally, phosphorylation downregulates microtubule binding of MAP65s; therefore, it may represent the means to abolish their localization from the mitotic spindle. This is supported by mutagenesis studies, showing that change of the consensus CDK-targeted site of MAP65-1 causes its localization at the mitotic spindle (Mao et al., 2005). As mentioned earlier, MAP65-1 and presumably MAP65-2 are nonessential for the mitotic and cytokinetic progress (Lucas and Shaw, 2012), and they may affect spindle and phragmoplast formation only when artificially overexpressed (Mao et al., 2005). MAP65-3, on the other hand, is essential for cell plate formation, since its genetic depletion results in the formation of giant, multinucleated cells with incomplete cell walls. Similar cytokinetic phenotypes have been observed in *anp2anp3* and *mpk4* mutants, which are related to MAPK signaling. The above mutants show reduced but not abolished MAP65-3 expression (Beck et al., 2010). In this case, it is speculated that the cytokinetic phenotype of *anp2anp3* and *mpk4* mutants maybe partially attributed to reduced phosphorylation of MAP65-3 (Beck et al., 2010). MAP65-4 alone has negligible cytokinetic phenotypes when depleted but contributes to the *map65-3/pleiade* phenotype in double mutants (Li et al., 2017). Its spatial localization coincides with that of MAP65-3 at the PPB and the phragmoplast midzone. However, MAP65-4 exhibits persistent localization at the cortical division zone throughout mitosis, unlike MAP65-3 (Li et al., 2017). Although the cytokinetic role of MAP65-4 was just recently described, it is also likely to be regulated by phosphorylation. Its carboxyl-terminal region harbors proline-directed serine or threonine residues, which are predicted targets of CDKs and MAPKs (based on prediction using GPS2.1.2; Xue et al., 2008). It is also predicted to interact with AUR (https://string-db.org/cgi/network.pl?taskId=qRfSrQ0dHJdK; **Figure 2**).

Several Arabidopsis microtubule motors of the kinesin superfamily, namely those related to the progress of mitosis and cytokinesis were shown to be regulated by phosphorylation. One example is the kinesin-like calmodulin-binding protein (KCBP),
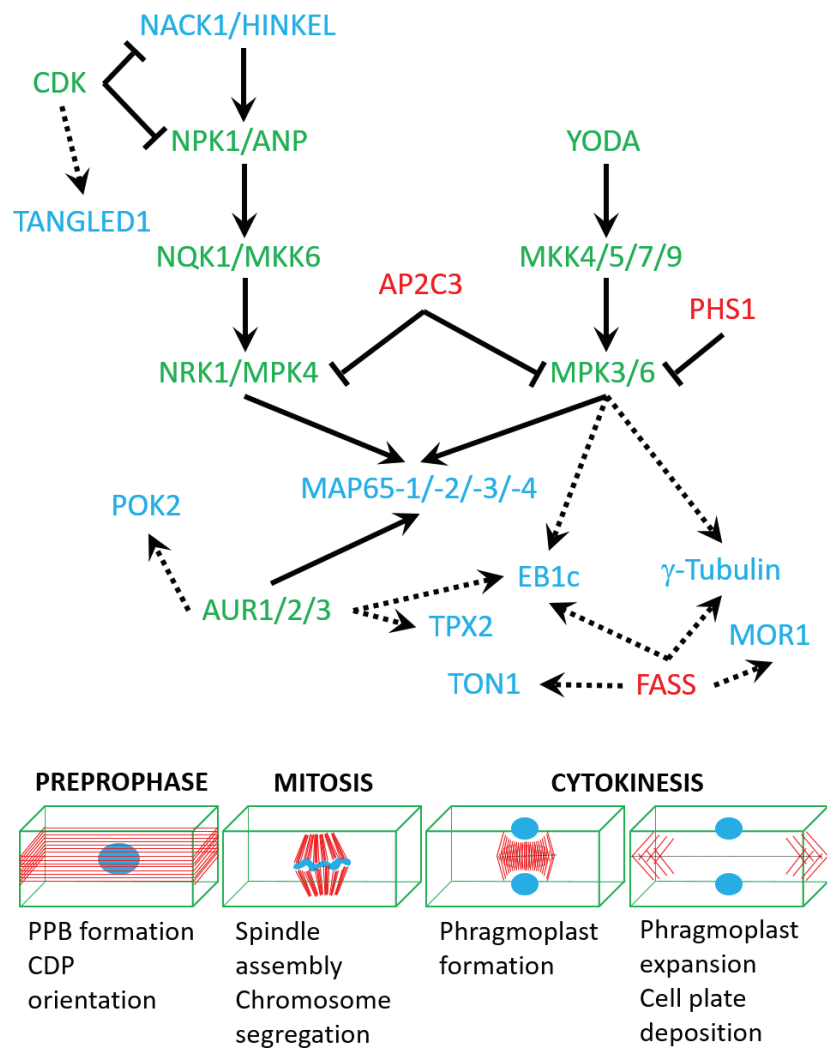
FIGURE 2 | A speculative network of protein kinases (green), phosphatases (red), and targeted cytoskeletal proteins (blue) based on either published interaction studies (full arrows) or in silico predictions (dashed arrows; see text for more details). Lower panel shows mitotic stages which are regulated by the above network of interactions.

which is involved in the tethering of phragmoplast margins to the CPFS (Buschmann et al., 2015; Buschmann and Zachgo, 2016). KCBP was shown to be regulated by phosphorylation (Day et al., 2000; Humphrey et al., 2015). The mitotic kinesin NACK1 (NPK1-activating kinesin-like protein 1) is an activator of the NPK1-NQK1-NRK1 MAPK pathway in tobacco (similarly, its *Arabidopsis* homologue HINKEL also activates the ANP-MKK6-MPK4 MAPK pathway; Nishihama et al., 2002), which is involved in the regulation of cytokinesis. The interaction between NACK1 and NPK1 is negatively regulated by CDK phosphorylation in residues of both the motor domain and the stalk region of NACK1. CDKs also target the carboxyl-terminal regulatory domain of NPK1, which is engaged in NACK1-NPK1 interactions (Sasabe et al., 2011a). Interruption of NACK1-NPK1 interaction by CDK-mediated phosphorylation abolishes the recruitment of the NPK1-NQK1-NRK1 module to the mitotic spindle. When

CDK activity declines during late anaphase, then the NPK1-NQK1-NRK1 module becomes localized to the phragmoplast (Sasabe et al., 2011a).

Interactions of kinesin motors with protein kinases may be reciprocal and may convey targeted transport or activity regulation to the kinase counterpart. For example, never in a mitosis (NIMA)-related kinase 6 (NEK6) is negatively regulated by the armadillo-repeat kinesin 1 (Eng et al., 2017). Also, NACK1 (and its Arabidopsis homologue HINKEL) directly activates the NPK1 MAPKKK (and its Arabidopsis homologues ANP1, 2, and 3; Nishihama et al., 2002; Takahashi et al., 2010).

Microtubule severing by the Arabidopsis KATANIN1 (Komis et al., 2017; Panteris et al., 2018) has not been shown to be regulated by phosphorylation yet. Moreover, the p60 catalytic subunit of the katanin holoenzyme is suspected to interact with FASS (https://string-db.org/cgi/network.pl?taskId=jBYrCeTF9nPv; **Figure 2**). In animals, phosphorylation is a major mechanism for the exclusion

of katanin activity from the mitotic spindle and connected to spindle sizing (Loughlin et al., 2011; Whitehead et al., 2013).

Apart from several MAPs that have been proven or predicted to be regulated by phosphorylation, tubulin has also been identified as a target of the atypical kinase domain of the protein phosphatase PROPYZAMIDE HYPERSENSITIVE 1 (PHS1; Fujita et al., 2013). So far, tubulin phosphorylation is related to conditional microtubule depolymerization (Ban et al., 2013), but it will be of interest to identify tubulin phosphorylation as a regulator of mitotic microtubule transitions.

KINASES REGULATING MAP ACTIVITY

Since MAPs play a role in microtubule dynamics while being regulated by reversible phosphorylation, kinases and phosphatases are master regulators of microtubule reorganization throughout cell cycle. Several kinases were implicated in phosphorylating MAPs, namely CDKs, AURs, MAPKs, and NEKs.

Since CDKs are master regulators of cell cycle progression, they are also implicated cell cycle-dependent cytoskeletal reorganizations (Costa, 2017). The mode of action on CDKs on the microtubule cytoskeleton of dividing cells is not well understood, since the only known cytoskeletal CDK substrate is NACK1 kinesin (Sasabe et al., 2011a), while MAP65-1 was only shown *in vitro* to be phosphorylated by CDK (Smertenko et al., 2006). Localization observations and pharmacological and genetic evidence favor the implication of CDK in regulating microtubules. For example, *Arabidopsis* CDK was shown to colocalize with PPB, spindle, and phragmoplast (Stals et al., 1997). Second, plant CDKs were found to participate in regulating mitotic microtubule structures (Weingartner et al., 2001). Third, CDKs are known to regulate microtubule dynamics by phosphorylating animal homologues of plant MAPs (Ookata et al., 1997; Vasquez et al., 1999). Last, several plant MAPs contain a CDK phosphorylation site (Hussey et al., 2002; Smertenko et al., 2006). CDKs may be also involved in CDP orientation through the phosphorylation of cytoskeletal markers of the cell division zone such as the microtubule binding protein TANGLED1 (https://string-db.org/cgi/network. pl?taskId=4lbkQFdWZfbv; **Figure 2**).

Apart from CDKs, Aurora kinases are another component of cell cycle progression machinery. These Ser/Thr kinases are on lower hierarchical position than CDKs (Schecher et al., 2017). They themselves are regulated by phosphorylation and ubiquitin-dependent proteolysis (Castro et al., 2002a,b). Therefore, they are known to play a more direct role in cytoskeleton rearrangements than CDKs (Ritchey and Chakrabarti, 2014). In plants, not only do they associate with mitotic structures (Demidov et al., 2005) but also they interact with MAPs (Boruc et al., 2017). Since AUR does not possess microtubule-binding domains, its colocalization with mitotic structures is most likely related to its functional interactions with MAPs (Petrovská et al., 2012; Tomaštíková et al., 2015). Out of three members of Aurora kinase family in *Arabidopsis* (Kawabe et al., 2005), two of them, AUR1 and AUR2, are essential for regulating the orientation of formative cell divisions

throughout plant ontogenesis (Van Damme et al., 2011). AUR phosphorylates MAP65-1 during metaphase (Boruc et al., 2017); however, the strength of AUR control over MAP65-1 is significantly weaker compared with the effect of another kinase, MAPK. Therefore, a hypothesis was presented, according to which the direct control of AUR over MAP65-1 is mild, yet the phosphorylation of MAP65-1 by AUR promotes phosphorylation by other kinases. This is in line with the observation that regulation of many eukaryotic proteins depends on multisite phosphorylation (Cohen, 2000; Repetto et al., 2018). Prediction studies show that other cytoskeletal regulators of mitosis and especially of CDP orientation like POK2 may interact and become regulated by Aurora kinases (https:// string-db.org/cgi/network.pl?taskId=f13kHLYXYV1W; **Figure 2**).

MAPKs are well known to phosphorylate MAPs (Hoshi et al., 1992; Shiina et al., 1992). In *Arabidopsis*, MPK4 and MPK6 phosphorylate proteins from MAP65 family (Smertenko et al., 2006; Sasabe et al., 2011b; Smékalová et al., 2014; Zhou et al., 2017), and MPK6 also phosphorylates EB1c (Kohoutová et al., 2015). MAPKs are governed by MAPK kinases (MAPKKs), which, in turn, are regulated by MAPKK kinases (MAPKKKs). In plants, two MAPK signaling cascades were implicated in regulating microtubule dynamics during cell division and described in detail as follows. A third pathway which involves the MAPK MPK18 and the MAPK phosphatase PROPYZAMIDE HYPERSENSITIVE 1 (PHS1) is somehow elusive without knowledge on microtubule-associated substrates which may justify their role in microtubule regulation (Naoi and Hashimoto, 2004; Walia et al., 2009; Fujita et al., 2013). However, the role of PHS1 may be broader since it is presumably interacting and deactivating other MAPKs as well, including MPK3 and MPK6 (https://string-db. org/cgi/network.pl?taskId=j8pmY8S1UlbB; **Figure 2**).

The first MAPK cascade described to play a role in microtubule reorganization was the NACK-PQR pathway (Calderini et al., 1998, 2001; Bögre et al., 1999; Nishihama, 2001). In *Arabidopsis*, this pathway consists of ANP2/ANP3 (*Arabidopsis* nucleus and phragmoplast-localized kinase, MAP3K), MKK6, and MPK4/MPK6 (Krysan et al., 2002; Strompen et al., 2002), and it plays a crucial role during phragmoplast and cell plate formation (Takahashi et al., 2010). It affects the organization of mitotic structures *via* reversible phosphorylation of MAP65 proteins (Beck et al., 2010). Interestingly, activation of this MAP3K is negatively regulated by CDKs (Sasabe et al., 2011a). Moreover, CDKs also interfere with MAPK phosphorylating MAP65-1, since the single MAPK targeting motif in MAP65-1 overlaps with a CDK targeting site (Smertenko et al., 2006). In conclusion, this MAPK cascade controls microtubule organization and dynamics during phragmoplast and cell plate formation, and the temporal regulation of this module is facilitated by CDKs.

The other plant MAPK pathway, which is integral to cell division directionality, consists of YODA (YDA, MAP3K), MKK4/MKK5, and MPK3/MPK6. YODA is implicated in several types of asymmetrical divisions, e.g., first division of zygote and stomatal development (Lukowitz et al., 2004; Bergmann et al., 2004). However, the characterization of *YODA*

mutants revealed its function in CDP orientation of regular cell divisions underlying tissue patterning of vegetative organs such as the root (Müller et al., 2010; López-Bucio et al., 2014). These observations are further supported by microscopic studies, which proved MPK6 colocalization with mitotic microtubule structures (Müller et al., 2010; Smékalová et al., 2014; Komis et al., 2018). Interaction studies showed that MAP65-1 is interacting with MPK6 and possibly phosphorylated by it (Smékalová et al., 2014). Interestingly, knockout mutants of YDA have deregulated transcript levels of CPFS markers (specifically TAN and phragmoplast orienting kinesin 1). Therefore, YODA may be involved at multiple levels of CPFS orientation (Smékalová et al., 2014).

The last family of kinases involved in regulation of mitotic microtubule structures is NEKs. This family of Ser/Thr protein kinases is highly conserved in eukaryotes, where it supervises crucial points in mitosis and cell division (O'Connell et al., 2003; Brieño-Enríquez et al., 2017). In plants, NEKs were shown to regulate cortical microtubules and, in turn, to affect cell expansion, organ growth, and stress responses (Vigneault et al., 2007; Agueci et al., 2012; Takatani et al., 2017). As for their role in rearrangement of microtubules during mitosis, NEK6 is known to associate with spindle and phragmoplast (Motose et al., 2011), but its function remains obscure.

PROTEIN PHOSPHATASES REGULATING MAP ACTIVITY

The reversibility of phosphorylation is ensured by cooperation between kinases and phosphatases. Numerous protein phosphatases were found in plants, with Ser/Thr specific phosphoprotein phosphatases (PPPs) being a prominent group among them. PPPs encompass large number of proteins, which can be grouped in several protein families. Three of these families were implicated to regulate microtubule dynamics during cytokinesis (Samofalova et al., 2017).

Type one protein phosphatases (TOPPs, also called PP1s) were predicted to be part of cell cycle regulation (Farkas et al., 2007; Boyer and Simon, 2015), which is supported by finding putative CDK recognition sites (Kwon et al., 1997) as well as noting crucial role of animal PP1s in cell cycle progression (Rodrigues et al., 2015). However, the functions of these proteins were not comprehensively studied to this date.

More progress was achieved in solving the function of protein phosphatase type 2A (PP2A). These PPs consist of three subunits—scaffolding (A), regulatory (B), and catalytic (C). They were characterized in both monocots (Wright et al., 2009) and dicots (Camilleri et al., 2002). Moreover, their animal homologs were found to be essential for regulating microtubule structures in both meiosis and mitosis (Tang et al., 2016; Enos et al., 2017; Varadkar et al., 2017). In plants, PP2A controls organization and dynamics of both cortical and mitotic microtubules (**Figure 1**; Camilleri et al., 2002; Yoon et al., 2018). This view is supported by observing knockout mutants displaying abnormal arrangement of cortical microtubules and severe problems with PPB formation and cell division plane orientation (Torres-Ruiz and Jurgens, 1994; Traas

et al., 1995; McClinton and Sung, 1997). During mitosis, PP2A forms a complex with tonneau 1 (TON1) and TON1 recruiting motif proteins (TRMs) (Spinner et al., 2013). TON1 and TRMs recruit this complex to site where PPB forms (Drevensek et al., 2012), and there the complex governs PPB development. As it remains at this site even after PPB disassembly, it is possibly involved in CPFS maintenance (Wright et al., 2009). Targets of PP2A-driven dephosphorylation could be MAPs marking cytokinetic structures (specifically MOR1, TON1, and CLASP; Twell et al., 2002; Kawamura, 2005; Xu et al., 2008; Ambrose et al., 2011). PP2A could temporally and spatially restrict common MAP activities and this would allow microtubule stabilization and formation of PPB (Walker et al., 2007; Wright and Smith, 2007; Lipka et al., 2015).

Metallo-dependent protein phosphatases (PP2C) might be part of cell division machinery as well, since knockout mutants display improper cell division orientation (Song et al., 2006). These phosphatases are also implicated in regulating MAPKs and CDK (Meskiene et al., 1998; Umbrasaite et al., 2010). Currently, their role in cortical microtubule rearrangement in response to environmental stimuli has been explored (Bhaskara et al., 2017; Qu et al., 2018). However, details on how PP2C is integrated into the regulatory network of cytokinesis remain undisclosed.

Although plenty of research has been done in elucidating the role of kinases in microtubule reorganization during cell cycle, phosphatases involved in these events remain largely understudied. The cause of this lies mainly in the fact that these phosphatases form multiprotein complexes, which is a serious challenge for both analysis and evaluation. Nevertheless, the current advances in understanding the role of PP2A in regulating microtubule dynamics shows it is not an impossible task.

CONCLUSIONS/FUTURE DIRECTIONS

In summary, reversible phosphorylation of several different MAPs is essential for regulating microtubule dynamics and organization during the plant cell division. The affinity of MAPs for microtubules can be downregulated or restored pending on their phosphorylation status. To this extend, several protein kinases and phosphatases have been shown to target cytoskeletal proteins with various roles in the regulation of mitotic spindle and phragmoplast assembly and progression. However, many questions remain unanswered and are expected to be addressed in the near future:

1. How phosphorylation may affect microtubule nucleation during acentrosomal mitotic spindle formation?
2. Is phosphorylation related to the transition from PPB to mitotic spindle?
3. How phosphorylation really controls microtubule bundling during phragmoplast expansion?
4. Which phosphatases are reinstating microtubule binding of MAP65 proteins?
5. Which mechanisms allow the regulation of the same cytoskeletal proteins (e.g., MAP65-1, -2, and -3) by different

protein kinases (e.g., MPK4 and MPK6 or auroras) with a different biological outcome (i.e., progression of cytokinesis and CDP orientation, respectively)?

6. How global phosphoproteomics analyses will help to decipher reversibly phosphorylatable cytoskeletal substrates in model cell suspension systems that can be synchronized?

7. How differential (phospho)proteomics comparing wild types with protein kinase/phosphatase mutants will advance our knowledge in the identification of cytoskeletal substrates?

AUTHOR CONTRIBUTIONS

TV drafted the manuscript and drawn **Figure 1**. JŠ contributed critical evaluation and editing of the text. GK conceived the

topic, supervised TV during drafting of the manuscript and edited its final form together with JŠ.

REFERENCES

Agueci, F., Rutten, T., Demidov, D., and Houben, A. (2012). *Arabidopsis* AtNek2 kinase is essential and associates with microtubules. *Plant Mol. Biol. Report.* 30, 339–348. doi: 10.1007/s11105-011-0342-1

Ambrose, C., Allard, J. F., Cytrynbaum, E. N., and Wasteneys, G. O. (2011). A CLASP-modulated cell edge barrier mechanism drives cell-wide cortical microtubule organization in *Arabidopsis*. *Nat. Commun.* 2:430. doi: 10.1038/ncomms1444

Ambrose, J. C., Shoji, T., Kotzer, A. M., Pighin, J. A., and Wasteneys, G. O. (2007). The *Arabidopsis* CLASP gene encodes a microtubule-associated protein involved in cell expansion and division. *Plant Cell* 19, 2763–2775. doi: 10.1105/tpc.107.053777

Ayaydin, F., Vissi, E., Mészáros, T., Miskolczi, P., Kovács, I., Fehér, A., et al. (2000). Inhibition of serine/threonine-specific protein phosphatases causes premature activation of cdc2MsF kinase at G2/M transition and early mitotic microtubule organisation in alfalfa. *Plant J.* 23, 85–96. doi: 10.1046/j.1365-313x.2000.00798.x

Ban, Y., Kobayashi, Y., Hara, T., Hamada, T., Hashimoto, T., Takeda, S., et al. (2013). α-tubulin is rapidly phosphorylated in response to hyperosmotic stress in rice and *Arabidopsis*. *Plant Cell Physiol.* 54, 848–858. doi: 10.1093/pcp/pct065

Beck, M., Komis, G., Müller, J., Menzel, D., and Šamaj, J. (2010). *Arabidopsis* homologs of nucleus- and phragmoplast-localized kinase 2 and 3 and mitogen-activated protein kinase 4 are essential for microtubule organization. *Plant Cell* 22, 755–771. doi: 10.1105/tpc.109.071746

Bergmann, D. C., Lukowitz, W., and Somerville, C. R. (2004). Stomatal development and pattern controlled by a MAPKK kinase. *Science* 304, 1494–1497. doi: 10.1126/science.1096014

Bhaskara, G. B., Wen, T. -N., Nguyen, T. T., and Verslues, P. E. (2017). Protein phosphatase 2Cs and microtubule-associated stress protein 1 control microtubule stability, plant growth, and drought response. *Plant Cell* 29, 169–191. doi: 10.1105/tpc.16.00847

Binarova, P., Cihalikova, C., Dolezel, J., Gilmer, S., and Fowke, L. C. (1996). Actin distribution in somatic embryos and embryogenic protoplasts of white spruce (*Picea glauca*). *In Vitro-Plant* 32, 59–65. doi: 10.1007/BF02823132

Bögre, L., Calderini, O., Binarova, P., Mattauch, M., Till, S., Kiegerl, S., et al. (1999). A MAP kinase is activated late in plant mitosis and becomes localized to the plane of cell division. *Plant Cell* 11, 101–114. doi: 10.1105/tpc.11.1.101

Boruc, J., Weimer, A. K., Stoppin-Mellet, V., Mylle, E., Kosetsu, K., Cedeño, C., et al. (2017). Phosphorylation of MAP65-1 by *Arabidopsis* Aurora kinases is required for efficient cell cycle progression. *Plant Physiol.* 173, 582–599. doi: 10.1104/pp.16.01602

Boyer, F., and Simon, R. (2015). Asymmetric cell divisions constructing *Arabidopsis* stem cell niches: the emerging role of protein phosphatases. *Plant Biol.* 17, 935–945. doi: 10.1111/plb.12352

Brieño-Enríquez, M. A., Moak, S. L., Holloway, J. K., and Cohen, P. E. (2017). NIMA-related kinase 1 (NEK1) regulates meiosis I spindle assembly by

altering the balance between α-Adducin and Myosin X. *PLoS One* 12:e0185780. doi: 10.1371/journal.pone.0185780

Brumbarova, T., and Ivanov, R. (2016). Differential gene expression and protein phosphorylation as factors regulating the state of the *Arabidopsis* SNX1 protein complexes in response to environmental stimuli. *Front. Plant Sci.* 7:1456. doi: 10.3389/fpls.2016.01456

Buschmann, H., and Zachgo, S. (2016). The evolution of cell division: from streptophyte algae to land plants. *Trends Plant Sci.* 21, 872–883. doi: 10.1016/j.tplants.2016.07.004

Buschmann, H., Chan, J., Sanchez-Pulido, L., Andrade-Navarro, M. A., Doonan, J. H., and Lloyd, C. W. (2006). Microtubule-associated AIR9 recognizes the cortical division site at preprophase and cell-plate insertion. *Curr. Biol.* 16, 1938–1943. doi: 10.1016/j.cub.2006.08.028

Buschmann, H., Dols, J., Kopischke, S., Peña, E. J., Andrade-Navarro, M. A., Heinlein, M., et al. (2015). *Arabidopsis* KCBP interacts with AIR9 but stays in the cortical division zone throughout mitosis via its MyTH4-FERM domain. *J. Cell Sci.* 128, 2033–2046. doi: 10.1242/jcs.156570

Caillaud, M. -C., Lecomte, P., Jammes, F., Quentin, M., Pagnotta, S., Andrio, E., et al. (2008). MAP65-3 microtubule-associated protein is essential for nematode-induced giant cell ontogenesis in *Arabidopsis*. *Plant Cell* 20, 423–437. doi: 10.1105/tpc.107.057422

Calderini, O., Bogre, L., Vicente, O., Binarova, P., Heberle-Bors, E., and Wilson, C. (1998). A cell cycle regulated MAP kinase with a possible role in cytokinesis in tobacco cells. *J. Cell Sci.* 111, 3091–3100.

Calderini, O., Glab, N., Bergounioux, C., Heberle-Bors, E., and Wilson, C. (2001). A novel tobacco mitogen-activated protein (MAP) kinase kinase, NtMEK1, activates the cell cycle-regulated p43Ntf6 MAP kinase. *J. Biol. Chem.* 276, 18139–18145. doi: 10.1074/jbc.M010621200

Camilleri, C., Azimzadeh, J., Pastuglia, M., Bellini, C., Grandjean, O., and Bouchez, D. (2002). The *Arabidopsis* TONNEAU2 gene encodes a putative novel protein phosphatase 2A regulatory subunit essential for the control of the cortical cytoskeleton. *Plant Cell* 14, 833–845. doi: 10.1105/tpc.010402

Castro, A., Arlot-Bonnemains, Y., Vigneron, S., Labbé, J. -C., Prigent, C., and Lorca, T. (2002a). APC/fizzy-related targets Aurora-A kinase for proteolysis. *EMBO Rep.* 3, 457–462. doi: 10.1093/embo-reports/kvf095

Castro, A., Vigneron, S., Bernis, C., Labbé, J. -C., Prigent, C., and Lorca, T. (2002b). The D-Box-activating domain (DAD) is a new proteolysis signal that stimulates the silent D-Box sequence of Aurora-A. *EMBO Rep.* 3, 1209–1214. doi: 10.1093/embo-reports/kvf241

Chan, J., Jensen, C. G., Jensen, L. C. W., Bush, M., and Lloyd, C. W. (1999). The 65-kDa carrot microtubule-associated protein forms regularly arranged filamentous cross-bridges between microtubules. *Proc. Natl. Acad. Sci.* 96, 14931–14936. doi: 10.1073/pnas.96.26.14931

Chang, H. -Y., Smertenko, A. P., Igarashi, H., Dixon, D. P., and Hussey, P. J. (2005). Dynamic interaction of NtMAP65-1a with microtubules in vivo. *J. Cell Sci.* 118, 3195–3201. doi: 10.1242/jcs.02433

Chang-Jie, J., and Sonobe, S. (1993). Identification and preliminary characterization of a 65 kDa higher-plant microtubule-associated protein. *J. Cell Sci.* 105, 891–901.

Chen, H. -W., Persson, S., Grebe, M., and McFarlane, H. E. (2018). Cellulose synthesis during cell plate assembly. *Physiol. Plant.* 164, 17–26. doi: 10.1111/ppl.12703

Cohen, P. (2000). The regulation of protein function by multisite phosphorylation – a 25 year update. *Trends Biochem. Sci.* 25, 596–601. doi: 10.1016/S0968-0004(00)01712-6

Costa, S. (2017). Are division plane determination and cell-cycle progression coordinated? *New Phytol.* 213, 16–21. doi: 10.1111/nph.14261

Day, I. S., Miller, C., Golovkin, M., and Reddy, A. S. (2000). Interaction of a kinesin-like calmodulin-binding protein with a protein kinase. *J. Biol. Chem.* 275, 13737–13745. doi: 10.1074/jbc.275.18.13737

de Keijzer, J., Kieft, H., Ketelaar, T., Goshima, G., and Janson, M. E. (2017). Shortening of microtubule overlap regions defines membrane delivery sites during plant cytokinesis. *Curr. Biol.* 27, 514–520. doi: 10.1016/j.cub.2016.12.043

Demidov, D., Damme, D. V., Geelen, D., Blattner, F. R., and Houben, A. (2005). Identification and dynamics of two classes of Aurora-like kinases in *Arabidopsis* and other plants. *Plant Cell* 17, 836–848. doi: 10.1105/tpc.104.029710

Dhonukshe, P., and Gadella, T. W. J. (2003). Alteration of microtubule dynamic instability during preprophase band formation revealed by yellow fluorescent protein–CLIP170 microtubule plus-end labeling. *Plant Cell* 15, 597–611. doi: 10.1105/tpc.008961

Drevensek, S., Goussot, M., Duroc, Y., Christodoulidou, A., Steyaert, S., Schaefer, E., et al. (2012). The *Arabidopsis* TRM1-TON1 interaction reveals a recruitment network common to plant cortical microtubule arrays and eukaryotic centrosomes. *Plant Cell.* 24, 178–191. doi: 10.1105/tpc.111.089748

Eng, R. C., Halat, L. S., Livingston, S. J., Sakai, T., Motose, H., and Wasteneys, G. O. (2017). The ARM domain of ARMADILLO-REPEAT KINESIN 1 is not required for microtubule catastrophe but can negatively regulate NIMA-RELATED KINASE 6 in *Arabidopsis thaliana*. *Plant Cell Physiol.* 58, 1350–1363. doi: 10.1093/pcp/pcx070

Enos, S. J., Dressler, M., Ferreira Gomes, B., Hyman, A. A., and Woodruff, J. B. (2017). Phosphatase PP2A and microtubule pulling forces disassemble centrosomes during mitotic exit. *Biol. Open.* doi: 10.1242/bio.029777

Farkas, I., Dombrádi, V., Miskei, M., Szabados, L., and Koncz, C. (2007). Arabidopsis PPP family of serine/threonine phosphatases. *Trends Plant Sci.* 12, 169–176. doi: 10.1016/j.tplants.2007.03.003

Fujita, S., Pytela, J., Hotta, T., Kato, T., Hamada, T., Akamatsu, R., et al. (2013). An atypical tubulin kinase mediates stress-induced microtubule depolymerization in Arabidopsis. *Curr. Biol.* 23, 1969–1978. doi: 10.1016/j.cub.2013.08.006

Gaillard, J., Neumann, E., Van Damme, D., Stoppin-Mellet, V., Ebel, C., Barbier, E., et al. (2008). Two microtubule-associated proteins of *Arabidopsis* MAP65s promote antiparallel microtubule bundling. *Mol. Biol. Cell* 19, 4534–4544. doi: 10.1091/mbc.e08-04-0341

Herrmann, A., Livanos, P., Lipka, E., Gadeyne, A., Hauser, M. T., Van Damme, D., et al. (2018). Dual localized kinesin-12 POK2 plays multiple roles during cell division and interacts with MAP65-3. *EMBO Rep.* 19:e46085. doi: 10.15252/embr.201846085

Hoshi, M., Ohta, K., Gotoh, Y., Mori, A., Murofushi, H., Sakai, H., et al. (1992). Mitogen-activated-protein-kinase-catalyzed phosphorylation of microtubule-associated proteins, microtubule-associated protein 2 and microtubule-associated protein 4, induces an alteration in their function. *Eur. J. Biochem.* 203, 43–52.

Humphrey, T. V., Haasen, K. E., Aldea-Brydges, M. G., Sun, H., Zayed, Y., Indriolo, E., et al. (2015). PERK-KIPK-KCBP signalling negatively regulates root growth in *Arabidopsis thaliana*. *J. Exp. Bot.* 66, 71–83. doi: 10.1093/jxb/eru390

Hussey, P. J., Hawkins, T. J., Igarashi, H., Kaloriti, D., and Smertenko, A. (2002). The plant cytoskeleton: recent advances in the study of the plant microtubule-associated proteins MAP-65, MAP-190 and the *Xenopus* MAP215-like protein, MOR1. *Plant Mol. Biol.* 50, 915–924. doi: 10.1023/A:1021236307508

Kawabe, A., Matsunaga, S., Nakagawa, K., Kurihara, D., Yoneda, A., Hasezawa, S., et al. (2005). Characterization of plant Aurora kinases during mitosis. *Plant Mol. Biol.* 58, 1–13. doi: 10.1007/s11103-005-3454-x

Kawamura, E. (2005). MICROTUBULE ORGANIZATION 1 regulates structure and function of microtubule arrays during mitosis and cytokinesis in the *Arabidopsis* root. *Plant Physiol.* 140, 102–114. doi: 10.1104/pp.105.069989

Kirik, A., Ehrhardt, D. W., and Kirik, V. (2012). TONNEAU2/FASS regulates the geometry of microtubule nucleation and cortical array organization in interphase Arabidopsis cells. *Plant Cell* 24, 1158–1170. doi: 10.1105/tpc.111.094367

Kohoutová, L., Kourová, H., Nagy, S. K., Volc, J., Halada, P., Mészáros, T., et al. (2015). The *Arabidopsis* mitogen-activated protein kinase 6 is associated with γ-tubulin on microtubules, phosphorylates EB1c and maintains spindle orientation under nitrosative stress. *New Phytol.* 207, 1061–1074. doi: 10.1111/nph.13501

Komaki, S., Abe, T., Coutuer, S., Inzé, D., Russinova, E., and Hashimoto, T. (2010). Nuclear-localized subtype of end-binding 1 protein regulates spindle organization in Arabidopsis. *J. Cell Sci.* 123, 451–459. doi: 10.1242/jcs.062703

Komis, G., Luptovčiak, I., Ovečka, M., Samakovli, D., Šamajová, O., and Šamaj, J. (2017). Katanin effects on dynamics of cortical microtubules and mitotic arrays in *Arabidopsis thaliana* revealed by advanced live-cell imaging. *Front. Plant Sci.* 8:866. doi: 10.3389/fpls.2017.00866

Komis, G., Novák, D., Ovečka, M., Šamajová, O., and Šamaj, J. (2018). Advances in imaging plant cell dynamics. *Plant Physiol.* 176, 80–93. doi: 10.1104/pp.17.00962

Kosetsu, K., Matsunaga, S., Nakagami, H., Colcombet, J., Sasabe, M., Soyano, T., et al. (2010). The MAP kinase MPK4 is required for cytokinesis in *Arabidopsis thaliana*. *Plant Cell* 22, 3778–3790. doi: 10.1105/tpc.110.077164

Krysan, P. J., Jester, P. J., Gottwald, J. R., and Sussman, M. R. (2002). An *Arabidopsis* mitogen-activated protein kinase kinase kinase gene family encodes essential positive regulators of cytokinesis. *Plant Cell* 14, 1109–1120. doi: 10.1105/tpc.001164

Kwon, Y. -G., Lee, S. Y., Choi, Y., Greengard, P., and Nairn, A. C. (1997). Cell cycle-dependent phosphorylation of mammalian protein phosphatase 1 by cdc2 kinase. *Proc. Natl. Acad. Sci.* 94, 2168–2173. doi: 10.1073/pnas.94.6.2168

Lee, J., Das, A., Yamaguchi, M., Hashimoto, J., Tsutsumi, N., Uchimiya, H., et al. (2003). Cell cycle function of a rice B2-type cyclin interacting with a B-type cyclin-dependent kinase. *Plant J.* 34, 417–425. doi: 10.1046/j.1365-313X.2003.01736.x

Li, H., Sun, B., Sasabe, M., Deng, X., Machida, Y., Lin, H., et al. (2017). *Arabidopsis* MAP65-4 plays a role in phragmoplast microtubule organization and marks the cortical cell division site. *New Phytol.* 215, 187–201. doi: 10.1111/nph.14532

Lin, F., Krishnamoorthy, P., Schubert, V., Hause, G., Heilmann, M., and Heilmann, I. (2019). A dual role for cell plate-associated PI4Kβ in endocytosis and phragmoplast dynamics during plant somatic cytokinesis. *EMBO J.* (In Press). doi: 10.15252/embj.2018100303

Lipka, E., Gadeyne, A., Stöckle, D., Zimmermann, S., Jaeger, G. D., Ehrhardt, D. W., et al. (2014). The phragmoplast-orienting kinesin-12 class proteins translate the positional information of the preprophase band to establish the cortical division zone in *Arabidopsis thaliana*. *Plant Cell.* 26, 2617–2632. doi: 10.1105/tpc.114.124933

Lipka, E., Herrmann, A., and Mueller, S. (2015). Mechanisms of plant cell division. *Wiley Interdiscip. Rev. Dev. Biol.* 4, 391–405. doi: 10.1002/wdev.186

López-Bucio, J. S., Dubrovsky, J. G., Raya-González, J., Ugartechea-Chirino, Y., López-Bucio, J., Luna-Valdez, D., et al. (2014). *Arabidopsis thaliana* mitogen-activated protein kinase 6 is involved in seed formation and modulation of primary and lateral root development. *J. Exp. Bot.* 65, 169–183. doi: 10.1093/jxb/ert368

Loughlin, R., Wilbur, J. D., McNally, F. J., Nédélec, F. J., and Heald, R. (2011). Katanin contributes to interspecies spindle length scaling in *Xenopus*. *Cell* 147, 1397–1407. doi: 10.1016/j.cell.2011.11.014

Lucas, J. R., and Shaw, S. L. (2012). MAP65-1 and MAP65-2 promote cell proliferation and axial growth in *Arabidopsis* roots. *Plant J.* 71, 454–463. doi: 10.1111/j.1365-313X.2012.05002.x

Lukowitz, W., Roeder, A., Parmenter, D., and Somerville, C. (2004). A MAPKK kinase gene regulates extra-embryonic cell fate in *Arabidopsis*. *Cell* 116, 109–119. doi: 10.1016/S0092-8674(03)01067-5

Mao, T., Jin, L., Li, H., Liu, B., and Yuan, M. (2005). Two microtubule-associated proteins of the *Arabidopsis* MAP65 family function differently on microtubules. *Plant Physiol.* 138, 654–662. doi: 10.1104/pp.104.052456

Marcus, A. I., Dixit, R., and Cyr, R. J. (2005). Narrowing of the preprophase microtubule band is not required for cell division plane determination in cultured plant cells. *Protoplasma* 226, 169–174. doi: 10.1007/s00709-005-0119-1

McClinton, R. S., and Sung, Z. R. (1997). Organization of cortical microtubules at the plasma membrane in *Arabidopsis*. *Planta* 201, 252–260. doi: 10.1007/s004250050064

Meskiene, I., Bogre, L., Glaser, W., Balog, J., Brandstotter, M., Zwerger, K., et al. (1998). MP2C, a plant protein phosphatase 2C, functions as a negative regulator of mitogen-activated protein kinase pathways in yeast and plants. *Proc. Natl. Acad. Sci.* 95, 1938–1943. doi: 10.1073/pnas.95.4.1938

Motose, H., Hamada, T., Yoshimoto, K., Murata, T., Hasebe, M., Watanabe, Y., et al. (2011). NIMA-related kinases 6, 4, and 5 interact with each other to regulate microtubule organization during epidermal cell expansion in *Arabidopsis thaliana*. *Plant J.* 67, 993–1005. doi: 10.1111/j.1365-313X.2011.04652.x

Müller, J., Beck, M., Mettbach, U., Komis, G., Hause, G., Menzel, D., et al. (2010). *Arabidopsis* MPK6 is involved in cell division plane control during early root development, and localizes to the pre-prophase band, phragmoplast, trans-Golgi network and plasma membrane. *Plant J.* 61, 234–248. doi: 10.1111/j.1365-313X.2009.04046.x

Müller, S., Han, S., and Smith, L. G. (2006). Two kinesins are involved in the spatial control of cytokinesis in *Arabidopsis thaliana*. *Curr. Biol.* 16, 888–894. doi: 10.1016/j.cub.2006.03.034

Müller, S., Smertenko, A., Wagner, V., Heinrich, M., Hussey, P. J., and Hauser, M. -T. (2004). The plant microtubule-associated protein AtMAP65-3/PLE is essential for cytokinetic phragmoplast function. *Curr. Biol.* 14, 412–417. doi: 10.1016/j.cub.2004.02.032

Murata, T., Sano, T., Sasabe, M., Nonaka, S., Higashiyama, T., Hasezawa, S., et al. (2013). Mechanism of microtubule array expansion in the cytokinetic phragmoplast. *Nat. Commun.* 4:1967. doi: 10.1038/ncomms2967

Naoi, K., and Hashimoto, T. (2004). A semidominant mutation in an Arabidopsis mitogen-activated protein kinase phosphatase-like gene compromises cortical microtubule organization. *Plant Cell* 16, 1841–1853. doi: 10.1105/tpc.021865

Nishihama, R. (2001). The NPK1 mitogen-activated protein kinase kinase kinase is a regulator of cell-plate formation in plant cytokinesis. *Genes Dev.* 15, 352–363. doi: 10.1101/gad.863701

Nishihama, R., Soyano, T., Ishikawa, M., Araki, S., Tanaka, H., Asada, T., et al. (2002). Expansion of the cell plate in plant cytokinesis requires a kinesin-like protein/MAPKKK complex. *Cell* 109, 87–99. doi: 10.1016/S0092-8674(02)00691-8

O'Connell, M. J., Krien, M. J. E., and Hunter, T. (2003). Never say never. The NIMA-related protein kinases in mitotic control. *Trends Cell Biol.* 13, 221–228. doi: 10.1016/S0962-8924(03)00056-4

Oh, S. A., Allen, T., Kim, G. J., Sidorova, A., Borg, M., Park, S. K., et al. (2012). Arabidopsis fused kinase and the kinesin-12 subfamily constitute a signalling module required for phragmoplast expansion. *Plant J.* 72, 308–319. doi: 10.1111/j.1365-313X.2012.05077.x

Oh, S. A., Johnson, A., Smertenko, A., Rahman, D., Park, S. K., Hussey, P. J., et al. (2005). A divergent cellular role for the FUSED kinase family in the plant-specific cytokinetic phragmoplast. *Curr. Biol.* 15, 2107–2111. doi: 10.1016/j.cub.2005.10.044

Ookata, K., Hisanaga, S., Sugita, M., Okuyama, A., Murofushi, H., Kitazawa, H., et al. (1997). MAP4 is the in vivo substrate for CDC2 kinase in HeLa cells: identification of an M-phase specific and a cell cycle-independent phosphorylation site in MAP4. *Biochemist* 36, 15873–15883. doi: 10.1021/bi971251w

Panteris, E., Diannelidis, B. -E., and Adamakis, I. -D. S. (2018). Cortical microtubule orientation in *Arabidopsis thaliana* root meristematic zone depends on cell division and requires severing by katanin. *J. Biol. Res. Thessalon.* 25:12. doi: 10.1186/s40709-018-0082-6

Petrovská, B., Cenklová, V., Pochylová, Ž., Kourová, H., Doskočilová, A., Plíhal, O., et al. (2012). Plant Aurora kinases play a role in maintenance of primary meristems and control of endoreduplication. *New Phytol.* 193, 590–604. doi: 10.1111/j.1469-8137.2011.03989.x

Petrovská, B., Jeřábková, H., Kohoutová, L., Cenklová, V., Pochylová, Ž., Gelová, Z., et al. (2013). Overexpressed TPX2 causes ectopic formation of microtubular arrays in the nuclei of acentrosomal plant cells. *J. Exp. Bot.* 64, 4575–4587. doi: 10.1093/jxb/ert271

Pickett-Heaps, J. D., and Northcote, D. H. (1966). Organization of microtubules and endoplasmic reticulum during mitosis and cytokinesis in wheat meristems. *J. Cell Sci.* 1, 109–120.

Qu, Y., Song, P., Hu, Y., Jin, X., Jia, Q., Zhang, X., et al. (2018). Regulation of stomatal movement by cortical microtubule organization in response to darkness and ABA signaling in *Arabidopsis*. *Plant Growth Regul.* 84, 467–479. doi: 10.1007/s10725-017-0353-5

Repetto, M. V., Winters, M. J., Bush, A., Reiter, W., Hollenstein, D. M., Ammerer, G., et al. (2018). CDK and MAPK synergistically regulate signaling dynamics via a shared multi-site phosphorylation region on the scaffold protein Ste5. *Mol. Cell* 69, 938–952.e6. doi: 10.1016/j.molcel.2018.02.018

Ritchey, L., and Chakrabarti, R. (2014). Aurora A kinase modulates actin cytoskeleton through phosphorylation of Cofilin: implication in the mitotic process. *Biochim. Biophys. Acta BBA Mol. Cell Res.* 1843, 2719–2729. doi: 10.1016/j.bbamcr.2014.07.014

Rodrigues, N. T. L., Lekomtsev, S., Jananji, S., Kriston-Vizi, J., Hickson, G. R. X., and Baum, B. (2015). Kinetochore-localized PP1–Sds22 couples chromosome segregation to polar relaxation. *Nature* 524, 489–492. doi: 10.1038/nature14496

Samaj, J., Baluska, F., and Hirt, H. (2004). From signal to cell polarity: mitogen-activated protein kinases as sensors and effectors of cytoskeleton dynamicity. *J. Exp. Bot.* 55, 189–198. doi: 10.1093/jxb/erh012

Samaj, J., Ovecka, M., Hlavacka, A., Lecourieux, F., Meskiene, I., Lichtscheidl, I., et al. (2002). Involvement of the mitogen-activated protein kinase SIMK in regulation of root hair tip growth. *EMBO J.* 21, 3296–3306. doi: 10.1093/emboj/cdf349

Samofalova, D. O., Karpov, P. A., Raevsky, A. V., and Blume, Y. B. (2017). Protein phosphatases potentially associated with regulation of microtubules, their spatial structure reconstruction and analysis. *Cell Biol. Int.* doi: 10.1002/cbin.10810

Sasabe, M., Boudolf, V., Veylder, L. D., Inzé, D., Genschik, P., and Machida, Y. (2011a). Phosphorylation of a mitotic kinesin-like protein and a MAPKKK by cyclin-dependent kinases (CDKs) is involved in the transition to cytokinesis in plants. *Proc. Natl. Acad. Sci.* 108, 17844–17849. doi: 10.1073/pnas.1110174108

Sasabe, M., Kosetsu, K., Hidaka, M., Murase, A., and Machida, Y. (2011b). *Arabidopsis thaliana* MAP65-1 and MAP65-2 function redundantly with MAP65-3/PLEIADE in cytokinesis downstream of MPK4. *Plant Signal. Behav.* 6, 743–747. doi: 10.4161/psb.6.5.15146

Schaefer, E., Belcram, K., Uyttewaal, M., Duroc, Y., Goussot, M., Legland, D., et al. (2017). The preprophase band of microtubules controls the robustness of division orientation in plants. *Science* 356, 186–189. doi: 10.1126/science.aal3016

Schecher, S., Walter, B., Falkenstein, M., Macher-Goeppinger, S., Stenzel, P., Krümpelmann, K., et al. (2017). Cyclin K dependent regulation of Aurora B affects apoptosis and proliferation by induction of mitotic catastrophe in prostate cancer: cyclin K in prostate cancer. *Int. J. Cancer* 141, 1643–1653. doi: 10.1002/ijc.30864

Sedbrook, J. C., Ehrhardt, D. W., Fisher, S. E., Scheible, W. R., and Somerville, C. R. (2004). The *Arabidopsis sku6/spiral1* gene encodes a plus end-localized microtubule-interacting protein involved in directional cell expansion. *Plant Cell* 16, 1506–1520. doi: 10.1105/tpc.020644

Shiina, N., Moriguchi, T., Ohta, K., Gotoh, Y., and Nishida, E. (1992). Regulation of a major microtubule-associated protein by MPF and MAP kinase. *EMBO J.* 11, 3977–3984. doi: 10.1002/j.1460-2075.1992.tb05491.x

Smékalová, V., Luptovčiak, I., Komis, G., Šamajová, O., Ovečka, M., Doskočilová, A., et al. (2014). Involvement of YODA and mitogen activated protein kinase 6 in *Arabidopsis* post-embryogenic root development through auxin up-regulation and cell division plane orientation. *New Phytol.* 203, 1175–1193. doi: 10.1111/nph.12880

Smertenko, A. P., Chang, H. -Y., Sonobe, S., Fenyk, S., Weingartner, M., Bögre, L., et al. (2006). Control of the AtMAP65-1 interaction with microtubules through the cell cycle. *J. Cell Sci.* 119, 3227–3237. doi: 10.1242/jcs.03051

Smertenko, A. P., Kaloriti, D., Chang, H. -Y., Fiserova, J., Opatrny, Z., and Hussey, P. J. (2008). The C-terminal variable region specifies the dynamic properties of *Arabidopsis* microtubule-associated protein MAP65 isotypes. *Plant Cell* 20, 3346–3358. doi: 10.1105/tpc.108.063362

Smertenko, A., Hewitt, S. L., Jacques, C. N., Kacprzyk, R., Liu, Y., Marcec, M. J., et al. (2018). Phragmoplast microtubule dynamics - a game of zones. *J. Cell Sci.* 131, 1–11. doi: 10.1242/jcs.203331

Song, S. -K., Lee, M. M., and Clark, S. E. (2006). POL and PLL1 phosphatases are CLAVATA1 signaling intermediates required for *Arabidopsis* shoot and floral stem cells. *Development* 133, 4691–4698. doi: 10.1242/dev.02652

Spinner, L., Gadeyne, A., Belcram, K., Goussot, M., Moison, M., Duroc, Y., et al. (2013). A protein phosphatase 2A complex spatially controls plant cell division. *Nat. Commun.* 4:1863. doi: 10.1038/ncomms2831

Stals, H., Bauwens, S., Traas, J., Montagu, M. V., Engler, G., and Inzé, D. (1997). Plant CDC2 is not only targeted to the pre-prophase band, but also co-localizes with the spindle, phragmoplast, and chromosomes. *FEBS Lett.* 418, 229–234. doi: 10.1016/S0014-5793(97)01368-9

Strompen, G., El Kasmi, F., Richter, S., Lukowitz, W., Assaad, F. F., Jürgens, G., et al. (2002). The *Arabidopsis HINKEL* gene encodes a kinesin-related protein involved in cytokinesis and is expressed in a cell cycle-dependent manner. *Curr. Biol.* 12, 153–158. doi: 10.1016/S0960-9822(01)00655-8

Takahashi, Y., Soyano, T., Kosetsu, K., Sasabe, M., and Machida, Y. (2010). HINKEL kinesin, ANP MAPKKKs and MKK6/ANQ MAPKK, which phosphorylates and activates MPK4 MAPK, constitute a pathway that is required for cytokinesis in *Arabidopsis thaliana*. *Plant Cell Physiol.* 51, 1766–1776. doi: 10.1093/pcp/pcq135

Takatani, S., Ozawa, S., Yagi, N., Hotta, T., Hashimoto, T., Takahashi, Y., et al. (2017). Directional cell expansion requires NIMA-related kinase 6 (NEK6)-mediated cortical microtubule destabilization. *Sci. Rep.* 7:7826. doi: 10.1038/s41598-017-08453-5

Tang, A., Shi, P., Song, A., Zou, D., Zhou, Y., Gu, P., et al. (2016). PP2A regulates kinetochore-microtubule attachment during meiosis I in oocyte. *Cell Cycle* 15, 1450–1461. doi: 10.1080/15384101.2016.1175256

Tomaštíková, E., Demidov, D., Jeřábková, H., Binarová, P., Houben, A., Doležel, J., et al. (2015). TPX2 protein of *Arabidopsis* activates Aurora kinase 1, but not Aurora kinase 3 in vitro. *Plant Mol. Biol. Report.* 33, 1988–1995. doi: 10.1007/s11105-015-0890-x

Torres-Ruiz, R. A., and Jurgens, G. (1994). Mutations in the FASS gene uncouple pattern formation and morphogenesis in *Arabidopsis development*. *Development* 120, 2967–2978.

Traas, J., Bellini, C., Nacry, P., Kronenberger, J., Bouchez, D., and Caboche, M. (1995). Normal differentiation patterns in plants lacking microtubular pre-prophase bands. *Nature* 375, 676–677. doi: 10.1038/375676a0

Twell, D., Park, S. K., Hawkins, T. J., Schubert, D., Schmidt, R., Smertenko, A., et al. (2002). MOR1/GEM1 has an essential role in the plant-specific cytokinetic phragmoplast. *Nat. Cell Biol.* 4, 711–714. doi: 10.1038/ncb844

Umbrasaite, J., Schweighofer, A., Kazanaviciute, V., Magyar, Z., Ayatollahi, Z., Unterwurzacher, V., et al. (2010). MAPK phosphatase AP2C3 induces ectopic proliferation of epidermal cells leading to stomata development in *Arabidopsis*. *PLoS One* 5:e15357. doi: 10.1371/journal.pone.0015357

Van Damme, D. V., De Rybel, B., Gudesblat, G., Demidov, D., Grunewald, W., De Smet, I., et al. (2011). *Arabidopsis* α Aurora kinases function in formative cell division plane orientation. *Plant Cell.* 23, 4013–4024. doi: 10.1105/tpc.111.089565

Varadkar, P., Abbasi, F., Takeda, K., Dyson, J. J., and McCright, B. (2017). PP2A-B56γ is required for an efficient spindle assembly checkpoint. *Cell Cycle* 16, 1210–1219. doi: 10.1080/15384101.2017.1325042

Vasquez, R. J., Gard, D. L., and Cassimeris, L. (1999). Phosphorylation by CDK1 regulates XMAP215 function in vitro. *Cell Motil.* 43, 310–321. doi: 10.1002/(SICI)1097-0169(1999)43:4<310::AID-CM4>3.0.CO;2-J

Vigneault, F., Lachance, D., Cloutier, M., Pelletier, G., Levasseur, C., and Séguin, A. (2007). Members of the plant NIMA-related kinases are involved in organ development and vascularization in poplar, *Arabidopsis* and rice. *Plant J.* 51, 575–588. doi: 10.1111/j.1365-313X.2007.03161.x

Walia, A., Lee, J. S., Wasteneys, G., and Ellis, B. (2009). Arabidopsis mitogen-activated protein kinase MPK18 mediates cortical microtubule functions in plant cells. *Plant J.* 59, 565–575. doi: 10.1111/j.1365-313X.2009.03895.x

Walker, K. L., Müller, S., Moss, D., Ehrhardt, D. W., and Smith, L. G. (2007). *Arabidopsis* TANGLED identifies the division plane throughout mitosis and cytokinesis. *Curr. Biol.* 17, 1827–1836. doi: 10.1016/j.cub.2007.09.063

Weingartner, M., Binarova, P., Drykova, D., Schweighofer, A., David, J. -P., Heberle-Bors, E., et al. (2001). Dynamic recruitment of Cdc2 to specific microtubule structures during mitosis. *Plant Cell* 13, 1929–1943. doi: 10.1105/tpc.13.8.1929

Whitehead, E., Heald, R., and Wilbur, J. D. (2013). N-terminal phosphorylation of p60 katanin directly regulates microtubule severing. *J. Mol. Biol.* 425, 214–221. doi: 10.1016/j.jmb.2012.11.022

Wong, J. H., and Hashimoto, T. (2017). Novel *Arabidopsis* microtubule-associated proteins track growing microtubule plus ends. *BMC Plant Biol.* 17:33. doi: 10.1186/s12870-017-0987-5

Wright, A. J., and Smith, L. G. (2007). "Division plane orientation in plant cells" in *Cell division control in plants plant cell monographs*. (Berlin, Heidelberg: Springer), 33–57.

Wright, A. J., Gallagher, K., and Smith, L. G. (2009). Discordia1 and alternative discordia1 function redundantly at the cortical division site to promote preprophase band formation and orient division planes in maize. *Plant Cell* 21, 234–247. doi: 10.1105/tpc.108.062810

Wu, S. -Z., and Bezanilla, M. (2014). Myosin VIII associates with microtubule ends and together with actin plays a role in guiding plant cell division. *elife* 3:e03498. doi: 10.7554/eLife.03498

Xu, X. M., Zhao, Q., Rodrigo-Peiris, T., Brkljacic, J., He, C. S., Muller, S., et al. (2008). RanGAP1 is a continuous marker of the *Arabidopsis* cell division plane. *Proc. Natl. Acad. Sci.* 105, 18637–18642. doi: 10.1073/pnas.0806157105

Xue, Y., Ren, J., Gao, X., Jin, C., Wen, L., and Yao, X. (2008). GPS 2.0, a tool to predict kinase-specific phosphorylation sites in hierarchy. *Mol. Cell. Proteomics* 7, 1598–1608. doi: 10.1074/mcp.M700574-MCP200

Yoon, J. -T., Ahn, H. -K., and Pai, H. -S. (2018). The subfamily II catalytic subunits of protein phosphatase 2A (PP2A) are involved in cortical microtubule organization. *Planta* 248, 1–17. doi: 10.1007/s00425-018-3000-0

Zhou, S., Chen, Q., Li, X., and Li, Y. (2017). MAP65-1 is required for the depolymerization and reorganization of cortical microtubules in the response to salt stress in *Arabidopsis*. *Plant Sci.* 264, 112–121. doi: 10.1016/j.plantsci.2017.09.004

Conflict of Interest Statement: The authors declare that the research was conducted in the absence of any commercial or financial relationships that could be construed as a potential conflict of interest.

Publication 3.

<u>Title:</u> Multicolour three dimensional structured illumination microscopy of immunolabeled plant microtubules and associated proteins.

<u>Authors:</u> <u>Tereza Vavrdová,</u> Olga Šamajová, Pavel Křenek, Miroslav Ovečka, Pavlína Floková, Renata Šnaurová, Jozef Šamaj and George Komis

Plant Methods 2019; **15**(1): 22.

My contribution: I was helping with selection of transformed plants and handling plants. I contributed to image acquisition, post-acquisition image processing and to the manuscript preparation.

METHODOLOGY

Multicolour three dimensional structured illumination microscopy of immunolabeled plant microtubules and associated proteins

T. Vavrdová, O. Šamajová, P. Křenek, M. Ovečka, P. Floková, R. Šnaurová, J. Šamaj and G. Komis*

Abstract

Background: In the present work, we provide an account of structured illumination microscopy (SIM) imaging of fixed and immunolabeled plant probes. We take advantage of SIM, to superresolve intracellular structures at a considerable z-range and circumvent its low temporal resolution capacity during the study of living samples. Further, we validate the protocol for the imaging of fixed transgenic material expressing fluorescent protein-based markers of different subcellular structures.

Results: Focus is given on 3D imaging of bulky subcellular structures, such as mitotic and cytokinetic microtubule arrays as well as on the performance of SIM using multichannel imaging and the quantitative correlations that can be deduced. As a proof of concept, we provide a superresolution output on the organization of cortical microtubules in wild-type and mutant Arabidopsis cells, including aberrant preprophase microtubule bands and phragmoplasts in a cytoskeletal mutant devoid of the p60 subunit of the microtubule severing protein KATANIN and refined details of cytoskeletal aberrations in the mitogen activated protein kinase (MAPK) mutant *mpk4*. We further demonstrate, in a qualitative and quantitative manner, colocalizations between MPK6 and unknown dually phosphorylated and activated MAPK species and we follow the localization of the microtubule associated protein 65-3 (MAP65-3) in telophase and cytokinetic microtubular arrays.

Conclusions: 3D SIM is a powerful, versatile and adaptable microscopy method for elucidating spatial relationships between subcellular compartments. Improved methods of sample preparation aiming to the compensation of refractive index mismatches, allow the use of 3D SIM in the documentation of complex plant cell structures, such as microtubule arrays and the elucidation of their interactions with microtubule associated proteins.

Keywords: Immunofluorescence, Microtubules, Microtubule associated proteins, Structured illumination microscopy

Background

Fluorescence microscopy, is the most powerful method to specifically interrogate subcellular infrastructure and the dynamics of distinct compartments and macromolecular assemblies [9]. Depending on the various confocal or widefield platforms that exist and the labeling strategies employed, it is possible to address intracellular architecture and dynamics of specific compartments at a wide range of spatiotemporal resolution (e.g., [24, 36]).

The need of imaging subcellular architecture, necessitates microscopy approaches with adequate resolving power at all three dimensions, since many such structures occupy a significant volume. 3D imaging has to cope with issues of light scattering due to refractive index mismatches and out-of-focus signal (e.g., [56]). Confocal laser scanning microscopy (CLSM), is being routinely used for 3D imaging, as it provides optical sectioning and exclusion of out-of-focus light by means of an adjustable pinhole [19]. However, CLSM in practice has very poor resolving capacity that may be slightly below

*Correspondence: georgios.komis@upol.cz
Department of Cell Biology, Centre of the Region Haná
for Biotechnological and Agricultural Research, Faculty of Science, Palacký University Olomouc, Olomouc, Czech Republic

Vavrdová *et al. Plant Methods* (2019) 15:22

Page 2 of 17

300 nm at the XY-plane and more than twice as much at the Z-dimension depending on the excitation light wavelength, the numerical aperture of the collecting objective and the pinhole settings (e.g., [8, 19, 24] and references therein), while for volumetric imaging, CLSM is time limited, although this issue is currently circumvented with resonant scanning at the expense of spatial resolution [19].

The diffraction limitations of widefield or confocal scanning fluorescence microscopy methods have been overcome to a considerable extend by different superresolution modalities [23, 24]. Such methods, convey structural information below Abbe's diffraction limits, either by patterned light illumination strategies (such as structured illumination microscopy, SIM; [15], or stimulated emission depletion microscopy, STED; [16]), while others exemplified by photoactivation localization microscopy (PALM; [7]) and the closely related stochastic optical reconstruction microscopy (STORM; [41]), utilize photochemical properties of fluorophores and highly sensitive acquisition systems to improve the precision of localization of individual molecules. The dimensional resolution using such methods can be isotropic (as is the case with STED and PALM/STORM), or slightly inferior at the Z-dimension (as in the case of SIM; [23]).

Within limits, all superresolution methods are able to resolve subcellular structures in living cells labeled with genetically encoded fluorescent markers but they differ in both terms of temporal resolution and their effective z-range.

Unlike TIRF-based methods such as PALM or dSTORM, SIM is a widefield approach that can offer superresolution at large fields of view (FOVs). This allows imaging of considerable tissue areas and facilitates quantitative deductions of the subcellular distribution of organelles in many cells. Moreover, employment of 3D-SIM via commercially available SIM platforms can offer an effective z-range of more than 10 μm (e.g., [55]), allowing the documentation of voluminous subcellular structures such as interphase nuclei [13, 26, 47, 49–51], mitotic chromosomes [1, 3, 29, 39, 48], the meiotic and mitotic spindle [29, 57], or plasmodesmata organization [14] with a z-resolution which can be easily half that of CLSM (reviewed in [42]). In all commercially available SIM platforms, volumetric imaging is limited by the temporal component, suggesting that imaging of structures occupying considerable volumes, is best done in stabilized and appropriately labeled cells. Until recently, commercial SIM platforms (including Zeiss Elyra S.1, Nikon NSIM and Deltavision OMX), presented limitations in the extend of volumetric imaging, either with restrictions

of the z-range (which for all platforms is between 5 and 15 μm), acquisition speed (which can be very limiting for volumetric imaging), or channel range which can be visualized (e.g., the configuration of Elyra S.1 allows only one camera by default meaning that multichannel imaging requires time consuming sequential acquisition). Such problems have been largely resolved with the new generation SIM microscopes such as the Zeiss Elyra 7 and the Deltavision OMX SR. By using unique modes of illumination (e.g., with lattice illumination in Elyra 7 and interferometric light pattern generation in the Deltavision OMX SR) and default configurations which may include from 2 up to 4 cameras, they allow very high acquisition frame rates (between 255 fps for Elyra 7 and 400 fps for OMX SR) and simultaneous multichannel imaging, suitable for high-throughput volumetric imaging of multiple labeled samples at affordable time scales (https://www.zeiss.com/micro scopy/int/products/elyra-7-with-lattice-sim-for-fast-and-gentle-3d-superresolution-microscopy.html; https ://www.gelifesciences.com/en/us/shop/cell-imaging-and-analysis/high-and-super-resolution-microscope s/instruments/deltavision-omx-sr-imaging-system-p-03020). It should be noted, however, that SIM relies on computer-assisted image reconstruction which is prone to several errors that might arise from the quality of the sample and principally from insufficient signal-to-noise ratios (e.g., due to poor labeling, high background etc.). Most notably, 3D-SIM is prone to artefactual reconstruction owing to spherical aberrations [2, 12, 25] from refractive index mismatches in the optical path.

We have routinely used and established protocols for live cell imaging of plant cells expressing fluorescent protein-based markers of different subcellular structures in order to extrapolate and quantify dynamic features of microtubules, actin filaments and endoplasmic reticulum among others [22, 24, 25]. Imaging of fixed and immunolabeled samples offers the advantage of signal amplification compared to fluorescent proteins and allows the elucidation of details in subcellular architecture that would have escaped the capacity of live cell imaging. We show case studies as proofs-of-principle on the efficiency of the preparatory labeling protocol, and potential biological outputs of 2-D, 3-D and multichannel SIM imaging. In particular, we show how 2D SIM can be used to resolve and quantify the organization of widespread intracellular structures such as cortical microtubules, the potential of 3D SIM to document subcellular structures with considerable three dimensional occupancy, and some applications of multichannel imaging with emphasis on the use of multicolor SIM in colocalization experiments.

Vavrdová *et al. Plant Methods*   (2019) 15:22

Page 3 of 17

Results

Validation of the immunolabeling procedure

By carefully controlling fixation and enzymatic digestion of the cell walls, it was possible to maintain the cellular and tissue integrity of the root tip, to structurally preserve microtubular appearance and integrity and to allow primary and secondary antibodies to diffuse throughout the entire volume of the sample. By increasing the stringency of blocking by prolonging blocking time and using a combination of blocking agents (BSA and BSAc) it was possible to reduce background fluorescence and to increase signal-to-noise ratio (SNR) to levels adequate for high quality SIM imaging which is particularly important for diffusely distributed antigens such as MAPK species. Finally, the use of controlled RI mounting media adequately compensated for spherical aberrations that may hamper SIM image acquisition at considerable RI mismatches during 3D acquisition.

Cortical microtubule organization in Col-0, *mpk4* and *ktn1-2*

Microtubule appearance, integrity and overall organization is a classical example to demonstrate labeling efficiency of a labeling and imaging process. For this reason we followed and documented microtubular structures in root whole-mount preparations by means of SIM. With optimized conditions of sample preparation, mounting and imaging, we acquired a series of images corresponding to microtubule organization of interphase root cells in either wild-type Col-0 root tips, or in cells of *ktn1-2* and *mpk4* mutants, in order to identify minute details that may underlie the phenotypes of the respective mutants and quantify microtubule angular distribution [5, 6, 21].

In interphase cells cortical microtubules are predominantly parallel to each other (Fig. 1a), showing a quite narrow angular distribution at angles perpendicular or slightly oblique with respect to the cell axis (Fig. 1b). In such cells of the *ktn1-2* mutant, cortical microtubule systems are disorganized without a prevalent pattern (Fig. 1c) and this is also reflected by their broader angular distribution (Fig. 1d). Similarly, cortical microtubules of *mpk4* root epidermal cells (Fig. 1e) are disorganized without prevalent orientation which is again evident from their broad angular distribution (Fig. 1f).

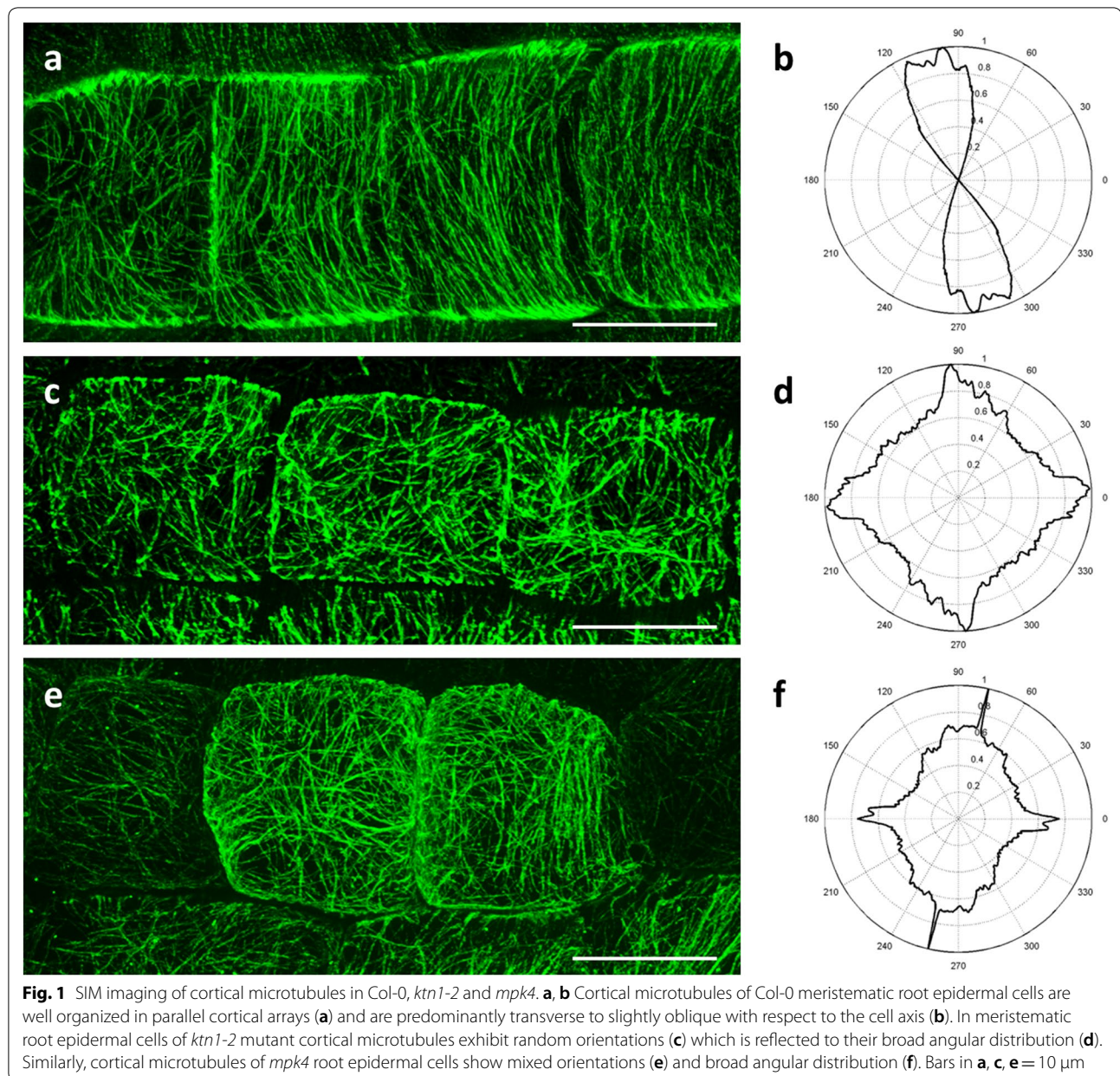### PPB organization in Col-0 and *ktn1-2*

In a previous study we followed the dynamic course of PPB formation and organization in *ktn1-2* mutants which exhibit an aberrant cell division plane orientation. In that study we identified that PPB shows marked delays in its progressive narrowing and that this is accompanied by reduced clearing of cortical microtubules outside the PPB region [21]. Herein, we addressed PPB organization in fixed and immunolabeled preprophase root cells of Col-0 (Fig. 2a) and *ktn1-2* mutant (Fig. 2b–e, g, h). Consistent with absent severing activity owing to the lack of the p60 subunit of KATANIN, PPBs in *ktn1-2* mutant appear considerably broader than those of Col-0 (Fig. 2b, c.f. Fig. 2a). In particular the PPB width of Col-0 preprophase cells was 3 ± 0.9 µm (mean $\pm$ SD; N $=50$) while in *ktn1-2* mutants it was nearly twice as much (5.5 ± 2 µm; mean $\pm$ SD; N $=22$). In all cases examined, the cortical cytoplasm surrounding the PPB area is populated with microtubules unlike what is observed in wild-type cells (Fig. 2b, c, e, g, c.f. Fig. 2a). Closer inspection of such cells showed that among others, the occurrence of such cortical microtubules is owing to excessive microtubule branching formation (Fig. 2c, d, g, h). Even at later stages when a clear bipolar spindle forms around the nucleus and the PPB is considerably narrower in Col-0 (Fig. 2b, c.f. Fig. 2a), the PPB of *ktn1-2* remains broad as in earlier stages of its formation (Fig. 2e, g, c.f. Fig. 2f).

Volumetric imaging of the mitotic spindle and the phragmoplast

Imaging of the mitotic spindle and the cytokinetic phragmoplast requires a considerable z-range capacity of the microscope since the spindle may expand at a depth of ca. 5 µm while the fully expanded phragmoplast may exceed 15–20 µm when it is occupying the entire circumference of the cell. As discussed earlier, 3D-SIM is very much prone to reconstruction artefacts due to spherical aberrations [2, 12]. For the purpose of mitotic spindle and phragmoplast visualization by means of 3D-SIM, we mounted immunolabeled whole-mount preparations in a thiodiethanol-based mounting medium supplemented with paraphenylene diamine as an antifade agent, at a TDE concentration that approximates the refractive index of the glass and the immersion oil (i.e., ca. 97% v/v with RI ≈ 1.52; [54]). Other studies have reported that Vectashield mounting medium may be used for 3D SIM acquisitions at a z-range of approximately 10 µm ([51] and references therein; [4] and references therein).

In such immunolabeled root whole-mount preparations of Col-0 we were able to document all the stages of the mitotic spindle including prophase (Fig. 3a), prometaphase (Fig. 3b), metaphase (Fig. 3c), anaphase (Fig. 3d) and telophase (Fig. 3e) in the three dimensions. During cytokinesis, it was possible to follow all stages of phragmoplast formation (Fig. 3e–h). Owing to refractive index compensations it was possible to follow the entire volume of the mitotic spindle as exemplified by appropriate 3D rendering (e.g., Figure 3i, j; Additional file 1: Video 1 and Additional file 2: Video 2). Finally 3D-SIM was

Vavrdová *et al. Plant Methods*   (2019) 15:22

Page 4 of 17

Fig. 1 SIM imaging of cortical microtubules in Col-0, *ktn1-2* and *mpk4*. **a, b** Cortical microtubules of Col-0 meristematic root epidermal cells are well organized in parallel cortical arrays (**a**) and are predominantly transverse to slightly oblique with respect to the cell axis (**b**). In meristematic root epidermal cells of *ktn1-2* mutant cortical microtubules exhibit random orientations (**c**) which is reflected to their broad angular distribution (**d**). Similarly, cortical microtubules of *mpk4* root epidermal cells show mixed orientations (**e**) and broad angular distribution (**f**). Bars in **a**, **c**, **e** = 10 μm

used to document an aberrant mitotic spindle of *ktn1-2* mutant with ectopic microtubule occurrence (Fig. 3k, l; Additional file 3: Video 3).

Detailed observation of early (Fig. 4a, b) or late (Fig. 4c, d) cytokinetic cells of *ktn1-2* revealed the occurrence of multiple events of de novo branched formation of microtubules within the phragmoplast (Fig. 4a, c, insets) and finally we documented abortive phragmoplasts of *mpk4* mutant (e.g., Fig. 4e).

Using SIM for colocalization studies

SIM might improve colocalization studies since its lateral resolution is at least two-fold better than that of the CLSM. In the next sections we demonstrate examples of erroneous colocalizations deciphered by CLSM and how they are corrected by SIM, while we also show how SIM can provide spatial interrelations at minute details.

Localization of MAP65-3 with cytokinetic microtubules

MAP65-3 is a microtubule crosslinking protein whose expression is restricted to mitotic stages, whereby it is associated conspicuously with telophase and cytokinetic

Vavrdová *et al. Plant Methods*   (2019) 15:22

Page 5 of 17
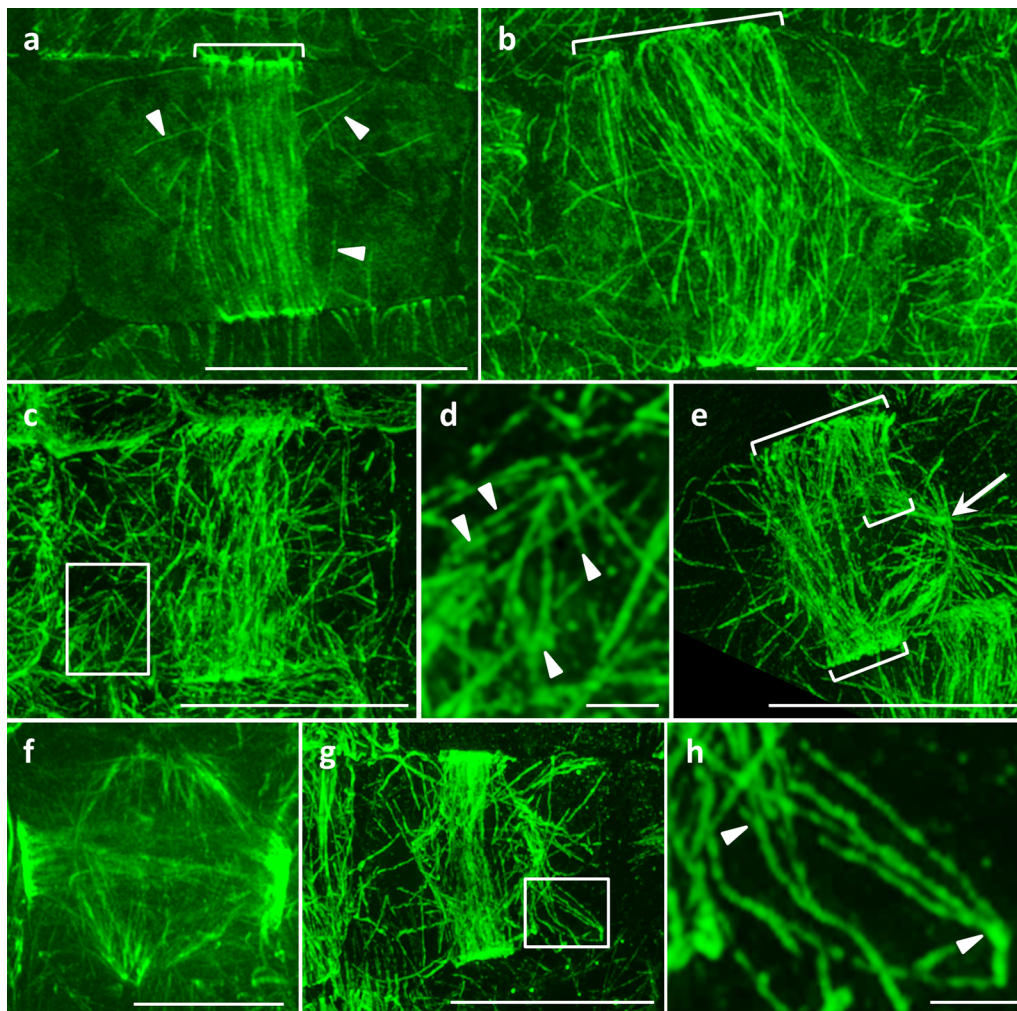
Fig. 2 SIM imaging of PPB formation in Col-0 and *ktn1-2*. **a** Early PPB in Col-0 (bracket). With few exceptions (arrowheads) the cortical cytoplasm outside of the PPB is cleared from microtubules. **b** An example of a very broad PPB (bracket) in *ktn1-2*. **c**, **d** Another example of an early *ktn1-2* PPB showing a wealth of cortical microtubules outside the PPB (**c**, rectangle) and excessive microtubule branching (**d**; arrowheads) in some instances. **e** An abnormally broad late PPB (long bracket) of an early prophase *ktn1-2* cell showing an incomplete part (short brackets) and the formation of perinuclear spindle (arrow). **f** By comparison to (**e**), a late PPB of a Col-0 early prophase cell is shown. PPB is considerably more narrow. **g**, **h** Overview (**g**) and detail (**h**) of another abnormal preprophase cell of *ktn1-2* showing excessive de novo branched formation of microtubules (arrowheads). Bars in **a**–**c**, **e**, **g** = 10 μm; **f** = 5 μm; **d**, **h** = 1 μm

microtubular systems [17]. MAP65-3 is of particular interest in the study of plant cytokinesis since its absence is associated with severe cytokinetic phenotypes [30], while its function is subjected to regulation via MAPKs or phosphoinositide kinases (e.g., [5]) either by means of phosphorylation [45], or by regulation of its localization [27].

In the absence of specific antibodies against MAP65-3, we rather localized eGFP-MAP65-3 (aminoterminal fusion of MAP65-3 with enhanced green fluorescent protein) in plant cells, using instead commercial anti-GFP nanobodies conjugated to Atto 488. Tubulin was detected with a rat monoclonal antibody and Alexa Fluor 647-conjugated anti-rat IgGs. Although a red dye (such as AlexaFluor 546 or AlexaFluor 594) is expected to yield better resolution than AlexaFluor 647, the latter exhibits an outstanding brightness, photostability and pH-tolerance (https://www.thermofisher.com/cz/en/home/life-science/cell-analysis/fluorophores/alexa-fluor-647.html), allowing for high signal-to-noise ratio labeling necessary for the efficient modulation of the sample with the light pattern. Nanobody-based detection is a relatively novel detection tool with several advantages over commercial
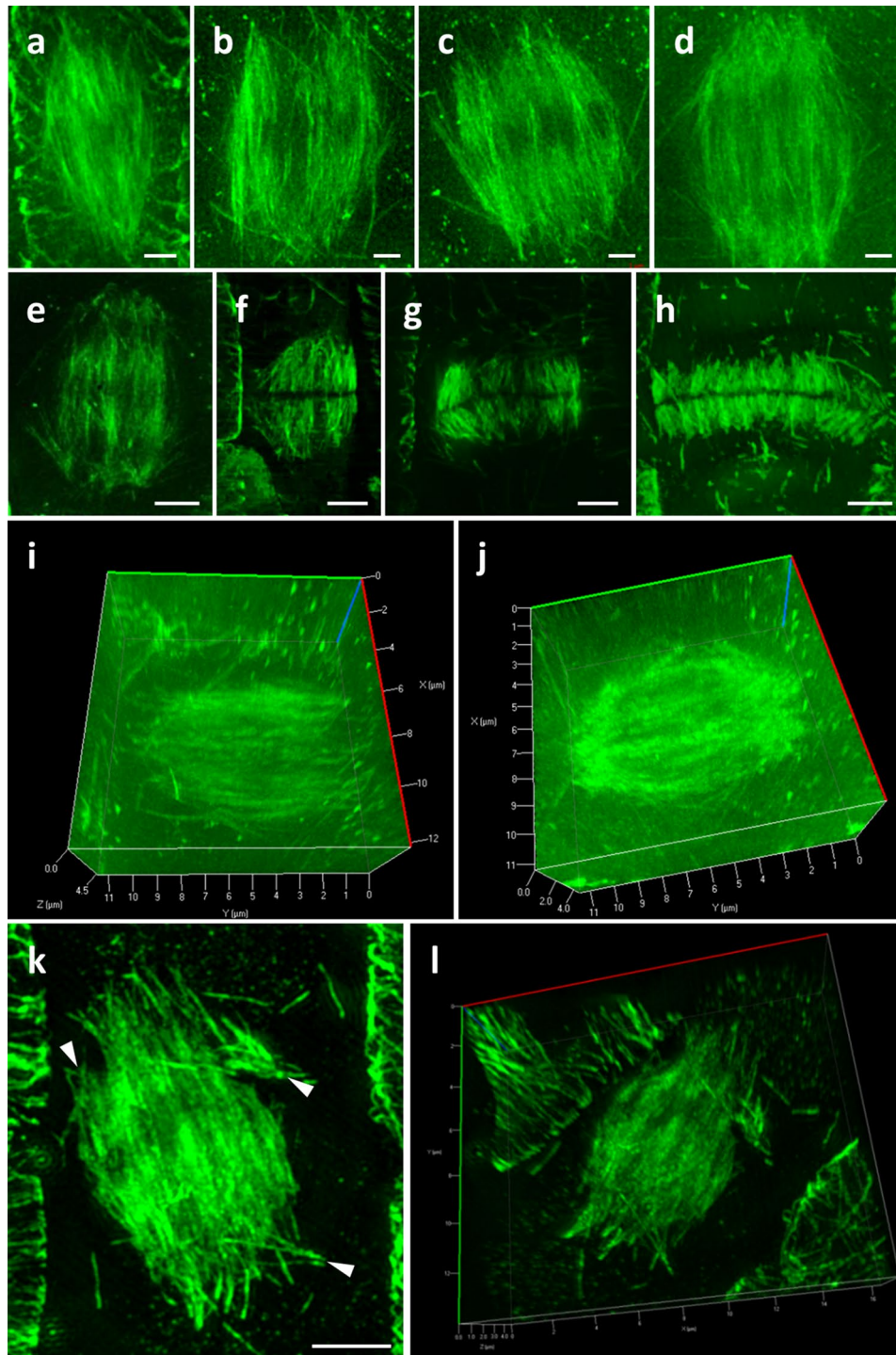
Vavrdová *et al. Plant Methods*   (2019) 15:22

Page 6 of 17

Fig. 3 Potential of 3D-SIM in visualizing mitotic and cytokinetic microtubule configurations. **a** Maximum intensity projection of a prophase spindle. **b** Maximum intensity projection of a prometaphase spindle. **c** Maximum intensity projection of a metaphase spindle. **d** Maximum intensity projection of an early anaphase spindle. **e** Maximum intensity projection of a telophase spindle. **f**–**h** Successive stages of centrifugal phragmoplast expansion. **i**, **j** Examples of 3D rendering of cells depicted in **b** and **d** respectively (see also Additional file 1: Video 1 and Additional file 2: Video 2), showing the potential of SIM to capture the entire volume of the mitotic apparatus. **k**, **l** Maximum intensity projection (**k**) and 3D (**l**) rendering of an aberrant mitotic spindle of *ktn1-2* (see also Additional file 3: Video 3). Arrowheads show ectopic microtubules occurrence (**k**). Bars in **a**–**h**, **k**, **l** = 2 μm

Vavrdová *et al. Plant Methods*   (2019) 15:22

Page 7 of 17
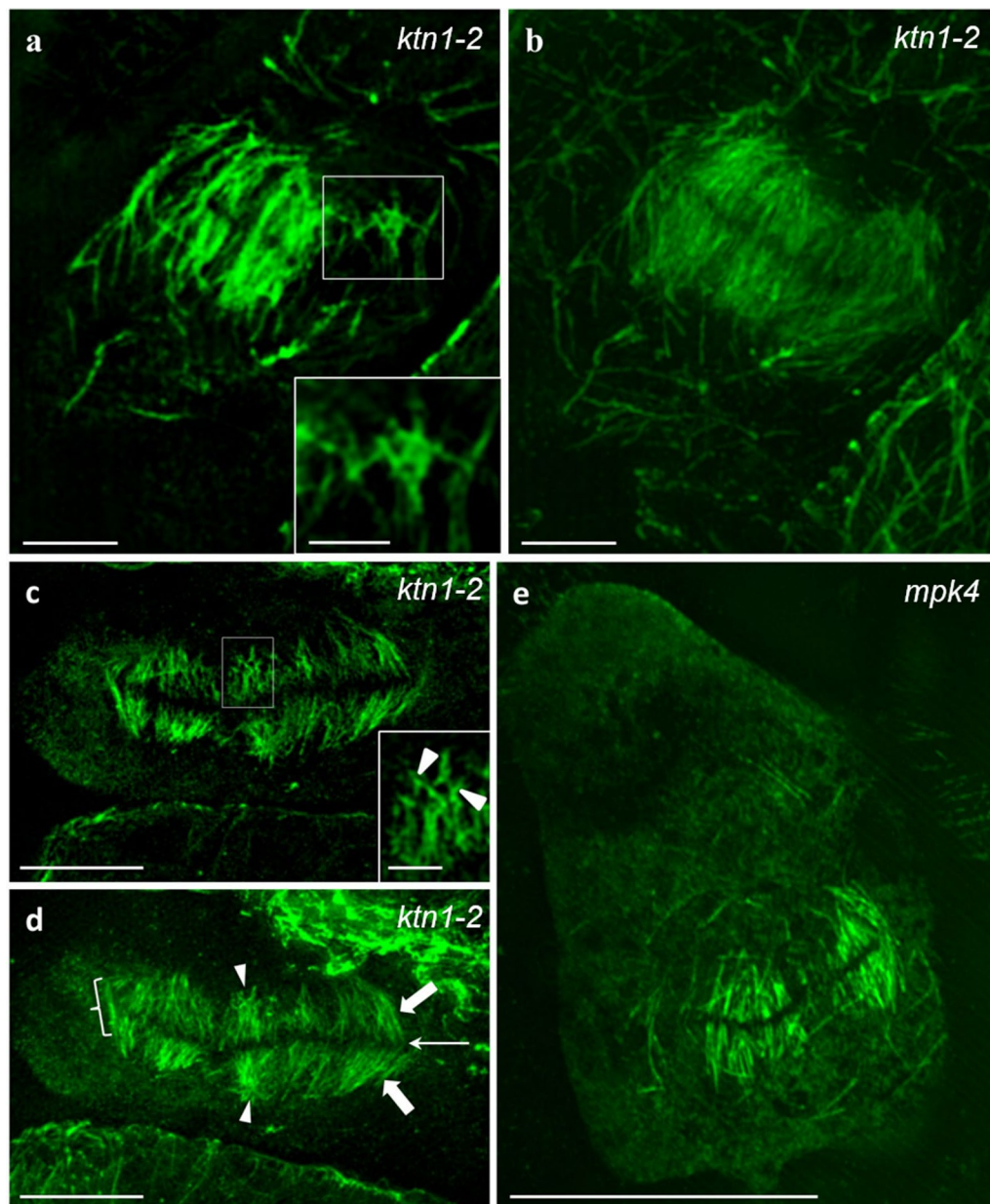
Fig. 4 Observation of abnormal phragmoplast formation in the *ktn1-2* and *mpk4* mutants. **a**, **b** Single optical section (**a**) and maximum intensity projection (**b**) of an early phragmoplast of a *ktn1-2* cytokinetic root cell, showing an area with extensively branched microtubules (**a**, inset) at the phragmoplast periphery. **c**, **d** Single optical section (**c**) and maximum intensity projection (**d**) of an aberrant late phragmoplast of the *ktn1-2* mutant. Excessive microtubule branching (arrowheads) is observed within the phragmoplast (**a**, **c**; inset). **e** Ectopic and abortive phragmoplast of an aberrant root epidermal cell of the *mpk4* mutant. Bars in **e** = 10 μm; **c**, **d** = 5 μm; **a**, **b** = 2 μm; insets of **a** and **c** = 1 μm

tetrameric IgGs and presents an emerging method in the plant field (e.g., [40]).

MAP65-3 starts to colocalize with microtubules during telophase (Fig. 5a; bottom spindle; arrow) as at earlier stages, mitotic spindles are devoid of MAP65-3 signal (Fig. 5a; top spindle; bracket) and the telophase signal of MAP65-3 corresponds to a rather broad band around the spindle midzone (Fig. 5a; arrowheads). During cytokinesis, MAP65-3 became narrowly localized to the midplane of the phragmoplast (coinciding with the position of cell plate; Fig. 5b–d; arrowheads).

The phragmoplast is a cellular structure that expands considerably during the course of cytokinesis, therefore it was a challenge to see whether SIM could be used to
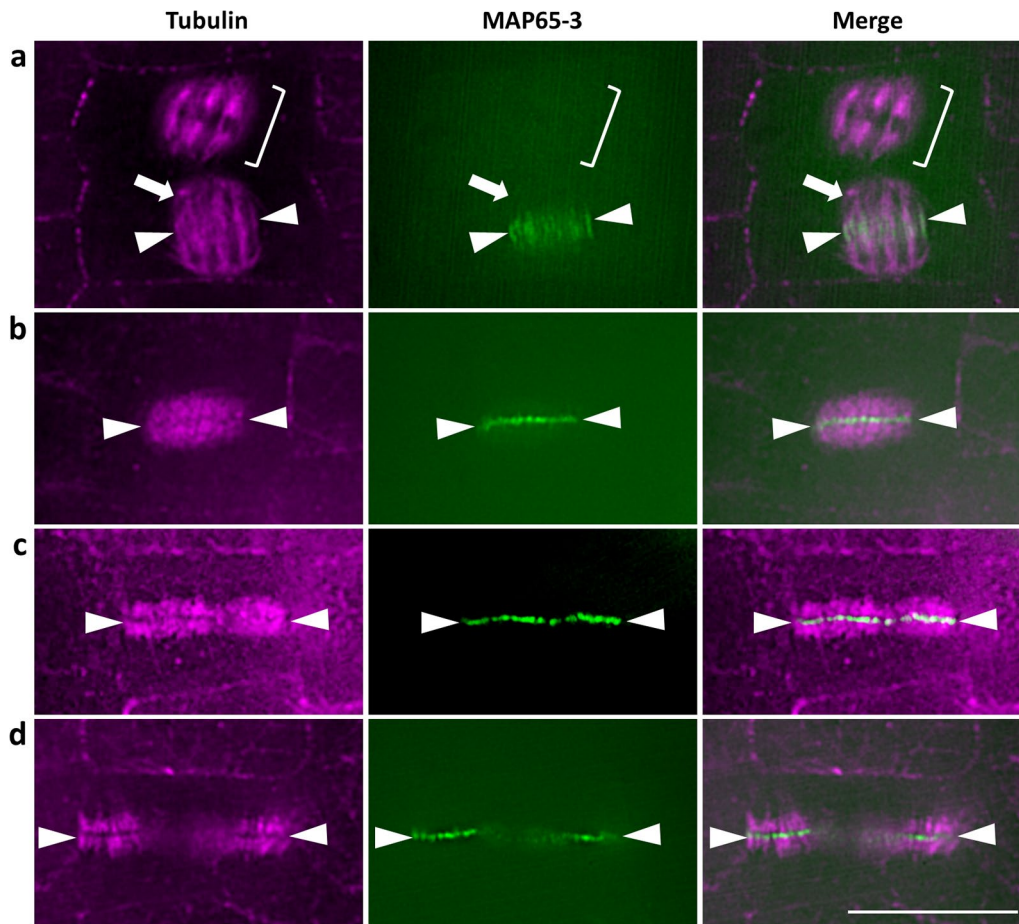
Fig. 5 Differential localization of eGFP-MAP65-3 with mitotic and cytokinetic microtubule systems. **a** Microtubule, MAP65-3 and overlay of a metaphase spindle (top bracket) devoid of MAP65-3 signal and a telophase spindle (arrow) showing broad accumulation of MAP65-3 at the midplane (arrowheads). **b** Colocalization of microtubules and MAP65-3 at the midzone (arrowheads). **c** A more advanced phragmoplast with similar midplane distribution of MAP65-3 (arrowheads). **d** Restriction of MAP65-3 signal at phragmoplast edges (arrowheads) and its disappearance from central areas of the phragmoplast devoid of microtubules. Bars in **a**–**d** = 10 μm

visualize cytokinesis at different stages. As examples we used again cells co-immunolabeled for microtubules and eGFP-MAP65-3 and documented their distribution during early (Fig. 6a–d; Additional file 4: Video 4) and late (Fig. 6e–h; Additional file 5: Video 5) stages of phragmoplast formation. This experiment revealed that in contrast to 2D imaging of either single optical sections (Fig. 5), or maximum intensity projections (Fig. 6b–d, f–h), 3D-SIM was able to show differences in the distribution of the two signals during different stages of the phragmoplast expansion.

Nuclear localization of MPK6 and active MAPK species

MAPKs are known to shuttle between the nucleus and the cytoplasm on an activity-based manner (reviewed in [38]). Therefore, it is reasonable to assume that a nuclear resident MAPK might be active, and this can

be addressed by colocalizing the MAPK itself by a specific antibody and by an activation-pendant (phospho-specific) antibody. To test this hypothesis we colocalized MPK6, previously shown to have a predominant nuclear localization [53] and activated plant MAPKs recognized by antibody against dually phosphorylated extracellular signal related protein kinases 1 and 2 of mammalian cells (ERK1/2). The antibody against MPK6 recognizes a 14-aminoacid carboxylterminal epitope, while the anti-pERK antibody recognizes a restricted epitope which encompasses the TEY motif present in MPK6 and other MAPKs [18], only when this motif is dually phosphorylated (https://www.cellsignal.com/products/primary-antibodies/phospho-p44-42-mapk-erk1-2-thr202-tyr204-antibody/9101).

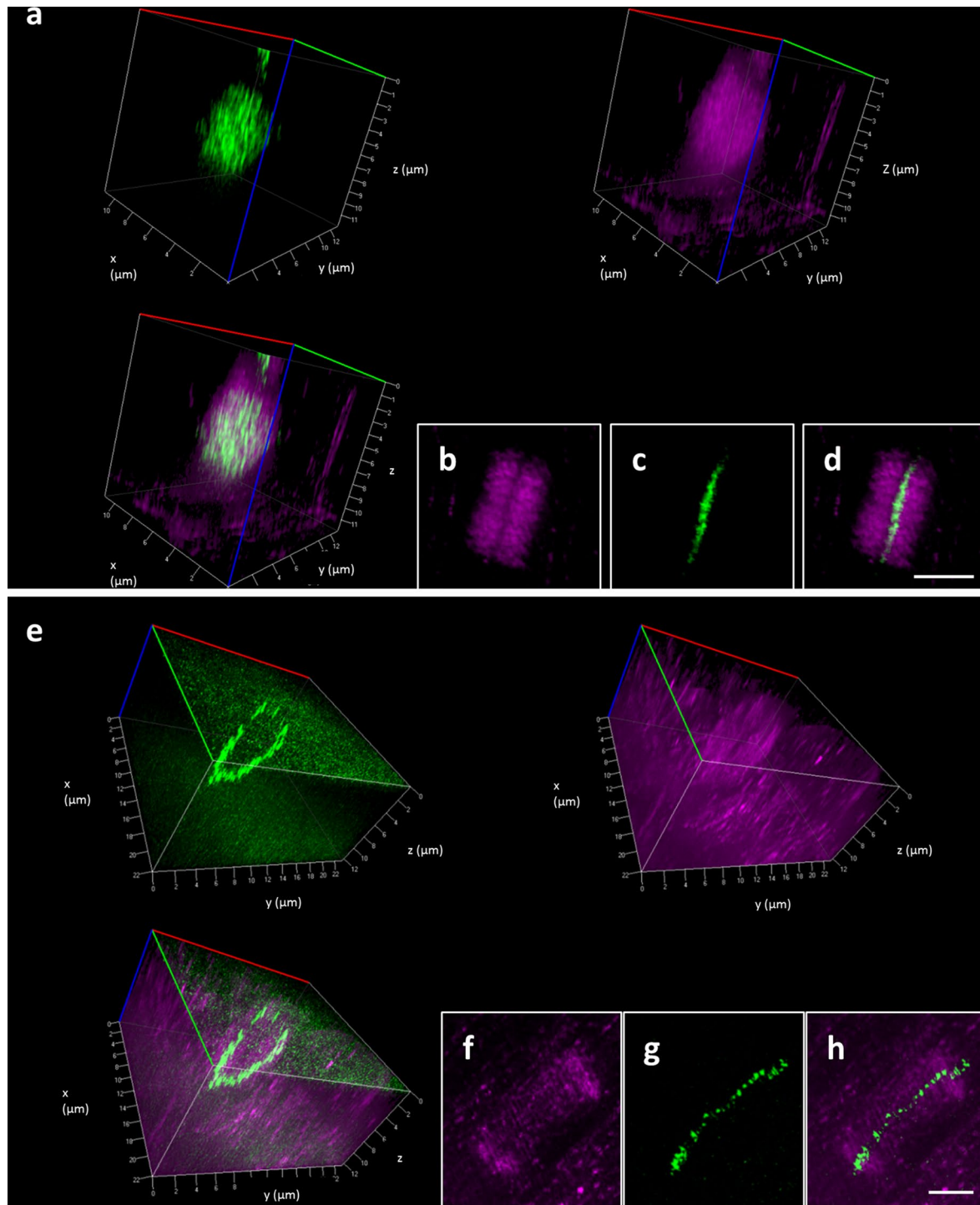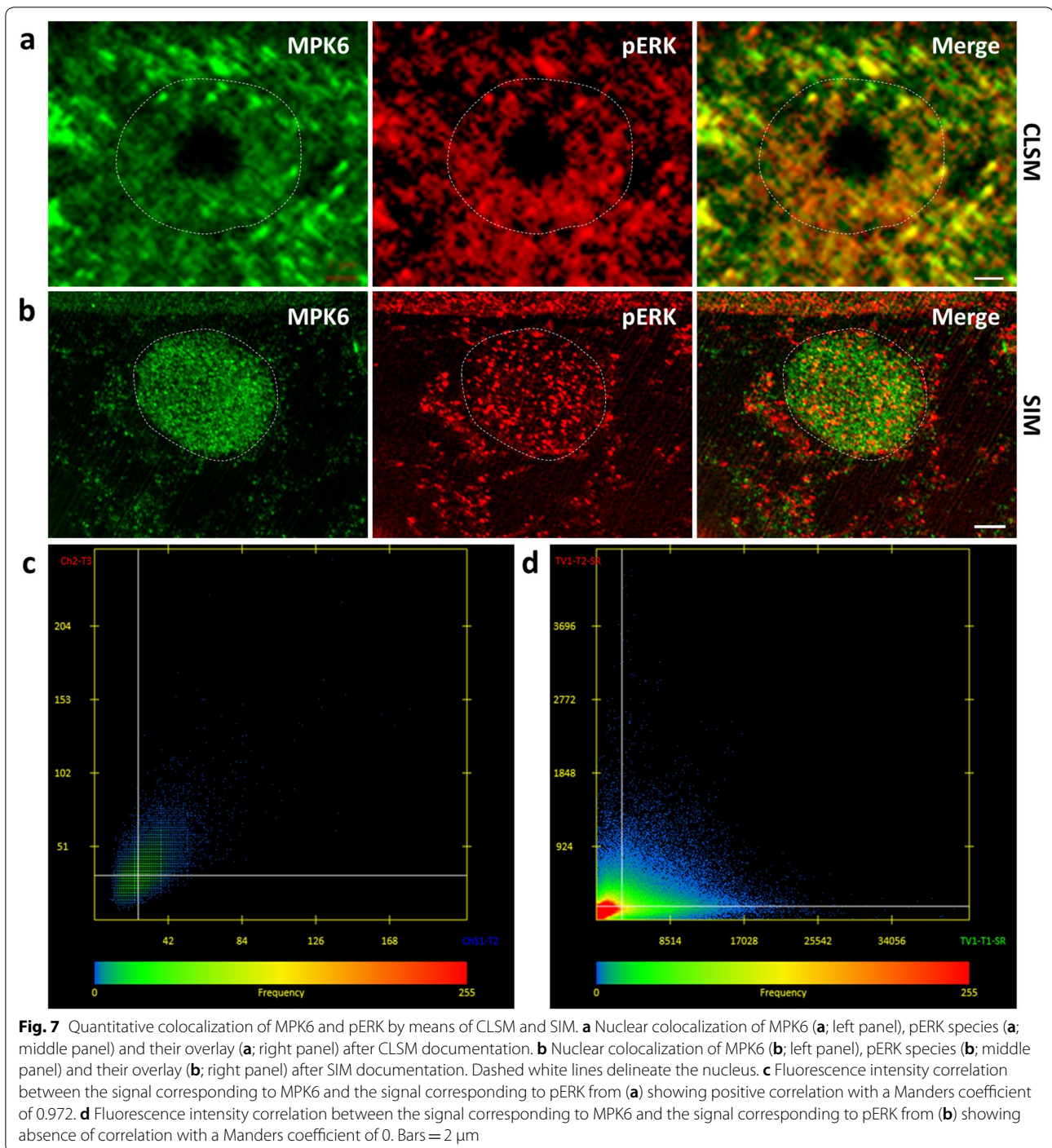By means of CLSM imaging, MPK6 (Fig. 7a; left panel) and pERK species (Fig. 7a; middle panel) were

Vavrdová *et al. Plant Methods*   (2019) 15:22

Page 9 of 17

Fig. 6 2-color 3D-SIM of MAP65-3 and microtubule distribution in cytokinesis. **a** Clockwise 3D rendering of MAP65-3, microtubules and their overlay in an early phragmoplast wherein both signals occupy the entire surface of the phragmoplast (corresponding to Additional file 4: Video 4). **b**–**d** Maximum intensity projection showing microtubule (**b**), MAP65-3 (**c**) and their overlay (**d**) in the same phragmoplast as in **a**. **e** Clockwise 3D rendering of MAP65-3, microtubules and their overlay in an late phragmoplast wherein both signals are restricted in the edges of the phragmoplast (corresponding to Additional file 5: Video 5). **f**–**h** Maximum intensity projection showing microtubule (**f**), MAP65-3 (**g**) and their overlay (**h**) in the same phragmoplast as in **e**. Bars = 2 μm

Fig. 7 Quantitative colocalization of MPK6 and pERK by means of CLSM and SIM. **a** Nuclear colocalization of MPK6 (**a**; left panel), pERK species (**a**; middle panel) and their overlay (**a**; right panel) after CLSM documentation. **b** Nuclear colocalization of MPK6 (**b**; left panel), pERK species (**b**; middle panel) and their overlay (**b**; right panel) after SIM documentation. Dashed white lines delineate the nucleus. **c** Fluorescence intensity correlation between the signal corresponding to MPK6 and the signal corresponding to pERK from (**a**) showing positive correlation with a Manders coefficient of 0.972. **d** Fluorescence intensity correlation between the signal corresponding to MPK6 and the signal corresponding to pERK from (**b**) showing absence of correlation with a Manders coefficient of 0. Bars = 2 μm

found in nuclei of wild-type root cells while quantitative colocalization [28] showed a good correlation between the two signals (Fig. 7a; right panel) with a correlation coefficient of 0.972 (Fig. 7c). When similar samples were documented with SIM (Fig. 7b), due to the achieved higher resolution it was found that the signals owing to MPK6 (Fig. 7b; left panel) and pERK (Fig. 7b; middle panel), are not colocalizing (Fig. 7b; right panel; d). This suggests that nuclear active MAPK species are other than MPK6 and support the previous idea that active MPK6 and its closely related *Medicago sativa* homologue SIMK are exported from the nucleus when active [35, 44]. In this particular case, Manders

coefficient was 0 suggesting the absence of colocalization, while inspection of the respective scatterplot shows the coincidence of red and green pixels occurs behind the Costes threadlines (Fig. 7d).

Association of cytoplasmic MAPKs with microtubule arrays

As previously shown, the MPK6 of *Arabidopsis thaliana* has a dominant nuclear localization [53] although a fraction may associate with the plasma membrane and cytoplasmic vesicular structures [31] as well as with

microtubular PPBs, mitotic spindles and phragmoplasts [24, 53].

A survey of the occurrence of MPK6 in the cortical cytoplasm of interphase cells showed its conspicuous localization in vesicular structures that form intimate association with cortical microtubule walls and tips (Fig. 8a–f), while qualitative and quantitative colocalization studies showed a stunning correlation of MPK6 with the localization of pERK species (Fig. 8g–j).

Fig. 8 Colocalization of MPK6 and pERK in microtubule bound spots analyzed by SIM. **a–e** Microtubule (**a**), MPK6 (**b**), pERK (**c**), MPK6-pERK overlay (**d**) and microtubule-MPK6-pERK overlay (**e**) in root epidermal cells of Col-0. **f** Close-up view of the boxed area of **e**, showing pERK and MPK6-labeled spots associated with the walls (full arrowheads) or the tips (outlined arrowheads) of cortical microtubules. **g–i** MPK6 (**g**), pERK (**h**) and overlay (**i**) in spots of the outlined area of **b–d**. **j** Fluorescence intensity of the profile drawn in **g–i**, showing absolute coincidence between the signals corresponding to MPK6 and pERK. Bars in **a–e** = 5 μm; **c** = 2 μm; **g-i** = 1 μm

Vavrdová *et al. Plant Methods*   (2019) 15:22

Page 12 of 17

Discussion

In the present study we provide an improved version of standard immunolabeling procedures, mostly applicable to root whole-mount preparations. This protocol is designed to improve antibody penetration within the z-range limits of 3D-SIM, and preserve intracellular structure and antigenicity at the standards set by superresolution imaging. Using this protocol, it was possible to label vast intracellular structures such as the microtubule cytoskeleton, to allow for sufficient labeling density and to achieve the high SNR values required for adequate SIM. Likewise it was possible to label less abundant and more diffusely distributed structures such as MPK6 and pERK positive spots and provide a correlative output based on multichannel imaging.

The use of TDE instead of glycerol as a mountant, compensated well for refractive index mismatches and made possible the recording of Z-stacks ranging from ca. 5 μm deep, covering the axial occupancy of a typical mitotic spindle, to depths ranging from 15 to 20 μm encompassing fully expanded phragmoplasts. The amount of time necessary for such acquisitions prohibits the use of SIM to document such structures in living cells, especially in the case of multichannel documentation. The importance of mounting media in the z-range of SIM, was very recently addressed [55]. In our case TDE helped to speed up sample preparation as compared to other laborious immunofluorescence-compatible tissue clearing approaches (e.g., [37, 58]) which may additionally compromise the integrity of the structurally-labile root after enzymatic cell wall digestion. Emission intensity of fluorescent proteins is reportedly impaired in high TDE concentrations [32], and this problem was alleviated by using fluorophore-tagged anti-GFP antibodies.

We expect that other mounting media can be efficiently used for purposes of 3D SIM imaging and the ultimate choice depends on both how stable is the sample during the documentation which is an essential consideration of root whole-mount preparations which are not stably fixed but rather immersed and free-floating in a liquid mounting medium (e.g., TDE-based, glycerol- paraphenylenediamine-based or Vectashield and other mounting media commercially available).

The volumetric documentation of subcellular architecture poses several challenges related to the speed of acquisition, the possibilities of multicolor imaging and importantly the means to compensate for light scattering issues that are increased by extending the desired z-range of imaging. Superresolution methods such as 2D and 3D SIM have provided the adequate means to visualize subcellular architecture below Abbe's limit for reasons that have been exhaustively reviewed (e.g., [23–25, 51] and references therein). However such methods require

proper sample preparation procedures aiming to achieve high SNRs and sufficient tissue clearing to compensate for light scattering issues. In this sense, the choice of an appropriate mounting medium is of paramount importance. The formulation of TDE used herein has a refractive index matching that of glass and immersion oil so basically any mounting medium with this property should be used to deal with light scattering. For this reason we tried hardset Vectashield with a refractive index of 1.46 after curing (https://vectorlabs.com/amfile/file/download/file_id/1770/product_id/298/). Unfortunately, residual PBS around the roots created refractive index mismatches that compromised image quality. This was not the case with TDE which was allowed to be infiltrated at stepwise increasing concentrations until the desired one was reached.

Since fixed samples are observed, laser power and camera exposure times can be set to yield the best possible results in terms of spatial resolution. This allowed us to document mitotic and cytokinetic microtubule arrays at unprecedented quality and allowed the visualization of minute defects underlying phragmoplast formation in *ktn1-2* mutant. In particular, we observed multiple de novo branched microtubule formation sites and this might underlie delays previously observed during phragmoplast expansion in living cytokinetic *ktn1-2* cells [21]. In this respect it would be interesting to superresolve KATANIN1 localization and relate it to microtubule nucleation sites by means of SIM.

The importance of resolution in colocalization studies and especially when those are meant to be quantified was demonstrated in the case of MPK6 and pERK species in nuclei. CLSM documentation and subsequent quantification of the two signals gave the erroneous impression of tight correlation of the two signals, whereas SIM showed that the two signals are completely unrelated.

On the other hand, the sequential documentation of microtubules, MPK6 and pERK species after triple labeling revealed that spots at the cortical cytoplasm, previously identified to contain MPK6 [31], are closely associated with microtubules. Most importantly they also contain pERK species raising the possibility that this presumably vesicular fraction of MPK6 is in an active, dually phosphorylated state. It will be of interest to follow up such a study and reveal substrates of MPK6 involved in vesicular trafficking.

Conclusions/future prospects

Plant tissues impose severe obstacles in the microscopic documentation of intracellular structures, owing to the contribution of the cell wall, the cortical cytoplasm and the vacuole to refractive index mismatches with the optical path of the microscope (reviewed in [52]). Such

Vavrdová *et al. Plant Methods*   (2019) 15:22

Page 13 of 17

mismatches may hamper the visualization of voluminous subcellular structures such as the mitotic spindle and the expanding phragmoplast. Refractive index mismatches are particularly limiting in the case of superresolution methods such as SIM which are heavily influenced by spherical aberrations [2, 12]. We find herein that the use of relatively simple mounting media containing TDE, sufficiently rectifies the contribution of the sample to the optical path and allows to make use of the high z-range of SIM. In this way it is possible to document spatial interrelations between different subcellular compartments at the subdiffraction resolution limits offered by SIM.

Speed of acquisition is another, possibly the most limiting aspect for 3D SIM since each plane has to be documented and reconstructed from some 9–25 Moire patterns resulting by the rotations and the phase-shifting of the light pattern used to illuminate the sample. Such time concerns become even more limiting during multichannel imaging. However very recent commercial developments such as those mentioned earlier, have overcome temporal issues and now the market provides SIM modules with outstanding acquisition frame rates and the possibility of simultaneous multichannel imaging.

Materials and methods
Plant material
Arabidopsis thaliana seedlings were used throughout. As wild-type we selected to work with the Columbia ecotype (Col-0). On the Col-0 background, we generated stably transformed lines of *proMAP65-3::eGFP-MAP65-3*, to express N-terminal eGFP fusions of the MAP65-3 microtubule crosslinking protein.

Moreover, we worked on two T-DNA insertion mutants, namely *ktn1-2* [34] and *mpk4* [5] which have been also raised in a Col-0 background. Wild-type, transformants and mutant seeds were surface-sterilized, plated on Phytagel or gellan gum solidified half-strength Murashige–Skoog (MS) basal salt mixture supplemented with 1% w/v sucrose as a carbon source, stratified at 4 °C for 1–4 days and finally allowed to germinate at controlled environmental conditions. Seedlings between 3 and 4 days after germination were selected for subsequent whole-mount immunolocalization experiments.

Molecular cloning and genetic crosses
The construct for N-terminal EGFP fusion of AtMAP65-3 was developed using the binary destination vector pGWB502 [33]. Initially, a multiple cloning site linker, generated by annealing of complementary oligonucleotides pGWB502link-F (ggttaattaatcctaggaatctgaagcactgccttgtggtacctgagct) and pGWB502link-R (caggtaccacaaggcagtgcttcagattcctaggattaattaacctgca), was cloned into SbfI and SacI digested pGWB502, in

order to replace vector fragment containing CaMV 35 promoter and Gateway® cloning cassette. The resulting vector was designated pGWB502link. Subsequently, a 1239 bp DNA fragment of MAP65-3 native promoter region was amplified from wild-type Col-0 genomic DNA using PCR with primers pMAP65-3-F (ctctcttaattaaacactcttccctacacaaaaccg) and pMAP65-3-R (aggtctaggtaccttcgaaatgcttaagcctgtaac), which contain PacI and Acc65I restriction site, respectively. Resulting PCR product was digested with PacI and Acc65I and cloned into PacI and Acc65I digested vector pGWB502link to generate construct pGWB502link-pMAP65-3. An open reading frame of MAP65-3 including stop codon was amplified from wild-type Col-0 cDNA using PCR with primers MAP65-3cDNA-F (acactagggtaccatggcaagtgttcaaaaagatcc) and MAP65-3cDNA-R (agatctacgtacgggatcctcaaaccaaacgacattcagact), which contain Acc65I and BsiWI restriction site, respectively. Obtained PCR product was digested with Acc65I and BsiWI and cloned into Acc65I digested pGWB502link-pMAP65-3 to generate construct pGWB502link-pMAP65-3::MAP65-3. Acc65I and BsiWI digest different restriction sites, but produce the same sticky ends. Therefore, in pGWB502link-pMAP65-3::MAP65-3 only unique Acc65I restriction site is present in between pMAP65-3 and MAP65-3 start codon. ORF of EGFP was PCR amplified with primers EGFP-F (tcctgtcaggtaccaagaagaaaaatggtgagcaagggcgaggagctgttca) and EGFP-R (cacagtttggtaccccttagcagctgcctcttttgcggcagcctctttagcagcagcttccttgtacagctcgtccatgccgagagtga) both of which contain Acc65I restriction site, while reverse primer contains no stop codon and DNA sequence encoding rigid linker (EAAAK)3, which joins EGFP tag with AtMAP65-3 [59]. Generated PCR product was digested with Acc65I and cloned into Acc65I digested pGWB502link-pMAP65-3::MAP65-3 to create construct pMAP65-3::EGFP:MAP65-3. pMAP65-3::EGFP:MAP65-3 construct was transformed into *Agrobacterium tumefaciens* strain GV3101::pMP90 and recombinant GV3101::pMP90 clones were used for simplified floral dip transformation of *Arabidopsis thaliana* Col-0 ecotype [11]. Primary transformants of *Arabidopsis thaliana* were selected on MS media (4.3 g/L MS + vitamins, 10 g sucrose/L, 500 μl/L MES, 5.7 g/L Gellan gum, pH 5.7) supplemented with 30 mg/L hygromycine (Roche).

Chemicals
All standard chemicals were ordered from Sigma unless stated otherwise. MS basic salt mixture without vitamins was from Duchefa. Gellan gum (a substitute for Phytagel) was from ThermoFisher (Kandel) GmbH. Electron microscopy grade fixatives were from Polysciences Inc.

Table 1 Labeling reagents, commercial source and dilution guide

Labeling reagent	Company/catalogue number	Dilution (diluent)
Rat monoclonal anti-α tubulin antibody (clone YOL1/34)	BioRad/MCA78G	1:300 (3% w/v BSA in PBS pH 7.3)
Alpaca anti-GFP nanobody-Atto 488 conjugated (GFP-Booster)	Chromotek/gba488	1:500 (3% w/v BSA and 0.5% w/v BSAc in PBS pH 7.4)
Rabbit polyclonal anti-MPK6 antibody	Sigma/A7104	1:750 (3% w/v BSA in PBS pH 7. 3)
Rabbit polyclonal anti-pERK antibody	Cell Signaling/9101 s	1:400 (3% w/v BSA in PBS pH 7.3)
Goat anti-rat IgGs-Alexa Fluor 488 conjugated	ThermoFischer Scientific/A11006	1:500 (3% w/v BSA in PBS pH 7.3)
Goat anti-rat IgGs-Alexa Fluor 647 conjugated	ThermoFischer Scientific/A21247	1:500 (3% w/v BSA in PBS pH 7.3)
Goat anti-rabbit IgGs-Alexa Fluor 546 conjugated	ThermoFischer Scientific/A11010	1:1000 (3% w/v BSA and 0.5% w/v BSAc in PBS pH 7.4)
Goat anti-mouse IgGs-Alexa Fluor 555 conjugated	ThermoFischer Scientific/A21422	1:500 (3% w/v BSA 3 in PBS pH 7.3)

A list of primary and secondary antibodies used in the immunolocalizations of the present study, information on their commercial availability and their dilutions used herein

(16% v/v methanol-free aqueous formaldehyde and 25% v/v aqueous glutaraldehyde). Cell wall digesting enzymes were from Desert Biologicals. Primary and secondary antibodies used herein are listed in Table 1. Reagents for molecular cloning are mentioned in the respective section.

Whole-mount immunofluorescence localization

For root whole-mount immunolocalization studies of microtubules, associated proteins and MAPKs we basically followed previously published procedures [43, 46] but with notable changes which follow. Fixatives included 1.5% v/v formaldehyde and 0.1% v/v glutaraldehyde buffered with microtubule stabilizing buffer (MTSB; 25 mM K-PIPES, pH 6.8; 2.5 mM EGTA and 2.5 mM $MgSO_4 \times 7H_2O$) and supplemented with 0.01% v/v Triton X-100 (at room temperature for 1 h). For fixation of seedlings expressing fusion proteins with eGFP, glutaraldehyde was omitted and formaldehyde concentration was raised to 4% v/v at the same buffer conditions.

After fixation cell walls were digested with an enzyme cocktail prepared in MTSB, comprising of 2% w/v Cellulase Onozuka R10, 0.5% w/v Cellulase Onozuka RS, 1% w/v Macerozyme R10, 1% w/v Meicelase and 0.1% w/v Pectolyase Y23 (30 min, room temperature). Subsequently seedlings were washed two times with MTSB and 2 times with PBS pH 7.4 (10 min each, room temperature) and then residual aldehyde groups were reduced by 15 min incubation in 0.1% w/v sodium borohydride ($NaBH_4$; this step was omitted when glutaraldehyde was not included in the fixative). Then, samples were sequentially permeabilized with 10% v/v DMSO, 2% v/v Nonidet P40 and 0.01% v/v Triton X-100 in PBS pH 7.4 for 15 min, washed in PBS pH 7.4 and blocked overnight in 3% w/v bovine serum albumin (BSA) and 0.5% w/v polyacetylated BSA (BSAc; Aurion) in PBS pH 7.4, prior to antibody incubation.

Subsequently samples were incubated in primary antibody (Table 1) diluted in 3% w/v BSA and 0.5% w/v BSAc in PBS pH 7.4 at room temperature overnight. During the following day, samples were extensively washed in PBS pH 7.4 (6 times, 10 min each), blocked with 3% w/v BSA and 0.5% w/v BSAc in PBS pH 7.4 for 1 h and incubated with secondary antibody diluted in 3% w/v BSA and 0.5% w/v BSAc in PBS pH 7.4 overnight at 37 °C. Finally, samples were washed in plain PBS pH 7.4 (at least 6 times 10 min each), counterstained with (4′,6-diamidine-2′-phenylindole dihydrochloride) DAPI and mounted in a mounting media supplemented with 0.1% w/v para-phenylene diamine as an antifade agent. For standard imaging, mounting medium was made in 90% v/v glycerol buffered with 100 mM tris(hydroxymethyl)aminomethane-HCl pH 8.8.

For improving the z-range necessary for 3D imaging, we replaced glycerol with 2,2′-thiodiethanol (TDE) at a concentration that was shown to have matching refractive index (RI) with that of the glass coverslip and the immersion oil (97% v/v; RI = 1.52; [54]). In order to achieve adequate infiltration of TDE in root whole-mount preparations, those were incubated to an increasing gradient of TDE in 100 mM Tris–Cl pH 8.8. Briefly, samples were infiltrated sequentially with 5% v/v, 10% v/v, 20% v/v, 30% v/v, 40% v/v, 50% v/v, 75% v/v and 97% v/v TDE in 100 mM Tris–Cl pH 8.8 for 10 min at room temperature per step. At the final step the samples were infiltrated in 97% v/v TDE in 100 mM Tris–Cl pH 8.8 supplemented with 0.01% w/v para-phenylene diamine and were prepared for microscopy.

We also tested hard set Vectashield (ThermoFischer Scientific) as a potential mounting medium but in our hands it introduced considerable spherical aberrations, light scattering and substandard image quality at acquisition.

Vavrdová *et al. Plant Methods*   (2019) 15:22

Page 15 of 17

Microscopy, image acquisition and processing

Microscopy of all samples described was done using an Elyra PS.1 (Zeiss) platform using settings as described in previously published works [22, 25]. Samples were mostly documented using a $63\times/1.40$ NA (numerical aperture) oil immersion objective and rarely a $100\times/1.46$ NA oil immersion objective. AlexaFluor 488, Atto 488, eGFP were excited with a 488 nm laser line. AlexaFluor 546 and AlexaFluor 555 were excited with a 561 nm laser line and AlexaFluor 647 and Atto 647 N were excited with a 642 nm laser line. For imaging of AlexaFluor 488 and Atto 488 a band pass emission filter (495–550 nm). For AlexaFluor 546 and AlexaFluor 555 we used a band pass emission filter (570–620 nm). Finally for AlexaFluor 647 and Atto 647 N we used a long pass filter (655 nm). Especially for 3D imaging, the grating pattern was rotated 5 times (at 72° increments) with 5 additional phase shifts (at $3\pi/2$ increments) per angular position. In all cases, laser power and camera exposure time was adjusted appropriately to ensure high SNR, and visible modulation of the sample with the emission light pattern (in this case this is achieved when the grating is visible on the screen during the acquisition).

For z-sampling the Nyquist criterion was applied for the channel with the smallest λ_{exc} (in this particular case the channel corresponding to AlexaFluor 488 and Atto 488). Since the sampling rate of this channel is higher than that required for red (AlexaFluor 546) or far-red (AlexaFluor 647) the respective channels were over-sampled. All images were acquired with a PCO.Edge 5.5 scientific complementary metal-oxide semiconductor (sCMOS) camera with exposure times ranging between 80 and 500 ms.

Raw images were reconstructed using the appropriate tool of Zeiss Zen software (Black version with Structured Illumination module) using settings as previously described [25]. Especially Wiener filtering was adjusted appropriately to avoid commonly occurring artefacts such as ringing and honeycomb background [12, 25]. As a rule of thumb, relatively high filter values (ranging from -7.0 to -5.2) were chosen for 2D snaps, whereas lower filter values (ranging from -5.0 to -4.2) were chosen for entire Z-stacks. Based on full width at half maximum values of transverse fluorescence intensity profiles drawn along individual microtubules (as in [22]), XY-resolution was never worse than ca. 150 nm.

To demonstrate the angular distribution of cortical microtubules in example images of Col-0, *mpk4* and *ktn1-2*, we used the stand-alone software Cytospectre ([20]; http://www.tut.fi/cytospectre/).

In order to ensure the validity of quantitative colocalization studies, channels were aligned using the channel alignment plugin of the Zen software with TetraSpeck™

Microspheres, 0.1 µm, fluorescent blue/green/orange/dark red as a sample (Thermofischer Scientific). Alternatively the align RGB planes Image J plugin was used (https://imagej.net/Align_RGB_planes) either with TetraSpeck™ Microspheres, or with documented root whole-mount sample images. Quantitative colocalizations were done using the colocalization tool of Zeiss Zen Black or Zen 2 (Blue Version). Scatterplots were automatically thresholded accordingly [10] and for quantitative purposes the Manders coefficient was also automatically extrapolated [28].

3D rendering of reconstructed z-acquisitions was done using the appropriate tool of ImageJ, or the volume rendering plugin of Zen software. The output was saved as an *.avi file.

Additional files

Additional file 1: Video 1. 360° Rotational view of the 3D rendering shown in Fig. 3i.

Additional file 1: Video 2. 360° Rotational view of the 3D rendering shown in Fig. 3j.

Additional file 3: Video 3. 360° Rotational view of the 3D rendering shown in Fig. 3l.

Additional file 4: Video 4. 360° Rotational view of the 3D rendering shown in Fig. 6a.

Additional file 5: Video 5. 360° Rotational view of the 3D rendering shown in Fig. 6e.

Vavrdová *et al. Plant Methods*   (2019) 15:22

Page 16 of 17

Publisher's Note
Springer Nature remains neutral with regard to jurisdictional claims in published maps and institutional affiliations.

References
1. Antosch M, Schubert V, Holzinger P, Houben A, Grasser KD. Mitotic lifecycle of chromosomal 3xHMG-box proteins and the role of their N-terminal domain in the association with rDNA loci and proteolysis. New Phytol. 2015;208:1067–77.
2. Arigovindan M, Sedat JW, Agard DA. Effect of depth dependent spherical aberrations in 3D structured illumination microscopy. Opt Express. 2012;20:6527–41.
3. Banaei-Moghaddam AM, Schubert V, Kumke K, Weiß O, Klemme S, Nagaki K, Macas J, González-Sánchez M, Heredia V, Gómez-Revilla D, González-García M, Vega JM, Puertas MJ, Houben A. Nondisjunction in favor of a chromosome: the mechanism of rye B chromosome drive during pollen mitosis. Plant Cell. 2012;24:4124–34.
4. Baroux C, Schubert V. Technical review: microscopy and image processing tools to analyze plant chromatin: practical considerations. In: Baroux MBC, editor. Plant chromatin dynamics: methods and protocols, vol. 1675. New York: Humana Press; 2018. p. 537–89.
5. Beck M, Komis G, Müller J, Menzel D, Samaj J. Arabidopsis homologs of nucleus- and phragmoplast-localized kinase 2 and 3 and mitogen-activated protein kinase 4 are essential for microtubule organization. Plant Cell. 2010;22:755–71.
6. Beck M, Komis G, Ziemann A, Menzel D, Samaj J. Mitogen-activated protein kinase 4 is involved in the regulation of mitotic and cytokinetic microtubule transitions in *Arabidopsis thaliana*. New Phytol. 2011;189:1069–83.
7. Betzig E, Patterson GH, Sougrat R, Lindwasser OW, Olenych S, Bonifacino JS, Davidson MW, Lippincott-Schwartz J, Hess HF. Imaging intracellular fluorescent proteins at nanometer resolution. Science. 2006;313:1642–5.
8. Cole RW, Jinadasa T, Brown CM. Measuring and interpreting point spread functions to determine confocal microscope resolution and ensure quality control. Nat Protoc. 2011;6:1929–41.
9. Combs CA. Fluorescence microscopy: a concise guide to current imaging methods. Curr Protoc Neurosci. 2010. https://doi.org/10.1002/04711 42301.ns0201s50.
10. Costes SV, Daelemans D, Cho EH, Dobbin Z, Pavlakis G, Lockett S. Automatic and quantitative measurement of protein-protein colocalization in live cells. Biophys J. 2004;86:3993–4003.
11. Davis AM, Hall A, Millar AJ, Darrah C, Davis SJ. Protocol: streamlined sub-protocols for floral-dip transformation and selection of transformants in *Arabidopsis thaliana*. Plant Methods. 2009;5:1–7. https://doi.org/10.1186/1746-4811-5-3.
12. Demmerle J, Innocent C, North AJ, Ball G, Müller M, Miron E, Matsuda A, Dobbie IM, Markaki Y, Schermelleh L. Strategic and practical guidelines for successful structured illumination microscopy. Nat Protoc. 2017;12:988–1010.
13. Fišerová J, Efenberková M, Sieger T, Maninová M, Uhlířová J, Hozák P. Chromatin organization at the nuclear periphery as revealed by image analysis of structured illumination microscopy data. J Cell Sci. 2017;130:2066–77.
14. Fitzgibbon J, Bell K, King E, Oparka K. Super-resolution imaging of plasmodesmata using three-dimensional structured illumination microscopy. Plant Physiol. 2010;153:1453–63.
15. Gustafsson MG. Surpassing the lateral resolution limit by a factor of two using structured illumination microscopy. J Microsc. 2000;198:82–7.
16. Hell SW, Wichmann J. Breaking the diffraction resolution limit by stimulated emission: stimulated-emission-depletion fluorescence microscopy. Opt Lett. 1994;19:780–2.
17. Ho CM, Hotta T, Guo F, Roberson RW, Lee YR, Liu B. Interaction of antiparallel microtubules in the phragmoplast is mediated by the microtubule-associated protein MAP65-3 in Arabidopsis. Plant Cell. 2011;23:2909–23.
18. Jonak C, Okrész L, Bögre L, Hirt H. Complexity, cross talk and integration of plant MAP kinase signalling. Curr Opin Plant Biol. 2002;5:415–24.
19. Jonkman J, Brown CM. Any way you slice it—a comparison of confocal microscopy techniques. J Biomol Tech. 2015;26:54–65.
20. Kartasalo K, Pölönen RP, Ojala M, Rasku J, Lekkala J, Aalto-Setälä K, Kallio P. CytoSpectre: a tool for spectral analysis of oriented structures on cellular and subcellular levels. BMC Bioinform. 2015;16:344. https://doi.org/10.1186/s12859-015-0782-y.
21. Komis G, Luptovčiak I, Ovečka M, Samakovli D, Šamajová O, Šamaj J. Katanin effects on dynamics of cortical microtubules and mitotic arrays in *Arabidopsis thaliana* revealed by advanced live-cell imaging. Front Plant Sci. 2017;8:866. https://doi.org/10.3389/fpls.2017.00866.
22. Komis G, Mistrik M, Samajová O, Doskočilová A, Ovečka M, Illés P, Bartek J, Samaj J. Dynamics and organization of cortical microtubules as revealed by superresolution structured illumination microscopy. Plant Physiol. 2014;165:129–48.
23. Komis G, Mistrik M, Šamajová O, Ovečka M, Bartek J, Šamaj J. Superresolution live imaging of plant cells using structured illumination microscopy. Nat Protoc. 2015;10:1248–63.
24. Komis G, Novák D, Ovečka M, Šamajová O, Šamaj J. Advances in imaging plant cell dynamics. Plant Physiol. 2018;176:80–93.
25. Komis G, Šamajová O, Ovečka M, Šamaj J. Super-resolution microscopy in plant cell imaging. Trends Plant Sci. 2015;20:834–43.
26. Kraus F, Miron E, Demmerle J, Chitiashvili T, Budco A, Alle Q, Matsuda A, Leonhardt H, Schermelleh L, Markaki Y. Quantitative 3D structured illumination microscopy of nuclear structures. Nat Protoc. 2017;12:1011–28.
27. Lin F, Krishnamoorthy P, Schubert V, Hause G, Heilmann M, Heilmann I. A dual role for cell plate-associated PI4Kbeta in endocytosis and phragmoplast dynamics during plant somatic cytokinesis. EMBO J. 2019. https://doi.org/10.15252/embj.2018100303.
28. Manders EM, Stap J, Brakenhoff GJ, van Driel R, Aten JA. Dynamics of three-dimensional replication patterns during the S-phase, analysed by double labelling of DNA and confocal microscopy. J Cell Sci. 1992;103:857–62.
29. Marques A, Schubert V, Houben A, Pedrosa-Harand A. Restructuring of holocentric centromeres during meiosis in the plant *Rhynchospora pubera*. Genetics. 2016;204:555–68.
30. Müller S, Fuchs E, Ovecka M, Wysocka-Diller J, Benfey PN, Hauser MT. Two new loci, PLEIADE and HYADE, implicate organ-specific regulation of cytokinesis in Arabidopsis. Plant Physiol. 2002;130:312–24.
31. Müller J, Beck M, Mettbach U, Komis G, Hause G, Menzel D, Samaj J. Arabidopsis MPK6 is involved in cell division plane control during early root

Vavrdová *et al. Plant Methods*   (2019) 15:22

Page 17 of 17

development, and localizes to the pre-prophase band, phragmoplast, trans-Golgi network and plasma membrane. Plant J. 2010;61:234–48.

32. Musielak TJ, Slane D, Liebig C, Bayer M. A versatile optical clearing protocol for deep tissue imaging of fluorescent proteins in *Arabidopsis thaliana*. PLoS ONE. 2016;11(8):e0161107. https://doi.org/10.1371/journal.pone.0161107.

33. Nakagawa T, Suzuki T, Murata S, Nakamura S, Hino T, Maeo K, et al. Improved gateway binary vectors: high-performance vectors for creation of fusion constructs in transgenic analysis of plants. Biosci Biotechnol Biochem. 2007;71:2095–100.

34. Nakamura M, Ehrhardt DW, Hashimoto T. Microtubule and katanin-dependent dynamics of microtubule nucleation complexes in the acentrosomal Arabidopsis cortical array. Nat Cell Biol. 2010;12:1064–70.

35. Ovečka M, Takáč T, Komis G, Vadovič P, Bekešová S, Doskočilová A, Šamajová V, Luptovčiak I, Samajová O, Schweighofer A, Meskiene I, Jonak C, Křenek P, Lichtscheidl I, Škultéty L, Hirt H, Šamaj J. Salt-induced subcellular kinase relocation and seedling susceptibility caused by overexpression of Medicago SIMKK in Arabidopsis. J Exp Bot. 2014;65:2335–50.

36. Ovečka M, von Wangenheim D, Tomančák P, Šamajová O, Komis G, Šamaj J. Multiscale imaging of plant development by light-sheet fluorescence microscopy. Nat Plants. 2018;4:639–50.

37. Palmer WM, Martin AP, Flynn JR, Reed SL, White RG, Furbank RT, Grof CP. PEA-CLARITY: 3D molecular imaging of whole plant organs. Sci Rep. 2015;5:13492. https://doi.org/10.1038/srep13492.

38. Plotnikov A, Zehorai E, Procaccia S, Seger R. The MAPK cascades: signaling components, nuclear roles and mechanisms of nuclear translocation. Biochim Biophys Acta. 2011;1813:1619–33.

39. Ribeiro T, Marques A, Novák P, Schubert V, Vanzela AL, Macas J, Houben A, Pedrosa-Harand A. Centromeric and non-centromeric satellite DNA organisation differs in holocentric Rhynchospora species. Chromosoma. 2017;126:325–35.

40. Rocchetti A, Hawes C, Kriechbaumer V. Fluorescent labelling of the actin cytoskeleton in plants using a cameloid antibody. Plant Methods. 2014;10:12. https://doi.org/10.1186/1746-4811-10-12.

41. Rust MJ, Bates M, Zhuang X. Sub-diffraction-limit imaging by stochastic optical reconstruction microscopy (STORM). Nat Methods. 2006;3:793–5.

42. Sahl SJ, Hell SW, Jakobs S. Fluorescence nanoscopy in cell biology. Nat Rev Mol Cell Biol. 2017;18:685–701.

43. Samajová O, Komis G, Šamaj J. Immunofluorescent localization of MAPKs and colocalization with microtubules in Arabidopsis seedling whole-mount probes. Methods Mol Biol. 2014;1171:107–15.

44. Šamaj J, Ovečka M, Hlavacka A, Lecourieux F, Meskiene I, Lichtscheidl I, Lenart P, Salaj J, Volkmann D, Bögre L, Baluska F, Hirt H. Involvement of the mitogen-activated protein kinase SIMK in regulation of root hair tip growth. EMBO J. 2002;21:3296–306.

45. Sasabe M, Kosetsu K, Hidaka M, Murase A, Machida Y. *Arabidopsis thaliana* MAP65-1 and MAP65-2 function redundantly with MAP65-3/PLEIADE in cytokinesis downstream of MPK4. Plant Signal Behav. 2011;6:743–7.

46. Sauer M, Paciorek T, Benková E, Friml J. Immunocytochemical techniques for whole-mount in situ protein localization in plants. Nat Protoc. 2006;1:98–103.

47. Schmid VJ, Cremer M, Cremer T. Quantitative analyses of the 3D nuclear landscape recorded with super-resolved fluorescence microscopy. Methods. 2017;123:33–46.

48. Schubert V, Lermontova I, Schubert I. Loading of the centromeric histone H3 variant during meiosis—how does it differ from mitosis? Chromosoma. 2014;123:491–7.

49. Schubert V, Lermontova I, Schubert I. The Arabidopsis CAP-D proteins are required for correct chromatin organisation, growth and fertility. Chromosoma. 2013;122:517–33.

50. Schubert V. RNA polymerase II forms transcription networks in rye and Arabidopsis nuclei and its amount increases with endopolyploidy. Cytogenet Genome Res. 2014;143:69–77.

51. Schubert V. Super-resolution microscopy—applications in plant cell research. Front Plant Sci. 2017;8:531.

52. Shaw SL, Ehrhardt DW. Smaller, faster, brighter: advances in optical imaging of living plant cells. Annu Rev Plant Biol. 2013;64:351–75.

53. Smékalová V, Luptovčiak I, Komis G, Šamajová O, Ovečka M, Doskočilová A, Takáč T, Vadovič P, Novák O, Pechan T, Ziemann A, Košútová P, Šamaj J. Involvement of YODA and mitogen activated protein kinase 6 in Arabidopsis post-embryogenic root development through auxin up-regulation and cell division plane orientation. New Phytol. 2014;203:1175–93.

54. Staudt T, Lang MC, Medda R, Engelhardt J, Hell SW. 2,2′-thiodiethanol: a new water soluble mounting medium for high resolution optical microscopy. Microsc Res Tech. 2007;70:1–9.

55. Szczurek A, Contu F, Hoang A, Dobrucki J, Mai S. Aqueous mounting media increasing tissue translucence improve image quality in structured illumination microscopy of thick biological specimen. Sci Rep. 2018;8:13971. https://doi.org/10.1038/s41598-018-32191-x.

56. Török P, Hewlett SJ, Varga P. The role of specimen-induced spherical aberration in confocal microscopy. J Microsc. 1997;1997(188):158–72.

57. Vyplelová P, Ovečka M, Komis G, Šamaj J. Advanced microscopy methods for bioimaging of mitotic microtubules in plants. Methods Cell Biol. 2018;145:129–58.

58. Warner CA, Biedrzycki ML, Jacobs SS, Wisser RJ, Caplan JL, Sherrier DJ. An optical clearing technique for plant tissues allowing deep imaging and compatible with fluorescence microscopy. Plant Physiol. 2014;166:1684–7.

59. Werner S, Marillonnet S, Hause G, Klimyuk V, Gleba Y. Immunoabsorbent nanoparticles based on a tobamovirus displaying protein A. Proc Natl Acad Sci USA. 2006;103:17678–83.

PALACKÝ UNIVERSITY OLOMOUC

Faculty of Science

Department of Biochemistry

Cell division plane regulation in plants by MAPK cascades

PhD Thesis summary

P1416 Biochemistry

Tereza Vavrdová

Olomouc

2020

This PhD thesis has been completed at the Department of Cell Biology, Centre of the Region Haná for Biotechnological and Agricultural Research, Faculty of Science, Palacký University Olomouc.

PhD candidate:	Mgr. Tereza Vavrdová
	Department of Cell Biology, Centre of the Region Haná for Biotechnological and Agricultural Research, Faculty of Science, Palacký University Olomouc
	Šlechtitelů 27, 783 71 Olomouc
Supervisor:	doc. George Komis, PhD
	Department of Cell Biology, Centre of the Region Haná for Biotechnological and Agricultural Research, Faculty of Science, Palacký University Olomouc
	Šlechtitelů 27, 783 71 Olomouc
Consultant:	Despina Samakovli, PhD
	Department of Cell Biology, Centre of the Region Haná for Biotechnological and Agricultural Research, Faculty of Science, Palacký University Olomouc
	Šlechtitelů 27, 783 71 Olomouc
Reviewers:	prof. RNDr. Viktor Žárský, CSc.
	Department of Experimental Plant Biology, Faculty of Science, Charles University
	Viničná 5, Prague 2 128 44
	Mgr. Matyáš Fendrych, PhD
	Department of Experimental Plant Biology, Faculty of Science, Charles University
	Viničná 5, Prague 2 128 44

The summary of the thesis was sent for distribution on ....

The defense of this thesis takes place at the Faculty of Science, Šlechtitelů 27, Olomouc on...

The PhD thesis is available at the library of the Biological Centre, Šlechtitelů 27, Olomouc.

Contents

Abstract

Plant mitogen activated protein kinases (MPK) are involved in a plethora of signalling events, integrating extrinsic cues to cellular responses. The focus of this thesis is to examine the role of MPKs in the cell division plane orientation. Specifically, the function of the YODA-MPK3/6 pathway is described in formative cell divisions during early embryonic development and in tissue patterning of the primary root tip of the model plant *Arabidopsis thaliana*. The interaction between the YODA-MPK3/6 pathway and the protein phosphatase 2A (PP2A) and heat shock proteins 90 (HSP90) was assessed.

PP2A phosphatases are known to affect cell division plane orientation and are expected to execute this function by regulating the phosphorylation status of proteins involved in cell division plane positioning. Herein, it is assumed that the PP2A cooperates with the YODA-MPK3/6 in determining the cell division plane orientation.

In the second part of the thesis, the involvement of HSP90s in early embryonic development is investigated in light of their previously described physical partnership with the YODA-MPK3/6 pathway.

Finally, the present thesis also provides a description and comparison of advanced microscopic techniques, with potential applications for imaging live cells expressing appropriate fluorescent protein fusions, or fixed and accordingly immunolabelled samples. Methods such as structured illumination microscopy and Airyscan laser scanning microscopy are applied to visualize microtubules together with two prominent microtubule associated proteins, microtubule associated protein 65 2 (MAP65-2) and MAP65-3.

Conclusively, this thesis presents information on the role of the YODA-MPK3/6 cascade in the cell division plane orientation and the cell fate determination as well as its interaction with PP2A and HSP90s while executing these functions. Furthermore, it reports on advanced microscopic methods which may be employed in future studies aiming to elucidate mechanisms behind cytoskeleton organization and dynamics in plants.

Objectives

1. Summary of recent knowledge on the role of phosphorylation in cell division plane orientation in both symmetric and asymmetric cell divisions. This part will be focused on describing mitogen-activated protein kinases (MPKs), microtubule associated proteins 65 (MAP65s) and protein phosphatase 2A (PP2A). Additionally, the role of heat shock proteins 90 (HSP90s) in plant development will be reviewed.

2. Documentation of the putative interaction between PP2A and MPK.

3. Phenotypic characterization of mutants defective in genes encoding PP2A subunits regarding the formative cell divisions.

4. Characterization of the role of HSP90s in modulating the function of YODA-MPK pathway in different types of formative cell divisions.

5. Visualization of MAP65s by employing advanced microscopy techniques.

1. Introduction

1.1. Cell division in plants

The plant cell division is markedly different from cytokinesis in animal cells. This property can be assign to the sessile life style and rigid cell walls, which lead to evolution of unique plant cell division mechanisms. The plant cell division depends on the two components of cytoskeleton, actin and microtubules. Microtubules form several structures during plant cell mitosis, some of them unique to plants (**Fig. 1**). Before prophase, the cortical microtubules typical for interphase rearrange into a belt-like structure (Dhonukshe and Gadella 2003). These microtubules forms the preprophase band together with actin filaments, organelles and specific proteins. Together they mark plasma membrane region denoted as cortical division zone providing a correction mechanism pivoting the nascent cell plate at the correct plane (Zhang and Dong 2018). While the position of the preprophase band is in symmetrically dividing cells determined by cell geometry (Flanders *et al.* 1990), and the position of the nucleus (Murata and Wada 1991), these positional cues are overridden in asymmetrically dividing cells. The preprophase band disassembles before prometaphase. As plant cells do not have a microtubule organizing centre, the spindle forms in an acentrosomal fashion just before the nuclear envelope breakdown (Buschmann and Zachgo 2016) and it drives the segregation of chromatids in anaphase. Subsequently, daughter nuclei are reconstituted and the plant-
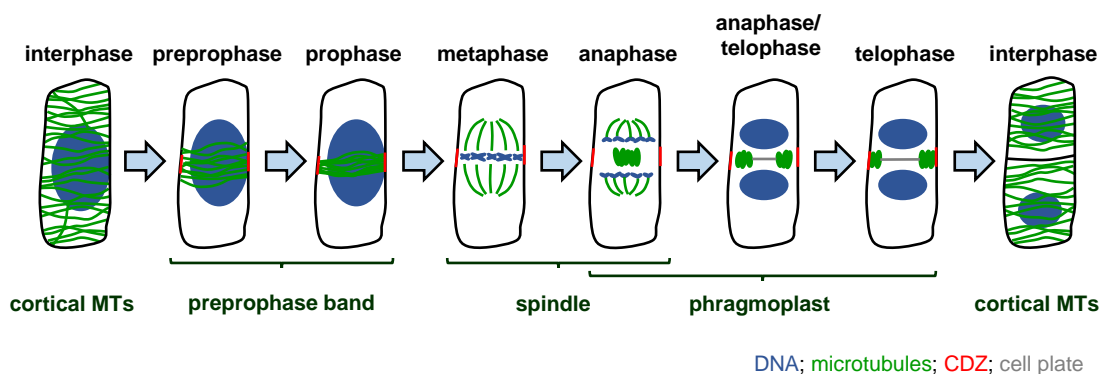

Figure 1. Organization of microtubules during the cell cycle. Adapted from Vavrdová *et al.* (2019). Cortical microtubules reorganize into the preprophase band at the onset of mitosis. The preprophase band starts as a broad ring of microtubules, it narrows during prophase and its site is marked as the cortical division zone, a place of the future cell plate fusion site. The preprophase band is disassembled before the metaphase as the spindle is formed. After the segregation of chromatids, the disc phragmoplast is formed at the centre of the cell. The phragmoplast guides the construction of the cell plate. Next, the ring phragmoplast is continuously degraded at its centre, where the cell plate is being built, and it expands towards the cell cortex. After the discontinuous phragmoplast reaches the cell plate fusion site, the cell plate is formed and two daughter cells are created, where microtubules again rearrange into cortical microtubules.

4

specific cytokinetic apparatus, the phragmoplast, is formed. The phragmoplast is formed between the sister nuclei in the central part of the cell and it serves as a frame guiding the movement of Golgi-derived vesicles carrying material for cell plate assembly. As the new cell wall is being built within the phragmoplast midzone, the phragmoplast is gradually degraded (Chen *et al.* 2018) while it continuously expands towards the cell plate fusion site marked by the cortical division zone (reviewed in Smertenko, 2018). Through the guidance of phragmoplast, the cell division plane is determined and the cell plate is assembled, resulting in completion of cytokinesis.

For proper progression of cytokinesis is essential precise spatiotemporal regulation of microtubule organization and dynamics. This is usually accomplished by microtubule associated proteins, which are affecting microtubule nucleation, de/polymerisation, and de/stabilization. One of the protein families involved in the organization of microtubule arrays is the MICROTUBULE ASSOCIATED PROTEIN 65 (MAP65) family. Plant MAP65s form homodimers through their N-terminal domains and they bind to microtubules with their C-terminal domains (Smertenko *et al.* 2004). MAP65s form crossbridges 25 nm wide between microtubules (Chan et al. 1999) and their main function is to slow down microtubule depolymerization (Van Damme et al. 2004). The activity and subcellular localization of MAP65s is regulated by reversible phosphorylation (Smertenko et al. 2006) and the members of this protein family differ in their colocalization with microtubule arrays. While MAP65-1 and MAP65-2 are colocalizing with cortical microtubules, preprophase band and phragmoplast (Lucas and Shaw 2012), MAP65-3 and MAP65-4 are associated only with mitotic microtubule arrays and their function appears essential for cytokinesis (Müller *et al.* 2004; Li *et al.* 2017).

The activity of the microtubule associated proteins is crucial for proper progression of cell division. Therefore, there is a need for precise spatiotemporal control of microtubule associated proteins. Plant cells employ several regulatory mechanisms to achieve this, among them the reversible protein phosphorylation. Several kinases were implicated in regulating the phosphorylation status of microtubule associated proteins during cell division, including MITOGEN ACTIVATED PROTEIN KINASEs (MPK; Smékalová *et al.* 2014; Kohoutová *et al.* 2015).

MPKs are Ser/Thr kinases and they form signalling cascades, where MPK is activated by MITOGEN ACTIVATED PROTEIN KINASE KINASE (MKK), which is in turn phosphorylated by MITOGEN ACTIVATED PROTEIN KINASE KINASE

KINASE (MKKK). In plants, two MPK signalling pathways are well-described regarding their activity in plant cell division. One of them is essential for the majority of cell divisions (Calderini *et al.* 1998; Bögre *et al.* 1999), while the function of the other cascade is more distinct. The latter pathway consists of YODA (YDA; MKKK), MKK4 and MKK5, MPK3 and MPK6 ((Wang *et al.* 2007) and its members are involved in stress responses, innate immunity (Colcombet and Hirt 2008) and plant development (reviewed in Komis *et al.* 2018a). This pathway is essential for several formative cell divisions, among them the first division of the zygote (Lukowitz *et al.* 2004), stomatal differentiation pathway (Bergmann *et al.* 2004; Wang *et al.* 2007), and root development (Müller *et al.* 2010; Smékalová *et al.* 2014).

The reversibility of phosphorylation is executed by protein phosphatases, which makes them indispensable for correct spatiotemporal regulation of microtubule organization and dynamics (Bhaskara *et al.* 2017). In the context of mitosis and cytokinesis, the Ser/Thr specific phosphoprotein phosphatases are of major importance (Samofalova *et al.* 2019). Plant phosphoprotein phosphatases are known to interact with tubulin (Awotunde *et al.* 2003; Voss *et al.* 2013), microtubule associated proteins (Spinner *et al.* 2013) and MPKs (Umbrasaite *et al.* 2010; Kohoutová *et al.* 2015). Notably, PHOSPHOPROTEIN PHOSPHATASE 2A (PP2A) is involved in establishing and maintaining the cortical division zone (Camilleri *et al.* 2002).

1.2. Asymmetric cell divisions in plants

Asymmetric cell divisions are indispensable for all multicellular organisms as they generate daughter cells with diverging cell fates (Shao and Dong 2016). There are numerous formative cell divisions during the plant ontogenesis, e.g. the first division of the zygote and stomatal differentiation pathway. The prerequisite for a successful asymmetric cell division is overriding the rules governing the symmetric cell division. The regulation of microtubules and microtubule associated proteins appear to be involved in these processes (Park *et al.* 1998; Oh *et al.* 2010). Several kinases and phosphatases have been implicated in asymmetric cell divisions (e.g. Tanaka *et al.* 2002; Wang *et al.* 2018; Li *et al.* 2019).

The YDA-MKK4/5-MPK3/6 signalling cascade targets microtubule associated proteins involved in the organization of mitotic microtubule arrays (Smertenko *et al.*

2006; Kohoutová *et al.* 2015) as well as cell fate determination factors (Lampard *et al.* 2009; Ueda *et al.* 2017). Members of this pathway affect several types of formative cell divisions during plant ontogenesis (reviewed in Komis *et al.* 2018a). This can be exemplified within the context of the early embryonic development. In Arabidopsis, the early embryonic development encompasses a series of extremely ordered cell divisions (Yoshida *et al.* 2014). The YDA-MKK4/5-MPK3/6 pathway is indispensable for the first asymmetric division of the zygote (Zhang *et al.* 2017), as it integrates several signalling cues (Bayer *et al.* 2009; Yu *et al.* 2016) and it secures transcriptional activation of cell fate determination factors (Ueda *et al.* 2017). The activity of the YDA-MKK4/5-MPK3/6 pathway is negatively regulated either by phosphorylation (Kim *et al.* 2012), or by dephosphorylation of MPK3/6 by PP2C and MAPK PHOSPHATASE 1 (Umbrasaite *et al.* 2010; Tamnanloo *et al.* 2018). Presumably, other phosphatases are involved in regulating this pathway.

1.3. The role of HSP90s in plant development

The HEAT SHOCK PROTEIN 90 (HSP90) protein family encompasses a large group of evolutionarily conserved prokaryotic and eukaryotic proteins. The members of this family act as chaperones enabling other proteins to correctly fold or re-fold their tertiary structures (Taipale *et al.* 2010). From the seven members of the HSP90 protein family in Arabidopsis, four are present in cytoplasm, while the other three localize to distinct compartments (Krishna and Gloor 2001). The cytoplasmic HSP90.1 has low expression levels under normal conditions, but they dramatically increase under stress conditions (Haralampidis *et al.* 2002). On the other hand, the other three cytoplasmic HSP90s, HSP90.2-4, which share high sequence homology, are constitutively expressed.

Generally, *hsp90* mutants exhibit pleiotropic phenotypes because they provide plant cells with genetic buffering (Queitsch *et al.* 2002), which means that they can mask mutations or polymorphisms by correctly folding mutant proteins. Once HSP90s are depleted, the genetic buffering is lost leading to pleiotropic phenotypes, especially under conditions challenging protein homeostasis (Taipale *et al.* 2010). Nevertheless, *hsp90* loss-of-function mutants were described to have morphological defects, and the protein levels of cytoplasmic HSP90s alter throughout plant ontogenesis (Prasinos *et al.* 2005). Thus, HSP90s play a role in plant development (Xu *et al.* 2012). The uncovering of their

role in plant development is challenging due to their functional redundancy and complex interactions with co-chaperones and plethora of client proteins. Several studies revealed their integration in developmental signalling networks (reviewed in Tichá *et al.* 2020). Through the interaction with signalling networks, cytoplasmic HSP90s serve as a central hub connecting these pathways with environmental cues. Moreover, they are known to colocalize with cortical microtubules and phragmoplast (Krtková *et al.* 2012) and to affect microtubule remodelling through yet unknown mechanism, which possibly includes other client or interacting proteins (Queitsch *et al.* 2002; Weis *et al.* 2010). Conclusively, their integration in developmental signalling pathways and their activity in microtubule remodelling proposes them as candidates in modulating the cell division plane orientation.

2 Materials and methods

Herein the material and methods are briefly introduced. Detailed information are presented in the thesis.

Arabidopsis thaliana (L.) Heynh. plants of the Columbia (Col-0) ecotype were used as wild type. All mutant lines and marker lines are listed in **Table 1**.

Macroscopic images of seedlings were taken on the stereo microscope M165 FC (Leica, Germany) and the distance between the root tip and first root hair was measured in ImageJ (Schneider *et al.* 2012). Statistical analysis was calculated by the software STATISTICA (version 13.4.0.14; Statsoft, USA) and Microsoft Excel Workbook (Gaetano 2013).

The roots of 5 days after germination old seedlings were stained with 5 µM FM4-64 staining (Thermo Fisher Scientific, USA) and observed under confocal laser scanning microscope (CLSM) LSM 710 (Carl Zeiss, Germany).

Modified pseudo-Schiff propidium iodide staining was performed as described previously (Truernit *et al.* 2008). Samples were observed on CLSM. Images had their colour inverted in ImageJ.

Table 1: **List of lines used in this study.**

Genotype	Description	Reference/source
hsp90.1	T-DNA insertional mutation in *HSP90.1* (At5g52640; SALK_007614)	(Hubert *et al.* 2009)
mpk3-1	T-DNA insertional mutation in *MPK3* (At3g45640; SALK_151594)	(Alonso *et al.* 2003)
mpk6-2	T-DNA insertional mutation in *MPK6* (At2g43790; SALK_073907)	(Liu and Zhang 2004)
rcn1-6	T-DNA insertional mutation in *RCN1* (At1g25490; SALK_059903)	(Blakeslee *et al.* 2008)
yda	insertional mutation in *YDA* (At1g63700)	(Lukowitz *et al.* 2004)
ΔNyda	deletion in N-terminal regulatory domain of *YDA* (At1g63700); gain-of-function	(Bergmann *et al.* 2004)
CaMV35S::TUA6:GFP (TUA6-GFP)	GFP-labelled tubulin driven under constitutively active promoter	(Shaw *et al.* 2003)
MAP65-2::eGFP:MAP65-2 (eGFP-MAP65-2)	eGFP-MAP65-2 fusion protein driven under native promoter	Pavel Křenek
MAP65-2::tagRFP:MAP65-2 (tagRFP-MAP65-2)	tagRFP-MAP65-2 fusion protein driven under native promoter	Pavel Křenek
MAP65-2::eGFP:MAP65-3 (eGFP-MAP65-3)	eGFP-MAP65-3 fusion protein driven under native promoter	Pavel Křenek

The visualization of eGFP-MAP65-2, tagRFP-MAP65-2, and eGFP-MAP65-3 was performed on either the Axio Observer LSM 880 with Airyscan (ACLSM; Carl Zeiss, Germany) or the Axio Observer Z.1 equipped with the Elyra PS.1 superresolution system supporting the structured illumination microscopy (SIM) module (Carl Zeiss, Germany). All microscopic data were reconstructed and analysed on appropriate Zeiss Zen software (Carl Zeiss, Germany), which was also used for fluorescence intensity profiling (Komis *et al.* 2014). For measuring the full-width at half maximum (FWHM), the profile measurements were first normalized based on the minimum-maximum scaling, then the FWHM was measured in ImageJ in the graphs presenting the normalized signal intensity plotted against the distance.

To prepare samples for the light-sheet Z.1 fluorescence microscope (Carl Zeiss, Germany), plants expressing both GFP and tagRFP were prepared according to the "open system" protocol (Ovečka *et al.* 2015).

The root wholemount immunolocalization was based on previously published protocols (Sauer *et al.* 2006; Šamajová *et al.* 2014) with notable changes. Seedlings were fixed in 4% (v/v) formaldehyde (Polysciences, USA) in microtubule stabilizing buffer (MTSB) supplemented with Triton X-100. Cell walls were digested using enzyme solution. After washing with MTSB and phosphate buffered saline (PBS), samples were incubated in the permeabilization solution. Blocking was performed overnight in blocking solution (3% (w/v) BSA and 0.5% (w/v) polyacetylated BSA in PBS). Subsequently, samples were incubated in primary antibody: rat anti-α tubulin antibody (Bio-Rad, USA), Atto 488-conjugated anti-GFP nanobody (Chromotek, Germany), or rabbit anti-RFP antibody (Thermo Fisher Scientific, USA). Next day, samples were incubated with secondary antibody: Alexa Fluor 647-conjugated anti-rat antibody (Thermo Fisher Scienticific, USA), or Alexa Fluor 546-conjugated anti-rabbit antibody (Thermo Fisher Scienticific, USA). Samples were counterstained with DAPI (4',6-diamidino-2-phenylindole dihydrochloride) and mounted on slides. Samples were observed on the SIM platform.

3 Results

3.1. PP2A affects the functions of MPK3 and MPK6 in plant development

Previous reports documented the involvement of both the YDA-MPK pathway and PP2A in the regulation of the cell division plane orientation (reviewed in Komis *et al.* 2018a; Samofalova *et al.* 2019). To examine whether these two modules are part of a common pathway, loss-of-function *mpk3* and *mpk6* mutants were subjected to the treatment with cantharidin, a phosphatase inhibitor with high selectivity towards PP2A (Li *et al.* 2010).

Wild type plants treated with cantharidin had reduced root length (**Fig. 2A**), corroborating previous results (Deruere *et al.* 1999). This trend was more pronounced in the *rcn1-6* mutant (**Fig. 2A**), confirming the sensitivity of the *rcn1-6* mutant to cantharidin. While the growth of *mpk3-1* and *mpk6-2* mutants was visibly affected by higher concentration of cantharidin in media (**Fig. 2B**), *mpk3-1* and *mpk6-2* mutants were less sensitive to cantharidin at lower concentrations compared to wild type (**Fig. 2A,B**).

Treatment with cantharidin lead to smaller distance between the root tip and first root hair in both the wild type and *rcn1-6* mutant (**Fig. 2C**), with *rcn1-6* showing more progressive changes in the increasing concentrations of cantharidin (**Fig. 2D**). Moreover, the concentrations of 3 and 5 µM cantharidin lead to the phenocopy of *rcn1*-6 (**Fig. 2C**). Conversely, both *mpk3-1* and *mpk6-2* mutants were insensitive to lower concentrations of cantharidin showing no significant changes in the distance between the root tip and first root hair (**Fig. 2C**).

Next, the cell division plane orientation defects in the primary root tips of *mpk6,* and *rcn1-6* mutants were examined by the staining with FM4-64, a lipophilic dye staining plasma membrane (**Fig. 3**). The root tip anatomy of the wild type is well-organized (**Fig. 3A,B**), which is in contrast with the aberrations in cell wall positioning in the *rcn1-6* and *mpk6-2* mutants (**Fig. 3C-F**), corroborating the previously published results (Blakeslee *et al.* 2008; Müller *et al.* 2010). Disorganization of the cell division plane orientation was especially strong in the *mpk6-2* mutant (**Fig. 3F**). Genetic depletion of RCN1 in the *mpk6-2 rcn1-6* mutant lead to partial rescue in the root tip anatomy (**Fig. 3G,H**) compared to both parent lines (**Fig. 3D,F**).

Both pharmacological and genetic depletion of RCN1 suggest that PP2A and MPK3/6 belong to a common pathway. This is evidenced by the partial insensitivity of *mpk3-1* and *mpk6-2* mutants to lower concentrations of cantharidin; and by the partial
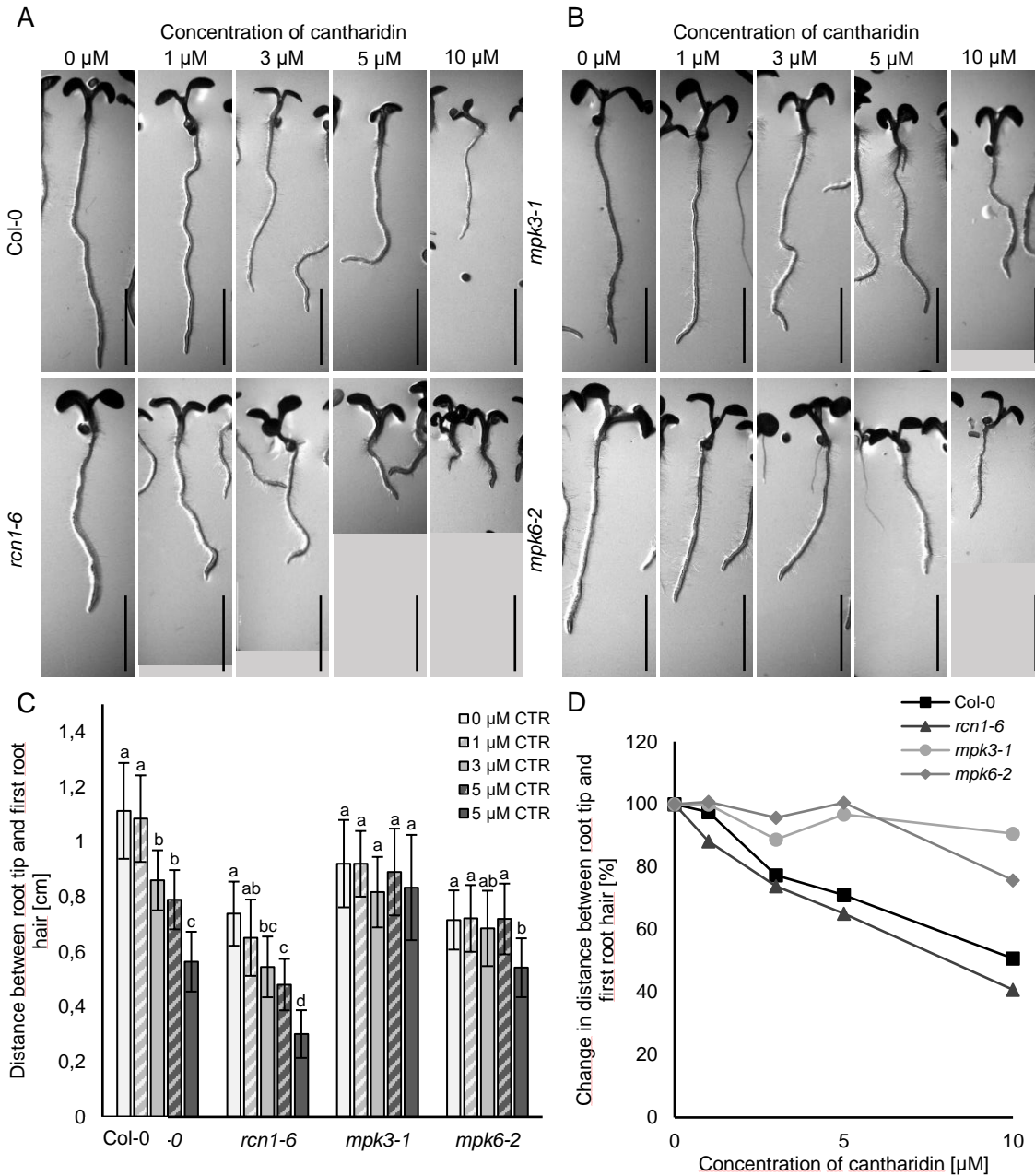
Fig. 2. *mpk3, mpk6* mutants are less sensitive to phosphatase inhibitor cantharidin. Plants of the indicated genotypes were grown on media with different concentration of cantharidin (CTR; 0/1/3/5/10 μM) up to 5 days after germination. (A,B) Representative pictures of 5 days old seedlings of Col-0, *rcn1-6* (A) and *mpk3-1, mpk6-2* (B). Scale bars, 5 mm. (C) Measurements of distances between the root tip and the first root hair presented as mean±SD (N≥50, three technical repetitions; two-way ANOVA followed by Scheffé's test and Holm-Bonferroni correction; statistical comparison is shown within groups sharing the same genotype; letters in the graph are shared by groups without statistically significant differences at the 0.001 probability level). (D) Change in the distance between the root tip and the first root hair relative to the same parameter in media without cantharidin.

rescue of abnormally oriented cell walls in the root tip of *mpk6-2* mutant after genetic depletion of RCN1.
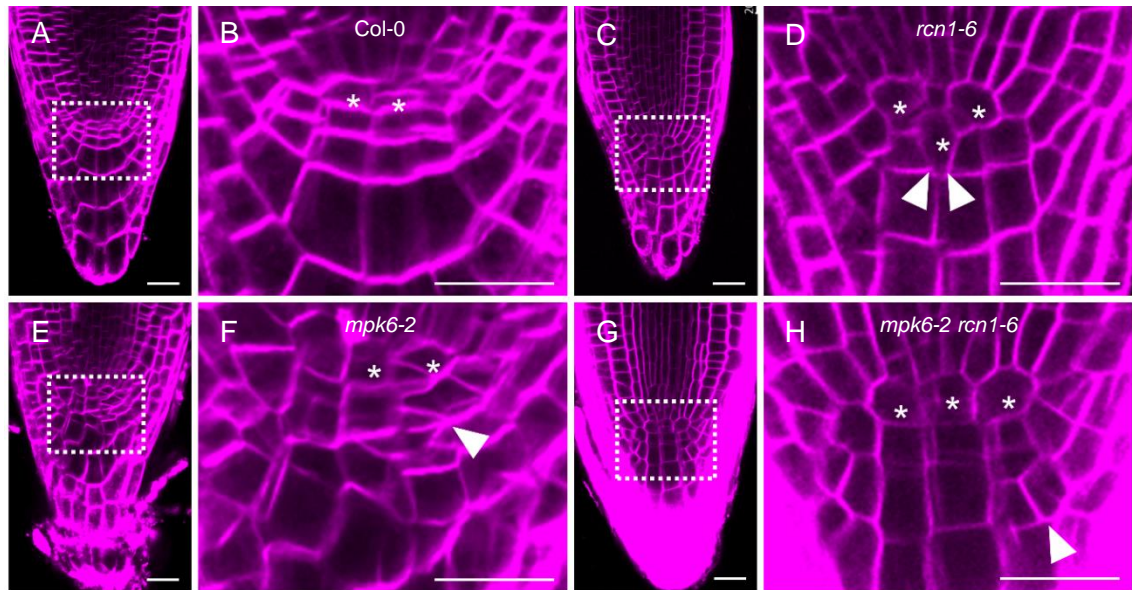
Fig. 3. *RCN1* **depletion partially rescues morphological defects in the root tip of** *mpk6* **mutant.** Primary root architecture in 5 days old seedlings stained with FM4-64. Images of the root tip meristem area of the wild type (A,B), *rcn1-6* (C,D), *mpk6-2* (E,F), *mpk6-2 rcn1-6* (G,H). Boxed areas in (A,C,E,G) are enlarged in (B,D,F,H). White stars mark cells of the quiescent centre (identified based on the anatomy), white arrowheads point to the abnormally positioned plasma membranes. Scale bars, 20 μm.

3.2. HSP90.1 is affecting asymmetric cell divisions via modulating YDA-MPK pathway

Recently, cytoplasmic HSP90.1 was shown to directly interact with the YDA-MPK3/6 pathway and to modulate its function during the differentiation of stomata (Samakovli *et al.* 2020). Because the YDA-MAPK pathway is also involved in other types of formative cell division, e.g. in early embryogenesis (Lukowitz *et al.* 2004) and primary root tissue patterning (Smékalová *et al.* 2014), the aim was to investigate whether HSP90.1 affects the function of the YDA-MPK3/6 pathway in these processes as well.

The embryonic development in *hsp90.1, yda* single and double mutants was examined by using the pseudo-Schiff propidium iodide staining. The highly ordered organization of cell walls, which is typical for early embryonic development in Arabidopsis (Yoshida *et al.* 2014; **Fig. 4A,B**), was distorted in both the loss-of-function *yda* and gain-of-function *ΔNyda* mutants (**Fig. 4C-F**), corroborating the previous reports (Lukowitz *et al.* 2004). Surprisingly, the positioning of the cell division plane was also compromised in the *hsp90.1* mutant (**Fig. 4G,H**), but to a smaller extent. The genetic

depletion of HSP90.1 resulted in partial rescue of the severe *yda* and *ΔNyda* phenotype in *hsp90.1 yda, hsp90.1 ΔNyda* double mutants (**Fig. 4I-L**).

To examine, whether HSP90.1 also affects primary root development, the roots of *hsp90.1, yda* single and double mutants had their plasma membranes stained with FM4-64 and then their root tip architecture was observed (**Fig. 5**). The well-organized root tip anatomy of the wild type (**Fig. 5A,B**), was also observed in the *hsp90.1* mutant
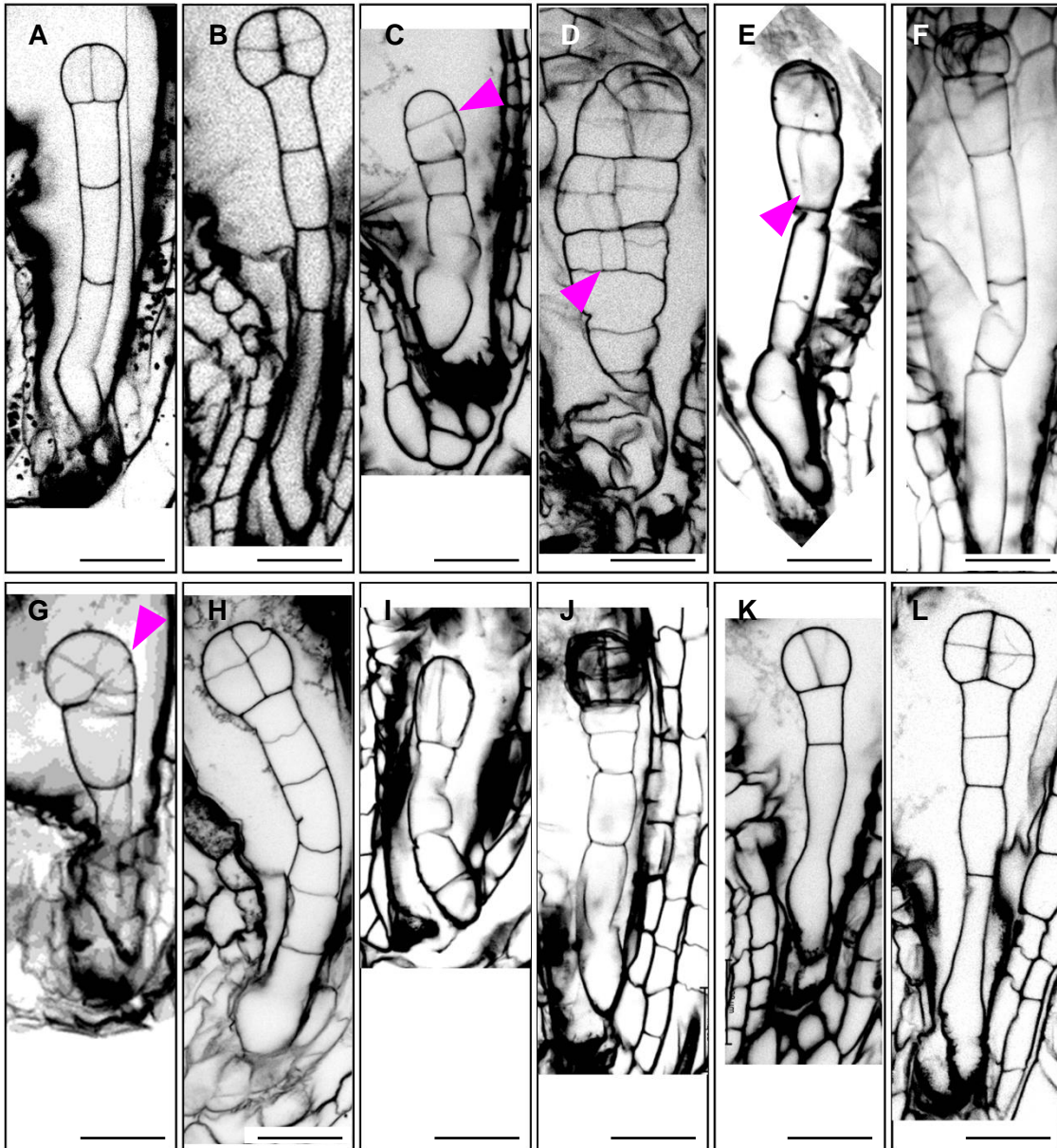

Figure 4. Genetic depletion of HSP90.1 restores defects in the cell division plane orientation in early embryogenesis of *yda* mutants. Adapted from Samakovli *et al.* (unpublished). Early embryonic development of the wild type (A,B), *yda* (C,D), *ΔNyda* (E,F), *hsp90.1* (G,H), *hsp90.1 yda* (I,J), *hsp90.1 ΔNyda* (K,L) was visualized by modified pseudo-Schiff propidium iodide staining. Magenta arrowheads point to wrongly oriented cell walls. Scale bars, 20 μm.
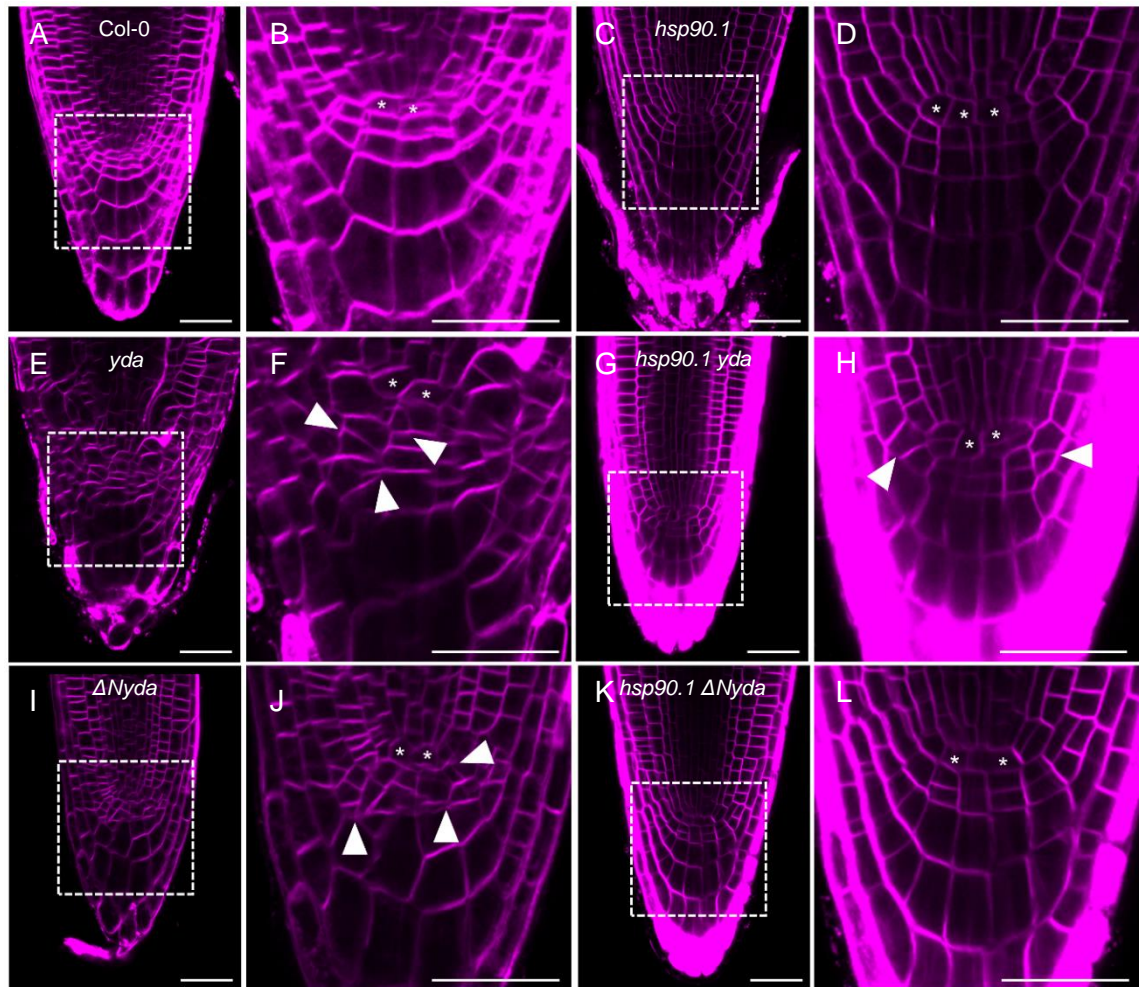
Figure 5. HSP90 depletion rescues morphological defects in root tip of *yda* mutants. Five days after germination old seedlings were stained with FM4-64 to observe the primary root architecture in Col-0 (A,B; **Fig. 3A,B**), *hsp90.1* (C,D), *yda* (E,F), *hsp90.1 yda* (G,H), *ΔNyda* (I,J) and *hsp90.1 ΔNyda* (K,L). White stars mark the quiescent centre, white arrowheads point to the abnormally positioned plasma membranes. Scale bars, 20 μm.

(**Fig. 5C,D**). On the other hand, both in *yda* and *ΔNyda* mutants, severe aberrations in the organization of cell walls were observed (**Fig. 5E,F,I,J**).

Similarly to the observations regarding the early embryonic development (**Fig. 4**), genetic depletion of HSP90.1 in *yda* and *ΔNyda* mutants lead to partial rescue in the cell division plane orientation defects in *hsp90.1 yda, hsp90.1, ΔNyda* double mutants (**Fig. 5G,H,K,L**). Conclusively, HSP90.1 modulates the regulation the cell division plane orientation in both the embryonic and root postembryonic development downstream of the YDA-MPK3/6 pathway.

3.3. Visualization of MAP65s with advanced microscopy techniques

Functions of microtubule associated proteins are crucial for regulating microtubule arrays. However, the molecular mechanisms of their activity are often examined by *in vitro* experiments and they should be confirmed *in vivo*. The aim of this part is to report on advanced microscopic techniques, which were improved and optimized to enable resolving the colocalization of microtubule associated proteins with microtubules and tracking their dynamic behaviour.

The organization and dynamics of MAP65-2 decorating cortical microtubules was visualized by two superresolution approaches, the ACLSM and the SIM. First, these two platforms were compared regarding their resolution potential (**Fig. 6**). Using both the ACLSM and SIM with the 63×/1.40 NA oil immersion objective, MAP65-2 decorating cortical microtubules in hypocotyl epidermal cells expressing eGFP-MAP65-2 was observed (**Fig. 6A,B**). Within these images, fluorescence intensity profiles were drawn perpendicular to the thinnest observed MAP65-2 decorating microtubules (**Fig. 6C,D**). The intensity profiles were normalized and plotted against distance (**Fig. 6E,F**) and within the resulting graphs, the FWHM was measured. The MAP65-2 tagged with fluorescent proteins were resolved by the ACLSM at 177±19 nm (mean±SD; N=36, **Fig. 6G**) and by the SIM platform at 133±20 nm (mean±SD; N=39, **Fig. 6H**). The SIM platform outperformed the ACLSM in its resolution potential while visualizing eGFP-MAP65-2.

Cortical microtubules create bundles consisting of various numbers of individual filaments. It has been shown previously, that the composite nature of cortical microtubules can be discriminated as the increase in the fluorescence intensity maximum of a bundle is linear compared to the fluorescence intensity maximum of its respective branches (Komis *et al.* 2014). To determine whether MAP65-2 follows the same trend, images of line expressing both tagRFP-MAP65-2 and TUA6-GFP were searched to find events where microtubule bundles were branching into two smaller bundles (**Fig. 7A-C**). In such places, the fluorescence intensity profiles were drawn perpendicularly to the two smaller bundles and the larger bundle. The fluorescence intensity profiles were plotted against distance (**Fig. 7D-E**). The fluorescence intensity maxima of the composite bundle and its smaller and larger branch can be differentiated in both TUA6-GFP (**Fig. 7D,F**) and tagRFP-MAP65-2 (**Fig. 7E,G**). Moreover, the linear correlation coefficients reached
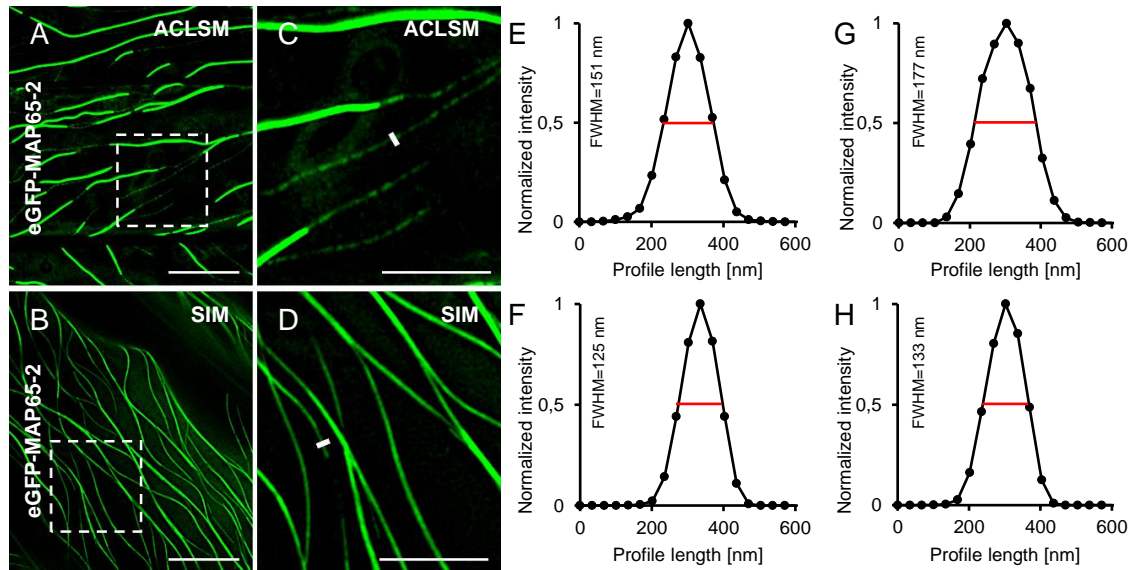
Figure 6. Resolving details of eGFP-MAP65-2 decoration of cortical microtubules by either ACLSM or SIM. Adapted from Vavrdová *et al.* (2020). MAP65-2 decoration of cortical microtubules in hypocotyl epidermal cells were visualized with eGFP-MAP65-2. (A) Image from the ACLSM (objective 63×/1.40 NA); (B) Image from the SIM (objective 63×/1.40 NA); (C-D) show area boxed in (A) and (B), respectively; (E-F) present normalized intensity measurements for the profile measurements marked by white line in (C) and (D), respectively; (G-H) provide a quantitative analysis showing averaged, coaligned, and normalized intensity profiles of individual eGFP-MAP65-2-labeled microtubule bundles from the ACLSM (G; N=36) and the SIM (H; N=36). Scale bars, 10 μm (A, B), or 5 μm (C, D), respectively. Abbreviations: ACLSM, Airyscan confocal laser scanning microscopy; FWHM, full-width at half maximum; SIM, structured illumination microscopy,

high values for both TUA6-GFP (R^2=0.9966; **Fig. 7F**) and tagRFP-MAP65-2 (R^2=0.9786; **Fig. 7G**). This is in line with the previous observation of a linear increase in maximum fluorescence intensity upon the inclusion of microtubules within a bundle (Komis *et al.* 2014) and the MAP65-2 appears to follow this trend. Thus, the maximum signal intensity of tagRFP-MAP65-2 corresponds to the amount of individual microtubules constituting the bundle.

The MAP65-2 colocalizes with cortical microtubules and also with the preprophase band and phragmoplast (Lucas and Shaw 2012). These two mitotic arrays are also decorated by the MAP65-3 (Müller *et al.* 2004). The diversification of the MAP65 family in plants (exemplified by differential subcellular localization) signifies that its members have distinct functions in organizing microtubule arrays (Gaillard *et al.* 2008). To reveal these functional differences, it is necessary to first characterize the subtle nuances in their subcellular localization throughout the cell cycle.
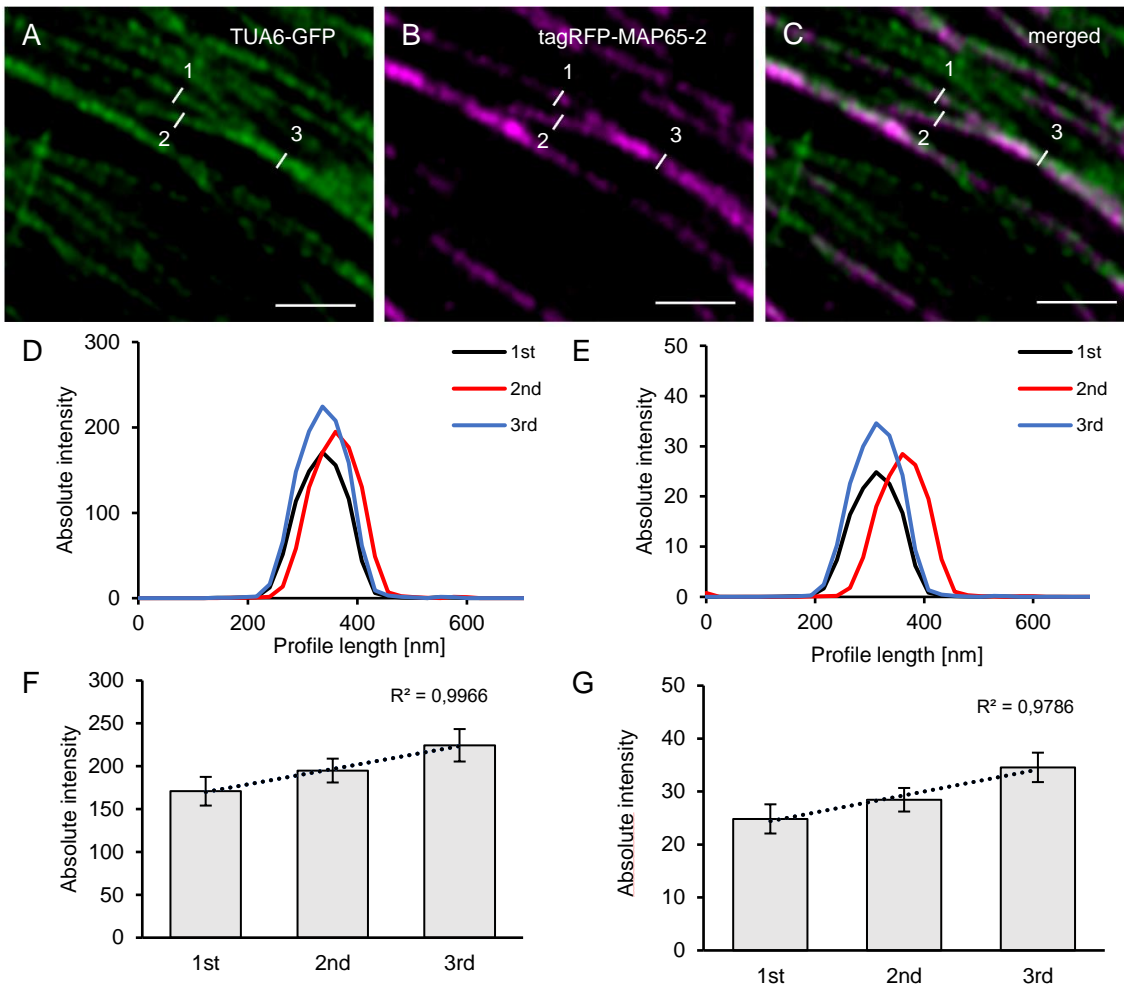
Figure 7. Signal intensity of tagRFP-MAP65-2 reflects the microtubule bundle composition. Adapted from Vavrdová *et al.* (2020). Hypocotyl epidermal cells of stably transformed lines expressing both tagRFP-MAP65-2 and TUA6-GFP were observed in the Airyscan confocal lased scanning microscope (objective 63×/1.40 NA). (A-C) overview of an area with microtubule branching with TUA6-GFP shown in the green channel (A), tagRFP-MAP65-2 in the magenta channel (B) and (C) is a merged picture; measured microtubule bundles are visualized with white lines and labeled with numbers according to their strength (1 being the weakest and 3 the strongest bundle). Microtubule bundles were quantified by fluorescence intensity profiling and averaged values are shown in (D) for TUA6-GFP and (E) for tagRFP-MAP65-2. Quantitative evaluation is given in (F) for TUA6-GFP and (G) for tagRFP-MAP65-2 (mean±SD; R^2, linear correlation coefficient; N=8, 5 technical repetitions). Scale bars, 2 μm.

To confirm the colocalization of MAP65-2 and MAP65-3 with specific mitotic microtubule arrays, the lines coexpressing tagRFP-MAP65-2 and eGFP-MAP65-3, were first observed using light sheet fluorescence microscopy (LSFM; **Fig. 8**). At the cost of lower resolution, the LSFM is capable of long-term time-lapsed imaging of whole roots (Ovečka *et al.* 2015). This enabled observation of whole root tips with multiple cell divisions, thus, repeated examination of MAP65-2, MAP65-3 localization throughout cell division (**Fig. 8A-C**). From the time-lapsed imaging was apparent, that both
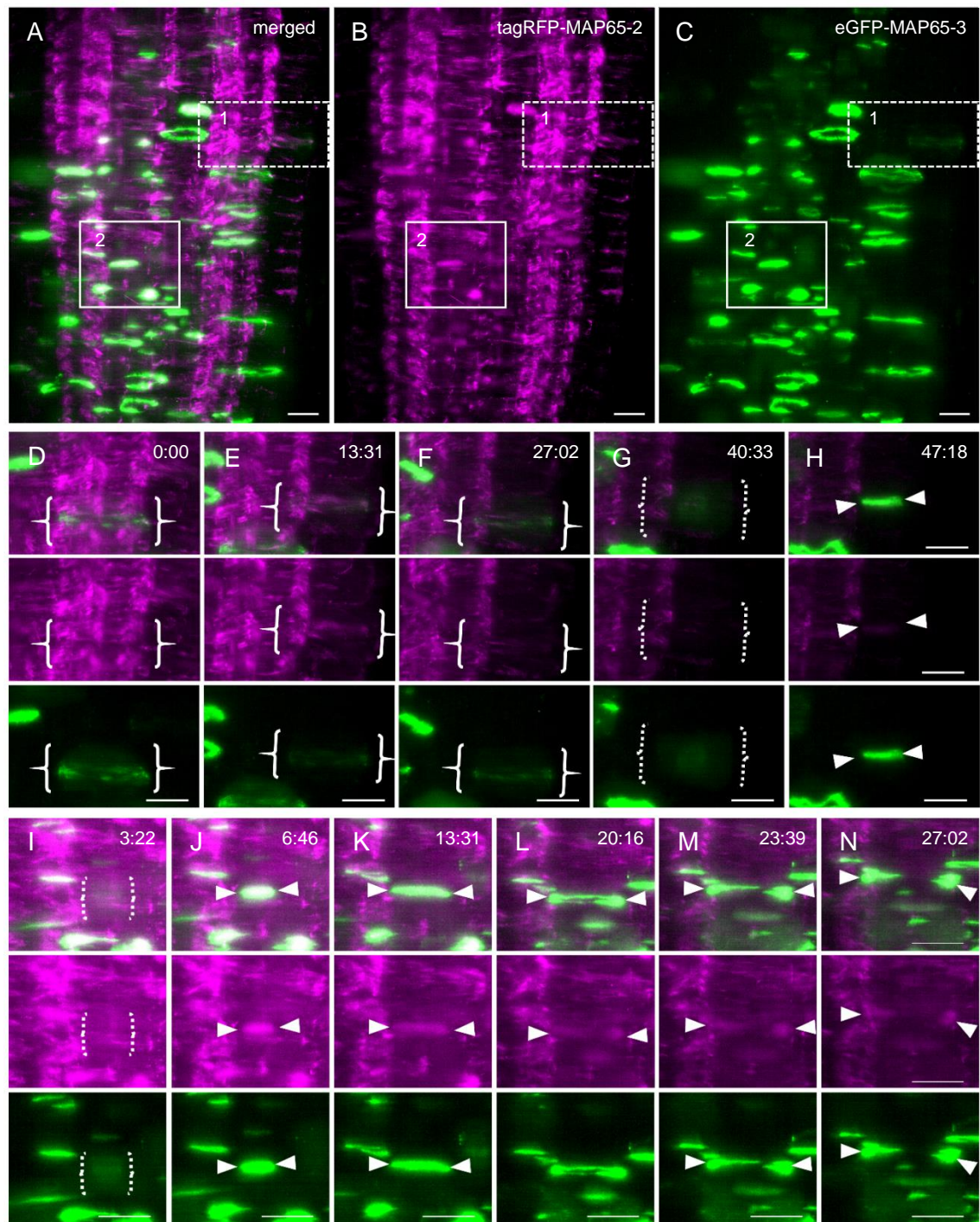
Figure 8. Differential colocalization of MAP65-2 and MAP65-3 with mitotic microtubule structures. Light sheet microscopy was used to capture growing root of Arabidopsis line expressing both tagRFP-MAP65-2 and eGFP-MAP65-3. (A-C) an overview showing merged picture (A), magenta channel reporting on tagRFP-MAP65-2 signal (B) and green channel depicting eGFP-MAP65-3 signal (C). The boxed area marked by dashed line and numbered as 1 in (A-C) is shown stills in (D-H), while the full-line box marked as 2 in (A-C) corresponds to stills shown in (I-N). In (D-N) the stills are presented as merged pictures, with corresponding images from magenta and green channel bellow them. White full-line brackets mark preprophase band (D-F), dotted brackets surround spindle (G, I), white arrowheads point to phragmoplast, specifically disc (H, J), ring (K, L) and discontinuous phragmoplast (M, N). Scale bars = 10 μm; time format, min:s.

tagRFP-MAP65-2 and eGFP-MAP65-3 decorate the preprophase band (**Fig. 8D-F**), while they are absent from the spindle (**Fig. 8G,I**). As the phragmoplast begins to form, the signals of tagRFP-MAP65-2 and eGFP-MAP65-3 reappear (**Fig. 8H,J**) and both follow the expansion of the phragmoplast towards the cell division site (**Fig. 8K-N**).

The LSFM provided information on the general localization of MAP65-2 and MAP65-3 during the cell cycle, which was later on confirmed by the SIM platform (data not shown). The main advantage of the live cell imaging is that it provides profound information on the cellular processes. On the other hand, its applicability is limited. In this study, the live cell colocalization studies were restricted to the visualization of two fluorophores. For this purpose an optimized protocol for the immunolabelling of Arabidopsis roots has been used (Sauer *et al.* 2006; Šamajová *et al.* 2014) to colocalize MAP65-2, MAP65-3, and tubulin.

In the fixed samples were observed the microtubules forming the metaphase spindle and the ring phragmoplast (**Fig. 9A**). The subcellular localization of both MAP65-2 and MAP65-3 (**Fig. 9B,C**) was visualized. The cell cycle stages were confirmed by staining the DNA with DAPI (**Fig. 9D**). The MAP65-2 and MAP65-3 were not colocalizing with microtubules of the metaphase spindle (**Fig. 9E-H**), corroborating the results of the live cell imaging (**Fig. 8**). On the other hand, both MAP65-2 and MAP65-3 were detected at the ring phragmoplast (**Fig. 9F-H**). While MAP65-2 was detected along the whole phragmoplast (**Fig. 9E**), MAP65-3 was localized more discretely at the phragmoplast midzone (**Fig. 9F-H**). Despite the MAP65-2 and MAP65-3 localizing at the same mitotic array, their subcellular localization is different, suggesting differential roles for these proteins in the organization of phragmoplast.

The fixed-sample microscopy is inferior to the live cell imaging in terms of the information value on cellular processes. Nevertheless, this approach provided useful details on the subcellular localization of proteins of interest while validating the observations from live cell imaging. Furthermore, by simultaneous visualization of microtubules, MAP65-2, MAP65-3 and DNA, it was possible to describe the localization MAP65-2 and MAP65-3 in relation to microtubules at well-specified cell cycle stages.
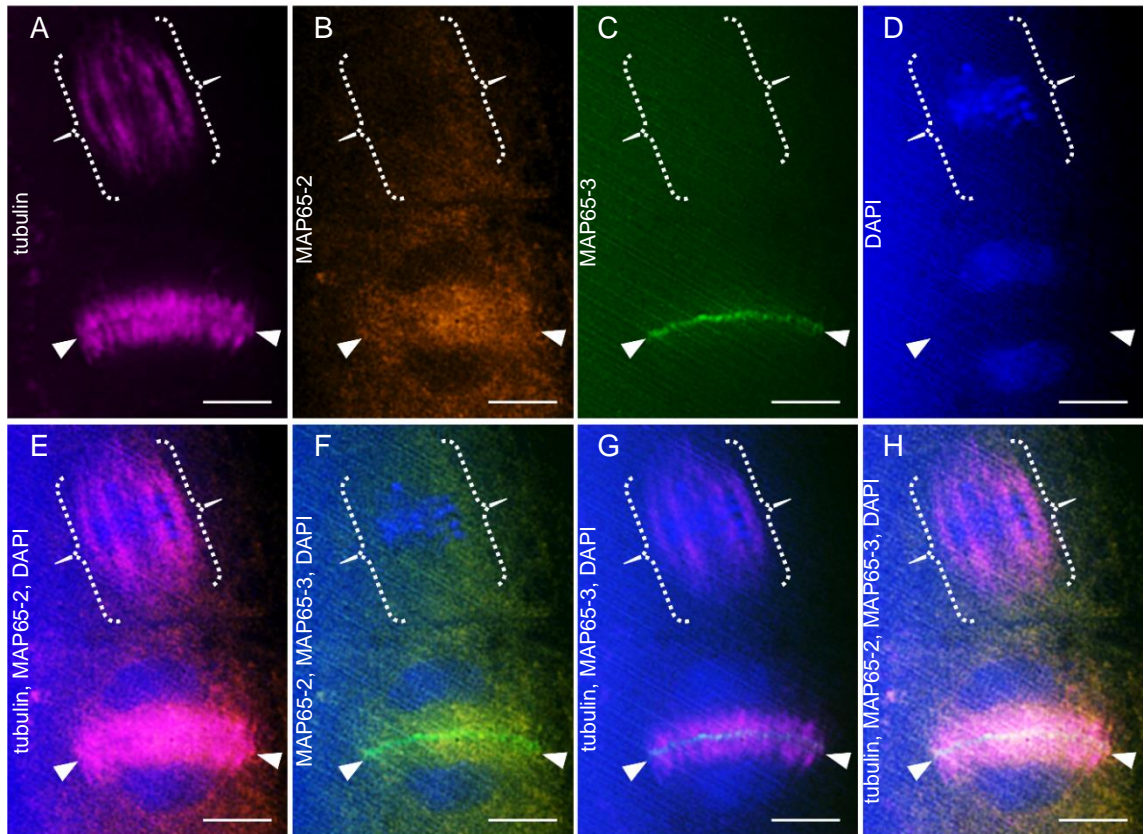
Figure 9. Colocalization of MAP65-2 and MAP65-3 with mitotic microtubular arrays.
Immunolocalization of tubulin (A), tagRFP-MAP65-2 (B) and eGFP-MAP65-3 (C) combined with DAPI staining (D) in roots of line coexpressing tagRFP-MAP65-2 and eGFP-MAP65-3. (E-H) present merged images showing combinations of: tubulin, MAP65-2, DAPI (E); MAP65-2, MAP65-3, DAPI (F); tubulin, MAP65-3, DAPI (G); tubulin, MAP65-2, MAP65-3, DAPI (H). White dotted brackets mark the metaphase spindle, white full arrowheads point to the ring phragmoplast. Arrowheads and brackets are positioned at the same places in all images. Scale bars, 2 μm. Image acquisition by Renata Šnaurová.

4 Discussion

4.1. The interplay of PP2A and MPK3, MPK6 in cell division plane orientation

The role of plant phosphoprotein phosphatases in formative cell divisions is usually described as an indirect one (Michniewicz *et al.* 2007), although there are examples of their direct involvement (Song and Clark 2005; Song *et al.* 2008). Moreover, the function of YDA-MPK3/6 pathway in establishing asymmetric divisions during stomatal development is regulated by two different phosphatases (Umbrasaite *et al.* 2010; Tamnanloo *et al.* 2018). A question arose, whether the plant PP2A, which was reported to affect the cell division plane orientation during embryonic and postembryonic development (Traas *et al.* 1995; Camilleri *et al.* 2002; Blakeslee *et al.* 2008), might control the function of the YDA-MPK3/6 pathway regarding its role in plant development.

The loss-of-function *mpk3* and *mpk6* mutants were treated with a phosphatase inhibitor to test whether the pharmacological depletion of PP2A affects the function of MPK3/6. Both *mpk3* and *mpk6* mutants are partially insensitive to lower concentrations of cantharidin suggesting that PP2A and MPK3/6 act in a common pathway, which affects the root tip.

Next, the root tip anatomy was examined in *mpk6* and *rcn1* single and double mutants. In the *mpk6* and *rcn1* single mutants were observed defects in cell division plane orientation, corroborating the previous results (Blakeslee *et al.* 2008; Müller *et al.* 2010). In the *mpk6 rcn1* double mutant, fewer defects in the cell wall orientation were noted. The observation of milder phenotype in double mutant compared to single mutants supports the hypothesis that RCN1 and MPK6 are controlling the cell division plane orientation through a common pathway. Future studies should elucidate whether PP2A directly interacts with and affects phosphorylation status of MPK3/6.

4.2. HSP90s affect asymmetric cell divisions through modulating YDA-MPK cascade

According to recent report, cytoplasmic HSP90s modulate the function of YDA-MPK3/6 cascade in the stomatal differentiation pathway (Samakovli *et al.* 2020). Since this signalling cascade is involved in other developmental processes (reviewed in Komis *et al.*

2018a), it was of interest to investigate whether HSP90s affect the function of YDA in other developmental events as well.

In embryogenesis, the YDA-MPK cascade plays a role in establishing asymmetric cell divisions and regulating the expression of cell fate determination factors (Ueda *et al.* 2017). Notably, the *yda* loss-of-function and *ΔNyda* gain-of-function mutants exhibit wrongly positioned cell walls during early embryogenesis, corroborating previous reports (Lukowitz *et al.* 2004). Interestingly, the cell division plane orientation defects were also noted for *hsp90.1*, although they were milder compared to *yda* mutants. Genetic depletion of HSP90.1 rescued the cell division plane orientation defect in *yda* mutants. Furthermore, genetic depletion of HSP90.1 also rescued the cell division plane orientation defect in the postembryonic primary root of *yda* mutants (Smékalová *et al.* 2014). These observations suggest that HSP90s affect both embryonic and postembryonic developmental events downstream of YDA, which is in line with the report on the overall improved phenotype of *hsp90 yda* double mutants (Závorková 2019).

It remains unknown, how exactly does the interaction between HSP90.1 and YDA-MPK3/6 pathway affect the cell division plane orientation. Recently, HSP90s were reported to be involved in the polarization of YDA in stomatal precursors (Samakovli *et al.* 2020), which is critical for the progression of asymmetric cell division during the stomatal differentiation pathway (Zhang *et al.* 2015; Houbaert *et al.* 2018). It has been suggested that similarly to the polarization during the stomatal differentiation pathway, the subcellular localization of YDA could be restricted prior to the formative cell division during embryogenesis as well (Jeong *et al.* 2016). This leads to speculations, that if YDA is indeed polarized in early embryogenesis, HSP90s might play a role in it. Another possibility is direct involvement of HSP90.1 in the cell division plane orientation, since HSP90s were reported to colocalize with phragmoplast (Krtková *et al.* 2012) and to affect microtubule remodelling (Queitsch *et al.* 2002).

4.3. Visualizing organization and dynamics of MAP65s

Plant cytoskeleton consists of fine structures which cannot be resolved by the light microscopy, as it is limited by the Abbe´s limitation. To circumvent this problem, the transmission electron microscopy (Kremer *et al.* 2015) or superresolution microscopic methods can be employed (Komis, *et al.* 2018b). Alas, the electron miscroscopy and many of the superresolution techniques are limited to fixed samples,

which restrains their applicability for observation of dynamic processes. Herein, two advanced light microscopy platforms, the ACLSM and the SIM, are compared regarding their resolution potential and applicability for live cell imaging. The SIM platform outperformed the ACLSM regarding the resolution, however, its phototoxicity proved to be exceedingly intense for tagRFP-labelled proteins. By contrast, the ACLSM enabled simultaneous imaging of GFP- and tagRFP-labelled proteins with fewer issues concerning photobleaching. While the ACLSM presents an improved CLSM platform (Huff 2016), the performance of SIM might be further improved by implementing other microscopy techniques (Vizcay-Barrena *et al.* 2011; Chen *et al.* 2014). Another possibility of obtaining high resolution images during live cell imaging is to employ one of the recently developed modification of single molecule localization microscopy (Dertinger *et al.* 2009; Cox *et al.* 2012; Gustafsson *et al.* 2016).

The MAP65-2 and MAP65-3 were previously described to colocalize with mitotic structures, even though there are some discrepancies in the reports (Müller *et al.* 2004; Caillaud *et al.* 2008; Lucas *et al.* 2011). To determine the subcellular localization of MAP65-2 and MAP65-3 throughout the cell cycle, the LSFM was used for mesoscopic observation of multiple cell divisions in growing plants. The localization pattern was confirmed by high-resolution imaging on the SIM platform.

MAP65-2 localizes to the preprophase band and the phragmoplast, corroborating the previous reports (Lucas and Shaw 2012). Moreover, the MAP65-3 localization pattern was described to be similar to the one observed in previous immunolocalization studies (Müller *et al.* 2004; Ho *et al.* 2012), which contrasts with the report from live cell imaging (Caillaud *et al.* 2008). This discrepancy is caused by different construction of chimeric fluorescent proteins. The N-terminal eGFP-MAP65-3 fusion used in this study appears to more faithfully report on the subcellular localizaton of MAP65-3 than the previously reported C-terminal MAP65-3-GFP fusion (Caillaud *et al.* 2008), because the C-terminal domain is reposible for subcellular localization of MAP65s (Smertenko *et al.* 2006; Ho *et al.* 2012).

Within the phragmoplast, MAP65-2 appears to colocalize with microtubules in the entire phragmoplast, while MAP65-3 was detected in the phragmoplast midzone. This was observed both in living cells and in fixed samples. The immunolabelling of fixed samples enabled simultaneous detection of MAP65-2, MAP65-3, tubulin and DNA, and this helped to prove the localization pattern of MAP65-2 and MAP65-3 throughout the cell cycle, as well as their differential subcellular localization at the phragmoplast.

Conclusively, the choice of the microscopic platforms for live cell imaging depends on the tradeoff between resolution capacity and phototoxicity. Moreover, the immunolabelling proved to be a valuable tool for confirming the observations from live cell imaging. The advanced microscopic techniques provided valuable information on the organization and dynamics of MAP65s. In future studies, these methods could be employed for ellucidating the differential functions of the members of MAP65 protein family.

5 References

Alonso, J.M., Stepanova, A.N., Leisse, T.J., Kim, C.J., Chen, H., Shinn, P., … Ecker, J.R. (2003). Genome-Wide Insertional Mutagenesis of Arabidopsis thaliana. *Science* **301**(5633):653–657. doi: https://doi.org/10.1126/science.1086391.

Awotunde, O.S., Lechward, K., Krajewska, K., Zołnierowicz, S. and Muszyńska, G. (2003). Interaction of maize (Zea mays) protein phosphatase 2A with tubulin. *Acta Biochimica Polonica* **50**(1):131–138. doi: https://doi.org/10.18388/abp.2003_3720.

Bayer, M., Nawy, T., Giglione, C., Galli, M., Meinnel, T. and Lukowitz, W. (2009). Paternal Control of Embryonic Patterning in Arabidopsis thaliana. *Science* **323**(5920):1485–1488. doi: https://doi.org/10.1126/science.1167784.

Bergmann, D.C., Lukowitz, W. and Somerville, C.R. (2004). Stomatal Development and Pattern Controlled by a MAPKK Kinase. *Science* **304**(5676):1494–1497. doi: https://doi.org/10.1126/science.1096014.

Bhaskara, G.B., Wen, T.-N., Nguyen, T.T. and Verslues, P.E. (2017). Protein Phosphatase 2Cs and *Microtubule-Associated Stress Protein 1* Control Microtubule Stability, Plant Growth, and Drought Response. *The Plant Cell* **29**(1):169–191. doi: https://doi.org/10.1105/tpc.16.00847.

Blakeslee, J.J., Zhou, H.-W., Heath, J.T., Skottke, K.R., Barrios, J.A.R., Liu, S.-Y. and DeLong, A. (2008). Specificity of RCN1-Mediated Protein Phosphatase 2A Regulation in Meristem Organization and Stress Response in Roots. *Plant Physiology* **146**(2):539–553. doi: https://doi.org/10.1104/pp.107.112995.

Bögre, L., Calderini, O., Binarova, P., Mattauch, M., Till, S., Kiegerl, S., … Heberle-Bors, E. (1999). A MAP Kinase Is Activated Late in Plant Mitosis and Becomes Localized to the Plane of Cell Division. *The Plant Cell* **11**(1):101–113. doi: https://doi.org/10.1105/tpc.11.1.101.

Buschmann, H. and Zachgo, S. (2016). The Evolution of Cell Division: From Streptophyte Algae to Land Plants. *Trends in Plant Science* **21**(10):872–883. doi: https://doi.org/10.1016/j.tplants.2016.07.004.

Caillaud, M.-C., Lecomte, P., Jammes, F., Quentin, M., Pagnotta, S., Andrio, E., … Favery, B. (2008). MAP65-3 Microtubule-Associated Protein Is Essential for Nematode-Induced Giant Cell Ontogenesis in Arabidopsis. *The Plant Cell* **20**(2):423–437. doi: https://doi.org/10.1105/tpc.107.057422.

Calderini, O., Bogre, L., Vicente, O., Binarova, P., Heberle-Bors, E. and Wilson, C. (1998). A cell cycle regulated MAP kinase with a possible role in cytokinesis in tobacco cells. *Journal of Cell Science* **111**(20):3091–3100.

Camilleri, C., Azimzadeh, J., Pastuglia, M., Bellili, Catherine, Grandjean, O. and Bouchez, D. (2002). The Arabidopsis TONNEAU2 Gene Encodes a Putative Novel Protein Phosphatase 2A Regulatory Subunit Essential for the Control of the Cortical Cytoskeleton. *The Plant Cell* **14**(4):833–845. doi: https://doi.org/10.1105/tpc.010402.

Chan, J., Jensen, C.G., Jensen, L.C.W., Bush, M. and Lloyd, C.W. (1999). The 65-kDa carrot microtubule-associated protein forms regularly arranged filamentous cross-bridges between microtubules. *Proceedings of the National Academy of Sciences* **96**(26):14931–14936. doi: https://doi.org/10.1073/pnas.96.26.14931.

Chen, B.-C., Legant, W.R., Wang, K., Shao, L., Milkie, D.E., Davidson, M.W., … Betzig, E. (2014). Lattice light-sheet microscopy: Imaging molecules to embryos at high spatiotemporal resolution. *Science* **346**(6208). doi: https://doi.org/10.1126/science.1257998.

Chen, H.-W., Persson, S., Grebe, M. and McFarlane, H.E. (2018). Cellulose synthesis during cell plate assembly. *Physiologia Plantarum* **164**(1):17–26. doi: https://doi.org/10.1111/ppl.12703.

Colcombet, J. and Hirt, H. (2008). Arabidopsis MAPKs: a complex signalling network involved in multiple biological processes. *Biochemical Journal* **413**(2):217–226. doi: https://doi.org/10.1042/BJ20080625.

Cox, S., Rosten, E., Monypenny, J., Jovanovic-Talisman, T., Burnette, D.T., Lippincott-Schwartz, J., … Heintzmann, R. (2012). Bayesian localization microscopy reveals nanoscale podosome dynamics. *Nature Methods* **9**(2):195–200. doi: https://doi.org/10.1038/nmeth.1812.

Dertinger, T., Colyer, R., Iyer, G., Weiss, S. and Enderlein, J. (2009). Fast, background-free, 3D super-resolution optical fluctuation imaging (SOFI). *Proceedings of the National Academy of Sciences* **106**(52):22287–22292. doi: https://doi.org/10.1073/pnas.0907866106.

Deruere, J., Jackson, K., Garbers, C., Soll, D. and DeLong, A. (1999). The RCN1-encoded A subunit of protein phosphatase 2A increases phosphatase activity in vivo. *The Plant Journal* **20**(4):389–399. doi: https://doi.org/10.1046/j.1365-313x.1999.00607.x.

Dhonukshe, P. and Gadella, T.W.J. (2003). Alteration of Microtubule Dynamic Instability during Preprophase Band Formation Revealed by Yellow Fluorescent Protein–CLIP170 Microtubule Plus-End Labeling. *The Plant Cell* **15**(3):597–611. doi: https://doi.org/10.1105/tpc.008961.

Flanders, D.J., Rawlins, D.J., Shaw, P.J. and Lloyd, C.W. (1990). Nucleus-associated microtubules help determine the division plane of plant epidermal cells: avoidance of four-way junctions and the role of cell geometry. *Journal of Cell Biology* **110**(4):1111–1122. doi: https://doi.org/10.1083/jcb.110.4.1111.

Gaetano, J. (2013). Holm-Bonferroni Sequential Correction: An EXCEL Calculator.

Gaillard, J., Neumann, E., Van Damme, D., Stoppin-Mellet, V., Ebel, C., Barbier, E., … Vantard, M. (2008). Two microtubule-associated proteins of Arabidopsis MAP65s promote antiparallel microtubule bundling. *Molecular Biology of the Cell* **19**(10):4534–4544. doi: https://doi.org/10.1091/mbc.e08-04-0341.

Gustafsson, N., Culley, S., Ashdown, G., Owen, D.M., Pereira, P.M. and Henriques, R. (2016). Fast live-cell conventional fluorophore nanoscopy with ImageJ through super-resolution radial fluctuations. *Nature Communications* **7**(1):1–9. doi: https://doi.org/10.1038/ncomms12471.

Haralampidis, K., Milioni, D., Rigas, S. and Hatzopoulos, P. (2002). Combinatorial Interaction of Cis Elements Specifies the Expression of the Arabidopsis AtHsp90-1Gene. *Plant Physiology* **129**(3):1138–1149. doi: https://doi.org/10.1104/pp.004044.

Ho, C.-M.K., Lee, Y.-R.J., Kiyama, L.D., Dinesh-Kumar, S.P. and Liu, B. (2012). Arabidopsis Microtubule-Associated Protein MAP65-3 Cross-Links Antiparallel Microtubules toward Their Plus Ends in the Phragmoplast via Its Distinct C-Terminal Microtubule Binding Domain. *The Plant Cell* **24**(5):2071–2085. doi: https://doi.org/10.1105/tpc.111.092569.

Houbaert, A., Zhang, C., Tiwari, M., Wang, K., Serrano, A. de M., Savatin, D.V., … Russinova, E. (2018). POLAR-guided signalling complex assembly and localization drive asymmetric cell division. *Nature* **563**(7732):574–578. doi: https://doi.org/10.1038/s41586-018-0714-x.

Hubert, D.A., He, Y., McNulty, B.C., Tornero, P. and Dangl, J.L. (2009). Specific Arabidopsis HSP90.2 alleles recapitulate RAR1 cochaperone function in plant NB-LRR disease resistance protein regulation. *Proceedings of the National Academy of Sciences* **106**(24):9556–9563. doi: https://doi.org/10.1073/pnas.0904877106.

Huff, J. (2016). The Fast mode for ZEISS LSM 880 with Airyscan: high-speed confocal imaging with super-resolution and improved signal-to-noise ratio. *Nature Methods* **13**(11):i–ii. doi: https://doi.org/10.1038/nmeth.f.398.

Jeong, S., Eilbert, E., Bolbol, A. and Lukowitz, W. (2016). Going mainstream: How is the body axis of plants first initiated in the embryo? *Developmental Biology* **419**(1):78–84. doi: https://doi.org/10.1016/j.ydbio.2016.05.002.

Kim, T.-W., Michniewicz, M., Bergmann, D.C. and Wang, Z.-Y. (2012). Brassinosteroid regulates stomatal development by GSK3-mediated inhibition of a MAPK pathway. *Nature* **482**(7385):419–422. doi: https://doi.org/10.1038/nature10794.

Kohoutová, L., Kourová, H., Nagy, S.K., Volc, J., Halada, P., Mészáros, T., … Binarová, P. (2015). The Arabidopsis mitogen-activated protein kinase 6 is associated with γ-tubulin on microtubules, phosphorylates EB1c and maintains spindle orientation under nitrosative stress. *New Phytologist* **207**(4):1061–1074. doi: https://doi.org/10.1111/nph.13501.

Komis, G., Mistrik, M., Šamajová, O., Doskočilová, A., Ovečka, M., Illés, P., … Šamaj, J. (2014). Dynamics and Organization of Cortical Microtubules as Revealed by Superresolution Structured Illumination Microscopy. *Plant Physiology* **165**(1):129–148. doi: https://doi.org/10.1104/pp.114.238477.

Komis, G., Novák, D., Ovečka, M., Šamajová, O. and Šamaj, J. (2018b). Advances in Imaging Plant Cell Dynamics. *Plant Physiology* **176**(1):80–93. doi: https://doi.org/10.1104/pp.17.00962.

Komis, G., Šamajová, O., Ovečka, M. and Šamaj, J. (2018a). Cell and Developmental Biology of Plant Mitogen-Activated Protein Kinases. *Annual Review of Plant Biology* **69**(1):237–265. doi: https://doi.org/10.1146/annurev-arplant-042817-040314.

Kremer, A., Lippens, S., Bartunkova, S., Asselbergh, B., Blanpain, C., Fendrych, M., … Guérin, C.J. (2015). Developing 3D SEM in a broad biological context. *Journal of Microscopy* **259**(2):80–96. doi: https://doi.org/10.1111/jmi.12211.

Krishna, P. and Gloor, G. (2001). The Hsp90 family of proteins in Arabidopsis thaliana. *Cell Stress & Chaperones* **6**(3):238–246.

Krtková, J., Zimmermann, A., Schwarzerová, K. and Nick, P. (2012). Hsp90 binds microtubules and is involved in the reorganization of the microtubular network in angiosperms. *Journal of Plant Physiology* **169**(14):1329–1339. doi: https://doi.org/10.1016/j.jplph.2012.06.010.

Lampard, G.R., Lukowitz, W., Ellis, B.E. and Bergmann, D.C. (2009). Novel and Expanded Roles for MAPK Signaling in Arabidopsis Stomatal Cell Fate Revealed by Cell Type–Specific Manipulations. *The Plant Cell* **21**(11):3506–3517. doi: https://doi.org/10.1105/tpc.109.070110.

Li, H., Cai, Z., Wang, X., Li, M., Cui, Y., Cui, N., … Gou, X. (2019). SERK Receptor-like Kinases Control Division Patterns of Vascular Precursors and Ground Tissue Stem Cells during Embryo Development in Arabidopsis. *Molecular Plant* **12**(7):984–1002. doi: https://doi.org/10.1016/j.molp.2019.04.011.

Li, H., Sun, B., Sasabe, M., Deng, X., Machida, Y., Lin, H., … Liu, B. (2017). Arabidopsis MAP65-4 plays a role in phragmoplast microtubule organization and marks the cortical cell division site. *New Phytologist* **215**(1):187–201. doi: https://doi.org/10.1111/nph.14532.

Li, W., Xie, L., Chen, Z., Zhu, Y., Sun, Y., Miao, Y., … Han, X. (2010). Cantharidin, a potent and selective PP2A inhibitor, induces an oxidative stress-independent growth inhibition of pancreatic cancer cells through G2/M cell-cycle arrest and apoptosis. *Cancer Science* **101**(5):1226–1233. doi: https://doi.org/10.1111/j.1349-7006.2010.01523.x.

Liu, Y. and Zhang, S. (2004). Phosphorylation of 1-Aminocyclopropane-1-Carboxylic Acid Synthase by MPK6, a Stress-Responsive Mitogen-Activated Protein Kinase, Induces Ethylene Biosynthesis in Arabidopsis. *The Plant Cell* **16**(12):3386–3399. doi: https://doi.org/10.1105/tpc.104.026609.

Lucas, J.R., Courtney, S., Hassfurder, M., Dhingra, S., Bryant, A. and Shaw, S.L. (2011). Microtubule-Associated Proteins MAP65-1 and MAP65-2 Positively Regulate Axial Cell Growth in Etiolated Arabidopsis Hypocotyls. *The Plant Cell* **23**(5):1889–1903. doi: https://doi.org/10.1105/tpc.111.084970.

Lucas, J.R. and Shaw, S.L. (2012). MAP65-1 and MAP65-2 promote cell proliferation and axial growth in Arabidopsis roots. *The Plant Journal* **71**(3):454–463. doi: https://doi.org/10.1111/j.1365-313X.2012.05002.x.

Lukowitz, W., Roeder, A., Parmenter, D. and Somerville, C. (2004). A MAPKK Kinase Gene Regulates Extra-Embryonic Cell Fate in Arabidopsis. *Cell* **116**(1):109–119. doi: https://doi.org/10.1016/S0092-8674(03)01067-5.

Michniewicz, M., Zago, M.K., Abas, L., Weijers, D., Schweighofer, A., Meskiene, I., … Friml, J. (2007). Antagonistic Regulation of PIN Phosphorylation by PP2A and PINOID Directs Auxin Flux. *Cell* **130**(6):1044–1056. doi: https://doi.org/10.1016/j.cell.2007.07.033.

Müller, J., Beck, M., Mettbach, U., Komis, G., Hause, G., Menzel, D. and Šamaj, J. (2010). Arabidopsis MPK6 is involved in cell division plane control during early root development, and localizes to the pre-prophase band, phragmoplast, trans-Golgi network and plasma membrane. *The Plant Journal* **61**(2):234–248. doi: https://doi.org/10.1111/j.1365-313X.2009.04046.x.

Müller, S., Smertenko, A., Wagner, V., Heinrich, M., Hussey, P.J. and Hauser, M.-T. (2004). The Plant Microtubule-Associated Protein AtMAP65-3/PLE Is Essential for Cytokinetic Phragmoplast Function. *Current Biology* **14**(5):412–417. doi: https://doi.org/10.1016/j.cub.2004.02.032.

Murata, T. and Wada, M. (1991). Effects of centrifugation on preprophase-band formation in Adiantum protonemata. *Planta* **183**(3):391–398. doi: https://doi.org/10.1007/BF00197738.

Oh, S.A., Pal, M.D., Park, S.K., Johnson, J.A. and Twell, D. (2010). The tobacco MAP215/Dis1-family protein TMBP200 is required for the functional organization of microtubule arrays during male germline establishment. *Journal of Experimental Botany* **61**(4):969–981. doi: https://doi.org/10.1093/jxb/erp367.

Ovečka, M., Vaškebová, L., Komis, G., Luptovčiak, I., Smertenko, A. and Šamaj, J. (2015). Preparation of plants for developmental and cellular imaging by light-sheet microscopy. *Nature Protocols* **10**(8):1234–1247. doi: https://doi.org/10.1038/nprot.2015.081.

Park, S.K., Howden, R. and Twell, D. (1998). The Arabidopsis thaliana gametophytic mutation gemini pollen1 disrupts microspore polarity, division asymmetry and pollen cell fate. *Development* **125**(19):3789–3799.

Prasinos, C., Krampis, K., Samakovli, D. and Hatzopoulos, P. (2005). Tight regulation of expression of two Arabidopsis cytosolic Hsp90 genes during embryo development. *Journal of Experimental Botany* **56**(412):633–644. doi: https://doi.org/10.1093/jxb/eri035.

Queitsch, C., Sangster, T.A. and Lindquist, S. (2002). Hsp90 as a capacitor of phenotypic variation. *Nature* **417**(6889):618–624. doi: https://doi.org/10.1038/nature749.

Šamajová, O., Komis, G. and Šamaj, J. (2014). Immunofluorescent Localization of MAPKs and Colocalization with Microtubules in Arabidopsis Seedling Whole-Mount Probes. In: Komis, G. and Šamaj, J. (eds.). *Plant MAP Kinases: Methods and Protocols*. New York, NY: Springer, pp. 107–115.

Samakovli, D., Tichá, T., Vavrdová, T., Ovečka, M., Luptovčiak, I., Zapletalová, V., … Šamaj, J. (2020). YODA-HSP90 Module Regulates Phosphorylation-Dependent Inactivation of SPEECHLESS to Control Stomatal Development under Acute Heat Stress in Arabidopsis. *Molecular Plant* **13**(4):612–633. doi: https://doi.org/10.1016/j.molp.2020.01.001.

Samofalova, D.O., Karpov, P.A., Raevsky, A.V. and Blume, Y.B. (2019). Protein phosphatases potentially associated with regulation of microtubules, their spatial structure reconstruction and analysis. *Cell Biology International* **43**(9):1081–1090. doi: https://doi.org/10.1002/cbin.10810.

Sauer, M., Paciorek, T., Benková, E. and Friml, J. (2006). Immunocytochemical techniques for whole-mount in situ protein localization in plants. *Nature Protocols* **1**(1):98–103. doi: https://doi.org/10.1038/nprot.2006.15.

Schneider, C.A., Rasband, W.S. and Eliceiri, K.W. (2012). NIH Image to ImageJ: 25 years of image analysis. *Nature Methods* **9**(7):671–675. doi: https://doi.org/10.1038/nmeth.2089.

Shao, W. and Dong, J. (2016). Polarity in plant asymmetric cell division: Division orientation and cell fate differentiation. *Developmental Biology* **419**(1):121–131. doi: https://doi.org/10.1016/j.ydbio.2016.07.020.

Shaw, S.L., Kamyar, R. and Ehrhardt, D.W. (2003). Sustained Microtubule Treadmilling in Arabidopsis Cortical Arrays. *Science* **300**(5626):1715–1718. doi: https://doi.org/10.1126/science.1083529.

Smékalová, V., Luptovčiak, I., Komis, G., Šamajová, O., Ovečka, M., Doskočilová, A., … Šamaj, J. (2014). Involvement of YODA and mitogen activated protein kinase 6 in Arabidopsis post-embryogenic root development through auxin up-regulation and cell division plane orientation. *New Phytologist* **203**(4):1175–1193. doi: https://doi.org/10.1111/nph.12880.

Smertenko, A. (2018). Phragmoplast expansion: the four-stroke engine that powers plant cytokinesis. *Current Opinion in Plant Biology*. doi: https://doi.org/10.1016/j.pbi.2018.07.011.

Smertenko, A.P., Chang, H.-Y., Wagner, V., Kaloriti, D., Fenyk, S., Sonobe, S., … Hussey, P.J. (2004). The Arabidopsis Microtubule-Associated Protein AtMAP65-1: Molecular Analysis of Its Microtubule Bundling Activity. *The Plant Cell* **16**(8):2035–2047. doi: https://doi.org/10.1105/tpc.104.023937.

Smertenko, A.P., Cheng, Hsin-Yu, Sosobe, Seiji, Fenyk, Stepan I., Weingartner, M., Bögre, L. and Hussey, P.J. (2006). Control of the AtMAP65-1 interaction with microtubules through the cell cycle. *Journal of Cell Science* **119**(15):3227–3237. doi: https://doi.org/10.1242/jcs.03051.

Song, S.-K. and Clark, S.E. (2005). POL and related phosphatases are dosage-sensitive regulators of meristem and organ development in Arabidopsis. *Developmental Biology* **285**(1):272–284. doi: https://doi.org/10.1016/j.ydbio.2005.06.020.

Song, S.-K., Hofhuis, H., Lee, M.M. and Clark, S.E. (2008). Key Divisions in the Early Arabidopsis Embryo Require POL and PLL1 Phosphatases to Establish the Root Stem Cell Organizer and Vascular Axis. *Developmental Cell* **15**(1):98–109. doi: https://doi.org/10.1016/j.devcel.2008.05.008.

Spinner, L., Gadeyne, A., Belcram, K., Goussot, M., Moison, M., Duroc, Y., … Pastuglia, M. (2013). A protein phosphatase 2A complex spatially controls plant cell division. *Nature Communications* **4**(1):1–13. doi: https://doi.org/10.1038/ncomms2831.

Taipale, M., Jarosz, D.F. and Lindquist, S. (2010). HSP90 at the hub of protein homeostasis: emerging mechanistic insights. *Nature Reviews Molecular Cell Biology* **11**(7):515–528. doi: https://doi.org/10.1038/nrm2918.

Tamnanloo, F., Damen, H., Jangra, R. and Lee, J.S. (2018). MAP KINASE PHOSPHATASE1 Controls Cell Fate Transition during Stomatal Development. *Plant Physiology* **178**(1):247–257. doi: https://doi.org/10.1104/pp.18.00475.

Tanaka, H., Watanabe, M., Watanabe, D., Tanaka, T., Machida, C. and Machida, Y. (2002). ACR4, a Putative Receptor Kinase Gene of Arabidopsis thaliana, that is Expressed in the Outer Cell Layers of Embryos and Plants, is Involved in Proper Embryogenesis. *Plant and Cell Physiology* **43**(4):419–428. doi: https://doi.org/10.1093/pcp/pcf052.

Tichá, T., Samakovli, D., Kuchařová, A., Vavrdová, T. and Šamaj, J. (2020). Multifaceted roles of HEAT SHOCK PROTEIN 90 molecular chaperones in plant development. *Journal of Experimental Botany*. doi: https://doi.org/10.1093/jxb/eraa177.

Traas, J., Bellini, C., Nacry, P., Kronenberger, J., Bouchez, D. and Caboche, M. (1995). Normal differentiation patterns in plants lacking microtubular preprophase bands. *Nature* **375**(6533):676–677. doi: https://doi.org/10.1038/375676a0.

Truernit, E., Bauby, H., Dubreucq, B., Grandjean, O., Runions, J., Barthélémy, J. and Palauqui, J.-C. (2008). High-Resolution Whole-Mount Imaging of Three-Dimensional Tissue Organization and Gene Expression Enables the Study of Phloem Development and Structure in Arabidopsis. *The Plant Cell* **20**(6):1494–1503. doi: https://doi.org/10.1105/tpc.107.056069.

Ueda, M., Aichinger, E., Gong, W., Groot, E., Verstraeten, I., Vu, L.D., … Laux, T. (2017). Transcriptional integration of paternal and maternal factors in the *Arabidopsis* zygote. *Genes & Development* **31**(6):617–627. doi: https://doi.org/10.1101/gad.292409.116.

Umbrasaite, J., Schweighofer, A., Kazanaviciute, V., Magyar, Z., Ayatollahi, Z., Unterwurzacher, V., … Meskiene, I. (2010). MAPK Phosphatase AP2C3 Induces Ectopic Proliferation of Epidermal Cells Leading to Stomata Development in Arabidopsis. *PLoS ONE* **5**(12):e15357. doi: https://doi.org/10.1371/journal.pone.0015357.

Van Damme, D., van Poucke, K., Boutant, E., Ritzenthaler, C., Inzé, D. and Geelen, D. (2004). In Vivo Dynamics and Differential Microtubule-Binding Activities of MAP65 Proteins. *Plant Physiology* **136**(4):3956–3967. doi: https://doi.org/10.1104/pp.104.051623.

Vizcay-Barrena, G., Webb, S.E.D., Martin-Fernandez, M.L. and Wilson, Z.A. (2011). Subcellular and single-molecule imaging of plant fluorescent proteins using total internal reflection

fluorescence microscopy (TIRFM). *Journal of Experimental Botany* **62**(15):5419–5428. doi: https://doi.org/10.1093/jxb/err212.

Voss, M., Campbell, K., Saranzewa, N., Campbell, D.G., Hastie, J., Peggie, M., … Cohen, P. (2013). Protein phosphatase 4 is phosphorylated and inactivated by Cdk in response to spindle toxins and interacts with γ-tubulin. *Cell Cycle* **12**(17):2876–2887. doi: https://doi.org/10.4161/cc.25919.

Wang, B., Liu, G., Zhang, J., Li, Y., Yang, H. and Ren, D. (2018). The RAF-like mitogen-activated protein kinase kinase kinases RAF22 and RAF28 are required for the regulation of embryogenesis in Arabidopsis. *The Plant Journal* **96**(4):734–747. doi: https://doi.org/10.1111/tpj.14063.

Wang, H., Ngwenyama, N., Liu, Y., Walker, J.C. and Zhang, S. (2007). Stomatal Development and Patterning Are Regulated by Environmentally Responsive Mitogen-Activated Protein Kinases in Arabidopsis. *The Plant Cell* **19**(1):63–73. doi: https://doi.org/10.1105/tpc.106.048298.

Weis, F., Moullintraffort, L., Heichette, C., Chrétien, D. and Garnier, C. (2010). The 90-kDa Heat Shock Protein Hsp90 Protects Tubulin against Thermal Denaturation. *Journal of Biological Chemistry* **285**(13):9525–9534. doi: https://doi.org/10.1074/jbc.M109.096586.

Xu, Z.-S., Li, Z.-Y., Chen, Y., Chen, M., Li, L.-C. and Ma, Y.-Z. (2012). Heat Shock Protein 90 in Plants: Molecular Mechanisms and Roles in Stress Responses. *International Journal of Molecular Sciences* **13**(12):15706–15723. doi: https://doi.org/10.3390/ijms131215706.

Yoshida, S., Barbier de Reuille, P., Lane, B., Bassel, G.W., Prusinkiewicz, P., Smith, R.S. and Weijers, D. (2014). Genetic Control of Plant Development by Overriding a Geometric Division Rule. *Developmental Cell* **29**(1):75–87. doi: https://doi.org/10.1016/j.devcel.2014.02.002.

Yu, T.-Y., Shi, D.-Q., Jia, P.-F., Tang, J., Li, H.-J., Liu, J. and Yang, W.-C. (2016). The Arabidopsis Receptor Kinase ZAR1 Is Required for Zygote Asymmetric Division and Its Daughter Cell Fate. *PLoS Genetics* **12**(3). doi: https://doi.org/10.1371/journal.pgen.1005933.

Závorková, N. (2019). *Molekulární a funkční charakterizace embryonálního vývoje u dvojitých mutantů HSP90 a YODA*. Bachelor Thesis, Palacký University Olomouc.

Zhang, M., Wu, H., Su, J., Wang, H., Zhu, Q., Liu, Y., … Zhang, S. (2017). Maternal control of embryogenesis by MPK6 and its upstream MKK4/MKK5 in Arabidopsis. *The Plant Journal* **92**(6):1005–1019. doi: https://doi.org/10.1111/tpj.13737.

Zhang, Y. and Dong, J. (2018). Cell polarity: compassing cell division and differentiation in plants. *Current Opinion in Plant Biology* **45**:127–135. doi: https://doi.org/10.1016/j.pbi.2018.06.003.

Zhang, Y., Wang, P., Shao, W., Zhu, J.-K. and Dong, J. (2015). The BASL Polarity Protein Controls a MAPK Signaling Feedback Loop in Asymmetric Cell Division. *Developmental Cell* **33**(2):136–149. doi: https://doi.org/10.1016/j.devcel.2015.02.022.

List of publications

Vavrdová, T.[*], Křenek, P.[*], Ovečka, M., Šamajová, O., Floková, P., Illešová, P., Šnaurová, R., Šamaj, J., Komis, G. (2020). Complementary superresolution visualization of composite plant microtubule organization and dynamics. *Frontiers in Plant Sciences* **11**. doi: https://doi.org/10.3389/fpls.2020.00693.

Tichá, T., Samakovli, D., Kuchařová, A., Vavrdová, T., Šamaj, J. (2020). Multifaceted roles of HEAT SHOCK PROTEIN 90 molecular chaperones in plant development. *Journal of Experimental Botany*. doi: https://doi.org/10.1093/jxb/eraa177.

Samakovli, D., Tichá, T., Vavrdová, T., Ovečka, M., Luptovčiak, I., Zapletalová, V., Kuchařová, A., Křenek, P., Krasylenko, Y., Margaritopoulou, T., Roka, L., Milion, D., Komis, G., Hatzopoulos, P., Šamaj, J. (2020). YODA-HSP90 Module Regulates Phosphorylation-Dependent Inactivation of SPEECHLESS to Control Stomatal Development under Acute Heat Stress in Arabidopsis. *Molecular Plant* **13**(4):612–633. doi: https://doi.org/10.1016/j.molp.2020.01.001.

Vavrdová, T., Šamaj, J. and Komis, G. (2019). Phosphorylation of Plant Microtubule-Associated Proteins During Cell Division. *Frontiers of Plant Sciences*, **10**: 238. https://doi.org/10.3389/fpls.2019.00238.

Vavrdová, T., Šamajová, O., Křenek, P., Ovečka, M., Floková, P., Šnaurová, R., Šamaj, J. and Komis, G. (2019). Multicolour three dimensional structured illumination microscopy of immunolabeled plant microtubules and associated proteins. *Plant Methods* **15**(1): 22. doi: https://doi.org/10.1186/s13007-019-0406-z.

6 Abstrakt

Mitogenem aktivované proteinkinázy (MPK) se v rostlinných buňkách zapojují do řady signalizačních drah. Díky tomu propojují reakce na podněty z okolí s mezibuněčnou komunikací. Cílem této práce bylo prozkoumat funkce MPK ve stanovení roviny buněčného dělení. Práce byla zaměřena na signální dráhu skládající se z YODA a MPK3, MPK3, MPK6 kináz, i které je známé její zapojení do regulace asymetrických buněčných dělení během ranné embryogeneze a vývoje primárního kořene u modelové rostliny *Arabidopsis thaliana*. Předmětem zájmu bylo zhodnotit, zda je signalizace YODA-MPK3/6 kaskádou ovlivněna proteinovou fosfatázou 2A (PP2A) a proteiny teplotního šoku 90 (HSP90).

Funkce PP2A fosfatázy je spojena s kontrolou stanovení roviny buněčného dělení a předpokládá se, že tuto úlohu plní regulací fosforylace proteinů zapojených do relevantních procesů. Tato práce předkládá hypotézu, podle které PP2A koordinuje funkci YODA-MPK3/6 signální dráhy během stanovení roviny buněčného dělení.

Druhá část této práce je zaměřena na zdokumentování zapojení HSP90 do regulace ranné embryogeneze. I v tomto příkladě se předpokládá, že HSP90 by embryonální vývoj mohli ovlivňovat skrze interakci s YODA-MPK3/6 signální dráhou.

V této práci jsou též popsány a porovnány pokročilé mikroskopické techniky. Zvláštní důraz je věnován popisu možností jejich praktického využití pro mikroskopické pozorování živých buněk exprimujících chimerické fluorescenční proteiny, nebo fixních preparátů se strukturami značenými pomocí protilátek. Strukturní iluminační mikroskopie a laserová rastrovací konfokální mikroskopie využívající detektor typu Airyscan byly využity pro současné zobrazení mikrotubulů a dvou významných proteinů asociovaných s mikrotubuly, konkrétně protein asociovaný s mikrotubuly 65 2 (MAP65-2) a MAP65-3.

Výsledkem této práce je informování o roli YODA-MPK3/6 signální dráhy ve stanovení roviny buněčného dělení a v určení buněčného osudu, a dále o interakci této signální kaskády s PP2A and HSP90. Dále je předloženo porovnání pokročilých mikroskopických technik, které mohou být využity v budoucích studiích pro objasnění mechanismů organizace a dynamických změn cytoskeletu v rostlinných buňkách.